CONTROL OF PWM AC MOTOR-DRIVE SYSTEMS UNDER FAULTY CONDITIONS

by

Ahmed Mohamed Sayed Ahmed , B.S., M.S.

A Dissertation Submitted to the Faculty of the
Graduate School, Marquette University,
in Partial Fulfillment of the Requirements for the
Degree of Doctor of Philosophy

Milwaukee, Wisconsin
December 2009

ABSTRACT

CONTROL OF PWM AC MOTOR-DRIVE SYSTEMS UNDER FAULTY CONDITIONS

Ahmed Mohamed Sayed Ahmed

Marquette University, 2009

The main contribution of this dissertation is the conception and development of a new control strategy that allows Delta-connected induction motors to operate under a faulty two-phase open-Delta mode of operation with a resulting performance characterized by nearly balanced line currents and acceptable levels of torque pulsations in either the open-loop mode of operation, or the vector-controlled closed-loop mode of operation. The main aim and accomplishment of this control strategy is to maintain a quality of performance of a two-phase open-Delta mode of operation of a faulty motor as close as possible to the quality of performance of such a motor under normal healthy three-phase Delta-connection. Hence, one anticipates that such a procedure would be triggered after the process of isolating the faulty phase is accomplished successfully. Typical applications that can rely on the benefits of this newly introduced control strategy are in cases that involve open-coil faults that may occur due to internal winding rupture, loose internal connections, or in cases that involve an inter-turn short-circuit fault that has been diagnosed and successfully isolated in an incipient stage. This control topology does not require any hardware modification or even oversizing of the drive. However, oversizing of the motor may be necessarily if it is required to develop the motor's rated power under this faulty two-phase open-Delta mode of operation. Another advantage of

this newly conceived control strategy is that it can be enabled in the three-phase normal mode of operation as well as the two-phase open-Delta mode of operation with hardly any transient disturbance affecting the quality of the torque or the balanced line currents. Thus, this newly conceived control strategy enhances the “robustness” of the system. This is because this control strategy avoids transients that may occur during the transfer between a control algorithm that is provided to control the machine under a healthy operating condition, and another control algorithm that is provided to control the machine under a faulty operating condition “fault mitigation algorithm”. The newly conceived control strategy was thoroughly explained and successfully verified through numerous results obtained from several simulation runs and corresponding experimental tests in this dissertation.

PREFACE

CONTROL OF PWM AC MOTOR-DRIVE SYSTEMS UNDER FAULTY CONDITIONS

Ahmed Mohamed Sayed Ahmed

Under the supervision of Professor Nabeel A.O. Demerdash

Marquette University, 2009

AC induction motor-drive systems are considered to be the backbone for numerous industrial processes as well as many other critical applications such as aerospace, medical equipment, thermal and nuclear power generation plants. This is in addition to various marine and land transportation systems. The wide-spread use of such motor-drive systems is mainly due to their reliability, high efficiency, controllability, and high power density. However, the utilization of such systems in numerous critical applications mandate extremely high levels of reliability and survivability. These applications were the main incentive to trigger numerous investigations in the areas of early fault diagnostics and reconfigurable fault-tolerant designs of such systems, such that a fault can be detected in an incipient stage in order to safely shutdown the system and avoid catastrophic failures, as well as minimize such systems' repair costs and downtimes. The other alternative was to isolate the fault and provide a reconfigurable arrangement that enables continued operation of such a motor-drive system with a tolerable/acceptable, though partially impaired performance.

The main contribution of this dissertation is the conception and development of a new control strategy that allows Delta-connected induction motors to operate under a faulty two-phase open-Delta mode of operation with a resulting performance characterized by nearly balanced line currents and acceptable levels of torque pulsations in either the open-loop mode of operation, or the vector-controlled mode of operation. The main aim and accomplishment of this control strategy is to maintain a quality of performance of a two-phase open-Delta mode of operation of a faulty motor as close as possible to the quality of performance of such a motor under normal healthy three-phase Delta-connection. That is, one anticipates that such a procedure would be triggered after the process of isolating the faulty phase is accomplished successfully. Typical applications that can rely on the benefits of this newly introduced control strategy are in cases that involve open-coil faults that may occur due to internal winding rupture, loose internal connections, or in cases that involve an inter-turn short-circuit fault that has been diagnosed and successfully isolated in an incipient stage. This control topology does not require any hardware modification or even oversizing of the drive. However, oversizing of the motor may be necessarily if it is required to develop the motor's rated power under this faulty two-phase open-Delta mode of operation. Another advantage of this newly conceived control strategy is that it can be enabled in the three-phase normal mode of operation as well as the two-phase open-Delta mode of operation with hardly any transient disturbance affecting the quality of the torque or the balanced line currents. Thus, this newly conceived control strategy enhances the "robustness" of the system. This is because this control strategy avoids transients that may occur during the transfer between a control algorithm that is provided to control the machine under a healthy

operating condition, and another control algorithm that is provided to control the machine under a faulty operating condition “fault mitigation algorithm”. The newly conceived control strategy was thoroughly explained and verified through numerous results obtained from several simulation runs and corresponding experimental tests in this dissertation.

In addition to the previously mentioned contribution, two other distinct contributions in the areas of fault identification and fault diagnostics were conceived in this research. These contributions were developed and experimentally verified in this dissertation. The first contribution is centered on the development of a theoretical foundation for a new technique that is capable of identifying the faulty phase in polyphase ac machines and estimating the associated fault severity, when such machines encounter an inter-turn short-circuit fault in an incipient stage. This is achieved without any requirement for additional sensors, wiring constrains, or knowledge of any other details of the machine design for the case of machines with concentric wound stators beyond what is normally included in the nameplate data. However, detailed design of a machine may be required for the case of motors with lap wound stators. This technique was verified through several experimental test results. The second contribution is the conception, development and verification of a theoretical foundation for a new technique for diagnosing an inter-turn short-circuit fault in vector-controlled motor-drive systems that is not affected by a motor-drive system interaction, which tends to mask fault signatures in such systems. This technique was validated and verified through several results obtained from experimental tests.

To my parents, my wife and my daughter

ACKNOWLEDGEMENTS

Ahmed Mohamed Sayed Ahmed

Marquette University, 2009

Over the four and half years of my Ph.D. course work and research, I was very fortunate to enjoy the guidance, friendship, and support of many individuals who enriched my research and my life all over these years either through their supervision, suggestions, insightful comments and technical discussion.

Words cannot express my appreciation and gratefulness to my adviser professor Nabeel Demerdash. His in-depth knowledge of my research area, outstanding teaching skills, interactive technical discussions, patience, and strong command of technical writing are key elements and main reasons for the success of this work. I will never forget the weekends he spent with me reviewing and following up my research. In addition to his close supervision in my research area, he was generous enough to share with me his wide knowledge in other subjects such as history, science and arts. I will be always seeking his guidance and support.

I would like also to express my sincere appreciation to my committee members Prof. Michael Johnson, Prof. Fabien Josse, Prof. Edwin Yaz of Marquette University, Dr. Russel Kerkman of Rockwell Automation, and Dr.Thomas Nehl of Delphi Automotive Research, for the time they have dedicated to examine and review my work and also for their insightful comments and technical discussions. I enjoyed taking digital signal processing classes under Prof. Johnson, which were very important for my research work. Also, I do really appreciate the knowledge I have gained from the advanced mathematics class and the probability and stochastic class I took with Prof.Josse. I wish also to express

my gratitude and appreciation to Prof. Yaz for his technical help and support throughout these four and half years, our technical discussions along with the two seminars he taught me, had a significant effect on enhancing and improving the quality of my research. I am also very fortunate to have Dr. Kerkman as a member in my committee and an industrial adviser as well as a senior co-worker with a wide depth of experience at my current employer / department of Rockwell Automation. He has been always generous enough to discuss any technical question with me whenever I ask for help.

My managers' support and understanding at Rockwell Automation through this entire research was a key element without which the completion of this work would have been a very difficult task to achieve, especially the perpetual encouragement and endless support of Mr. Richard Lukaszewski, who was my direct manager during the period in which most of my research work was accomplished. I would like also to express my sincere appreciation to Mr. Ray Sladky and Mr. Kevin Baumann for their support and understanding throughout my research.

I consider myself very fortunate to work with a group of talented individuals. The insightful comments, practical experience, and technical hints of my co-workers Mr. Reese, Dr. Tallam, Mr. Seibel, Dr. Rowan, Dr. Skibinski, Mr. Brown, Dr. Wei and Mr. Leggate of Rockwell Automation were very helpful to my research.

In addition, I cannot forget to express my appreciation to my previous co-workers Mr. Buck, Mr.Bhadkamkar, Mr.Wallace, Dr. Bhavaraju, and Dr.Kikuchi of Eaton Innovation Center, in which I have spent a wonderful year as a power electronics intern. That year at Eaton was full of creation, inventions and hard work.

I am very grateful to my peers and colleagues at the Electrical Machines and Drives laboratory at Marquette University. The help and support of Dr. Mirafzal, Dr.

Yeh, and Mr.Sizov throughout my research were very important and had a significant beneficial impact on the quality of my research. I would like also to thank Ms. Anushree Kadaba, Ms.Peng Zhang, and Mr. Bojian Cao for their friendship, assistance and enjoyable discussions. I also enjoyed taking classes with my friend and colleague Steven Vitullo, I hope that our friendship lasts forever.

I wish also to acknowledge the financial support of the NSF grants ECS-0322974 and OISE-0609731. In addition, the support of Rockwell Automation, A.O Smith and Eaton Corporation in donating test motors, drives, and other electronic equipment, is greatly acknowledged. The experimental portion of this research would not have been possible without their support.

I would like also to thank and apologize to everyone I did not have a chance to mention his/her name here, and he/she has directly or indirectly helped and supported me throughout the work of this research.

Last but not least, I would like to express my sincere love and gratefulness to the closest people to my heart, my parents, my wife and my daughter. I would like to thank my parents for everything they have done for me and for encouraging my desire to learn as well as their perpetual support and blessing prayers. I would like also to thank my sole mate and life partner, my wife “Ghadeer”, her love and support enrich my life day by day. I would like to also thank and apologize to my daughter “Reem” for not sharing enough time with her over the last years and being tied up in my work and my research most of the time.

TABLE of CONTENTS

Chapter 3

Control of open-loop motor-drive systems under stator windings failure

Chapter 4

Control of vector-controlled motor-drive systems under stator windings failure

Chapter 5

The operation of a motor-drive system under a short-circuit fault

Chapter 6

Research summary, contributions, and recommendations for future work

LIST OF TABLES

LIST OF FIGURES

CHAPTER 1

1. INTRODUCTION

1.1 Historical review

There is no doubt that the invention of the ac induction motor by Nichola Tesla in 1888, [1], and the squirrel-cage induction motor by Dolivo-Dobrovolsky in 1889,[2], was a technological leap in industrial drive systems due to the robustness, ruggedness and the outstanding reliability of this kind of electrical machine compared to its alternatives such as dc motors which require frequent maintenance of their brushes and commutators. In addition, the existence of sparks as a result of the commutation action in dc machines limited their utilization in chemically volatile environments in which the existence of such sparks represents unacceptable hazardous conditions. Moreover, the ac induction motor is considerably less costly in dollars to power ratio in comparison to its counterparts. Since the advent of the ac induction motor, especially the squirrel-cage construction type, this machine has replaced its alternatives in numerous industrial applications. However, prior to the “power electronics” age, induction motors had several limitations compared to their dc counterparts, such as their limited speed and torque control. This is in addition to the limited starting torque of induction motors. These limitations made induction motors represent unattractive solutions as prime movers for some applications such as in automation industries that require precise speed and torque control, and traction applications that require very high starting torques and a wide range of speed control. The dawn of the “power electronics and ac drives” age started at the GE

research labs in 1957 where a six-step drive was introduced, [3]. This drive utilized Silicon Controlled Rectifiers "SCR" as the power devices. Later, the advancements and the enhancements in the characteristics of SCRs with reduced turn-on time and turn-off time improved the performance of SCR based six-step Current Source Inverters "CSI" in the 1970's, [3]. The requirement of commutation circuits, and the extensive harmonic content in the output current of these inverters, that introduces undesirable torque ripples and excessive heat losses in a motor, imposed significant limitations on their applications, [3]. Meanwhile, the invention of the Bipolar Junction Transistor (BJT) in 1950, [4, 5] which led to the invention of the power Bipolar Junction Transistor in 1960, [6], introduced another technological leap in drive systems. The relatively fast switching of the power (BJT) enabled the invention of the constant Voltage per Hertz (V/f) scalar controlled Voltage Source Inverter "VSI", [6] that can be matched to an ac induction motor to allow variable speed operation of such types of machines. Over the last decades, the advances in power devices that have relatively short turn-on and turn-off times, and reduced switching and conduction losses, enabled the invention of several PWM techniques such as Sinusoidal PWM "SPWM", harmonic elimination, etc, which consequently led to much improved inverter technology, [7]. Typically, with recent advances in modern power devices, the switching frequencies of these PWM techniques may vary depending on the applications from a few hundred Hertz to 20 kHz, [7]. These techniques have significantly reduced harmonic contents in motor current waveforms, and consequently minimized torque pulsations and thermal losses in such motors. In general, over the last decades, the performance of such type of motor-drive systems was found to be quite acceptable in a wide range of applications, [3]. The fact still remained

that dc motor-drive systems had superior torque controllability and performance, with quite simple control algorithms as compared to their counterpart ac induction motors. Because of the highly nonlinear dynamic characteristics of ac induction motors, in the presence of strong dynamic motor-controller system interaction, that requires much more complicated control algorithms, their acceptance in variable speed drives (VSDs)/ adjustable speed drives (ASDs) needed further technological developments in solid state power switches and associated control electronics.

The early work of Blaschke, [8], followed by the work of Hasse, [9], was the foundation of the so called "vector-control" in recent motor-drive systems. The vector-control concept is a computationally extensive technique that enables an ac induction motor-drive to replicate the superior performance of a dc motor-drive system. This is mainly achieved by decoupling the stator current's flux component, d-axis component, and the stator current's torque component, q-axis component, and control each of them independently of the other. Later, several enhancements to this technique were introduced by the pioneering work of several other investigators such as in references [11-20]. The main limitation of the vector-control technique at that stage was its high requirements of intensive real time computations vis-à-vis the computational power of available processing units.

Meanwhile, several enhancements have been introduced to improve the performance of the conventional open-loop control (constant Volts per Hertz) technique which is known for its simplicity and reduced computation requirements. The introduction of the so called "slip compensation" technique to the literature [21], and later to industrial VSDs such as in [22-24], was a significant improvement in the performance

of open-loop motor-drive systems. The slip compensation technique compensates for an induction motor's natural droop in speed with load.

The continued breakthroughs in digital electronics rendered available to investigators in the ac motor-drive area, as well as ASD manufactures modern digital processing units with high speed processing capabilities that are able to host and execute real time complex control algorithms. This was taken advantage of in numerous investigations, which were centered on enhancing the performance of motor-drive systems. This was achieved through the utilization of modern full-order adaptive state observers such as Extended Luenberger Observer "ELO" and Extended Kalman Filter "EKF" observer, both of which required extensive computational processing power [25,26]. Further research and development efforts were also directed towards applying modern Fuzzy Logic techniques in motor parameters estimation as well as motor control, [25, 26]. Other research efforts were centered on the utilization of modern artificial intelligence techniques and advanced machine learning algorithms, [25, 26], for motor parameters' estimation as well as motor control.

Enhancements in motor-drive technology were not only limited to advances in motor control algorithms but extended to other sides of market requirements such as reduction in a drive's size, weight and cost. In addition, the reliability of an ac motor-drive system has been significantly improved over the last few decades. Other features were also introduced in modern ac motor-drive systems such as dynamic braking, flux braking, dc braking, and reconnecting to spinning motor, [3]. Investigators and manufactures of ac motor-drive systems were also confronted by several technical challenges with the increasingly widespread use of this type of ac motor-drive systems in

numerous applications, [27-39]. These challenges included stator winding failures due to reflected wave phenomenon, [27-29], motor bearing failures due to bearing currents, [30-32], mechanical resonance that may occur due to nonlinear effects in the drives, [33], electromagnetic interference, [34-36], and power quality issues, [37-39]. Intensive research efforts, [27-39], enabled the ac motor-drive industry to overcome most of these hurdles or alleviate their effects.

Advances in modern ac motor-drive technology are a continuing process, especially with the fierce competition in the market place between numerous manufactures. Nowadays, researchers and manufactures are addressing other issues such as enhanced communication for automated processes, fail-safe mechanisms and fault-tolerant capabilities.

1.2 Definition of the problem

1.2.1 An overview

In spite of the fact that modern ac induction motor-drive systems already posses acceptable levels of reliability and robustness in typical industrial applications, the widespread use of ac induction motor-drive systems in critical applications require more intelligent systems with enhanced reliability and survivability. A standard engineering approach used to overcome the problem of reliability is accomplished by introducing the concept of redundancy such that for example, several identical motor-drive units (n) should be available to perform the same task. Usually, several (n-1) of them are kept in service while one of them is in a standby mode. This solution introduces a significant increase in cost, and is not efficient in applications which have severe space and weight

limitations/constrains such as offshore oil and gas platforms, naval crafts, submarines, aircraft and spacecraft. This represents a very strong incentive that triggered a large amount of research towards ac motor-drive system fault diagnostics and mitigation that can provide only one unit with enhanced reliability and survivability. Typically, in order to implement an intelligent ac induction motor-drive system with enhanced reliability and lesser vulnerability, the control scheme should preferably contain three algorithms. The first algorithm is running under normal operation in order to control the healthy system and provide optimum operation. Meanwhile, a second algorithm is a diagnostic algorithm, which should be hosted within the system's controller, and should be running continuously in order to detect any abnormal conditions or any imminent fault possibilities. It should be mentioned that this diagnostic algorithm should acquire an acceptable level of sensitivity to detect a fault in its incipient (early) stage and significant reliability against false alarms, such that it should not be triggered by any possible no-fault operating conditions such as current unbalances due to inherent asymmetry in the machine, sudden load variation or load fluctuation. A third algorithm should be available, such that once a fault condition is detected, it can trigger a proper fault isolation and mitigation action to enable continued sub-optimal system operation under this faulty condition, even if it is for a limited period of time. The power structure of the converter should be designed to accommodate system operation under this faulty condition, with attempts to find control strategies that minimize subsequent stresses resulting from such faulty conditions. The control algorithm should be also designed to diminish, if not eliminate, the effect of the fault and guarantee system operation with an acceptable performance. Any ac motor-drive system can fail due to either a fault in the power

converter itself with its associated power electronic components, control system or a fault in the motor itself. Faults in an ac motor can be either in its stator winding, squirrel-cage rotor, or in its bearings and the overall mechanical system. Meanwhile, a fault in a drive can either be a fault in the rectifier bridge, the dc-link capacitor or a power device, such as IGBTs normally used in the inverter bridge of the drive.

1.2.2 AC induction motor faults

Stator winding short-circuits are estimated to constitute about 36% of ac motor faults according to a survey carried out by EPRI in 1985 [40]. These faults can be either inter-turn short-circuit faults, open-coil faults, phase to phase short-circuit faults, or phase to ground faults, [41]. At that time in 1985, most of the motors surveyed were line-fed motors. More on-site short-circuit stator failures have been reported later in [42] as a result of the so-called reflected wave phenomena in PWM motor-drives with considerable length of cables between the power converter (drive) and its associated motor [27-29]. Kerkman and Skibniski showed that fast voltage rise rates associated with inverters in which new generations of fast-switching IGBTs are used, are the root cause of this problem, [27-29]. Traditional motor protection schemes, such as over current, over load and differential protection, have been employed in industry since the early times of use of motors throughout industry. However, most of these techniques fail to detect a fault in its incipient or early stage. It is worth mentioning that outstanding advancements in the field of switchgear and protection have also been achieved throughout the recent decades. Solid-state and microprocessor multifunction protection relays have replaced traditional electro-mechanical relays in numerous applications throughout the power and energy industry due to their reliability, robustness, speed and programming flexibility.

Still more sophisticated diagnostic algorithms are required in systems that mandate enhanced reliability and early detection of stator faults in their premature stages. Several interesting stator winding diagnostic techniques for inter-turn short-circuit faults have been introduced in the literature [43-62] under different control schemes. Some of these techniques require the addition of intrusive sensors such as described in [44] for axial flux detection, or the accessibility of a poly-phase motor winding's neutral point [51]. Other techniques require insertion of search coils [57, 58]. Meanwhile, some require only measuring the stator currents and carry out frequency-domain spectrum analysis of these currents [44-49]. Tallam et al. showed that measuring the negative sequence component in the motor currents can be a strong indication of inter-turn short-circuit winding faults [50, 52]. This technique was even extended for the case of closed-loop drives by measuring the negative sequence component in the measured voltage, [50, 52]. Mirafzal et al. introduced a new diagnostic technique based on detecting oscillations in the motor's magnetic field and relating such oscillations to fault conditions [54, 56]. The investigations presented in [59-62] were also concerned with open-coil stator faults. Heinzmann et al. introduced in [59] a generalized model-based approach for open-coil fault detection in a motor's stator winding. This technique is mainly based on monitoring the voltage, current and the speed of the motor. The amplitude of a motor's inrush current during starting was also used for detection of open-turn faults as reported in [61]. In [60], a model-based test platform has been implemented and introduced by Aguayo et al. for the detection of open-coil faults in induction motor-drive systems. The main concept of this technique is to compare actual current and voltage measurement with their counterparts estimated using a reference model.

Rotor broken-bar and end ring faults have been also reported in the aforementioned survey carried out by EPRI [40], and were reported to constitute about 9 % of motor faults. Broken-bar faults are mainly due to thermal and mechanical stresses especially due to frequent starting operations, aging effects and/or manufacturing defects. To the best of this author's knowledge, unlike stator winding faults, no reports or publications are yet in the literature regarding the vulnerability of induction motors with respect to broken bar faults when these motors are fed from fast switching variable speed drives. Most modern ac motor-drive systems existing in the market [63, 64] have soft staring capabilities that mitigate mechanical and thermal stresses during the starting transient. However, prolonged low speed operation under rated torque may cause thermal stresses especially for shaft-mounted totally-enclosed fan cooled motor designs [65]. Dynamic braking by dc current injection may also cause high rotor bar currents and subsequent thermal and mechanical stresses, [65]. Numerous broken-rotor-bar diagnostic techniques have been introduced in the literature [66-84]. Kliman et al. introduced in the literature an innovative technique to detect rotor-broken-bars using a so called "motor current signature analysis (MCSA)", [70]. This is achieved by detecting the side band components of the FFT spectrum of the motor current waveform around the fundamental frequency. This technique was further enhanced by Filippeto et al. using a means of artificial intelligence to strengthen system reliability and sensitivity of the diagnostic process [78]. Other techniques rely on vibration signal measurements and analysis [75]. Most of these products depend on the MCSA concept for fault detection coupled to artificial intelligence algorithms for enhanced reliability and sensitivity, [85].

Bearing-related faults appear to be the most common type of faults according to the survey given in the aforementioned EPRI report [40], in which these bearing failures constitute about 41% of motor faults. Improper maintenance, inadequate engineering design and external contamination are the most common reasons behind bearing premature failure, [86-87]. Bearing-failures have also been reported in ac motor-drive systems as a result of significant motor bearing currents that appear as a result of fast switching action of PWM drive systems. This phenomenon has been thoroughly discussed in several papers [30-32].

An assortment of other mechanical faults was also reported in the aforementioned EPRI report [40] and is estimated to constitute 9% of motor faults. These faults are related to external component failures, and the detailed nature of which is not specified in the survey.

1.2.3 Power converter "drive" faults

The main function of power converters "drives" in ac induction motor-drive systems is controlling motor terminal currents and voltages in order to achieve stable operating conditions, either manually selected by the user, or by an automated system in case of automated processes. In other words, the electrical energy fed to the motor is adequately processed and controlled by the power converter to guarantee stable operation at a preset speed and torque operating point. The main components of a conventional drive in ac motor-drive systems are a standard uncontrolled diode rectifier bridge or thyristor controlled rectifier bridge, which is responsible for converting the electrical ac voltage supplied by the electric utility line to a dc voltage, which is usually filtered and

smoothed by bulk dc link electrolytic capacitors at the so-called dc bus, which is then inverted again to an ac voltage with an appropriate selected frequency and voltage magnitude by an inverter bridge that consists of three legs, each leg consist of two IGBTs connected in series across the dc link, see the schematic of Fig.1.1. This power structure is the most common one already existing in numerous products. Failure in a drive can occur in any part. Several fault scenarios that may occur in a conventional drive with the previously mentioned power structure will be briefly discussed next, [89].

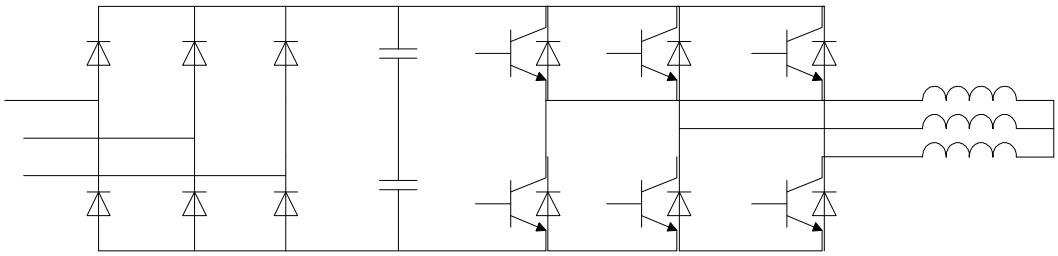

Fig.1.1 A standard power structure for the power converter

Single phase operation from the rectifier side can either occur due to failure in one of the diodes in the rectifier bridge, failure in the cable, or in the power fuse connecting the mains to the rectifier. This kind of fault introduces high voltage and current ripples across the dc link which may cause capacitor failure or undesirable current and torque harmonics, [89]. Proper de-rating of the drive should be considered in this case in order to avoid subsequent failures in other components.

The fact that dc link electrolytic capacitors constitute very critical components in such drives was a strong incentive for several researchers to investigate capacitor failure modes and capacitor life prediction [90-93]. Typically, there are three failure modes; wear-out, early-life and operating-life failures, [90-93]. Wear-out is the most common failure mode and it is due to loss of electrolytic dielectric strength or ESR “equivalent

series resistance" increase [93-95]. Other failures are due to aging effects, thermal stresses or high current ripples due to either improper design or due to the existence of other fault condition.

Power switch, IGBT, failures constitute the most significant category of failure modes of the power converter. These failures can be due to external fault, thermal stresses, voltage spikes or internal failure in the device itself, [96-99]. Failures of IGBT power switches in inverter bridges may lead to a single phase motor operation mode. Operating the motor in this faulty mode can cause significant damage to the motor as well as the drive. The interested reader should refer to [89] for further detailed discussion and analysis on several fault modes in power converters "drives".

1.2.4 Fault tolerant motor-drive systems

As mentioned before, early detection of incipient faults in ac motor-drive systems has outstanding advantages such as avoiding catastrophic system failures and avoiding unplanned shutdowns. Meanwhile, various applications in critical industrial functions mandate continuous operation of such systems till complete unit failure adopting "run to fail" concept. Such industrial functions include motor-drive systems for water feed pumps in nuclear plants and associated cooling tower functions, various motor-drive functions in naval vessels, ventilation systems in mines, aircraft critical electrical loads, or medical functions associated with equipment in operating or intensive-care rooms of hospitals which may have severe life threatening and other unacceptable consequences as well as many other examples in which sudden system failures are intolerable.

Therefore, several designs for fault tolerant motor-drive systems have been proposed in [100-127,130-131].

Early work in the area of fault-tolerant motor-drive systems traces back to 1978, [100] and 1980, [101]. In this work, Jahns introduced to the literature the concept of phase redundancy in fault-tolerant motor-drive systems. This technique is based on the fact that an n-phase motor is capable of continued operation with only "n-1" energized phases provided that the n-phase drive is capable of withstanding the stresses associated with "n-1" phase operation. The scope of this research was mainly directed towards semiconductor device failures.

Langley et al. introduced in [102] a motor with redundant winding sets and its associated power devices. Consequently, only the faulty winding can be isolated upon the detection of a faulty condition in this winding. The sets of the windings are physically placed apart from each other to minimize the magnetic coupling between these windings. This physical and magnetic separation distinguishes this design from other conventional designs in which two or more motor phase windings might occupy the same slot simultaneously such as in double layer winding designs. The advantage of this design is that it reduces the probability of fault propagation from one phase to another especially for inter-turn short-circuit faults.

Vaidya proposed in [103] a special stator winding arrangement with multi-dimension regions, in which each region has its separate set of windings and its associated power channels. Hence, the main objective of this work was to provide multiple motive power redundancy that cooperates with a rotor structure to produce a net electromagnetic torque summation. This enables the operation of the motor even in the

presence of failure in the winding or its associated energizing circuitry after electrically isolating the faulted circuit or faulted portion of the winding.

Oliveira introduced to the literature an innovative technique in [104] to enable balanced operation of three phase induction motors with Delta-connected stators with only one phase (single-phase) supply upon failure of one of the phases. The method is based on using a properly designed capacitor in parallel with one of the motor phases in order to minimize or eliminate the backward rotating MMF component in the airgap.

Enjeti et al. introduced in [105] a new technique to reject dc-link voltage ripples by modifying the modulating signal fed to the PWM generator. Existence of dc-link voltage ripples may be mainly due to supply unbalance, [106], single phase supply to the input rectifier bridge, [89], or dc-link capacitor failure [105]. These voltage ripples if not compensated through the modifications of the PWM algorithm, may propagate to the load side and cause highly undesirable sub-harmonics in the line currents, [107,108], and the output torque which in-turn may cause resonance in the mechanical system, [33].

In order to produce a perfect rotating field with a backward MMF component equal to zero, the currents in at least two of the motors' phases should be independent of each other, [109, 110]. This degree of freedom is not available in the single-phase mode of operation, with an isolated neutral as will be discussed in details in Chapter 3. Therefore, the topology suggested by Liu et al. in [109] and Elch-Heb et al. in [110] is to connect the neutral point of a motor to the midpoint of capacitors connected to the dc-voltage link as shown in Fig.1.2 for vector-controlled motor-drive systems. This provides the system with an additional degree of freedom and the currents of the two phases can be controlled independently to produce a perfect rotating field with a backward component

equal to zero. This requires a phase shift between the currents in these two phases that is equal to 60 elect. degree, [109,110]. This topology requires the neutral of the motor to be available which implies that the machine's stator should be Wye-connected with an accessible neutral point. In addition, proper sizing of the dc-link capacitors and a static (solid-state) switch is mandatory in order to connect the motor's neutral to the midpoint of the dc-voltage link. At this point, it should be highlighted that it is a common practice that Wye-connected stator windings with isolated neutrals are designed with an appropriate pitch factor to eliminate or alleviate the fifth and seventh order MMF space harmonics which may produce fifth and seventh order time harmonics that may cause undesirable torque ripples, [2,111]. Meanwhile, the third harmonic cannot circulate in the motor winding as the neutral current should be equal to zero for a case with an isolated neutral point. Therefore, the coil pitch is not designed to suppress the third order space harmonic component in airgap MMFs, [2, 111]. However, the configuration presented in [109,110] and depicted in Fig1.2 allows the existence of a third order time domain harmonic component in the motor line currents. This time domain harmonic component in the motor windings will produce a resultant third order space harmonic in the airgap flux density. The existence of this third order space harmonic in the airgap flux density waveform may cause undesirable torque ripples as will be detailed in Chapters 3 and 4.

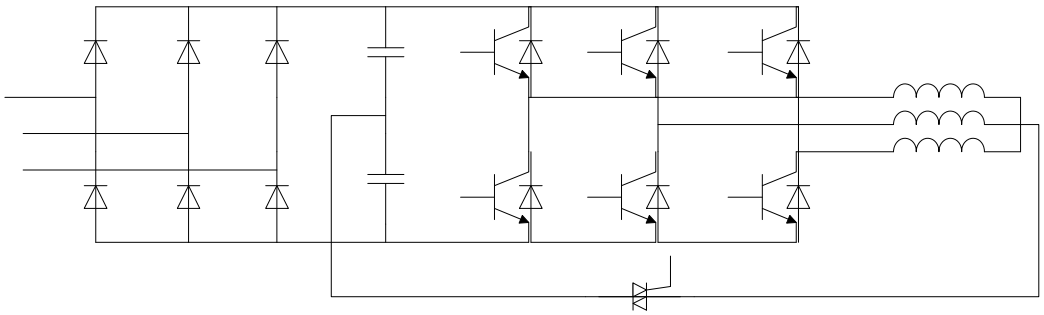

Fig.1.2 Power structure of the converter with the neutral of the motor connected to the midpoint of the dc-link, [109,110].

The concept of redundancy has been used for several decades to increase system reliability. This concept can be achieved either by using two separate motors with their associated control systems, or using only one machine with n-number of phases controlled by power converter with n-legs. In [112], Jen-Ren Fu et al. emphasized and extended the concept of phase redundancy previously introduced in [100, 101]. The basic principle of the proposed technique is that using five-phase and six-phase machines has an outstanding advantage over conventional three-phase machines for vector-controlled motor-drive systems. The multiphase configuration also can be used to provide the required degrees of freedom, if one of the machine's phases is completely isolated. The power structure for the ac motor-drive system with a 5-phase topology is shown in Fig.1.3. Again, this work was mainly directed towards vector-controlled motor-drive systems.

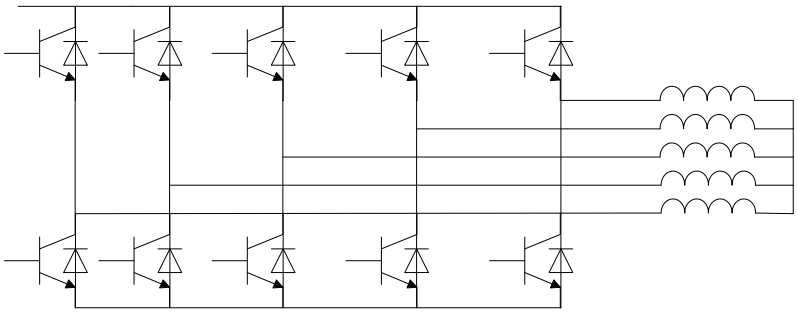

Fig.1.3 Multiphase ac motor-drive system topology,[112].

Kastha and Bose presented in [113] a new technique for open-loop motor-drive systems to improve the torque pulsations resulting from single phase operation by means of harmonic injection. This technique is based on the fact that the main target in open-loop scalar constant (V/f) control applications is to control the motor speed. In single-phase operation mode, the pulsating torque component is filtered out due to the inertia effect at high speed operation. However, at low speed, the low pulsating field torque frequency component will result in speed oscillations which can induce mechanical resonance. The main idea of the control algorithm in this technique is to inject odd harmonic voltages at the appropriate phase angle with respect to the fundamental voltage component. For instance, a third harmonic voltage will result in a positive sequence third harmonic current component. This third harmonic current component will result in a third order space harmonic in the airgap flux density waveform and the airgap MMF, this third harmonic component will interact with the fundamental component of the MMF to produce a second order harmonic component in the output torque. This second order harmonic component in the output torque can be controlled by controlling the phase shift of this third harmonic current component. This is in order to naturalize the second harmonic torque component produced due to the single phase mode of operation, [113]. However, a fourth harmonic torque component of equal magnitude will be produced. Therefore, the pulsating torque frequency can be shifted to a higher value in the spectrum that can be filtered by the inertia, even at low operating speeds. The authors of this technique [113], further suggested a search algorithm to determine the appropriate phase shift at which the voltage should be applied, [114]. It should be mentioned that this technique can only be used in applications where speed control is only considered. High

torque pulsations are produced at higher frequency, rather than the original produced pulsation torque at lower frequency, namely at double the line frequency. In addition, injecting a higher order harmonic current component to neutralize the pulsating torque may result in a considerable increase in the stator rms current, hence these authors suggested that an appropriate machine de-rating should be considered.

The so-called cascaded inverter topology is based on a special power structure for the power converter. In this configuration, each phase in the motor is independently controlled through a separate single phase inverter bridge, commonly known as an H-Bridge, as shown in Fig.1.4. This topology is suggested for fault tolerant vector-controlled induction motor-drive systems by Huggett et al. in [115]. Since each phase of the motor's stator windings is controlled independently by a separate H-bridge, this topology provides sufficient degrees of freedom to independently control the current of the remaining two phases of the machine. This topology may render a motor-drive system with high reliability against several fault scenarios such as switching device failure and winding failure. However, it can be noticed that this technique requires an inverter with twelve power switches, with their associated gate drive circuits and control algorithm rather than the six power switches of a conventional power converters.

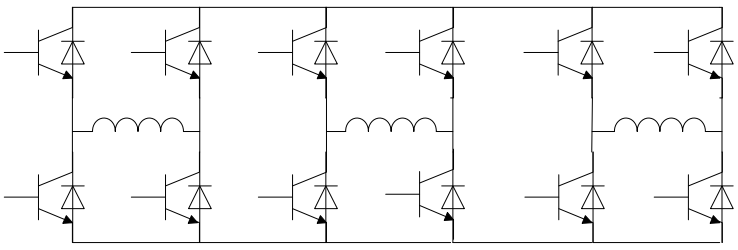

Fig.1.4 Cascaded inverter topology,[115].

The stator winding designs presented earlier by Langley in [102], and Vaidya in [103] utilized the distributed winding design which might increase the possibility of phase to phase short-circuit due to the overlap between winding end-turns. Hence, stator complete failure is still possible in this design especially for winding failures occurring due to short-circuit faults, [116] .To overcome this design limitation, Trago et al. proposed in [116] a special machine design that minimizes winding overlap and crossing with reinforced insulation between different phases overlapping or located in the same slot. This technique provides an effective means to prohibit spreading the fault from the faulty coil to other coils in the machine. Thus, enables the machine to operate even in the presence of a partial winding failure.

Haylock et al. presented in [117] a new fault-tolerant motor-drive system with respect to inter-turn short-circuit faults for permanent magnet machines. The main concept of the design is that the entire winding containing the fault must be shorted from its terminals upon detection of the fault. The strong mutual coupling between the turns in this winding ensures that the turns in this winding will share the same current which is limited by winding reactance that is 1p.u. in this design. It should be mentioned also that in this design each separate winding is controlled by a separate H-inverter bridge.

Seper et al. proposed in [118] a fault-tolerant motor-drive system in case of current sensors failure or encoder failure. The basic principle of this method is to provide a smooth transfer from a vector-controlled motor-drive operation to open-loop constant (V/f) control through proper reconfiguration of the control system that minimizes or eliminates transients during the transfer between the two modes.

Riberio et al. presented in [119] a new fault tolerant motor-drive system topology by providing a means of controlled connection of the motor winding to the dc-link mid point as depicted in Fig.1.5 This topology is mainly focused on faults in the converter such as switching device failure and/or misfiring. Upon detection of misfiring or switching device failure, the associated motor winding is connected to the dc link mid-point by means of a static switch as depicted in Fig.1.5

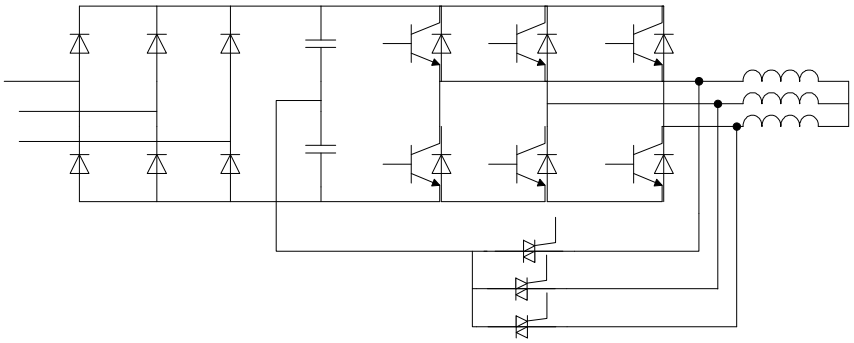

Fig.1.5 Fault tolerant topology for misfiring or switch failure, [119].

The work presented by Etrugrul in [120] is based on the concept of segment redundancy. The basic principle of this design is to use two separate motor-drive systems. However, the rotors of the motors are mechanically mounted on one shaft. This design provides fault-tolerant potential with respect to several types of faults either in the drive or in the motor. However, the size and the cost of this design may limit its practicality in many applications.

Stanley et al. presented in [121] a new electrical machine design mainly intended for high power synchronous machines. The main principle of the invention is to provide a nonmagnetic sleeve in the airgap between the rotor and the stator of the machine which is affixed to the stator. Therefore, one or more segments of high permeability material can be inserted to the slots with the shorted turns. Therefore, this segment will provide a low

reluctance path to the magnetic flux and hence minimize or eliminate flux coupling to the failed winding and consequently the faulty loop current in this winding.

The concept of fault-tolerance using cascaded inverter topology was introduced for permanent magnet motor-drive systems by Welchko et al. in [122]. This topology has been used by Welchko et al. in [122] to null/ reduce the flux linked to the faulty phase by controlling the zero sequence current in order to produce an effective zero current command in the faulted phase in permanent magnet machines.

A comprehensive survey was carried out by Welchko et al. in [123] to compare fault mitigation strategies presented in the literature. The comparison was mainly based on the consideration of the additional cost with respect to the relevant enhanced reliability of the system.

Gerada et al. showed in [124] that reduction of the machine flux level may enable extended period of operating the machine during the time in which there is an inter-turn short-circuit fault in one of its coils.

Schulz et al. proposed in [125] a fault-tolerant motor-drive system vis-à-vis current sensors failures when such sensors are used in an associated drive. These sensors are very critical for a large class of vector-controlled motor-drive systems. The method includes the utilization of state observers. This approach also includes a test method to detect current sensor failure. Upon detection of a current sensor failure, the readings of this sensor are ignored and the estimated values by the state observer are used instead.

In [126], Welchko et al. enhanced the technique previously presented in [122] to null or reduce magnet flux in order to improve the response to short-circuit faults for interior PM machines. This technique utilized the degree of freedom existing in the

cascaded inverter power topology, [115, 122], in order to produce a demagnetizing flux that neutralize the magnet flux in the faulty winding.

Instead of applying a special winding design for a fault tolerant motor-drive system, Youngkook et al. showed in [127] that reducing the machine flux significantly reduces the induced voltage and the circulating current in the shorted-turns without isolating the faulty winding. This helps to eliminate or reduce the propagation of the fault due to thermal stresses associated with it. This aspect can be utilized to minimize the faulty loop circulating current to an acceptable level. However, in this case, sever de-rating of the machine is mandatory. In addition, in spite of the fact that this technique might alleviate the effects of thermal stresses resulting from the short-circuit condition, keeping the failed winding connected to the supply without electrical isolation might lead to further propagation of the fault, and acceleration of the failure mechanism due to associated voltage stresses ,[128,129].

As an extension to the work proposed earlier by Fu in [112], Miranda et al. introduced in [130] a new control scheme that enables a six-phase motor-drive system to continue operation while one of the inverter switching devices has a short-circuit fault. The introduced control technique utilizes the inherent redundancy of voltage vectors in this type of motor-drive systems.

The concept of modular design was also presented by Su et al. in [131] for hybrid electrical vehicle applications. In this work, a modular design for axial gap permanent magnet machines as depicted in Fig.1.6, [131], in which each module was energized by a separate inverter bridge. This design provides increased reliability and enhanced fault-

tolerant capability. On the other hand, this configuration mandates increased system cost and size.

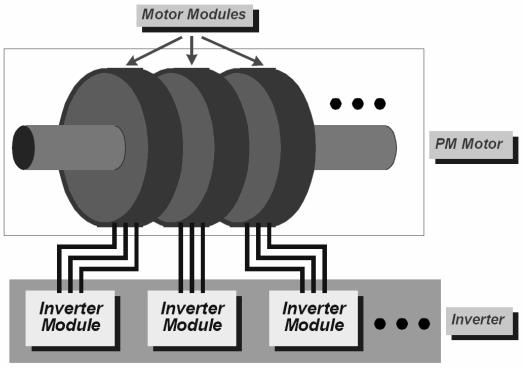

Fig.1.6 Modular PM fault-tolerant motor-drive system design, [131].

El-Rafie et al. examined in [132] the performance of several stator fractional slot concentric winding "FSCW" designs in induction machines compared to lap-type distributed winding designs using Time Stepping Finite Element "TSFE" analysis. The analysis included fractional slot concentric winding designs, non-overlapping end-turns (coils wound around teeth) for (2/5) slots/pole/phase and (1/2) slots/pole/phase. These stator winding designs that have non-overlapping end-turns are highly desirable in applications that require fault-tolerant capabilities, [116,117]. Other concentric winding designs were investigated as well in this work, [132].The advantages of a stator with a concentric-coil winding design/layout has been discussed in [117] for permanent magnet machines. The work presented in [132] using the same concepts of FSCW designs shows that design with (1/2) slot/ pole/phase is the most promising with respect to torque production. However, significant increase in the rotor losses has been observed compared to distributed winding designs.

The research introduced in [112] was further extended by Zhu et al. in [133] through developing a new fault tolerant strategy for DTC brushless ac motor-drive systems that enables a continued operation of such a motor-drive system in a case of open –circuit faults. The topology requires having an additional leg in the inverter and accessibility to the motor's neutral. Consequently, this topology obligates an increase in the size and the cost of such a motor-drive system.

A comprehensive review of the state of the art of fault-tolerant permanent magnet machines that can maintain comparable performance under faulty operating conditions was introduced by El-Rafie in [134].

1.3 Research objective

Diagnostic and robust control of ac motor-drive systems under faulty conditions is rather a sophisticated and widely ranging topic that can not be comprehensively covered in one dissertation, but rather a series of integrated research efforts. The discussion in the previous section has already demonstrated that numerous research efforts have been directed toward this general research area. Consequently, the work in this dissertation targets research topics that are still in their immature stage and require more investigative efforts. Stator inter-turn short-circuit faults in motors constitute one of the significant faults in ac motor-drive systems as reported in [40]. Although this topic was investigated in several previously published work, [42-62, 68-69], it is still considered to be an open research area with substantial gaps that need to be bridged. Therefore, this work is an attempt to bridge some of these gaps. Mainly, the research in this dissertation is centered on the detection and location of stator winding faults as well as providing a reliable

control algorithm to extend the useful period of operation of the motor upon the detection of the fault.

Knowledge of the specific faulty phase constitutes vital information to the design of the proper control strategy of the system. Thus, the faulty phase can be properly isolated in an early stage of the fault, and a proper control approach or strategy can be invoked to guarantee continued operation under this faulty condition. Another means of isolation of this type of faults can be provided by other protection means such as fast reacting fuses. Since continual fuse protection will only be activated at an advanced fault stage. Once the faulty winding has been isolated a proper fault mitigation strategy "robust control scheme" should be invoked to maintain acceptable system performance.

It can be noticed from the literature review conducted in the previous section that in spite of the fact that substantial research efforts were directed toward fault mitigation for motor-drive systems [100-132], most of these investigations were directed towards Wye-connected motors in vector-controlled closed-loop drives. In addition, from the literature review conducted in the previous section, to the best of this author's knowledge, only a few works addressed open-loop motor-drive systems in Wye-connected machines, [113, and 114]. Also, fault mitigation strategies focused on Delta-connected motors are almost absent from the literature. Therefore, the topology in this work is mainly directed to both vector-controlled closed-loop and open-loop motor-drive systems with Delta-connected stator windings. This topology utilizes the "open-Delta" configuration to control the current in each phase independently. A new control technique associated with this topology is also introduced in this dissertation. Mainly, this control technique is based on the theory of multiple reference frames previously applied to the

control of Uninterrupted Power Supply "UPS" units used in critical industrial applications, [136]. The new control technique presented in this dissertation is responsible for mitigating/alleviating any torque pulsations resulting from any asymmetrical conditions associated with this class of faults. This is accomplished by forcing the negative sequence component of the three line currents to zero. The implementation of this topology with its associated control scheme is analyzed and discussed in this dissertation for both open-loop ac induction motor-drive systems and for vector-controlled ac induction motor-drive systems.

The basic concepts of the new techniques and the control strategies presented in this dissertation are valid for induction machines, as well as permanent magnet machines which commonly share the same stator poly-phase winding design configurations/layouts. However, the analysis and the discussions contained in this dissertation have been experimentally verified only on an available case-study 5-hp induction motor.

1.4 Dissertation Organization

In addition to this chapter, this dissertation contains five other chapters. In the next chapter, Chapter 2.0, the mechanisms of winding insulation failures in VSD-fed induction motor are discussed. Naturally, these failure mechanisms should be well understood in order to establish a proper diagnostic and robust post-fault control strategies and/or algorithms. Two distinct contributions will be introduced in this chapter. First, a new technique is being introduced that can be utilized as a foundation for a rule-based artificial intelligent method to identify the faulty phase in a three-phase induction

motor when an inter-turn short-circuit occurs in one of its phases. This new technique is based on analyzing the disturbance in the internal magnetic field of this machine. The advantages and the limitations of this technique are also discussed. Simulation and experimental results are also included to establish and validate this approach. Second, a new technique to detect inter-turn short-circuit faults in closed-loop vector-controlled motor-drive systems is introduced. This technique is based on the motor's internal magnetic field pendulous oscillation concept introduced earlier in several previous publications [54, 56]. Hence, this second new technique extends the so called "swing angle" approach, [54, 56], for detecting inter-turn short-circuit faults in line-fed and inverter-fed open-loop induction motors to the cases involving vector-controlled closed-loop drives. The associated newly developed algorithms can potentially be coupled to advanced artificial intelligence based algorithms to form a robust on-line fault diagnostic and fault isolation approach. This aspect will be discussed further in Chapter 6 with regard to future extensions of the research subject of this dissertation.

In Chapter 3, a new technique is introduced to diminish torque oscillations associated with the two-phase open-Delta mode of operation of a three-phase induction motor that is after the detection of the failed phase winding and its isolation. This technique is mainly based on the theory of multiple-reference frames [135,136], in which the negative sequence component of the three-phase currents appears as a dc component in a clockwise synchronously rotating reference frame. In which case, the counter-clockwise rotating reference frame is associated with the positive sequence component of the motor's three-phase currents. Subsequently, this negative sequence component can, through the control algorithm, be driven to zero in this reference frame. The analysis

introduced in Chapter 3 is mainly focused on open-loop drives. Simulation work and experimental results are also included to support and validate the presented analysis.

In Chapter 4, the analysis presented in Chapter 3 is extended for the case of vector-controlled closed-loop motor-drive systems, and their associated control algorithm. Again, the presented analysis is supported by simulation and experimental verification.

In Chapter 5, inter-turn short-circuit faults are considered as a special case of stator winding failures. The performance of the system with this type of fault is thoroughly discussed. The effect of inter-turn short-circuit faults on the machine is analyzed using an in-depth Time Stepping Finite Element (TSFE) model of the three phase 5-hp, 6 poles, case study motor as well as the dynamics of the drive's controller. The prototype motor stator windings were connected in a Delta configuration.

In Chapter 6, the conclusions regarding the new contributions of this dissertation and possible future work are presented in detail.

CHAPTER 2

2. DIAGNOSTICS OF STATOR WINDINGS INTER-TURN SHORT-CIRCUIT FAULTS

2.1 Introduction

It was shown in Chapter 1 that stator winding faults are a major cause of motor premature failures. In addition to the financial loss associated with this kind of faults, such faults present significant hazardous conditions. Therefore, international testing standards, [137], and associated conventional mandatory protection systems, [41,137], were established to ensure motor-drive system reliability and productivity with regard to such types of faults.

Premature stator winding insulation failures are mainly due to thermal stresses, electrical stresses, mechanical stresses, or a combination of all of them, [138-145]. The effects of these stresses on predicted insulation life and insulation life modeling were studied in references [138-145], and they will be briefly summarized in the second section of this chapter for the sake of the reader's convenience. Prediction and/or early detection of an inter-turn short-circuit fault in a motor's stator phase windings can prevent severe financial loss, and prevent motor permanent damage. Moreover, such diagnostic methods/tools can be used to invoke a fault mitigation control strategy/ topology that may result in a prolonged system operation under such a faulty condition.

The significant increase in motor-drive systems in numerous critical applications necessitated the establishment of advanced diagnostic techniques in addition to the well established conventional protection means currently used in electrical facilities. The survey presented in Chapter 1 showed that in spite of the fact that intensive research efforts, [43-62], have been directed to provide industry with an advanced and reliable technology that enables early detection of inter-turn short-circuit faults, this research topic is still in its immature stages with substantial gaps that need to be bridged.

Therefore, in this chapter, two separate contributions are introduced to the literature in this research area, the first one, which is discussed in the third section of this chapter, is related to the identification of the faulty phase in a three-phase ac machine in which an inter-turn short-circuit fault does exist in one of its phases. The technique was validated using results obtained from several experimental tests. The advantages and the limitations of the introduced technique are also pointed out and discussed.

The second contribution in this research area that is discussed in the fourth section of this chapter is the introduction of a new inter-turn short-circuit fault diagnostic technique for vector-controlled closed-loop motor-drive systems. The introduced technique was validated using results obtained from several experimental tests.

From this author's vantage point, the fault detection algorithm introduced in this chapter, or any similar advanced stator winding fault detection algorithm, should not replace any other means of well known traditional protection schemes such as short-circuit, over-load, ground protection, differential protection, etc, particularly common to large-power rating, of motor-drive systems. In addition, the fault detection algorithm introduced in this chapter is not a substitute for, or reason to change any regular

maintenance schedules or any design criteria established in all accepted and well established practices based on international standards. Therefore, the main objective of this work is to provide a means to detect such types of faults in augmentation to the benefits that are relied upon through these traditional practices. Even if the lead time of the fault detection might be very short, this will enable the operation of a standby unit to avoid severe financial loss or a certain hazardous condition.

2.2 Stresses on insulation and failure mechanism

As mentioned earlier, the insulation of a line-fed motor's stator windings is subjected to several stresses that may accelerate the aging process and cause premature failure. These can be thermal, dielectric, mechanical stresses or a combination of all of them. Insulation of an-inverter fed motor's stator windings is further subjected to severe voltage stresses resulting from repetitive voltage pulses with a very fast rise time from an inverter applied voltage at motor terminals, [27-29,144-145]. The magnitude of these voltage pulses may be multiplied by a factor of three to four times of the dc bus voltage at the motor terminals due to the well known successive reflection phenomenon, [27-29,144-145]. The various above mentioned stresses and their corresponding adverse effects on insulation life are described below.

Mechanical Stresses:

Motor windings are subjected to several mechanical stresses that may cause excessive vibrations in motor windings and possible coil movement in the slots, [143,144]. In addition, excessive vibration may result in abrasion due to either turn-to-

turn movement or coil-to-coil movement, which consequently may cause insulation degradation and an inevitable premature failure, [144].

Thermal Stresses:

Thermal stresses are considered to be among the major causes of insulation premature failures and are usually caused by an increase in the winding/ core temperature or a failure in the cooling mechanism which results in elevated operating temperatures that adversely degrade winding insulation, [138-144]. In addition, physical and chemical breakdown/aging processes are highly accelerated due to these thermal stresses, [138-144].

Electric Stresses:

Electric stresses are caused by a significant increase in the voltage applied to a coil above its rated value. In line-fed motors, these electric stresses are mainly caused by manufacturing defects especially in a winding impregnation process, [129,143]. Presence of gas/air bubbles in the insulation causes non-uniform and concentrated electric field distributions and cause increased dielectric stresses around these gas bubbles. If the electric field exceeds a certain critical value an internal arcing may occur which is known as corona or gas discharge. Frequent arcing adversely damages the insulation and eventually leads to a complete breakdown. Line surges resulting from power grid transients and severe lightening may also result in insulation failure if proper surge protection was not followed, [138]. Introducing the third generation of fast-switching IGBT devices to the market that allowed increased switching frequencies with minimized turn-on / turn-off times in the range of hundreds of nanoseconds, resulted in improved system performance and significant reduction in the size of the ac drives, which initially

appeared to be an outstanding milestone in the technology of motor-drive systems. On the other hand, repetitive failures in inverter-fed motors, that utilized this recent technology, were reported in several industrial applications. Investigations in references [143-145] showed that extremely short voltage rise times impose severe stresses on a motor's phase windings while most of these voltage stresses are distributed non-uniformly and largely across the first few turns of a motor's phase windings causing Partial Discharge, PD, and consequently imminent insulation failure, [143-145]. These stresses can be further increased due to the well known successive reflection phenomenon that occurs when the inverter and the motor are connected through a long cable. In this case, the magnitudes of these voltage pulses at the motor terminals may increase to three or four times the magnitude of the dc bus voltages, [143-145].

Environmental stresses:

Corrosive chemical environment, moisture, and improper maintenance may also accelerate insulation failure mechanism and cause stator windings' premature failure if proper sizing and application guidelines are not followed.

Insulation failure mechanism:

Insulation failure mechanism depends on a combination of the previously mentioned stresses. It was shown in references [129,142-145] that an inter-turn insulation breakdown is due to a series of PDs which usually happens when the voltage stresses are not high enough to cause complete breakdown of the insulation. However, the internal electric field intensity in the insulation may exceed the dielectric strength of the insulation material at certain weak points "such as areas surrounding gas/air bubbles" and hence an internal breakdown process in the insulation will be initiated. The PD process

transfers the capacitively stored energy into heat and radiation. The resulting heat leads to elevated temperatures which significantly reduce the PD inception voltage and consequently increases the rate/ repetition of PD events and so on till complete failure of the insulation takes place. In addition, high rates of voltage rise versus time (dv/dt) during IGBT transistor switching increases the magnitude of capacitive/displacement-type dielectric currents which may cause additional heating, and consequently leading to acceleration of failure mechanisms. The experimental testing shown in reference [129] demonstrated that an increase in the temperature of an insulation class F specimen to 155° C has reduced the PD inception voltage, and breakdown voltage, by 15%. In addition, according to [129], temperature increase by 10°C results in reducing the expected life time of this specimen by 50 %.

Once a coil in a motor's stator phase windings encounters an inter-turn short-circuit, a very high circulating current will passe through the faulted-turns of this coil. It should be pointed out that this circulating current can not be detected by conventional protection technique such as overload protection, or differential current protection. This circulating current results in a significant increase in the thermal stresses which might lead to complete phase failure or rupture in the coil and consequently an open-coil fault, [142].

2.3 Analysis of stator winding inter-turn short-circuit faults in induction machines for identification of the faulty phase

Over the last decade, premature failures in stator windings of electrical machines have led to various investigations concerning the detection of commonly occurring stator winding shorts. Several interesting techniques have been introduced in the literature for purposes of diagnosing such types of faults at their early stages [43-62]. Moreover, intensive research has been centered on providing adequate fault mitigation strategies which can enable the motor-drive system to provide an acceptable performance [100-131] with an existing fault condition. Electric drive system reliability and minimized running cost are the major reasons for these investigations. Mainly, any fault mitigation topology does require three main pre-stages to be carried out effectively. This includes fault detection, fault identification, and fault isolation.

However, to the best of this authors' knowledge, most of these techniques do not offer the capability of identifying the specific faulty phase at an early stage of the fault unless the neutral point of a Wye-connected stator winding is accessible, or intrusive sensors are installed inside the machine, [44, 51]. In addition, these techniques lacked the capability of accurately estimating the extent of the fault severity based on the magnetic field unbalance produced in the machine as a result of this fault. In some of these investigations, additional sensors and/or knowledge of the details of a machine design were required [55]. This section tackles the previously mentioned problem based on a unique technique introduced here. This technique is based on a space-vector magnetic field analysis in case of a one-phase fault event occurring in a polyphase winding. The method utilizes the concept of magnetic field pendulous oscillation presented earlier in

references [54, 56] in order to identify the specific faulty phase and estimate the fault severity in that phase. Knowledge of the specific faulty phase and the severity of the fault are considered as vital information for purposes of devising a fault mitigation strategy. This novel technique at hand can be readily applied to identify the faulty phase without any required knowledge of the machine design or special wiring constrains for the case of concentric wound stators. However, for the case of lap wound stators, the faulty phase can be estimated provided that the stator winding layout is known.

In the next subsection, a space-vector analysis of the disturbance in a motor magnetic field due to an inter-turn short-circuit is analyzed and discussed. The result of this analysis will be utilized to extract a time domain correlation between the so-called magnetic field pendulous oscillation (MFPO), which was introduced in references [54, 56], and the applied motor phase voltage associated with the faulty phase. This analysis is extended in Subsection 2.3.2 to the use of the amplitude of the angle of the MFPO as an index for estimating the fault severity in a motor's winding. In Subsection 2.3.3, the theoretical development which is introduced in Subsection 2.3.1 is analyzed. This is carried out through the testing of a 2-hp, 460-volt, 60-Hz, 2-pole, concentric wound case study three-phase squirrel-cage induction motor. Meanwhile, in Subsection 2.3.4, the simulation results of a 5-hp, 460-volt, 60-Hz, 6-pole, lap wound case study three-phase squirrel-cage induction motor were introduced. In Subsection 2.3.5, the proposed technique is further verified using experimental results obtained for these case study motors.

2.3.1 Field space- vector analysis of an inter-turn short-circuit for identification of the faulty Phase

Consider an ideal case of a healthy three-phase induction motor with a balanced sinusoidal three-phase voltage applied at its terminals, and the sinusoidal three-phase currents passing through its windings. The voltage and the current space-vectors can be accordingly expressed as follows [25]:

$$\vec{v}_s(t) = V_s e^{j\omega t} \tag{2.1}$$

$$\vec{i}_s(t) = I_s e^{j(\omega t-\varphi)} \tag{2.2}$$

Consequently, under healthy conditions, the resultant forward rotating field, $\vec{f}_s$, in space-vector form can be written as follows [25]:

$$\vec{f}_s(t) = N_{se}\vec{i}_s(t) = N_{se}I_s e^{j(\omega t-\phi)} = F_s e^{j(\omega t-\phi)} \tag{2.3}$$

In the above equations, V_s and I_s are the peak values of the instantaneous voltage and current waveforms, respectively. Meanwhile, $\vec{v}_s$, $\vec{i}_s$, and $\vec{f}_s$ are the instantaneous space-vectors of the polyphase voltages, currents, as well as the resultant rotating stator MMF waveform in the airgap, respectively. Here, N_{se} , is the equivalent effective number of series stator turns per phase which include the winding factor effect, and ϕ is the power factor angle. In addition, F_s, is the amplitude of the stator MMF space-vector, where $F_s=N_{se}I_s$. It follows that when motor windings encounter an inter-turn short-circuit fault, see Fig.2.1, the previous formulations in (2.2) and (2.3) are no longer valid since the polyphase balanced currents condition would be violated. Hence, the faulty phase winding can be represented by a healthy winding and an additional shorted (faulty) one as

shown in Fig. 2.2, [54, 56]. The latter winding can be considered as a separate phase, the so-called shorted-coil, which is magnetically coupled to other phases/coils in the machine. Consequently, due to the flux linkage between the faulty coil and the other windings, a voltage will be induced in this shorted-coil. This induced voltage circulates a demagnetizing current through the closed-loop path, see Fig. 2.1, resulting from the fault [45]. The amplitude, I_f, of this instantaneous fault current, i_f, which is largely resistance limited depends on the fault resistance, R_f, which denotes the degraded resistance of the winding turn-to-turn insulation, and the induced voltage, v_{sc}, in the shorted-coil. This is particularly the case during the early stages of insulation deterioration when R_f has relatively high values. It should be observed here that this analysis and method are only intended for situations in which insulation degradation is happening over a relatively long time period at relatively slow rates of insulation breakdown. Consequently, i_f can be expressed as follows:

$$i_f = v_{sc} / R_f \tag{2.4}$$

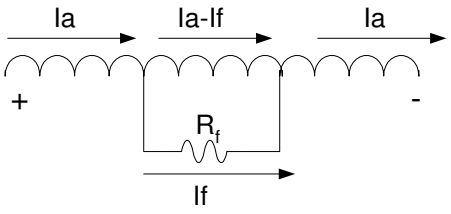

Fig. 2.1 Inter-turn short in a faulty phase "A" of a motor winding.

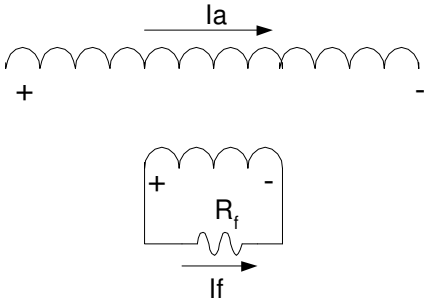

Fig. 2.2 The new resolved system.

Moreover, for frequencies below 10 kHz, the voltage gradient from winding turn-to-turn is constant and consequently the voltage is almost distributed uniformly across the turns of the phase winding [145]. In addition, for a winding factor approximately equal to one [147], the voltage in the shorted-turns can be expressed as follows:

$$v_{sc} = (N_{sc} / N_{ph}) v_{ph} = (N_{sc} / N_{ph}) V_m \cos(\omega t + \beta) \tag{2.5}$$

where, N_{sc} indicates the number of shorted-turns, N_{ph} is the effective number of series stator turns per phase, and v_{ph} is the voltage applied across the terminals of this faulty phase. This voltage is equal to the line voltage for the case of Delta-connected stator windings. Thus, it can be measured directly at the inverter output terminals after filtering high frequency components resulting from an inverter's switching action. On the other hand, this voltage is equal to the phase voltage for the case of Wye-connected stator windings, which can be calculated from the knowledge of the three line voltages applied to this motor as shown in [151], also after filtering high frequency components resulting from the inverter's switching action. Hence, the fundamental component of circulating current, i_f, in Fig. 2.1 can be expressed as follows:

$$v_{sc} = (V_m / R_f)(N_{sc} / N_{ph}) \cos(\omega t + \beta) \tag{2.6}$$

where, in general, β is the electrical space phase shift (in electrical radians) between the magnetic axis of the faulty coil and the original magnetic axis of phase-A. In a concentric-type winding distribution, see Fig.2.3a, β has a zero value, while in a lap-type winding distribution, see Fig.2.3b, β is not equal to zero and depends on the design of the phase winding layout. This induced voltage, v_{sc} , correspondingly depends on the number of shorted turns, N_{sc}, that belong to this shorted portion of the faulty phase winding in the machine. Hence, consider an inter-turn short-circuit which has been encountered in

phase-A in a concentric winding machine, the pulsating field waveform produced by the shorted-coil can be expressed in a forward and backward magnetic field space-vector form as follows:

$$\vec{f}_{sc} = \vec{f}_{scf} + \vec{f}_{scb} = \frac{1}{2} N_{sc} I_f [e^{j\omega t} + e^{-j\omega t}] = F_{sc} [e^{j\omega t} + e^{-j\omega t}] \tag{2.7}$$

where, $\vec{f}_{sc}$, is the space-vector representation of the magnetic field produced by the faulty loop, and F_{sc} is its amplitude. This magnetic field is equivalent to a pulsating field produced by a single-phase winding. Accordingly, from (2.3) and (2.7), the resultant MMF can be expressed in space-vector notation as follows:

$$\vec{f} = \vec{f}_s - \vec{f}_{sc} = e^{j\omega t} \{ N_{se} I_s e^{j(-\phi)} - \frac{1}{2} N_{sc} I_f - \frac{1}{2} N_{sc} I_f e^{-j(2\omega)} \} \tag{2.8}$$

Hence, from (2.8), the following can be rewritten with respect to a forward-rotating synchronous reference frame, see the ($e^{j\omega t}$) term in (2.8), as follows:

$$\vec{f} = \vec{f}_s - \vec{f}_{sc} = \vec{f}_s - \vec{f}_{scf} - \vec{f}_{scb} = \vec{f}_f - \vec{f}_{scb} = e^{j\omega t} \{ N_{se} I_s e^{j(-\phi)} - \frac{1}{2} N_{sc} I_f - \frac{1}{2} N_{sc} I_f e^{-j(2\omega)} \} \tag{2.9}$$

Notice here that the resultant forward component, $\vec{f}_f$, can be expressed as follows:

$$\vec{f}_f = \vec{f}_s - \vec{f}_{scf} \tag{2.10}$$

Also, equation (2.6) can be rewritten as follows for concentric wound machines:

$$v_{sc} = (V_m / R_f)(N_{sc} / N_{ph}) \cos(\omega t) \tag{2.11}$$

The first two terms in (2.9), namely, $\vec{f}_s$ and, $\vec{f}_{scf}$ are the forward field components produced by the original rotating field in a normal healthy machine and the forward field

component produced by the shorted-coil, respectively. The third term in (2.9), $\vec{f}_{scb}$, is the backward component produced by the shorted-coil.

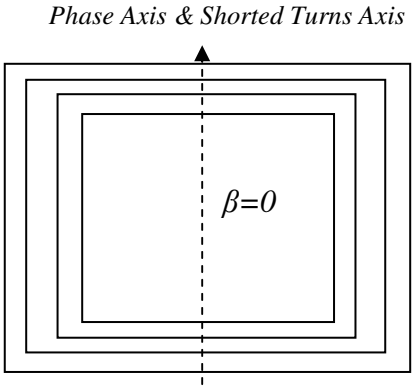

Fig. 2.3a Concentric winding distribution

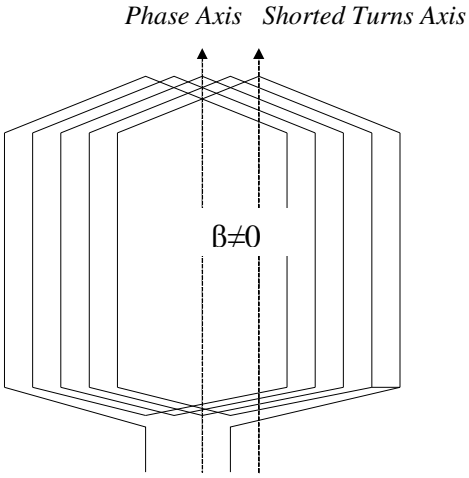

Fig.2.3b Lap winding distribution.

At this point, it should be noticed that (2.9) represents a formulation of the magnetic disturbance in the motor magnetic field as a result of an inter-turn short-circuit fault. Also, it can be noticed that in the aforementioned frame of reference, the forward rotating field appears as a stationary space-vector component and the backward rotating component appears as a space-vector rotating in the backward direction with a speed equal to twice the synchronous speed. Hence, the previously mentioned forward and backward magnetic field components can be depicted vectorially as shown in the space-vector diagram of Fig. 2.4. Here, Fig.2.4 demonstrates, at a given time instant, the relationship between the space-vectors of the resultant field, $\vec{f}$, given in (2.12), the forward field component, $\vec{f}_{scf}$, given in (2.10) above, and the backward field component, $\vec{f}_{scb}$, given in (2.7). Notice that this figure is drawn with respect to the same synchronously forward rotating reference frame used in (2.9).

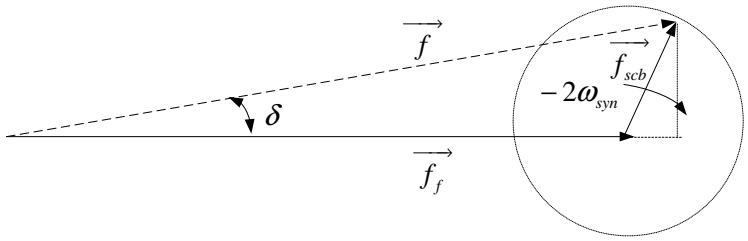

Fig.2.4 Fields space-vectors at a given time instant.

Again, Fig.2.4 shows a time domain correlation between the instantaneous MFPO angle, δ (the angle subtended between the resultant MMF and the forward MMF component), and the backward field component, $\vec{f}_{scb}$, in such a manner that the instantaneous value of δ is equal to zero at the same time instants ,δ , the angle of the space-vector , $\vec{f}_{scb}$, reaches a zero value (where δ = [(nπ)/(2ω)], and n=0,1,2,3,…etc). Meanwhile, the instantaneous value of the faulty loop current is equal to zero, see (2.11), at time instants, t (where t = [(nπ)/(2ω)], and n=1,3,5,…etc). Hence, it can be noticed that both the instantaneous values of the MFPO angle and the faulty loop current are zero at time instants t= [(nπ)/(2ω)], where n=1,3,5,..etc. However, it should be noticed that the MFPO angle is changing with a frequency equal to double the line frequency and the faulty loop current is changing with a frequency equal to the line frequency.

Naturally, in practical applications, it is almost impossible to measure the faulty loop current. The only available quantities are the motor terminal line voltages and currents. These line voltages are directly applied on the motor phase windings for the case of Delta-connected stator windings, and it can be easily measured at the inverter's output terminals after filtering out high frequency components resulting from the switching action. In addition, for Wye-connected stator windings, phase voltages can be directly measured if the neutral point is accessible, or it can be calculated from the line voltages, [151]. Hence, it is of paramount importance to closely examine (2.11) because it presents

the time domain relationship between the voltage applied across the faulty phase, and the faulty loop current for the case of concentric wound machines. Again, it should be emphasized that this voltage, the voltage in (2.11), is the phase voltage for Wye-connected stator windings, and the line voltage for Delta-connected stator windings.
It can be shown from (2.11) that for the case of concentrically wound stators, the faulty current is in phase with the voltage applied across the faulty phase. Thus, the zero-crossings of the MFPO angle, δ, are congruent with the zero-crossings of the faulty loop current and the phase voltage applied to the faulty motor winding at time instants t= [(nπ)/(2ω)], where n=1,3,5,..etc. The phase voltages can be readily measured from the motor terminals if the neutral is available or calculated from the line voltages provided that the supply is balanced, which is almost the case for all open-loop drives. However, for lap wound machines, the angle, β , see (2.6), depends on the location of the shorted-coil, the number of coils per phase and the distribution of the coils in the stator slots. Consequently, it is harder to detect the faulty phase in those types of machines unless the complete winding layout is known and one is able to take into considerations the fact that the most probable turns to fail in a phase are those located nearest to the terminals connected to the drive, [145]. This will be elaborated-on in details later.

2.3.2 Estimation of the fault severity as a function of the MFPO angle

Now, one proceeds to estimate the severity of a fault in stator windings. Here, (2.9) can be depicted by the space-vector diagram shown in Fig.2.5 at an instant at which the magnetic field pendulous oscillation (MFPO) angle, δ, is at its maximum value, δ_{max}. From basic trigonometric identities, upon examination of the right angled triangles (1-2-

4-1) and (2-3-4-2) shown in Fig.2.5, one can write the following relationship:

$$f_f^2 = (f_s - F_{sc}\cos\phi)^2 + F_{sc}^2 \sin^2\phi \tag{2.12}$$

where, F_{sc} , is the amplitude of both the backward and forward rotating field components produced by the shorted portion of the winding. Based on the space-vector diagram depicted in Fig.2.5, the magnetic disturbance in the motor field "fault severity factor" as a result of the fault can be defined in terms of the maximum value of the MFPO angle, δ_{max}. Hence, one can define the severity factor as the ratio between the amplitude of the shorted turns' MMF, $F_{sc,}$ to the amplitude of the healthy stator MMF. Hence, one can write the severity factor as follows based on the geometry of the space-vector diagram of Fig. 2.5.

$$severity \quad factor = \frac{F_{sc}}{F_s} = \frac{1}{\lambda} = \frac{1}{\cos\phi \pm \sqrt{\cos^2\phi + \cos ec^2\delta_{\max} - 1}} \tag{2.13}$$

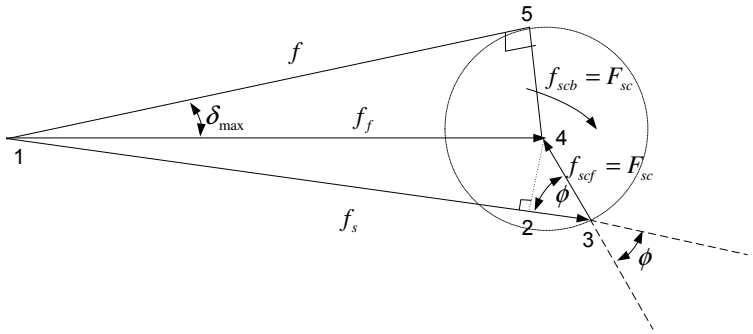

Fig.2.5 Space-vector representation at the instant of maximum MFPO angle, δ_{max} .

Here in (2.13) , $\lambda = \cos\phi \pm \sqrt{\cos^2\phi + \cos ec^2\delta_{\max} - 1}$, is the inverse of the severity factor. Again in (2.13), $F_{sc} = (N_{sc}I_f)/2$ and $F_s = N_{se}I_s$. Accordingly, (2.13) can be rewritten as follows:

$$\lambda^2 - 2\lambda\cos\phi + [1 - \cos ec^2(\delta_{\max})] = 0 \tag{2.14}$$

Notice that, λ is the inverse of the severity factor, where, $\lambda = \frac{F_s}{F_{sc}}$. A direct relationship between the disturbance in the magnetic field (the severity factor, $1/\lambda$ and the amplitude of the MFPO angle, δ, is implicitly given in (2.14).

2.3.3 Analysis of the case study concentric wound motor

Concentric wound machines may have 1, 2, 3, or more different coil spans, and they might have different numbers of turns per coil. Concentric wound machines are usually used for lower capacity motors of 100-hp or less in rated output, [2].The case-study motor to be analyzed in this section is the above-mentioned 2-hp, 460-volt, 60-Hz, 2-pole squirrel-cage three-phase induction motor, having 24 stator slots and 8 coils per phase with 216 turns in each phase. The cross section of this machine is depicted in Fig.2.6 and its winding layout is depicted according to the phase labeling of its two layers as outlined in Table 2.1.

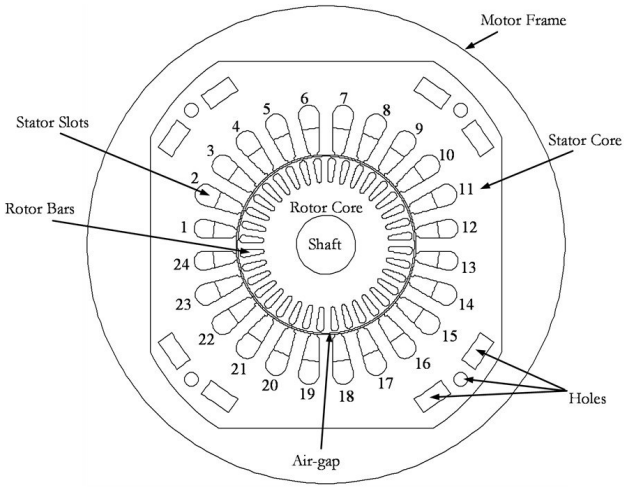

Fig.2.6 The 2-hp, 2-pole induction motor cross-sectional view.

In this case, the magnetic axis of each of the coils belonging to a specific phase coincides with the magnetic axis of this phase. Consequently, there is no phase shift between the magnetic axis of the faulty phase and the faulty coil in this winding design, that is $\beta=0$, as explained earlier in association with Fig.2.3a.

The aforementioned machine was modeled and simulated using the commercially available Time Stepping Finite Element (TSFE) software "MAGSOFT-Flux2D" package [146]. The model takes into account the nonlinearity effects of the B-H curve of the rotor and stator cores, as well as the intricacies pertaining to tooth/slot patterns and tooth tip saturation patterns in the stator and rotor magnetic circuit structures. A flux plot at a given instant of time for this machine is depicted in Fig.2.7 for a case of 5 shorted turns through a 0.8Ω resistor in one phase, where the inclusion of the resistor is to limit the short-circuit circulating current, i_f, to a safe level. Also, the corresponding resulting time domain relationship between the "scaled" phase voltage, the "scaled" fault current, and the angle in degrees of the MFPO , δ, obtained from this TSFE software are given in Fig. 2.8.

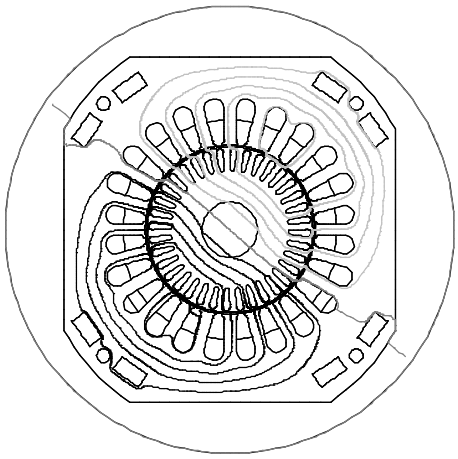

Fig.2.7 Flux plot for the 2-hp case-study motor.

1	2	3	4	5	6	7	8	9	10	11	12	13	14	15	16	17	18	19	20	21	22	23	24
A	A	A	A					A'	A'	A'	A'	A'	A'	A'	A'					A	A	A	A
B'	B'	B'	B'	B'	B'	B'	B'					B	B	B	B	B	B	B	B				
				C	C	C	C	C	C	C	C					C'	C'	C'	C'	C'	C'	C'	C'

Table 2.1 Winding layout for the 2-hp, concentric wound machine.

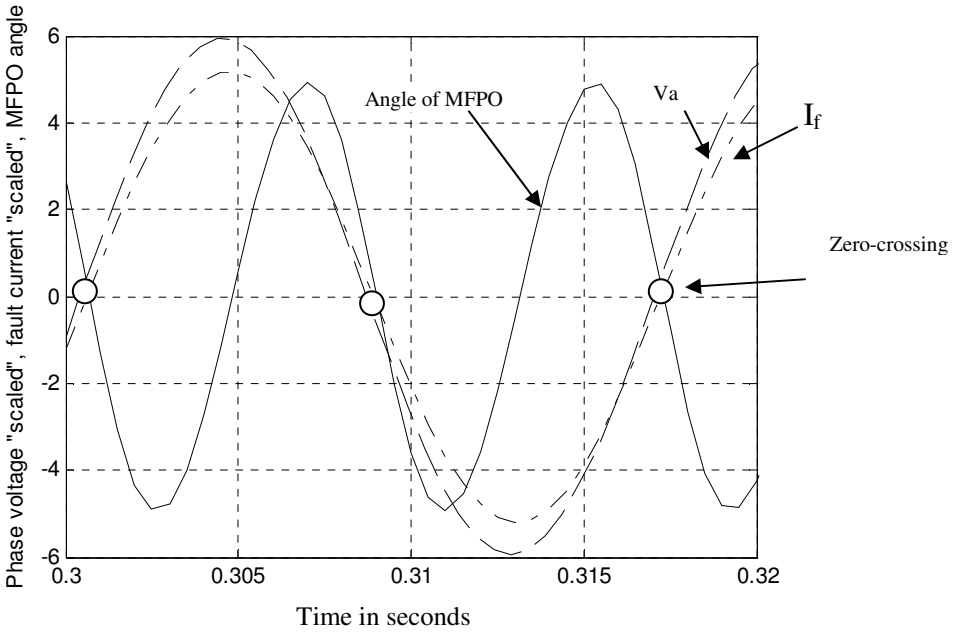

Fig.2.8 The time domain relationship between the "scaled" phase voltage, the "scaled" faulty current, and the angle in degrees of the MFPO from TSFE simulation (phase-A is the faulty phase).

Examining Fig.2.8 shows that the zero-crossings of the profile of the MFPO angles are very close (almost congruent) with the zero-crossings of the phase voltage of the faulty phase. Note that these zero-crossings are circled in this figure. It can be noticed that the angle of the MFPO is varying in time at double the line frequency. This confirms the validity of the theoretical analysis presented above and the corresponding mathematical derivation delineated earlier. At this point, it should be highlighted as mentioned earlier that, as argued in reference [124], the aforementioned assumption that the fault current is mainly limited by the resistance of the faulty loop is valid only for a fault in its early stages when the fault resistance is very high in ohmic value or in the case

when the motor is running at very low speed such that the resistance effect of the coil is dominant over its leakage inductance.

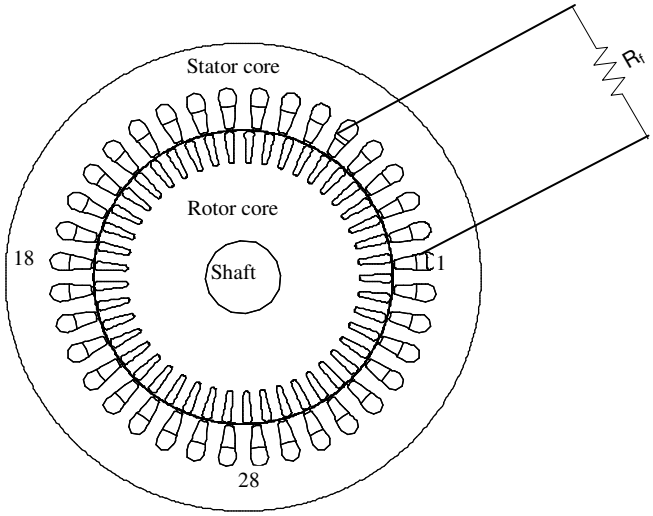

Fig.2.9 The 5-hp, 6-pole induction motor cross-sectional view.

Otherwise, when the current increases at lower fault resistance values, the leakage inductance of the faulty loop plays a dominant role and hence the current is resistance-inductance limited. This leakage inductance of this faulty loop introduces a phase shift between the phase voltage and the faulty loop current. It is worth mentioning that the simulation is carried out for the case in which phase-A is the faulty phase. Experimental tests were carried out to emulate faults in the three phases one at a time, and the results were confirming to the TSFE simulation of Fig.2.8, as will be shown later-on in this section.

2.3.4 Analysis of case study lap wound motor

In most of the lap wound machines, the coil span and the number of turns per coil are the same. In addition, the number of coils in this type of machines is equal to the number of stator slots for a double-layer winding distribution and half of the number of stator slots for a single-layer winding distribution. Higher horsepower motors are usually

lap wound [2]. The second case study is a lap wound 5-hp, 460-volt, 60Hz, 6-pole induction machine. This motor has a double-layer winding distributed in 36 stator slots (2 slots per pole per phase) and 45 rotor bars. The machine's stator winding is designed such that there is one coil group per pole per phase, each coil group consists of two separate coils, each coil has 20 turns with a total of 240 turns per phase, and each coil has a short-pitched span of 150 electrical degree leading to a total of 6 coil groups per phase. The machine's cross-section is depicted in Fig.2.9, and its corresponding winding layout is given in Table 2.2. In addition, a schematic for the winding layout for phase-A is depicted in Fig.2.10.

1	2	3	4	5	6	7	8	9	10	11	12
A11+*	A12+	C11-	C12-	B11+	B12+	A21-	A22-	C21+	C22+	B21-	B22-
A62+	C61-	C62-	B61+	B62+	A11-*	A12-	C11+	C12+	B11-	B12-	A21+

13	14	15	16	17	18	19	20	21	22	23	24
A31+	A32+	C31-	C32-	B31+	B32+	A41-	A42-	C41+	C42+	B41-	B42-
A22+	C21-	C22-	B21+	B22+	A31-	A32-	C31+	C32+	B31-	B32-	A21+
25	26	27	28	29	30	31	32	33	34	35	36
A51+	A52+	C51-	C52-	B51+	B52+	A61-	A62-	C61+	C62+	B61-	B62-
A42+	C41-	C42-	B41+	B42+	A51-	A52-	C51+	C52+	B51-	B52-	A61+

Table 2.2. Winding layout for the 5-hp LAP wound machine

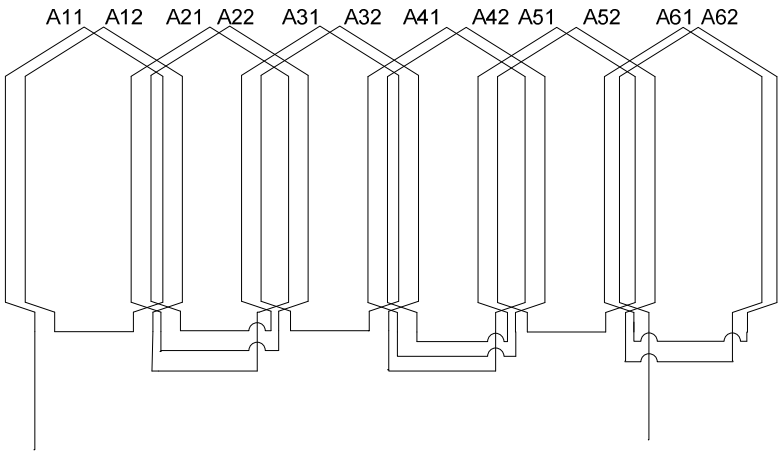

Fig.2.10 Winding layout for phase-A.

This design implies that the spatial space angles between the magnetic axes of each two adjacent coils per pole per phase in the machine are displaced by 30 electrical degree. This means that the overall magnetic axis of the phase is shifted from the individual magnetic axis of each coil in that phase. Hence, for this type of stator winding, the angle β depicted in Fig.2.3b is not equal to zero. This is unlike the case of concentric wound machines, see Fig.2.3a. Therefore, the MMF and the magnetic axis of each phase are obtained from the resultant vectorial summation of the MMF and the magnetic axis of each coil in this phase. Consequently, for this case, (2.1) to (2.5) can be rewritten with respect to the magnetic axis of the faulty coil as the reference axis as follows:

$$\vec{v}_s(t) = V_s e^{j(\omega t+\beta)} \tag{2.15}$$

$$\vec{i}_s(t) = I_s e^{j(\omega t+\beta-\varphi)} \tag{2.16}$$

$$\vec{f}_s(t) = N_{se}\vec{i}_s(t) = N_{se} I_s e^{j(\omega t+\beta-\phi)} = F_s e^{j(\omega t+\beta-\phi)} \tag{2.17}$$

$$v_{sc} = (N_{sc} / N_{ph}) v_{ph} = (N_{sc} / N_{ph}) V_m \cos(\omega t) \tag{2.18}$$

$$v_{sc} = (V_m / R_f)(N_{sc} / N_{ph}) \cos(\omega t) \tag{2.19}$$

Equations (2.7) to (2.11) are valid and do not need to be modified. However, the reader should notice that these equations are written with respect to the magnetic axis of the faulty phase (which coincides with the magnet axis of the faulty coil in concentric wound machines) , while the same equations are written with respect to the magnetic axis of the faulty coil in this section (which does not necessarily coincide with magnet axis of the faulty coil in lap wound machines). In this case, it will be realized from the winding layout and confirmed by the TSFE simulations that β=15 electrical degree for this machine. In order to obtain an insight into the electric and magnetic analysis for such a type of winding when an inter-turn stator winding fault occurs, this case study motor was modeled and simulated using the same commercial TSFE software package mentioned earlier "MAGSOFT-Flux2D". This software was used in this case study to obtain several key results which can not be obtained in the laboratory setup such as the voltage across each coil in the faulty phase of the machine, the airgap flux density distribution and fault-associated distortions, effects on local losses, etc. Here, Fig.2.11 shows the flux plot of this machine while Fig.2.12 shows the "scaled" phase voltage applied to the faulty phase, the phase current, the voltage across the coil A11, and the voltage across the coil A12 for the physically realizable test condition of an inter-turn short-circuit (6 turns were shorted through 1Ω resistor) in the stator winding of phase-A. This faulty condition resulted in 7 amps " r.m.s" circulating faulty loop current, while the rated current of this machine is 6.7 amps "r.m.s". It should be noticed that the fault detection and isolation system of the faulty phase should be activated as early as possible in order to avoid catastrophic failure of the motor. In order to understand the phase shift between the voltages in the coils A11 and A12, the winding layout in Table 2.2 should be carefully examined. Notice that the

motor was modeled such that the inter-turn short-circuit fault occurred in the coil A11, where again 6 turns were shorted through a 1Ω resistor. In Table 2.2, A11+ and A11- denote the phase-A coil number 1 group number 1 while, "+" denotes the positive conductor and "-" denotes the negative conductor of the coil.

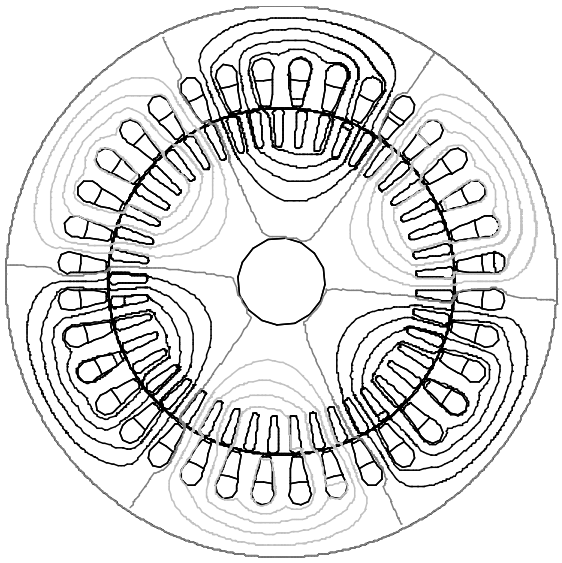

Fig.2.11 Flux plot for the 5-hp case study motor.

Now, let us consider an inter-turn fault in the coil A11, the faulty portion of the coil A11 can be considered as a separate coil A11F. Due to the flux linkage between that faulty coil "A11F" and the other coils in the machine, a circulating fault current will pass though this coil. It can be noticed that the voltages in the coils A11 and A12 are shifted from each other by a phase angle equal to 30 electrical degree and shifted from the phase voltage by a lead angle equal to 15 electrical degree for coil A11 and a lag angle for coil A12 also by 15 electrical degree. The voltage in each coil in the machine can be known from the stator winding layout, where the cross-section of the machine is depicted in Fig.2.9. It can also be noticed that the faulty loop current is in phase with the voltage across coil A11, which is in accordance with (2.18) and (2.19). In addition, as mentioned above in this case, the magnetic axis of each coil in one phase does not coincide with the

magnetic axis of phase-A. It can also be shown from the winding layout, see Fig.2.10, and the TSFE results that the induced voltages in coils A21, A31, A41, A51, and A61 are in phase with the voltage across coil A11, and the voltages in coils A22, A32, A42, A52, and A62 are in phase with the voltage across coil A12. The phase shift between the phase voltage applied to phase-A and the coils in this phase can be accordingly explained using Kirchhoff's law. In other words, the phase voltage applied to phase-A should be equal and opposite to the summation of the voltages across the coils in this phase. Hence, to satisfy this condition, the phase voltage applied on phase-A is lagging the voltage across the coils A11, A21, A31, A41, A51, and A61 by an angle 15 electrical degree and leading the voltage across the coils A12, A22, A32, A42, A52, and A62 by an angle 15 electrical degree as depicted in Fig.2.14. The same explanation can be applied to phase-B and phase-C. This means that the faulty loop current will be in phase with one of these six induced voltages depending on the faulty phase and the location of the faulty coil within the phase. The previous discussion can be confirmed through examining Fig 2.12 and Fig. 2.13, where the faulty loop current is in phase with the voltage across that faulty coil A11F which is shifted by 15 electrical degree leading from the phase-A voltage while the zero-crossings of the faulty loop current are congruent with the zero-crossings of the MFPO angle as shown in Fig.2.12 and Fig.2.13, which agrees with the analysis delineated earlier. Therefore, for lap wound machines which might have several coils overlapping with each other, identifying the faulty phase in a deterministic manner is not possible using this technique. At this stage, it should be pointed out that research studies and field investigations on motor-drive systems showed that the first few turns in the winding closest to the motor terminal are the ones which are most susceptible to

insulation failure in motor-drive systems,[27-29, 42,144-145], since most of the transient voltages resulting from the pulse-width modulation switching of the power modules of the drive are distributed across the first few turns nearest to the terminal of the motor. Hence, for this particular design in our case study, coils A11, B11 and C11 are the ones which are the most susceptible to fail in such motor-drive systems. Hence, for an inter-turn short-circuit fault in its early stage, and from (2.15) and (2.19), the faulty loop current and consequently the zero-crossings of the MFPO angle will be shifted from the phase voltage of that faulty phase by an angle, β=15 electrical degree (leading) in this 5-hp motor at hand. This was confirmed through the simulation results depicted above in Fig.2.12 where it can be noticed that the voltage across the coil A11 is leading the voltage across the coil A12 by an angle equal to 30 electrical degree , hence β = 15 electrical degree, see Fig. 2.14.

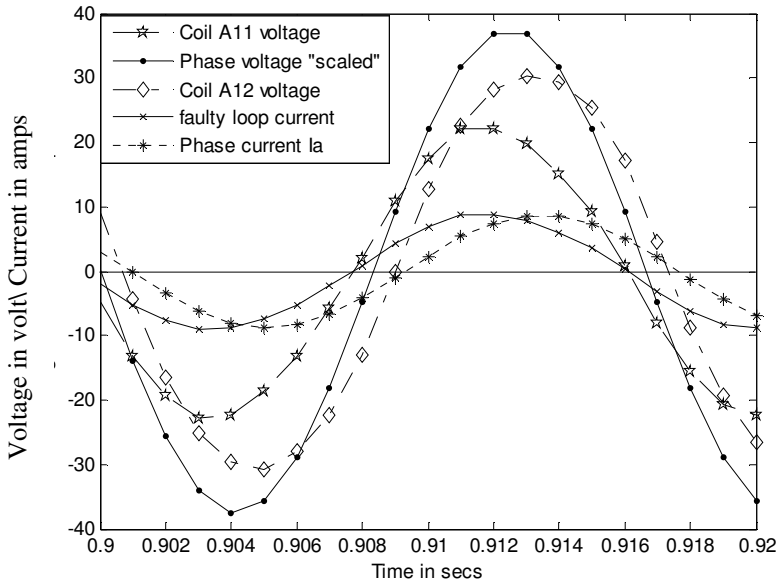

Fig. 2.12 "Scaled" phase voltage Van, phase current Ia, coil A11 voltage, and coil A12 voltage

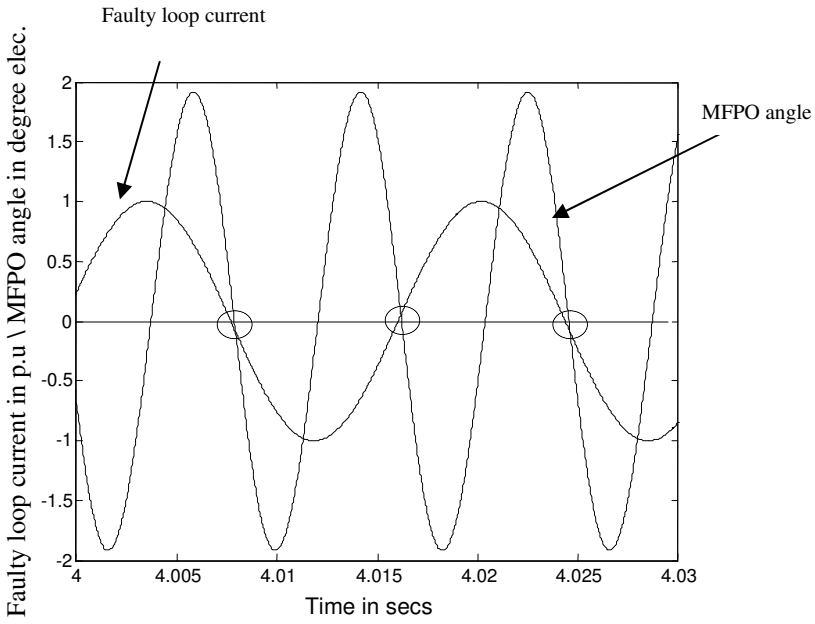

Fig.2.13 The faulty loop current in pu and the swing angle.

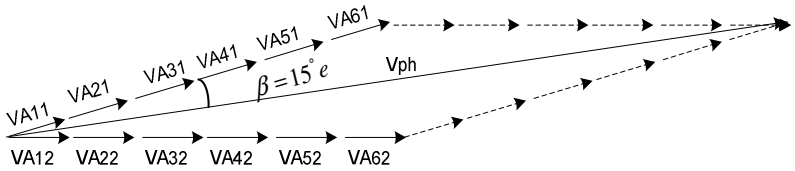

Fig.2.14 Vector diagram of the stator coils' induced voltages for phase-A and its corresponding phase voltage.

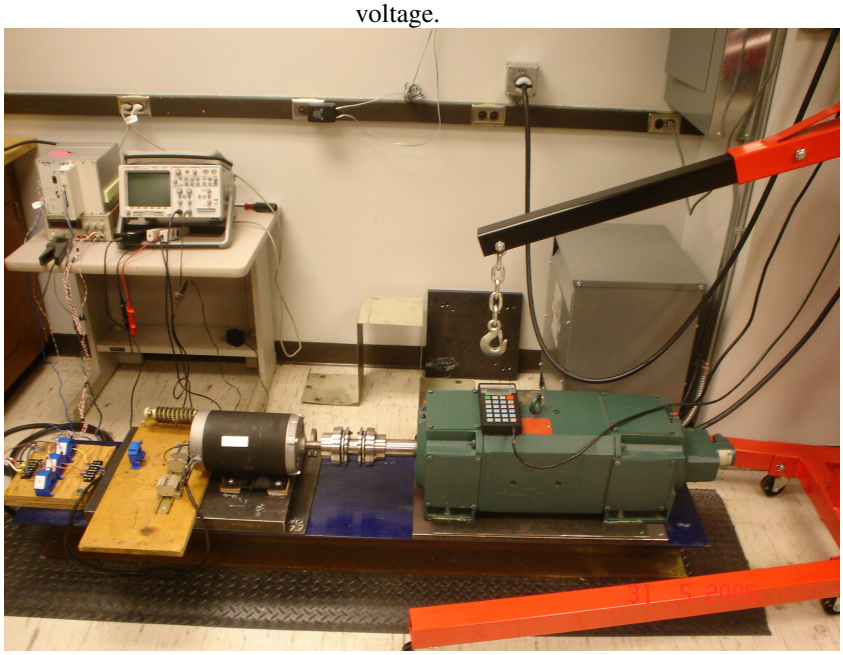

Fig.2.15 Experimental test set-up.

2.3.5 Experimental Results

In this section, the analysis and the discussion presented in the previous sections are verified through several experimental results. The aforementioned 2-hp and 5-hp motors used in these case studies described earlier were tested in the laboratory and the results are reported in this section for several faulty conditions. The taps are provided for only one phase in both motors, consequently in order to emulate a fault in different phases the motor terminal connections were mutated between the three outlet points of the 3-phase mains holding the same phase sequence. The experimental test set-up is shown in Fig.2.15 where the previously mentioned 2-hp, concentric wound motor was tested. The voltage and current waveforms were collected using a data acquisition system, with a sampling frequency of 50 kHz. The data has been collected and processed using a Matlab-Simulink program to calculate the instantaneous value of the MFPO angle from only measured line voltages and currents, a flow chart for the faulty phase identification algorithm subject of this study is depicted in Fig.2.16. Here, the reader should notice that the faulty phase identification algorithm introduced in this section should only be invoked in case of an inter-turn short-circuit fault detection algorithm, such as the ones presented in [43-62], has confirmed the existence of an inter-turn short-circuit fault in a motor stator winding.

The time-domain relationships between the angle of MFPO, the faulty loop current, and the phase voltage which corresponds to the faulty phase are shown in Figs.2.17 through 2.19 for a fault in phase-A, a fault in phase-B, and a fault in phase-C, respectively for this case study machine. Recall that this motor is of the concentric wound stator type as described earlier.

Obviously, for practical implementation of such types of fault detection systems, the fault current can not be measured or monitored. Only motor phase voltages and currents can be measured and the angle of the MFPO angle can be computed from sampling the motor's terminal voltages and currents, and extracting the fundamental components of these voltages and currents. Again, the phase voltage can either be directly measured if the neutral is accessible or it can be calculated from the line-to-line voltages under balanced conditions. It can be noticed that the zero-crossings of the faulty loop current, the zero-crossings of the phase voltage applied to that faulty phase and the zero-crossings of the MFPO angle are congruent with each other. This verifies the soundness of the theoretical idea and analysis delineated previously in this study, about the specific identification of the faulty phase in concentric wound machines.

In addition to this 2-hp concentric wound induction motor, the 5-hp lap wound induction motor described in Subsection 2.3.5 was also tested. It was mentioned before in Section V that in practical applications the first few turns closest to the supply side are the most prone to insulation failure in a coil. In this case, this applies to the coil A11 for this specific motor, see Table 2.2, Fig.2.9, and Fig.2.10. However, for this motor, the second coil A12 was wound with provision of external tapes for emulation of the winding inter-turn shorts. Hence, for this case, the voltage across that coil is lagging the phase voltage applied to that faulty phase by 15 electrical degree as discussed earlier regarding the winding layout and the accompanying TSFE analysis of Section V. Consequently, the main target of this test was to verify that the zero-crossings of a voltage waveform lagging the phase voltage by 15 electrical degree (that is the zero-crossings of the voltage across the faulty coil) are congruent with the zero-crossings of the MFPO angle of the

machine under fault. This verifies the concept and the analysis explained in Subsection 2.3.4. The time domain correlation between a waveform lagging the phase voltage by 15 electrical degree , see the TSFE simulation results of Fig.2.12, the MFPO angle, and the faulty loop current are shown in Figs.2.20 through 2.22. It can be noticed that the zero-crossings of this voltage are congruent with the zero-crossings of the MFPO angle. Hence, from the above experimental results, this verifies the idea of the zero-crossing congruencies as a means of recognizing the faulty phase in the 2-hp and 5-hp case study motors at hand.

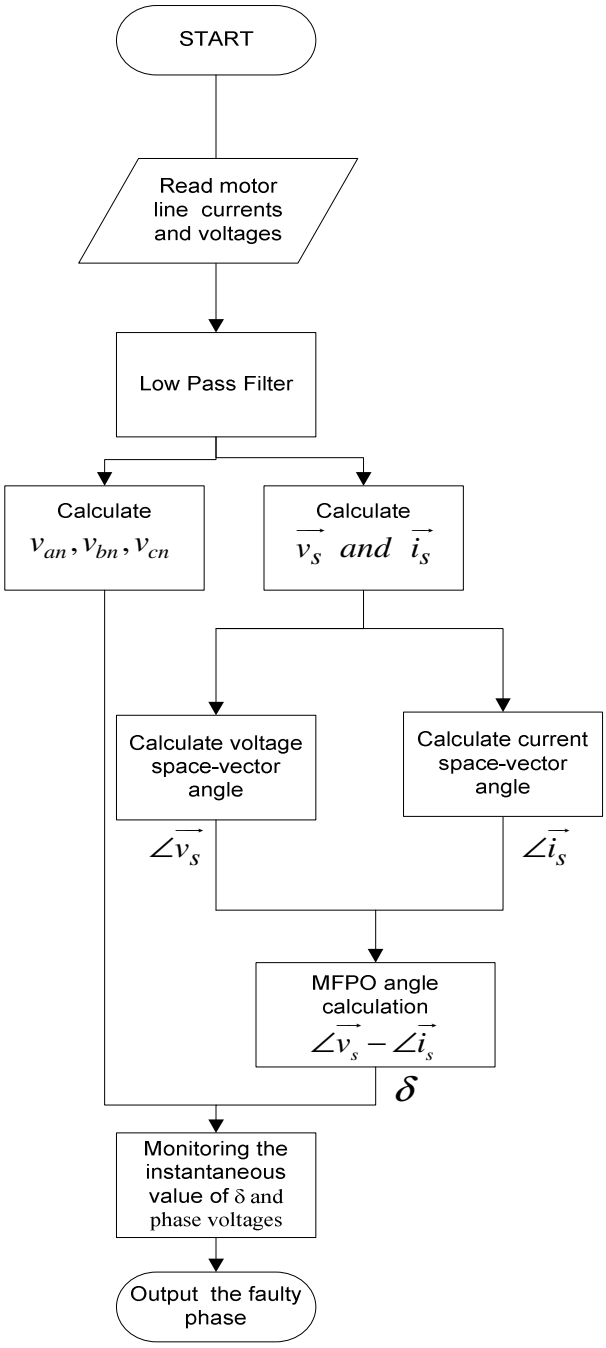

Fig. 2.16 A simplified flow chart for the algorithm used to identify the faulty phase.

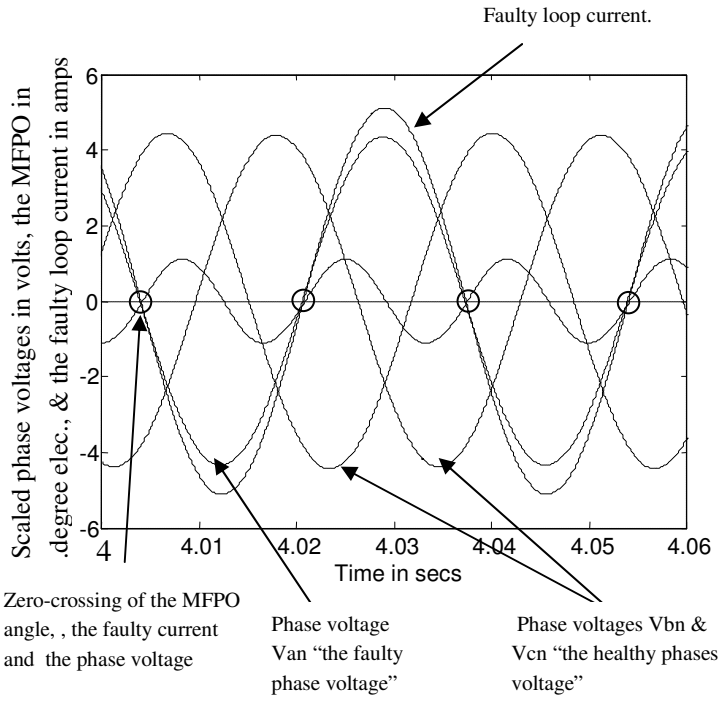

Fig.2.17 The time domain relationship between the phase voltages, the faulty current and the angle of the MFPO for the 2-hp motor (phase-A is the faulty phase).

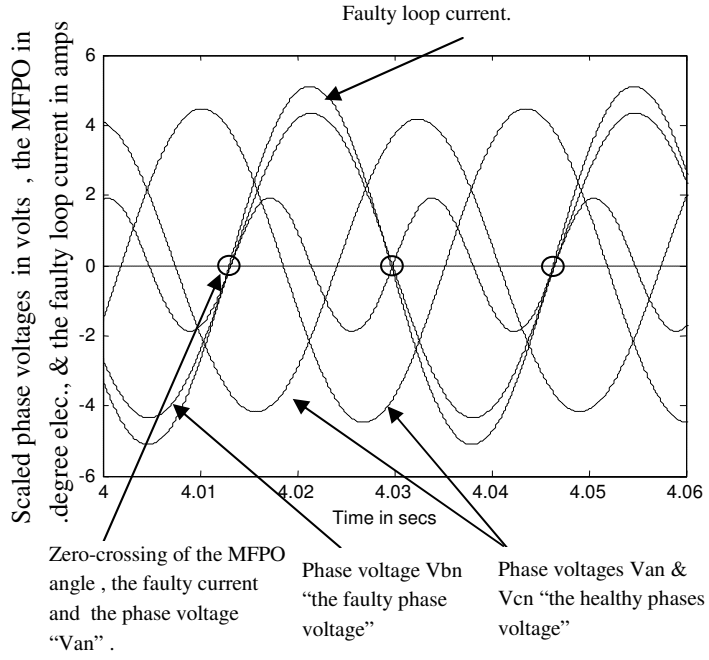

Fig.2.18 The time domain relationship between the phase voltages, the faulty current and the angle of the MFPO for the 2-hp motor (phase-B is the faulty phase).

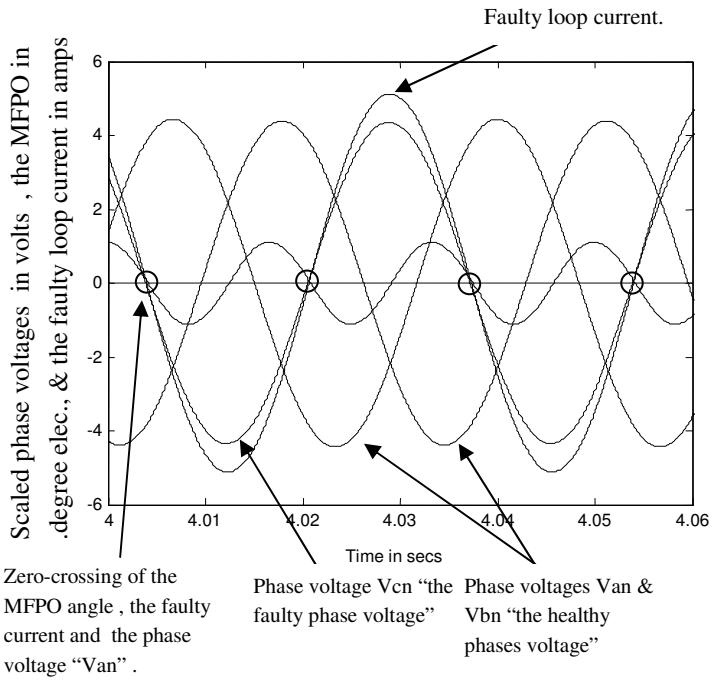

Fig.2.19 The time domain relationship between the phase voltages, the faulty current and the angle of the MFPO for the 2-hp motor (phase-A is the faulty phase).

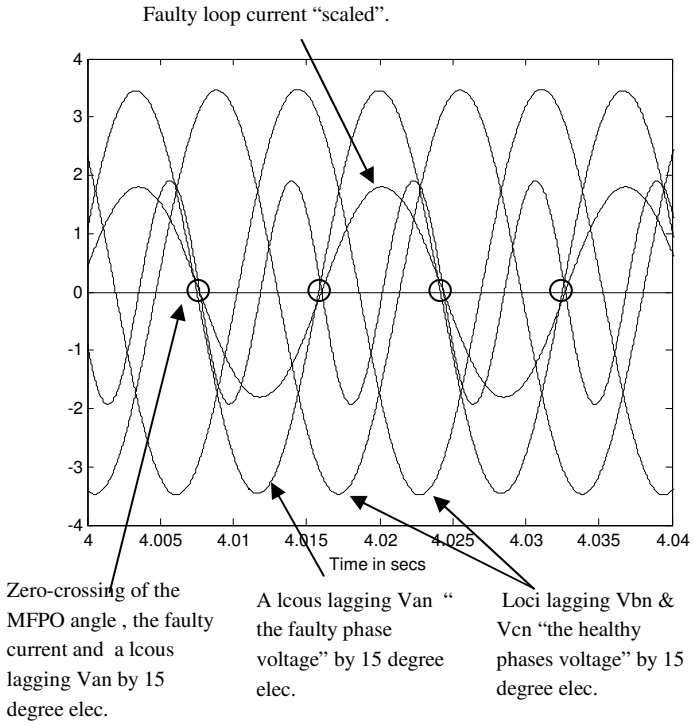

Fig. 2.20 The time domain relationship between loci lagging the phase voltages by 15 degree. elect, the faulty current and the angle of the MFPO for the 5-hp motor (phase a is the faulty phase).

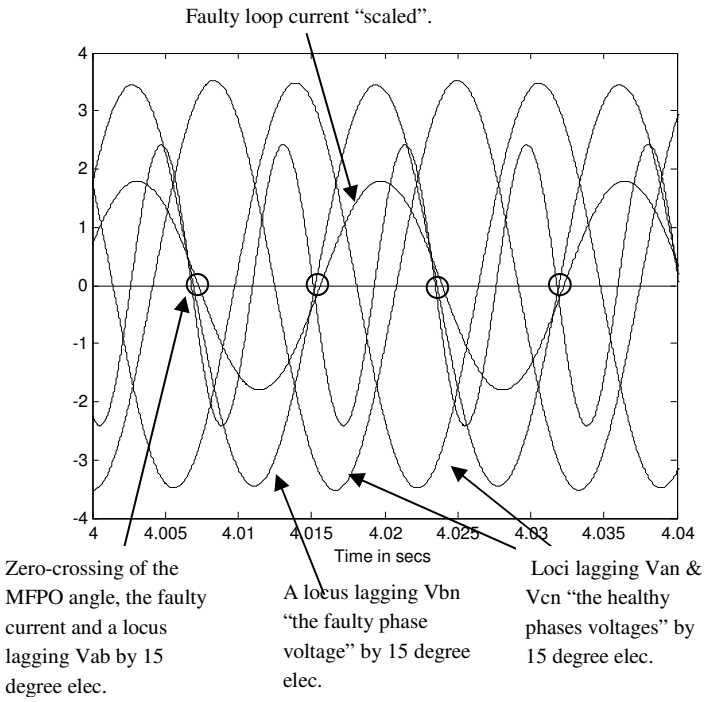

Fig.2. 21 The time domain relationship between loci lagging the phase voltages by 15 degree elec., the faulty current and the angle of the MFPO for the 5-hp motor (phase-B is the faulty phase).

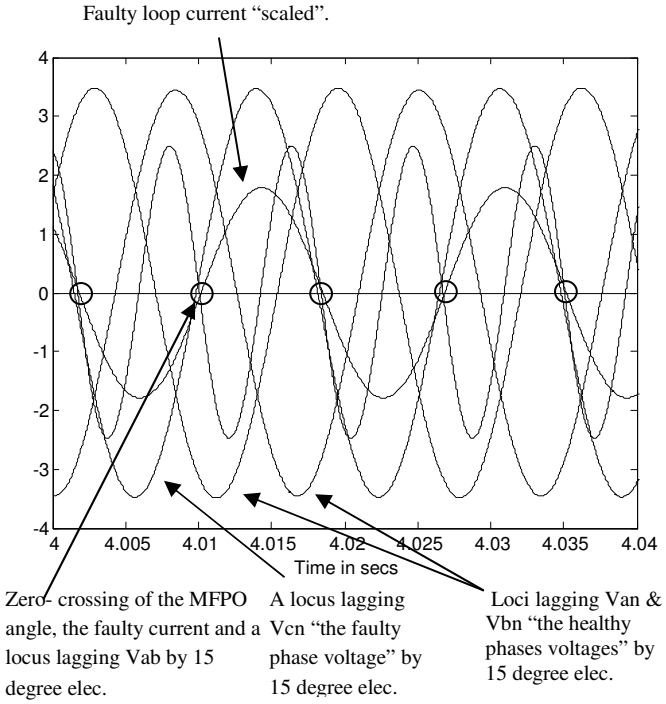

Fig.2 22 The time domain relationship between loci lagging the phase voltages by 15 degree. elect, the faulty current and the angle of the MFPO for the 5-hp motor (phase-C is the faulty phase

2.3.6 Summary of the introduced technique

A new technique for identifying the faulty phase in a squirrel-cage three-phase induction motor for either concentric or lap wound coil construction, when an inter-turn short-circuit in its early stage occurs in one of the phases, was conceived, developed and verified through several experimental tests in this section. This technique also does not require any additional sensors, wiring constrains, or knowledge of any other details of the machine design for the case of concentric wound machine beyond what is normally included in the nameplate data. However, machine detailed design may be required for the case of lap wound machines.

2.4 Diagnosis of stator inter-turn short-circuit for poly-polyphase induction motors in closed-loop vector-controlled drives

Induction motor ac drives have been used in numerous applications for more than three decades. This includes both open-loop and closed-loop drives. The former are the simplest form of ac motor-drive systems, and in such case there is no compensation with respect to the applied voltage space-vector which is generated by the drive's controller. On the other hand, closed-loop drives provide voltage space-vector compensation action through adjustment of the applied voltage space-vector. This action is initiated by the drive to minimize or eliminate the error between the feedback torque and speed signals and the corresponding reference signals. Vector-controlled drives constitute a special class of closed-loop drives which control the machine's torque as well as speed. This is in

order to obtain optimum motor-load dynamic response. This makes the ac induction motor replicate the traditional dc machine which is known for its precise and simple torque-speed control. Vector-controlled closed-loop drives have been used extensively in numerous applications which require precise torque and speed control. The breakthrough in the field of power electronics enabled ac vector-controlled motor-drive systems to replace dc motor-drive systems in a myriad of applications.

Meanwhile, motor and drive fault diagnostics have become a major concern from the industrial point of view, particularly in critical applications where motor-drive failure can be costly, catastrophic or life threatening. This remains the major incentive for a considerable amount of research in the area of motor-drive system fault diagnostics [43-62].

A comprehensive survey of the state of the art concerning this research area has been reported in [55, 62, 78]. Most of these techniques were dedicated to line-fed motors or open-loop ac motor-drive systems [47-49, 51, 53, 54-62]. The research conducted in [50, 52] was mainly concerned with inter-turn short-circuit fault diagnostics in vector-controlled closed-loop drives based on calculating the negative sequence components of the line voltages and currents, while the work reported in [49] was more centered on detecting such type of faults in direct-torque controlled motor-drive systems. The research conducted in [79] extends the application of the motor current signature analysis technique to tackling stator and rotor fault diagnostics using spectral analysis in closed-loop vector-controlled drives.

The main objective of this section is to introduce a so-called “flux pendulous-oscillation”, which supersedes the magnetic field/MMF pendulous oscillation

phenomenon previously utilized in the diagnosing of inter-turn short-circuit faults in open-loop drives and line-fed induction machines, see [54, 56], thus allowing the diagnostic process to be extended to the case involving closed-loop vector-controlled drives. Hence, providing the literature with an additional tool to be added to the "existing tool-kit" that is already available in the literature, [49, 50, 52, 79], for detecting such faults in closed-loop motor-drive systems should be helpful to the motor–drive manufacturers and users. In other words, the decision making algorithm can be based on a combination of all of these approaches rather than utilizing only one of them. This will enhance the reliability of a motor-drive unit and strengthen the fault discrimination capability of the diagnostic algorithm. This author also wishes to draw the reader's attention to the fact that the fault detection algorithm introduced in this section should not be a substitute for any other means of well known traditional protection schemes such as short-circuit, over-load, ground protection, differential protection, etc of a motor-drive system. In addition, the fault detection algorithm introduced in this section is not a substitute for, or reason to change any regular maintenance schedules, or any design criteria established in all accepted practices based on international standards. Therefore, the main objective of this work is to provide a means to detect such types of faults in augmentation to the benefits that are relied upon through these traditional practices. Even if the lead time of the fault detection might be very short, this new approach may enable the operation of a standby unit to avoid financial losses or hazardous conditions. In the next subsection, Subsection 2.4.1, the performance of closed-loop torque-regulated vector-controlled drives, following the on-set of the early stages of an inter-turn short-circuit in a motor in one of the phases of a stator winding, is analyzed. Meanwhile,

Subsection 2.4.2 centers upon discussing the new concept of the flux pendulous-oscillation (FPO), which utilizes the concept introduced here of a rotating space-vector reference whose rate of rotation is unaffected by the control compensation action of the closed-loop drive. Subsection 2.4.3 demonstrates and explains the experimental results which verify the validity of this new approach presented in this work. Finally, in the last subsection, Subsection 2.4.4, the contributions of the work carried out in this investigation are discussed.

2.4.1 Analysis of drive performance in case of stator winding inter-turn short-circuit faults

First, let us consider a healthy three-phase induction motor which is energized from a high performance vector-controlled voltage-source inverter (VSI) drive. It is well known that this type of drive utilizes an outer speed-control loop for speed control and an inner current-control loop in order to regulate the motor torque as shown schematically in Fig.2.23, [25]. At this point, it should be highlighted that the outlines of the control approach are almost identical in these inner and outer control loops. However, the details of the control algorithm might differ from one drive manufacturer to another. The error between a given speed reference and the actual motor speed is processed through the speed controller, which outputs a torque reference command to the torque controller. This torque reference command is compared with the actual torque produced by the motor. It should be mentioned that the motor torque is usually estimated in the drive controller from terminal current and voltage information. The error in the torque is processed through the torque controller which outputs a reference current to the current controller. The output current is processed through the decoupling circuit, which is responsible for converting the commanded current to a commanded voltage in which the *d-axis* and *q-*

axis voltage components are decoupled. Subsequently, the *d-q* voltage components are transformed to a stationary *abc* voltage frame of reference. The *abc* reference voltage signals are then used to generate the required switching pattern of the inverter switches.

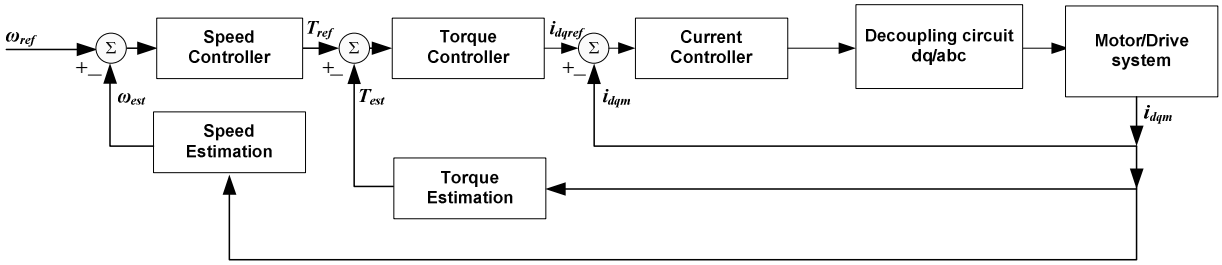

Fig.2.23 Simplified block diagram for typical vector-controlled closed-loop drives.

The previously described scheme is the backbone of any vector-controlled closed-loop drive, see [25]. According to reference [25], the developed machine torque, *T*, which is estimated in the drive, can be expressed as follows:

$$T = (3/4)P(\vec{\psi}_s \times \vec{i}_s) \tag{2.20}$$

where $\vec{\psi}_s = \int \left(\vec{v}_s - R_s \vec{i}_s\right) dt$

Here, P, is the number of poles, $\vec{\psi}_s$, is the stator flux (flux linkage) space-vector, $\vec{i}_s$, is the stator current space-vector, $\vec{v}_s$ is the applied stator voltage space-vector, and R_s is the stator phase resistance. This equation can be applied in any reference frame. However, for the purpose of our analysis, in this section, a counter clockwise synchronously rotating frame of reference is utilized throughout. One should notice that for a voltage source inverter (VSI) the voltage space-vector, $\vec{v}_s$, is the input to the motor. Consequently, based on (2.20) it follows that the stator flux space-vector is also controlled by the action of the drive through its voltage space-vector. Here, the current space-vector and the speed can be considered as the system state variables, while the

torque is the system output. Now, let us consider a case of an inter-turn short-circuit in one phase of a stator winding. The stator MMF can be resolved into a counter clockwise (CCW) forward MMF component rotating at synchronous speed and a clockwise (CW) backward field/MMF component rotating in the opposite direction, also at synchronous speed, [54,56]. Consequently, the current space-vector, $\vec{i}_s$, can be resolved into a forward component rotating CCW at synchronous speed and a backward component rotating CW also at synchronous speed. Thus, the resultant current space-vector, $\vec{i}_s$, can be resolved into two components and hence can be expressed as follows:

$$\vec{i}_s = \vec{i}_f + \vec{i}_b \tag{2.21}$$

where, $\vec{i}_f$, is the forward rotating component of the current space- vector, and $\vec{i}_b$, is the backward rotating component of the current space-vector, resulting from the asymmetry caused by the inter-turn short-circuit in the stator winding of the machine. Hence, from (2.20) and (2.21) the torque estimated in the drive for a faulty machine can be expressed by flux (flux linkage) and current space-vector cross-products as follows:

$$T = (3/4)P\vec{\psi}_s \times (\vec{i}_f + \vec{i}_b) = (3/4)P(\vec{\psi}_s \times \vec{i}_f + \vec{\psi}_s \times \vec{i}_b) \tag{2.22}$$

The first term, $(\vec{\psi}_s \times \vec{i}_f)$, in (2.22) represents a constant (dc) torque component which is produced due to the interaction between the stator flux space-vector and the forward component of the stator current space-vector. Meanwhile, the second term, $(\vec{\psi}_s \times \vec{i}_b)$, in (2.22) represents torque oscillations, with a frequency equal to double the fundamental operating frequency. This component is produced by the interaction between the stator flux space-vector, $\vec{\psi}_s$, and the backward component of the stator current space-vector,

$\vec{i}_b$. As mentioned before, the voltage space-vector, $\vec{v}_s$, is the only input to the motor from the VSI-drive, which directly impacts the stator flux space-vector, $\vec{\psi}_s$. Thus, it should be expected that the compensation action of the vector-controlled drive, which would tend to minimize these torque ripples, will appear as adjustments to the output voltage space-vector of the drive, $\vec{v}_s$. Hence, because of these adjustments, the drive's output voltage space-vector, $\vec{v}_s$, will end up being composed of two components. One of these components is resolvable into a forward, $\vec{v}_f$, component and another component which is resolvable into a backward, $\vec{v}_b$, component. Consequently, the stator flux space-vector, $\vec{\psi}_s$, will have to be resolved into a forward and a backward components, $\vec{\psi}_f$ and, $\vec{\psi}_b$ respectively, in which case,

$$\vec{\psi}_s = \vec{\psi}_f + \vec{\psi}_b \tag{2.23}$$

Accordingly, the torque in (2.22) can now be rewritten to include the compensation action (adjustments to $\vec{v}_s$) from the drive as follows:

$$\begin{aligned} T &= (3/4)P(\vec{\psi}_f + \vec{\psi}_b)\times(\vec{i}_f + \vec{i}_b) = \\ &\quad (3/4)P[(\vec{\psi}_f \times \vec{i}_f) + (\vec{\psi}_f \times \vec{i}_b) + (\vec{\psi}_b \times \vec{i}_f) + (\vec{\psi}_b \times \vec{i}_b)] \end{aligned} \tag{2.24}$$

It should be noticed that the first term in (2.24), $(\vec{\psi}_f \times \vec{i}_f)$, represents torque produced due to the interaction between the forward component of the stator flux space-vector, $\vec{\psi}_f$, and the forward component of the stator current space-vector, $\vec{i}_f$. This term produces a constant (dc) torque component which is the main developed/useful torque in the machine. The second term, $(\vec{\psi}_f \times \vec{i}_b)$, in (2.24) represents the torque produced by the

interaction between $\vec{\psi}_f$ and the backward component of the stator current space-vector, $\vec{i}_b$. This term produces torque ripples (pulsations) with a frequency equal to double the fundamental frequency of the applied voltage. The third term, $(\vec{\psi}_b \times \vec{i}_f)$, represents the interaction between the backward component of the stator flux space-vector, $\vec{\psi}_b$, and $\vec{i}_f$. This term, again, produces torque ripples with a frequency equal to double the fundamental frequency. The fourth term, $(\vec{\psi}_b \times \vec{i}_b)$, results from the interaction between $\vec{\psi}_b$ and $\vec{i}_b$. This term produces a constant (dc) torque component, acting in opposite direction to the main torque produced in the forward direction by the aforementioned first term in (2.24). This means that the average developed torque is reduced in the case of an inter-turn short-circuit. Now, the controller will try to track the reference torque, which will be assumed constant to simplify our analysis. Then, the drive has to increase the torque produced by the interaction between $\vec{\psi}_f$ and $\vec{i}_f$ to cancel out the torque produced in the opposite direction due to the interaction between $\vec{\psi}_b$ and $\vec{i}_b$. This is achieved by increasing the magnitude of $\vec{\psi}_f$ and consequently increasing the forward component of the applied stator voltage space-vector, $\vec{v}_f$. Meanwhile, the backward component of the stator flux space- vector, $\vec{\psi}_b$, should be adjusted to cancel or mitigate the ac torque ripples produced by the second and the third term in (2.24) by adjusting the backward component of the applied stator voltage space-vector, $\vec{v}_b$, to produce the desired total voltage space-vector, $\vec{v}_s = \vec{v}_f + \vec{v}_b$.

At this stage, one should notice that the compensation action of the drive depends on the tuning status of its controller. For a better physical understanding of the controller's

actions described above, the loci of the voltage space-vector, $\vec{v}_s$, the stator current space-vector, $\vec{i}_s$, and the stator flux space-vector, $\vec{\psi}_s$, under faulty conditions are depicted in the space-vector diagram of Fig. 2.24

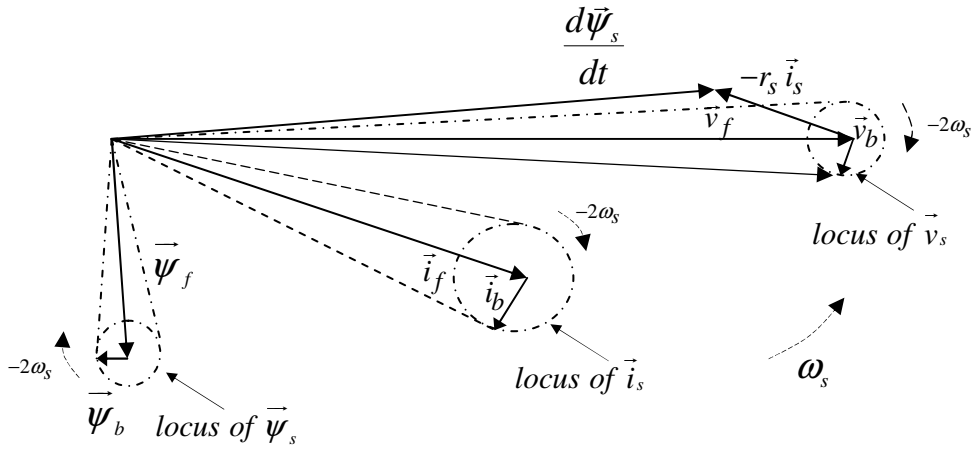

Fig.2.24 Space-vector diagram of vector-controlled motor-drive system for a case of inter-turn short-circuit in one of the stator winding fault (ω_s is the synchronous speed)

2.4.2 The concept of the Flux Pendulous Oscillation "FPO"

The concept of magnetic field (MMF) pendulous oscillation (MFPO) has been previously presented in several publications [54,56]. This MFPO concept can best be defined as the fluctuation of the speed of rotation of the resultant magnetic field (MMF) with respect to a synchronously rotating frame of reference, due to asymmetry either in the stator and/or the rotor circuits, which also produces torque ripples that might degrade system performance. These oscillations in the resultant rotating magnetic field (MMF) are measured with respect to the synchronously rotating voltage space-vector as a reference. However, as mentioned above, for a closed-loop motor-drive system, which has a well tuned torque regulator, the drive-controller attempts to compensate for these torque ripples by modulating the applied stator voltage space-vector, $\vec{v}_s$, at the motor

terminals. Consequently, for this case, the applied, $\vec{v}_s$, voltage space-vector, and hence the resultant rotating magnetic field (flux) space-vector, $\vec{\psi}_s$, also fluctuates with respect to a CCW synchronously rotating frame of reference. This is in order to alleviate the torque ripples which are produced as a result of the fault as explained above. Hence, in such a case, the oscillations in the stator current space-vector, $\vec{i}_s$, and the flux space-vector, $\vec{\psi}_s$, can be monitored separately using two reference frames produced by a Phase-Locked-Loop (PLL) algorithm. Although, the PLL concept has been explained in detail in several publications [147-148], it will be briefly summarized here for the sake of continuity and for the reader's convenience. A simplified block diagram for the PLL concept is depicted in the schematic of Fig.2.25, [147,148].

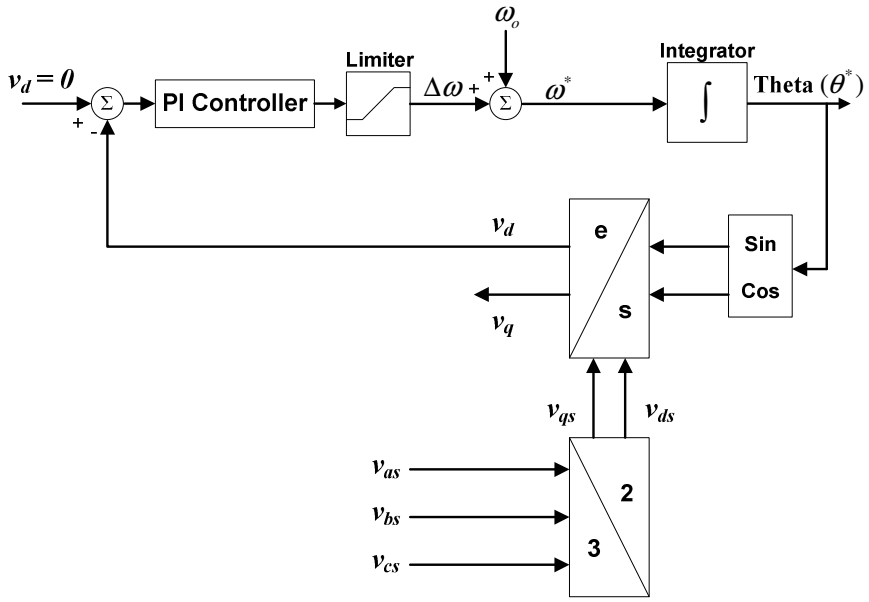

Fig.2.25 Simplified block diagram for the phase locked loop.

With regard to the voltage space-vector, $\vec{v}_s$, the drive's output line voltages, v_{ab}, v_{bc}, and v_{ca}, are measured (acquired) and then transformed from the abc stationary reference

frame to a synchronously rotating d-q reference frame leading to the voltage components, v_d and v_q. This rotating d-q frame is synchronized to the output frequency of the drive. The angle theta, θ^* , in Fig.2.25 , which is used in this transformation, is obtained by integrating an angular frequency command, ω^*. In this reference frame, v_d and v_q, appear as dc components depending on the angle, θ^* . The PI controller is used to obtain that value of ω^* (or θ^*) to render the transformed feedback voltage component, v_d, to a value nearly equal to a zero. At this point, it should be mentioned that the angle θ^* is not affected by any oscillations which might be produced as a result of a faulty condition. Accordingly, the angle, θ^*, can be used as a reference, which is CCW rotating with a speed equal to the synchronous speed. Now, for closed-loop drives, the new concept of "Flux Pendulous Oscillation" (FPO) can be defined as the oscillation of the stator voltage space-vector with respect to the angle, θ^*. Also, here the aforementioned MFPO can be measured as the oscillation of the stator current space-vector with respect to the angle θ^* , which is generated by the PLL algorithm. The diagnostic technique introduced here employs two PLLs running concurrently. One is dedicated to measuring the oscillation of the current space-vector, PLL*i*, while the other is dedicated to measuring the oscillation in the voltage space-vector, PLL*v*. Consequently, the flux space- vector traces a locus as shown in the space-vector diagram of Fig.2.26.

In this technique, the instantaneous oscillation in the current space-vector, $\vec{i}_s$, is measured with respect to the output angle of the PLL*i*, θ_{iref}, while the instantaneous oscillation in the voltage space-vector, $\vec{v}_s$, is measured with respect to the output angle of the PLL*v*, θ_{vref}, both of which are continuously monitored. It should also be noticed that the difference between the output angle of the PLL*v*, θ_{vref},, and the output angle of

the PLL*i*, θ_{iref}, , is the machine's power factor angle. Accordingly, this algorithm can also be used to monitor the machine's power factor angle.

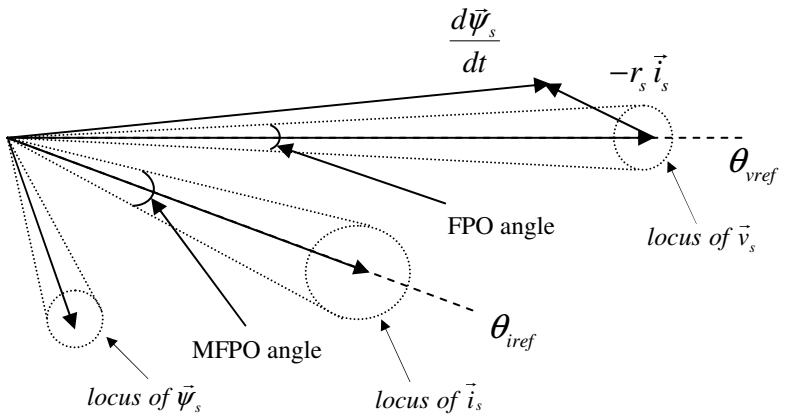

Fig.2.26 Space-vector diagram of vector-controlled motor-drive system illustrates the concept of the flux pendulous oscillation FPO and the magnetic field pendulous oscillation MFPO.

2.4.3 Analysis of the experimental results

In this subsection, the analysis and concepts presented in the previous sections are experimentally verified and explained through several motor-drive system tests. The experimental setup consists of a 5-hp, 460-Volt, 6-pole, 3-phase induction motor, in which one of the phases has been rewound to enable the investigator to emulate an inter-turn short-circuit, see the schematic winding diagram of Fig.2.27 , and the experimental setup's functional block diagram and physical components as depicted in Fig.2.28. This motor has been energized from a commercially available closed-loop drive. This drive can be programmed to run in either a closed-loop vector-control mode or open-loop mode. The voltage and current waveforms were collected using a data acquisition system, see Fig.2.28, with a sampling frequency of 50kHz. Notice that the faulty loop (shorted-turns loop) current, i_f, shown in Fig.2.27, is one of the measured variables being

monitored in the test results given below, only for purposes of analysis of the experimental results presented here, and is not needed or used in the diagnostic method or resulting algorithm.

The data has been collected and processed using a Matlab-Simulink program. A self-explanatory flow chart for the diagnostic algorithm subject of this study is depicted in Fig.2.29. The main features of this algorithm are the computation of the pendulous oscillation of the resultant stator flux space-vector, the so-called flux pendulous oscillation (FPO) angle, δ_v, and the pendulous oscillation of the stator current (MMF) space-vector, the so-called MMF pendulous oscillation (MFPO), δ_i.

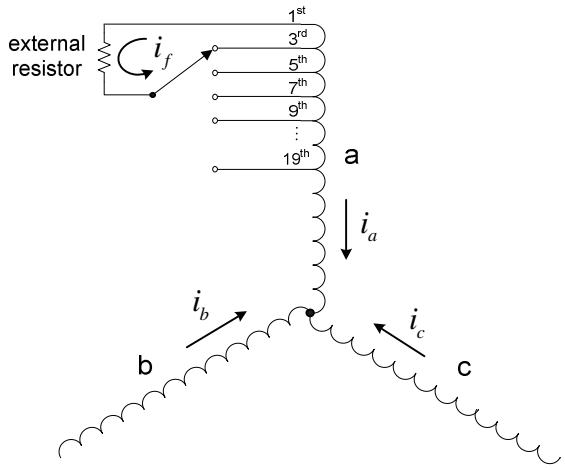

Fig.2.27 Schematic diagram of stator windings with taps.

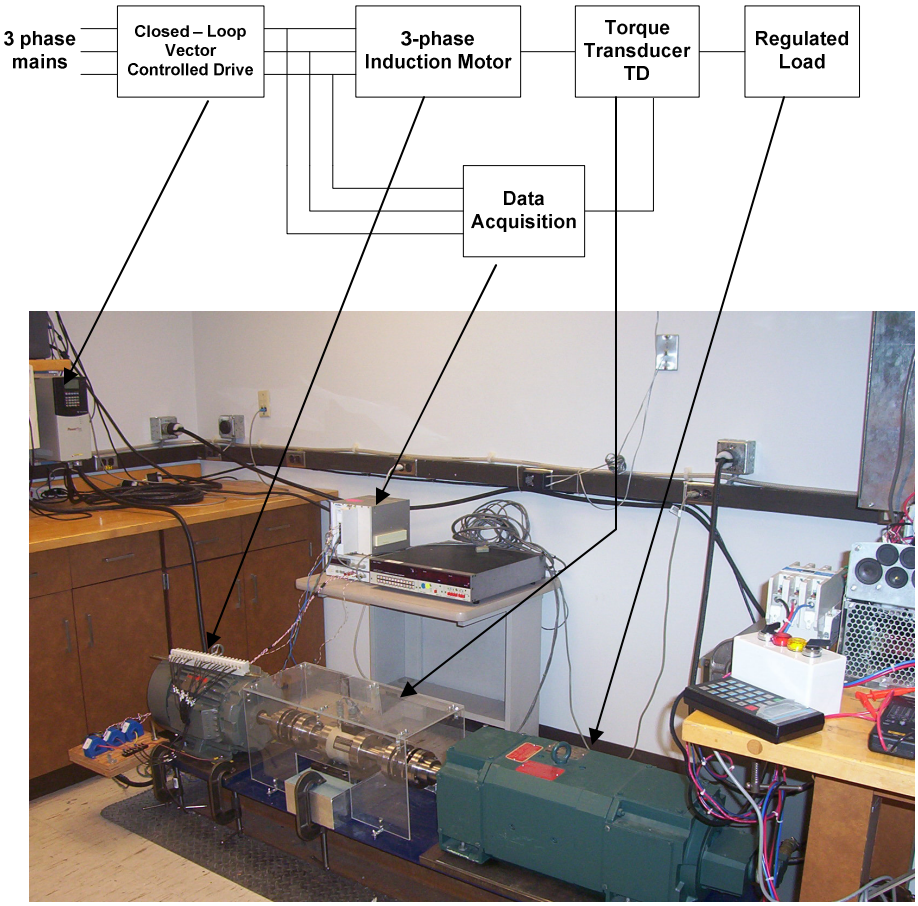

Fig.2.28 Experimental set up and it's associated function block diagram.

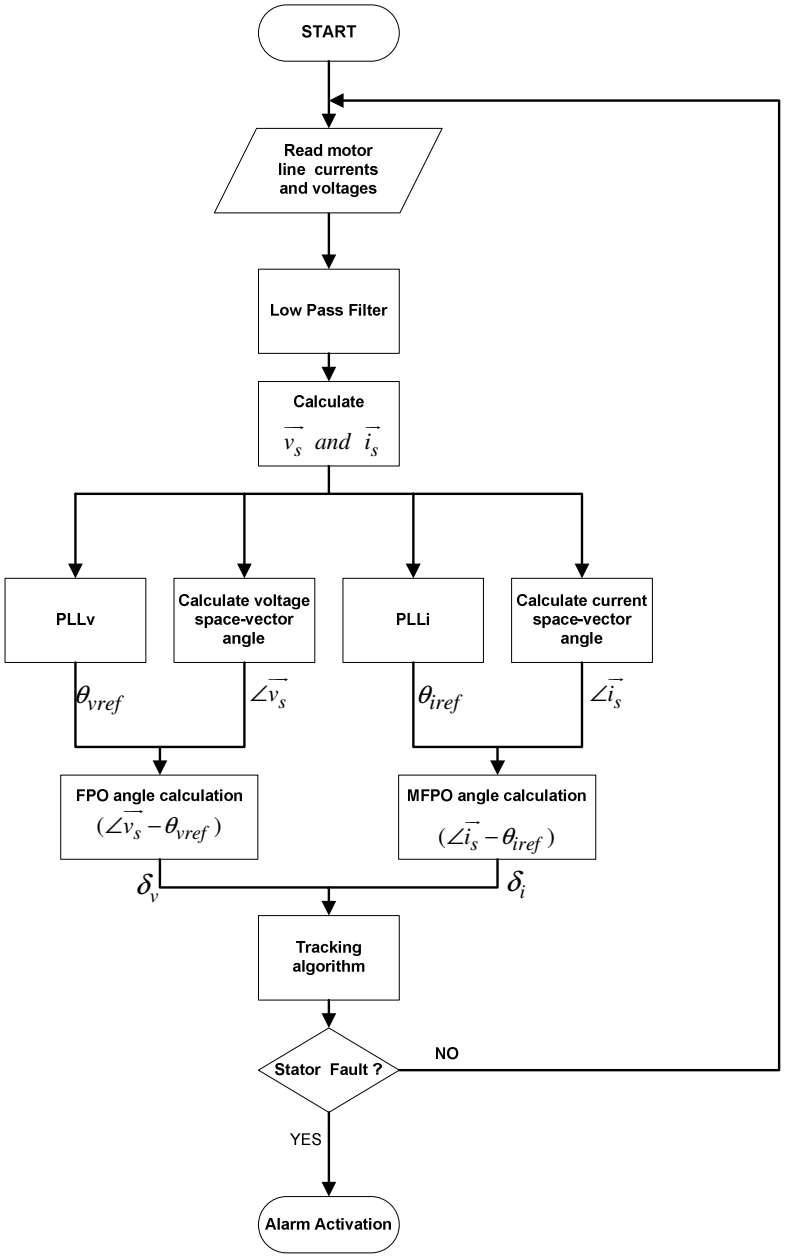

Fig.2.29 Flow chart for the diagnostic algorithm.

A set of experimental tests has been carried out using the previously explained setup to verify the validity of the concepts presented in this section, namely collection of the data for monitoring the angles, δ_v and δ_i, for diagnostic purposes. Here, the 5-hp motor-drive system was run at rated full-load with an output torque of 30Nm, with a circulating fault current, i_f = 2p.u. The tests results yielded time-domain profiles

(waveforms) for the FPO angle, $\delta_v = \angle\vec{v}_s - \theta_{vref}$, and the MFPO angle, $\delta_i = \angle\vec{i}_s - \theta_{iref}$, which are plotted versus time in Fig. 2.30a. Meanwhile, for further insight into the relationship between the fault current, i_f, and the phase currents, i_a , i_b and i_c , the waveforms of these motor currents for the faulty case, i_f = 2p.u., are plotted in Fig.2.30b.

A set of results for the FPO angle and the MFPO angle similar to these given in Fig. 2.30a was obtained for various fault currents, $0 \leq i_f \leq 2.0$p.u. From these results, plots of the FPO and the MFPO angles versus the fault current, i_f, were obtained and are given in Fig. 2.31. Thus, Fig. 2.31 depicts the variation in these two angles versus the fault current, i_f , expressed in per unit. It can be noticed that the FPO angle increases with respect to the faulty loop current while the MFPO angle almost experiences no change with respect to that current. This is due to the compensation action of the closed-loop drive's controller that mainly affects the applied voltage space-vector, which is in line with the theoretical concepts previously elaborated-on earlier. It can be also noticed from Fig. 2.30b that there is only a slight increase in one of the line currents in spite of the fact that the circulating faulty loop current has already reached a level equal to double the rated current. Thus the occurrence of such a fault is not easily detectable by only monitoring the magnitudes of the terminal currents. The data plotted in Fig.2.32 shows the corresponding results of the FPO and MFPO angles for the half-load condition of 15Nm. It can be noticed that the percentage increase in the FPO angle, δ_v, with respect to the circulating current of the faulty–loop, i_f, for the case of full-load (30Nm) is higher than that for the half-load (15 Nm) condition. Meanwhile, the variation of the MFPO angle, δ_i, versus i_f for a half-load torque condition (15Nm) is higher than that for a full-load condition. This may be attributed to the fact that the stator core may have a slightly

higher degree of saturation under half-load than full-load conditions, since the demagnetizing effect of the rotor MMF on the overall saturation level in the motor's magnetic circuit is weaker at half-load than at full-load conditions. This has been verified through time-stepping FE modeling of the motor, which is not given here in this dissertation, but can be found in [158, 159]. Some of the results can also be attributed to the closed-loop drive controller's response to the torque ripples developed as a result of the stator fault. Furthermore, this can also be attributed to the fact that the drive controller is tuned for optimum compensation at the full-load condition with its corresponding machine parameters and consequently less so (sub-optimally) at half-load condition.

Meanwhile, Fig. 2.33 shows a considerable increase in the magnitude of the applied stator voltage space-vector, $\| \vec{v}_s \|$, with respect to the faulty loop current, when $i_f \geq 0.6$ p.u., for both cases of full-load and half-load conditions. This increase can be attributed to the drive controller's response to the negative torque produced by the interaction of the backward component of the stator flux space-vector and the backward component of the current space-vector, $(\vec{\psi}_b \times \vec{i}_b)$, as pointed out earlier in discussing the fourth term in (2.24).

It was also interesting to monitor the variation of the summation of the MFPO angle, δ_i, and the FPO angle, δ_v, which is depicted in Fig. 2.34 for the full-load and half-load conditions. It can be noticed that the summation of the angles, δ_v plus δ_i, is increasing monotonically with respect to the faulty loop current, i_f, which suggests that this summation $(\delta_i + \delta_v)$ can be a very effective fault diagnostic index. The rate of increase of this fault index can be used as an indication of the fault condition. Thus, monitoring the summation $(\delta_i + \delta_v)$ is an effective indirect indicator of the status of the

circulating fault current, I_f. Since the circulating fault current can not be monitored directly from the drive, monitoring $(\delta_i + \delta_v)$ represents a means of indirectly monitoring the fault current, I_f. Therefore, one can envisage programming the DSP chip in a drive to continuously compute and track such an index $(\delta_i + \delta_v)$. With the knowledge of the range of values of $(\delta_i + \delta_v)$ with respect to the monitored (estimated) output torque of the machine under healthy conditions, one can use this monitoring process when the values of $(\delta_i + \delta_v)$ begin to increase without change in torque as indicative of "potential trouble" in the stator windings of a motor. Meanwhile, Fig. 2.35 demonstrates the variation of the MFPO angle, δ_i , and FPO angle, δ_v , with respect to the faulty-loop circulating current, i_f, for the case of the open-loop operating mode of the drive, in which case the drive's controller compensation action with regard to the applied voltage space-vector, $\vec{v}_s$, does not exist. Here, one should observe the significant increase in the value of the MFPO angle, δ_i, versus the faulty-loop current, I_f . In this case, it should be noticed that there is almost no change in the FPO angle, δ_v, which is naturally expected for the open-loop mode of operation of this drive. Again, this is because under this mode there is no controller compensation action with regard to the voltage space-vector, $\vec{v}_s$. These experimental results are also summarized in Table 2.3 for the convenience of the reader, for various values of the fault current, i_f, for both open-loop and closed-loop operating conditions in the drive.

Based on the previous discussion and the experimental results, a new diagnostic approach is being introduced in this work. The new diagnostic approach depends on monitoring the increase (upward creep) in the summation of both the MFPO angle and the FPO angle, namely the (MFPO+FPO) angle for a given torque condition, for the

purpose of diagnosing of inter-turn short-circuit faults for a given load torque condition, when a motor is energized from a vector-controlled closed-loop drive.

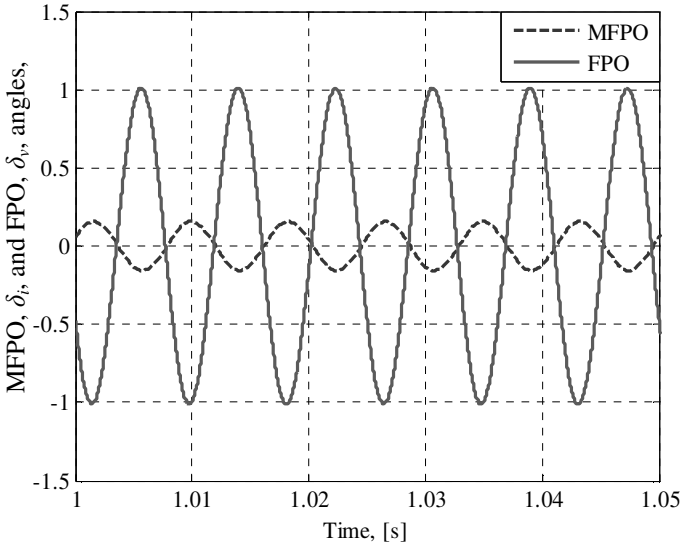

Fig. 2.30a FPO angle, δ_v, and MFPO angle, δ_i, time-domain profiles, vector-controlled closed-loop drive (full-load), with i_f = 2p.u

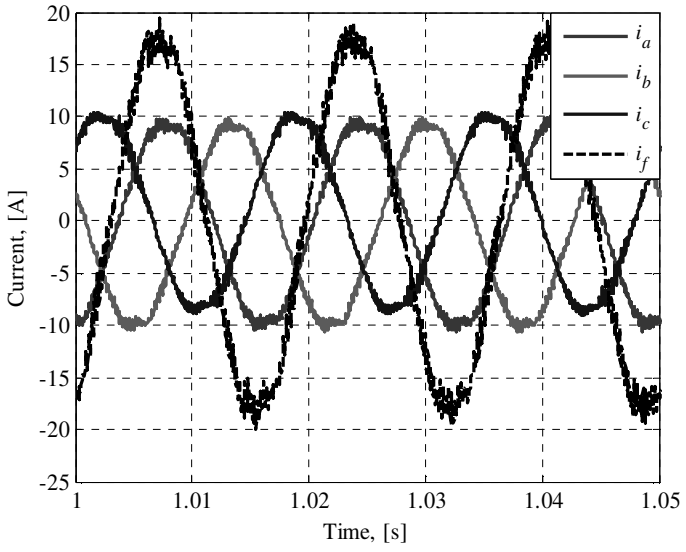

Fig. 2.30b Motor three-phase currents and circulating loop current, vector-controlled closed-loop drive (full-load), with i_f = 2p.u.

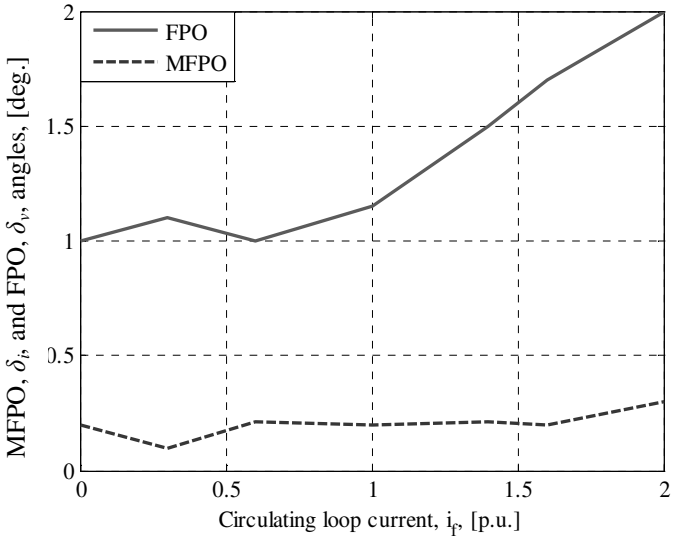

Fig. 2.31 FPO angle, δ_v, and MFPO angle, δ_i, versus the circulating loop current, i_f, for vector-controlled closed-loop drive (full-load).

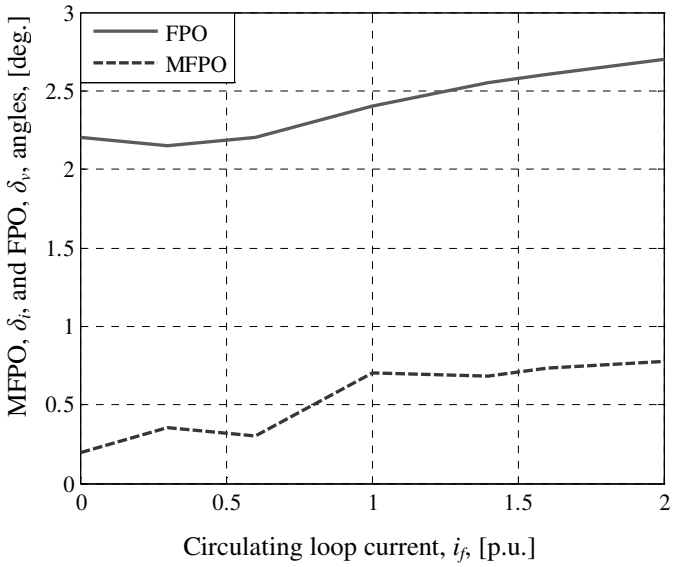

Fig.2.32 FPO angle, δ_v, and MFPO angle, δ_i, versus the circulating loop current, i_f, for vector-controlled closed-loop drive (half-load).

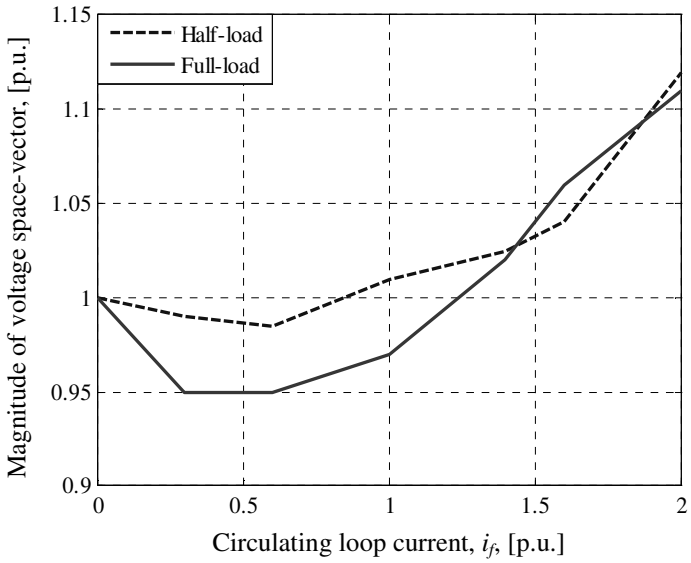

Fig.2.33 Magnitude of the voltage space-vector, $\|\vec{v}_s\|$, versus the circulating loop current, i_f, for vector-controlled closed-loop drive (half-load and full-load).

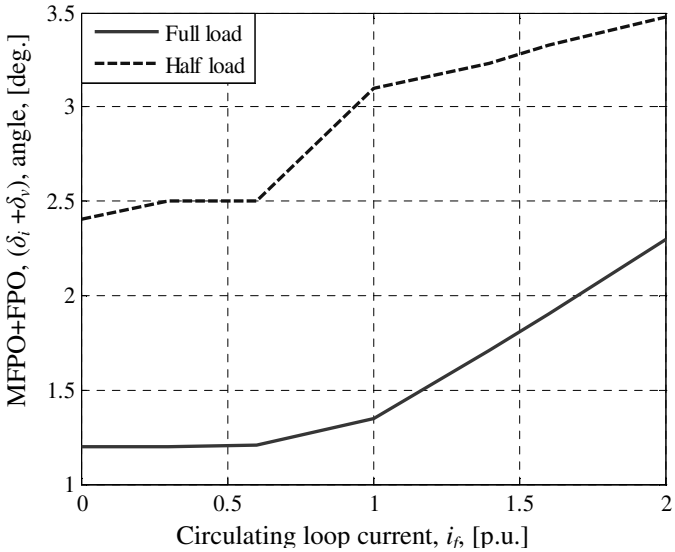

Fig.2.34 FPO+MFPO angle, ($\delta_i + \delta_v$), versus the circulating loop current, i_f, for vector-controlled closed-loop drive (full-load and half-load).

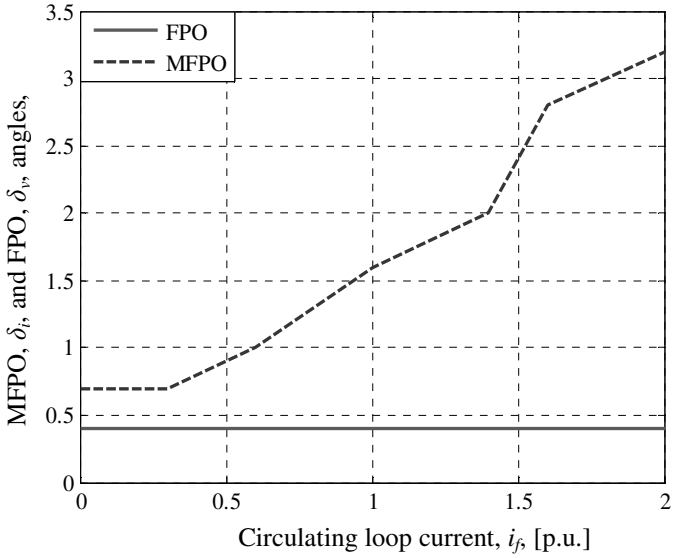

Fig. 2.35 FPO angle, δ_v, and MFPO angle, δ_i, versus the circulating loop current, i_f, for open-loop drive (full-load).

Circulating (fault) loop current, [p.u.]	**Open-loop (full-load)**			**Closed-loop (full-load)**			**Closed-loop (half-load)**		
	FPO, δ_v, [deg.]	MFPO, δ_i, [deg.]	FPO+MFPO, $(\delta_i+\delta_v)$, [deg.]	FPO, δ_v, [deg.]	MFPO, δ_i, [deg.]	FPO+MFPO, $(\delta_i+\delta_v)$, [deg.]	FPO, δ_v, [deg.]	MFPO, δ_i, [deg.]	FPO+MFPO, $(\delta_i+\delta_v)$, [deg.]
0	0.45	0.65	1.1	1.0	0.2	1.2	2.2	0.2	2.4
0.2	0.45	0.65	1.1	1.05	0.16	1.21	2.15	0.3	2.45
0.3	0.45	0.65	1.1	1.1	0.1	1.2	2.1	0.35	2.45
0.4	0.45	0.8	1.25	1.05	0.16	1.21	2.17	0.28	2.45
0.6	0.45	1.0	1.45	1.0	0.2	1.2	2.2	0.29	2.49
0.8	0.45	1.3	1.75	1.08	0.2	1.28	2.3	0.5	2.8
1	0.45	1.6	2.05	1.17	0.2	1.37	2.4	0.725	3.125
1.2	0.45	1.8	2.25	1.33	0.2	1.53	2.48	0.72	3.2
1.4	0.45	2.0	2.45	1.5	0.2	1.7	2.575	0.715	3.29
1.6	0.45	2.85	3.3	1.7	0.2	1.9	2 .6	0.75	3.35
1.8	0.45	3.0	3.45	1.85	0.25	2.1	2.65	0.77	3.42
2.0	0.45	3.2	3.65	2.0	0.3	2.3	2.7	0.79	3.49

Table 2.3 Numerical values of the FPO and the MFPO angles in electrical degrees at several test conditions.

2.4.4 Summary of the introduced technique

In this section, a new technique was introduced such that it can be utilized as a theoretical foundation for an artificial intelligent algorithm to detect inter-turn short-circuit faults in one phase of a motor's stator winding, when such a motor is supplied from a vector-controlled closed-loop drive used in high performance applications. Also, in this section, a new concept of the stator flux pendulous oscillation was introduced. This concept has been found by this author to be influenced by the compensation action

initiated by the drive, in its effort to alleviate (or mitigate) the torque ripples produced due the shorted-turn fault conditions The technique utilizes the phase locked loop (PLL) concept to track the angles of the voltage and current space-vectors. A new diagnostic index based on the summation of these two angles, $(\delta_i + \delta_v)$, the so-called MFPO and FPO angles, was introduced here for stator inter-turn short-circuit detection, when motors are operated from closed-loop drives. The magnitude of the summation of these two angles was found to be a good indirect indicator of the severity of the circulating faulty loop current, and hence the severity of the fault. The technique, which requires monitoring only motor terminal voltages and currents, was verified through a set of experimental results carried out at various load conditions.

2.5 Summary

In this chapter, two different contributions to the literature were introduced. The first contribution is to develop and experimentally verify a technique that can be used as a theoretical foundation for a rule-based advanced artificial intelligent algorithm to identify the faulty phase in a squirrel-cage three-phase induction motor for either concentric or lap wound coil construction, when an inter-turn short-circuit occurs in one of the phases. This work leads to a theoretical foundation for identifying the faulty phase in polyphase ac machines and estimating the associated fault severity. This is achieved without any requirement for additional sensors, wiring constraints, or knowledge of any other details of the machine design for the case of concentric wound machine beyond what is normally included in the nameplate data. However, machine design details may be required for the

case of lap wound machines. The theoretical analysis was verified through several experimental test results.

The second contribution is to present and experimentally verify a new technique that can be a basis for an advanced artificial intelligent algorithm to diagnose an inter-turn short-circuit fault in vector-controlled motor-drive systems. This technique is mainly based on monitoring the oscillation of the stator voltage space-vector and the stator current space-vector with respect to a reference unit space-vector that is not affected by the fault or the control action of a vector-control drive. The validity of the technique was verified through several results obtained from experimental tests that were carried out at different operating conditions of a case-study motor-drive system.

CHAPTER 3

3. CONTROL OF OPEN-LOOP MOTOR-DRIVE SYSTEMS UNDER STATOR WINDING FAILURES

3.1 Introduction

Open-loop Variable Speed Drives “VSDs” are wide-spread in numerous industrial and commercial applications. The control of most of these drives is based on the conventional scalar constant volts-per-hertz (V/f) control, [3]. In spite of the simplicity of this approach and its associated reduced processing requirement, it can provide a smooth speed-torque control over a wide dynamic range. Although this control approach can not provide precise speed-torque control as in the vector-controlled closed-loop systems, the scalar (V/f) control method is adequate for a wide variety of real-world drive applications. This approach is in essence the workhorse of the ac motor-drive industry, [3]. Nevertheless, the reliability and survivability of the motor-drive system remains a significant concern especially in critical applications in which the failure of a motor-drive system may cause substantial financial losses or even life threatening conditions.

As mentioned before, numerous investigations have been directed towards enhancing the reliability and the survivability of these motor-drive systems, [100-106, 109-110, 112-123, 125-128]. However, most of these works were focused on vector-controlled closed-loop type of drives, [109-110,112,122-130]. Little attention was given

to open-loop drives, except for the work presented in [113-114]. Most of these introduced techniques were based on adding extra hardware to the system and require more processing power. That means increasing the cost of the system. Therefore, this makes it more difficult for modern drives with enhanced fault-tolerant capabilities to compete in the market place with conventional drives. Moreover, with these complications in system components, the cost and size advantages between the concept of applying complete system redundancy and a motor-drive system with enhanced survivability/ reliability may not be significant. This might make the later approach not an attractive solution.

An innovative technique that enables the operation of an open-loop motor-drive system upon a failure in one of a motor's phase windings, presuming that the stator winding of a motor is Delta-connected, is presented in this chapter. This technique enables the operation of an ac motor as a two-phase open-Delta machine driven by a three-phase inverter. Unlike other techniques that require over-sizing/ over-rating the motor and the drive, such over-sizing is not required if one uses this approach at hand. However, over-sizing the motor may be necessary if it is required that the motor develops the same power under a faulty condition. Another advantage of the technique presented here is that the controller can be activated either in the case of normal mode of operation or faulty mode of operation. In other words, the compensation algorithm is running during healthy operation without any significant impact on the system performance. However, the compensation algorithm will have a significant impact on the system performance to diminish or alleviate the effect of the fault and therefore enhances the "robustness" of the system.

It should be pointed out that the technique presented here enhances the survivability of the motor-drive system in case of winding failures. It is presumed in the analysis presented in this chapter that the stator winding has either an open-coil "open-turn" due to winding rupture, [55,66,128,149], or the stator winding has an inter-turn short-circuit fault that has been detected and the faulty phase has been isolated in an early stage using one of the techniques already documented in the literature, [43-62].In this case, the circulating faulty loop current has negligible "ampere-turn" effect on the machine's net torque,[124]. However, it should be pointed out that the machine should be specially designed in replication to the work presented in [102-103,116,121]. The faulty case, where one of a stator winding coils is completely shorted is discussed and analyzed in Chapter 5.

In the first two sections of this chapter, the basic principles necessary to understand the contribution of this chapter will be reviewed for the sake of reader's convenience and for the sake of completeness. First, the basic principles of the scalar constant (V/f) control are briefly reviewed. Then, induction motors with Delta-connected stator phase windings are discussed under healthy operation, and under winding failure circumstances. In the third section of this chapter, a literature review of previously introduced motor-drive systems' fault mitigation strategies that are applicable to open-loop scalar constant (V/f) control is revisited. The basic concept of the algorithm introduced here is next described and analyzed in depth. This is followed by a controller design procedure to obtain an optimum performance under healthy and faulty modes of operation. This analysis is then supported by several time-domain simulation results

which are introduced in a later section in this chapter. Mainly, the simulation presented in this chapter is based on two different models.

In the first simulation model, the monitored currents are sampled and processed with a 10 kHz frequency. This is to replicate the operation of the real control algorithm implemented in the DSP used in the experimental work which is described in Appendix B of this dissertation while the actual simulation step size is 1μsec in order to accurately simulate the various transistor switching effects. The actual device switching also is included in this model. However, the motor model is presented in the d-q stationary frame of reference in which MMF space harmonics higher than the fundamental component and saturation effects are not included. The entire motor-drive model and the controller are developed in the environment of MATLAB Simpowersystem toolbox, [150]. The second model used in the analysis is a coupled analysis between two different commercial software packages, namely MATLAB and MAGSOFT-Flux2D. The control algorithm is developed in MATLAB Simulink toolbox and the motor model is implemented in time-stepping finite element software "MAGSOFT-Flux2D" where the entire machine design particulars/ characteristics are included in the simulation model. Finally, the simulation and experimental results will be compared and discussed, based on the analysis and the simulation work presented earlier in this chapter.

3.2 Basic principles of conventional scalar V/F control

As mentioned earlier, scalar constant (V/f) control is widely implemented in motor-drive systems due to its simplicity and reliability. This scheme is based mainly on changing the voltage to frequency ratio in a certain manner to keep the machine flux

constant throughout the normal rated operating range, [151]. Hence the machine can develop the same rated torque over a wide speed range. The relationship between the machine airgap flux and stator induced emf can be expressed as follows, [151]:

$$E = 4.44Nf\phi K_w \tag{3.1}$$

Where , E is the induced emf in the stator per phase(line-to-neutral)

N is the number of series turns per phase

ϕ is the resultant airgap flux per pole.

f is the frequency of the energization source (inverter or line).

K_w is the stator winding factor.

Hence from (3.1), the ratio between the stator induced emf and the supply frequency can be expressed as follows:

$$\frac{E}{f} = 4.44N\phi K_w K_d \tag{3.2}$$

Moreover, the relationship between the applied phase voltage and the induced emf in the stator winding can be expressed as follows:

$$\bar{E} = \bar{V} - \bar{I}(r + j\ x_l) \tag{3.3}$$

Where, $\bar{V}$ is the motor's applied voltage per phase, $\bar{E}$ is the corresponding phasor of the induced emf in this phase, r and x_l is the stator resistance and the leakage reactance per phase.

The voltage drop across the stator resistance and the leakage inductance is insignificant at relatively high speed operation and can be neglected. However, this voltage drop can not be neglected at low operating speed and should be compensated for in order to maintain the same airgap flux in the machine, [151]. Consequently, the machine speed can be fully controlled through controlling the magnitude of the applied

supply voltage and the corresponding supply frequency. A family of Torque-speed curves is depicted in Fig.3.1 at different supply voltages and frequencies such that (V/f) is constant. Speeds above the rated speed of the motor can be obtained by holding the line voltages at their rated values, while increasing the supply frequency, thus reducing the airgap flux, which is commonly known in the literature by the flux weakening region or constant power region, [151].

The desired line voltage and frequency are commonly obtained using reference voltage control signals which are converted to switching commands to the power switches in the inverter bridge using the well known PWM technique, [7,151]. The main concept of this technique is to compare theses reference signals with a carrier signal. The frequency of this carrier signal is usually chosen to be much higher than the fundamental frequency. This well established technique is known as Pulse Width Modulation "PWM" technique and is covered in text books and other publications, [7,151].

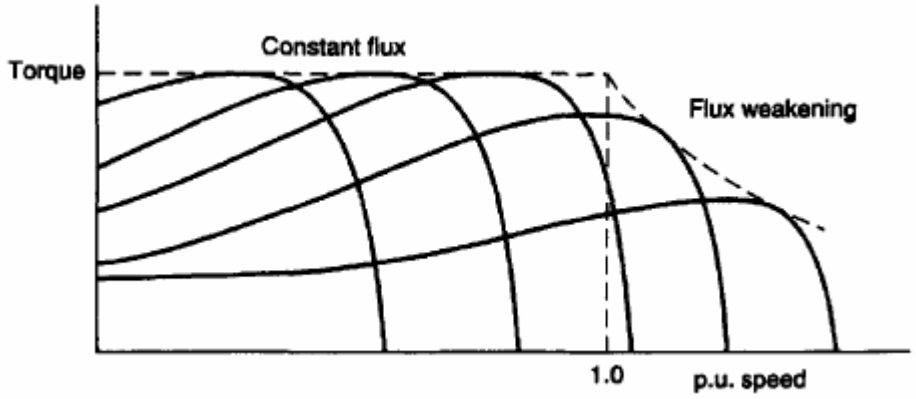

Fig.3.1 Torque-speed characteristics at variable frequencies, [2].

3.3 Analysis of Delta-connected stator windings in induction motors under two-phase open-Delta operation upon winding failures

Since the focus of this research is on Delta-connected three-phase induction motors, it is very important to review the basic differences between Wye-connected induction motors and Delta-connected induction motors from the design prospective, as well as from the operational prospective. The concept of Wye and Delta connections is well defined and established in electrical power systems and electrical machines for more than a century, [2,111,151]. The main intention of this section is to understand the advantages and disadvantages of using Delta- connection in induction motor stator windings either under normal condition or in the case of two-phase open-Delta mode of operation.

For healthy "normal" operation, the advantages of a Delta-connected stator winding connection can be summarized as follows, [2,111,151]:

- For the same power rating, the Delta-connection has less current in the motor phase windings, which means reduced thermal losses, smaller machine size and higher efficiency compared to a Wye-connection.
- For the same number of turns, a Delta -connection results in higher airgap flux and consequently less volume to power ratio compared to a Wye-connection design.
- Delta-connected machines usually provide higher breakdown torque.

On the other hand, the disadvantages of Delta-connected stator phase windings can be summarized as follows:

- Delta-connected windings permit circulation of zero sequence currents as well as harmonic current components of the third order and its multiples. Circulation of these current components may increase thermal losses and elevate the winding temperature as well as reduce the motor-drive efficiency. Therefore, proper design should be considered to minimize the values of these current components as much as possible, if not eliminating them altogether through pitch, distribution, and skew winding factors.
- The fact that the line-to-line voltage is directly applied to motor phase windings, leads to more costly winding insulation with a higher class.

Generally, three-phase induction motors with Delta-connected stator windings are more common in high horsepower applications [2].

3.3.1 Two-phase operation of induction machine with Wye-connected stator windings

In case of two-phase open-Delta operation, the performance of induction motors with Delta- connected stator windings differs from the performance of their counterparts with Wye-connected stator phase windings,[152]. This is due to the differences in the physical connections between the motor phases in each connection type. For instance, let us consider a Wye-connected motor with a healthy stator, the relationship according to Kirchoff Current Law "KCL" between the motor phase currents can be expressed as follows:

$$i_a + i_b + i_c = 0 \tag{3.4}$$

The fact that the three-phase currents are shifted by 120 deg.elect in the time-domain and the phase windings are shifted from each other by a space angle of 120 deg.elec results in producing a perfect rotating MMF with a speed equal to the synchronous speed,[151,153]. In this case, two of the motor phase currents can be controlled independently which means that the system has two Degrees of Freedom (DOF).

Meanwhile, if another case was considered, such that phase a is electrically isolated, according to KCL the relationship between the currents in the other two-phases " phase b and phase c" can be expressed as follows:

$$i_b + i_c = 0 \tag{3.5a}$$

Hence, for this case, if $i_b = I_m \cos(\omega t)$, it follows that $i_c = I_m \cos(\omega t - \pi)$ (3.5b)

That means that the phase angle between the phase currents in the remaining two active windings is shifted from each other by 180 deg.elec. and this phase shift does not depend on the supply voltage and can not be externally controlled and the system will have only one DOF as depicted in Fig.3.2. In this case, the stator MMF for each phase can be expressed as follows:

$$\begin{aligned} f_a &= 0 \\ f_b &= F_{\max} \cos(\omega t)\cos(\theta - 120) = \frac{F_{\max}}{2}[\cos(\theta - \omega t - 120) + \cos(\theta + \omega t - 120)] \\ f_c &= F_{\max} \cos(\omega t - 180)\cos(\theta - 240) = \frac{F_{\max}}{2}[\cos(\theta - \omega t - 60) + \cos(\theta + \omega t - 60)] \end{aligned} \tag{3.6}$$

Therefore, the resultant stator MMF_s, can be expressed as follows:

$$MMF_s = f_a + f_b + f_c = \frac{\sqrt{3}}{2} F_{\max} \sin(\theta - \omega t) - \frac{\sqrt{3}}{2} F_{\max} \sin(\theta + \omega t) \tag{3.7}$$

In (3.7), $F_{\max} = \frac{4}{\pi} K_w \frac{N_{ph}}{P} I_m$, where; k_w is the stator winding factor, N_{ph} is the series number of turns per phase, P is the number of poles, and I_m is the magnitude of the current in this phase.

The above means that resultant stator MMF_s can be decomposed into two main components, one is rotating Counter ClockWise (CCW) with a speed equal to the synchronous speed, while the other is rotating ClockWise (CW) also with a speed equal to the synchronous speed. Therefore, there will be two induction-induced MMF components produced by the rotor corresponding to these two stator MMF components. One MMF is rotating CCW at synchronous speed and the other is rotating CW also at a speed equal to the synchronous speed. The interaction between these two stator MMFs, and their two corresponding rotor MMFs results in four torque components. The first component results from interaction between the forward MMF component of the stator and the forward MMF component of the rotor and this produces a dc torque component in the forward direction which is the developed torque by the machine. The second component results from the interaction between the backward MMF component of the stator and the backward MMF component of the rotor and this component results in a dc torque component with a direction opposite to the forward component and hence it is a drag torque that reduces the available net developed useful torque by the machine. The ratio between these two dc components varies based on the motor slip, [151]. At stand still, these two components are equal to each other, and therefore the machine can not develop a starting torque, [152]. The last two components result from the interaction between the stator forward MMF component and the rotor backward MMF component,

in addition to the interaction between the stator backward MMF component and the rotor forward MMF component. These components produce high torque ripples with a frequency equal to double the line frequency and an average torque equals zero. These torque ripples may produce high mechanical vibrations and would accelerate system wearout. In addition, these torque ripples may cause catastrophic failure at low speed operation where the frequency of these ripples may be equal to the resonant frequency of the mechanical system.

At this stage it should be pointed out that even for a healthy machine with a slight unbalance or with unbalanced voltage supply, the stator backward MMF component and the rotor backward MMF component may exist during normal operation. However, the magnitudes of these components are very small and do not have significant effect on the motor performance.

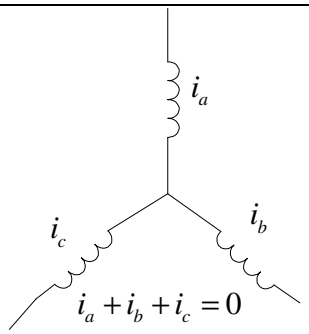

Fig.3.2a Wye-connected Stator winding during normal operation

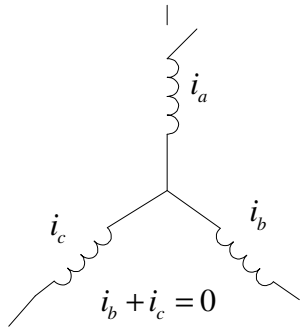

Fig.3.2b Wye-connected Stator winding during two-phase operation

3.3.2 Two-phase operation of induction machine with Delta-connected stator windings

The two-phase operation of an inverter-fed induction motor with Delta-connected stator phase windings has two possible configuration scenarios as depicted in Fig.3.3.

The first scenario is that one of the power lines connecting the supply voltage to the motor is disconnected as shown in Fig.3.3b. This might be due to a blown fuse, an accidental rupture in the cable connecting the drive to the motor, a faulty switch or failure of the gate drive circuit of a switch, [89]. The second scenario is that one of the phases in the stator winding is disconnected as shown in Fig.3.3c. This might be due to an accidental rupture in one of the motor phase windings, a loose connection between the internal motor coils, or disconnection of the winding upon detection of a fault by advanced fault diagnostic algorithms such as the ones reported in [43-62].The performance of the system in each of the above cases is completely different as described below.

In the first case, the supply to the motor will be equivalent to a single phase supply. The current in the motor windings will flow according to the current divider rule. The stator winding in this case is equivalent two parallel impedances. It can also be noticed here that the phase currents will have only one DOF and all the phase currents have to be dependent. Accordingly, the relationship between the phase currents can be expressed as follows:

$$i_a = -2i_b = -2i_c = I_{\max}\cos(\omega t) \tag{3.8}$$

The stator MMF for each phase of the stator winding can be expressed as follows:

$$\begin{aligned} f_a &= F_{\max}\cos(\theta)\cos(\omega t) = \frac{F_{\max}}{2}[\cos(\theta-\omega t)+\cos(\theta+\omega t)] \\ f_b &= \frac{1}{2}F_{\max}\cos(\theta-120)\cos(\omega t-180) = \frac{F_{\max}}{4}[\cos(\theta-\omega t+60)+\cos(\theta+\omega t+60)] \\ f_c &= \frac{1}{2}F_{\max}\cos(\theta-240)\cos(\omega t-180) = \frac{F_{\max}}{4}[\cos(\theta-\omega t-60)+\cos(\theta+\omega t-60)] \end{aligned} \tag{3.9}$$

Therefore, the resultant stator MMF can be expressed as follows:

$$MMF_s = f_a + f_b + f_c = \frac{3}{4} F_{\max} \cos(\theta - \omega t) + \frac{3}{4} F_{\max} \cos(\theta + \omega t) \tag{3.10}$$

Here again, $F_{\max} = \frac{4}{\pi} K_w \frac{N_{ph}}{P} I_m$

It can be noticed from (3.10) that the stator MMF is similar in nature to the stator MMF produced by a single phase induction motor with no auxiliary winding, [151]. Again, the machine can not develop a starting torque from stand-still, as the forward and the backward MMF components exist in the resultant stator MMF. In this case, the machine may operate with a high torque ripples equal to double the line frequency if a fault develops while the machine is rotating. However, it should be pointed out that the available developed torque will be dramatically reduced under such mode of operation.

In the second case, it is presumed that the motor windings are connected to the supply voltage. However, one of the motor phases is disconnected due to a fault as depicted in Fig.3.3c. Therefore, the relationship between the motor line currents, i_A, i_B, i_c and phase currents, i_a, i_b, i_c can be expressed as follows:

$$\begin{aligned} i_a &= I_{\max} \cos(\omega t - \phi) \\ i_b &= I_{\max} \cos(\omega t - \psi) \\ i_c &= 0 \\ i_A &= i_b - i_a \\ i_B &= -i_b \\ i_C &= i_a \end{aligned} \tag{3.11}$$

Where, ϕ and ψ are arbitrary phase angles which will be shown later to be controllable through the inverter operation.

In other words, examining (3.11) shows that the phase currents have two DOF, and the current in these two remaining active phases can be controlled independently. The MMFs

produced by the stator phase winding, presuming that "phase c" is the failed phase, can be expressed as follows:

$$\begin{aligned} f_a(\theta,t) &= F_{\max}\cos(\theta)\cos(\omega t-\phi) \\ f_b(\theta,t) &= F_{\max}\cos(\theta-120)\cos(\omega t-\psi) \\ f_c(\theta,t) &= 0 \end{aligned} \tag{3.12}$$

Therefore, the resultant stator MMF , F_s, can be expressed as follows:

$$\begin{aligned} F_s(\theta,t) = f_a + f_b + f_c &= \frac{1}{2}F_{\max}[\cos(\theta-\omega t+\phi)+\cos(\theta-\omega t+\psi-120)] \\ &+\frac{1}{2}F_{\max}[\cos(\theta+\omega t-\phi)+\cos(\theta+\omega t-\psi-120)] \end{aligned} \tag{3.13}$$

Examining (3.13) shows that the stator MMF consists of two main components, one is a forward MMF component and the second is a backward MMF component. The magnitudes of these components can be controlled by controlling the phase shift angles, ϕ and ψ. The backward MMF component of the stator can be set to zero by controlling the stator phase currents such that ψ-ϕ=60°[109-110]. This can be verified analytically as follows:

It follows from (3.13) that in order to eliminate the backward MMF component the following trigonometric identity should be satisfied:

$$\begin{aligned} &\cos(\theta+\omega t-\phi) = -\cos(\theta+\omega t-\psi-120) \\ &\textit{Therefore},\\ &\theta+\omega t-\psi-120 = \theta+\omega t-\phi+\pi \\ &\textit{Hence},\\ &\phi-\psi = \pi/3 \end{aligned} \tag{3.14}$$

In this case, the resultant stator MMF can be expressed as follows:

$$F_s(\theta,t) = f_a + f_b + f_c = \frac{\sqrt{3}}{2}F_{\max}\sin(\theta-\omega t) \tag{3.15}$$

Inspection of (3.15) shows that the magnitude of the remaining two active phase currents should be increased by a factor of $\sqrt{3}$.

This is in order to maintain the same stator MMF ($\frac{3}{2}F_{\max}$) in the airgap. In addition, eliminating the backward component of the stator MMF has two advantages. The first one is to increase the net developed torque produced by the machine. This is achieved by diminishing the dragging torque resulted from the interaction between the backward component of the stator MMF and the backward component of the rotor MMF. The second advantage is the alleviation of the torque ripples resulting from the interaction between the forward component of stator MMF and the backward component of the rotor MMF, and the interaction between the backward component of the stator MMF and the forward component of the rotor MMF.

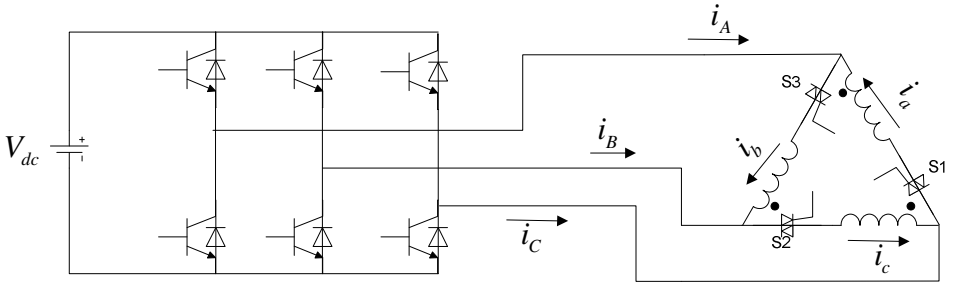

Fig.3.3a Inverter fed induction motor with a Delta-connected stator winding “three-phase operation”

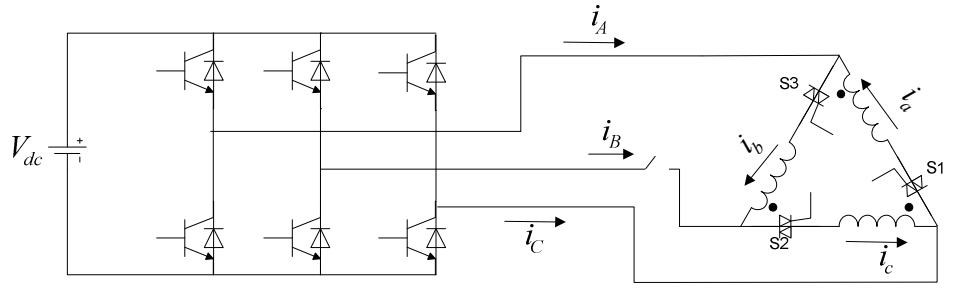

Fig.3.3b Inverter fed induction motor with a Delta-connected stator winding “single-phase operation”

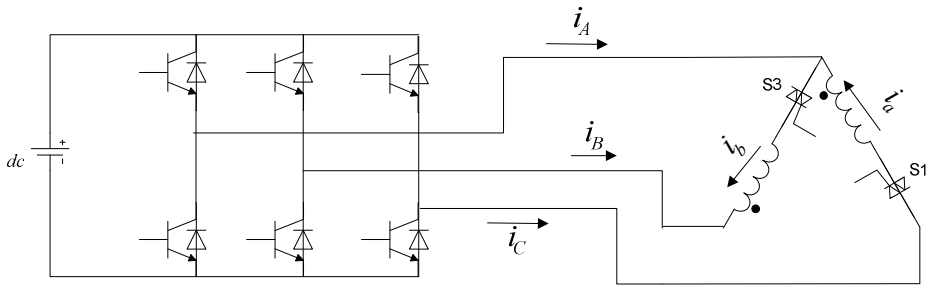

Fig.3.3c Inverter fed induction motor with a Delta-connected stator winding "two-phase open-Delta operation"

3.4 Previous work related to this investigation

As mentioned earlier in Chapter 1, most of investigations available in the literature, which centered on extending the survivability and reliability in motor-drive systems, are mainly focused on vector-controlled closed-loop drives rather than conventional open-loop drives with scalar constant (V/f) control. To the best of this author's knowledge, fault mitigation algorithms for open-loop constant Volts/Hz induction motor-drive systems are scarce to find in the literature, the exception is the work presented in [113-114]. The research presented in [113] was based on injecting current harmonics to neutralize the torque pulsations resulting from the single phase mode of operation of such polyphase motors. Meanwhile, the investigations in [102-103,115-117,122] were based on fault-tolerant stator winding designs that enable the machine to continue operation with an inter-turn short-circuit in one of its coils. The next section is centered on discussing, in more details, the control strategy introduced here that enables a three-phase induction motor to operate in the two-phase open-Delta mode of operation with the third of its phases (the faulty phase) electrically isolated.

3.5 An insight into the control strategy introduced here

The theoretical basics of the control strategy introduced here are applicable to any ac motor with Delta-connected stator windings. It is conceived in such a manner as to enhance the survivability of the motor-drive system, when a winding failure occurs in one of its' phases. This strategy does not require any special "fault activation algorithm" that alters the original motor-drive "operating algorithm". The analysis and discussion in this chapter is mainly focused on three-phase induction motors. The introduced compensation algorithm is intended to be activated immediately after the start-up of a machine. Hence it enhances the "robustness" of the existing open-loop scalar constant (V/f) control. Under healthy condition, conventional constant (V/f) control schemes are normally run in addition to the compensation control algorithm. It should be pointed out that the effect of the compensation algorithm on the overall control performance is negligible. Upon disconnecting one of the motor phases according to the second scenario described in sub-section 3.3.2, the output of the compensation algorithm will become dominant in order to diminish the backward MMF component of the stator due to the unbalance introduced by the faulty condition.

This new control strategy is based on the idea of multiple reference frames explored before in reference [135] with regard to the analysis of rectifier-inverter input currents and in reference [136] with regard to other applications such as controlling the output current of an Uninterrupted Power Supply "UPS". This is in order to provide a balanced set of currents even in the case of existing unbalanced loads, [136]. In such a case, unbalanced operation of UPS units result in high current ripples in their dc-link

capacitors and inductors, which may produce additional thermal stresses and significant reduction in such capacitor and inductor life-times. This is also the case for dc-link capacitors in drive systems, especially for the case of a two-phase mode of operation of a three-phase induction motor. In a motor-drive application with a Delta-connected motor, when one of the motor phases is disconnected, the currents flowing in the remaining active phase windings are highly unbalanced, and the resulting stator MMF is dependent on the phase shift between the currents flowing through the other two healthy phases as described before, see (3.13). Therefore, the compensation algorithm mainly controls the motor line currents to produce a near perfect rotating stator MMF only in the forward direction. This is achieved by forcing the stator backward MMF component to near zero through forcing the backward component of the stator current space-vector to zero. First, let us consider a healthy machine, the stator MMF can be expressed in space-vector notation as follows, [14]:

$$MMF_s = \frac{3}{2} N K_w \vec{i}_s \tag{3.16}$$

Where, $\vec{i}_s$ is the space-vector of the stator current and it can be expressed in terms of the three-phase currents and the complex operator $a = 1\angle 120^\circ$ as follows [14]:

$$\vec{i}_s = i_a + a i_b + a^2 i_c = I_s e^{j(\omega t - \theta)}$$

Now, when one of the phases is disconnected, the stator current space-vector can be decomposed into a forward component and a backward component as follows:

$$\vec{i}_s = \vec{i}_{sf} + \vec{i}_{sb}$$

Hence, the stator MMF that corresponds to these current components can be expressed as follows:

$$MMF_s = \frac{3}{2} NK_w \vec{i}_{sf} + \frac{3}{2} NK_w \vec{i}_{sb} \tag{3.17}$$

In (3.17), the first term represents the forward component of the stator MMF while the second term in (3.17) represents the backward component of that MMF. Consequently, the backward component of the stator current space-vector to near zero. Also, the three-phase line currents appearing on the side of the drive are thus rendered balanced with an amplitude value of each equal to the line currents under normal operation. This mean that modifications in the power structure of the drive are not required. A simplified diagram that describes the algorithms introduced here is depicted in Fig.3.4.

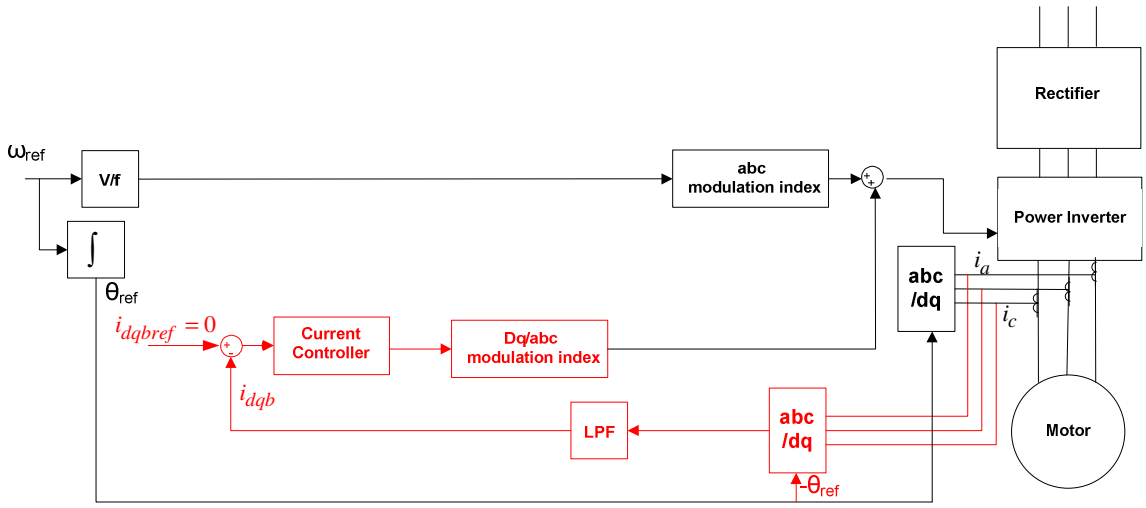

Fig.3.4a A simplified diagram for an open-loop scalar V/f control with the compensation algorithm.

As any conventional scalar constant (V/f) control, the ratio between the voltage and the frequency of the reference signal fed to the modulator is kept constant. In addition to this reference signal, the three-phase line currents are measured and transferred to a synchronous reference frame rotating backward in a Clock Wise (CW) at a speed equal to the synchronous speed. The angle, "θ_{ref}", see Fig.3.4a, used in the transformation is the result of the integration of the reference speed in electrical rad/sec,

and it is generated internally in the controller. In this frame of reference, the backward (CW) component of the stator current space-vector appears as a dc value in both the d-axis and the q-axis, while the forward Counter Clock Wise (CCW) component of the stator current space-vector appears as an ac component with a frequency equal to double the line frequency. This ac component is filtered through a low pass filter, while the dc components in the d-axis and in the q-axis are processed through two PI controllers to force these components to zero. At normal operation, for a balanced machine, the backward component of the stator current space-vector is very small or negligible. In this case, the dc component of the stator current space-vector in the synchronous CW frame of reference is almost zero. Consequently, the controller output will be negligible. Thus, in this case although the introduced compensation algorithm is activated during system's normal operation, the controller output is almost negligible or equal to zero. On the other hand, in the case of a two-phase open-Delta operation upon the failure of a third phase of the motor winding, the backward component of the stator current space-vector will have a significant value. This backward component will appear as a dc component in a CW synchronously rotating reference frame. Therefore, the introduced controller will act to drive this dc component to zero. The controller output is then added to the main reference signal normally generated in a conventional scalar constant (V/f) control system. The resultant summation is then fed to the modulator to generate the appropriate switching pattern. Forcing the backward component of the stator current space-vector to zero results in a balanced three-phase set of line currents with equal magnitudes and inter-phase shift angles of 120˚e. Meanwhile, the remaining two active phase currents are rendered with equal magnitudes and a phase shift angle of 60˚e, which leads to only CCW rotating

MMF component, recall (3.15). This can be explained as a result of the nature of a Delta-connected winding, in which the end (finish) of each phase is connected to the beginning (start) of the other, with phase-c deactivated, see Fig.3.3c. That is the corresponding active two-phase currents of phase-a and phase-b in a stator winding with open-Delta, are equal to each other in magnitude with a phase shift equal to 60˚e between each other. Hence, the overall result is a set of motor terminal line currents, i_A , i_B , and i_C, that are balanced with a sequential phase shift of 120˚e which results-in a balanced positive sequence set of three phase currents. This is because of the fact that, with reference to Fig.3.3c, one can state the following; $i_A=i_b-i_a$., $i_B=-i_b$, and $i_C=i_a$ (in other words, $i_a=i_C$, $i_b=-i_B$, and $i_c=0$). The relationship between the motor line current phasors $\overline{I}_A,\overline{I}_B,\overline{I}_C$ and phase current phasors $\overline{I}_a,\overline{I}_b,\overline{I}_c$ for the two phase-mode of operation is illustrated in the phasor diagram of Fig.3.4b.

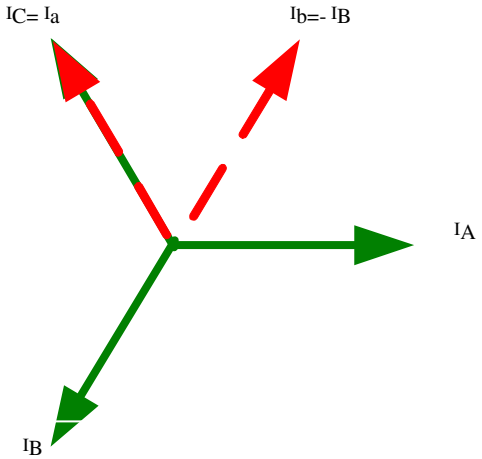

Fig.3.4b Phasor diagram of motor phase and line currents at two-phase open-Delta mode of operation (reference to Fig 3.4a and Fig.3.3c)

3.6 Controller Design

In this section, the design of the conceived controller is explained. This controller consists of two conventional PI controllers, [154].As mentioned before, this controller is

required to be running at both normal three-phase mode of operation, without any degradation of the system performance and in a two-phase open-Delta mode of operation. It is also required that the controller should be insensitive to most of the ac ripples that may exist in the input signals. It is well known that the induction motor can be simulated/emulated using various models with varying levels of complexity and order, depending on the applications and its performance requirements [155-156]. This can be starting from the simple first order model considering only the equation of motion up to more sophisticated models that can reach the order of 20,000 unknowns or more, such as in time stepping finite-element modeling of these inductions motors and associated drives [157-159]. The first step in the sound designing of any control system is to have an accurate model for the controlled system or plant. It is highly required to have as simple a model as possible, yet as accurate as possible. In our next discussion, two distinct models are explored here for use in the design of the system.

The first model is a fourth order state-space model in a synchronously rotating frame of reference that can be mathematically expressed by the following equations [25, 155-156]:

$$\begin{aligned} \dot{I} &= AI + BV \\ Y &= CI \end{aligned} \tag{3.17}$$

where,

$I = [I_d \ I_q \ I_{dr} \ I_{qr}]$ $,V = [V_d \ V_q \ 0 \ 0],$ $,Y = [I_d \ I_q \ 0 \ 0]$

$A = -L1^{-1}(R + L2)$

$B = L1^{-1}$

$$L1 = \begin{bmatrix} L_{ss} - L_{sm} & 0 & \frac{3}{2}L_{srm} & 0 \\ 0 & L_{ss} - L_{sm} & 0 & \frac{3}{2}L_{srm} \\ \frac{3}{2}L_{srm} & 0 & L_{rr} - L_{rm} & 0 \\ 0 & \frac{3}{2}L_{srm} & 0 & L_{rr} - L_{rm} \end{bmatrix}$$

$$L2 = \begin{bmatrix} 0 & \omega_s(L_{ss} - L_{sm}) & 0 & -\frac{3}{2}\omega_s L_{srm} \\ \omega_s(L_{ss} - L_{sm}) & 0 & \frac{3}{2}\omega_s L_{srm} & 0 \\ 0 & -\frac{3}{2}(\omega_s - \omega_r)L_{srm} & 0 & -(\omega_s - \omega_r)(L_{rr} - L_{rm}) \\ \frac{3}{2}(\omega_s - \omega_r)L_{srm} & 0 & (\omega_s - \omega_r)(L_{rr} - L_{rm}) & 0 \end{bmatrix}$$

$$R = \begin{bmatrix} R_s & 0 & 0 & 0 \\ 0 & R_s & 0 & 0 \\ 0 & 0 & R_r & 0 \\ 0 & 0 & 0 & R_r \end{bmatrix}$$

and

$$C = \begin{bmatrix} 1 & 0 & 0 & 0 \\ 0 & 1 & 0 & 0 \\ 0 & 0 & 0 & 0 \\ 0 & 0 & 0 & 0 \end{bmatrix}$$

In (3.17) L_{ss} is the stator self inductance.

L_{sm} is the stator mutual inductance.

L_{rm} is the rotor mutual inductance.

L_{srm} is the stator to rotor mutual inductance.

L_{rr} is the rotor self inductance.

ω_s is the motor synchronous speed.

ω_r is the rotor speed.

I_d is the d-axis component of the stator current

I_q is the q-axis component of the stator current.

I_{dr} is the d-axis component of the rotor current.

I_{qr} is the q-axis component of the rotor current.

V_d is the d-axis component of the applied voltage to the stator.

V_q is the q-axis component of the applied voltage to the stator.

R_s is the stator resistance.

R_r is the rotor resistance.

It can be noticed that the model described in (3.17) is considered to be linear if the equation of motion is not considered and the motor speed is considered to be constant and equal to "ω_r". Therefore, using classical control techniques system transfer functions, H(s), between the input voltages and output currents can be formulated as follows [161].

$$H(s) = \{C[SI - A]^{-1} B\} V(s) \tag{3.18}$$

This system is excited by a set of input line voltages, V_d and V_q

The second model is based on the fact that modern motor-drive systems usually operate at high switching frequency, in the range between 2 kHz and 15 kHz, [3]. At this fast electronic switching rate, the stator current will mainly depend on the applied voltages, V_d and V_q, stator resistance, R_s , rotor resistance, R_r , stator leakage inductances,

L_s , and rotor leakage inductance , L_r , all referred to the stator side. Accordingly in this case, a transient motor model can be mathematically expressed as follows [26]:

$$\frac{I_d}{V_d} = \frac{1}{(R_s + R_r) + (L_s + L_r)s}$$
$$\frac{I_q}{V_q} = \frac{1}{(R_s + R_r) + (L_s + L_r)s} \tag{3.19}$$

In this case-study, the parameters of a 5-hp, 6-poles, and Delta-connected three-phase induction motor are utilized in our analysis. This is a specially designed machine, [160], that can be configured either as a six-phase induction motor or a three-phase induction motor with it's stator connected either in a Wye or a Delta configuration. The design and the parameters of this machine are detailed in Appendix A. Meanwhile, the machine design procedure is detailed in [160].

In order to evaluate the performance of these models, their step responses are shown next. The transfer function of the first model expressed by (3.17) was calculated, using the matrix formulation given in (3.18) at two different speeds, at ω_o = 120 mech. rad/sec and at ω_o =60 mech. rad/sec. These transfer functions can be expressed for the 5-hp case-study motor as follows, [161]:

$$G_1(s) = \frac{I_d}{V_d} = \frac{I_q}{V_q} = \frac{139.7\ \ s^3 + 1.792e4\ \ s^2 + 7.752e6\ \ s + 2.445e8}{s^4 + 247\ \ s^3 + 8.641e4\ \ s^2 + 8.841e6\ \ s + 9.364e8} \tag{3.20}$$

$$G_2(s) = \frac{I_d}{V_d} = \frac{I_q}{V_q} = \frac{139.7\ \ s^3 + 1.792e4\ \ s^2 + 5.273e5\ \ s + 2.794e7}{s^4 + 247\ \ s^3 + 3.468e4\ \ s^2 + 2.382e6\ \ s + 6.915e7} \tag{3.21}$$

Meanwhile, the transfer functions of the second motor model expressed by (3.19) were accordingly obtained as follows:

$$G_3(s) = \frac{I_d}{V_d} = \frac{I_q}{V_q} = \frac{1}{0.0073066\ \ s + 1.038} \tag{3.22}$$

As depicted in Fig.3.5, it can be noticed that the step responses of the two model's transfer functions given in (3.20),(3.21), and (3.22) are very close to each other for high switching frequencies "greater than 2 kHz". Here, it was assumed that the step input was applied to the system at time, t=1sec, and the duration of the response of interest corresponds to a switching frequency of 2 kHz, which yield a cycle period of 0.0005 sec. Notice here that the input voltages, V_d and V_q . The period of interest is from 1.00 sec to 1.0005sec. Therefore, the second model expressed in (3.19) was chosen for the design of the controller gains due to its simplicity and reasonable accuracy.

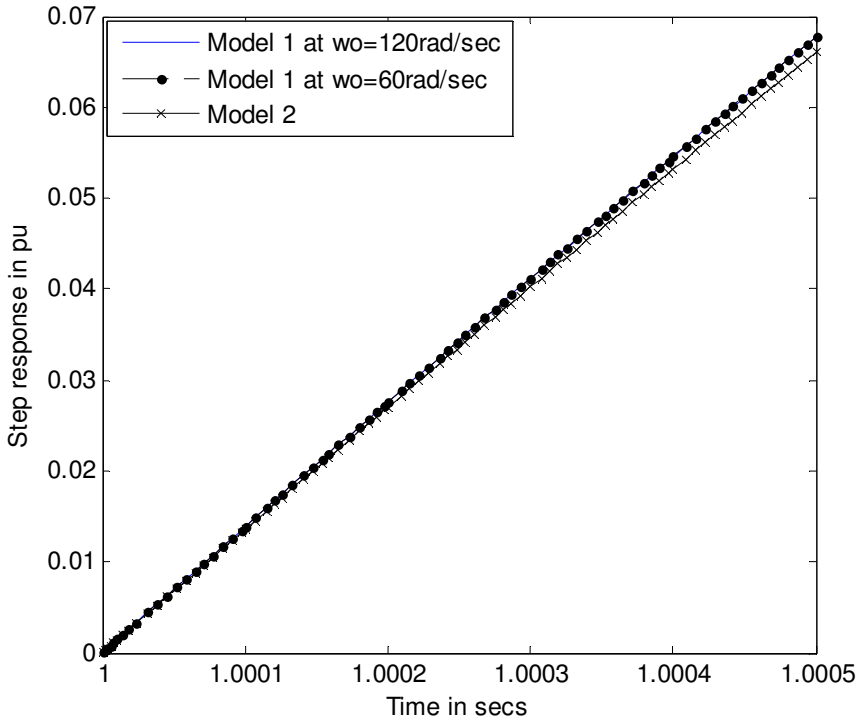

Fig.3.5 Step response for the three models

3.6.1 Controller design procedure

The controller design problem is that corresponding to the system/plant transfer function given by (3.22). It is required to design a PI-controller in the discrete domain to

yield design requirements in a synchronously rotating frame of reference that can be summarized as follows:

- Steady-state error <1%.
- Overshoot<5%
- The closed-loop system should have a disturbance gain less than -3dB for disturbance frequencies greater than 5Hz (31.4 rad/sec). These disturbances are mainly originating from the ac ripples resulting from the existence of the forward component "rotating CCW" of the stator current space-vector in the CW synchronously rotating frame of reference utilized in this controller.

Given the system transfer function in the continuous time-domain $G_3(s)=I_d/V_d=I_q/V_q = 1/(0.0073066\ s+1.038)$, and the PI-controller transfer function, $C(s) = K_p + (K_i/s)$, also in the continuous time-domain , it is required to calculate the values of the gains K_p and K_i that render the closed-loop system response conforming to the same design specifications given above. However, since this controller has to be implemented in a digital DSP chip, it is more rational to design the control system in the discrete time-domain. Consequently, this requires converting the motor model from the continuous time-domain to the discrete time-domain. A time step of 2μsec was chosen for the best accuracy which matches the simulation time step, as will be discussed later in the next section. Meanwhile, the sampling time for the controller was chosen to be 100μsec to match the actual implementation in the DSP chip. It can be noticed that for this case, it is required to drive the dc component to zero. In other words, one should aim at driving the backward component of the stator current space-vector to zero, and at the same time reject (or render the controller insensitive to) the ac ripples resulting from the existence of

the forward component of the stator current space-vector. The closed-loop system was implemented in MATLAB/Simulink as depicted in Fig.3.6. It should be noticed here that the ac ripples are presented as a disturbance added to the feedback signal.

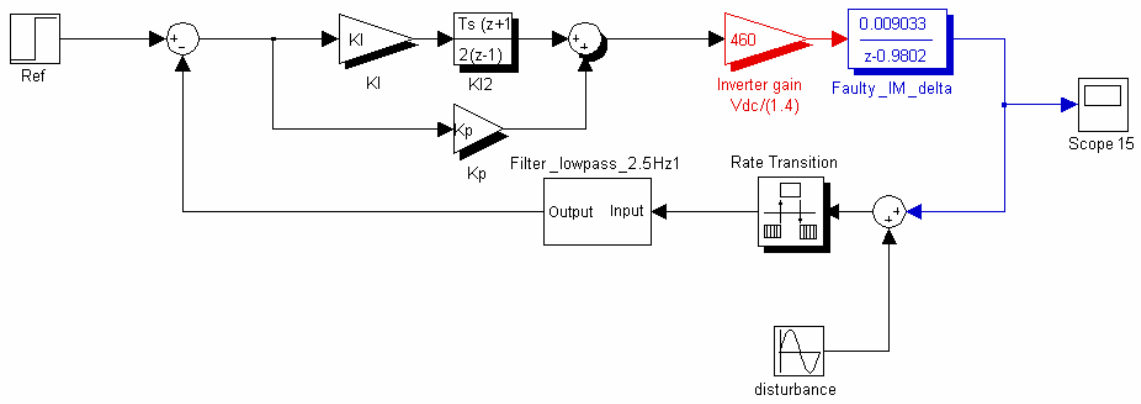

Fig.3.6 CW current control loop in the discrete time-domain

Therefore, based on the above, it is required here that one should find the proper values of K_p and K_i to achieve the stipulated design goals. The controller was deigned using conventional Bode-plot technique as described in [154] and MATLB Control-Design tool-box, [162], the system was discretized using approximated zero order hold method "ZOH", [162]. The low pass filter in Fig.3.6 is a first order low pass filter that has a gain equals to 0.0007848, a zero at z=-1, and a pole at z=0.9984 in a discrete domain with a sampling time equals 100μsec. This design yields an over damped filter response with a cut-off frequency that is equal to 2.5Hz. The open-loop and the closed-loop Bode plots are depicted in Fig.3.7 through Fig.3.9 for controller gain values, K_p =0.01 and K_i =0.1 which yielded the required design performance. It can be noticed from the system Bode-plot closed-loop disturbance response that the cut-off frequency of the closed-loop system is 5Hz (31.46 rad/sec), which guarantees high degree of rejection of the ac ripples. On the other hand, it can be noticed that the closed-loop system has a steady state error

less than 1%. Therefore, it can be concluded that this controller design is valid only for applications where the inverter supply frequency is greater than 5 Hz "which corresponds to ac ripples in the CW synchronous frame greater than 10 Hz". It should be pointed out that controller gains should be modified for applications that require a supply frequency less than 5 Hz. In general, the cut-off frequency of the closed-loop system should be less than twice the supply frequency. Otherwise, the ac ripples will propagate through the control system and will be amplified, which might cause unstable operation.

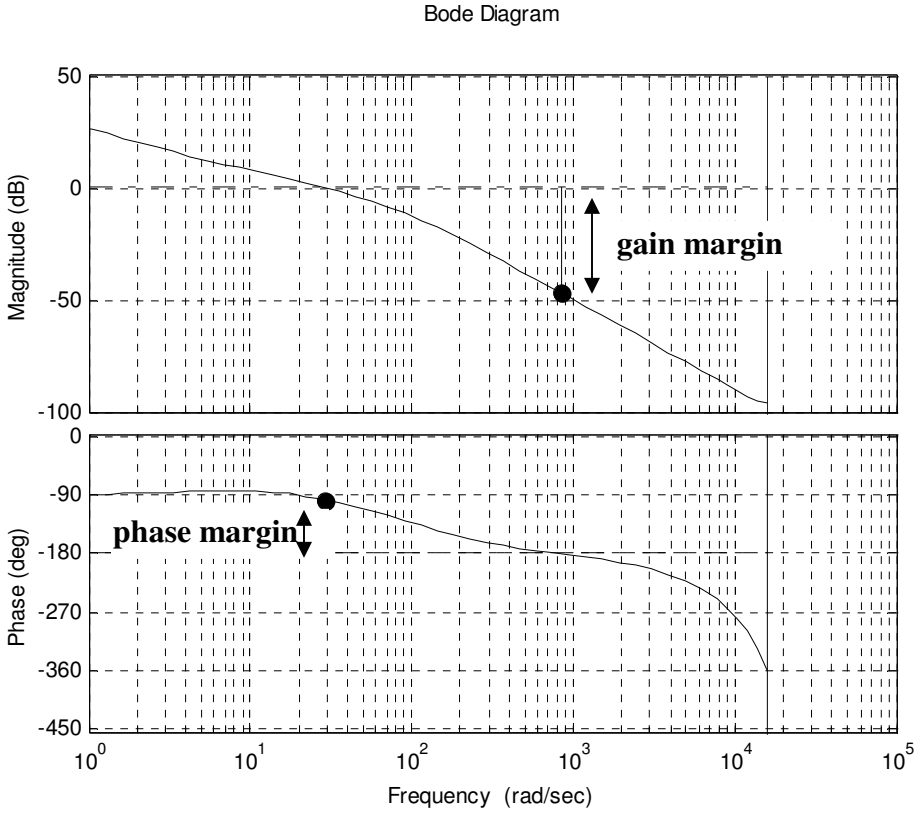

Fig.3.7 open-loop response for K_p =0.01 & K_i =0.1

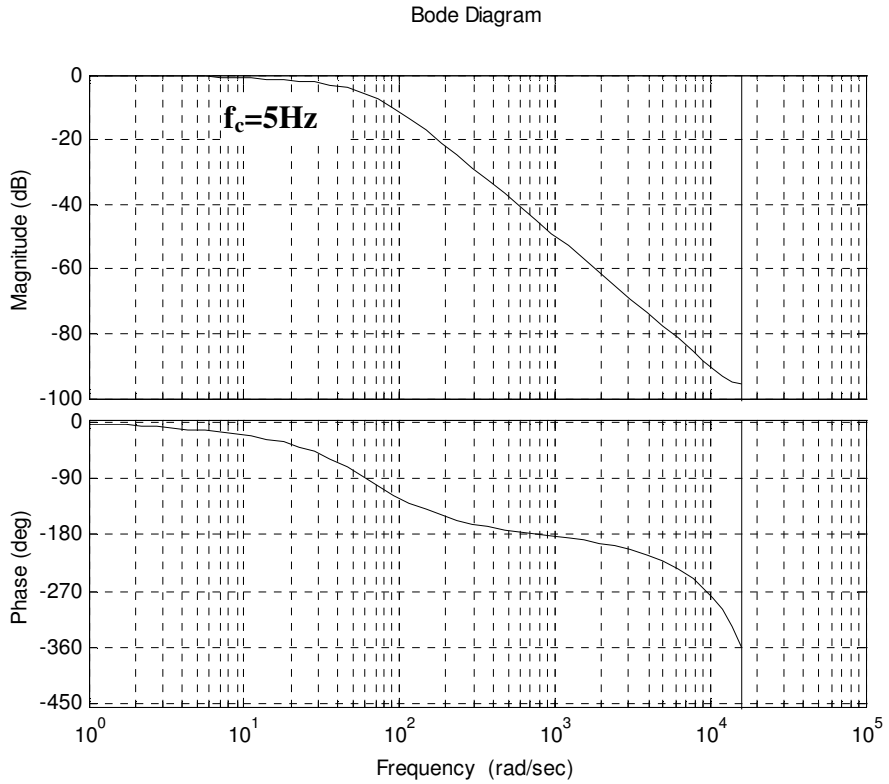

Fig.3.8 closed-loop response for Kp =0.01 & K_i =0.1

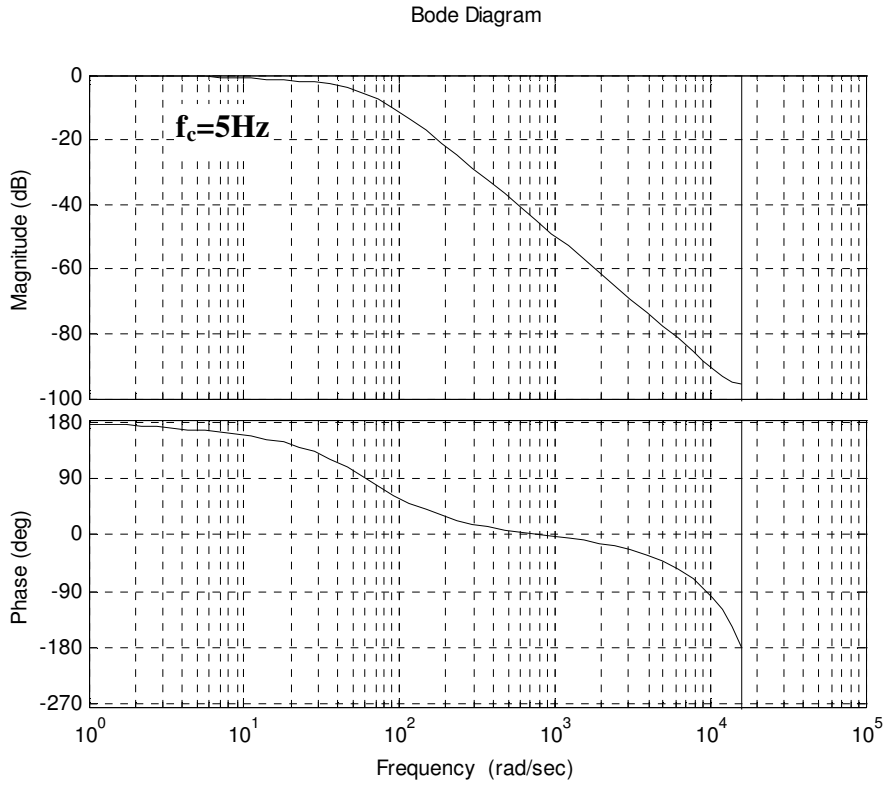

Fig.3.9 closed-loop disturbance response for Kp =0.01 & K_i =0.1

3.7 Simulation Work

As mentioned earlier, the simulation work was carried out using two different models. The first model is entirely implemented in MATLB "Simulink toolbox and Simpowersystem toolbox". The second model is implemented using MATLAB Simulink toolbox and commercial Finite element software, namely, Flux2D. The details of each model are given below.

3.7.1 An insight into the first simulation model

In the first model, a time-domain simulation that includes the system controller, the model of the drive including the transistors' switching effects, and lumped parameter model of the case-study 5-hp motor, see Appendix A and [160] for motor parameters and detailed motor design. The motor is modeled using the d-q stationary reference frame, in which saturation and effects of space harmonics higher than the fundamental airgap flux are neglected. In this frame of reference, the mathematical motor model is defined by the following equations [26]:

$$
\begin{aligned}
V_{qs}^{s} &= R_s i_{qs}^{s} + \frac{d}{dt}\psi_{qs}^{s} \\
V_{ds}^{s} &= R_s i_{ds}^{s} + \frac{d}{dt}\psi_{ds}^{s} \\
0 &= R_r i_{qr}^{s} + \frac{d}{dt}\psi_{qr}^{s} - \omega_r \psi_{dr}^{s} \\
0 &= R_r i_{dr}^{s} + \frac{d}{dt}\psi_{dr}^{s} + \omega_r \psi_{qr}^{s} \\
\psi_{ds}^{s} &= L_{ls} i_{ds} + L_m (i_{ds} + i_{dr}) \\
\psi_{qs}^{s} &= L_{ls} i_{qs} + L_m (i_{qs} + i_{qr}) \\
\psi_{dr}^{s} &= L_{lr} i_{dr} + L_m (i_{ds} + i_{dr}) \\
\psi_{qr}^{s} &= L_{lr} i_{qr} + L_m (i_{qs} + i_{qr})
\end{aligned}
\qquad (3.23)
$$

In (3.23), V^s_{qs}, and V^s_{ds} are the applied three-phase voltage components in the stationary d-q frame of reference. Meanwhile, in (3.23),

R_s is the stator resistance,

i^s_{qs} and i^s_{ds} are the balanced stator current components in the stationary d-q frame of reference,

Ψ^s_{ds} and Ψ^s_{qs} are the stator flux components in the stationary d-q frame of reference,

Ψ^s_{dr} and Ψ^s_{qr} are the rotor flux components in the stationary d-q frame of reference,

ω_r is the rotor speed,

R_r is the rotor resistance,

L_{ls} is the stator leakage inductance,

L_{lr} is the rotor leakage inductance,

L_m is the mutual inductance between the stator and the rotor.

The time-step of this model's simulation was chosen to be 1μsec to represent the power-electronic switching effects, while the controller sampling time was chosen to be 100μsec to replicate the actual implementation in the DSP chip used in the drive associated with this experimental work. The functional block diagram of the model is depicted in Fig.3.10, for which the controller subsystem is depicted in Fig.3.11. Notice here that an additional switch was utilized to simulate the case of open-coil/winding-rupture by opening this switch.

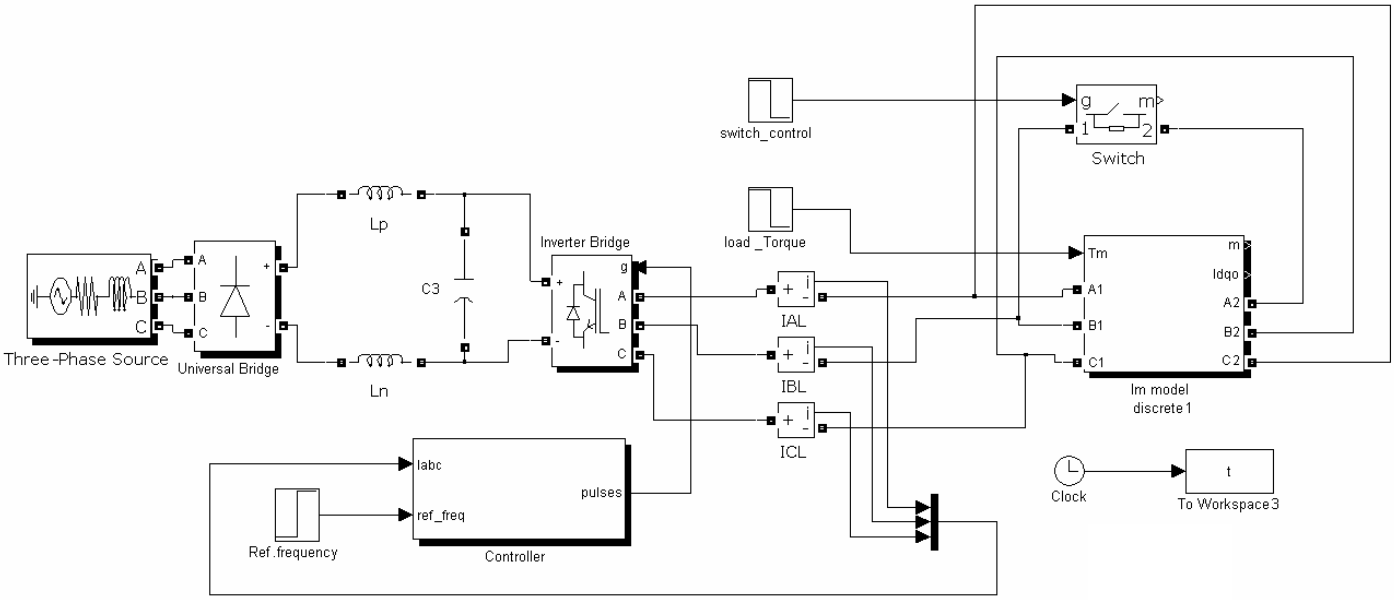

Fig.3.10 Simulation model implemented in MATLAB

3.7.2 An insight into the second simulation model

The second simulation model is a time-domain simulation that includes the system's controller model implemented in MATLAB/Simulink toolbox linked to a detailed TSFE software representation of the case-study motor that includes rigorous representation of the effects of MMF space harmonics and magnetic circuit configuration, as well as magnetic nonlinearities due to saturation. Meanwhile, electric transients due to power electronics transistor switching are not accounted for in this model, because the controllers' signals are assumed to operate two idealized instantaneously varying time-domain controlled voltage sources feeding lines (AB) and (BC) at the terminal of the motor, which are an "emulation" of the output voltage of the inverter. The inverter gain is only included where this gain equals (Vdc/$\sqrt{2}$) for the space-vector PWM, [26, 7], which was utilized in both the simulation and the experimental work.

The controller is linked to the TSFE software "MAGSOFT-Flux2D" through "Simulink to Flux2D block" hosted in the Simulink simulation model, [163], as shown in Fig.3.12. In this model, the calculated voltage is passed to the TSFE motor model, and the output currents are passed back from the TSFE software to the controller implemented in the Simulink environment for each time step. In addition to the advantage of including MMF space harmonics and saturation effects in this model, several magnetic quantities are also available such as airgap flux densities and nodal magnetic vector potentials. Knowledge of these magnetic quantities is highly desirable to thoroughly analyze the machine performance. The case-study motor is a six-pole induction motor, which is designed such that it can be configured either as a six-phase or as three-phase induction motor, with the stator connected either as Wye or Delta. The stator consists of 36 stator slots and 45 rotor bars with closed slots. These design particulars implied the existence of the third, fifth and seventh harmonics in the phase currents and fifth, and seventh harmonics in the line currents. The total harmonic distortion "THD" for the line current is 1.6% and the THD of the phase current is 3%. Again, the detailed motor design and parameters are elaborated on in Appendix A while detailed analyses of this case-study motor with its design procedure were included in [160]. Table 3.1 summarizes a comparison between the two models.

	First model	Second model
Modeling technique	MATLAB Simulink and Simpowersystem	MATLAB Simulink linked to Flux2D
Transistor switching effects	Included in the model	Not included in the model
Motor MMF space harmonics effects	Not included in the model	Included in the model
Magnetic saturation	Not included in the model	Included in the model
Step size	1μsec	100μsec
Magnetic Quantities	Not available in the model and can not be extracted	Available and can be extracted

Table 3.1 Comparison between the two simulation models

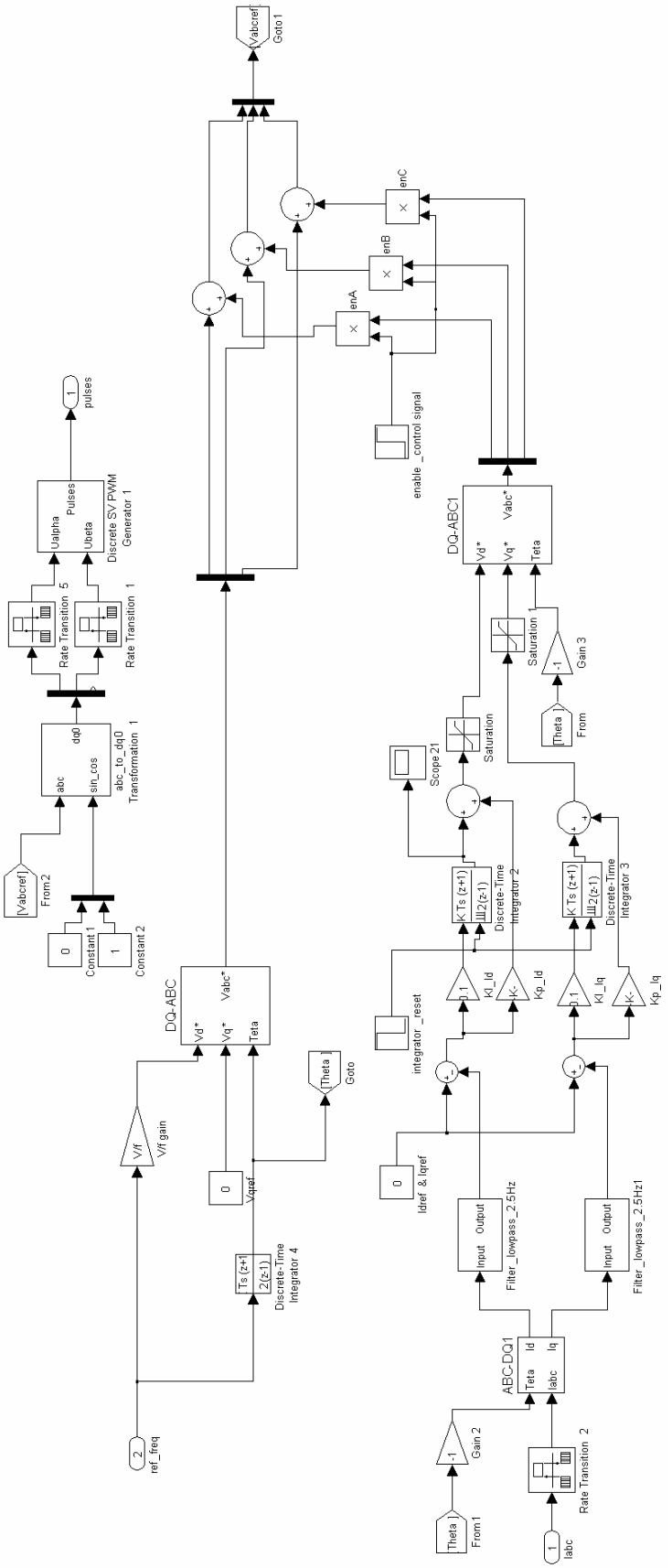

Fig.3.11 Controller Simulink Model

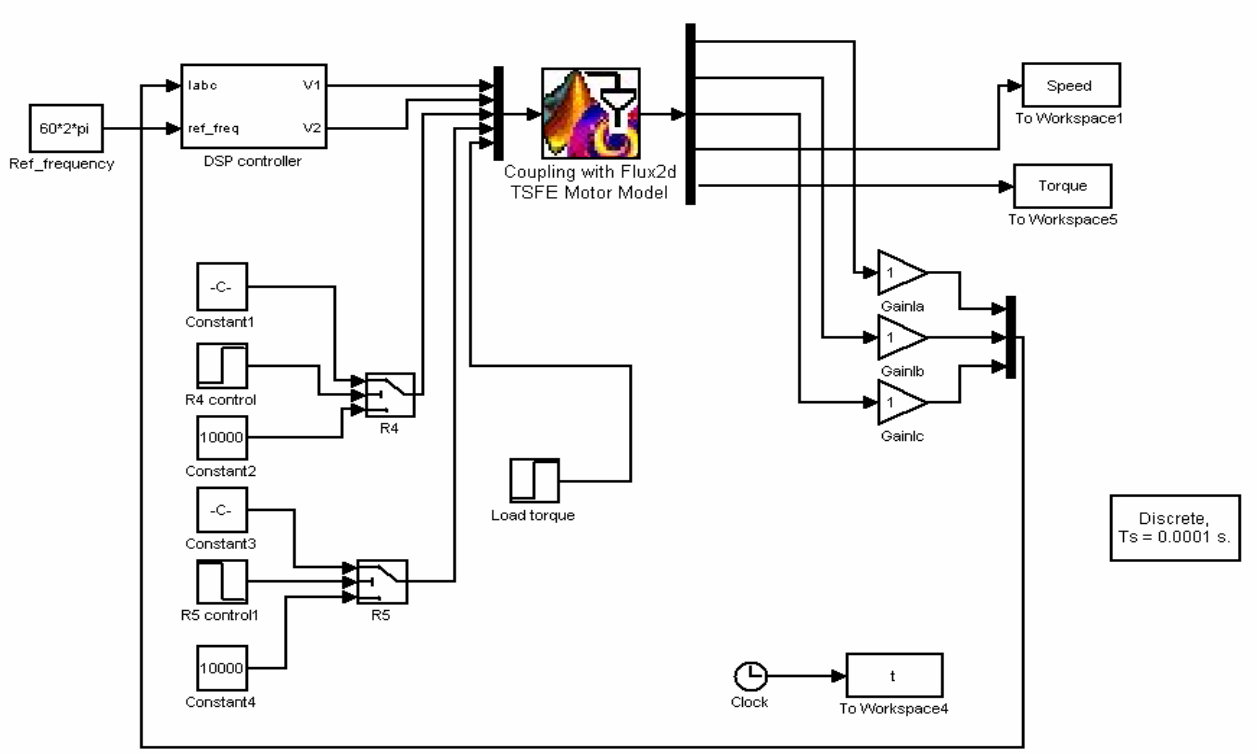

Fig.3.12 Simulation model implemented using Simulink/Flux2D link technology

3.8 Analysis of the simulation and experimental results

In order to examine the performance of the introduced technique discussed earlier, the motor-drive system was simulated and experimentally tested at several operating conditions. The power structure of a commercial drive was interfaced to a DSP board ezdsp F2812 from "Spectrum Digital" in which "TMS320F2812" is the main processor that hosted the algorithms introduced earlier,[164]. The currents sampling rate is 10 kHz. The conceived control algorithm was executed through an "interrupt service routine" called every 100μsec. The switching frequency is 10 kHz. A description of the experimental prototype and software implementation are discussed in Appendix B. The operation modes addressed in this section can be mainly divided to three categories. The first category is the normal "healthy" operation. In this category, the simulation and

experimental results were obtained for the case in which the new controller was deactivated and for the case in which this controller was activated. The main target of this category is to evaluate and verify the validity, accuracy, and the limitation of the models used in the simulation with respect to the actual experimental setup. This is in addition to investigating the effect of having this new controller activated during healthy "normal" operation. Analysis of the magnetic quantities is also provided through the TSFE model results. The second category is simulating the motor-drive system in the two-phase open-Delta mode of operation with and without having the new controller activated. Thorough analysis for the two separate cases is provided through comparing the experimental results with the Simulink/Simpowersystem simulation model, and the coupled MATLAB/Flux2D model. The third category examines the performance of the new controller "without altering the controller gains" for the case of two-phase open-Delta operation at 30Hz.

3.8.1 Healthy operation

The results presented here in Fig.3.13 through Fig.3.31 underline two main observations. The first one is to show the capabilities and the limitations of each one of the two models used in this analysis. As mentioned before, the model implemented in Simulink/ Simpowersystem includes the inverter switching effects and the interaction between the controller and the fundamental component of the motor MMFs. On the other hand, the coupled MATLAB/Flux2D model includes the controller action coupled to idealized controlled voltage source. However, this model fully includes the effects of the MMF space harmonics, as described in Appendix A. As will be seen throughout the forthcoming discussion, the space harmonics in the resultant airgap MMF can

significantly affect the system performance during abnormal operation. Examining the machine line current waveforms of Fig.3.13a and Fig.3.14a clearly shows the effect of the inverter transistor switching in introducing current ripples in these waveforms, see Fig.3.13a. The main frequency of these current ripples equals the PWM switching frequency, 10 kHz, and its associated side bands, which has been discussed and thoroughly analyzed in [7,165]. These various components are not in the scope of this work. Meanwhile, lower order harmonics such as the fifth and the seventh do not exist in the spectrum of the line currents waveforms depicted in Fig.3.13b. This is expected and it is due to the limitation of this model that assumes purely sinusoidal MMFs produced by the machine windings. Meanwhile, one should notice the existence of lower order harmonics with frequencies equal to the fifth and seventh multiplies of the fundamental in the line currents waveforms of Fig.3.14a and their associated spectrum depicted in Fig.3.14b, which were obtained from the detailed TSFE motor-drive simulation model. These harmonics in the line currents are mainly caused by the fifth and seventh space harmonics existing in the machine windings' MMFs which are inherently present in any detailed FE simulation of the machine's magnetic circuit. This model is as described in details in Appendix A. These harmonic components in the line currents are also noticed in the waveforms of the line currents obtained from the experimental test results which are depicted in Fig.3.15a and its associated spectrum depicted in Fig.3.15b. In addition, other harmonics of the second and fourth order can be observed in the spectrum of the line currents in Fig.3.15b.The existence of these harmonics may be due to inherent asymmetries either in the machine hardware (core, windings, etc) or in the drive, [7, 111]. It is also important to examine the waveforms of the motor phase currents which are

depicted in Fig.3.16a for the results obtained from the Simulink/Simpowersystem model. Again, current ripples with a frequency equal to the PWM switching frequency can be observed in the time-domain waveforms of Fig.3.16a. This is in addition to the lower order harmonics which are small enough to be ignored as shown in the spectrum of Fig.3.16b. Meanwhile, the phase current waveforms obtained using the Coupled Simulink/Flux2D TSFE model are depicted in Fig.3.17a, and their associated spectrum which is depicted in Fig.3.17b show the existence of a significant third harmonic component resulting from the third-order space harmonics in the machine's stator winding MMF. This is in addition to the presence of the fifth and seventh harmonics, which already can be observed in the line current. At this point, it should be pointed out that this third harmonic in the phase current waveform does not appear in the spectrum of the line current and does not produce any torque ripples in the machine in the healthy case. However, in a Delta-connection, this third harmonic current component circulates in the windings which may cause overheating if the machine is not properly de-rated. This third harmonic component is also observed in the phase current waveforms obtained from the experimental tests as depicted in Fig.3.18a and its associated spectrum in Fig.3.18b. In addition to this third harmonic component, it should be noticed that the phase current waveforms depicted in Fig.3.18a and its associated spectrum shown in Fig.3.18b contain the third, fifth and seventh harmonic components. Meanwhile, examining the time-domain torque profile obtained using Simulink/Simpowersystem model and shown in Fig.3.19a, and its associated spectrum depicted in Fig.3.19b, show the existence of torque ripples. The magnitudes of these torque ripples/harmonics are naturally small and are naturally filtered by the system inertia. These torque ripples are mainly caused by the

switching action associated with the inverter operation, [7, 72]. Meanwhile, the steady state torque profile resulting from the time-stepping simulation using the Simulink/Flux2D model, which is depicted in Fig.3.20a, and its associated spectrum depicted in Fig.3.20b, contain torque ripples/harmonics with a frequency mainly of the fourth order "240Hz" and sixth order "360Hz" of the 60-Hz fundamental frequency. It should be emphasized that these torque ripples shown in the spectrum of Fig. 3.20b are caused solely by the existence of the space harmonics in the machine's stator and rotor MMFs since the PWM inverter switching effect was not included in the Simulink/Flux2D model. Meanwhile, it should be re-emphasized that the torque ripples of Fig.3.19b are solely caused by the switching action of the inverter, since the space harmonic effects associated with the winding and magnetic circuit slotting layout are not included in the Simulink/Simpowersystem mode. Therefore, in tandom, the two models complement each other and both of them should be considered in order to carry out a comprehensive analysis of the system under study. The time-domain torque profile obtained from the experimental tests depicted in Fig.3.21a, and its associated frequency spectrum shown in Fig.3.21b, also contain torque ripples/harmonics with a frequency equal to the fourth and six harmonic orders of the 60Hz fundamental frequency. These torque harmonic components are the result of the harmonics produced due to the nonlinearities in the drive such as the dead-time effects in the switching process, ripples in the dc-link voltage, and also are due to the effect of the space harmonics inherent in the resultant airgap flux density waveform. In addition, a sub-harmonic with a frequency equal to 7 Hz is observed in the torque spectrum of Fig.3.21b. The existence of this sub-harmonic may be due to other effects such as the discrete nature of the PWM switching, ripples in the dc-

link voltage, dead time, etc, [7, 33, 35]. The analysis and compensation/mitigation techniques to reduce these sub-harmonics are detailed in [7]. Again, these aspects are beyond the scope of this research and are not considered in the present simulation and its corresponding experimental work. This airgap flux density is also depicted in Fig.3.22a with its associated spectrum in Fig.3.22b. The Magnetic Vector Potential "MVP" waveform over the six-pole mid-airgap arc is also shown in Fig.3.23 at a give instant in time in this TSFE solution. Again, both of the flux density and the MVP waveforms at mid-airgap circumference were obtained using the TSFE analysis software package "MAGSOFT-Flux 2D".

The second observation is that whether the new controller was deactivated or activated, the machine performance remained almost identical in both cases. This can be verified by examining the line current waveforms, phase current waveforms, and torque ripples depicted in Fig.3.24 through Fig.3.31. This verifies the notion that the newly introduced controller does not affect the system performance during normal operation, and it can be kept continuously activated after the machine starts regardless of its health status.

3.8.2 Two-phase open-Delta operation

The results presented from Fig.3.32 through Fig.3.50 document the performance of the motor-drive system, when the newly introduced controller was deactivated, and when this controller was activated for the two-phase open-Delta operation mode of the prototype three-phase induction motor used in this research. The results are shown at two different motor speeds corresponding to 60Hz and 30Hz voltage supply frequency.

The motor line current waveforms obtained using the simulation results of the Simulink/Simpowersystem model for the case of two-phase open-Delta mode of operation when the introduced controller was deactivated are depicted in Fig.3.32a when their associated frequency spectrum is shown in Fig.3.32b. It can be noticed that these currents are highly unbalanced with a significant negative sequence component. The existence of this negative sequence component has two undesirable effects that degrade the machine performance as elaborated on next. The first undesirable effect is that, in addition to the forward stator MMF component, MMF_{sccw}, and the forward rotor MMF component, MMF_{rccw} , a new backward stator MMF component, MMF_{scw}, *rotating* Clock Wise "CW" with a speed equal to synchronous speed is produced due to this unbalanced condition. This stator MMF will consequently induces a new backward rotor MMF component, MMF_{rcw}, which also rotates CW with a speed equal to the synchronous speed. The interaction between the forward stator MMF component, MMF_{sccw} , and the backward rotor MMF component, MMF_{rcw} produces torque pulsations with a frequency equal to double the line frequency. In addition, The interaction between the backward stator MMF component, MMF_{scw} , and the rotor forward MMF component, MMF_{rccw} produces torque pulsations with a frequency also equal to double the line frequency. The second effect is that the interaction between the backward stator MMF component, MMF_{scw} , and the backward rotor MMF component, MMF_{rcw} , produces a negative/drag torque opposite to the forward rotor rotation that reduces the net torque developed by the machine.

In addition to these torque pulsations produced due unbalance operation, the simulation results obtained from the time-stepping Simulink/Flux2D model show the

appearance of the third harmonic current component in the machine line current waveforms when the machine is running in the two-phase open-Delta mode of operation as depicted in Fig.3.33a and its associated frequency spectrum depicted in Fig.3.33b. As mentioned before, this third harmonic component is mainly caused by the space harmonics of the stator MMF, and in the healthy case, it appears only in the phase currents and not in the line currents because of the cancellation effect. It should be also pointed out that the existence of this third harmonic component in the phase currents for the healthy case causes only circulating current in the Delta-connected motor phase windings, and does not produce torque pulsations since the resultant flux due to this third harmonic component is identically equals zero. On the other hand, the third harmonic component in the motor phase windings will produce a resultant airgap flux in the case of the two-phase open-Delta mode of operation which will consequently produce torque ripples with a frequency equal to double the line frequency due to the interaction between the fundamental forward rotor MMF, and the third harmonic stator MMF component of the stator. Also, the interaction between the third harmonic stator MMF component and the induced backward MMF component of the rotor will produce torque pulsations with a frequency which equals four times that of the fundamental frequency. Again, it can be noticed that these harmonics do not appear in the results obtained using Simulink/Simpowersystem model, which does not include the effect of space harmonics associated with the machine's winding layouts and circuit slotting. In addition to the undesired torque pulsations resulting from the unbalanced operation of the machine, current unbalance dramatically reduces the expected lifetime of the dc-link capacitor and may eventually cause a premature failure of the drive, [136]. Meanwhile, the line current

waveforms obtained from the experimental tests for the same case are depicted in Fig.3.34a and their associated spectrums are depicted in Fig.3.34b. It can be noticed that the line current waveforms obtained from the experimental tests are in better agreement with the ones obtained from the time-stepping Coupled Simulink/ Flux2D model.

Using the Simulink/Simpowersystem model, the resulting line current waveforms for the case of the two-phase open-Delta mode of operation, when the newly introduced controller is activated are depicted in Fig. 3.35a, while their associated frequency spectrum is depicted in Fig.3.35b. The effectiveness of this newly introduced controller can be verified through comparing the unbalanced line current waveforms for the case of two-phase open-Delta operation, when the newly introduced controller was deactivated, see Fig.3.32a, and the balanced line current waveforms for the case of two-phase open-Delta operation, when this newly introduced controller was activated, see Fig.3.35a. These figures show that this controller has diminished the magnitude of the negative sequence component in the line currents which dramatically improves the output torque of the machine as will be demonstrated below. The corresponding simulation results for the same case using the time-stepping Coupled Simulink/Flux2D are depicted in Fig.3.33a, Fig.3.33b, Fig.3.36a, and Fig.3.36b in which the line current waveforms resulting from the two-phase open-Delta mode of operation are depicted in Fig.3.33a with its associated frequency spectrum is depicted in Fig.3.33b. The third, fifth and seventh order harmonic components can be observed in Figures 3.33b and 3.36b in the spectrum of the line currents for the case of the two-phase open-Delta mode of operation, when this controller was deactivated and while this controller was activated. The effectiveness of this newly introduced controller can be also verified through examining the unbalance in

the line currents depicted in Fig.3.33a for the case of the two- phase operation, when this introduced controller was deactivated, and when this controller was activated. However, it should be pointed out that this controller only compensates for the unbalance in fundamental components of the currents but not for the current harmonics in the motor windings. Meanwhile, the experimentally obtained line current waveforms for the case of the two-phase open-Delta mode of operation, when the new controller was deactivated are depicted in Fig.3.34a, while their associated frequency spectrum is depicted in Fig.3.34b. Meanwhile, the experimentally obtained line current waveforms for the case of two-phase open-Delta mode of operation, when the new controller was activated are depicted in Fig.3.37a, while their associated frequency spectrum is depicted in Fig.3.37b.It can be noticed that the experimental results are in close agreement with the simulation results obtained using Coupled Simulink/Flux2D. An increase in the magnitude of the third, fifth and seventh harmonic components which are existing in the spectrum of the motor line currents obtained from the experimental results can observed in comparison to the same components obtained from the time-stepping Coupled Simulink/Flux2D model. This may be attributed to the nonlinearity effects in the inverter such as the dead-time switching effects, ripples in the dc-link voltage…etc, [7,33]. The transient performance of the newly introduced controller was also examined through monitoring the magnitude of the negative sequence component of the line currents which is depicted in Fig.3.37c. It can be noticed that there is a sudden increase in the magnitude of the negative sequence component magnitude of the line currents at the instant that one of the phases was disconnected. However, this controller was able to reduce the

magnitude of the negative sequence component of the line currents to a value close to zero.

The presence of the previously explained time harmonics in the motor currents and the space harmonics in the motor MMFs have significant effects on the output torque of the machine the case of two-phase open-Delta mode of operation. This can be verified by examining the output torque profiles obtained from Simulink/Simpowersystem simulation for the case of the two-phase open-Delta mode of operation, when this controller was deactivated, versus the case when the controller was activated as shown in Fig.3.38a. A high torque ripples of 180% peak-to-peak of the developed torque can be observed for the case of two-phase open-Delta mode of operation, when the controller was deactivated, “case a”. It can also be observed from Fig.3.38b that the 120 Hz component is the dominant torque harmonic which is in agreement with the physical reasoning described earlier in this chapter. It can also be noticed from the output torque waveforms of Fig.3.38a and their associated spectrum depicted in Fig.3.38b that this harmonic is highly diminished when the controller was activated to a value approximately equal to 10% of the developed torque at steady state condition, “case b”. Meanwhile, the simulation results for the same two cases obtained from the time-stepping Coupled Simulink/Flux2D model are depicted in Fig.3.39a and their associated spectrum depicted in Fig.3.39b. Examining the results obtained from both Simulink/Simpowersystem model and Coupled Simulink/Flux2D model lead to two observations. The first observation is that torque ripples obtained from the Coupled Simulink/Flux2D model for the case of two-phase open-Delta mode of operation, when the controller was deactivated, are 133% peak to peak of the developed torque which is

less than the torque ripples obtained from the Simulink/Simpowersystem model. It should be pointed out that the torque ripples obtained from Simulink/Simpowersystem in the case of the two-phase open-Delta mode of operation are due to the backward MMF components, MMF_{scw} and $MMF_{rcw.}$ resulting from the unbalance in the machine as described earlier in this section. On the other hand, the torque ripples obtained from the Coupled Simulink/Flux2D include the torque ripples produced due to the interactions between the machine's MMF space harmonics, in addition to the torque ripples produced by the interaction between the stator backward MMF components, MMF_{scw} and $MMF_{rcw.}$, resulting from the unbalance in the machine currents and the forward MMF components MMF_{sccw} and MMF_{rccw}. Thus, the resultant torque ripples may randomly increase or decrease depending on the phase shift between the torque ripples produced due to the unbalanced operation of the machine and the torque ripples produced due to the interaction between the fundamental component of the airgap MMF and the third order harmonic component in the airgap. The second observation is that the peak to peak magnitude of the torque ripples depicted in Fig.3.39a when the introduced controlled was activated is slightly higher, 15% of the developed torque at steady state condition, than its counterpart obtained from the Simulink/Simpowersystem model, Again, this increase is resulting from the interaction between third harmonic MMF component and the fundamental harmonic MMF component in the airgap. In the experimental testing, the motor output torque was measured using a torque transducer that is mechanically coupled to the motor shaft, see torque transducer and torque measurement details in Appendix B. The torque profiles were measured when this controller was activated at steady state condition and for the case when this controller was deactivated under steady-state are

depicted in Fig.3.40a, while their associated frequency spectra are depicted in Fig.3.40b. Meanwhile, the torque profile at the instant of the transfer between the three-phase mode of operation and the two-phase open-Delta mode of operation is depicted in Fig.3.40c. This Fig.3.40c demonstrates the efficacy of this fault mitigation method and associated quality of the new controller in preserving the motor's torque quality under faulty operating conditions, almost to the same "goodness" of the healthy mode of operation.

The previous discussion demonstrates the effect of the newly introduced controller on the motor current, and torque pulsations. The main concept is that the controller is compensating for the unbalance in the machine through outputting a set of unbalanced voltages that render the resulting system currents to be almost in balance, thus minimizing the stator's backward MMF component. This is achieved through controlling the modulating signal. For instance, the modulating signal of the gate drivers of phases A and C while the controller was deactivated are depicted in Fig.3.41a, while the waveforms of Fig.3.41b depict the same modulating signals while the controller was activated. These signals were obtained during the experimental testing using a software data logger module provided by TI, [166].This software enables the user to obtain real time-domain waveforms of the values in the DSP internal registers. This fact can be also verified through examining the three line voltages, depicted in Fig.3.41c, that were obtained from a simulation run using Simulink/Flux2D model while the motor was running at open-Delta mode of operation with the introduced controlled activated The unbalance in the applied voltage also has a significant effect on the mid-airgap flux density waveform. The mid-airgap flux density waveform for the case of the two-phase open-Delta mode of operation, when the controller was deactivated is shown in Fig.3.42a,

while its associated spectrum depicted in Fig.3.42b. Examining the spectrum of Fig.3.42b shows the existence of the third order space harmonic in addition to the fifth and seventh order space harmonics as explained earlier. It is also important to highlight the fact that a third order time harmonic has also been observed in the motor line currents for the same case as explained earlier. Meanwhile, A significant increase in this third order and ninth order space harmonics in the mid-airgap flux density waveform for the case of the two-phase open-Delta mode of operation, when the introduced controller was activated is shown in Fig.3.43a, with its associated spectrum shown in Fig.3.43b. Meanwhile, the flux densities color shade plots are depicted in Fig.3.44a for the case of three-phase mode of operation when the introduced controller was activated, and in Fig.3.44b for the two-phase open-Delta mode of operation when the introduced controller was activated. These waveforms are given at the same time instant. Therefore, the compensation action of the controller renders a set of unbalanced voltages applied to motor terminals. The later is rendered as a distortion in the mid-airgap flux density waveform with a high percentage of the third and ninth order space harmonics. The increase in these third and fifth order harmonic components might also be attributed to the saturation in the machine's stator core which can be noticed by comparing the color shade plots of Fig.3.44b for abnormal two-phase open-Delta mode of operation and Fig.3.44a for normal three phase mode of operation. Six increased saturation spots can be observed in the color shaded plot of Fig.3.44b, see arrows, which corresponds to the number of poles in the machine. The existence of these increased saturation spots in the stator core can also be attributed to the effect of the absence of a phase current in winding C. These results could not have been

accessible without the use of the TSFE Coupled Simulink/Flux2D or similar TSFE model.

A one-to-one set of simulation and experimental results were also obtained for two-phase open-Delta mode of operation at 30Hz operating frequency, both when the newly introduced controller was deactivated and when this controller was activated, respectively. This was carried out in order to examine the controller performance at a different speed range without changing any software setting except for the reference speed. The effectiveness of the newly introduced controller was examined through comparing the line current waveforms obtained from Simulink/Simpowersystem model for the case of the two-phase open-Delta mode of operation when the controller was deactivated that is depicted in Fig.3.45a, and the two-phase open-Delta mode of operation when the introduced controller was deactivated that is depicted in Fig.3.45b. The corresponding results for these two cases obtained from the time-stepping Simulink/Flux2D model are depicted in Fig.3.46a and Fig.3.46b, respectively. Meanwhile, the results for these same two cases obtained from the experimental tests set-up are depicted in Fig.3.47a and Fig.3.47b, respectively. The time-domain torque profiles for the same operating frequency obtained from Simulink/Simpowersystem model for the case of two-phase open-Delta mod of operation when the controller was activated and when the controller was deactivated are depicted in Figures Fig.3.48a and Fig.3.48b, respectively. The results obtained from the time-stepping Simulink/Flux2D model for the same two cases are depicted in Fig.3.49a and Fig.3.49b, respectively. Meanwhile, the experimentally obtained torque profiles measured by the torque transducer for the same two cases are depicted in Fig.3.50. Again examining these figures

demonstrate the efficacy of the introduced controller in diminishing the unbalance in the line currents and minimizing the torque pulsations at the faulty two-phase open-Delta mode of operation.

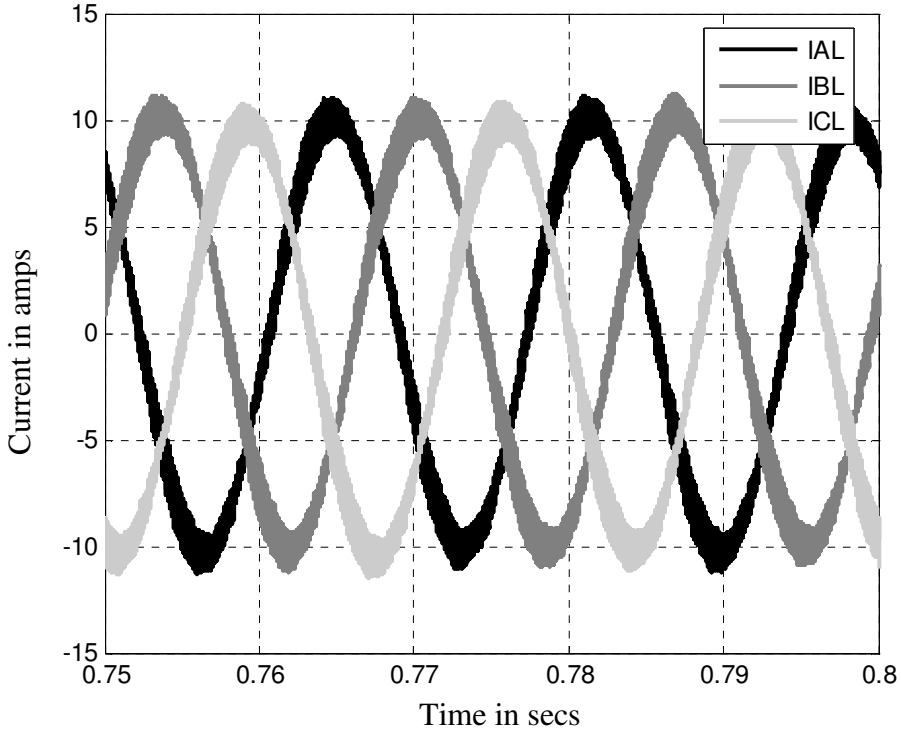

Fig.3.13a Line currents, open-loop, when the introduced controller was deactivated under healthy three-phase mode of operation, 60 Hz “Simulink/Simpower model”.

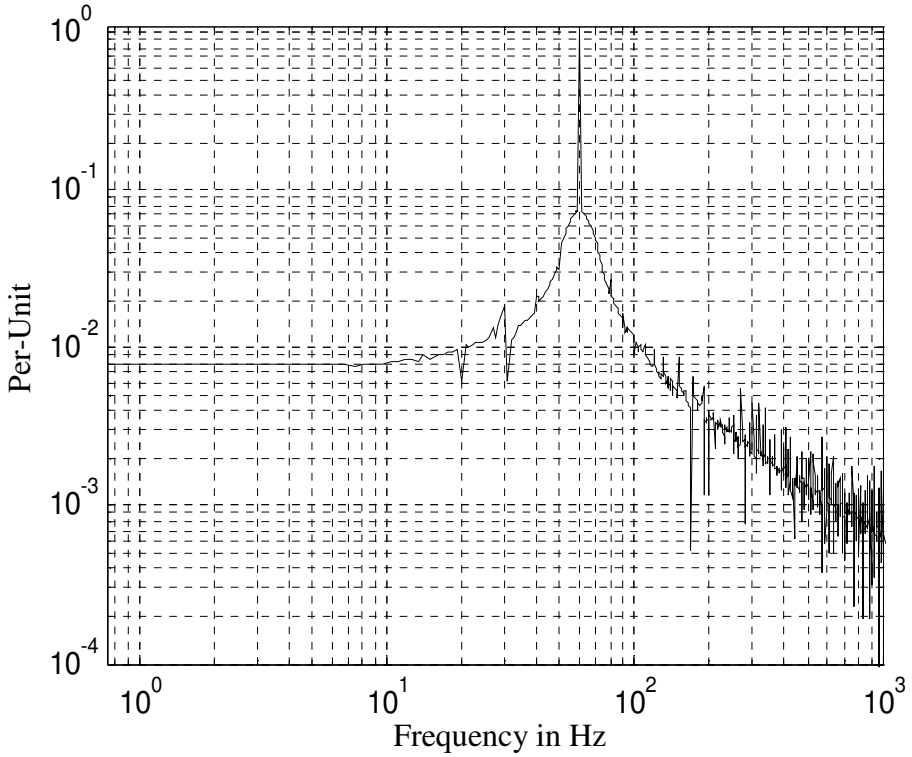

Fig.3.13b Line current spectrum, open-loop, when the introduced controller was deactivated under healthy three-phase mode of operation,60 Hz "Simulink/Simpowerswystem model".

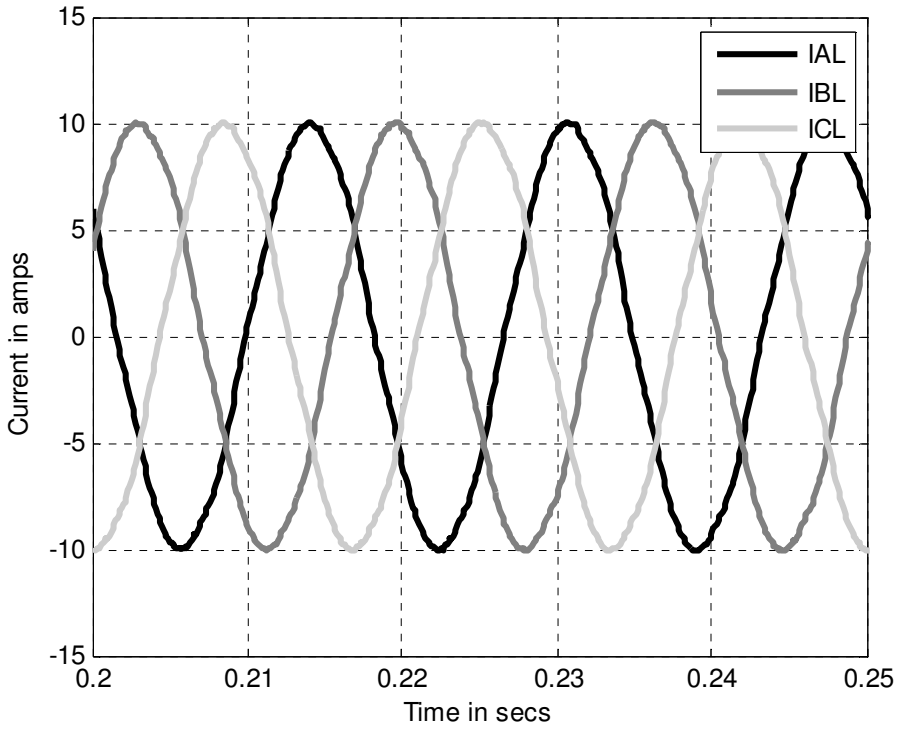

Fig.3.14a Line currents, open-loop , when the introduced controller was deactivated under healthy three-phase mode of operation, 60 Hz "Coupled Simulink/ Flux2D model".

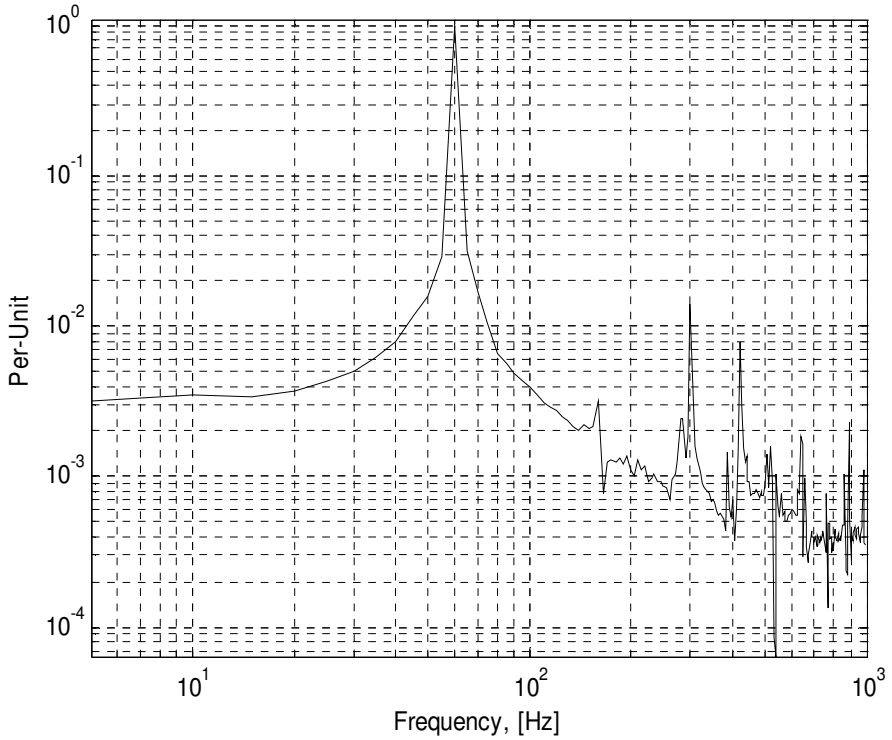

Fig.3.14b Line currents, open-loop, when the introduced controller was deactivated under healthy three-phase mode of operation, 60 Hz "Coupled Simulink/Flux2D model".

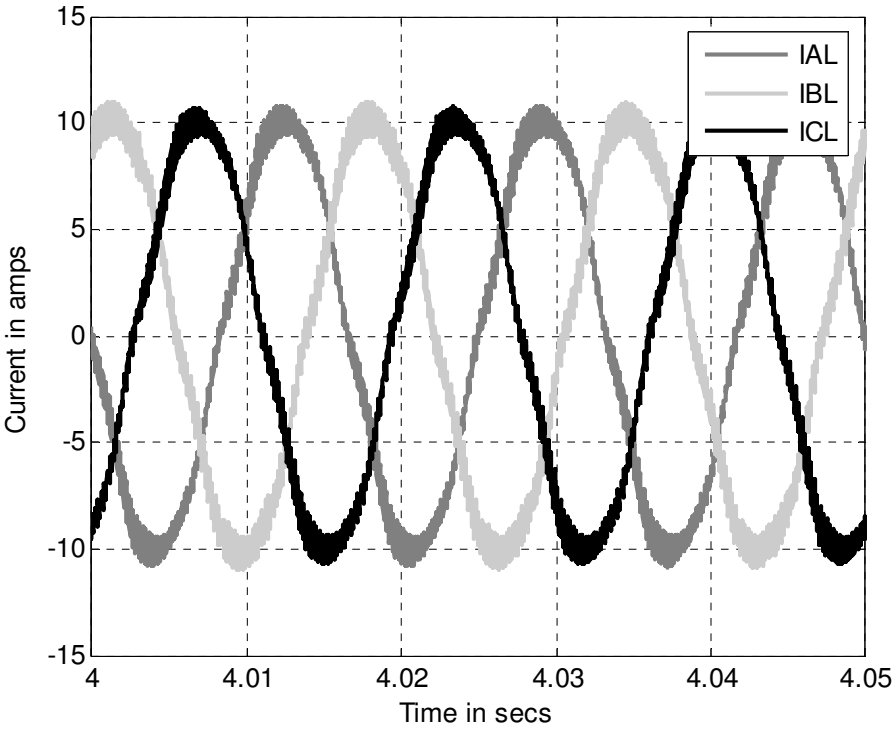

Fig.3.15a Experimentally obtained line currents, open-loop, when the introduced controller was deactivated under healthy three-phase mode of operation, 60 Hz.

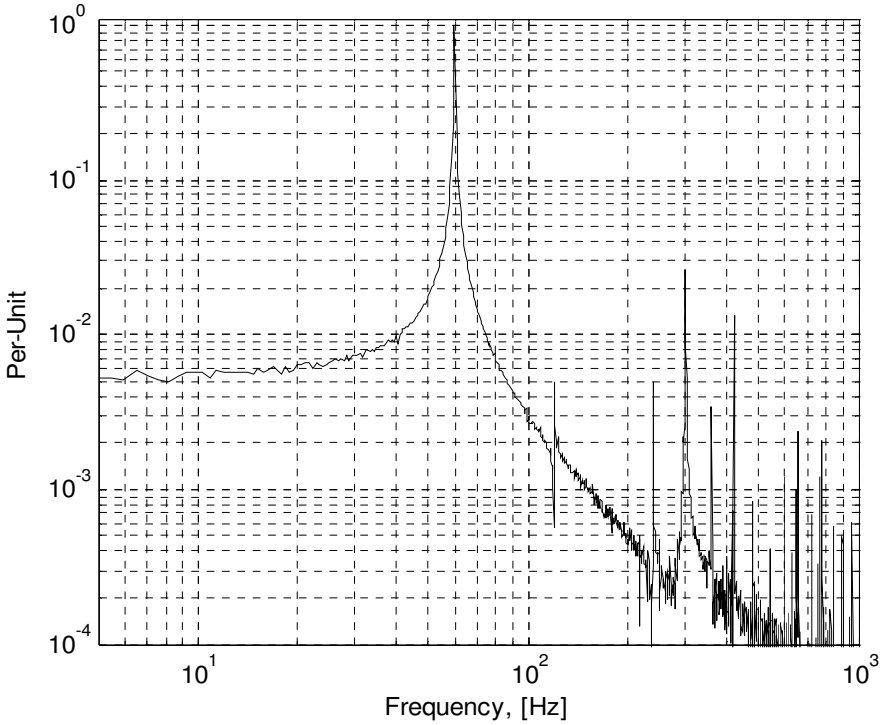

Fig.3.15b Experimentally obtained line current spectrum, open-loop, when the introduced controller was deactivated under healthy three-phase mode of operation, 60 Hz.

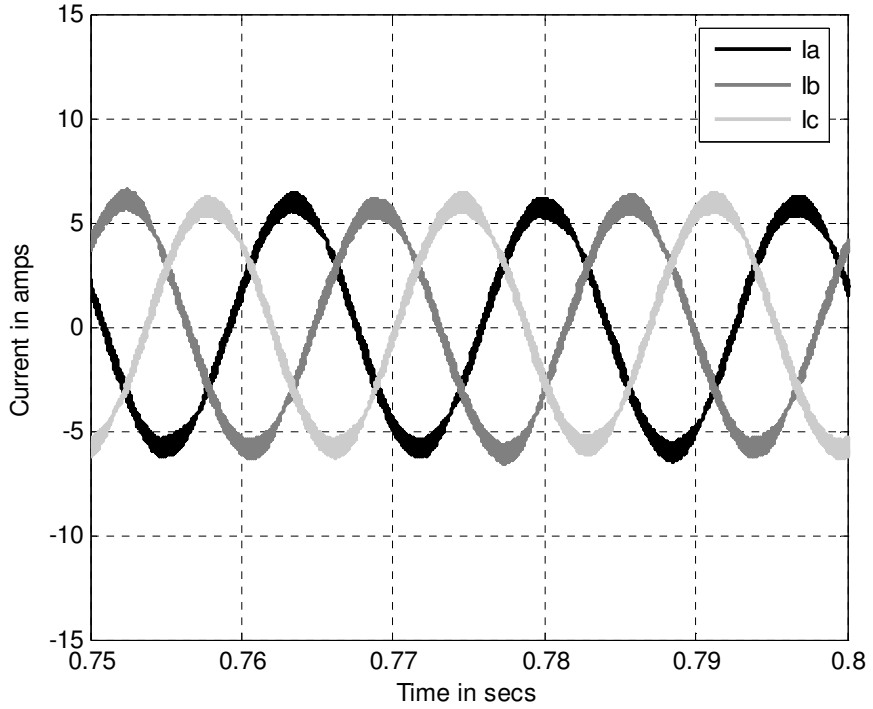

Fig.3.16a Phase currents, open-loop, when the introduced controller was deactivated under healthy three-phase mode of operation, 60 Hz "Simulink/Simpowersystem model".

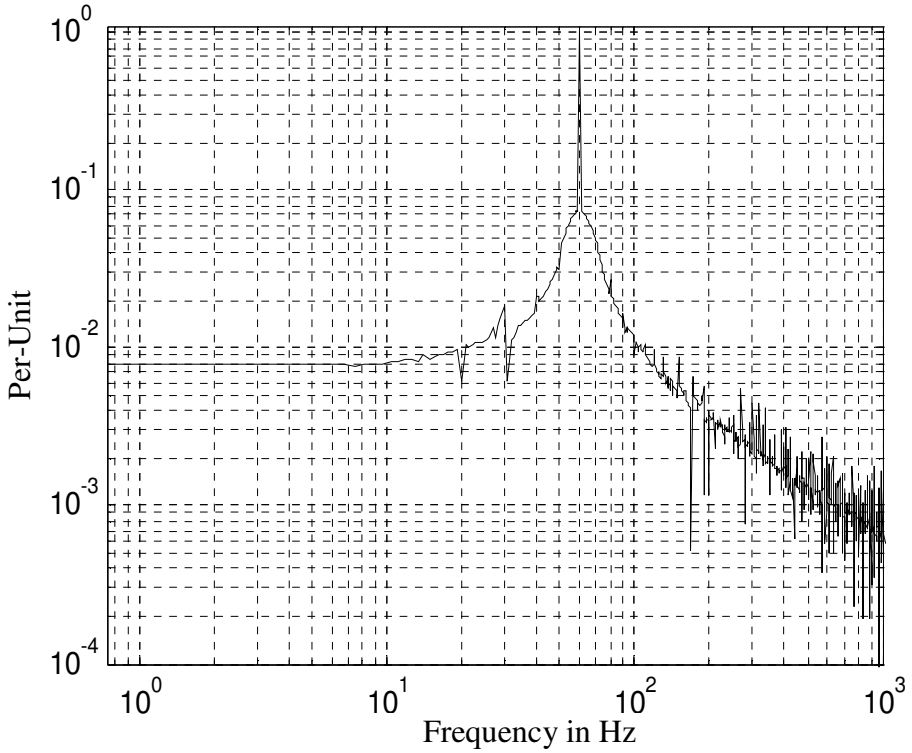

Fig.3.16b Phase current spectrum, open-loop, when the introduced controller was deactivated under healthy three-phase mode of operation, 60 Hz "Simulink/Simpowersystem model".

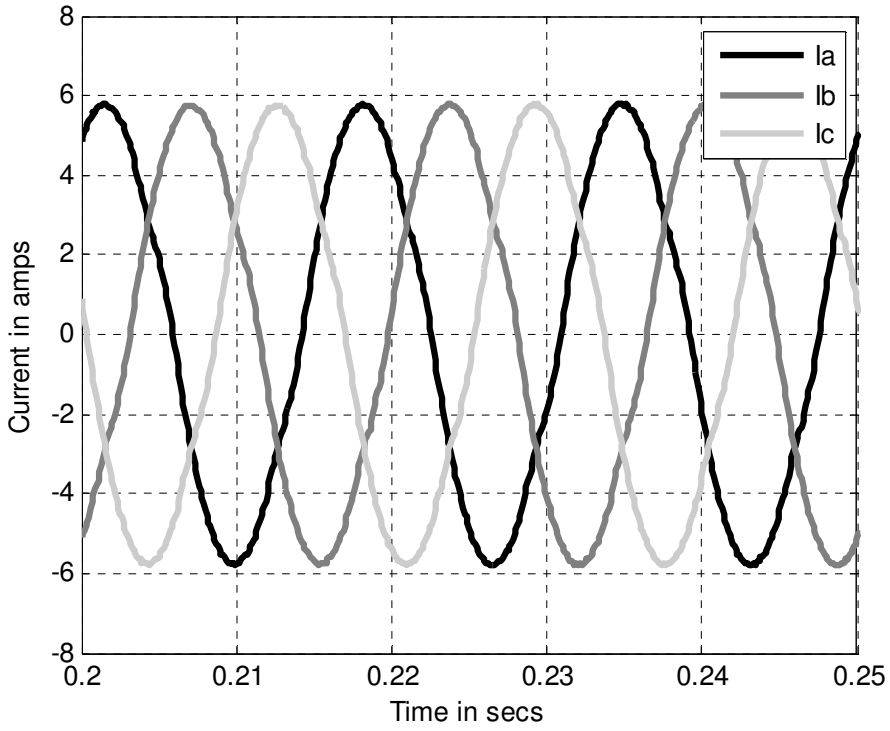

Fig.3.17a Phase currents, open-loop, when the introduced controller was deactivated under healthy three-phase mode of operation, 60 Hz "Coupled Simulink/Flux 2D model".

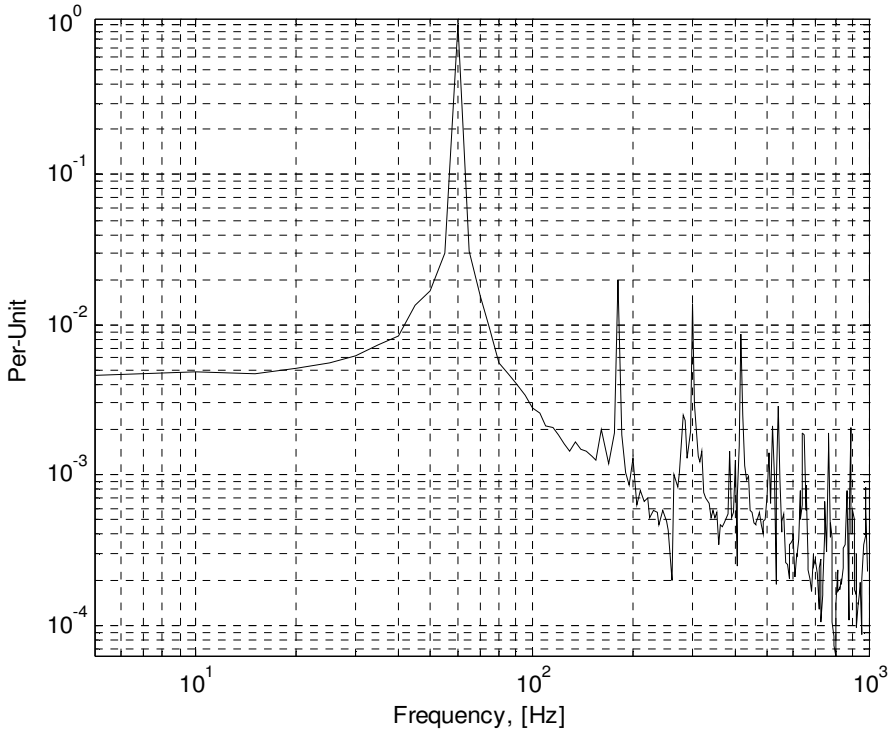

Fig.3.17b Phase currents, open-loop, when the compensation algorithm was deactivated under healthy three-phase mode of operation, 60 Hz "Coupled Simulink/Flux 2D model".

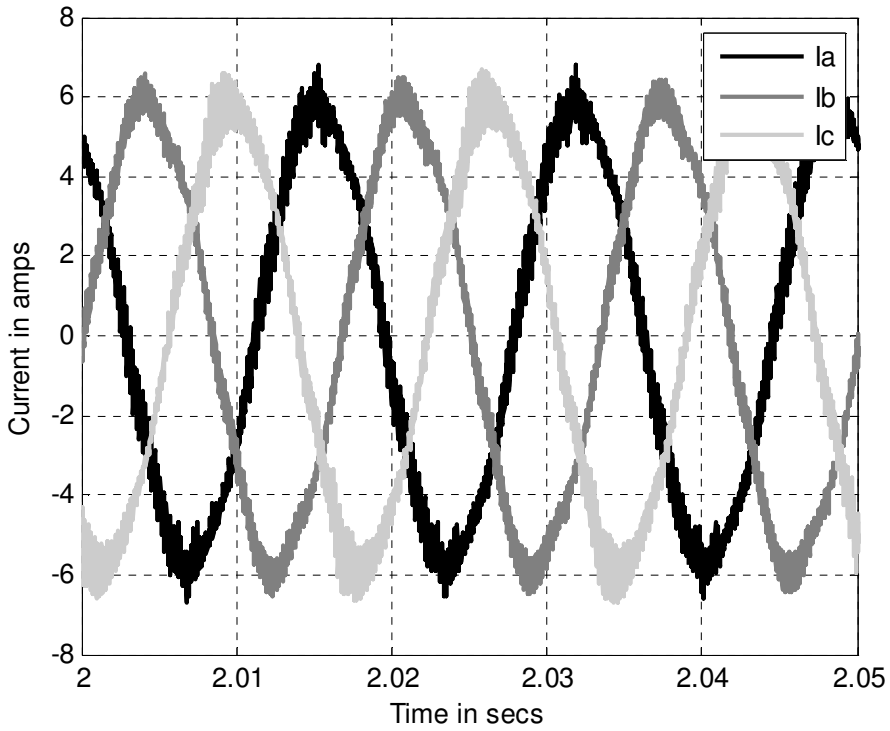

Fig.3.18a Experimentally obtained phase currents, open-loop, when the introduced controller was deactivated under healthy three-phase mode of operation, 60 Hz.

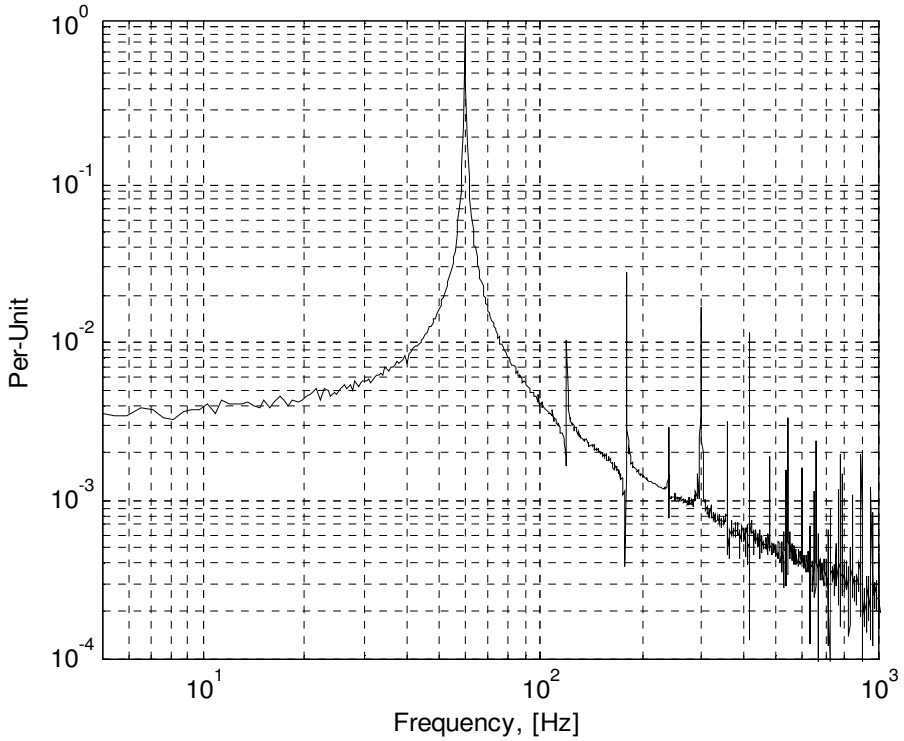

Fig.3.18b Experimentally obtained phase currents spectrum, open-loop, when the introduced controller was deactivated under healthy three-phase mode of operation, 60 Hz.

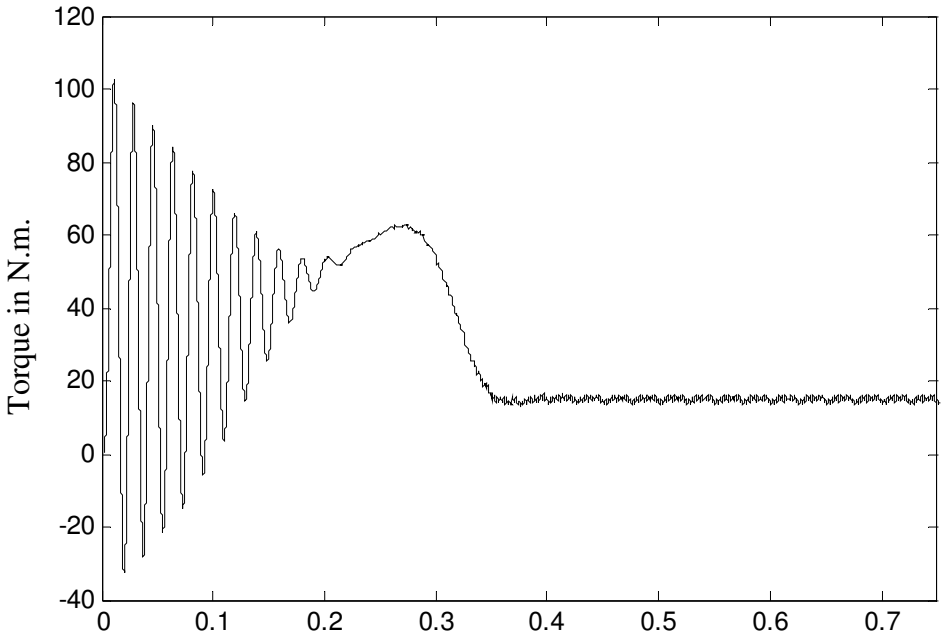

Fig.3.19a Output Torque, open-loop, when the introduced controller was deactivated under healthy three-phase mode of operation "Simulink/Simpowersystem model", 60 Hz.

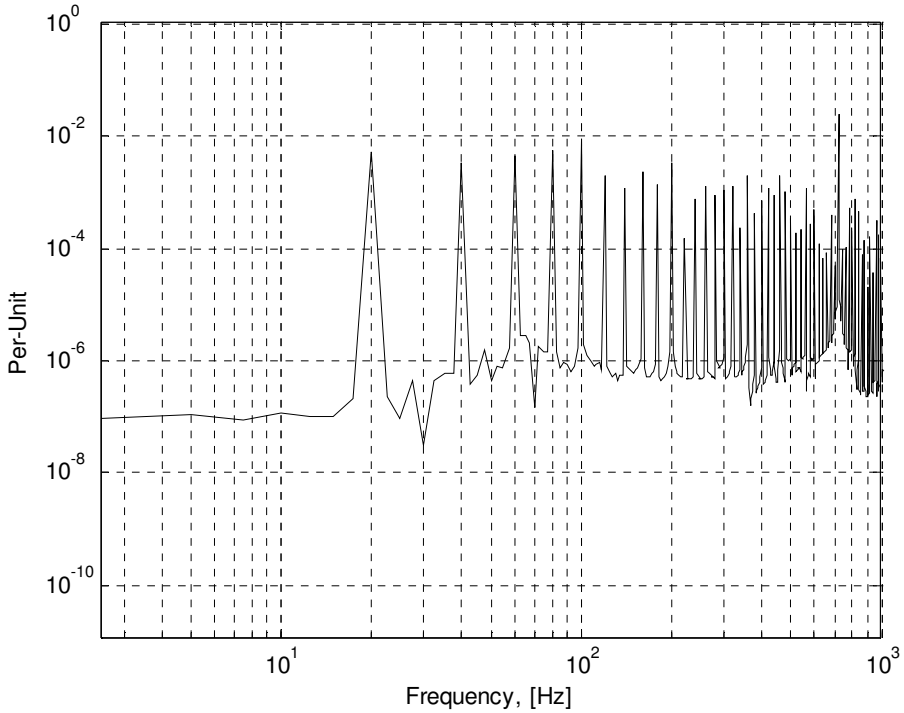

Fig.3.19b Output Torque, open-loop, when the introduced controller was deactivated under healthy three-phase mode of operation "Simulink/simpowersystem model", 60 Hz.

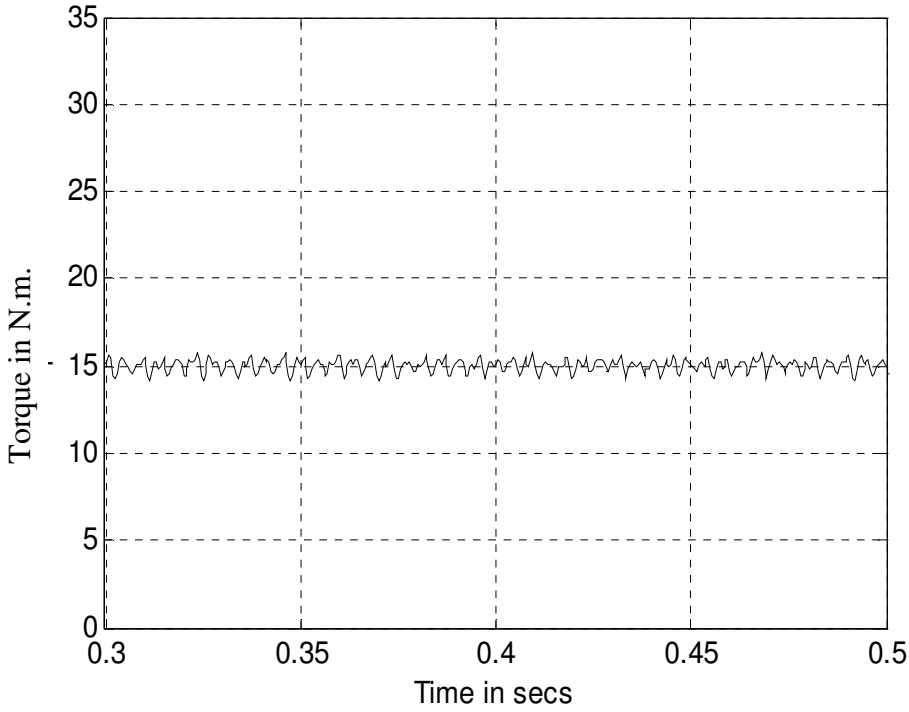

Fig.3.20a Output Torque, open-loop, when the introduced controller was deactivated under healthy three-phase mode of operation "Coupled Simulink/Flux2D model", 60 Hz.

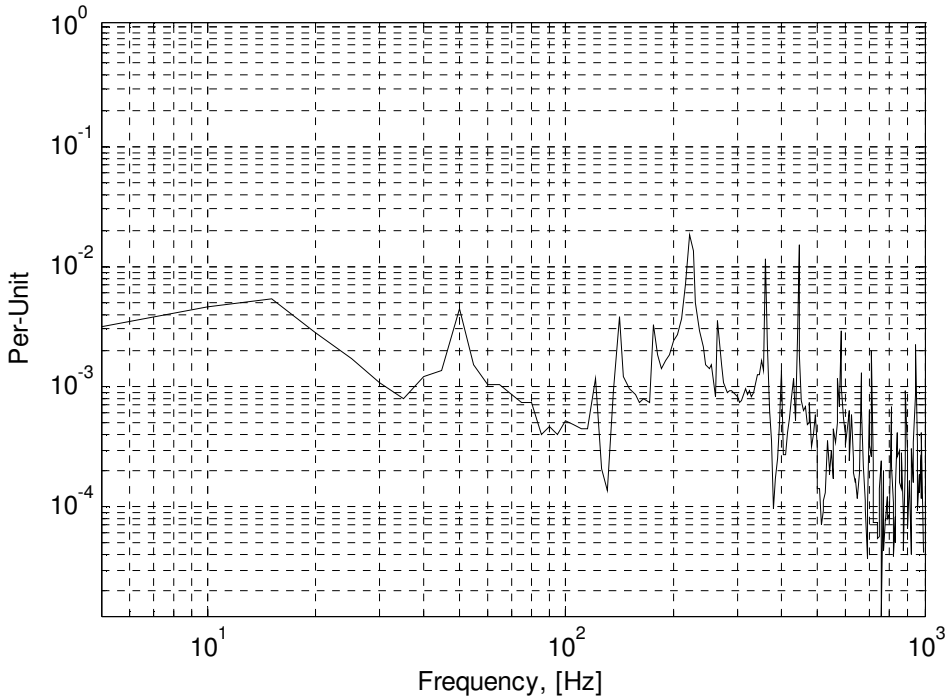

Fig.3.20b Output Torque, open-loop, when the introduced controller was deactivated under healthy three-phase mode of operation "Coupled Simulink/Flux2D model", 60 Hz.

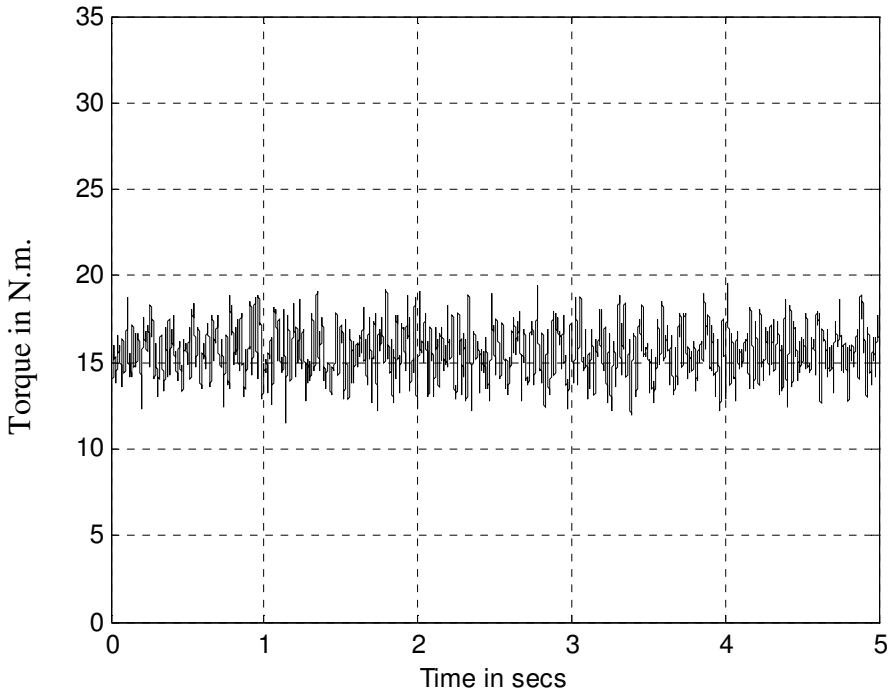

Fig.3.21a Experimentally obtained output Torque, open-loop, when the introduced controller was deactivated under healthy three-phase mode of operation, 60 Hz.

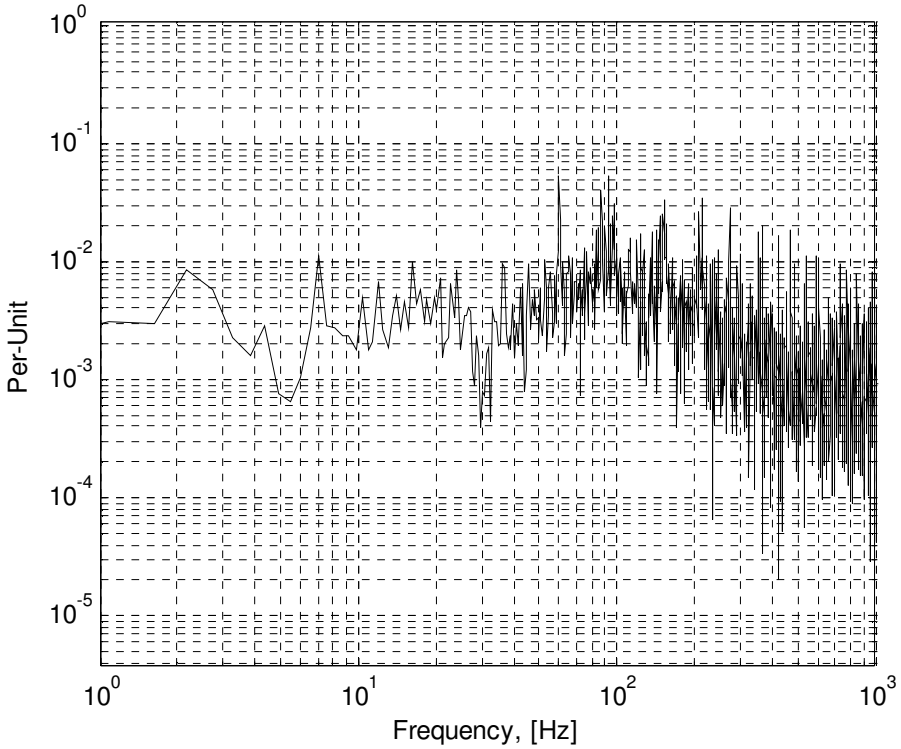

Fig.3.21b Experimentally obtained output Torque spectrum, open-loop, when the introduced controller was deactivated under healthy three-phase mode of operation, 60 Hz.

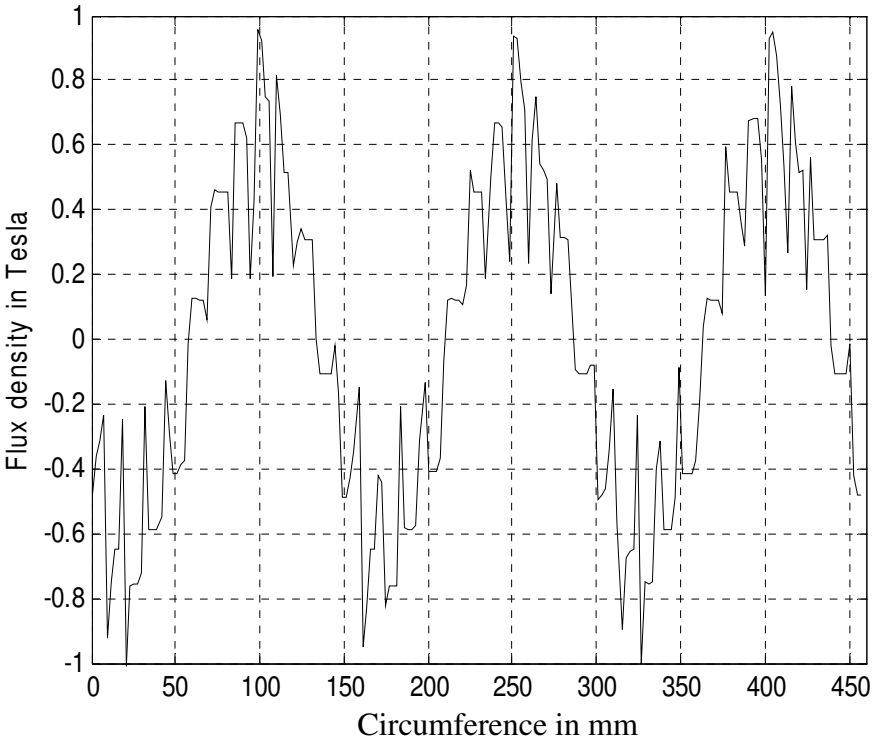

Fig.3.22a Airgab Flux Density, open-loop, when the introduced controller was deactivated under healthy three-phase mode of operation "Coupled Simulink/Flux2D model", 60 Hz.

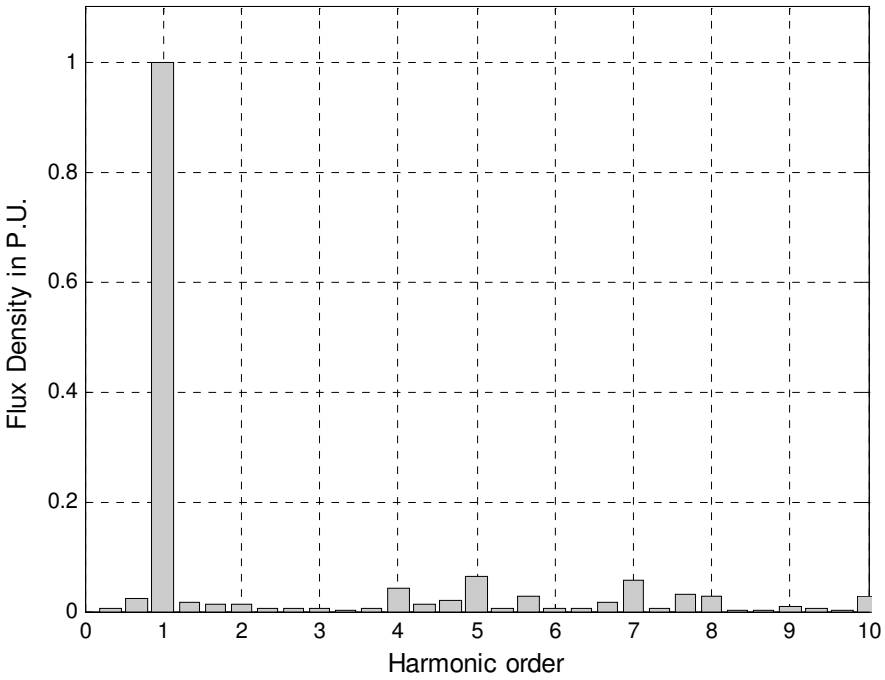

Fig.3.22b Spectrum of the airgab Flux Density, open-loop, when the introduced controller was deactivated under healthy three-phase mode of operation "Coupled Simulink/Flux2D model", 60 Hz.

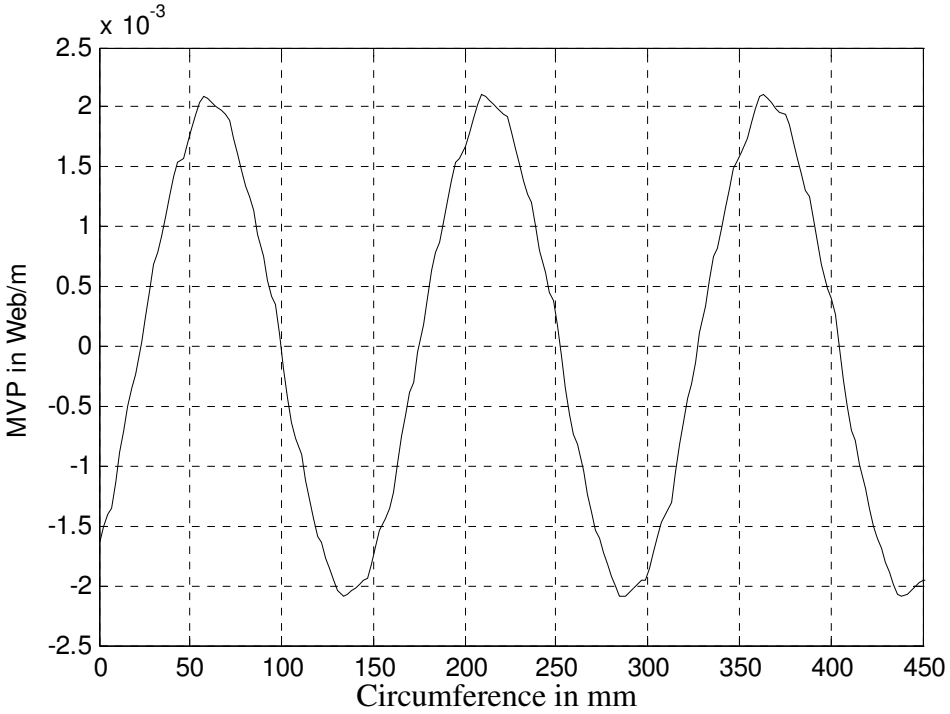

Fig.3.23 Airgab Magnetic Vector Potential, open-loop, when the introduced controller was deactivated under healthy three-phase mode of operation "Coupled Simulink/Flux2D model", 60 Hz.

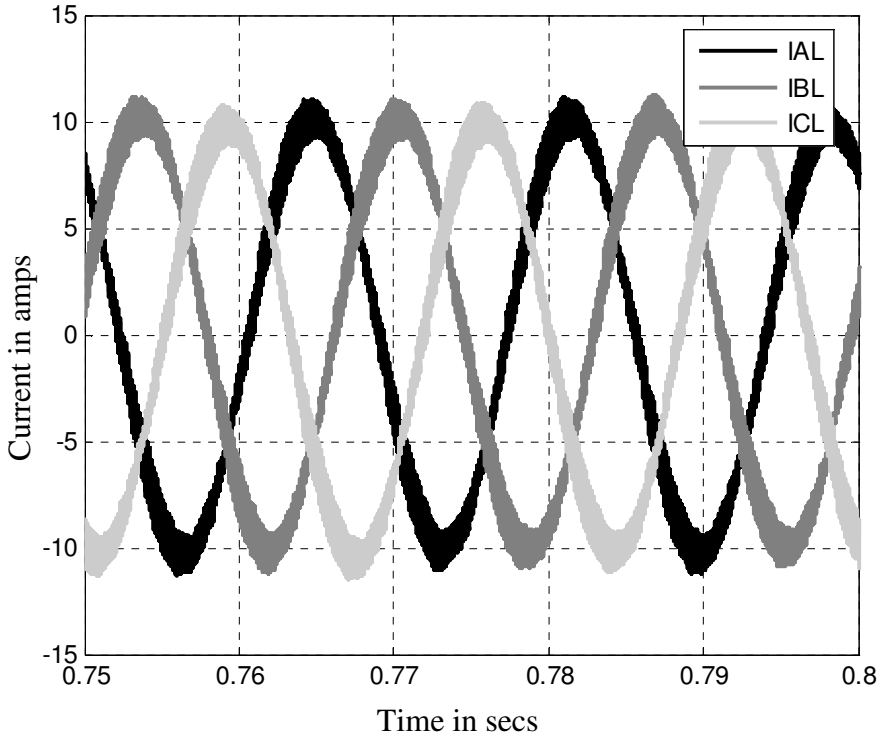

Fig.3.24a Line currents, open-loop, when the introduced controller was activated under healthy three-phase mode of operation "Simulink/Simpowersystem model", 60 Hz.

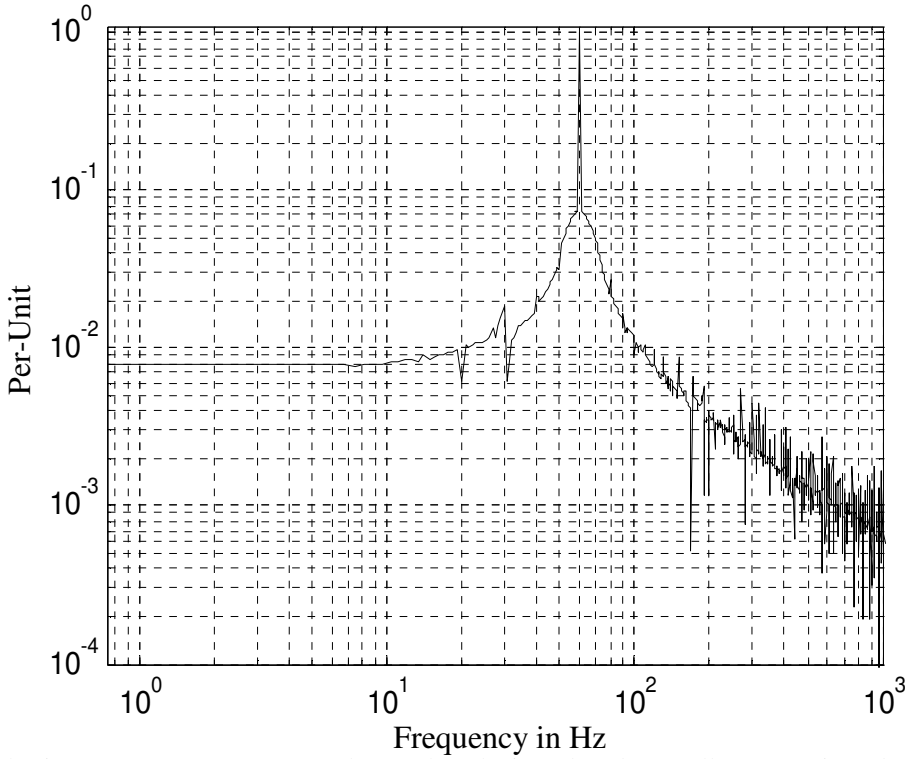

Fig.3.24b Line currents spectrum, open-loop, when the introduced controller was activated under healthy three-phase mode of operation "Simulink/Simpowersystem model", 60 Hz.

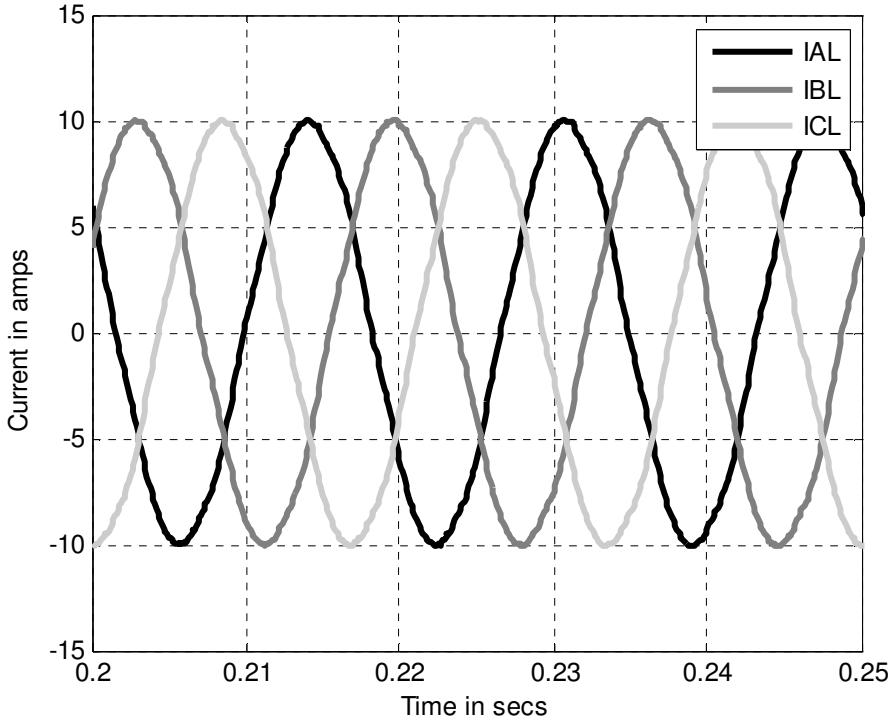

Fig.3.25a Line currents, open-loop, when the introduced controller was activated under healthy three-phase mode of operation "Coupled Simulink/Flux2D model", 60 Hz.

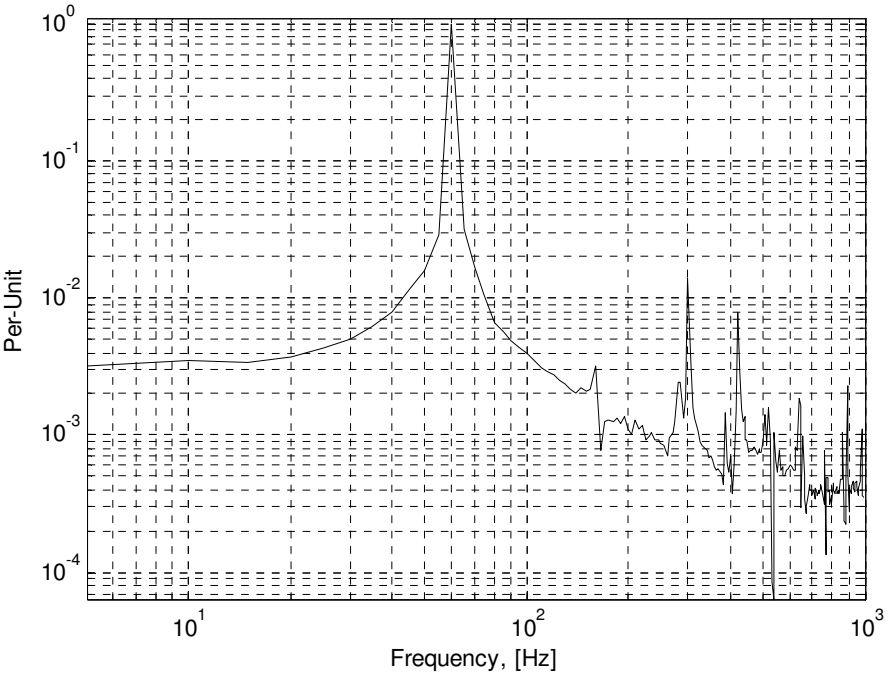

Fig.3.25b Line currents spectrum, open-loop, when the introduced controller was activated under healthy three-phase mode of operation "Coupled Simulink/Flux2D model".

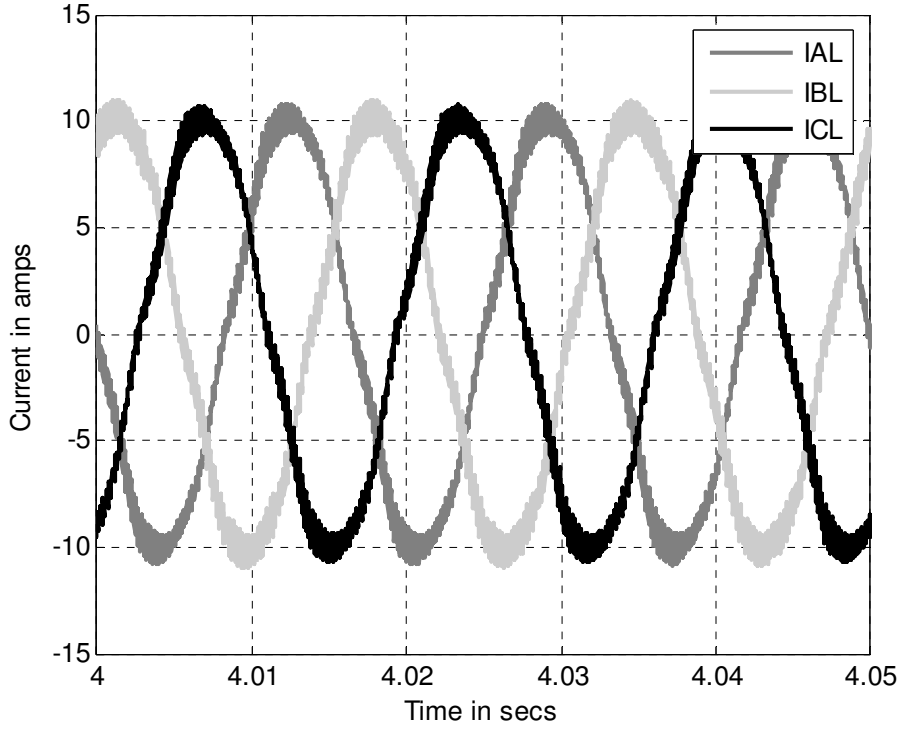

Fig.3.26a Experimentally obtained line currents, open-loop, when the introduced controller was activated under healthy three-phase mode of operation, 60 Hz.

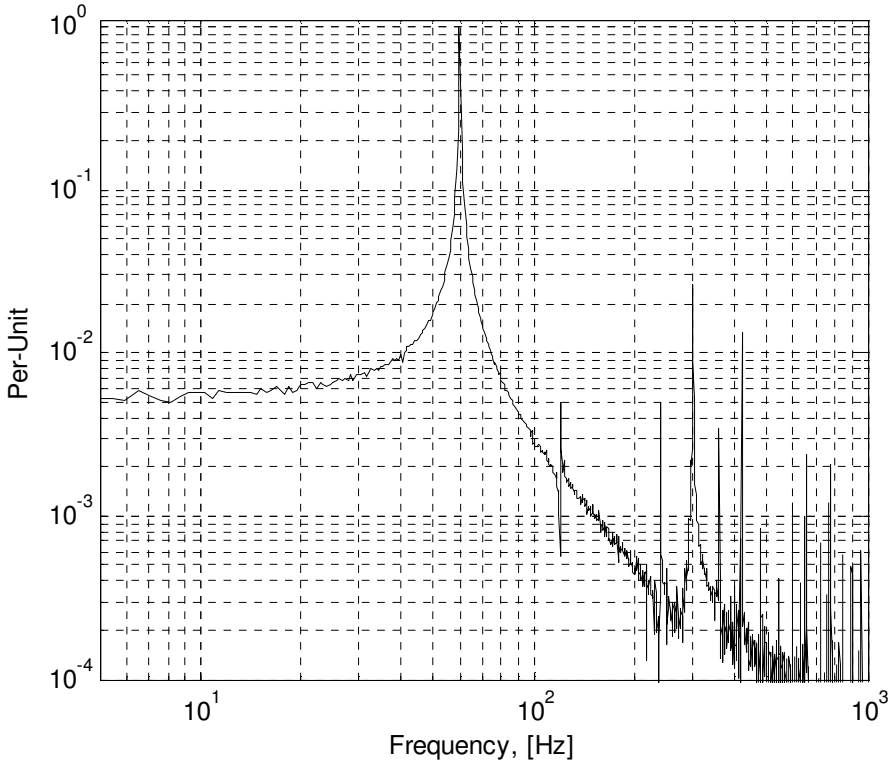

Fig.3.26b Experimentally obtained line current spectrum, open-loop, when the introduced controller was activated under healthy three-phase mode of operation, 60 Hz.

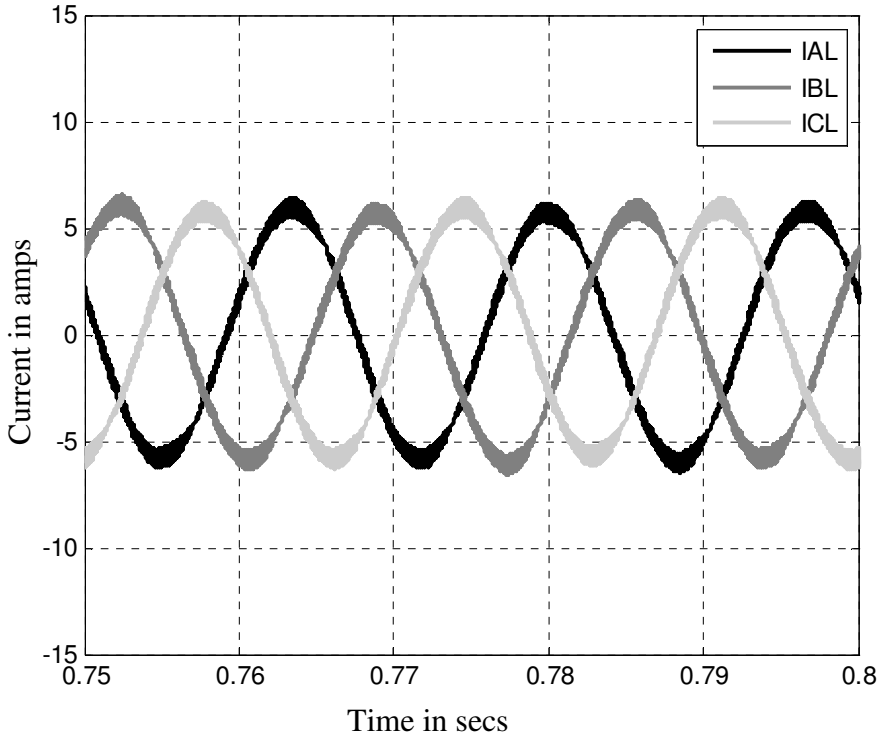

Fig.3.27a Phase currents, open-loop, when the introduced controller was activated under healthy three-phase mode of operation "Simulink/Simpowersystem model", 60 Hz.

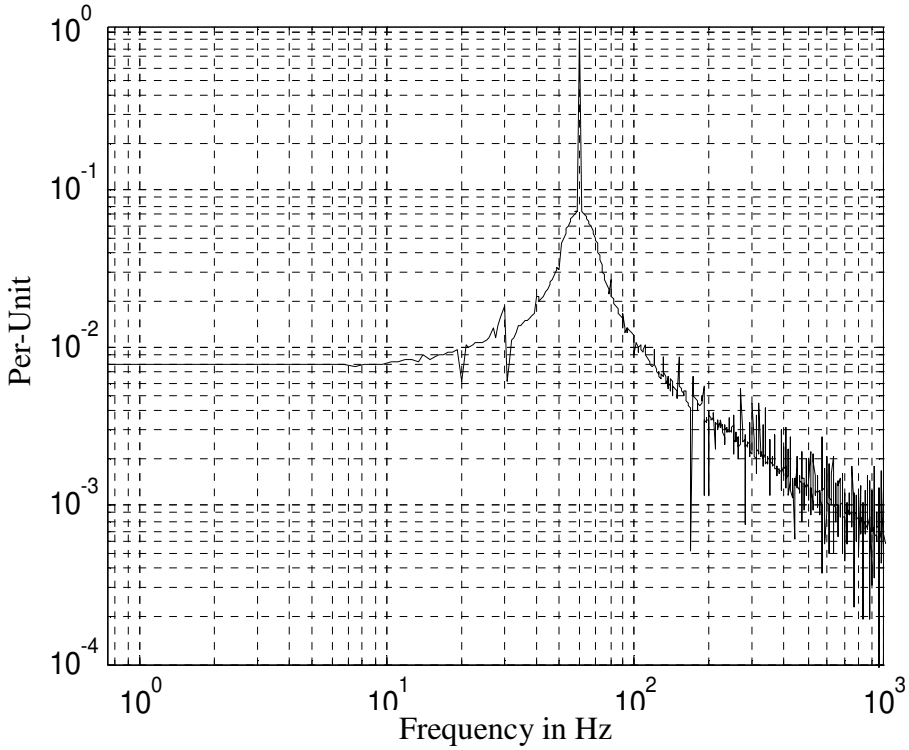

Fig.3.27b Phase current spectrum, open-loop, when the introduced controller was activated under healthy three-phase mode of operation "Simulink/Simpowersystem model", 60 Hz.

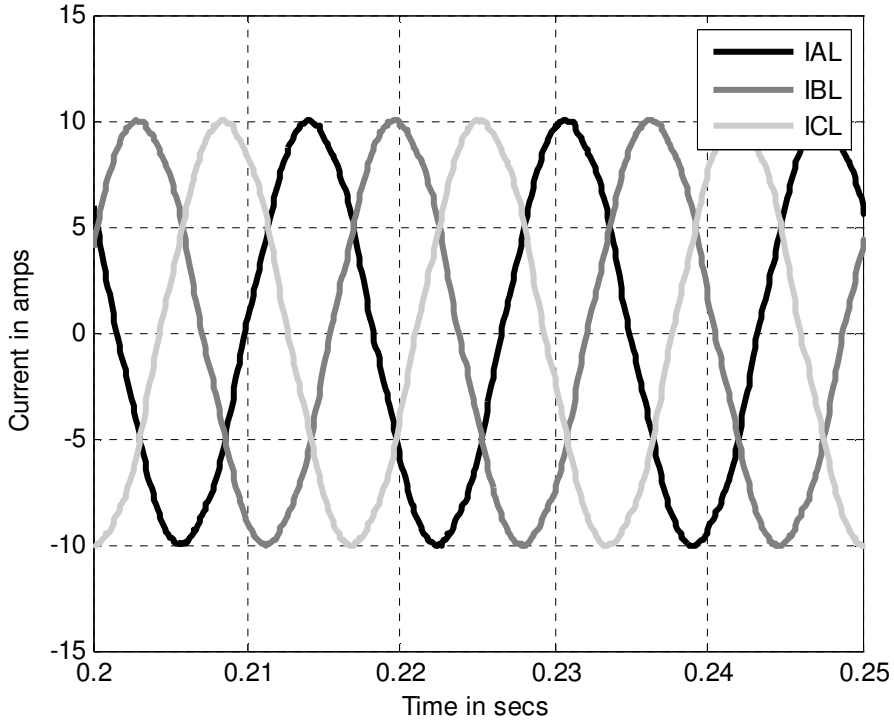

Fig.3.28a Phase currents, open-loop, when the introduced controller was activated under healthy three-phase mode of operation "Coupled Simulink/Flux2D model", 60 Hz.

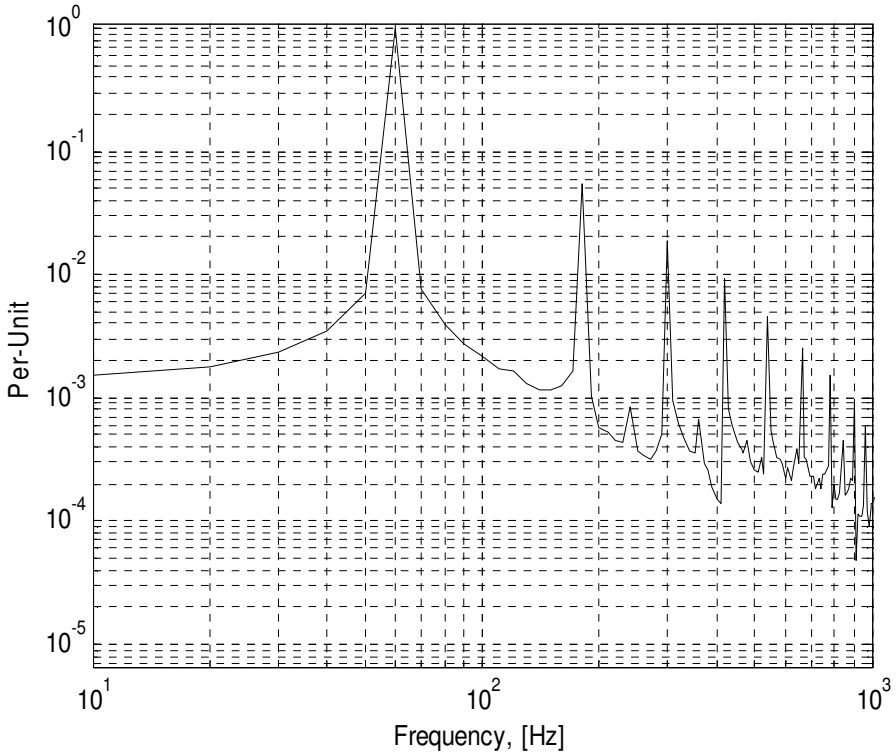

Fig.3.28b Phase currents spectrum, open-loop, when the introduced controller was activated under healthy three-phase mode of operation "Coupled Simulink/Flux2D model", 60 Hz.

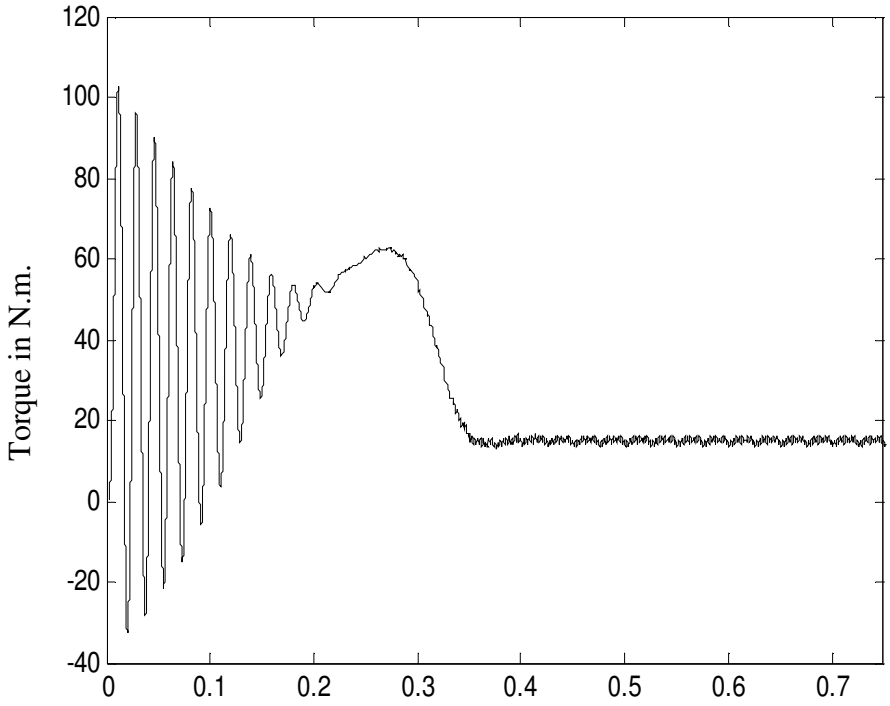

Fig.3.29a Output Torque, open-loop, when the introduced controller was activated under healthy three-phase mode of operation "Simulink/Simpowersystem model", 60 Hz.

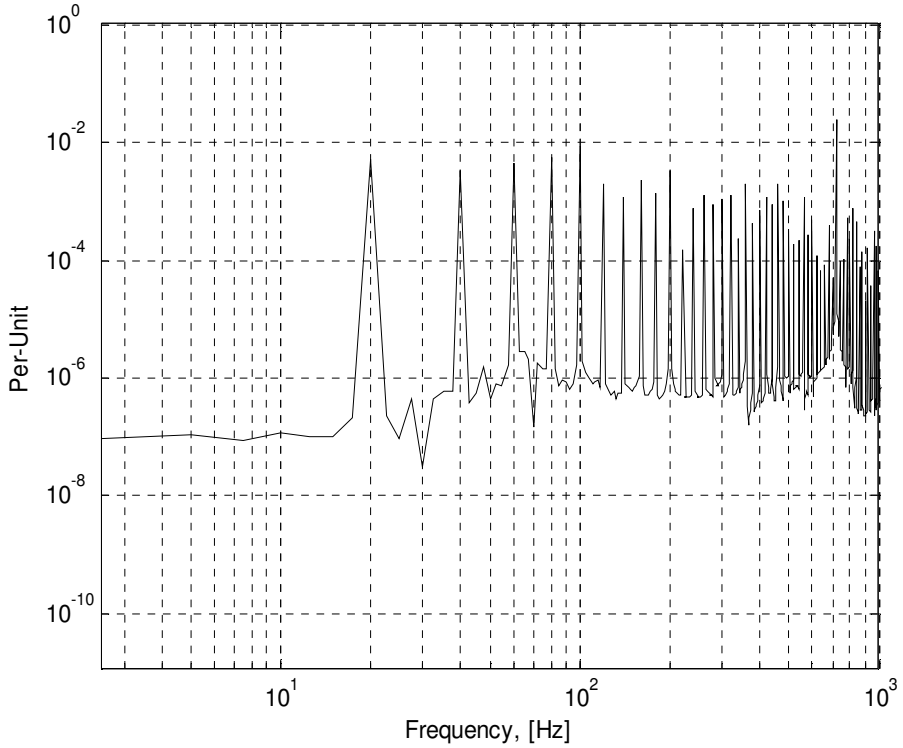

Fig.3.29b Output Torque spectrum, open-loop, when the introduced controller was activated under healthy three-phase mode of operation "Simulink/Simpowersystem model", 60 Hz.

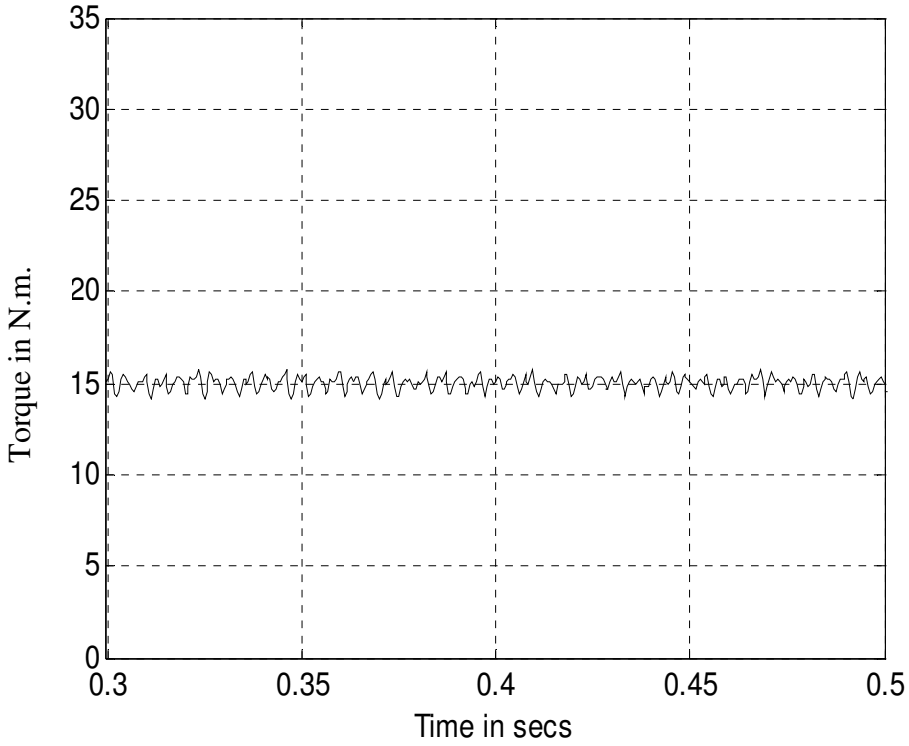

Fig.3.30a Output Torque, open-loop, when the introduced controller was activated under healthy three-phase mode of operation "Coupled Simulink/Flux2D model", 60Hz.

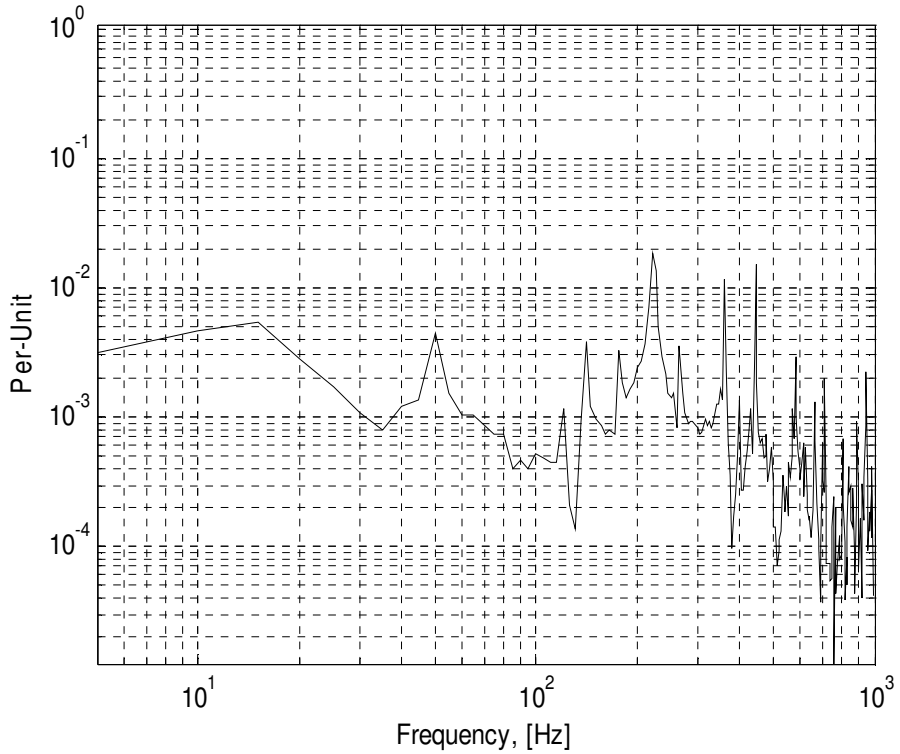

Fig.3.30b Output Torque, open-loop, when the introduced controller was activated under healthy three-phase mode of operation "Coupled Simulink/Flux2D model", 60 Hz.

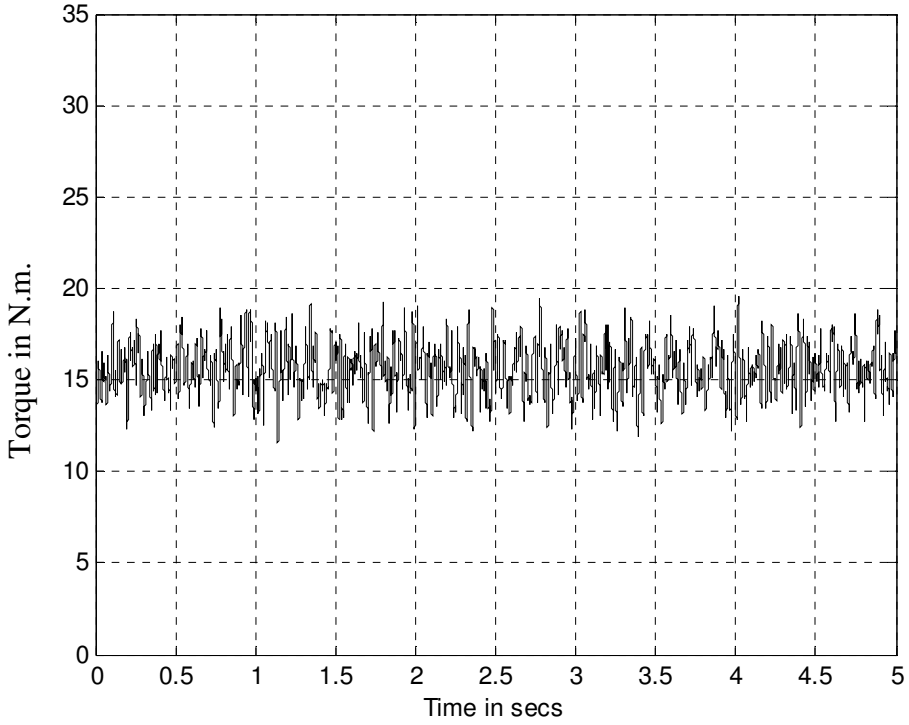

Fig.3.31a Experimentally obtained output torque, open-loop, when the introduced controller was activated under healthy three-phase mode of operation, 60 Hz.

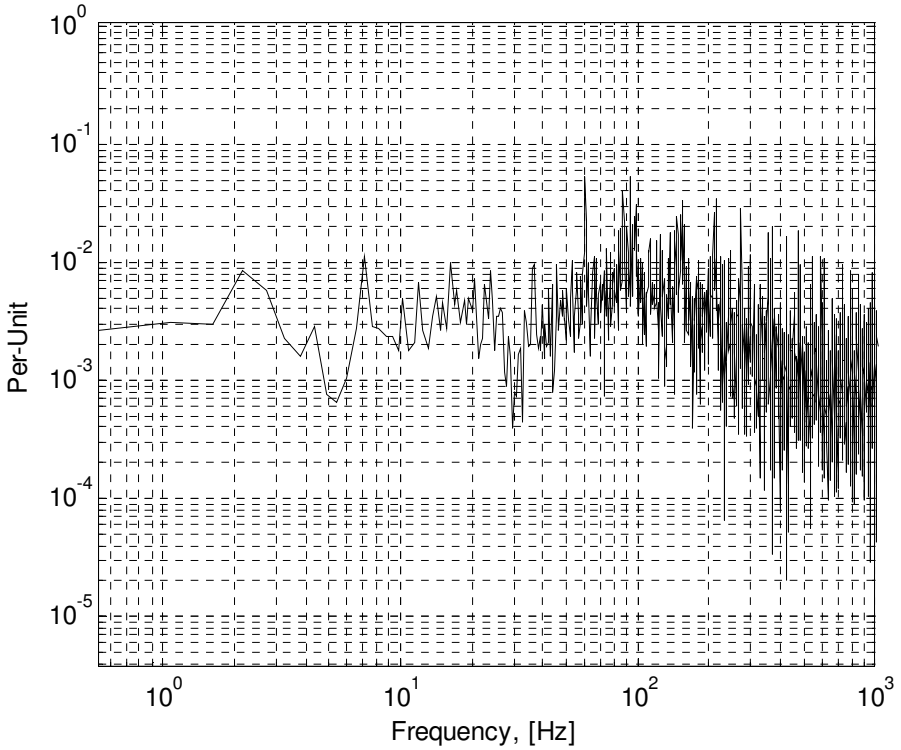

Fig.3.31b Experimentally obtained output torque spectrum, open-loop, when the introduced controller was activated under healthy three-phase mode of operation, 60 Hz.

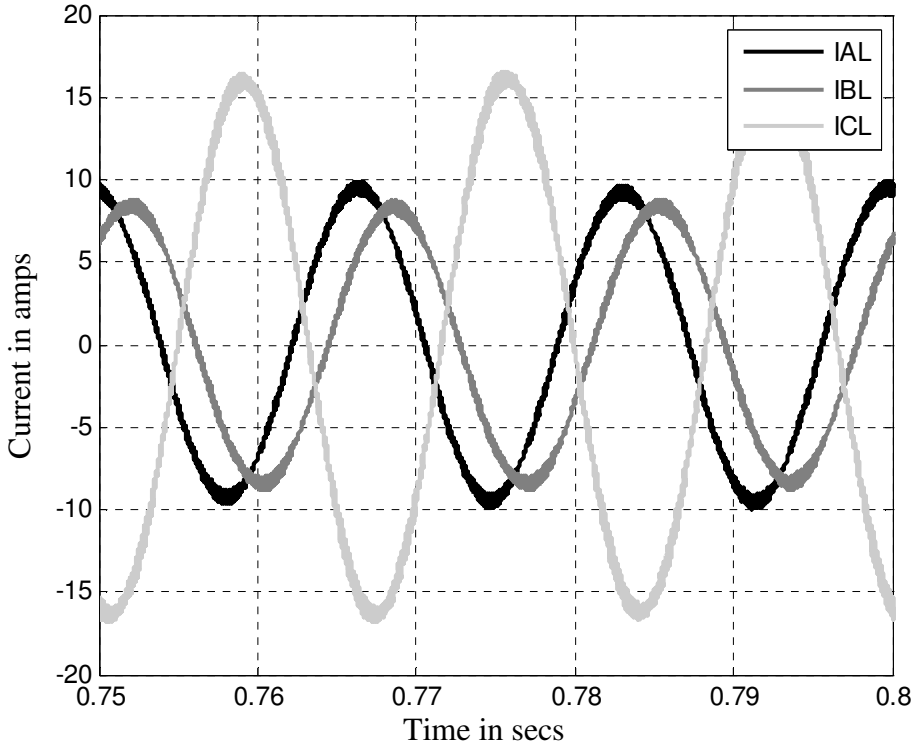

Fig.3.32a Line currents, open-loop, when the introduced controller was deactivated under two-phase open-Delta operation, 60 Hz "Simulink/Simpowersystem model".

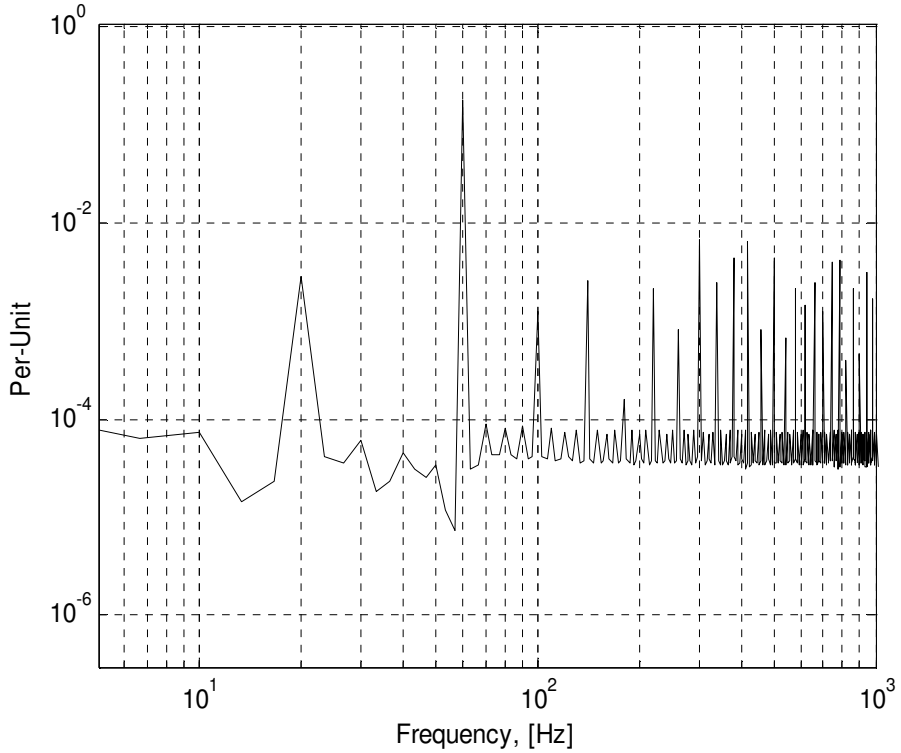

Fig.3.32b Line current spectrum, open-loop, when the introduced controller was deactivated under two-phase open-Delta operation, 60 Hz "Simulink/Simpowersystem model".

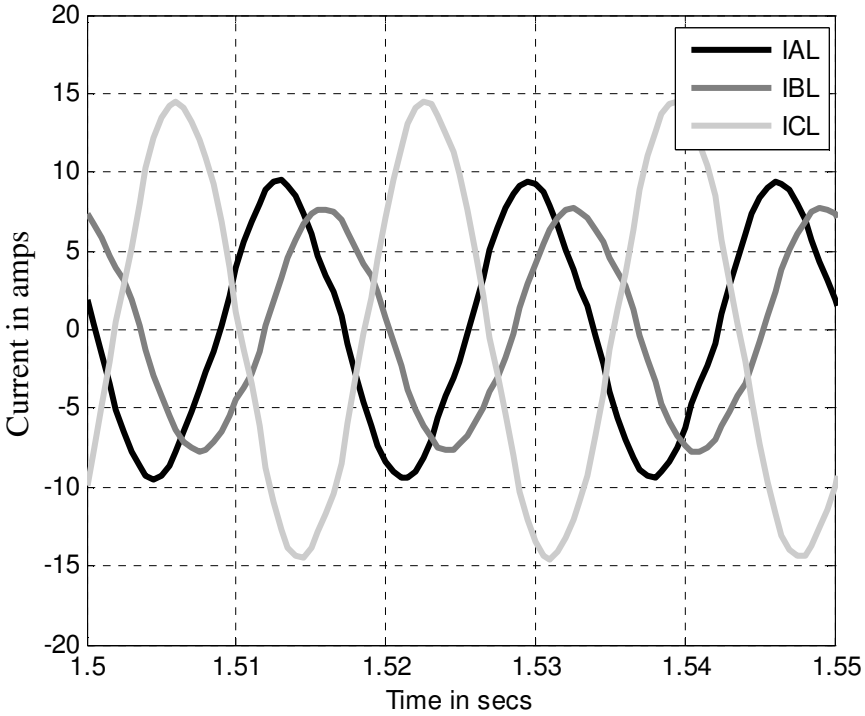

Fig.3.33a Line currents spectrum, open-loop, when the introduced controller was deactivated under two-phase open-Delta operation, 60Hz. "Coupled Simulink/Flux2D model".

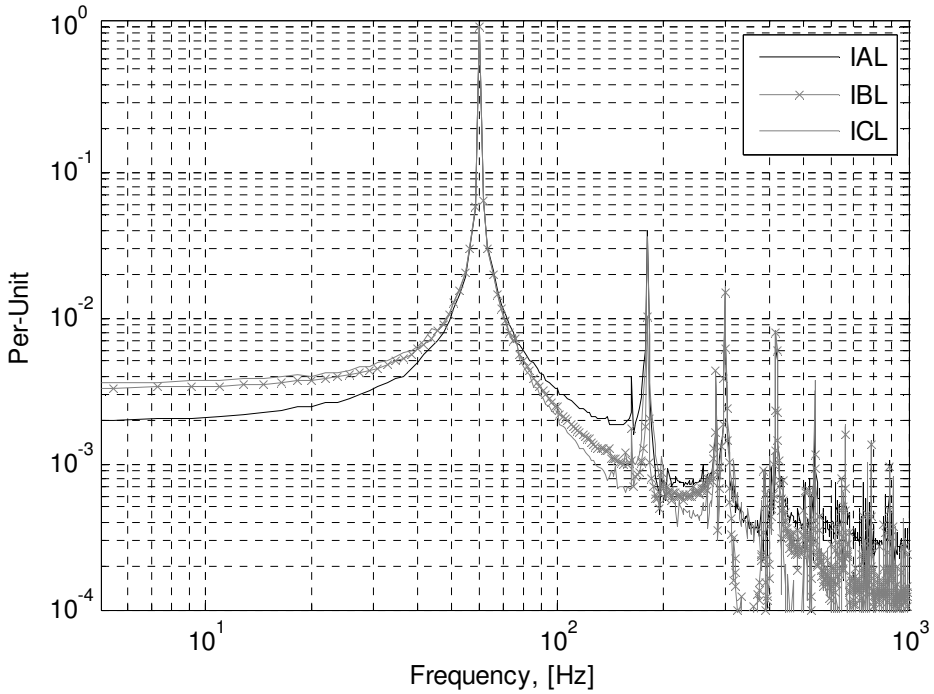

Fig.3.33b Line current spectrum, open-loop, when the introduced controller was deactivated under two-phase open-Delta operation., 60Hz. "Coupled Simulink/Flux2D model".

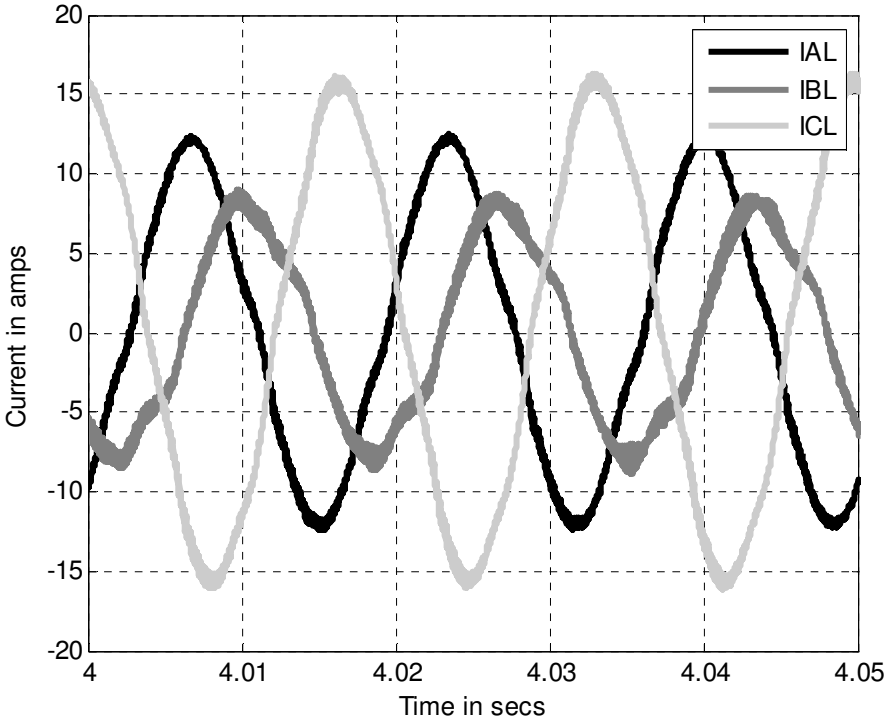

Fig.3.34a Experimentally obtained line currents, open-loop, when the introduced controller was deactivated under two-phase open-Delta operation, 60Hz..

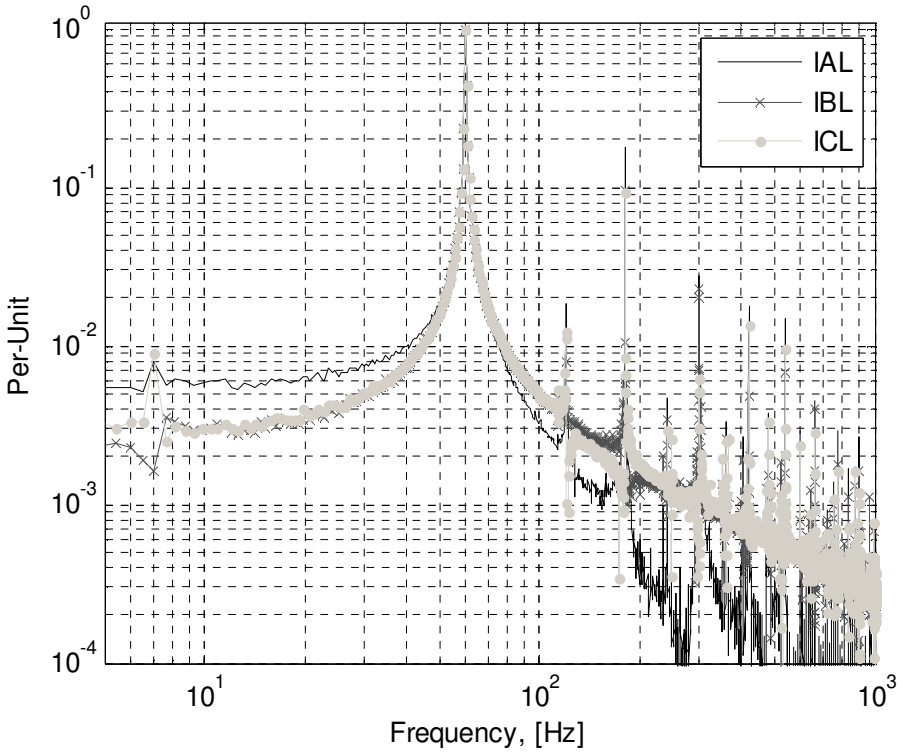

Fig.3.34b Experimentally obtained line currents spectrum, open-loop, when the introduced controller was deactivated under two-phase open-Delta operation. 60Hz.

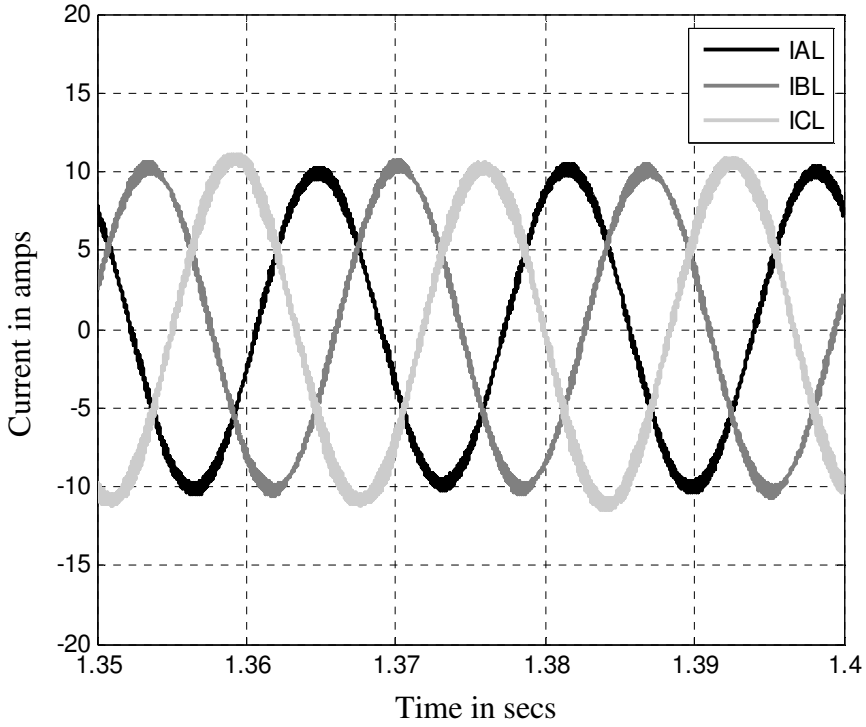

Fig.3.35a Line currents, open-loop, when the introduced controller was activated under two-phase open-Delta operation, 60Hz "Simulink/Simpowersystem model".

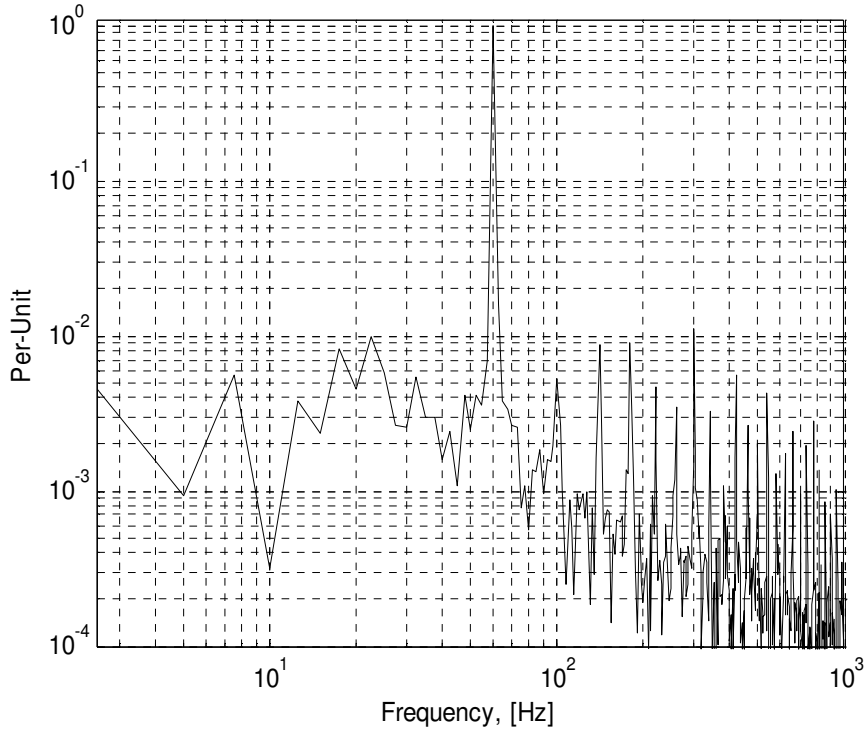

Fig.3.35b Line current spectrum, open-loop, when the introduced controller was activated under two-phase open-Delta operation, 60Hz."Simulink/Simpowersystem model".

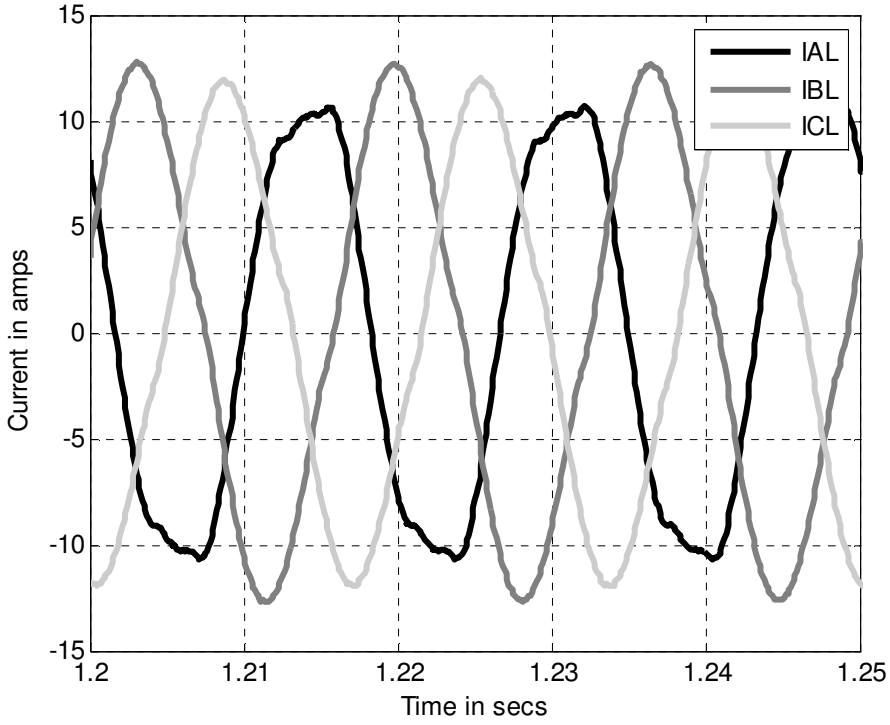

Fig.3.36a Line currents, open-loop, when the introduced controller was activated under two-phase open-Delta operation, 60Hz "Coupled Simulink/Flux2D model".

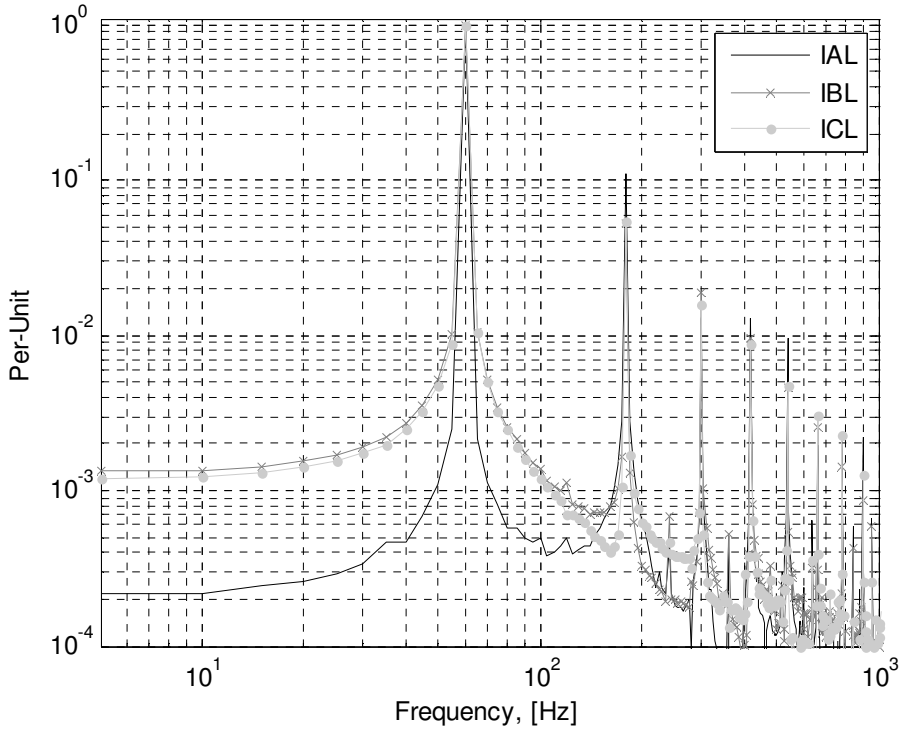

Fig.3.36b Line currents spectrum, open-loop, when the introduced controller was activated under two-phase open-Delta operation, 60Hz "Coupled Simulink/Flux2D model".

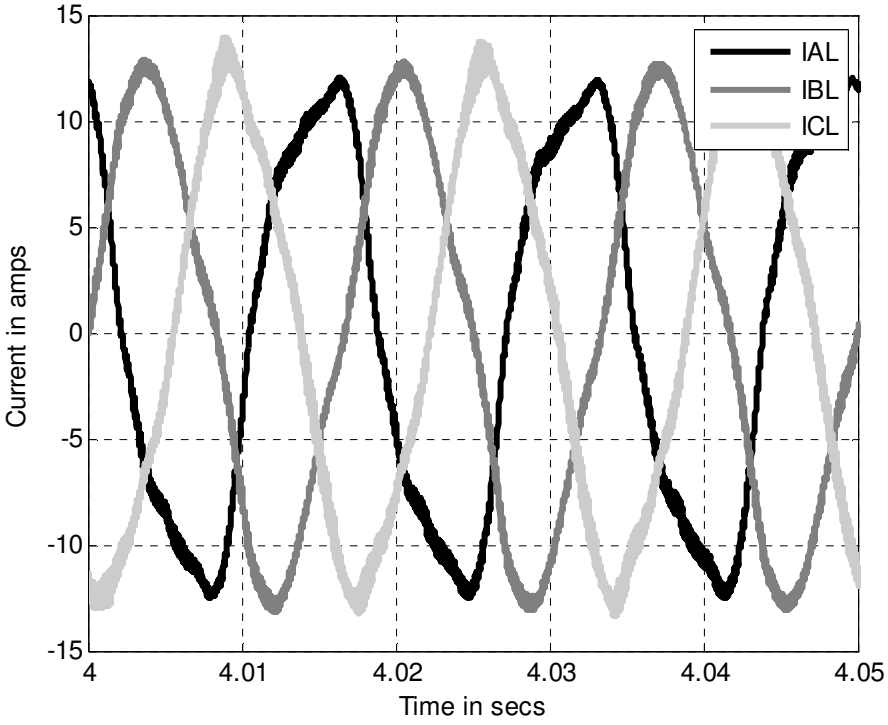

Fig.3.37a Experimentally obtained line currents, open-loop, when the introduced controller was activated under two-phase open-Delta operation, 60Hz.

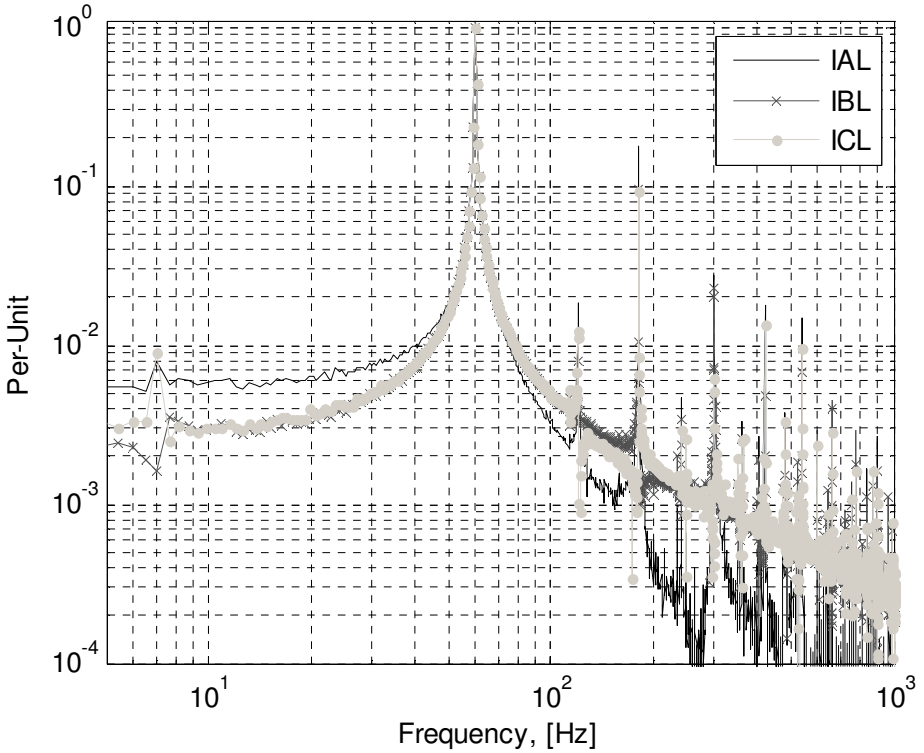

Fig.3.37b Experimentally obtained line currents spectrum, open-loop, when the introduced controller was activated under two-phase open-Delta operation, 60Hz.

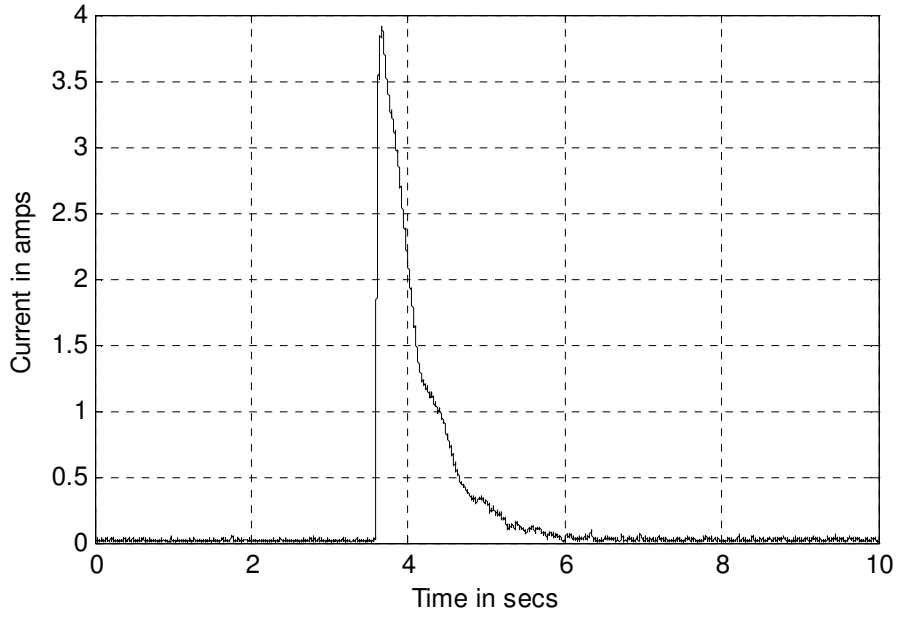

Fig.3.37c Experimentally obtained negative sequence component of the line currents at the instant of the transfer from three-phase mode to two-phase open-Delta mode when the introduced controller was activated, 60Hz.

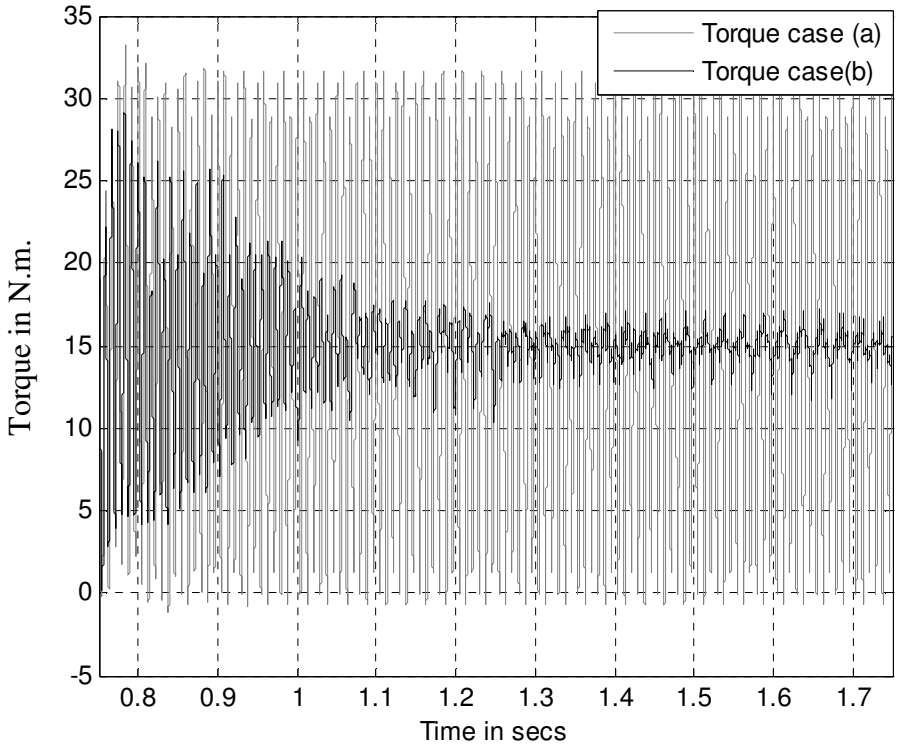

Fig.3.38a Output torque, open-loop, 60Hz, "Simulink/Simpowersystem model":
Case (a) The introduced control deactivated
Case(b) The introduced control activated

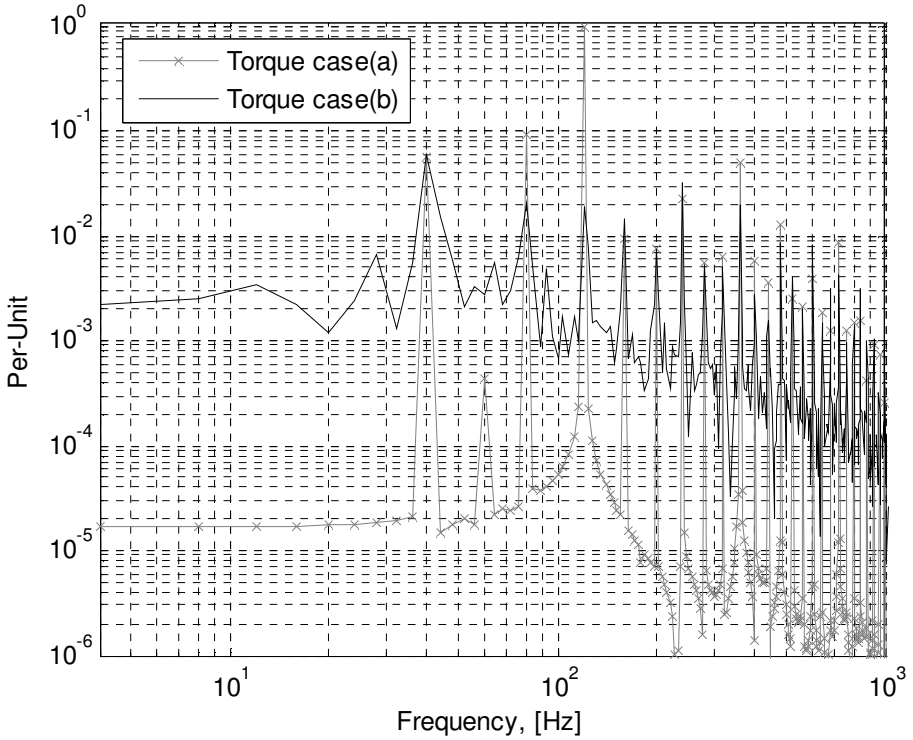

Fig.3.38b Output torque spectrum, 60Hz, "Simulink/Simpowersystem model": Case (a) The introduced controller deactivated ,Case(b) The introduced control activated

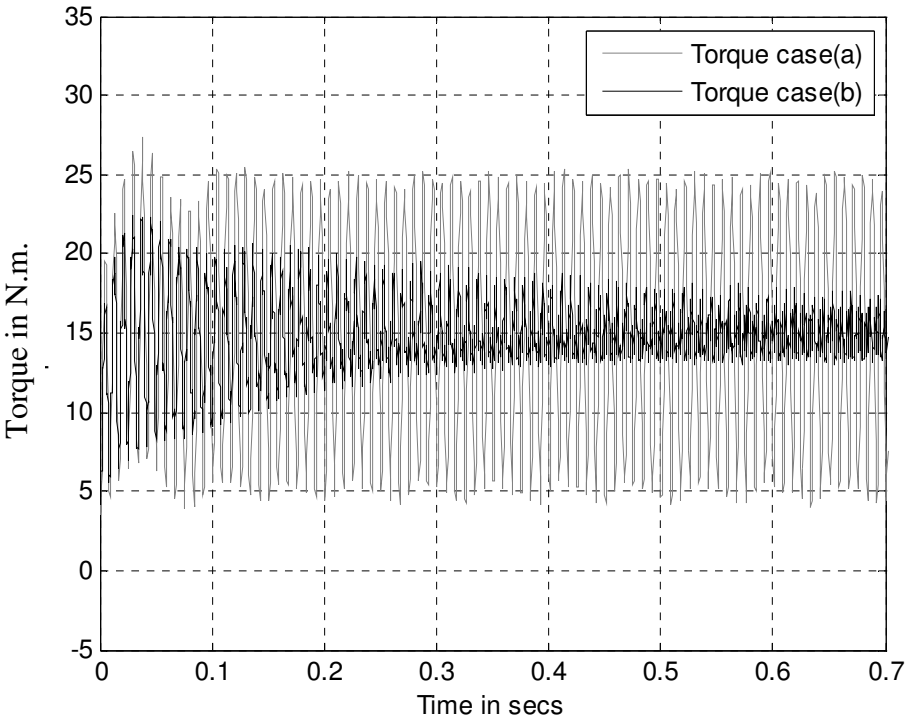

Fig.3.39a Output torque, open-loop , two-phase open-Delta operation, 60Hz, "Coupled Simulink / Flux2D":Case (a) The introduced controller deactivated. Case (b) The introduced control activated.

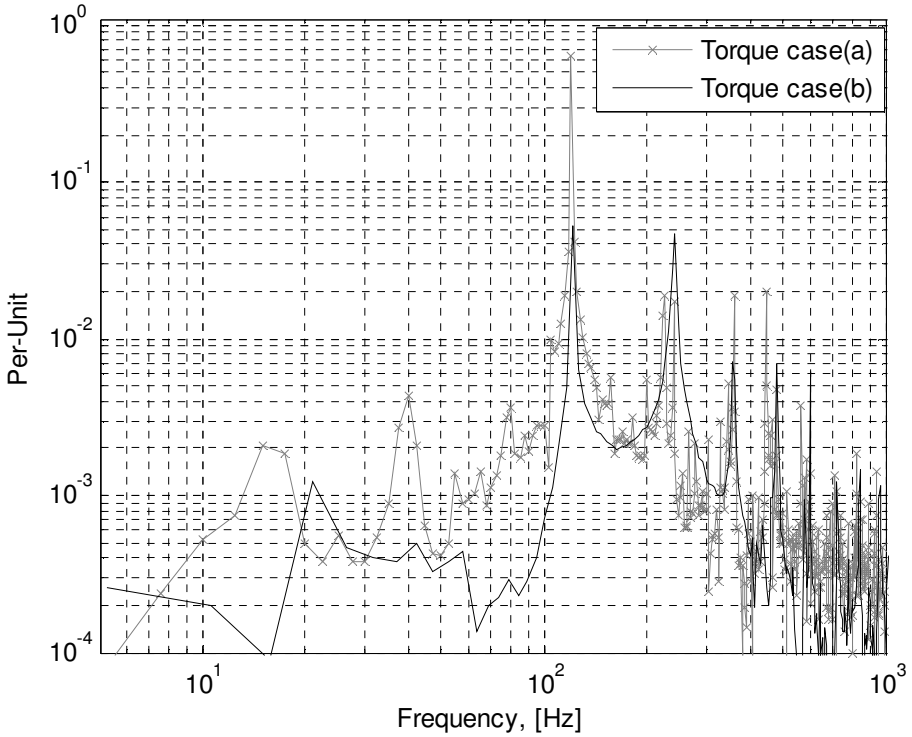

Fig.3.39b Output torque spectrum, open-loop , two-phase open-Delta operation, 60Hz, "Coupled Simulink / Flux2D": Case (a) The introduced controller deactivated, Case (b) The introduced control activated

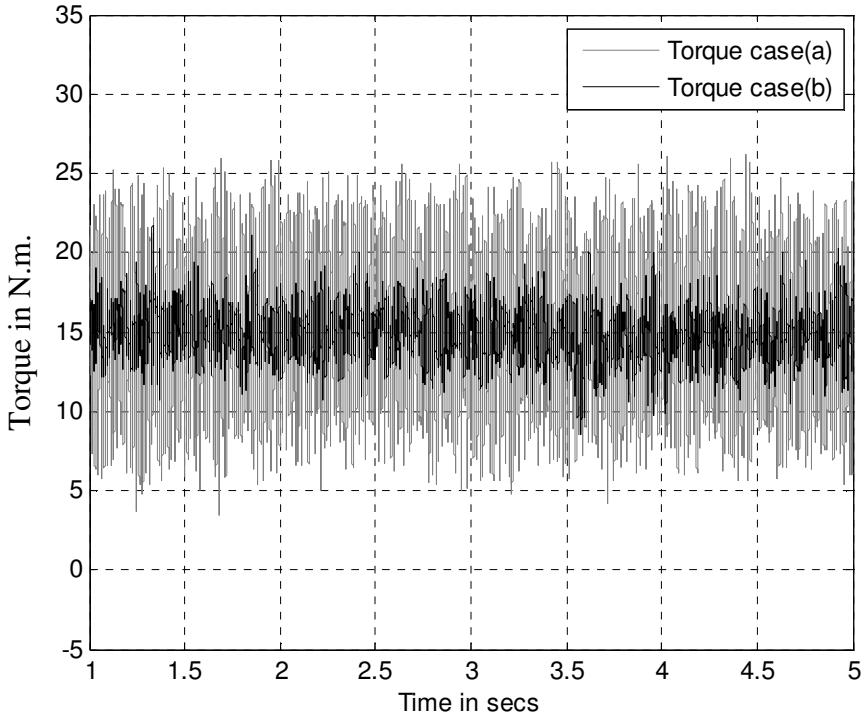

Fig.3.40a Experimentally obtained output torque with, open-loop , two-phase open-Delta operation, 60Hz: Case (a) The introduced controller deactivated, Case (b) The introduced control activated

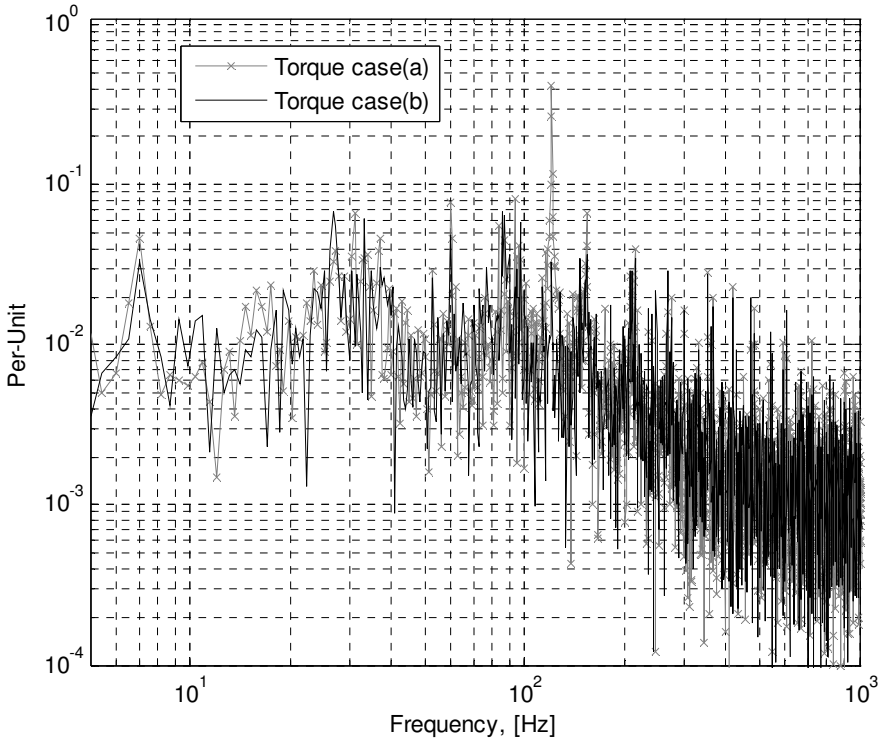

Fig.3.40b Experimentally output torque spectrum, open-loop, two-phase open-Delta operation, 60Hz: Case (a) The introduced controller deactivated, Case (b) The introduced control activated

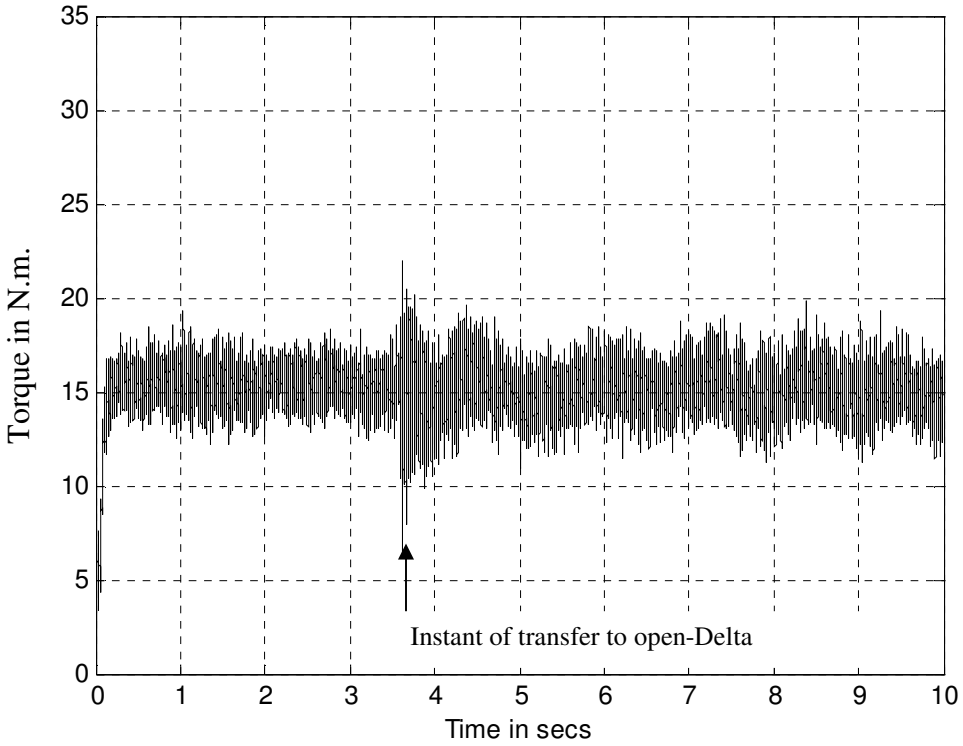

Fig.3.40c Experimentally obtained output torque , open-loop, at the instant of transfer from three-phase to two-phase open-Delta transient response, 60Hz.

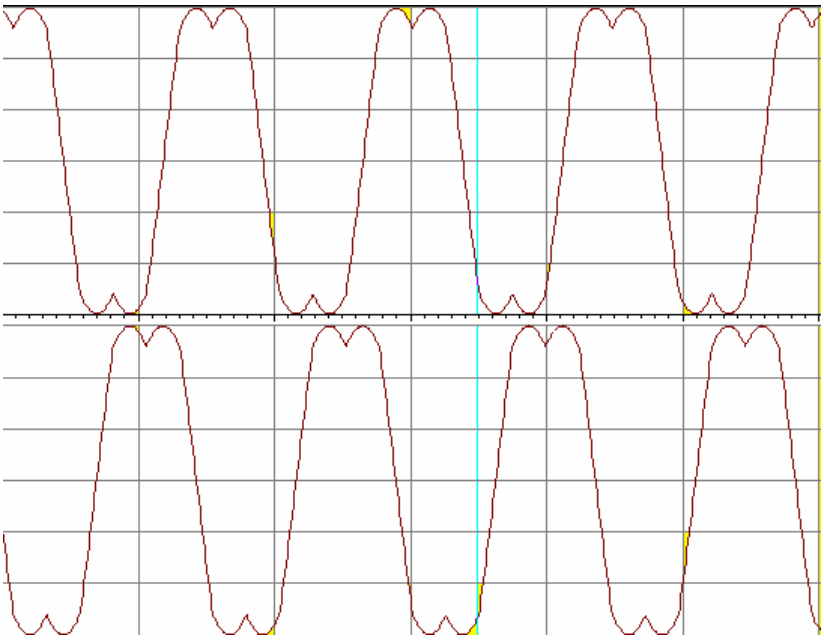

Fig.3.41a DSP output modulating signals for gate drives of phase A and phase C, open-loop 60Hz, two-phase open-Delta operation, the introduced controller deactivated
Horizontal Scale 5ms/div, Vertical scale 0.2 P.U.

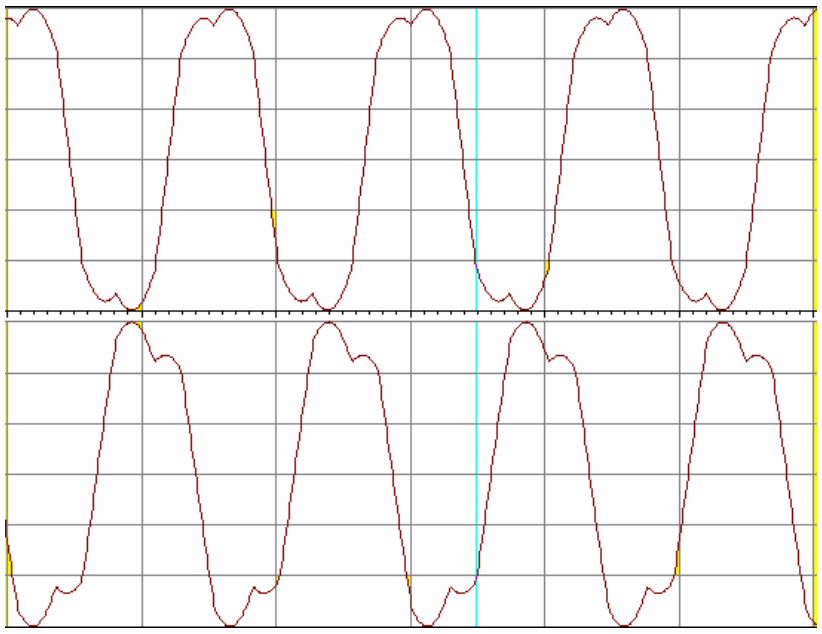

Fig.3.41b DSP output modulating signals for gate drives of phase A and phase C, open-loop 60Hz, two-phase open-Delta operation, the introduced controller activated
Horizontal Scale 5ms/div, Vertical scale 0.2 P.U.

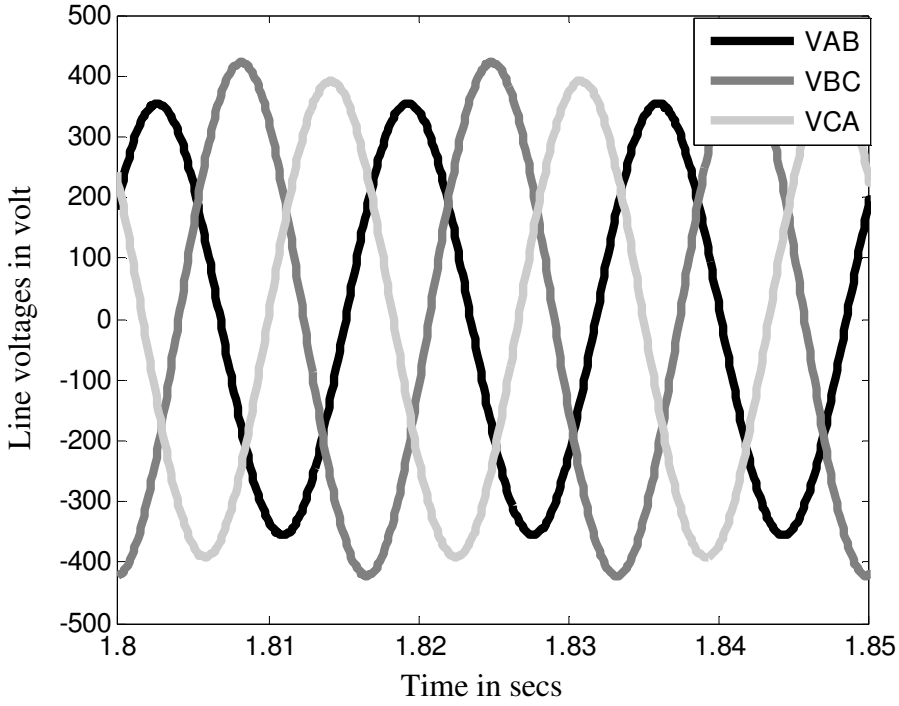

Fig.3.41c Three line voltages, open-loop mode, open-Delta mode of operation while the compensation controller was enabled, Simulink/Flux2D model

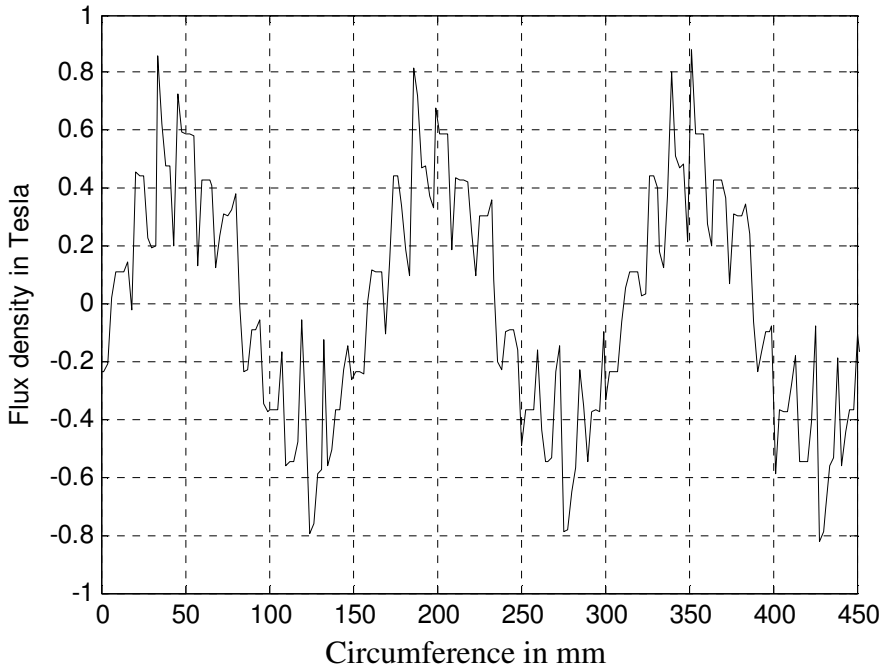

Fig.3.42a Airgap flux density, open-loop, when the introduced controller was deactivated under two-phase open-Delta operation, 60Hz "Coupled Simulink / Flux2D".

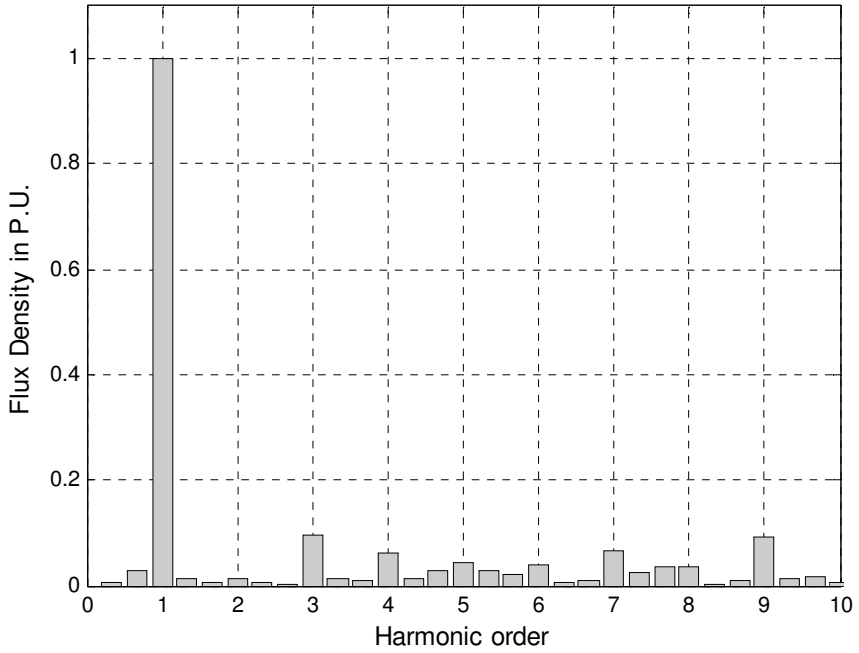

Fig.3.42b Spectrum of the airgap flux density, open-loop, when the introduced controller was deactivated under two-phase open-Delta operation, 60Hz "Coupled Simulink / Flux2D".

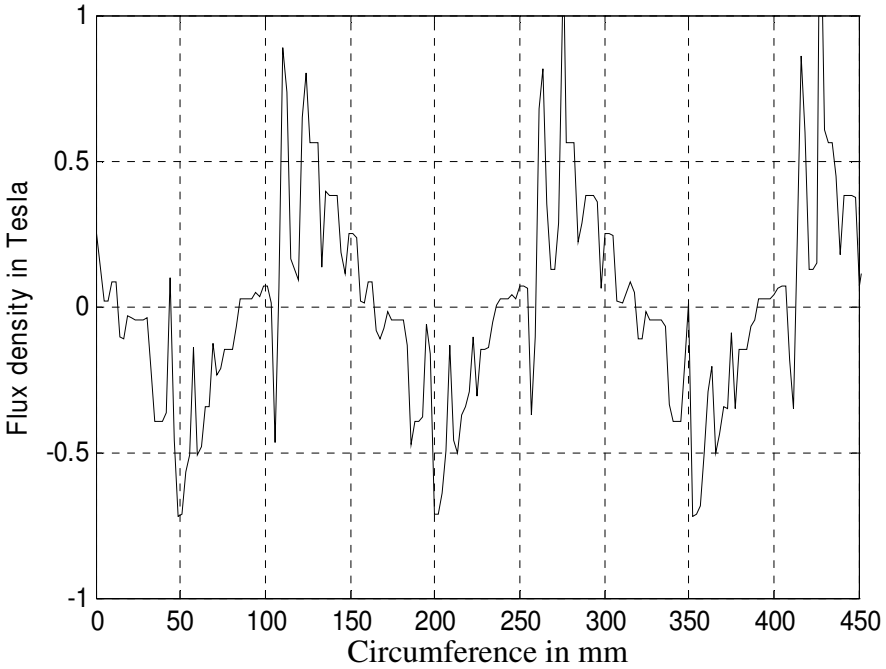

Fig.3.43a Airgap flux density at a given time instant, open-loop, when the introduced controller was activated under two-phase open-Delta operation, 60Hz "Coupled Simulink/Flux2D".

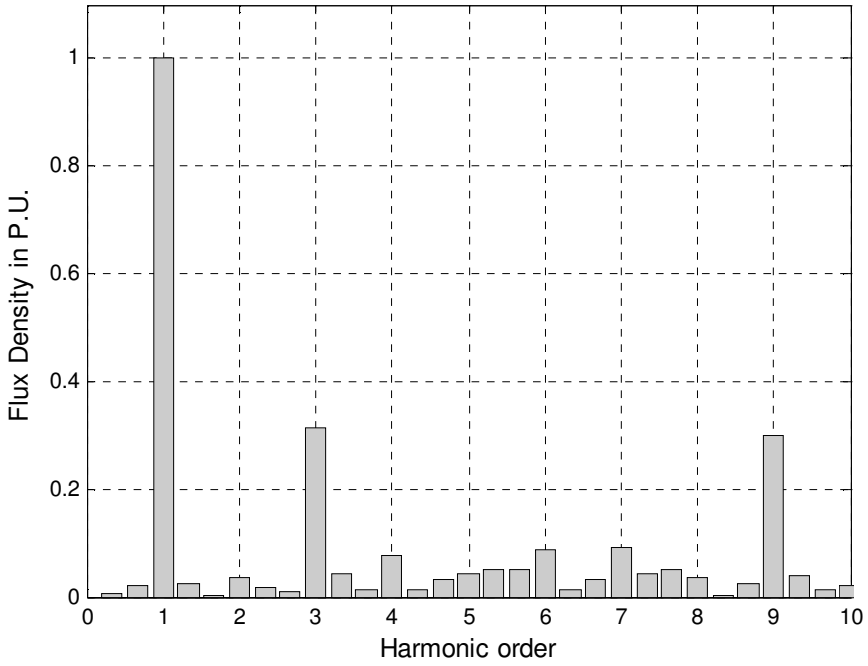

Fig.3.43b Spectrum of the airgap flux density, open-loop, when the introduced controller was activated under two-phase open-Delta operation, 60Hz "Coupled Simulink / Flux2D".

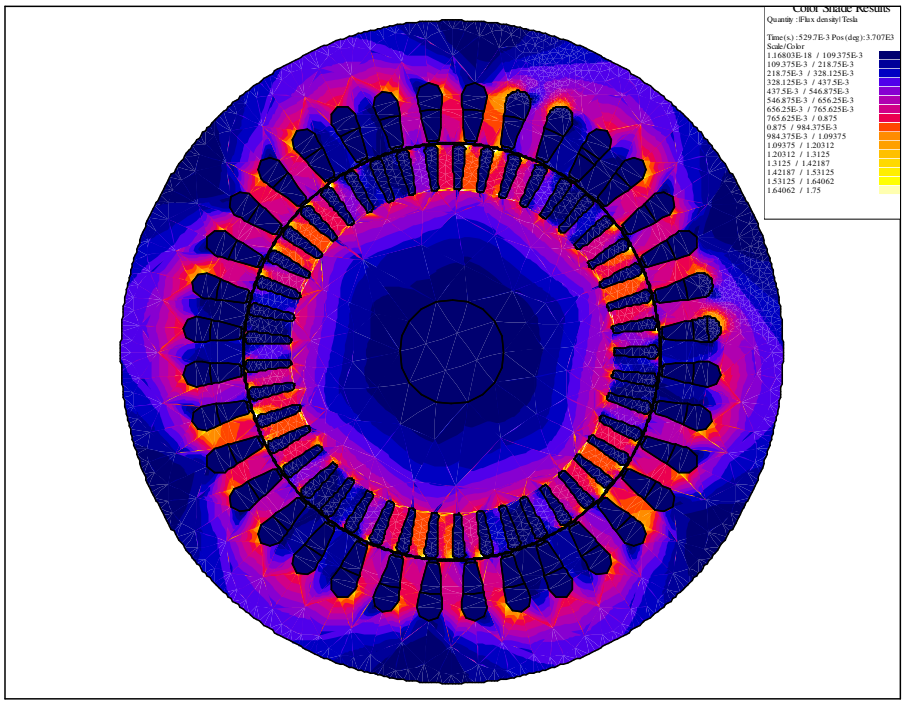

Fig.3.44a Flux density color shade plot at a given time instant, open-loop, the introduced controller was activated, three-phase operation, 60Hz, "Coupled Simulink / Flux2D"

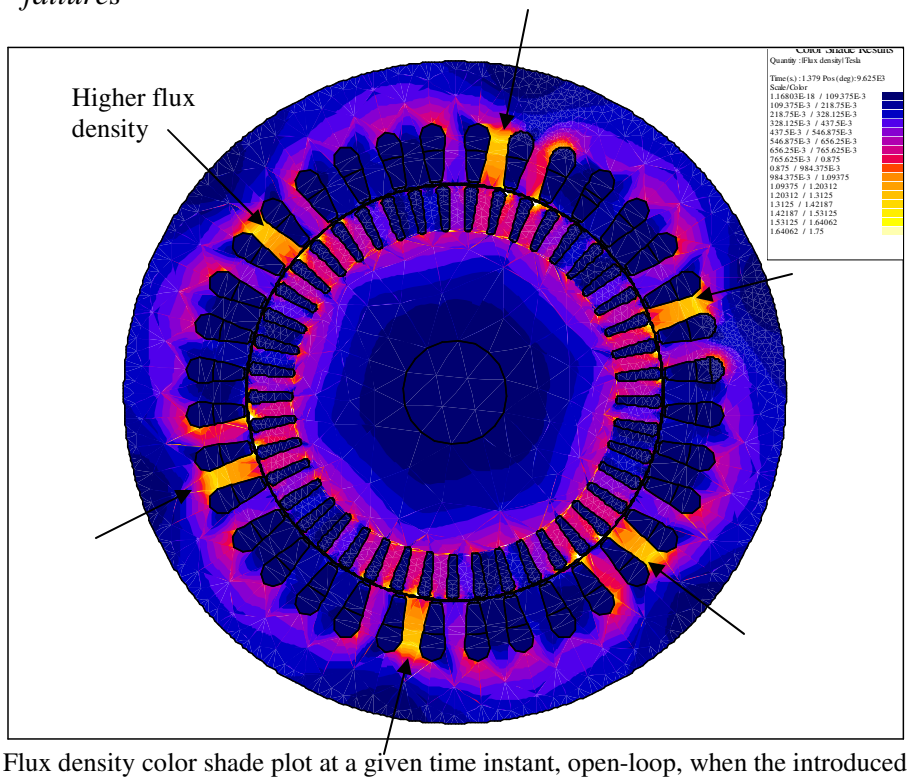

Fig.3.44b Flux density color shade plot at a given time instant, open-loop, when the introduced controller was activated, two-phase open-Delta operation, 60Hz "Coupled Simulink / Flux2D".

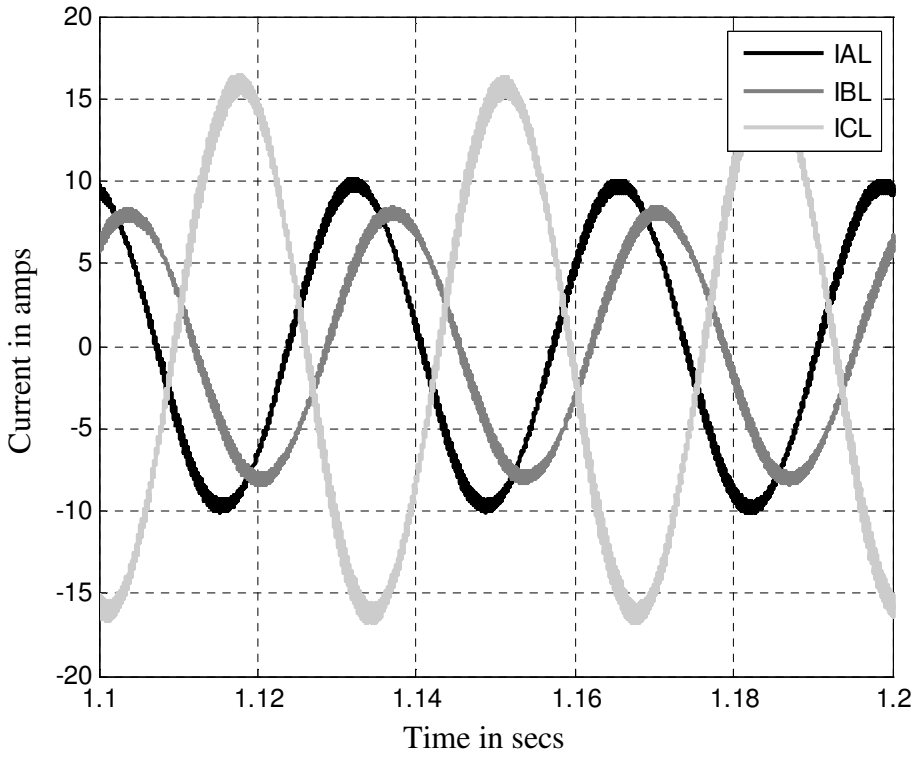

Fig.3.45a Line currents, open-loop, when the introduced controller was deactivated under two-phase open-Delta operation, 30 Hz "Simulink/Simpowersystem model".

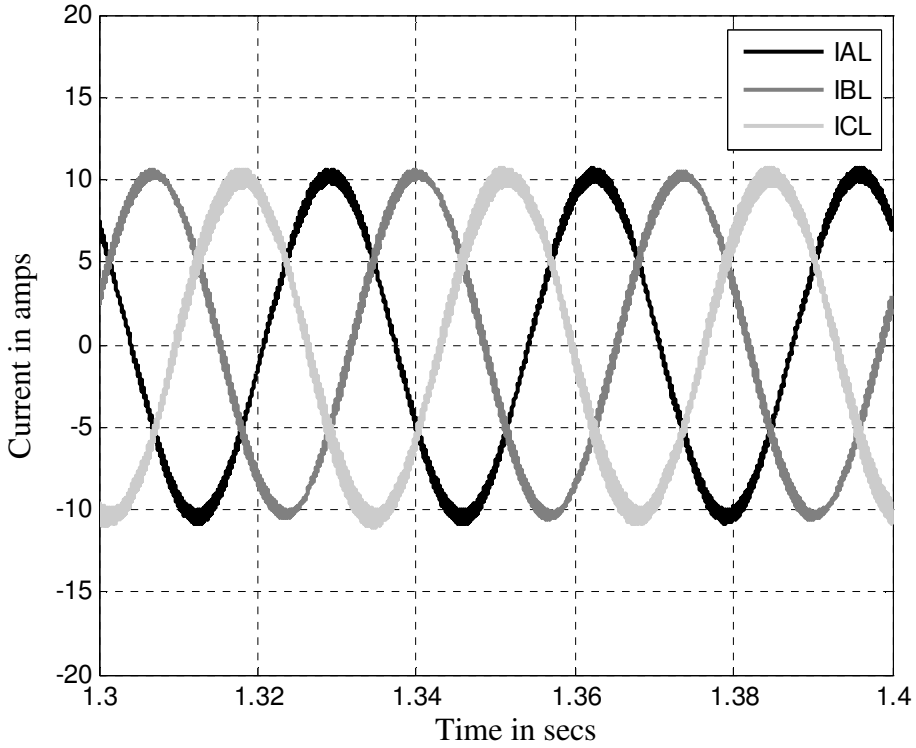

Fig.3.45b Line currents, open-loop, when the introduced controller was activated, under two-phase open-Delta operation, 30 Hz "Simulink/Simpowersystem model".

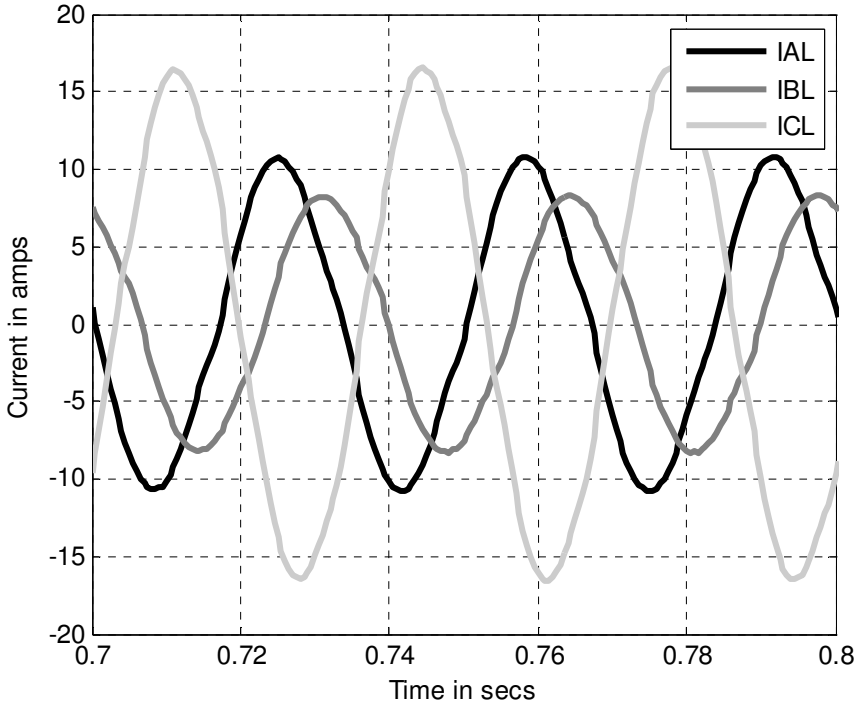

Fig.3.46a Line currents, open-loop, when the introduced controller was deactivated under two-phase open-Delta operation. 30Hz "Coupled Simulink / Flux2D".

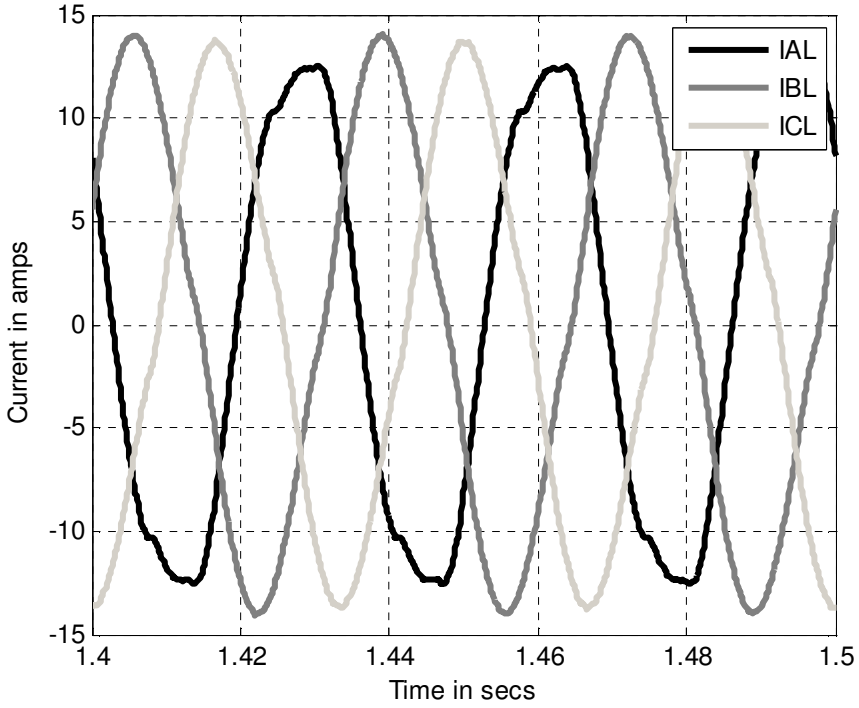

Fig.3.46b Line current spectrum, when the introduced controller was activated under two-phase open-Delta operation, 30Hz "Coupled Simulink / Flux2D".

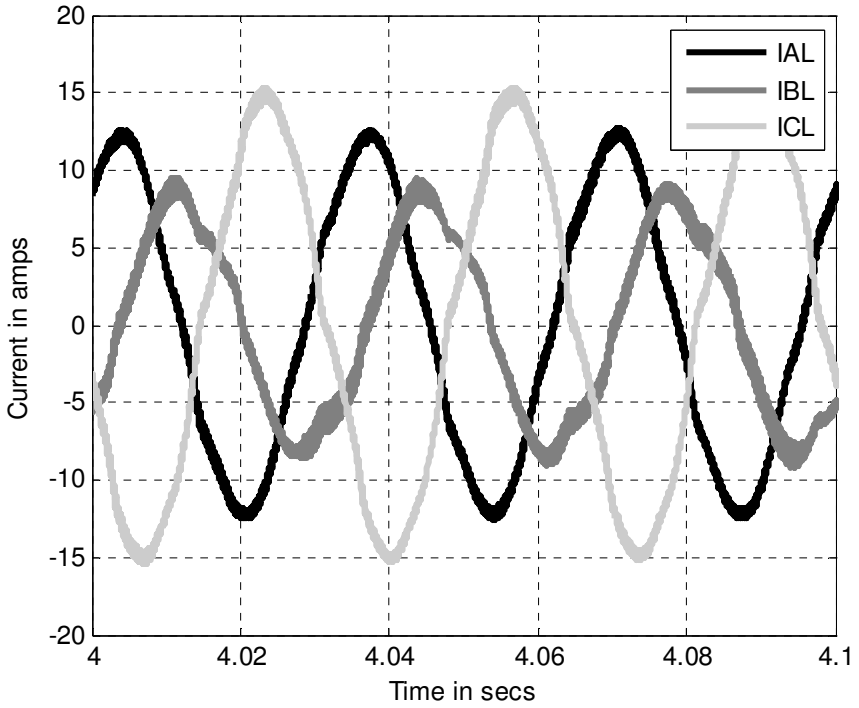

Fig.3.47a Experimentally obtained line currents, open-loop, when the introduced controller was deactivated under two-phase open-Delta operation, 30 Hz .

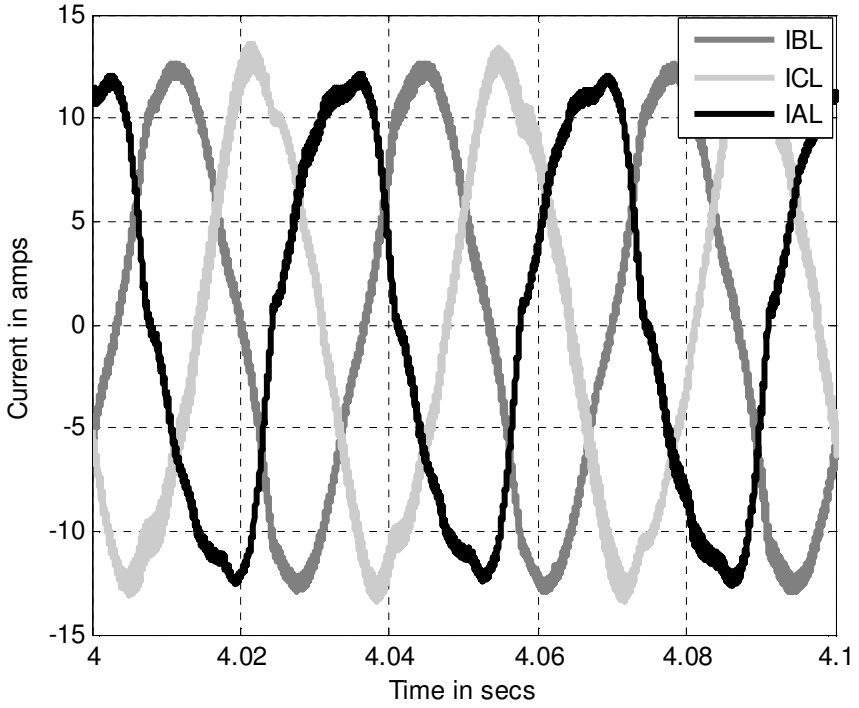

Fig.3.47b Experimentally obtained line current , open-loop, when the introduced controller was activated under two-phase open-Delta operation, 30 Hz.

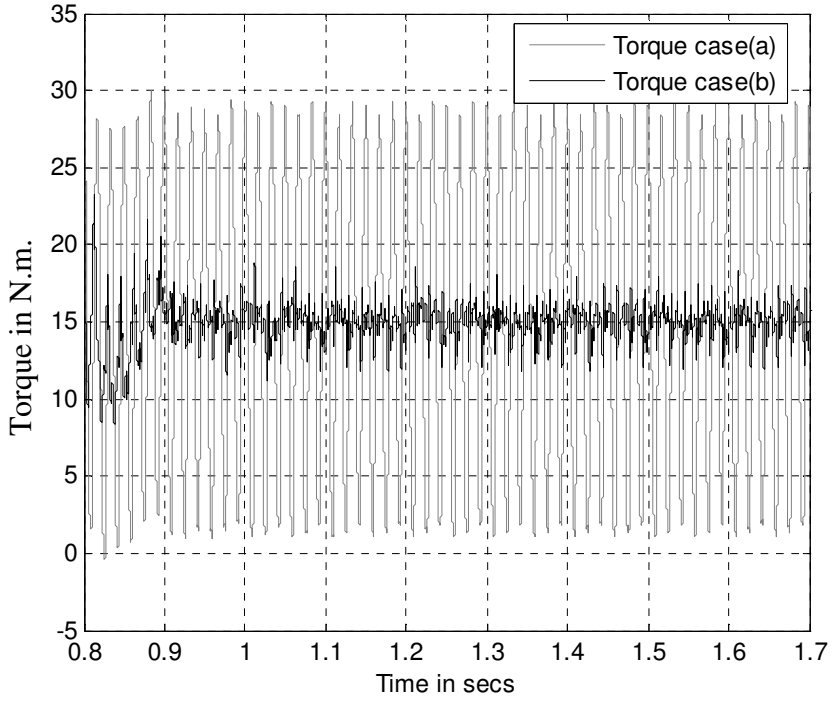

Fig.3.48 Output torque, open-loop, under two-phase open-Delta operation, 30Hz, "Simulink/Simpowersystem model":
Case (a) The introduced controller deactivated, Case (b) The introduced controller activated

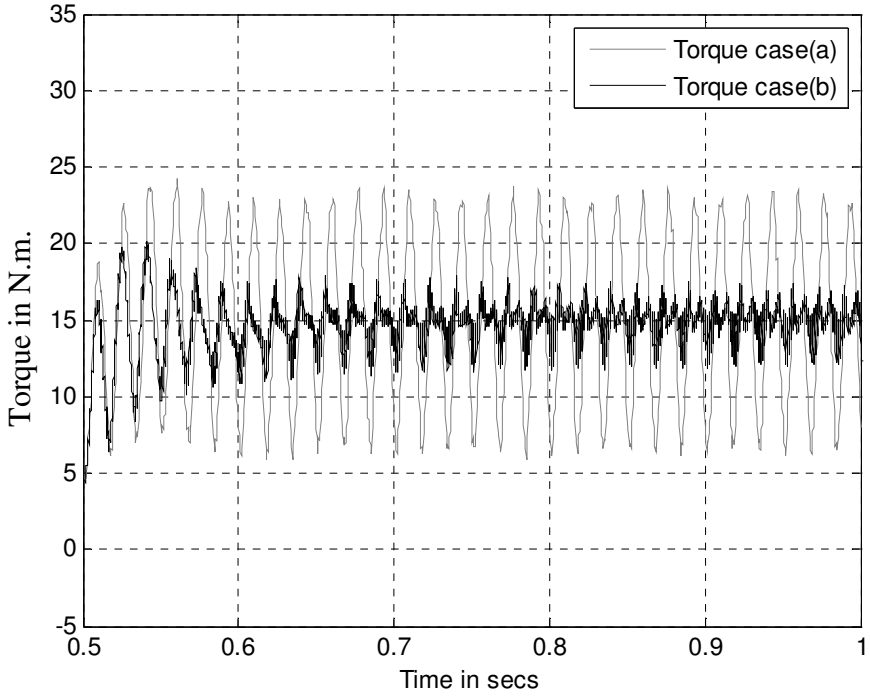

Fig.3.49 Output torque, open-loop, under two-phase open-Delta operation, 30Hz "Coupled Simulink / Flux2D"
Case (a) The introduced controller activated, Case (b) with the introduced controller deactivated

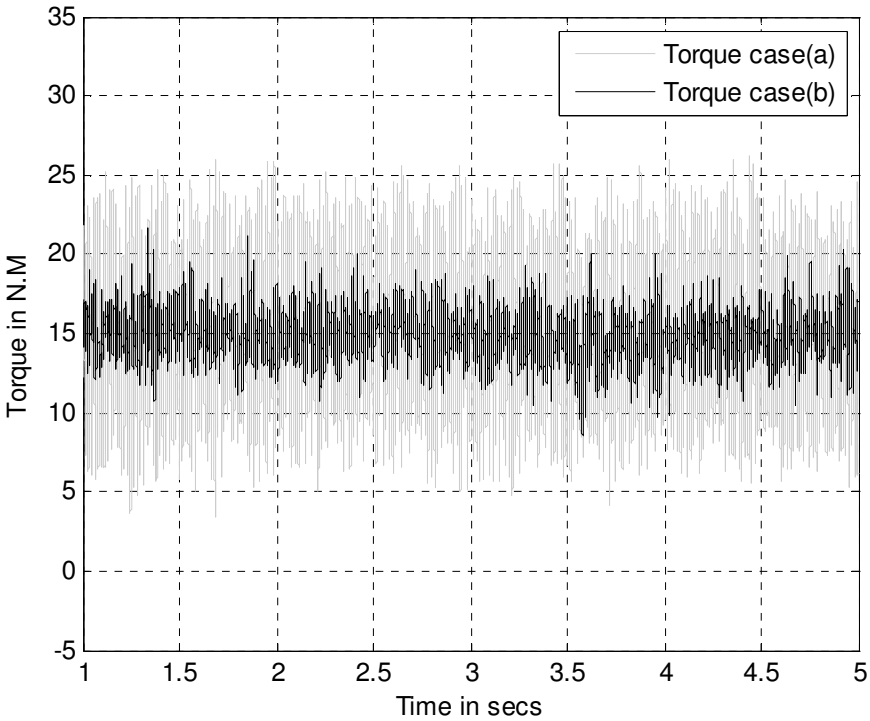

Fig.3.50 Experimentally obtained output torque, open-loop, under two-phase open-Delta operation, 30Hz.
Case (a) The introduced controller deactivated, Case (b) The introduced controller activated

3.9 Summary

The conceptual and theoretical background as well as the validating experimental results of a new control technique that enables the two-phase mode of operation of an open-loop motor-drive system, with a motor's stator winding connected in a Delta configuration was presented in this chapter. This technique takes advantage of the additional degree of freedom inherently provided in an open-Delta polyphase stator winding configuration in which the current in the two remaining active phases can be controlled independently. Also, in this chapter, it was shown that the controller introduced here can be activated at normal operation as well as at faulty operating conditions, which enhances the "robustness" of the control system. The control structure of this type of systems was thoroughly discussed and analyzed, followed by a detailed procedure for the controller design. It was also shown that one of the advantages of the open-Delta configuration is that the phase currents in the remaining active phases can be controlled independently such that an only forward rotating component (CCW) MMF can be produced while keeping balanced line currents with only a positive sequence component. The introduced control topology does not require oversizing of the drive. The theoretical analysis introduced in this chapter is also valid for permanent magnet ac machines with Delta-connected stator windings. It was also shown that the introduced controller can be activated at normal "three-phase" mode of operation without adversely affecting the drive's performance. Meanwhile, the introduced controller was able to significantly diminish unbalances in line currents, as well as diminish the torque pulsations resulting from the faulty "two-phase open-Delta" mode of operation. The concepts and the theoretical background introduced were verified through numerous

simulation and experimental results. Two different simulation models were utilized in this work. The first one was implemented in Simulink/Simpowersystem in which the machine's MMF space harmonics and core saturation effects were not accounted for. The second model was implemented using Simulink/Flux2D link technology in which the controller was implemented in a Simulink environment while the machine model was implemented using MAGSOFT-Flux2D TSFE software. The TSFE model accounts for saturation effects as well as space harmonics due to machine winding layouts and magnetic circuit configuration including saturation. In addition, the TSFE model provided access to key magnetic quantities required for rigorous analysis, and in depth study of the motor and system's performance. The introduced technique was experimentally implemented and tested using a 5-hp motor-drive set-up, where the control algorithms were hosted in the DSP TMS320F2812, manufactured by Texas Instruments, and interfaced with a commercial drive. As expected, the experimental results were in closer agreement to the simulation results obtained from the Simulink/Flux2D model than to the corresponding simulation results obtained from the Simulink/Simpowersystem model because of its simplified machine representation. The results obtained from the Simulation runs and the experimental testing demonstrated the efficacy of the introduced control topology in diminishing the torque pulsations at two-phase "open-Delta" mode of operation of Delta-connected induction motors, and its efficiency in diminishing the unbalances in their line currents.

CHAPTER 4

4. CONTROL OF CLOSED-LOOP VECTOR-CONTROLLED MOTOR-DRIVE SYSTEMS UNDER STATOR WINDING FAILURES

4.1 Introduction

A new fault mitigation strategy for open-loop scalar constant (V/f) control was discussed in the previous chapter. In this chapter, this fault mitigation strategy is extended to the case involving a closed-loop vector-controlled motor-drive system that is usually used when precise speed and torque control are required, [3]. The main advantage of a vector-controlled motor-drive system is that it decouples the motor flux and the motor torque such that each of them can be controlled independently, [14, 25, 26]. This unique capability enables the induction motor control system to replicate the unique torque and speed performance of a dc motor with a separate field excitation, [14, 25, 26]. On the other hand, a vector-controlled motor-drive system requires high processing power and relatively larger code memory compared to open-loop scalar (V/f) control. The wide availability and lower cost of modern DSPs (Digital Signal Processors) and Power PCs made this memory and processing speed hurdle easy to overcome. Therefore, the outstanding performance, relatively low cost, ruggedness and reliability of the induction motor enabled vector-control induction motor-drive systems to be widely accepted, and to invade the drives market in numerous applications replacing the former commonly used dc motor-drives, [25]. Meanwhile, the widespread use of this type of ac

motor-drive systems required the manufactures to enhance the robustness and the reliability of such system with respect to external faults such as external short-circuit, external power disturbances, immunity to electromagnetic interference etc, [3]. This is in addition to the reliability of internal drive components such as semiconductor devices, dc-link inductors, dc-link capacitors, and other power components that may exist in a drive, [3]. However, as mentioned before in Chapter 3, this relatively enhanced reliability and consequent increased mean time between failures were found to be not quite satisfactory in many critical applications that require extreme levels of equipment availability and reliability. Consequently, conventional design techniques usually apply the concept of redundancy to enhance and consolidate the overall system reliability and availability. Although redundancy is an ideal solution from the reliability prospective, size limitations, increased system weight and cost may make the redundancy principle unattractive, or even render such option to be an impractical solution in many applications as discussed in Chapter 3. Therefore, several investigations, [100-106, 109-110, 112-123, 125-128] were mainly focused on developing motor-drive systems that already posses all the existing system reliability, with additional capabilities that enable the system to continue further operation while a fault may exist either in the motor or in the drive. This is referred to in this dissertation as “limp-home” capability. To the best of this author’s knowledge, and based on the literature survey presented in Chapter 1, most of these techniques were mainly focused on electric machines that have Wye-connected stator windings [100,101, 109-110,112,122-130]. Fault mitigation for electrical machines that have Delta-connected stator windings are almost absent from the literature.

Therefore, the introduced fault mitigation strategy is mainly centered on vector-controlled motor-drive systems where the machine stator is Delta-connected. This fault mitigation strategy enhances system reliability with respect to stator winding failures, such that it enables the motor to run, with minimized torque ripples, in a two-phase open-Delta mode of operation. Also, the analysis and discussion presented in this chapter presumes that stator windings have an open-coil fault, that may result from rupture in the winding and/or internal loose connection, [55, 60,149], or the stator windings have an inter-turn short-circuit fault that has been detected in an early stage and the corresponding phase has been disconnected, using the diagnostic techniques already present in the literature [43-62]. The case which involves an inter-turn short-circuit fault in an advanced stage, with a significant faulty loop current circulating in these shorted turns is not discussed in this chapter but it is discussed in Chapter 5. As one proceeds through this chapter, first, the basic principles of vector-controlled motor-drive systems will be briefly discussed for the sake of completeness and for the reader's convenience. Then, a review of the state of the art of the literature will be presented underlining the capabilities and the limitations of each fault mitigation technique. The controller being introduced here together with an insight into its theory of operation is described for the case of vector-controlled motor-drive systems. This is followed by the presentation of a detailed procedure for the controller design. The details of the simulation models utilized in this chapter are described last. As described earlier in Chapter 3, two different types of simulation models are utilized in this work, the first model is based on a Simulink/Simpowersystem simulation and the second one is based on a Coupled Simulink/Flux2D time stepping FE simulation. Since these two models were detailed

earlier in Chapter 3, only the differences between the simulation models implemented for the work presented in Chapter 3 and the work presented in this chapter are discussed. Finally, the presented analysis and discussion in this chapter are verified using several simulation runs and experimental test data.

4.2 Basic principles of vector-controlled motor-drive systems

In a separately excited dc machine, the motor torque and the motor flux can be controlled independently. The developed torque, neglecting the armature reaction effect, can be expressed in terms of the machine design constant, *K,* the armature current, I_a , and the field current , I_f as follows,[151]:

$$T = K\ I_a\ I_f \tag{4.1}$$

Therefore, from (4.1), the machine's developed torque is a function of the armature current, I_a , and the field current, I_f . The field current is usually kept constant and it is usually adjusted to keep a constant flux in the machine that is equal to the rated machine flux in the constant torque mode of operation, [151]. Meanwhile, the motor's developed torque is adjusted through controlling the armature current, [151]. Since the motor flux and developed torque current components are completely decoupled, excellent torque and speed control performance can be achieved both under transient and at steady state operations.

The main target of the vector-controlled induction motor-drive system is to replicate the excellent speed and torque control performance of dc motor-drive systems. This can be achieved by transforming the motor equations into a suitable synchronously

rotating frame of reference in which the sinusoidal varying variables appear as dc components. It is also required to decouple the flux current component and the torque current component in this synchronously rotating frame of reference component in the motor current [14, 25, 26]. The basic equations for a three-phase induction motor in a synchronously rotating frame of reference can be expressed as follows, [14,25,26]:

$$v_d^e = R_s i_{ds}^e + \frac{d\psi_{ds}^e}{dt} - \omega_e \psi_{qs}^e \tag{4.2}$$

$$v_q^e = R_s i_{qs}^e + \frac{d\psi_{qs}^e}{dt} + \omega_e \psi_{ds}^e \tag{4.3}$$

$$0 = R_r i_{dr}^e + \frac{d\psi_{dr}^e}{dt} - (\omega_e - \omega_r)\psi_{qr}^e \tag{4.4}$$

$$0 = R_r i_{qr}^e + \frac{d\psi_{qr}^e}{dt} - (\omega_e - \omega_r)\psi_{dr}^e \tag{4.5}$$

In equations (4.2) through (4.5), v_d and v_q are the voltage components in synchronously rotating frame of reference, R_s is the stator resistance, i_{ds} and i_{qs} are the stator current components in a synchronously rotating frame of reference, Ψ_{ds} and Ψ_{qs} are the stator flux components in the synchronously rotating frame of reference, ω_e is the motor synchronous speed, R_r is the rotor resistance, i_{dr} and i_{qr} are the rotor current components in synchronously rotating frame of reference, Ψ_{dr} and Ψ_{qr} are the rotor flux components in the synchronously rotating frame of reference, ω_r is the motor speed, L_m is the mutual inductance, L_s is the stator inductance, L_r is the rotor inductance, P is the number of the motor poles. Meanwhile, in this frame of reference the developed machine torque can be expressed as follows, [14, 25, 26]:

$$T = (3/4)P \; L_m / L_r (i_{qs}^e \; \psi_{dr}^e - i_{ds}^e \; \psi_{qr}^e) \tag{4.6}$$

In addition, the rotor current components can be related to the rotor flux and stator current components as follows, [14, 25, 26]:

$$i_{qr}^{e} = \psi_{qr}^{e} / L_r - L_m / L_r \; i_{qr}^{e} \tag{4.7}$$

$$i_{dr}^{e} = \psi_{dr}^{e} / L_r - L_m / L_r \; i_{ds}^{e} \tag{4.8}$$

Substituting from (4.7) and (4.8) into (4.2)-(4.5) yields:

$$\frac{d\psi_{qr}^{e}}{dt} + \frac{R_r}{L_r}\psi_{qr}^{e} - \frac{L_m R_r}{L_r} i_{qs}^{e} + (\omega_e - \omega_r)\psi_{dr}^{e} = 0 \tag{4.9}$$

$$\frac{d\psi_{dr}^{e}}{dt} + \frac{R_r}{L_r}\psi_{dr}^{e} - \frac{L_m R_r}{L_r} i_{ds}^{e} + (\omega_e - \omega_r)\psi_{qr}^{e} = 0 \tag{4.10}$$

If the synchronously rotating frame of reference is particularly chosen with angular orientation such that the resultant rotor flux is aligned along the d-axis, it follows that $\psi^{e}_{qr} = 0$, and also $\frac{d\psi_{qr}^{e}}{dt} = 0$. Accordingly, equations (4.9) and (4.10) can be reduced to the following form:

$$\omega_e = \omega_r + \frac{L_m R_r}{L_r} \frac{i_{qs}^{e}}{\psi_{dr}^{e}} \tag{4.11}$$

$$\frac{d\psi_{dr}^{e}}{dt} + \frac{R_r}{L_r}\psi_{dr}^{e} = \frac{L_m R_r}{L_r} i_{ds}^{e} \tag{4.12}$$

Also, the torque expression in (4.6) can be simplified and rewritten as follows:

$$T = \frac{3}{4} P \; \frac{L_m}{L_r} i_{qs}^{e} \; \psi_{dr}^{e} \tag{4.13}$$

Accordingly, using equations (4.12) and (4.13), if the rotor flux , ψ^{e}_{dr} =constant, which is usually the case [14,25,26], the machine flux and torque can be controlled independently based on a reference Torque, T^* and a reference flux, $\psi_{dr}^{e\,*}$, such that, [14,25,26]:

$$i_{qs}^{e\,*} = \frac{4\ T^{*} L_r}{3 L_m P\ \psi_{dr}^{e}} \qquad \& \qquad i_{ds}^{e\,*} = \frac{\psi_{dr}^{e\,*}}{L_m} \tag{4.14}$$

Where, $i_{qs}^{e\,*}$ and $i_{ds}^{e\,*}$ are the stator reference current components in this frame of reference.

Therefore, in a voltage-source inverter in which the motor currents are controlled, the so-called voltage-source current-controlled inverter, the motor currents should be controlled in real- time to render these currents equal to the reference current components $i_{qs}^{e\,*}$ and $i_{ds}^{e\,*}$, which are correspondingly calculated based on the commanded reference torque, T^{*} ,and reference d-axis flux, $\psi^{e}{}_{dr}{}^{*}$. In the speed control mode, the reference torque is usually obtained from an outer speed loop. Meanwhile, reference torque may be also obtained from an external reference in automated processes. A functional block diagram of such a vector-controlled motor-drive system in speed control mode is depicted in Fig.4.1

In spite of the solid theoretical basis of the concept of vector-control for induction motors introduced above, accurate implementation in real-time of this scheme has the following challenges, [25]:

- Motor parameters should be accurately known
- Estimation of parameter variations and perturbation during normal operation, which is a relatively difficult task, should be accurately obtained.
- Motor speed should be accurately measured or estimated.
- Optimum tuning of the current controllers and speed controller gains are mandatory to guarantee optimum performance.

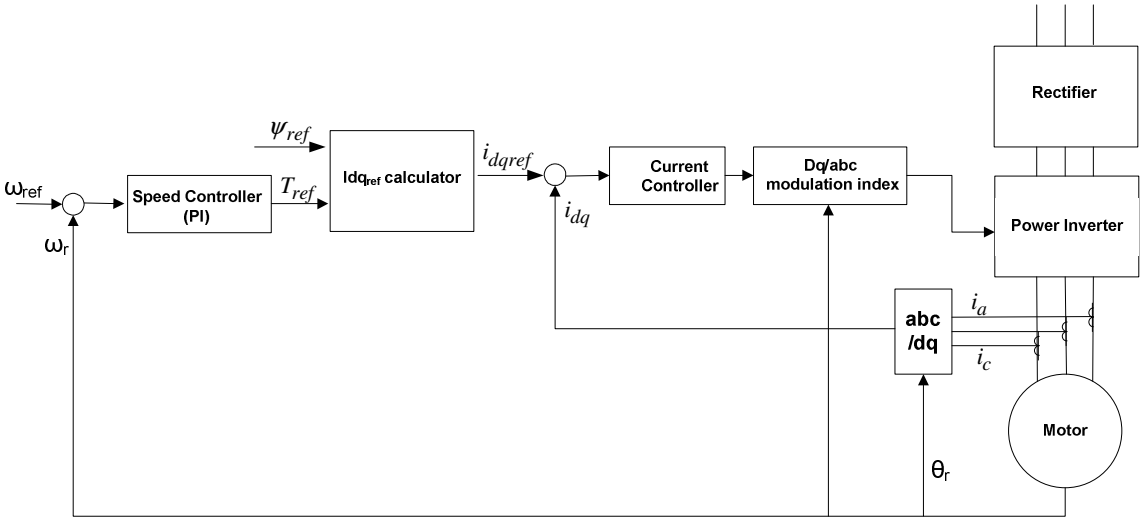

Fig.4.1 A simplified functional block diagram of a vector-controlled motor-drive system

Most of the previously mentioned challenges have been addressed and resolved either in several publications, [17-19, 21], or in patents that are intellectual properties for drives manufactures [20, 23]. Therefore, vector-controlled motor-drive systems were able to replace traditional dc motor-drive systems in new installations and in plant retrofitting projects in most industrial applications that require precise speed and torque control.

4.3 Previous work related to this investigation

Fault-mitigation topologies for vector-controlled motor-drive systems that may enable the motor to run in two-phase open-Delta mode of operation were briefly summarized in Chapter 1. These topologies are revisited in more detail in this section.

4.3.1 Connecting the neutral point of the motor to the midpoint on the dc bus-link

As discussed earlier in detail in Chapter 3, Wye-connected stator windings free from stator winding faults have two Degrees of Freedom (2-DOF) for three-phase normal mode of operation. On the other hand, Wye-connected stator windings have only 1-DOF

in a two-phase mode of operation, with one of the motor phases disconnected due to the presence of a fault in that phase. In this case, the winding currents of the two remaining active phases are dependent on each other, and have a phase shift of 180 deg.elect between each other for example that is $i_{a=}$-i_b. This topology is based on providing an additional Degree of Freedom (DOF) by connecting the neutral point of the Wye-connection of the stator to the mid point in the dc bus, [112]. This is in order to enable the motor-drive system to continue operation while only two phases of the motor are connected to the inverter. This topology is re-shown in Fig.4.2 for the reader's convenience.

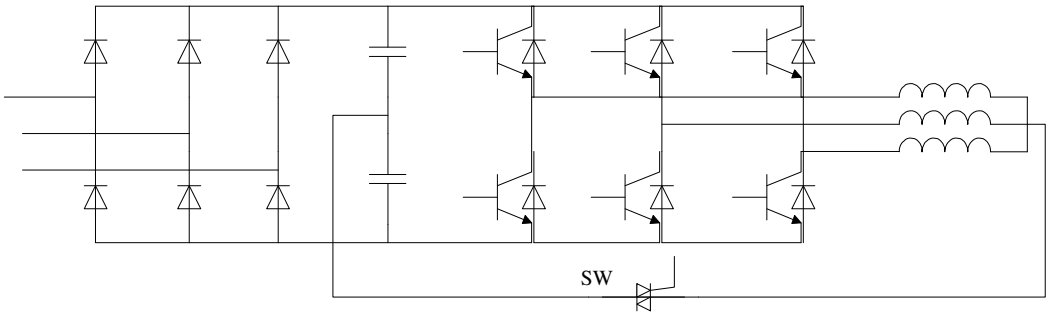

Fig.4.2 Power structure of the converter with the neutral of the motor connected to the midpoint of the dc-link,[112].

Under normal operation, the static switch, "SW", is kept open and the motor can run in the ordinary three-phase mode of operation. Upon fault detection, the faulty phase is deactivated and the motor-drive system should run in the two-phase open-Delta mode of operation with the switch "SW" in a closed status. The motor currents are controlled such that the phase shift between these remaining currents of the two-phase open-Delta is 60 deg.elect as depicted in the phasor diagram of Fig.4.3, [109, 112]. This enables the motor to have a predominantly rotating field component such as in the three-phase mode of operation, as described in Chapter 3 and explained earlier in [112]. This topology enhances the reliability of the motor-drive system with respect to several fault scenarios

such as an IGBT fault in an inverter, blown fuse, gate drive failure, and partial phase winding failure. On the other hand the disadvantages and limitations of this topology can best be summarized as follows:

- The topology is only applicable for Wye-connected stator windings with an accessible neutral connection.

- For the same power, motor line currents are increased to a value equal to $\sqrt{3}$ of the rated current value, thus the drive and windings have to be capable of carrying such overloads for extended periods of times.

- Also, for the same power, the neutral current is increased to a value equal to three (3) times that of the rated current value as shown in Fig.4.3. This may lead to premature failure of the dc-link capacitors if such capacitors are not properly designed and oversized to accommodate these current stresses resulting from this mode of operation.

- It is usually required to design a motor's stator winding with an appropriate pitch factor in order to eliminate or minimize the effects of the resultant airgap MMF space harmonics, [2,111]. Mainly, one seeks to suppress the fifth and seventh harmonics. Third order harmonic current and its multiplies can not circulate in the stator winding due to the physical nature of the Wye-connection, with an isolated neutral for a balanced three-phase mode of operation. However, for this configuration of Fig.4.2, a third harmonic current may circulate in the motor phase windings and return through the neutral connection of the motor to the drive. This third harmonic current will produce a corresponding third harmonic MMF component in the airgap. This third harmonic MMF

component in the airgap will interact with the fundamental MMF component in the airgap producing torque ripples with a frequency equal to double the fundamental frequency. To the best of this author's knowledge, this phenomenon has not been addressed in the literature except for the work presented in this dissertation.

- An additional static switch with its corresponding control circuit and its corresponding heat sink are required.

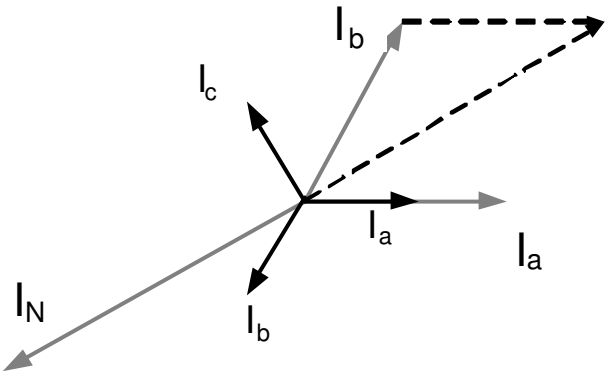

Fig.4.3 Phasor diagram of motor currents at normal operation and in two-phase open-Delta mode of operation.

4.3.2 Multiphase topology

This topology is based on providing additional DOF by using the concept of using multiphase systems instead of a three-phase system, [109]. Consequently, for an n- phase system, n>2, there is (n-1) DOF. The main target of this topology is to generate the same rotating MMF with a minimum possible current magnitude, and obtain a balanced set of currents with neither a negative sequence current component nor a zero sequence current component, [109,110]. For instance, a five-phase motor-drive system can continue to operate using only four phases, with one of its phases in an open-circuit condition "phase-1", while generating the same rotating MMF magnitude as that of a five-phase

machine. In this case, with "phase-1" in an open-circuit condition/status, the desired currents in the remaining healthy phases are depicted in Fig.4.4, [109,110,112]. Meanwhile, using the same design concepts for a seven-phase machine, with "phase-1" assumed to be in an open-circuit status, the desired currents in the remaining six phases if one of the phases is open are depicted in Fig.4.5, [109,112].

Although this multi-phase topology might be an attractive solution in some applications, widespread use of this topology might be limited in practice due to the significant extra cost resulting from the additional power switches "IGBTs" required to be added to the converter with their associated control and gate drive circuits, and the extra complexity of the winding layout with its associated implementation steps.

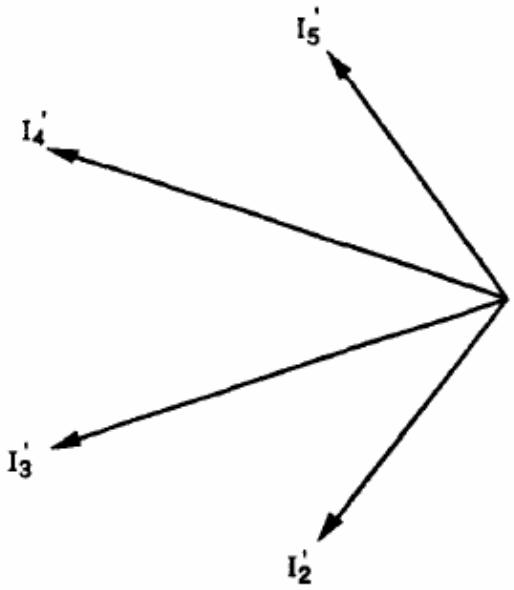

$$I_2^{\backprime} = 1.176I\cos(\theta - \frac{7\pi}{10}), I_3^{\backprime} = 1.902I\cos(\theta - \frac{9\pi}{10}), I_4^{\backprime} = 1.902I\cos(\theta + \frac{9\pi}{10}), I_5^{\backprime} = 1.176I\cos(\theta + \frac{7\pi}{10})$$

Fig.4.4 Phasor diagram of the desired currents for the remaining four phases of a five-phase motor operating in a four-phase mode of operation, [112].

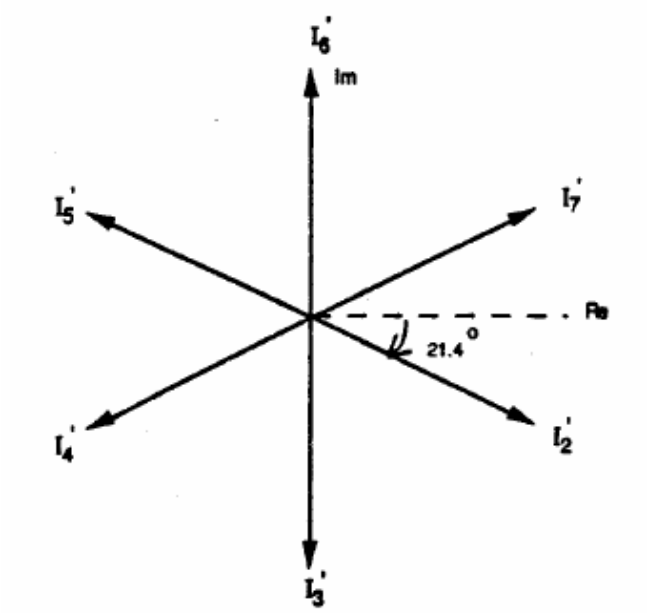

$$I_2^{\backprime} = 1.233I\cos(\theta - 21.4), I_3^{\backprime} = 1.233I\cos(\theta - \frac{\pi}{2}), I_4^{\backprime} = 1.233I\cos(\theta - 158.6),$$

$$I_5^{\backprime} = 1.233I\cos(\theta + 158.6), I_6^{\backprime} = 1.233I\cos(\theta + \frac{\pi}{2}), I_7^{\backprime} = 1.233I\cos(\theta + 21.4)$$

Fig.4.5 Phasor diagram of the desired currents for the remaining six phases of a seven-phase motor operating in a six-phase mode of operation.

4.3.3 Cascaded inverter topology

Additional DOF for a three-phase motor-drive system can be provided by controlling each phase independently through separate single phase bridges as shown in Fig.4.6, [115,123,126]. This topology has been used to provide enhanced reliability for an induction motor-drive system, [115], and for a PM motor-drive system, [123,126]. The three single-phase inverters can be fed through a common dc bus. This topology can enhance system reliability with respect to several fault types either in the motor or in the drive. These faults can be static switch "IGBT" failures, capacitor failures, gate drive failures, or winding failures, [123]. This topology has been used to null the flux through the shorted portion of the winding. The control principle associated with this topology

utilizes the additional DOF to control the zero sequence current component in the motor winding as well as the positive sequence current component, [115,123,126].

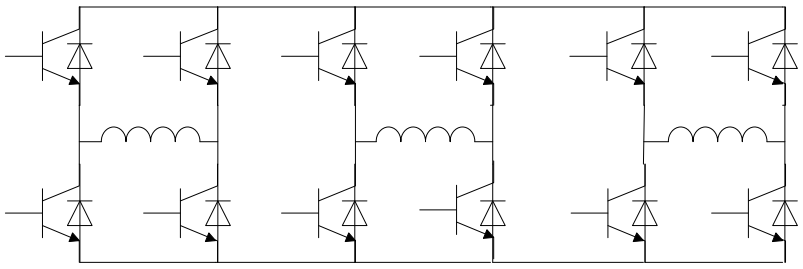

Fig.4.6 Cascaded inverter topology,[115, 123,126].

The reliability and robustness of the cascaded inverter topology with respect to several fault scenarios make it a very attractive choice in applications that requires high reliability. However, the extra cost associated with the additional power switches and their gate drives should be justified, particularly in the light of the additional significant size and weight increase.

4.3.4 Fault- tolerant machines

The reliability of the motor in a motor-drive system is as important as the reliability of the drive. Therefore, several investigations were mainly concerned with developing a motor design that is invulnerable to different fault scenarios, [102,103,115-117,121]. Among the possible fault scenarios that a motor may encounter, a special concern was given to inter-turn short-circuit faults. This is due to the existence of a circulating current with a very high magnitude resulting from this type of fault. This circulating current may produce excessive heat and elevate the windings temperature, thus jeopardizing other coils spatially ones overlapping with this faulted coil in the end-winding region, or in an adjacent coil occupying the same slot. The propagation rate of an inter-turn short-circuit fault is very high and is in range of milliseconds, [50,167-169],

and it is very difficult to accurately predict in advance with a sufficient period of time for implementing remedial action.

Therefore, most of fault-tolerant designs introduced into the literature, [102,103,115-117,121], were based on electrical, thermal and magnetic isolation of the faulty coil from other healthy portions of a winding, and hence eliminate or minimize the propagation of the fault. This can be achieved by minimizing or eliminating the overlap between the coils in the end-winding region, and use single-layer designs to guarantee complete isolation between different coils, [102,103,115-117,121].

The winding configuration introduced in [102], depicted in Fig.4.7, is based on minimizing the overlap between the windings, with a reinforced insulation at the regions of overlap. It was claimed in [102] that this winding configuration might be valid for any electrical machine. Meanwhile, the winding configuration introduced in [116], depicted in Fig 4.8, are entirely based on complete isolation between the stator phases, and elimination of any overlap between the phase windings. The concept of fractional slot concentric windings (FSCW) has been introduced in [132] for optimum operation of a three-phase induction machine. On the other hand, any FSCW design has a significant increase in the magnitude of the MMF space harmonics compared to distributed winding design, which increase the motor and introduce significant torque ripples. The research conducted in [132] studied in more details several stator FSCW designs focusing mainly on induction motors. This research showed that the design with 1/2 slot /pole/phase, depicted in Fig. 4.9, is the most promising design approach with respect to minimized torque ripples and improved efficiency.

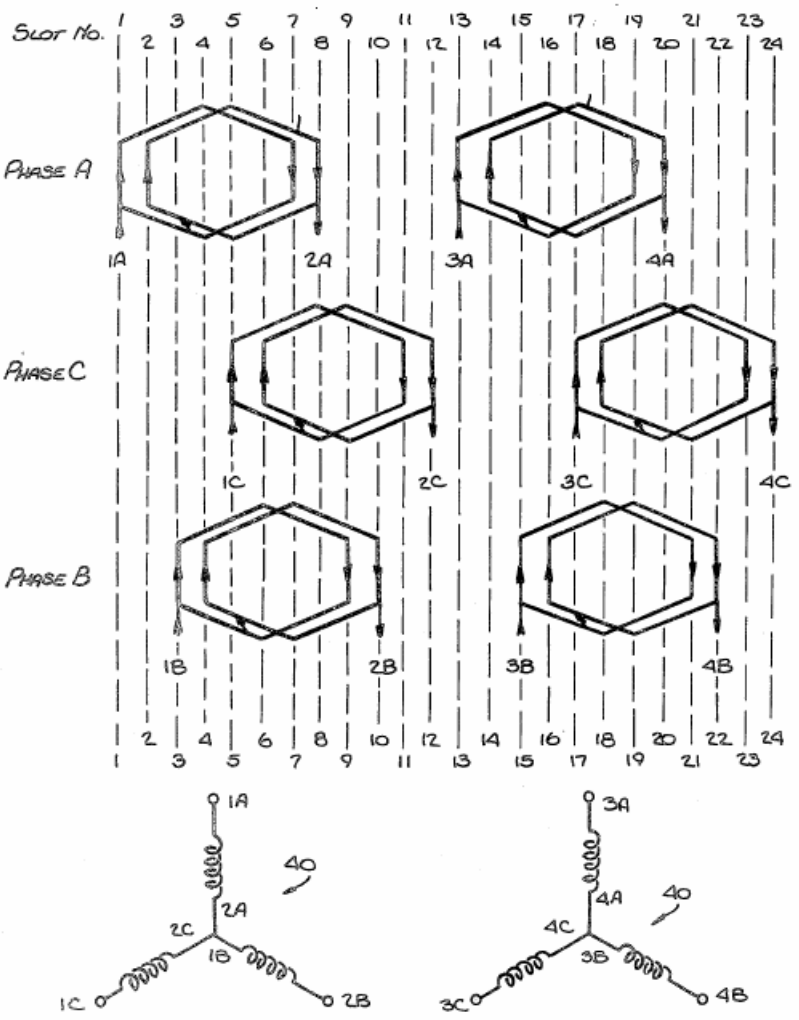

Fig.4.7 Stator winding design with two redundant winding sets with minimized overlap and re-enforced insulation in the overlapping regions, [102]

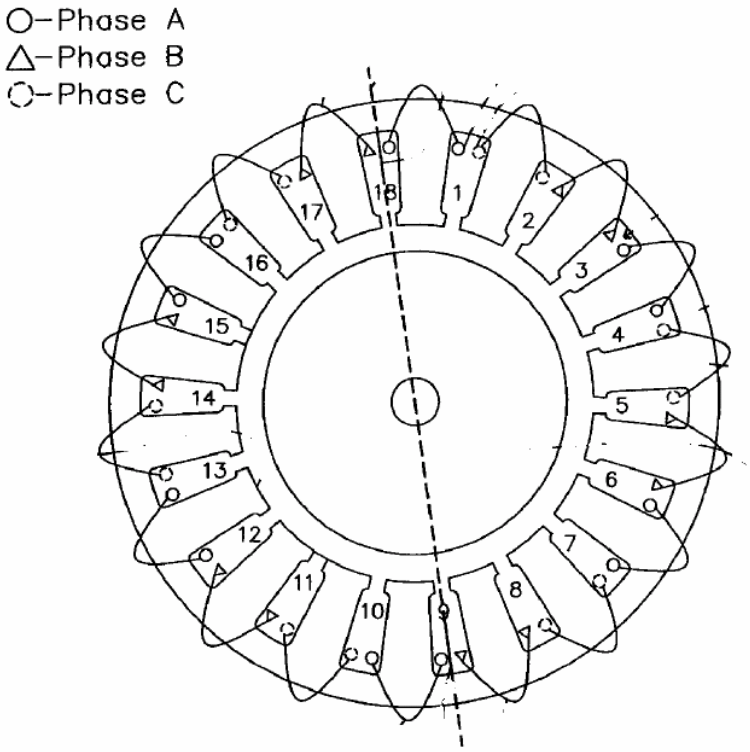

Fig.4.8 Stator winding design without overlapping windings, [116]

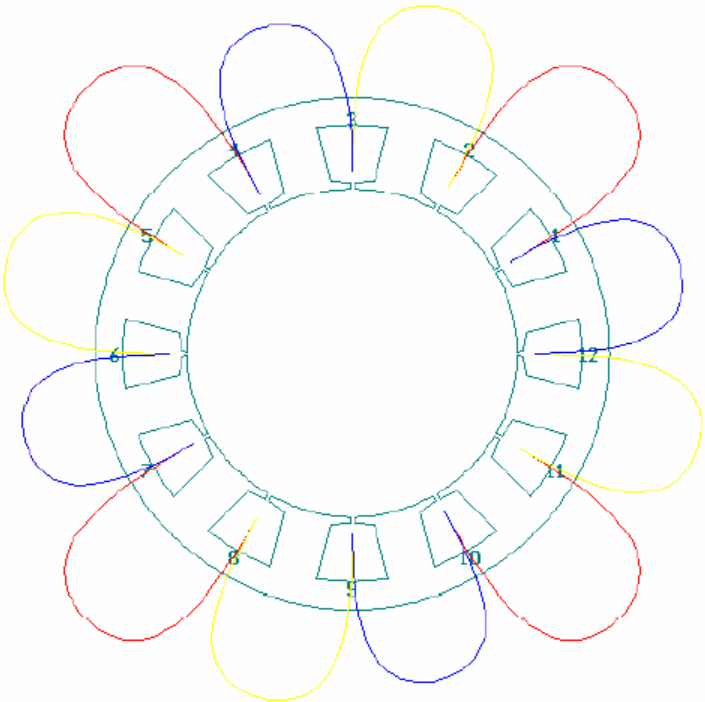

Fig.4.9 FSCW stator design with 1/2 slot/pole/phase, [132]

4.4 An insight into the introduced control strategy

The control strategy for open-loop motor-drive systems, introduced earlier in Chapter 3, is extended here to the case which involves a closed-loop vector-controlled motor-drive system. It was shown in section 4.2 that proper tuning of the d-axis current controller in the rotor flux frame of reference, the q-axis current controller in the rotor flux frame of reference, in addition to the speed control loop, is mandatory to obtain optimum performance during steady-state and transient operation. Modern drives available in the market have internal routines to estimate motor parameters and set the proper controller gains, [63, 64]. This feature in modern drives is also known as self-commissioning, [25]. In analogy to the robust control structure introduced in Chapter 3 for the case of open-loop motor-drive systems, two additional current control loops are added here to the conventional control scheme of the vector-controlled motor-drive system of Fig.4.1. The first control loop is a d-axis current controller also in the CW frame of reference and a q-axis current controller in the CW frame of reference. A functional block diagram of the new control structure is shown in Fig.4.10

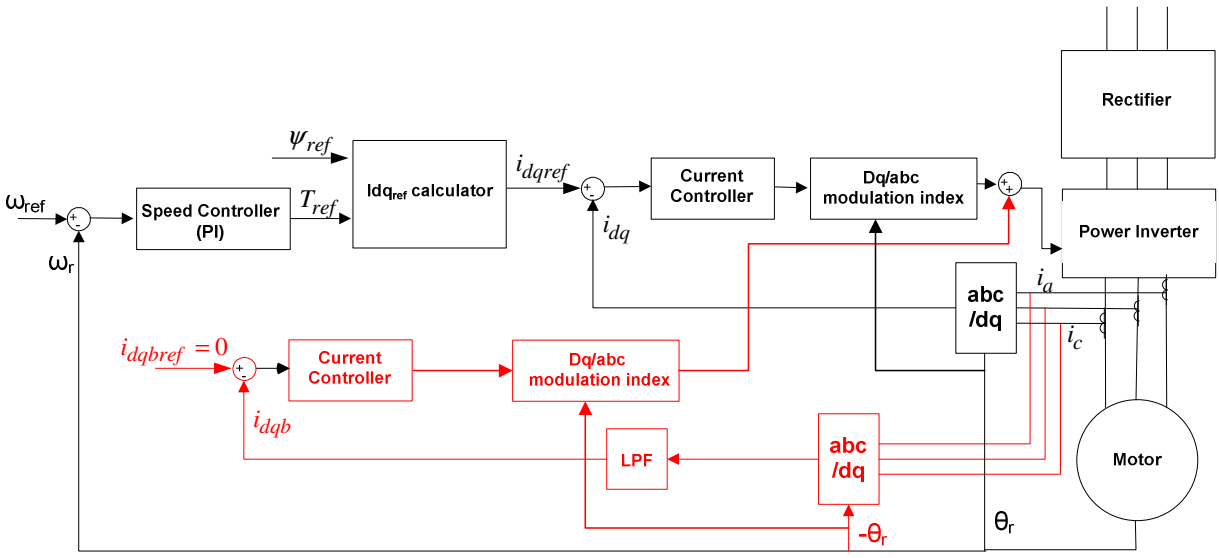

Fig.4.10 A simplified functional block diagram of the introduced vector-controlled motor-drive system

The theory of operation is based on forcing the negative sequence current component to value close or equal to zero. This is achieved through measuring the motor line currents, and then transforming the line currents from the abc stationary frame of reference into a d-q CW synchronously rotating frame of reference, utilizing an angle equal to but opposite to the rotor flux angle "θ_r". In this frame of reference, the negative sequence current component appears as a dc value and the positive sequence current component appears as ac current ripples with a frequency equal to double the line frequency. The ac ripples in this frame of reference are filtered out using a low pass filter with an appropriate cut-off frequency "the cut-off frequency should be much less than twice the line frequency". Then, the d-q current components in this frame of reference are processed through a PI controller to force these current components to a value close or equal to zero. The output of the PI controller is transformed again to the abc stationary frame of reference and added to the main control signal as shown in Fig.4.10, which is consequently processed to the modulator to generate the proper gating signals.

It has been shown in Chapter 3 that the introduced control strategy can be activated during normal operation without affecting system performance for the case of open-loop constant (V/f) scalar control. During normal operation in the three-phase, the magnitude of the negative sequence current component is very small or equal to zero. Hence, the magnitudes of the d-q current components in the previously mentioned CW frame of reference are very close or equals zero. Therefore, the outputs of the PI controllers in the CW current control loop are negligible and do not affect the modulator signal. On the other hand, the magnitude of the negative sequence current component will have a significant value for the case of the two-phase open-Delta mode of operation, in

which one of the motor phases is isolated upon the detection of a phase winding's failure or due to an internal winding rupture in this phase. In this case, the magnitudes of the d-q current components in the synchronously rotating CW frame of reference will have a significant dc value. This dc value is processed through a PI controller in the d-axis and a PI controller in the q-axis. This is in order to force the magnitudes of these current components to zero. The controllers' outputs are then converted to the stationary abc frame of reference which is added to the main modulator signal that correspondingly generates proper gating signals that render a balanced set of the motor line currents.

4.5 Controller Design

In this section, the controller design is explained. The control structure contains a speed regulator, a torque regulator, and a flux regulator commonly used in vector-controlled motor-drive systems in healthy three-phase modes of operation, [25, 26]. This is in addition to two current control loops in the CW synchronously rotating frame of reference to minimize or eliminate torque pulsations associated with the two-phase open-Delta mode of operation under fault conditions. The controller function is best explained as follows:

- The speed regulator, see Fig.4.10, is mainly responsible for controlling the motor speed. The difference between the desired reference speed and the actual measured speed is processed through a PI controller. The output of this PI controller presents a reference torque signal that is forwarded to the current control loop. The steady state and transient performance depend mainly on the

speed controller gains and the system's mechanical time constant which is usually much larger than the electrical time constant [25,26].

- Once the reference torque is obtained, the corresponding reference value of the q-axis current component in the rotor flux frame of reference can be calculated from (4.14). Therefore, the torque regulator is mainly responsible for controlling this current component to render the actual measured value of the q-axis current component in the rotor flux frame of reference equal to the commanded/ reference q-axis current component in the same frame of reference, using a traditional PI controller. The response of this control loop depends mainly on the motor electrical time constant and the controller gains. Consequently, the output torque is regulated through regulating the motor current.
- The flux regulator is mainly dedicated to control the machine airgap flux which is usually kept constant in the constant power region. The corresponding value of the d-axis current component in the rotor flux frame of reference can be calculated using (4.14). Therefore, the flux regulator is mainly responsible for controlling this current component to render the actual measured value of the d-axis current component in the rotor flux frame of reference equal to the commanded/ reference d-axis current component in the same frame of reference, using a traditional PI controller.
- The additional two current regulators introduced in this work are utilizing a CW synchronously rotating frame of reference in order to eliminate or minimize the dc value of the d-axis and q-axis current components in this frame of reference as described in the previous section. The performance of these current regulators

depends on the electrical time constant of the motor, the controller gains, and minimum operating speed.

4.5.1 Torque and flux regulators design

The previous discussion showed that both of the torque regulator and flux regulator designs depend mainly on the electrical time constant of the motor. The design problem is that for the system transfer function given by (3.22). It is required to design a PI controller for the d-axis current component, and for the q-axis current component, in the rotor flux frame of reference in the discrete time-domain to yield design requirements that can be summarized as follows:

- A Band Width BW >1500 rad/sec, in order to obtain an adequate transient response
- A gain margin >15dB, this is in order to ensure stable operation of the experimental control system that includes other nonlinearities which are not considered in this simplified control design procedure. These nonlinearities include dead time effects, dc-link voltage ripples, machine saturation, space harmonics in the machine's airgap flux density,…etc
- A steady-state error<1%

The control system is designed in the discrete time-domain, in which the motor currents are sampled and processed through the controller every 200μsec, in order to replicate the actual DSP implementation in the experimental prototype. Meanwhile, the motor first order model utilized in the controller design for the open-loop motor-drive system explained earlier in Chapter 3 is utilized throughout this chapter. The control system was designed using the Control System Design Toolbox in MATLAB, [162]. The performance of the controller is examined at healthy condition "three-phase mode of

operation", and faulty condition "two-phase open-Delta mode of operation". A simplified current control loop is depicted in Fig.4.11a. The well known space-vector PWM technique, [25, 26], is used to generate proper gating signals based on the reference commands. Therefore, the inverter gain in this case is equal to Vdc/√2, [25, 26]. The first order model for an induction motor, described earlier in Chapter 3 and in [26], is used in the design of the controller gains. The open-loop and the closed-loop responses are depicted in Fig.4.11b and Fig.4.11c for controller gain values, Kp=0.025 and Ki =2. It should be noticed from the open-loop response that the system has a gain margin equal to 16.2 and phase margin equal to 83 degrees. Meanwhile, in Fig.4.11c, it can be noticed from the closed-loop response that the system's BW equals 1830 rad/sec. The performance of the system is also examined for the case of the two-phase open-Delta mode of operation. In this case, the equivalent leakage inductance and the equivalent resistance are obtained by multiplying their original values by three because of the Delta to open-Delta reconnection, [151], and consequently the equivalent transfer function in the discrete time-domain can be calculated. The current control loop for this case is depicted in Fig. 4.12a. Meanwhile, it can be noticed from the open-loop response that the system has a gain margin equal to 25.6, and a phase margin equal to 89 degrees. It can be noticed from the closed-loop response that the system's BW equals 527 rad/sec.

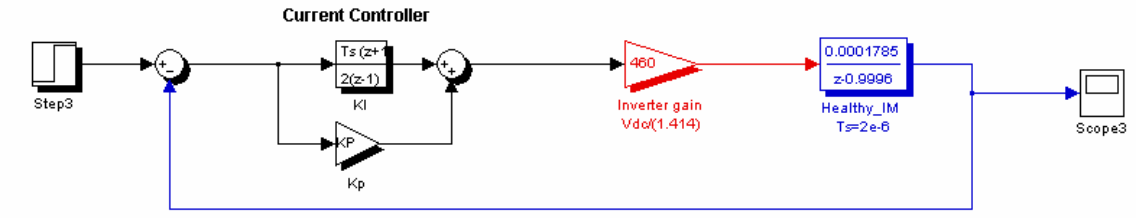

Fig.4.11a Torque/ Flux regulators in the discrete time-domain

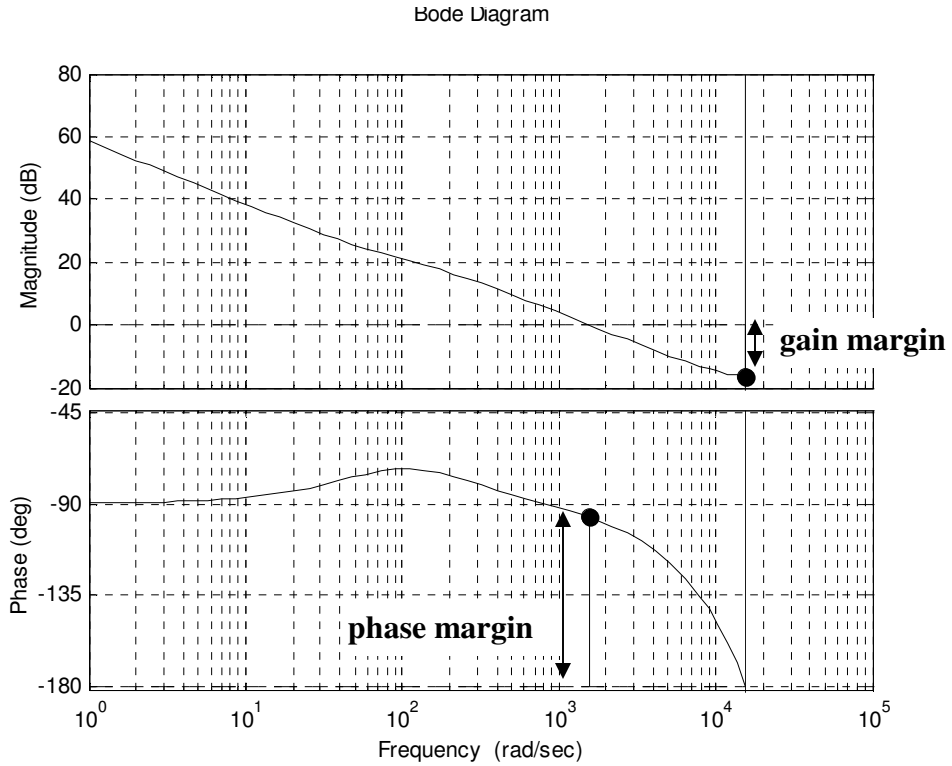

Fig.4.11b Open-loop response for Kp =0.025 & *Ki* =2 "three-phase mode of operation"

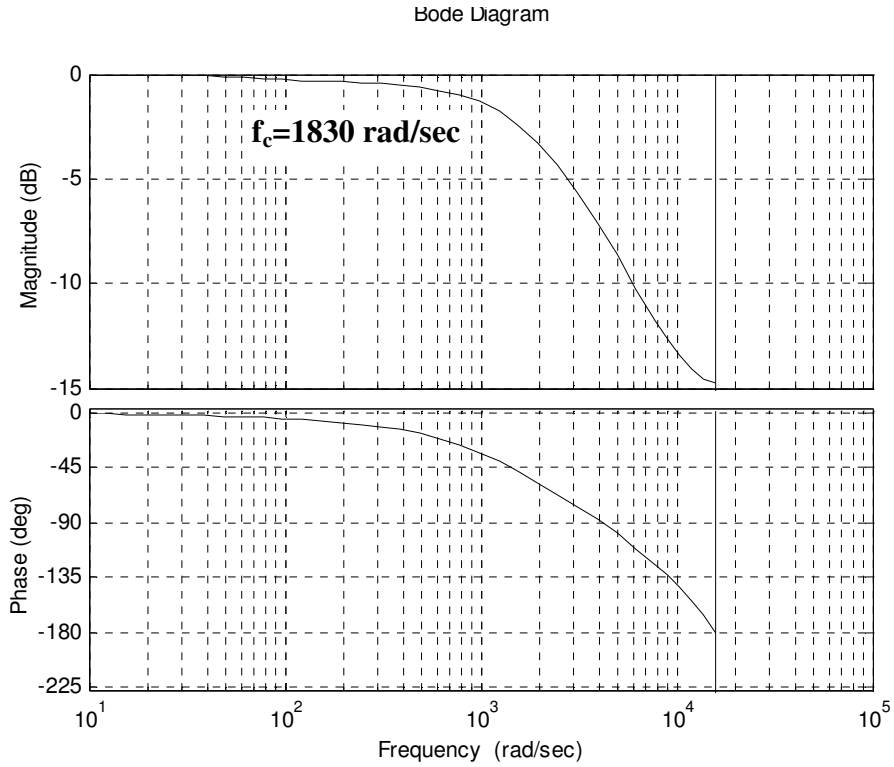

Fig.4.11c Closed-loop response for Kp =0.025 & *Ki* =2 "three-phase mode of operation"

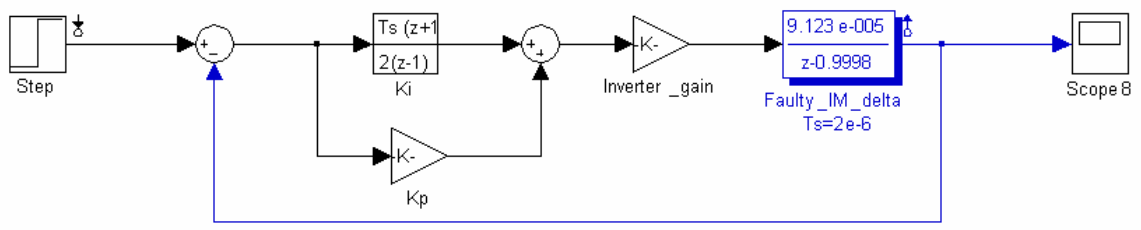

Fig.4.12a Torque/ Flux regulators in the discrete time-domain "two-phase open-Delta mode of operation"

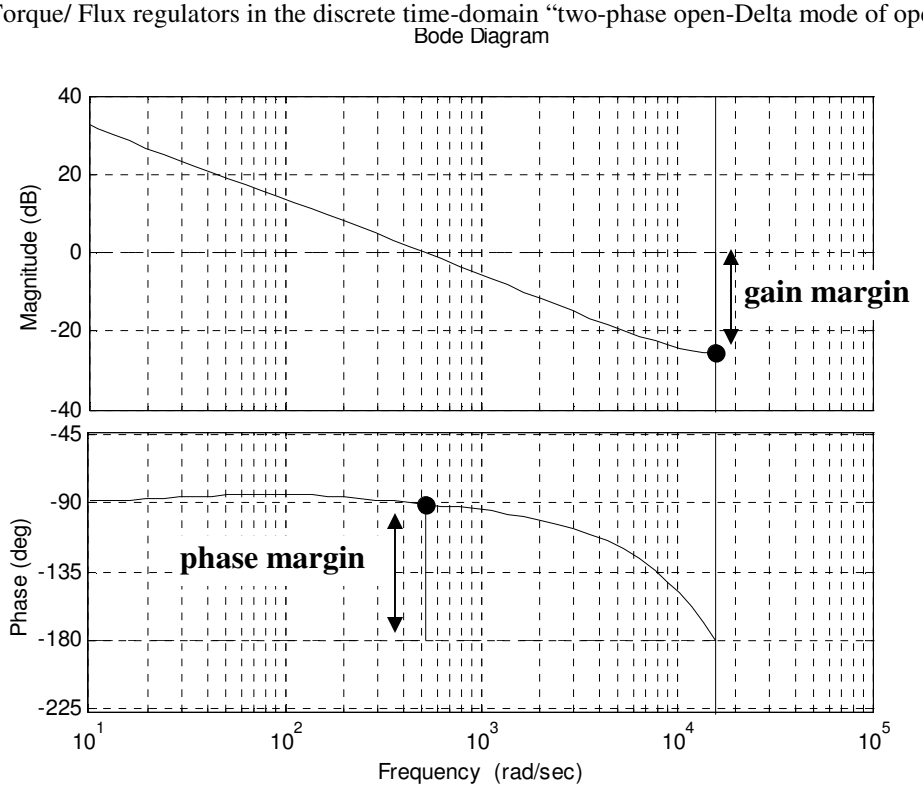

Fig.4.12b Open-loop response for Kp =0.025 & *Ki* =2 "two-phase open-Delta mode of operation"

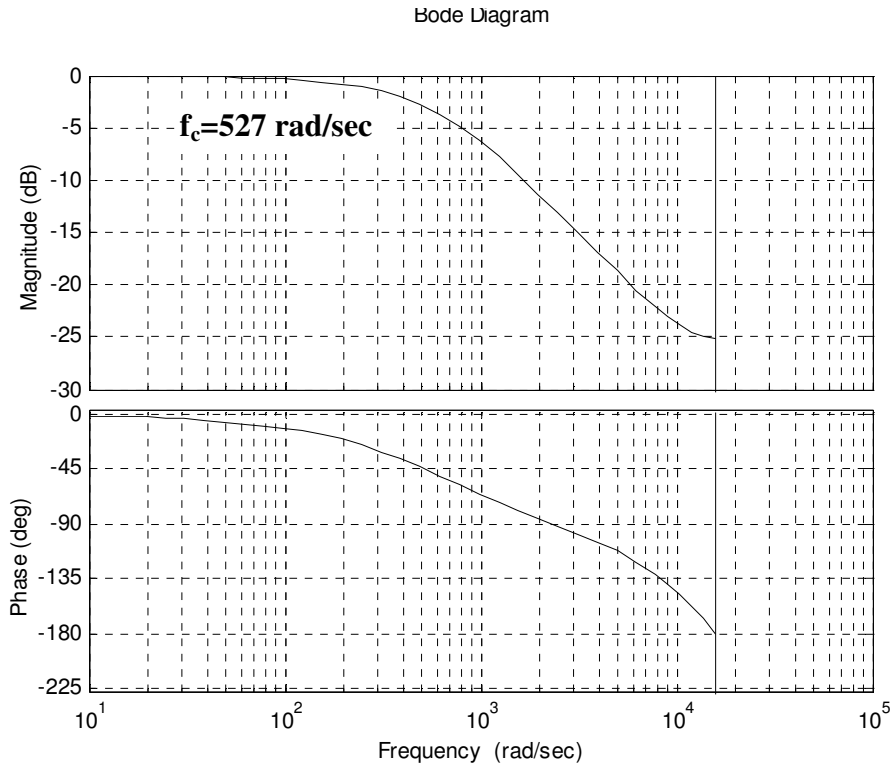

Fig.4.12c Closed-loop response for Kp =0.025 & *Ki* =2 "two-phase open-Delta mode of operation"

4.5.2 Current regulators design in the clockwise frame of reference

The main function of the current regulators in the CW frame of reference is to eliminate or minimize the backward component of the stator current space-vector and hence eliminate or minimize the backward MMF component in (3.16). In addition, the controller's d and q axes components should not be affected by the current ripples in this frame of reference. These ripples are present due to the forward (CCW) component of the stator current space-vector which appear as an ac component with a frequency equal to double the line frequency and is treated as a system disturbance in the CW current control loop design. The closed-loop system implemented in MATLAB/Simulink is depicted in Fig.4.13a for the case of a faulty operation "two-phase open-Delta mode of operation", and is depicted in Fig 4.13d for the case of healthy operation "three-phase mode of

operation". It is highly desirable to design the current control loop such that the dc component in the CW synchronously rotating frame of reference is forced to zero. Meanwhile, the double supply frequency ac ripples should be filtered out and shouldn't have any effect on the system performance.

Two different configurations are used for the control loop design. In the first configuration, the d-q current components in the CW synchronously rotating frame of reference are processed through a second order low pass filter with a cut-off frequency equal to 20Hz (125.67 rad/sec). The system closed-loop response with respect to an added disturbance is depicted in Fig.4.13b. It can be noticed that the disturbance signal is amplified, and it will have a significant effect for frequencies less than 30 Hz (cut-off frequency at 188.4 rad/sec) with a maximum gain of 10dB at 10Hz (162.5 rad/sec).This might lead to system instability for disturbances at these frequencies. However, the effect of the disturbance is significantly diminished for frequencies more than 30Hz. For instance, the gain at 120Hz (753.98) is -35dB. On the other hand, the second configuration does not imply the utilization of a low pass filter; however it utilizes the inherent frequency response of the PI controller to filter out higher frequency disturbances. The system response for this case is depicted in Fig.4.13c. It can be noticed that for this configuration, the closed-loop response with respect to the input disturbance has a cut-off frequency equal to 60.12 Hz (378 rad/sec). The gain is then reduced with respect to a frequency increase. For instance, the closed-loop gain equals -6dB at 120Hz.

Therefore, examining Bode plot response of these two different configurations, see Fig.4.13b and Fig.4.13c, show that the first configuration can not attenuate or diminish the effect of the ac current ripples at frequencies less than 30 Hz (188.49

rad/sec). Meanwhile, the second configuration can not attenuate frequencies less than 60.12 Hz. It can be noticed that the first configuration has much higher ripples rejection for frequencies greater than 30 Hz compared to the second configuration which does not utilize a low pass filter. The same conclusion can be drawn from the system response for the healthy case "three-phase mode of operation" depicted in Fig. 4.13e where the cut-off frequency is equal to 39Hz (245 rad/sec), and Fig.4.13f where the cut-off frequency is equal to 112Hz (701 rad/sec).

From the above discussion and analysis, the general control topology utilized in this work is to enable the CW current control loop for frequencies greater than 20 Hz (125.6 rad/sec) for both the three-phase mode of operation "healthy operation" and the two-phase open-Delta mode of operation "faulty operation". At this frequency, as explained earlier, the frequency of the ac current ripples in this frame of reference equals 40Hz (251.3 rad/sec), and the closed-loop gain equals -8dB, which is sufficient to diminish the effect of these ripples. Meanwhile, the d-axis and in the q-axis PI controllers in the CW frame of reference, are designed to act on the dc current components in this frame of reference and drive them to a value equal to zero. These dc current components are due to the two-phase open-Delta mode of operation. Meanwhile, the CW current control loop should be deactivated for frequencies less than 15Hz (94.24 rad/sec). At this low frequency range, the current controllers in the CCW control loop have enough bandwidth to suppress any torque pulsations that might result during faulty operation "two-phase open-Delta mode of operation" at this operating speed (94.24 rad/sec).

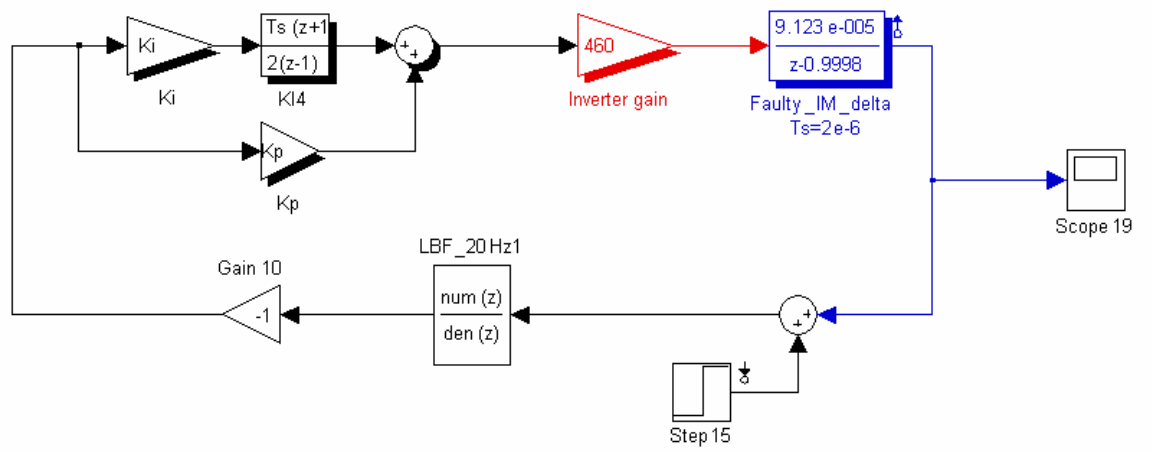

Fig.4.13a CW current control loop in the discrete time-domain "two-phase open-Delta mode of operation"

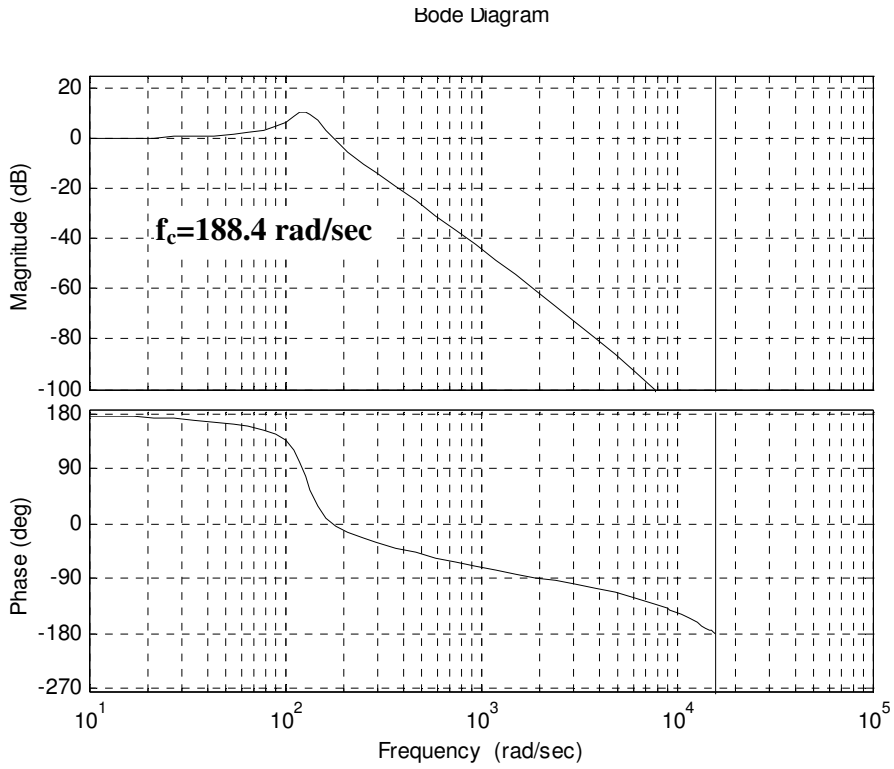

Fig.4.13b Closed-loop response with low pass filter in the loop, *Kp=0.02 &Ki=1*, "two-phase open-Delta mode of operation"

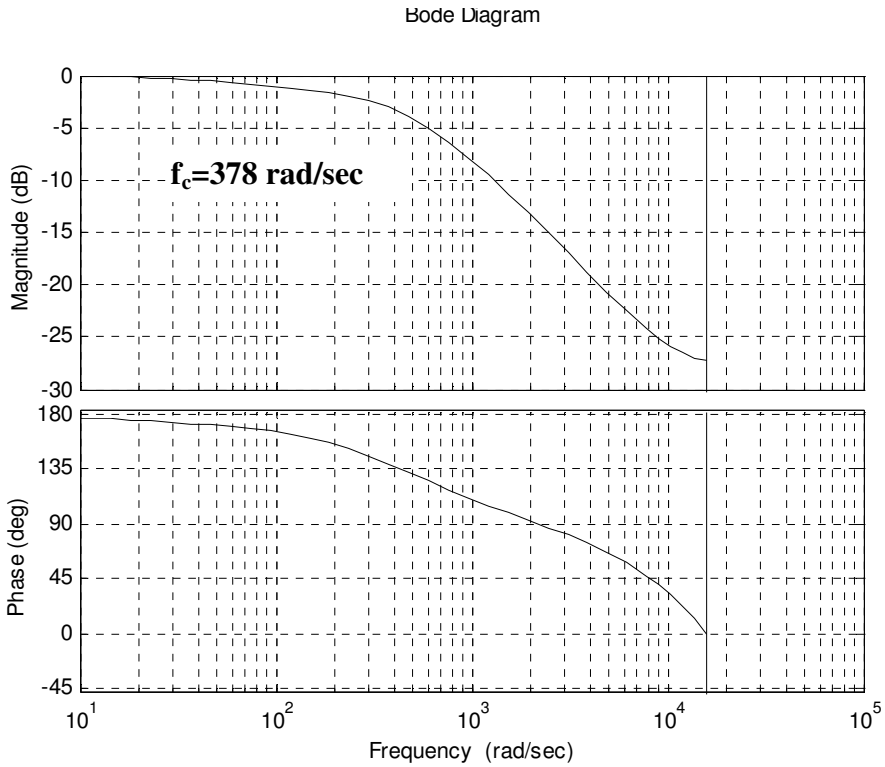

Fig.4.13c Closed-loop response without low pass filter in the loop, *Kp=0.02 & Ki=1*, "two-phase open-Delta mode of operation"

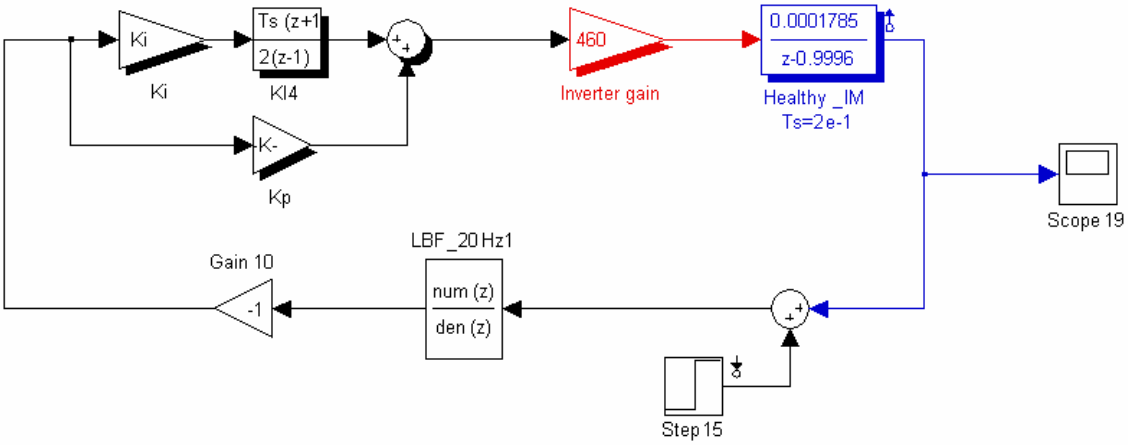

Fig.4.13d CW current control loop in the discrete time-domain "three-phase mode of operation"

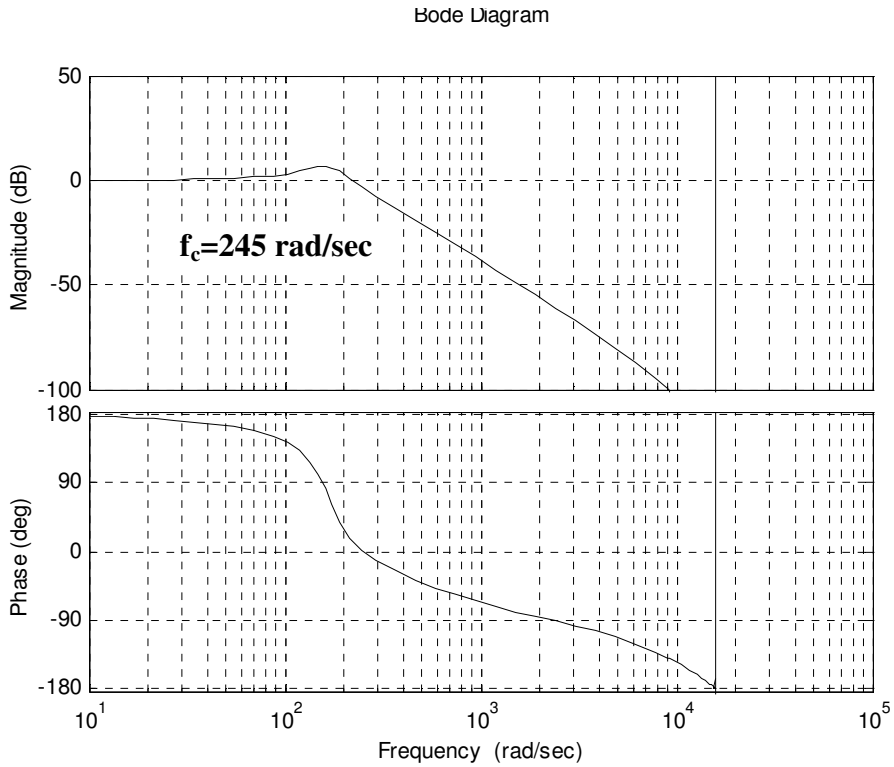

Fig.4.13e Closed-loop response with low pass filter in the loop, *Kp=0.02 &Ki=1*, "three-phase mode of operation"

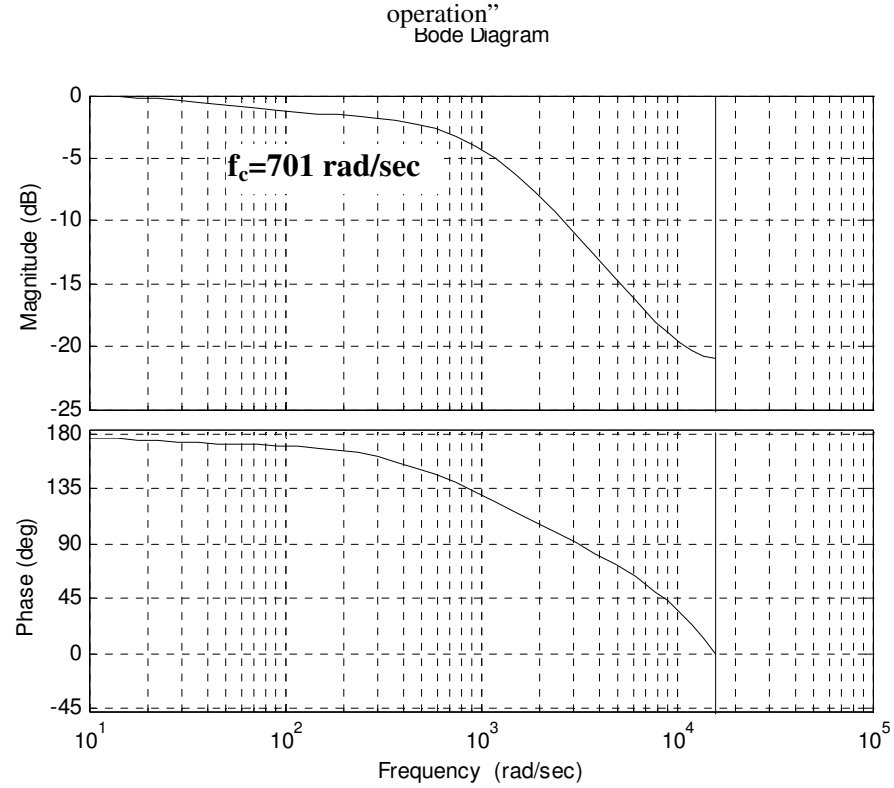

Fig.4.13f Closed-loop response without low pass filter in the loop, *Kp=0.02 &Ki=1*, "three-phase mode of operation"

4.5.3 Speed Regulator

The current control loop is known to be much faster than the speed control loop. This is due to the fact that the electrical time constant is much smaller than the mechanical time constant which is mainly based on a system's mechanical inertia and any viscous friction coefficient. Consequently, the speed regulator can be designed using the first order model described in [25, 26]. This model is based on the mechanical equation of motion that can be expressed as follows:

$$T_m - T_L = J\frac{\partial \omega_m}{\partial t} + b\omega_m \tag{4.15}$$

Therefore, the system input or the forcing function in this loop is the difference between the machine developed torque, T_m, the load torque, T_L, in which the T_L term was considered as a system disturbance. Meanwhile, to simplify the analysis, motor's friction can be neglected. Therefore, in (4.15), the rate of change of the motor mechanical speed with respect to time, $\frac{\partial \omega_m}{\partial t}$, depends mainly on the forcing function, T_m-T_L, and the system inertia , J. The viscous friction coefficient, b, usually has a typically very small value and can be neglected in order to simplify the design procedure. The simplified speed control loop is shown in Fig.4.14

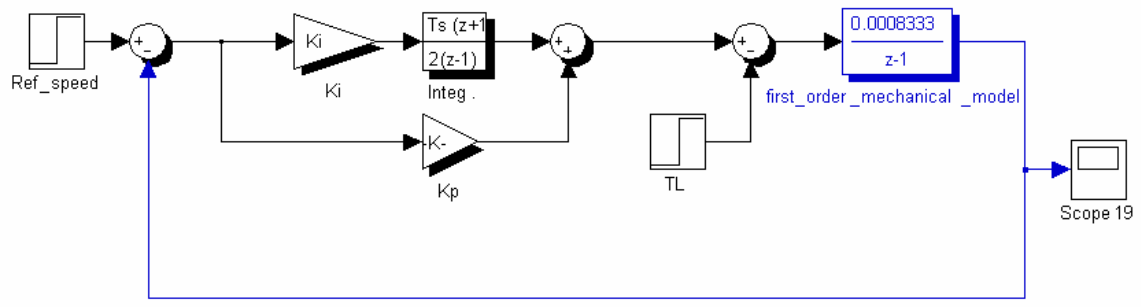

Fig.4.14 speed control loop in the discrete time-domain

4.6 Simulation Work

The simulation work was carried out using the two different models discussed earlier in details in Chapter 3. As mentioned in Chapter 3, the first simulation model was implemented in MATLB "Simulink toolbox and Simpowersystem toolbox". The time step of the simulation was chosen to be 2μSec to accurately model the switching effect, while the controller sample time was chosen to be 200μsec to replicate the actual implementation in the experimental work.

The second simulation model is a time-domain model that includes the system's controller model implemented in MATLAB/Simulink toolbox linked to a detailed Time Stepping Finite Element "TSFE" model for the case-study motor that includes the effects of MMF space harmonics, magnetic circuit configuration, and saturation. Meanwhile, the transistor switching is not included in this model. The inverter is modeled by a constant gain equal to Vdc/$\sqrt{2}$ for the space-vector PWM, [25, 26], which is utilized in the simulation and the experimental work. A comparison between the two modeling techniques is shown in Table 4.1 for the reader's examination.

The controller model, shown in Fig.4.15, was implemented in MATLAB/ Simulink in order to replicate the control structure depicted earlier in Fig.4.10.

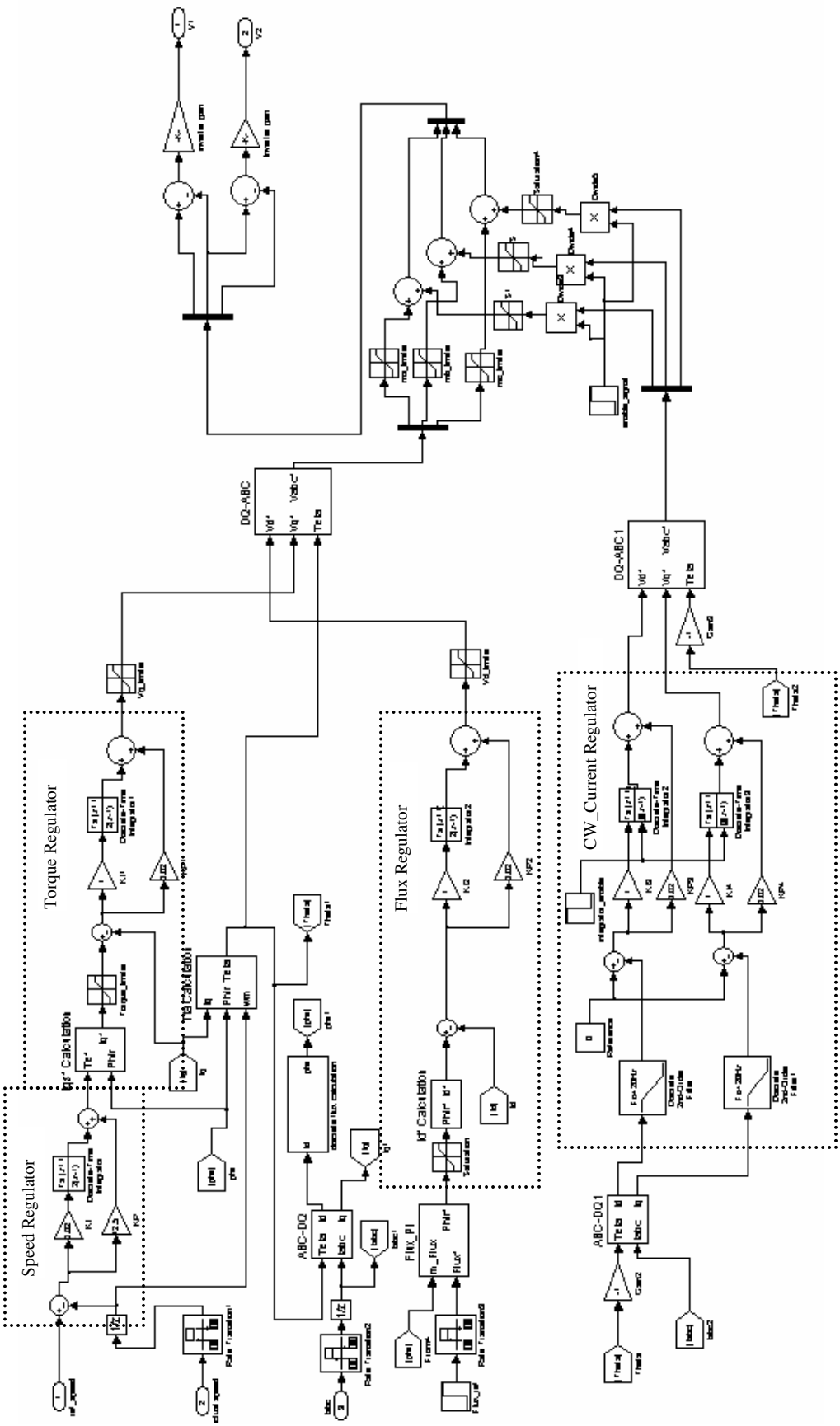

Fig.4.15 Controller Simulink Model

	First model	Second model
Modeling technique	MATLAB Simulink and Simpowersystem	MATLAB Simulink linked to Flux2D
Transistor switching effects	Included in the model	Not included in the model
Motor MMF space harmonics effects	Not included in the model	Included in the model
Magnetic saturation	Not included in the model	Included in the model
Step size	2μsec	200μsec
Magnetic variables	Not available in the model and can not be extracted	Available and can be extracted

Table 4.1 Comparison between the two simulation models

4.7 Analysis of the simulation and experimental results

The control system introduced here was simulated and experimentally tested in order to verify the theory and the analysis presented earlier in this chapter. As, elaborated on earlier, two different simulation models have been used in order to thoroughly analyze the effects of the space harmonics, saturation, and time harmonics on the system performance. The experimental prototype described in Appendix B was used for the experimental testing and verification of the validity of the introduced algorithms. The power structure of a commercial drive was interfaced to a DSP board "ezdsp F2812" from Spectrum Digital in which the DSP TMS320F2812 is the main processor that hosted the algorithms described earlier. The current sampling rate was 5 kHz, and the introduced control algorithm was executed through an interrupt service routine called every 200μsec. The carrier frequency was set to 5 kHz. The operation modes addressed in this section can be divided into three main categories. The first category is the healthy operation "three-phase mode of operation" when the introduced controller was activated. However, it will be shown that the introduced controller does not have any effect on the system performance. The second category is the faulty operation "two-phase open-Delta mode of operation", when the introduced controller was deactivated. Meanwhile, the

third category is the faulty mode of operation "two-phase open-Delta mode of operation" when the introduced controller was activated.

The three-phase line current waveforms obtained from simulation runs using the Simulink/Simpowersystem model and the coupled Simulink/Flux2D model under healthy operating condition and at a reference speed equal to 120 rad/sec are depicted in Fig.4.16a and Fig.4.16b, respectively. The corresponding three-phase line current waveforms obtained at the same reference speed from the experimental tests are depicted in Fig.4.16c. Meanwhile, the spectrum for the line current for this case is depicted in Fig.4.16d. The increased distortion in the line current waveforms obtained from the experimental tests compared to the results obtained from the simulation results is due to the dead time effects, and dc-link voltage ripples as explained in details in [7].

On the other hand, the three-phase line current waveforms obtained from the simulation runs using the Simulink/Simpowersystem model and the coupled Simulink/Flux2D model at faulty operating condition "two-phase open-Delta mode of operation", while the newly introduced controller was deactivated, and at a reference speed equal to 120 rad/sec are depicted in Fig.4.17a and Fig.4.17b respectively. The corresponding three-phase line current waveforms obtained from the experimental tests under the same operating conditions are depicted in Fig.4.17c. A significant current unbalance can be observed from the results obtained from both the simulation runs, and from the experimental tests. Operating the system under such condition is highly undesirable, and it may cause excessive torque ripples, significant temperature increase, increased capacitor current ripples, which may jeopardize the whole system and may cause complete system failure.

In order to explore the effect of the introduced controller on the system performance under such faulty condition, the system was re-simulated and experimentally tested when the introduced controller was activated at the same operating conditions. The three-phase line current waveforms obtained from simulation runs using the Simulink/Simpowersystem model and the coupled Simulink/ Flux2D model for this case are depicted in Fig.4.18a and Fig.4.18b respectively. Meanwhile, the three-phase line current waveforms obtained from the experimental tests at the same operating conditions are depicted in Fig.4.18c.The effectiveness of the introduced controller can be verified through comparing the unbalanced line current waveforms for the case of two-phase open-Delta mode of operation while the introduced controller was in a deactivated state, see Fig.4.17a, Fig.4.17b and Fig.4.17c and the balanced line currents waveforms for the case of two-phase open-Delta operation, while the introduced controller was activated, see Fig.4.18a, Fig.4.18b and Fig.4.18c. These figures show that the introduced controller has diminished the negative sequence current component of the three-phase line currents which significantly improves the machine output torque as will be demonstrated later. This is in addition to alleviating other undesirable effects resulting from unbalanced operation of the motor-drive system such as stresses on the dc-link capacitor and the dc-link inductor.

In addition, the magnitude of the negative sequence current component during the instant of the transfer from the three-phase mode of operation to two-phase open-Delta mode of operation is depicted in Fig.4.18d. A sudden increase in the magnitude of the negative sequence current component can be observed at the instant of switching.

However, this component was driven to zero due to the compensation action initiated by the CW current control loop as explained earlier in this chapter.

The effectiveness of the introduced controller can also be verified through examining the time-domain profiles of the output torque obtained from simulation runs at a reference speed equal to 120 rad/sec. The motor was operating at a faulty condition "two-phase open-Delta mode of operation", when the introduced controller was deactivated case (a) and when the introduced controller was activated case (b), are shown in Fig.4.19a and Fig.4.19b using the Simulink/Simpowersystem model and the coupled Simulink/Flux2D model, respectively. Significant torque ripples with a frequency equal to double the line frequency can be observed in the simulation results shown in Fig.4.19a and Fig.4.19b. This agrees with the analysis presented earlier in this chapter. The significant reduction of theses torque ripples when the introduced controller was activated can be easily observed also from these figures. The same conclusion can be drawn from the time-domain profiles of the output torque obtained from the experimental tests at the same operating condition, which are depicted in Fig.4.19c, where the torque was directly measured using a torque transducer which is mechanically coupled to the motor shaft. The transducer output signal was filtered out by a low pass filter with a cut-off frequency equals 300Hz.

As mentioned earlier in Chapter 3 and explained in details in Appendix A, the design constrains for the prototype machine in this research implied stator winding design with a full pitched coil. Design analysis in Appendix A shows the existence of a third harmonic MMF component in the frequency spectrum of the windings MMF. However, this third harmonic component will not appear in the resultant airgap flux density which

can be verified through examining Fig.4.20a and its associated spectrum depicted in Fig.4.20b. This is due to the fact that the resultant summation of the third harmonic MMF components is equal to zero for a balanced three-phase system. Meanwhile, a third harmonic current component will circulate in the machine windings for Delta-connected stator windings as shown earlier in Chapter 3. On the other hand, the third harmonic components will not cancel each other for the case of the two-phase open-Delta mode of operation, and a third harmonic component will appear in the airgap flux density as shown in Fig.4.20c and its associated spectrum depicted in Fig.4.20d. It should be highlighted that the existence of a third harmonic component in the frequency spectrum of the airgap flux density will also cause torque pulsations with a frequency equal to double the line frequency which may be suppressed by the CCW current control loop in vector-controlled drives provided that the controller has enough bandwidth much larger than the frequency of these torque oscillations..

The simulation runs and the experimental tests were repeated at a reference speed equal to 60 rad/sec and a load torque equal to 15N.M. for the healthy operation “three-phase mode of operation” and for the faulty operation “two-phase open-Delta mode of operation”. The three-phase line current waveforms obtained from the simulation runs using the Simulink/Simpowersystem model and the Simulink/Flux2D model for the healthy condition are depicted in Fig.4.21a and Fig.4.21b, respectively. The three-phase line current waveforms obtained from experimental tests at the same operating conditions are depicted in Fig.4.21c. An increased distortion in the line current time-domain waveforms obtained from the experimental tests compared to the line currents time-domain waveforms obtained from the simulation runs can be observed in the time-

domain profile of the line current waveforms. The existence of the fifth and seventh harmonic components in these line currents time-domain waveforms can be verified through examining the frequency spectrum of the line current depicted in Fig.4.21d. The increase of these harmonic components in the spectrum of the line current time-domain waveforms can be attributed to the inverter nonlinearities such as the dead time and ripples in the dc bus voltage, [7]. Meanwhile, a significant current unbalance can be noticed in the line current time-domain waveforms obtained from simulation results for the case of the faulty "two-phase open-Delta mode of operation", while the introduced controller was in a deactivated state as depicted in Fig.4.22a and Fig.4.22b, and the line current time-domain waveforms obtained from the experimental tests which are depicted in Fig.4.22c.On the other hand, the significant impact of the introduced controller on the system performance can be verified by examining the line currents time-domain waveforms which were obtained form the simulation runs and depicted in Fig. 4.23a and Fig.4.23b, respectively. Meanwhile, the line current time-domain waveforms obtained from the experimental tests at the same operating conditions are depicted in Fig.4.23c. The magnitude of the negative sequence current component during the transition from a three-phase mode of operation to a two-phase open-Delta mode of operation is depicted in Fig.4.23d. From this figure, a sudden increase in the magnitude of the negative sequence current component can be observed at the switching instant from a three-phase mode of operation to a two-phase open-Delta mode of operation. However, the CW current controller was able to drive the magnitude of the negative sequence current component of the line current and render a balanced set of the line currents. In addition, a significant reduction in the torque ripples can be observed for the case of the two-phase

open-Delta mode of operation when the introduced controller was activated, as compared to the same case when the introduced controller was deactivated. This can be verified through examining the time-domain torque profiles obtained from the simulation runs which are depicted in Fig.4.24a and Fig.4.24b and the time-domain torque profile acquired from the experimental test shown in fig.4.24c. It is also important to observe the decrease in the magnitude of the torque ripples when the introduced controller is in a deactivated state for the case of the two-phase open-Delta mode of operation at 60 rad/sec operating speed, depicted in Fig.4.24c compared to the case of the two-phase open-Delta mode of operation at 120 rad/sec operating speed, depicted in Fig.4.19c. The explanation of this phenomenon is that the compensation of the torque ripples depends on the ratio between the bandwidth of the CCW current control loop and the frequency of these torque ripples. It was shown earlier that the two-phase open-Delta mode of operation causes a significant increase in the torque ripples at a frequency equal to double the line frequency. Since the CCW current regulator BW is limited to 527 rad/sec as shown earlier. The ability of the CCW current control loop to suppress such torque ripples is much stronger for lower speed operation. On the other hand, these torque ripples appear as a dc component in the CW frame of reference, and hence they can be suppressed mainly by the CW current control loop at high speed modes of operation.

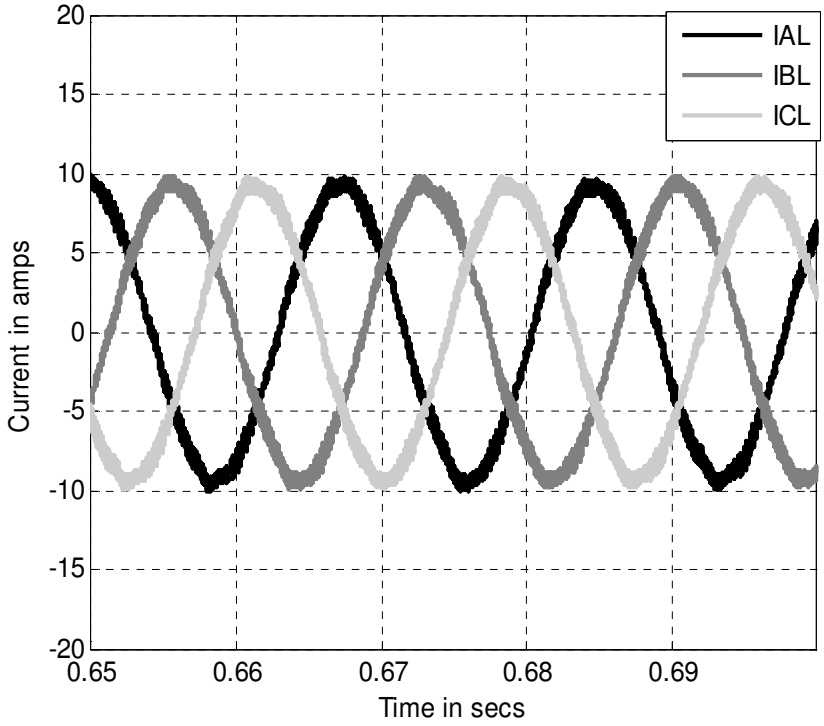

Fig.4.16a Line currents, vector-control, the introduced controller was activated, three-phase mode of operation, reference speed=120rad/sec, "Simulink/Simpowersystem model".

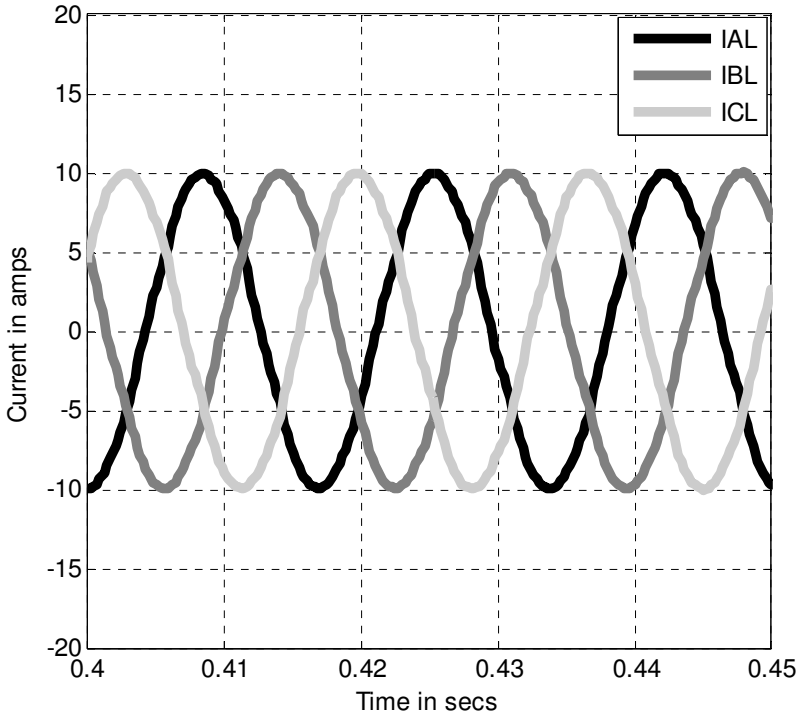

Fig.4.16b Line currents, vector-control, the introduced controller was activated, three-phase mode of operation, reference speed=120rad/sec, "Coupled Simulink / Flux2D".

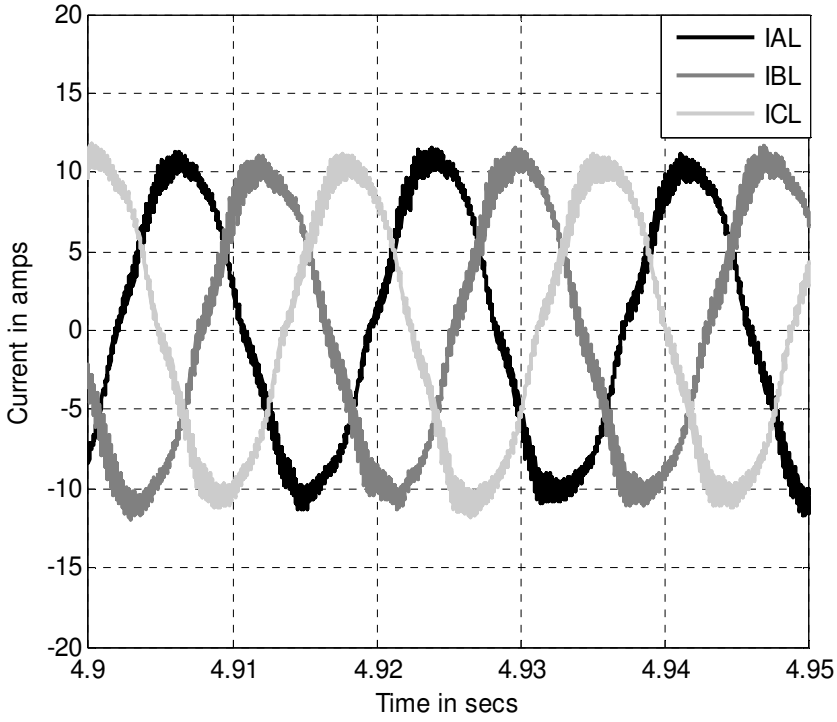

Fig.4.16c Experimentally obtained Line currents, vector-control, the introduced controller was activated, three-phase mode of operation, reference speed=120rad/sec.

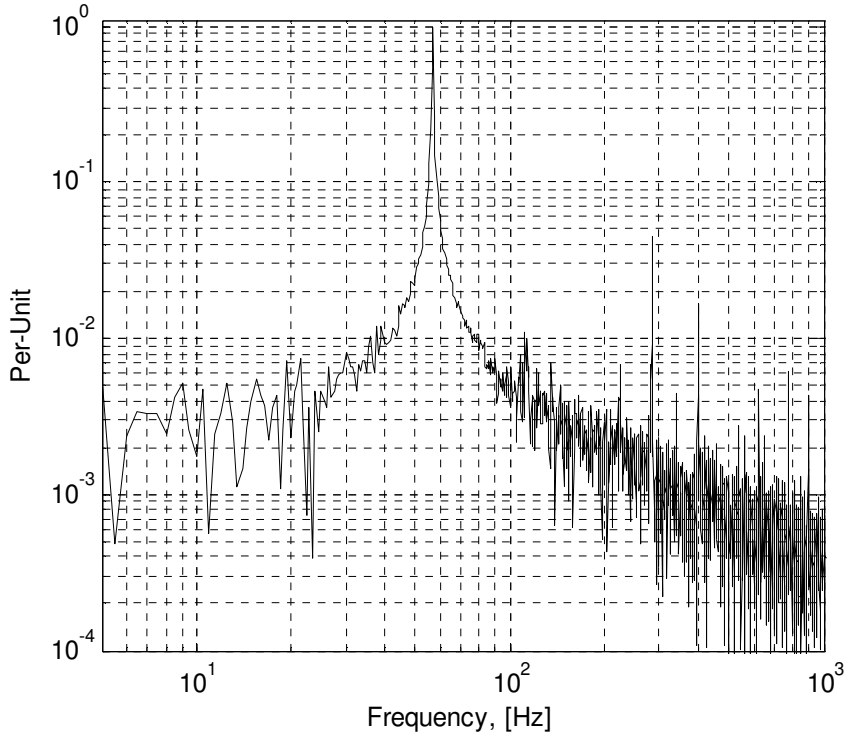

Fig.4.16d Spectrum of the experimentally obtained line currents, vector-control, the introduced controller was activated, two-phase open-Delta mode of operation, reference speed=120rad/sec.

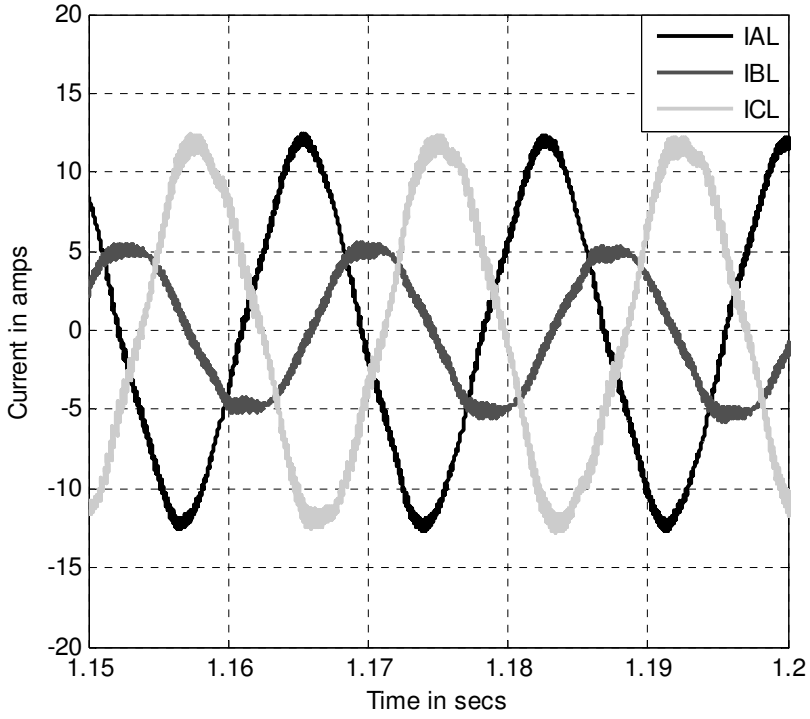

Fig.4.17a Line currents, vector-control, the introduced controller was deactivated, two-phase open-Delta mode of operation, reference speed=120rad/sec, "Simulink/Simpowersystem model".

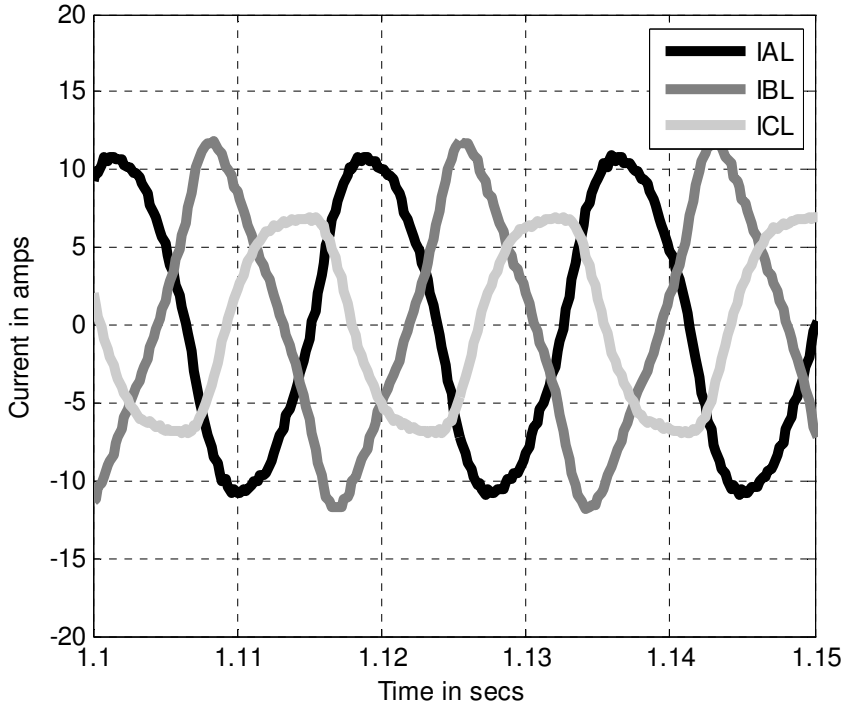

Fig.4.17b Line currents, vector-control, the introduced controller was deactivated, two-phase open-Delta mode of operation, reference speed=120rad/sec, "Coupled Simulink / Flux2D".

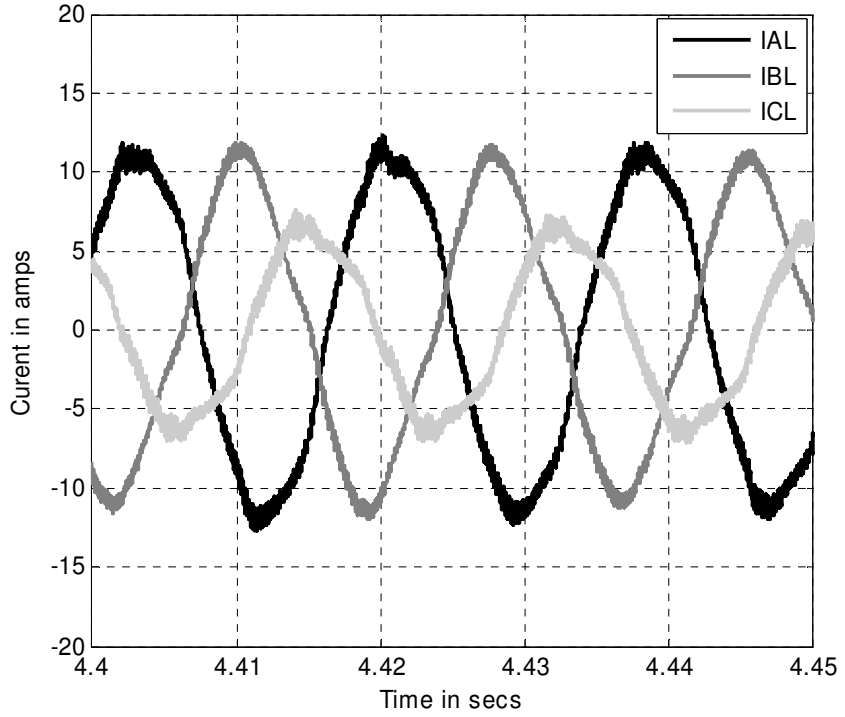

Fig.4.17c Experimentally obtained line currents, vector-control, the introduced controller was deactivated , two-phase open-Delta mode of operation, reference speed=120rad/sec.

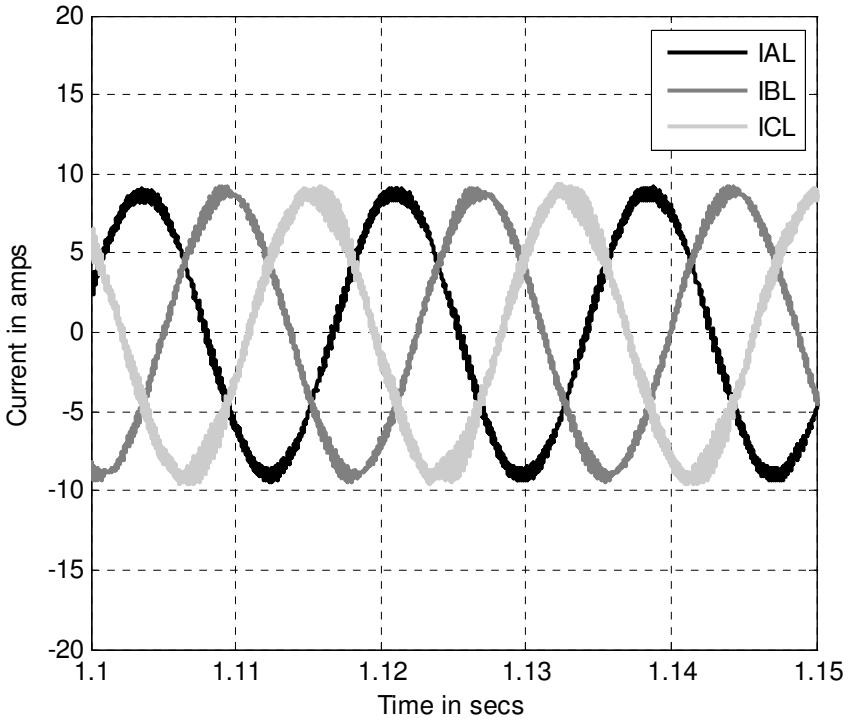

Fig.4.18a Line currents, vector-control, the introduced controller was activated, two-phase open-Delta mode of operation, reference speed=120rad/sec, "Simulink/Simpowersystem model".

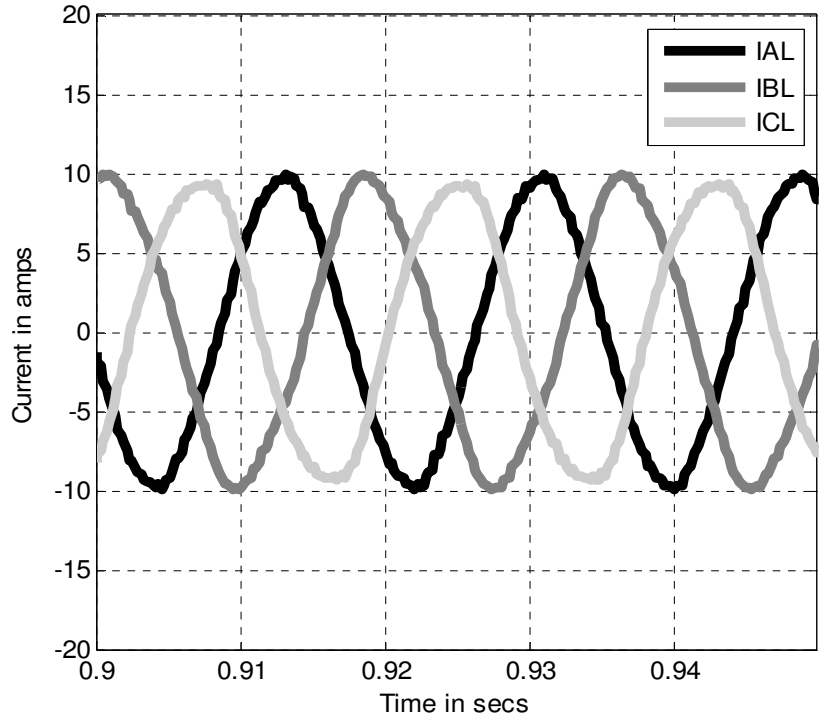

Fig.4.18b Line currents, vector-control, the introduced controller was activated, two-phase open-Delta mode of operation, reference speed=120rad/sec, "Coupled Simulink / Flux2D".

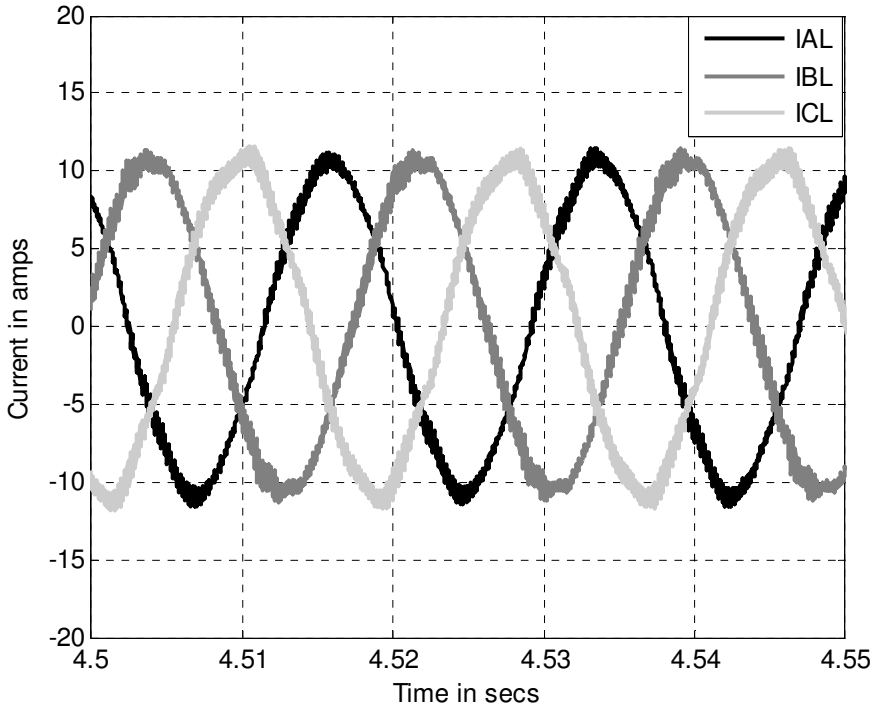

Fig.4.18c Experimentally obtained line currents, vector-control, the introduced controller was activated, two-phase open-Delta mode of operation, reference speed=120rad/sec.

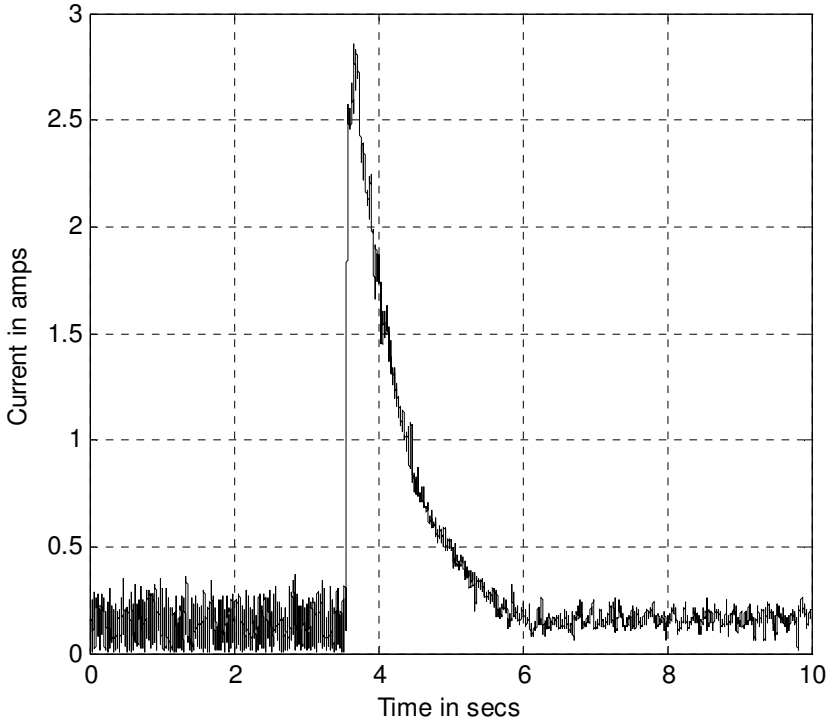

Fig.4.18d Experimentally obtained negative sequence component of the line currents, transfer from three-phase mode to two-phase open-Delta mode when the introduced controller was activated, reference speed=120rad/sec.

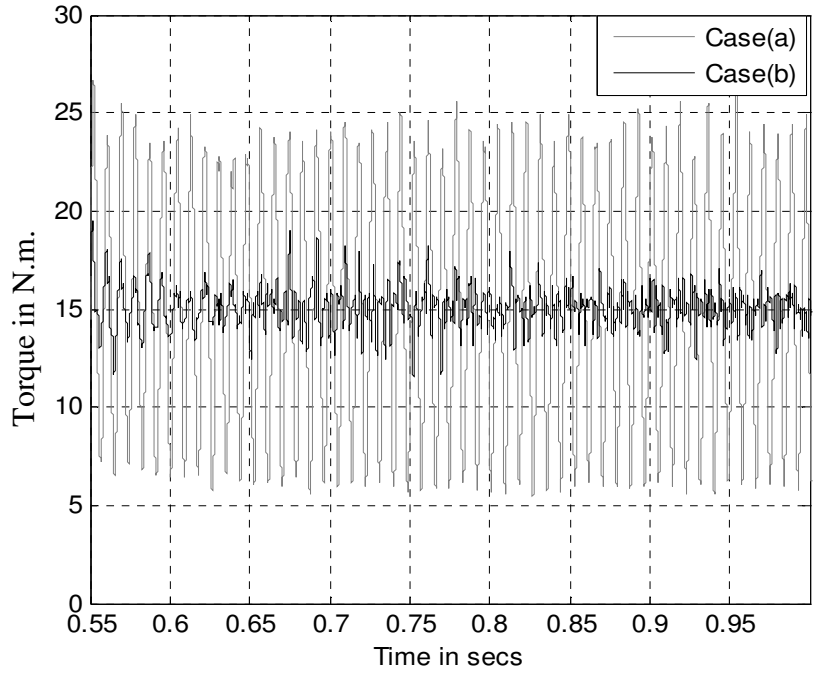

Fig.4.19a Output torque, vector-control, two-phase open-Delta mode of operation, reference speed =120rad/sec, "Simulink/Simpowersystem model":
Case (a) The introduced controller was deactivated. Case (b) The introduced controller was activated

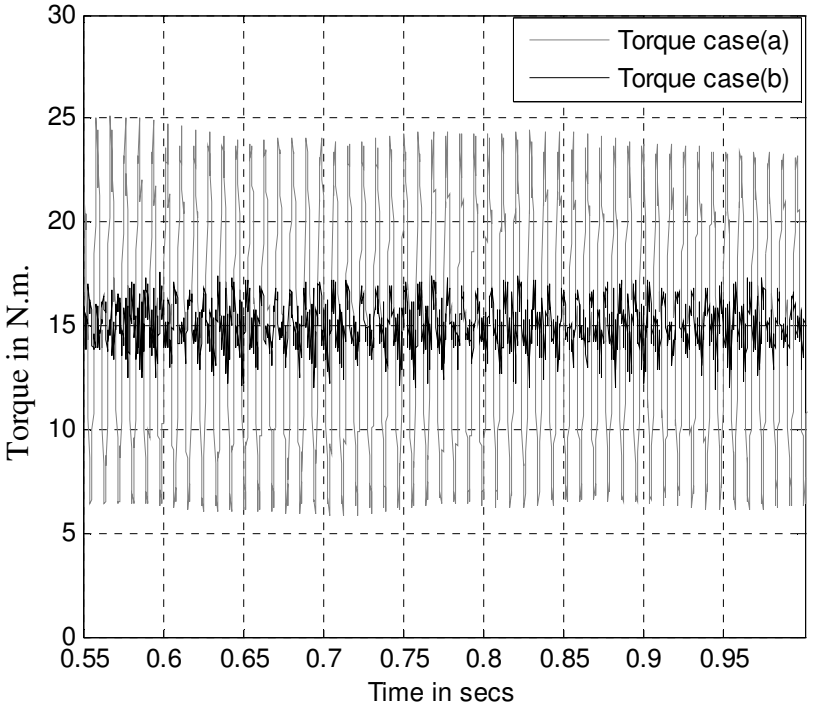

Fig.4.19b Output torque, vector-control, two-phase open-Delta mode of operation, speed ref=120rad/sec, "Coupled Simulink / Flux2D", Case (a) The introduced controller was deactivated. Case (b) The introduced control was activated.

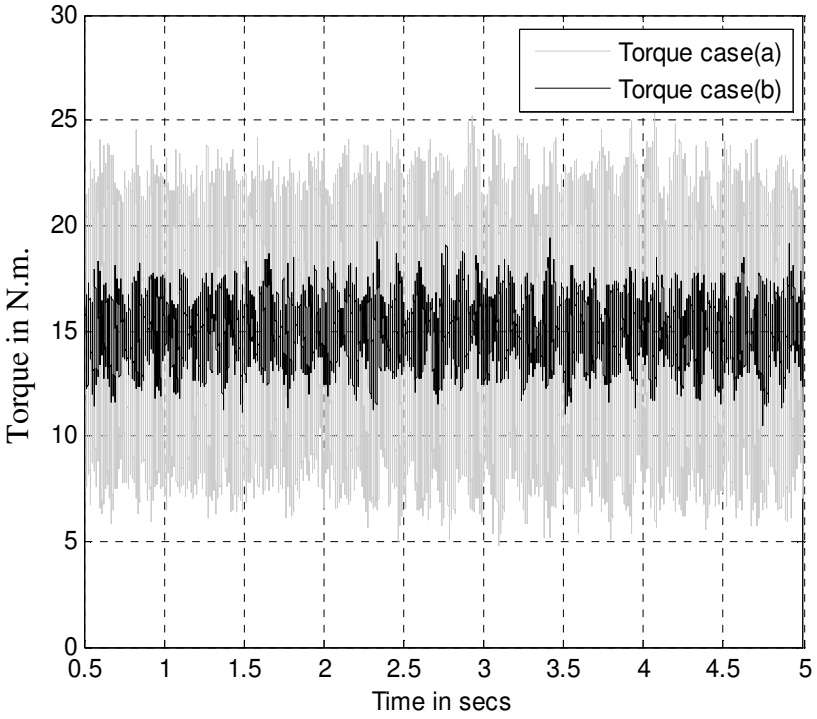

Fig.4.19c Experimentally obtained output torque, vector-control, two-phase open-Delta mode of operation, speed ref=120rad/sec, Case (a) The introduced controller was deactivated . Case (b) The introduced control was activated.

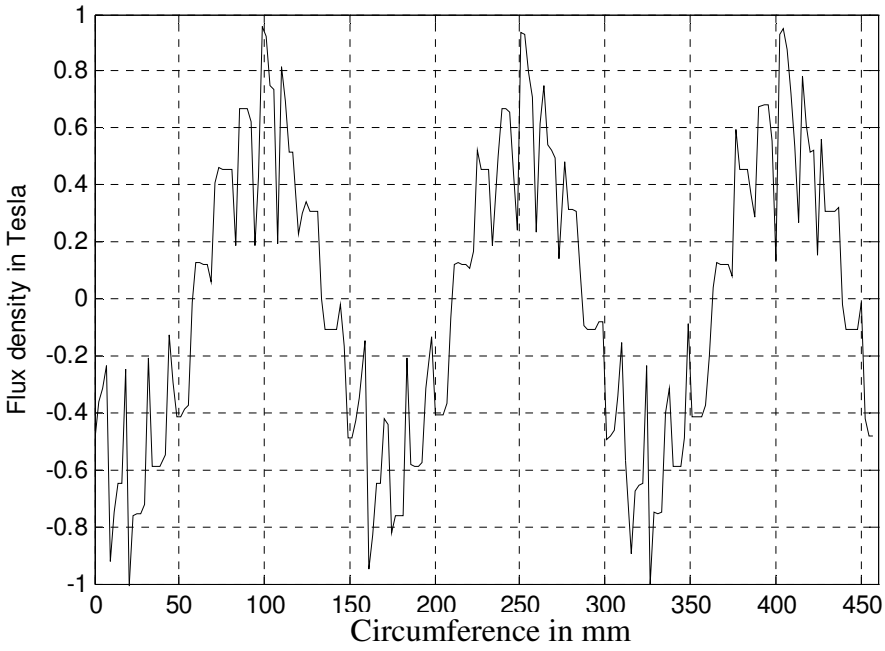

Fig.4.20a Airgab Flux Density, vector-control, when the introduced controller was activated under healthy three-phase mode of operation "Coupled Simulink/Flux2D model", speed ref=120rad/sec.

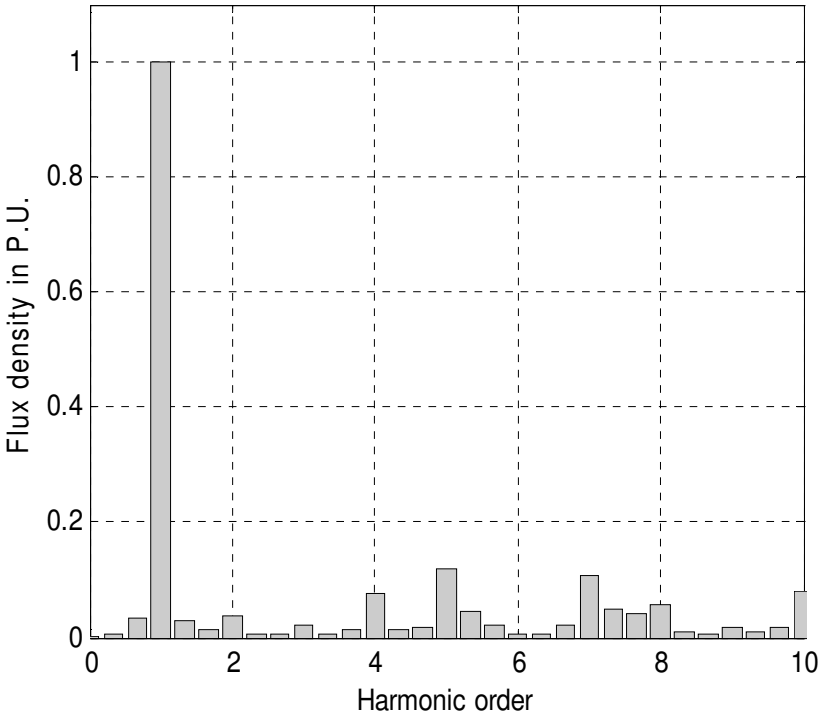

Fig.4.20b Spectrum of the airgap flux density, vector-control, the introduced controller was activated, three-phase mode of operation, speed ref=120rad/sec, "Coupled Simulink / Flux2D"

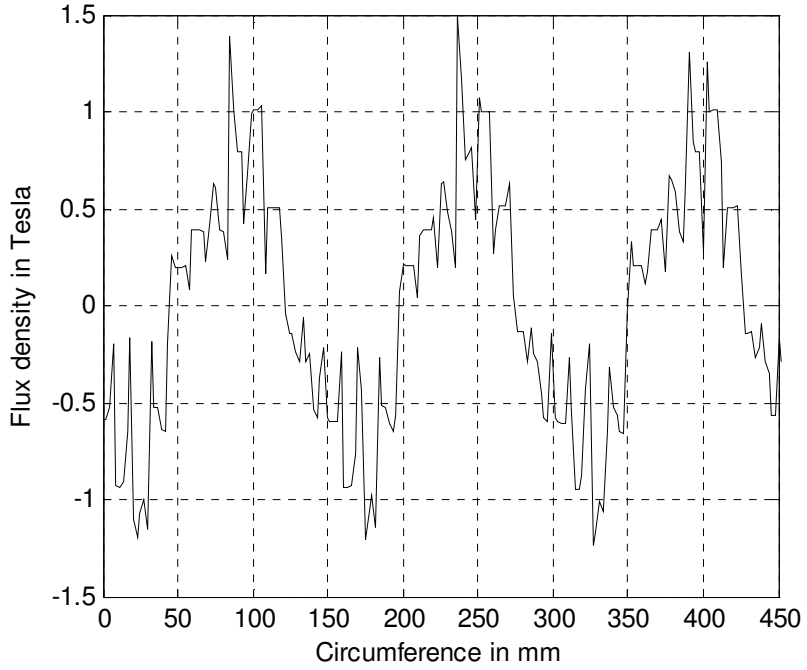

Fig.4.20c Airgab flux density, vector-control, when the introduced controller was activated, two-phase open-Delta mode of operation "Coupled Simulink/Flux2D model", speed reference=120rad/sec.

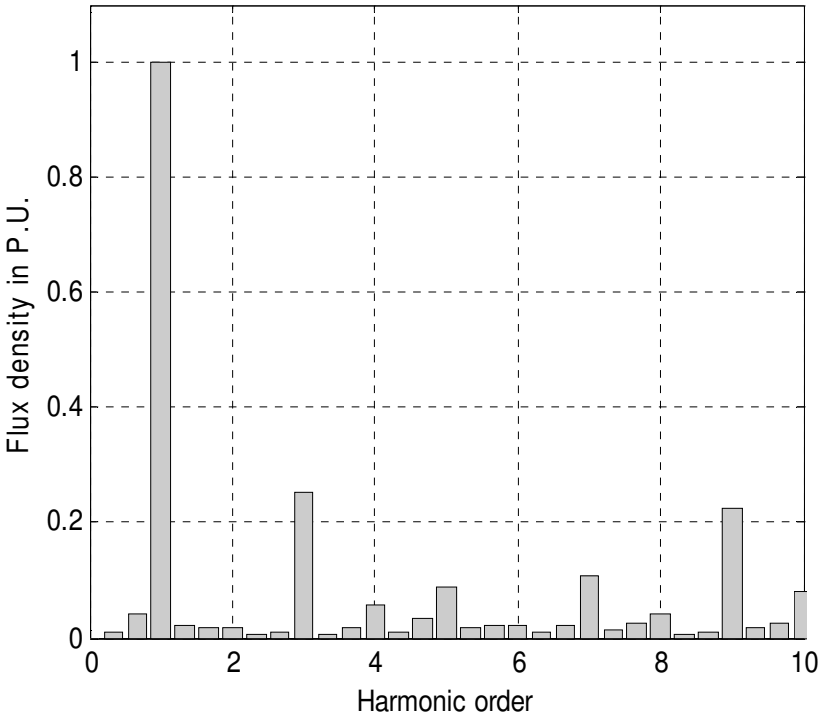

Fig.4.20d Spectrum of the airgap flux density, vector-control, the introduced controller was activated, two-phase open-Delta mode of operation, speed reference=120rad/sec, "Coupled Simulink / Flux2D"

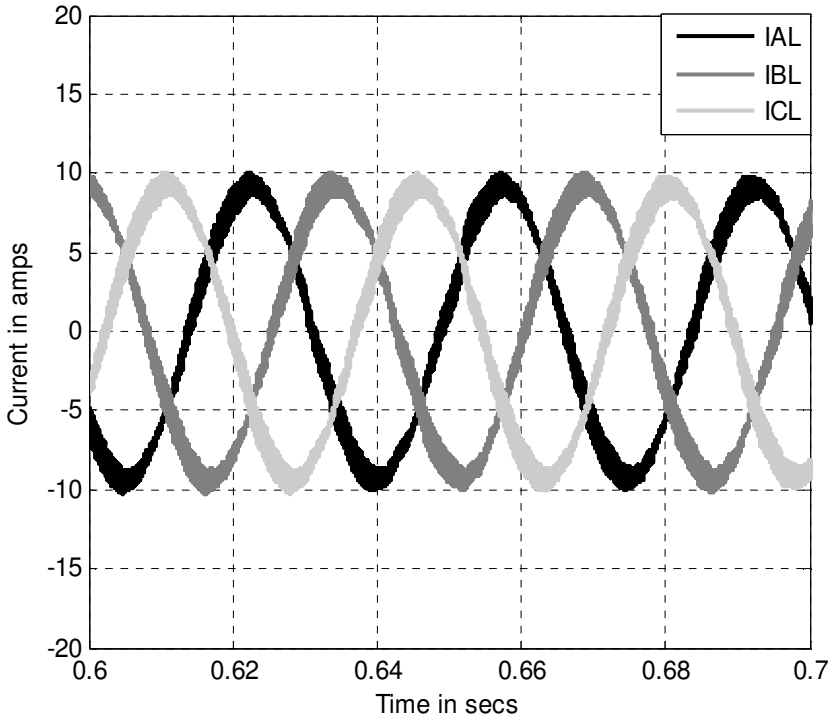

Fig.4.21a Line currents, vector-control, the introduced controller was activated, three-phase mode of operation, speed ref=60rad/sec, "Simulink/Simpowersystem model".

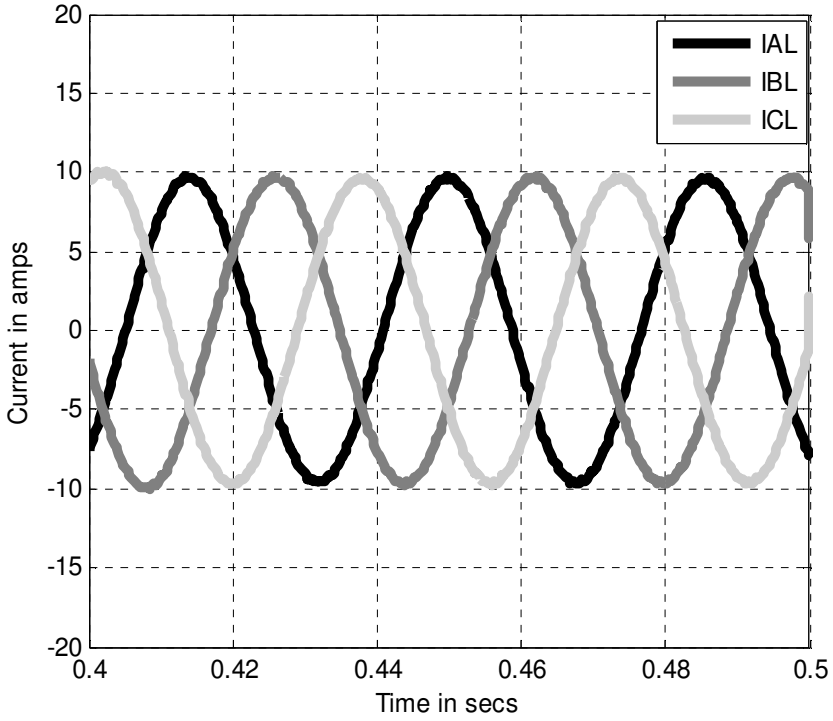

Fig.4.21b Line currents, vector-control, the introduced controller was activated, three-phase mode of operation, speed ref=60rad/sec, "Coupled Simulink / Flux2D".

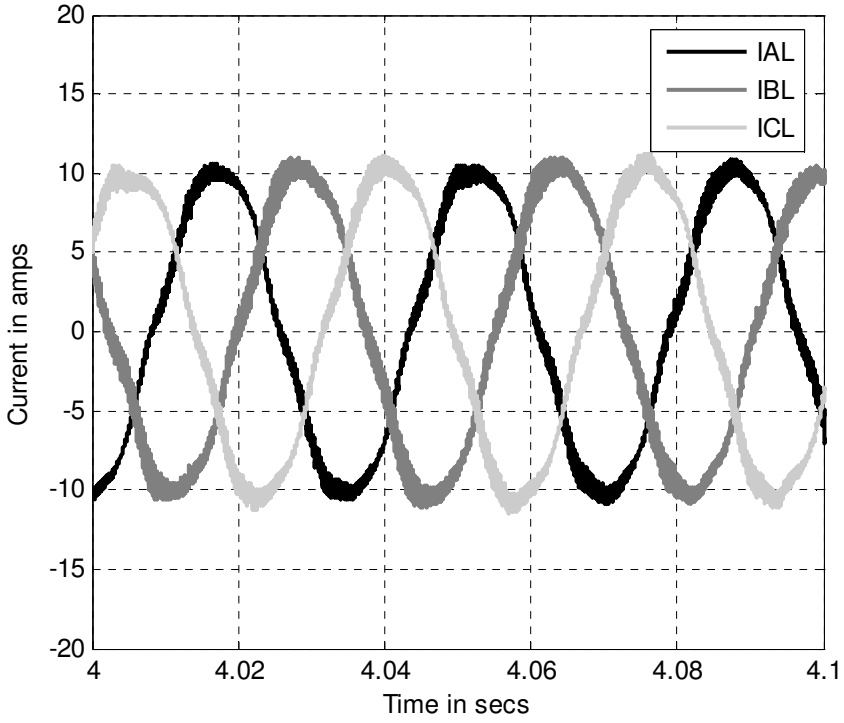

Fig.4.21c Experimentally obtained line currents, vector-control, the introduced controller was activated, three-phase mode of operation, reference speed=60rad/sec.

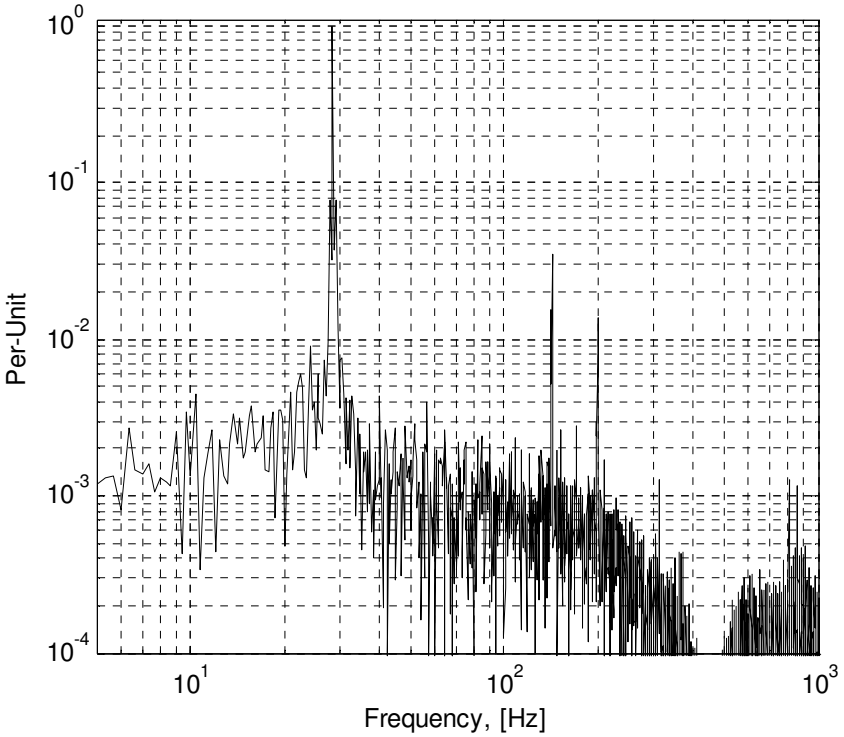

Fig.4.21d Experimentally obtained line currents spectrum, vector-control, the introduced controller was activated, three-phase mode of operation, reference speed=60rad/sec.

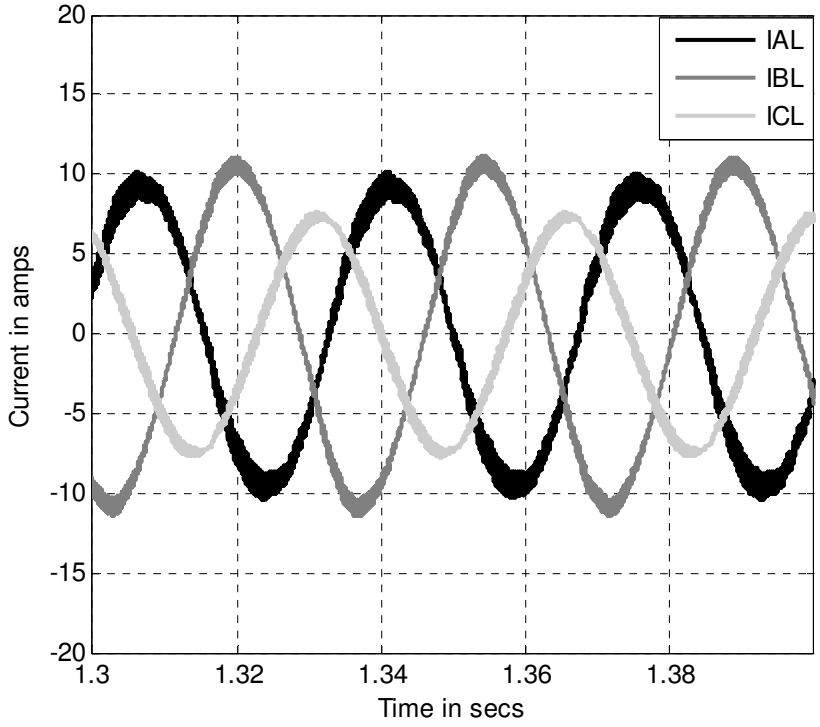

Fig.4.22a Line currents, vector-control, the introduced controller was deactivated, two-phase open-Delta mode of operation, reference speed=60rad/sec, "Simulink/Simpowersystem model".

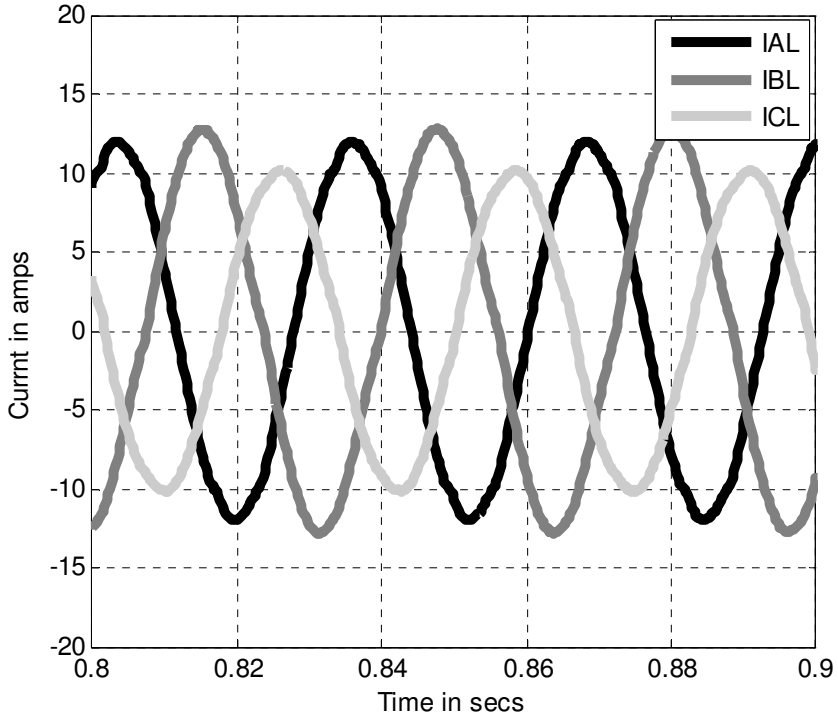

Fig.4.22b Line currents, vector-control, the introduced controller was deactivated, two-phase open-Delta mode of operation, reference speed=60rad/sec, "Simulink/Flux2D".

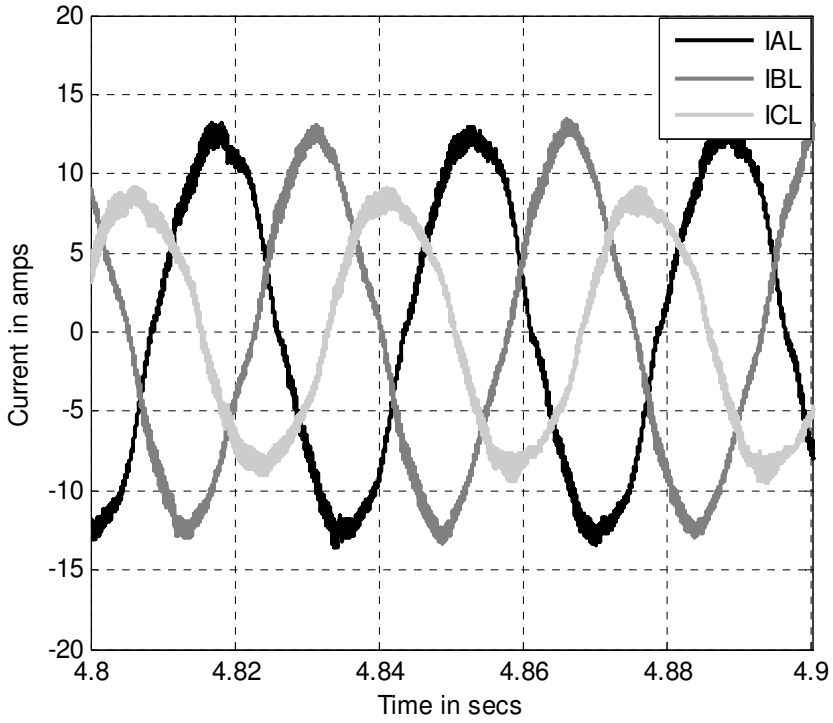

Fig.4.22c Experimentally obtained line currents, vector-control, the introduced controller was deactivated, two-phase open-Delta mode of operation, reference speed=60rad/sec.

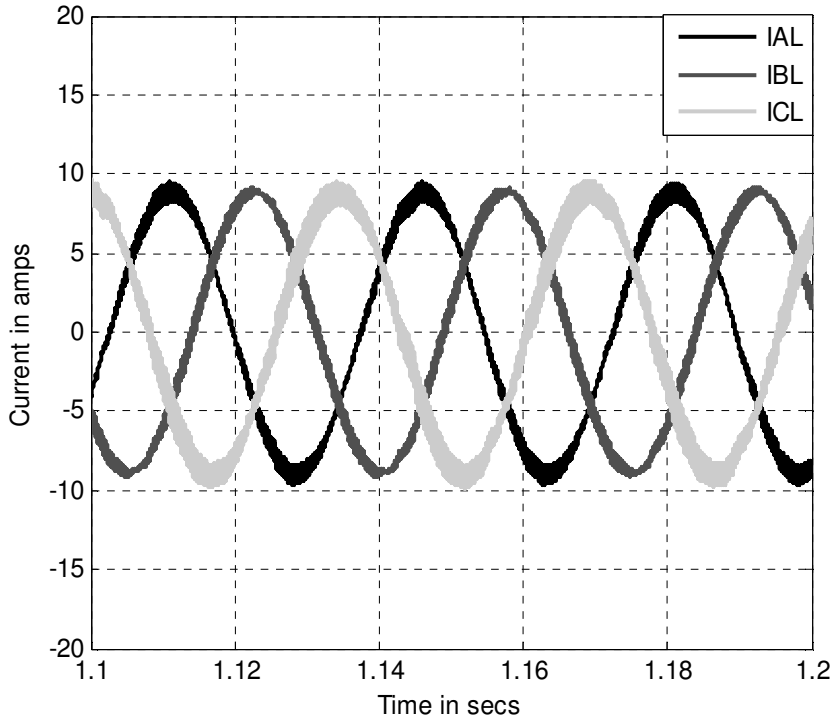

Fig.4.23a Line currents, vector-control, the introduced controller was activated, two-phase open-Delta mode of operation, reference speed =60rad/sec, "Simulink/Simpowersystem model".

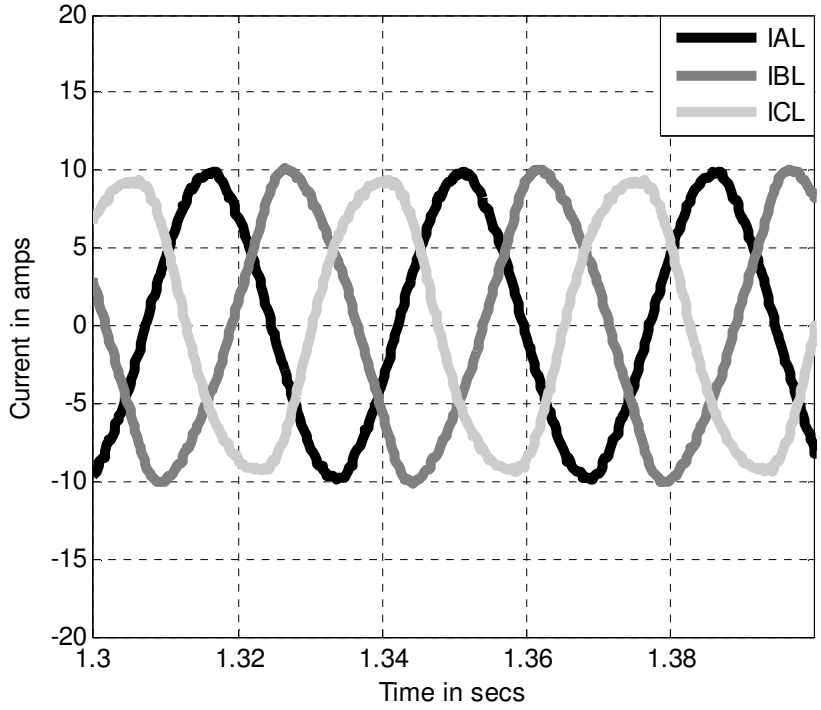

Fig.4.23b Line currents, vector-control, the introduced controller was activated, two-phase open-Delta mode of operation, reference speed=60rad/sec, "Simulink/Flux2D".

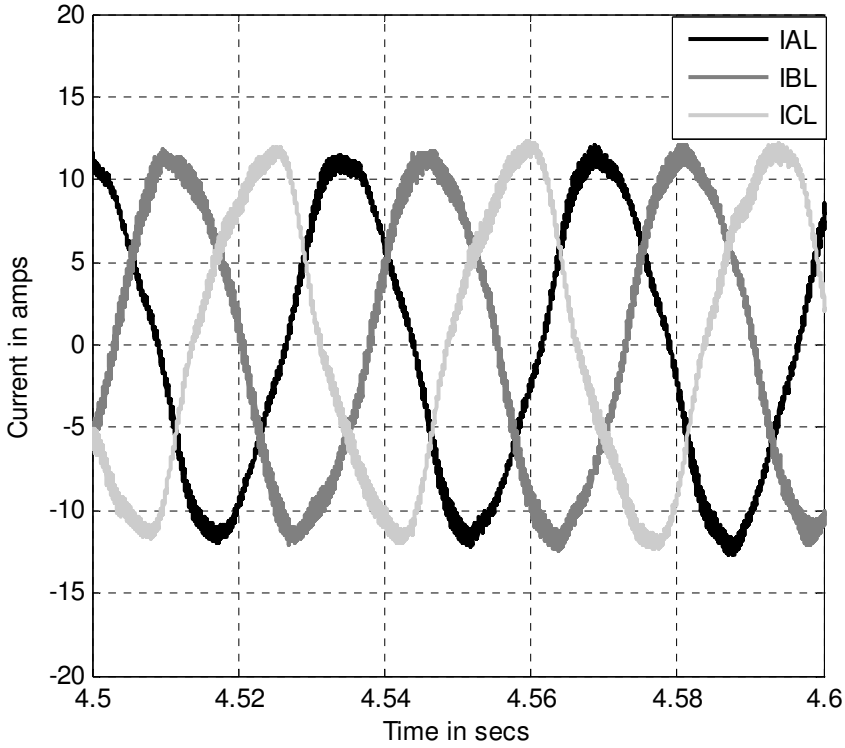

Fig.4.23c Experimentally obtained line currents, vector-control, when the introduced controller was activated, two-phase open-Delta mode of operation, reference speed=60rad/sec.

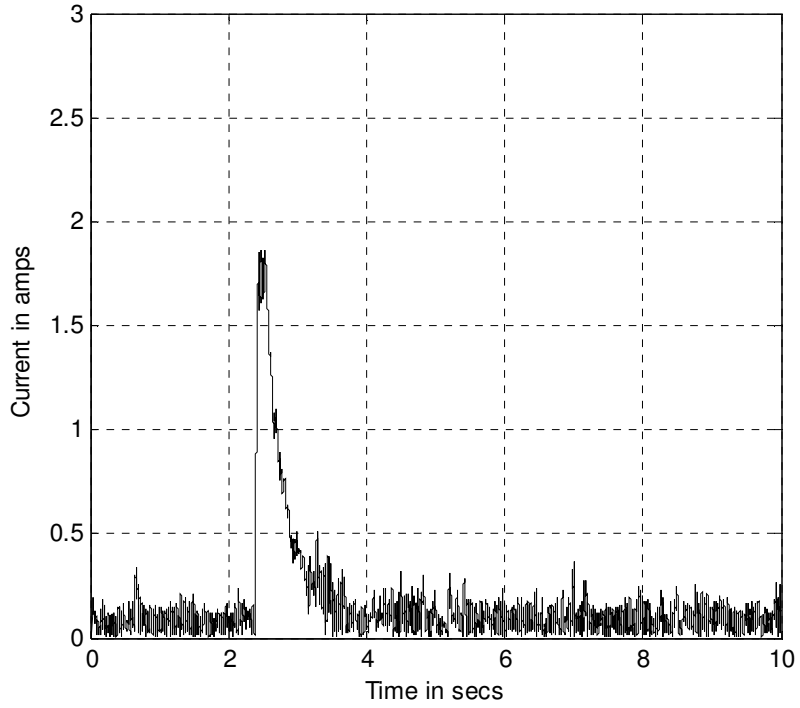

Fig.4.23d Experimentally obtained negative sequence component of the line currents, transfer from three-phase mode of operation to two-phase open-Delta mode of operation when the introduced controller was activated , reference speed=60 rad/sec.

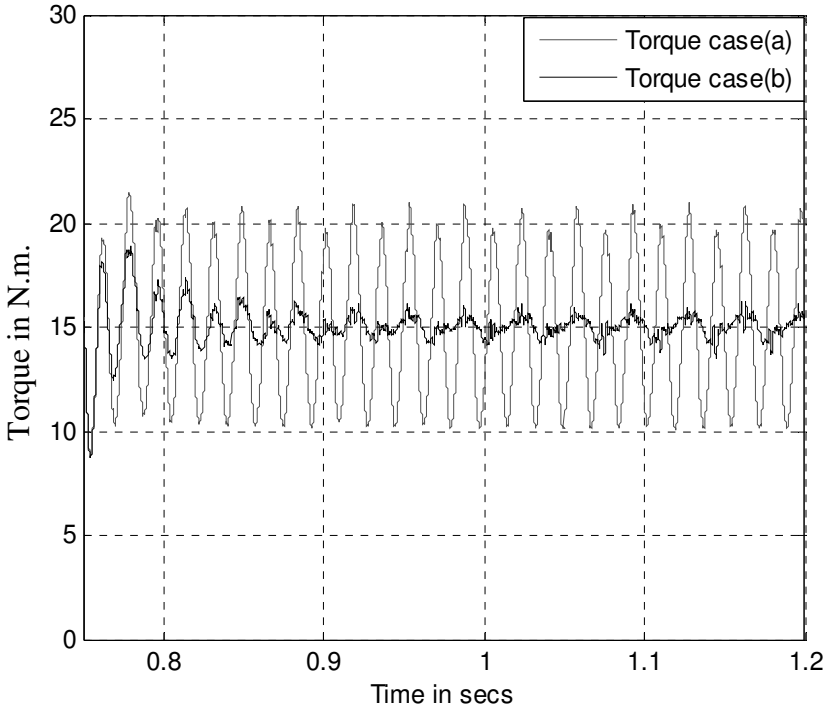

Fig.4.24a Output torque, vector-control, two-phase open-Delta mode of operation, reference speed=60 rad/sec, "Simulink/Simpowersystem model" Case (a) The introduced controller was deactivated. Case (b) The introduced control was activated.

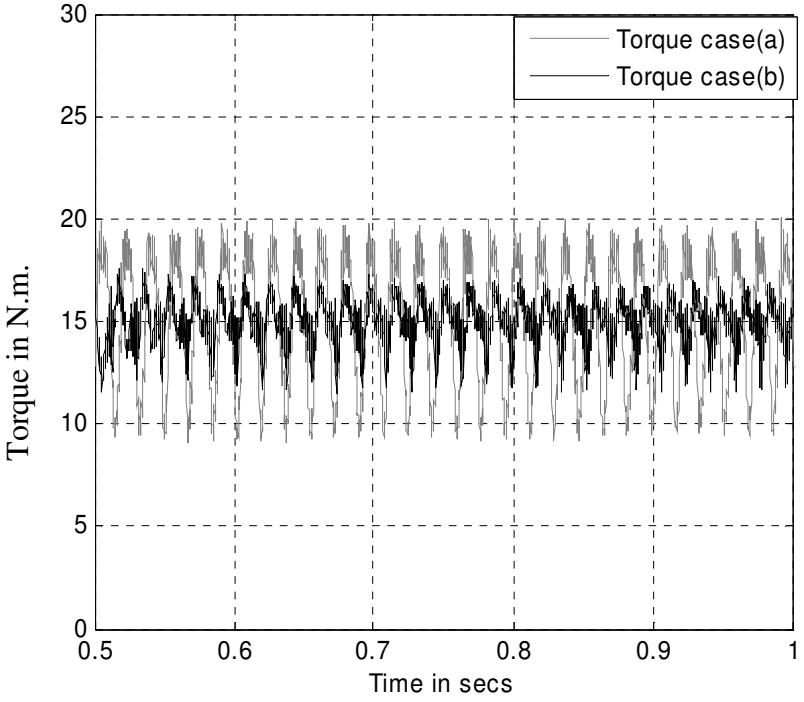

Fig.4.24b Output torque, vector-control, two-phase open-Delta mode of operation, reference speed=60 rad/sec, "Simulink/Flux 2D" Case (a) The introduced controller was deactivated. Case (b) The introduced control was activated.

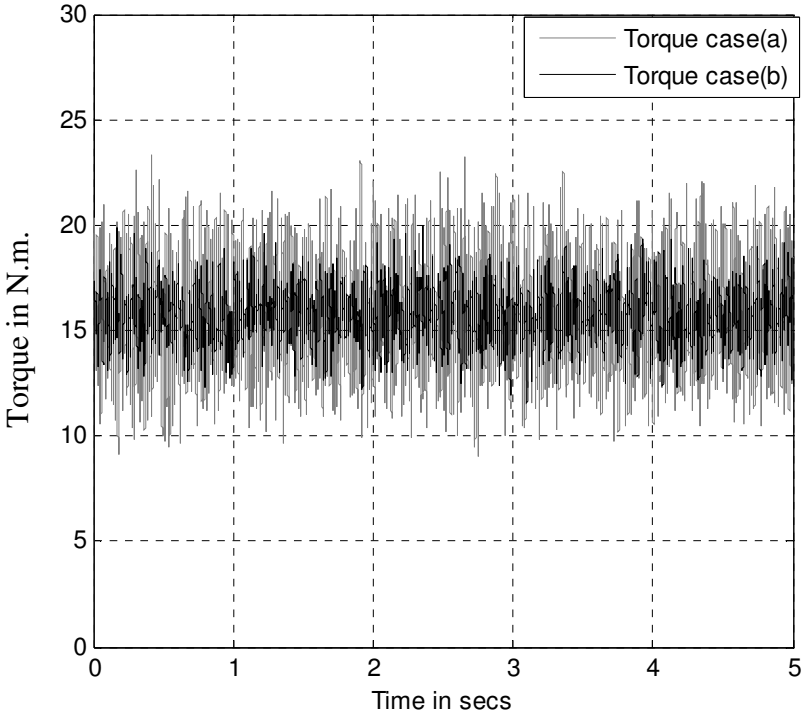

Fig.4.24c Experimentally obtained output torque, vector-control, two-phase open-Delta mode of operation, reference speed=60 rad/sec, Case (a) The introduced controller was deactivated. Case (b) The introduced control was activated.

4.8 Summary

In this chapter, the control topology introduced earlier in Chapter 3, to enable the operation of a three-phase motor-drive system in a two-phase open-Delta mode of operation where one of its phases is disconnected for the case of open-loop constant (V/f) control, was extended for the case of vector-controlled mode. The state of the art in this area was revisited giving a special attention to fault mitigation techniques in such control environments and to fault tolerant machine designs. The basic principles of vector-controlled motor-drive systems were briefly reviewed for the sake of continuity and for the reader's convenience. The control structure of this type of systems was thoroughly discussed and analyzed, followed by a detailed procedure for the controller design. Simulation and experimental results were documented in detail and were found to be in good agreement with the theoretical analysis explained earlier in this chapter. The efficacy of the newly introduced controller in suppressing the torque oscillations and the unbalance in the line currents resulting from a faulty two-phase open-Delta mode of operation were verified through numerous results obtained from several simulation runs and corresponding experimental tests. The simulation work in this chapter included two different models. The first one was based on a simplified motor d-q model in which a sinusoidal MMF in the airgap was assumed. The other model was based on a detailed TSFE simulation that accounts for machine nonlinearities, MMF space harmonics and magnetic circuit configuration. It was also shown that the torque pulsations resulting from the two-phase open-Delta mode of operation can be mostly suppressed by the CCW current control loop at low speed operation provided that the bandwidth of these

controllers is much higher than the frequency of these torque oscillations. However, at high operating speed, torque pulsations resulting from the two-phase open-Delta mode of operation are suppressed by the newly introduced CW current control loop. Therefore, the CW current control loop can be deactivated at low speed without adversely affecting the performance of such a faulty system. On the other hand, it should be activated at relatively high speed in order to suppress torque pulsations resulting from the two-phase open-Delta mode of operation.

CHAPTER 5

5. THE OPERATION OF A MOTOR-DRIVE SYSTEM UNDER A SHORT-CIRCUIT FAULT

5.1 Introduction

The operation of a motor-drive system, while one of such a motor's stator coils was shorted, for the case of an open-loop control drive and the case of a vector-controlled closed-loop motor-drive, is a hazardous condition that require immediate shutdown of the motor-drive system. However, in critical industries like aerospace, nuclear power plants, and military combat systems, immediate shutdown of a motor-drive system may lead to other severe consequences. In a commercial industrial application, this may also lead to sever financial losses or even a life threatening conditions. Therefore, several designs of fault tolerant machines that can tolerate such mode of operation were invented in several previous works, [134]. These designs may come at the expense of increased cost, increased losses and reduced efficiencies. Other investigators, [124,127,170], focused on implementing a fault mitigation control strategy that enables the operation of a standard motor-drive under such fault conditions. This comes at the expense of a degraded system performance, reduced output power, and reduced speed, [124,127,170].

The fault mitigation strategies introduced in this dissertation for open-loop scalar constant (V/f) control and for vector-controlled motor-drive systems were discussed in details in Chapters 3 and 4. This was accomplished for the case of open-coil fault, and as proposed in [124] for the case in which the "ampere-turn" effects of the faulty loop

circulating current can be ignored. The case which involves the operation of an ac motor, while an inter-turn short-circuit current does exist in one of its coils is discussed in details in this chapter. This is carried out through an in-depth simulation and analysis utilizing advanced TSFE modeling technique "Coupled Simulink/Flux2D model" that accounts for the dynamics of the interaction between the inverter's controller, which is usually a software algorithms hosted on a DSP chip, and the motor's saturation effects as well as space harmonics due to the machine winding layouts and magnetic circuit configuration. In addition, the TSFE model provided access to key magnetic quantities required for rigorous analysis, and in-depth study and understanding of the motor and system's performance. Thus, the work introduced in this chapter is centered on the possibility of continued operation of a Delta-connected motor in an "open-Delta" mode of operation while one of the coils in one of the stator phases was shorted.

Under such a mode of operation, a circulating current "faulty loop current" will be induced due to the magnetic coupling between this faulted coil and other energized windings in the machine. The magnitude of this faulty loop current can reach very high values of multiple-times the magnitude of the rated current of a motor, since it is only limited by the resistance, leakage inductance of the faulty coil, bearing in mind that localized core saturation will reduce the magnitude of such a leakage inductance. As will be shown later in this chapter, the rms value of this faulty loop current can reach up to 15 times the rated current of the prototype machine analyzed in this chapter. An excessive heat and temperature rise will be generated in such a coil, affecting the insulation of other coils overlapping with it, [128,170]. This process may cause very fast insulation degradation and accelerates the insulation failure mechanism. The faulty coil may be

electrically isolated to reduce the magnitude of this circulating current. However, a voltage will still be induced in this faulty coil as a result of the magnetic coupling between the faulty coil and other energized coils in the machine. Therefore, several designs have been proposed in references [102,103,115-117,121,134], as discussed earlier in Chapter 4, to minimize or eliminate the overlap between coils from different phases. That is preventing the propagation of the fault to other healthy coils and may allow continued operation of the machine under these faulty conditions. A Fractional Slot Concentric Winding "FSCW" design was applied in reference [132] to provide fault tolerant capability that may allow machine continued operation while a fault does exist in a motor's stator windings. However, a FSCW design may cause external losses in the machine, [132], which consequently reduce the overall system efficiency and may require special means of enhanced cooling for the same power rating of a motor as compared to a traditional double layer distributed windings configuration. In addition, as will be shown later in this chapter, the existence of this circulating faulty loop current produces torque pulsations that is very difficult to estimate or detect by the drive's controller unless the torque signal is measured through a torque transducer mechanically coupled to the motor's shaft.

The theoretical analysis presented in this chapter is mainly focused on the case of the existence of a faulty coil in a stator phase windings, where this coil is electrically isolated but magnetically coupled to the other machine phase windings. This is typically the case when the faulty winding is isolated by a standard fuse protection such as in reference [41], or an advanced diagnostic and a fault location scheme such as in references [44,171]. This analysis is supported by results from an in-depth simulation

using a coupled Simulink/Flux2D TSFE model developed for the 5-hp motor-drive set-up discussed earlier in Chapters 3 and 4. Accordingly, for this case, the model was implemented for simulation of an inter-turn short-circuit taking place in one of the machine phase winding coils. Therefore, the simulation and analysis presented in this chapter include the effects of the interaction between the controller implemented in MATLAB/Simulink, the magnetic disturbance resulting from the fault condition, the space harmonics, the saturation effects, and other machine nonlinearities implemented in a rigorous TSFE model using Magsoft/Flux2D. See Appendix A for details about the prototype machine parameters and the prototype machine TSFE model. The inverter switching action and inverter nonlinearities (dead-time, dc link ripples, etc) are not considered in this simulation work mainly due to hardware and software computation limitations.

A theoretical analysis that discusses the effects of circulating faulty loop current on the machine performance is discussed in detail in the next section for the case of an open-loop operation and a vector-controlled closed-loop operation. Meanwhile, the simulation model used in this analysis is discussed in Appendix A. A rigorous discussion and analysis of the simulation results obtained from several simulation runs at different operating conditions are presented in the third section of this chapter.

5.2 Theoretical analysis of machine performance under stator inter-turn winding faults

As discussed earlier in Chapter 2 and in references [138-144], insulation failure may be due to several reasons such as excessive voltages stresses, excessive thermal

stresses due to frequent overloading conditions, excessive vibrations, etc. The major concern regarding inter-turn short-circuit faults is that the rate of propagation of the fault is in range of one to four minutes as reported in references [50,167-168]. This condition does require immediate attention otherwise a catastrophic motor winding failure may result. Moreover, excessive temperature rise associated with this type of faults may cause irreparable core damage. Therefore, several investigations were centered on providing a reliable diagnostic technique to detect such faults and disconnect the machine as soon as possible upon the detection of such a faulty condition. On the other hand, several critical applications such as in aerospace systems, medical equipment, and nuclear power plant water-feed pumps and cooling systems, mandate continued system operation adopting "run to fail" concept, [134], provided that a system's failure does not cause a safety compromising hazardous situation.

Continued operation of a machine while an inter-turn short-circuit exists in its windings is a hazardous condition that require proper machine and converter design to allow such mode of operation. In this section, the case involving an electrically isolated faulty is investigated in details, for the case of open-loop drives and vector-controlled drives. The analysis presumes that the coil is completely shorted through an external fault resistance equal to zero, which is the severest type of such a class of faults.

The analysis introduced earlier in Chapter 2 is repeated her, but for a case involving a solid short-circuit across one of the stator winding coils. Let us consider an ideal case for a healthy three-phase induction motor, with a sinusoidal three-phase balanced voltage source applied on its terminals, and sinusoidal three phase currents

passing through its phase windings, the voltage space-vector, $\vec{v}_s$, and the current space-vector, $\vec{i}_s$,for this case can be expressed as follows, [25]:

$$\vec{v}_s(t) = V_s e^{j(\omega t)} \tag{5.1}$$

$$\vec{i}_s(t) = I_s e^{j(\omega t - \varphi)} \tag{5.2}$$

where, V_s and I_s are the peak voltage and the current amplitudes, φ is the power factor angle, ω is the supply frequency in rad/sec.

Consequently, under a healthy condition, the resultant forward rotating field, $\vec{f}_s$, in space-vector form can be written as follows, [25]:

$$\vec{f}_s(t) = N_{se}\vec{i}_s(t) = N_{se} I_s e^{j(\omega t - \varphi)} = F_s e^{j(\omega t - \varphi)} \tag{5.3}$$

Meanwhile $\vec{v}_s, \vec{i}_s, \vec{f}_s$ are the instantaneous space-vectors of the polyphase voltages, currents, as well as the resultant rotating forward stator MMF waveform in the airgap, respectively. Here, N_{se}, is the equivalent effective number of series stator turns per phase. In addition, F_s, is the amplitude of the stator MMF space-vector, where F_s=$N_{se}I_s$.

It was shown earlier in Chapters 3 and 4 that for Delta-connected stator windings, high unbalance in both the line currents and the phase currents will result when one of the motor phases is disconnected and electrically isolated upon the detection of an inter-turn short-circuit in one of its coils. This unbalance in the currents can be measured and compensated for using two current control loops in the CW frame of reference in both the d-axis and in the q-axis. This technique was discussed and verified earlier in Chapter 3 for the case of open-loop motor-drive systems and in Chapter 4 for the case of vector-controlled closed-loop motor-drive systems. Meanwhile, the faulty coil which is electrically isolated but magnetically coupled to the other coils in the machine phase

windings can be considered as a separate phase, the so-called shorted-coil, which is magnetically coupled to these other coils. Consequently, due to the flux linkage between the faulty coil and the other coils, a voltage will be induced in this shorted-coil. This induced voltage circulates a demagnetizing current through the closed loop path as discussed earlier in Chapter 2. The amplitude, I_f, of this instantaneous faulty loop current, i_f, is mainly limited by the faulty coil's leakage inductance, L_{lsc} and the faulty coil's resistance, r_{coil}. Therefore, the faulty loop current can be expressed in steady state condition as follows:

$$i_f = v_{sc} /(r_{coil} + j\omega\ L_{lsc}) \tag{5.4}$$

It can be noticed from (5.4) that at a very low operating speeds, $r_{coil} >> \omega\ L_{lsc}$ and the faulty loop current is limited by the coil resistance. On the other hand, at relatively high operating speeds, $\omega\ L_{lsc} >> r_{coil.}$ Hence, the faulty loop current is limited by the inductive reactance "$\omega\ L_{lsc}$" of the shorted-coil.

Meanwhile, if the faulty coil is electrical isolated but magnetically coupled to other windings in the machine, the relationship between the faulty loop current, i_f, and the shorted-coil's mutual flux linkage, λ_{sc}, can be expressed as follows, [170]:

$$0 = r_{coil}\ i_f + \frac{d\lambda_{sc}}{dt} + L_{lsc}\frac{di_f}{dt} \tag{5.5}$$

In addition, assuming that the shorted-coil is located in phase C, the shorted-coil's mutual flux linkage, λ_{sc}, can be expressed as follows:

$$\lambda_{sc} = \lambda_{scas} + \lambda_{scbs} + \lambda_{scar} + \lambda_{scbr} + \lambda_{sccr} \tag{5.6}$$

In (5.6), λ_{scas}, λ_{scbs}, λ_{scar}, λ_{scbr}, λ_{sccr} are the mutual flux linkage between the shorted-coil and stator phase a, stator phase b, rotor phase a, rotor phase b, and rotor phase c, respectively. These flux linkage components can be approximately expressed in terms of

the stator mutual inductance, L_{sm} , stator-to-rotor mutual inductance, L_{srm}, the stator currents in phase A and phase B , i_A and i_B, as well as the three phase rotor currents , i_{ar} , i_{br} and i_{cr} , respectively, as follows:

$$\begin{aligned}
\lambda_{scas} &= \mu L_{sm}\ i_A \\
\lambda_{scbs} &= \mu L_{sm}\ i_B \\
\lambda_{scar} &= [\mu L_{srm}\cos(\delta_0 + \omega_r t)]\ i_{ar} \\
\lambda_{scbr} &= [\mu L_{srm}\cos(\delta_0 + \omega_r t + 2\pi/3)]\ i_{br} \\
\lambda_{sccr} &= [\mu L_{srm}\cos(\delta_0 + \omega_r t + 4\pi/3)]\ i_{cr}
\end{aligned} \tag{5.7}$$

In (5.7), μ is the ratio between the number of the shorted turns in phase C to the total number of series turns in that phase, and $(\delta_0 + \omega_r t)$, $(\delta_0 + \omega_r t + 2\pi/3)$, $(\delta_0 + \omega_r t + 4\pi/3)$ are the instantaneous displacement angles between the stator phase C axis and the rotor a, b, c phase axes. Here, δ_0 is an arbitrary initial position angle depending on the motor operating condition.

Therefore, substituting from (5.7) in (5.6) yields to

$$\begin{aligned}
\lambda_{sc} &= \mu L_{sm}\ i_A + \mu L_{sm}\ i_B + \mu L_{srm}\cos(\delta_0 + \omega_r t)\ i_{ar} \\
&+ \mu L_{srm}\cos(\delta_0 + \omega_r t + 2\pi/3)\ i_{br} + \mu L_{srm}\cos(\delta_0 + \omega_r t + 4\pi/3)\ i_{cr}
\end{aligned} \tag{5.8}$$

It is obvious from (5.8) that the flux linkage between the shorted-coil in the faulty phase “Phase C” and other windings in the machine depends on the machine design parameters, L_{sm} and L_{srm} , and stator and rotor currents. It should be also mentioned that the mutual inductance between the shorted-coil and one of the remaining active phases may not be equal to the mutual inductance between this shorted-coil and the other active phase. This is mainly due to the fact that the magnetic coupling between the faulty coil and each of the remaining two healthy phases depends on the winding layout and the location of this faulty coil especially in lap-wound machines. This fact is not considered

in (5.8) for the sake of simplicity. However, it is inherently included in the TSFE simulation runs carried throughout this chapter, this is as a result of the distributed nature of magnetic FE machine modeling. Now, let us consider a case in which the currents in the two remaining active phases are controlled such that they are equal in magnitude with a phase shift angle maintained at a value of $\pi/3$ between them. With these constrains, a perfect rotating field is produced , as described earlier in Chapters 3 and 4, where the fault was supposedly detected and isolated at an early stage. Accordingly, the stator and the rotor currents can be expressed as follows:

$$\begin{aligned} i_A &= I_m \cos(\omega t) \\ i_B &= I_m \cos(\omega t - \pi/3) \\ i_{ar} &= I_{mr} \cos(s\omega t + \theta_o) \\ i_{br} &= \mathrm{I}_{mr} \cos(s\omega t + \theta_o - 2\pi/3) \\ i_{cr} &= \mathrm{I}_{mr} \cos(s\omega t + \theta_o - 4\pi/3) \end{aligned} \tag{5.9}$$

In (5.9), s is the slip, [151], ω is fundamental frequency of the inverter in rad/sec, and θ_o is a phase shift angle that depends on the motor circuit parameters and operating/load conditions. Hence, substituting from (5.9) into (5.8) yields the following:

$$\begin{aligned} \lambda_{sc} &= \mu L_{sm} \ \mathrm{I}_m \cos(\omega t) \\ &+ \mu L_{sm} \ \mathrm{I}_m \cos(\omega t - \pi/3) \\ &+ \mu L_{srm} \cos(\delta_0 + \omega_r t) \ \ \mathrm{I}_{mr} \cos(\theta_0 + s\omega t) \\ &+ \mu L_{srm} \cos(\delta_0 + \omega_r t + 2\pi/3) \ \ \mathrm{I}_{mr} \cos(\theta_0 + s\omega t - 2\pi/3) \\ &+ \mu L_{srm} \cos(\delta_0 + \omega_r t + 4\pi/3) \ \ \mathrm{I}_{mr} \cos(\theta_0 + s\omega t - 4\pi/3) \end{aligned} \tag{5.10}$$

Simplifying (5.10), yields:

$$\lambda_{sc} = \sqrt{3} \ \mu L_{sm} \ I_m \cos(\omega t - \pi/6) + (3/2)\mu L_{srm} I_{mr} \cos(\delta_0 + \theta_0 + \omega t) \tag{5.11}$$

Hence, from (5.11), the induced voltage in the shorted-coil, v_{sc}, can be expressed as the rate of change of the mutual flux linkage between this shorted-coil and other windings in the machine, and can be expressed as follows:

$$v_{sc} = \frac{\partial \lambda_{sc}}{\partial t} = -\sqrt{3}\ \mu L_{sm}\omega\ I_m \sin(\omega t - \pi/6) - (3/2)\mu L_{srm}\omega I_{mr} \sin(\delta_0 + \theta_0 + \omega\, t) \quad (5.12)$$

Hence, (5.12) is an approximated analytical expression to calculate the induced voltage in the shorted-coil. Moreover, at no load or light load conditions, the current in the rotor circuit can be ignored, thus $I_{mr} \approx 0$. Therefore, in this case, (5.12) can be re-expressed as follows:

$$v_{sc} = \frac{\partial \lambda_{sc}}{\partial t} = -\sqrt{3}\ \mu L_{sm}\omega\ I_m \sin(\omega t - \pi/6) \quad (5.13)$$

In the two-phase open-Delta mode of operation with the faulty phase electrically isolated but magnetically coupled to other windings in the machine, the faulty coil can be considered as an additional phase carrying a current, i_f , with a number of series turns, N_{coil} , [56]. Thus, the MMF produced by this faulty coil can be expressed as follows:

$$MMF_{coil} = N_{coil}\ i_f = N_{coil} \cos(\theta - \beta)\ I_f \cos(\omega t - \alpha) \quad (5.14)$$

In (5.14), θ is the spatial space angle, β is the phase shift between the magnetic axis of the faulty coil and the magnetic axis of the phase that contains this faulty coil. This angle "β" equals zero for the case of concentric winding and it depends on the location of the coil for the case of lap winding as described earlier in Chapter 2, and is re-depicted in Fig.5.1 and Fig.5.2 below for the reader's convenience and for the sake of continuity.

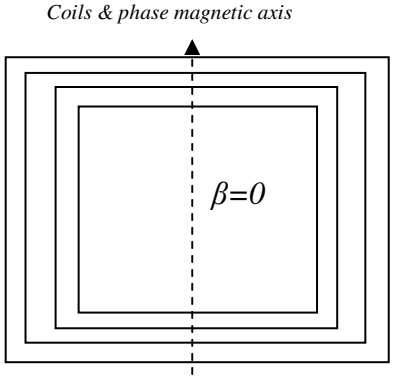

Fig. 5.1 Concentric winding distribution.

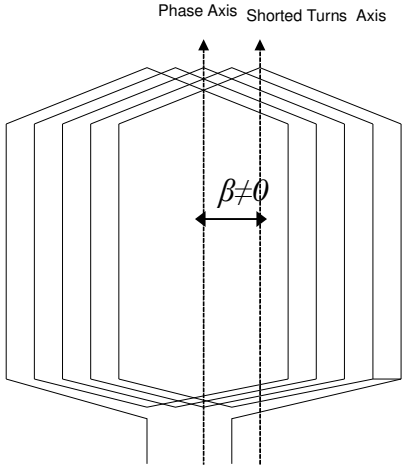

Fig. 5.2 Lap winding distribution.

The MMF expressed in (5.14) can be resolved into a forward rotating MMF component and a backward rotating MMF component as follows:

$$MMF_{coil} = \frac{N_{coil} I_f}{2}[\cos(\theta - \omega t - \beta + \alpha) + \cos(\theta + \omega t - \beta - \alpha)] \tag{5.15}$$

The first term in (5.15) represents a forward rotating field component which can be added vectorially to the main rotating field in the machine. The second term in (5.15) is a backward field component that is rotating CW at a speed equal to the synchronous speed. This backward rotating MMF component can not be estimated or compensated by the drive from only measuring the three-phase line currents, [49]. This backward *MMF* component interacts with the forward *MMF* component and produces torque pulsations with a frequency that is equal to double the line frequency. The magnitude of these torque pulsations depends mainly on the magnitude of the MMF produced by this faulty coil which consequently depends on the number of shorted turns and the faulty loop current.

Therefore, it can be realized from the previous analysis that having an inter-turn short-circuit in a coil in a machine's stator windings has several undesirable

consequences even if this coil is electrically isolated from the circuit. These consequences can be in the form of excessive thermal stresses that elevate the temperature of this coil, thus jeopardizing other coils either overlapping with its coil in the end-region, or located in the same slot with it. The other effect is the presence of torque pulsations resulting from the field disturbance produced by this faulty coil. The dynamic performance of a motor-drive system resulting from the effects of the faulty loop current circulating in one of the stator phase winding coils depends mainly on the interaction between the drive's controller and the faulty motor. For open-loop motor-drive systems with constant (V/f) control, the drive's controller action does not depend on the machine's performance. Therefore, there is no interaction between the motor and the drive's controller. On the other hand, for the case of vector-controlled motor-drive systems, the drive's controller action depends on the measured motor line currents and measured or estimated speed. In both cases, there are two different sources of torque pulsations in the system. The frequency of both is equal to double the fundamental frequency.

The first source of torque pulsations is caused by the negative sequence MMF component resulting from the two-phase open-Delta mode of operation of the machine as described earlier in detail in Chapters 3 and 4. This negative sequence MMF result in significant magnetic unbalance in the machine, that appears at the terminals as line current unbalance that can be sensed by the drive's current sensors. The analysis in Chapters 3 and 4 showed that this current unbalance and torque pulsations can be compensated for by adding two current control loops in the CW frame of reference, in which the negative sequence component of the line currents is driven to a value very

close or equal to zero. It was also shown in Chapter 4 that these torque pulsations can be neutralized/ compensated for by the conventional current control loop in the CCW frame of reference at low speed operation provided that the bandwidth of these current control loops is much higher than the frequency of these torque pulsations.

The second source of torque pulsations in this case is the pulsating field resulting from the circulating faulty loop current in the shorted-coil. Although the faulty winding might be electrically isolated, the magnetic coupling between the faulty coil and other coils in the machine produces an induced voltage in the faulty coil. Consequently, a faulty loop current circulates in this faulty coil through the fault resistance which is considered to be equal to zero in the analysis described in this chapter. The circulating current in the faulty coil and its associated torque pulsations are extremely difficult to measure or estimate by the drive. However, depending on the operating speed and system's inertia, these torque pulsations may produce speed oscillations. These speed oscillations may be significant and detectable at low speed operations.

5.3 Analysis of the simulation results

In the previous section, the theoretical background that is necessary to understand the operation of a three-phase machine in the two-phase open-Delta mode of operation, in the presence of a shorted-coil in the third phase was discussed. It was shown that although this faulty coil is electrically isolated, it is magnetically coupled to other windings in the machine which induces a circulating current in this coil. This circulating current may also cause additional magnetic disturbance in the airgap that is very difficult to estimate or to compensate for by the drive from measuring only the motors' line

currents. The magnitude of the faulty loop current and the torque pulsations depend on several factors like a motor's operating speed and airgap flux density, as well as other motor parameters.

Detailed simulation studies under several operating conditions are thoroughly discussed and analyzed in this chapter. These studies include several simulation runs using the Coupled Simulink/Flux2D TSFE model described earlier in Chapter 4. In spite of the fact that the detailed Finite Element "FE" model of the prototype machine is discussed in Appendix A, it will be briefly discussed here for the sake of continuity and for the reader's convenience.

The simulation runs and their corresponding results discussed in this section are mainly focused on the case of a solid short-circuit case in one coil in one of the motor phase windings. The simulation includes the effects of space harmonics, complete windings layout, saturation effects as well as the interaction between the control system dynamics and this detailed TSFE model.

5.3.1 Prototype Motor Finite Element Model

The Machine model was implemented using a commercial software package, namely "Magsoft/Flux2D". The entire machine geometry, winding layout and circuit connection were entered to the software package, [146]. The mesh of the geometry includes 13,667 nodes and 6,674 elements. The prototype machine consists of three phases, each phase consists of 12 coils, and each coil has 20 turns. Therefore, the total number of turns per phase is 240 turns. The geometry of the machine with the mesh is shown in Fig.5.3. Meanwhile the circuit connection is shown in Fig.5.4.

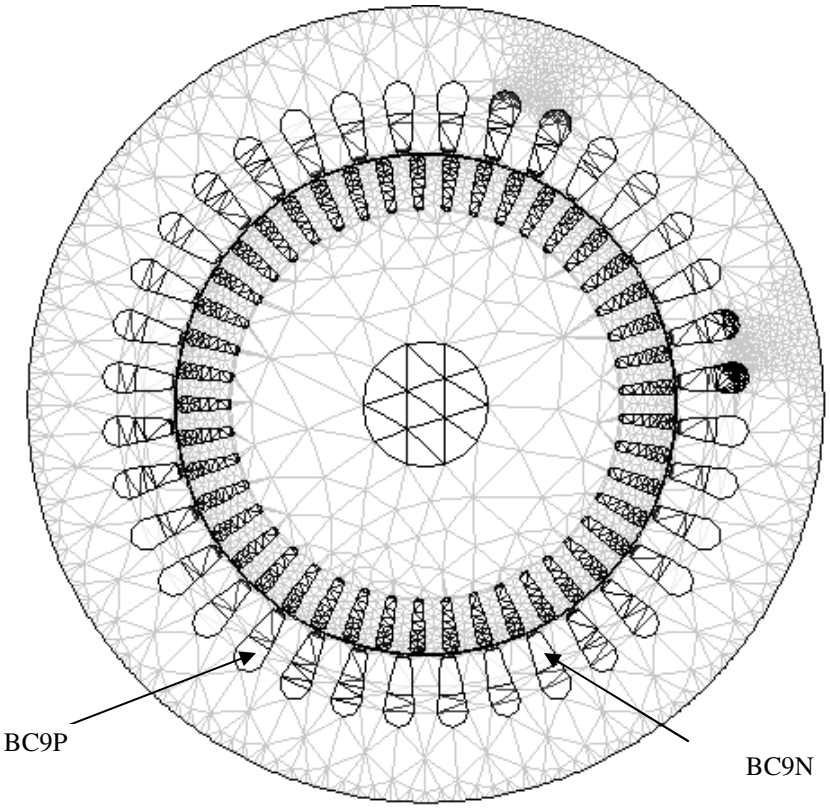

Fig.5.3 Geometry mesh for the 5-hp prototype machine

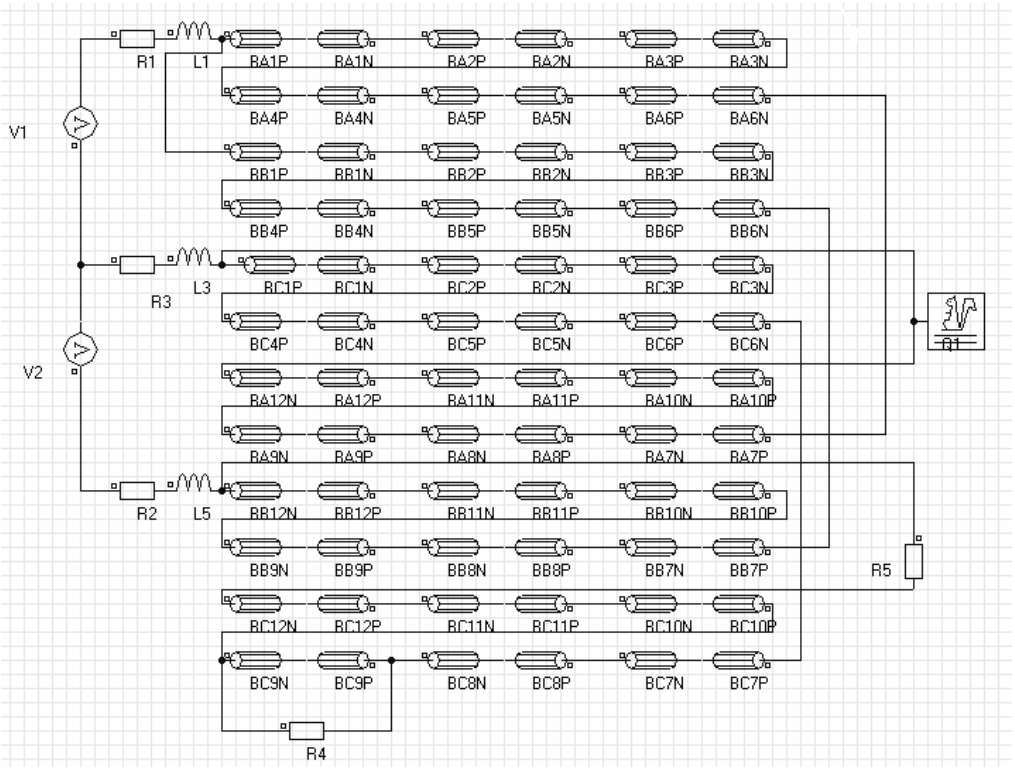

Fig.5.4 circuit connection for the 5-hp prototype machine

It can be noticed from Fig.5.4 that two additional virtual resistors are added to one of the phases in the circuit connection, namely R4 and R5. These two resistors do not physically exist in the actual circuit of the motor. The resistor, R4, was added and connected across the terminals of one of the coils, namely coil "BC9" in the circuit of Fig.5.4 in order to simulate a solid short-circuit fault across this coil by setting its value to zero ohms, and in order to simulate a healthy condition for this coil one sets the value of this resistance to a very large number, say 10000Ohms. Meanwhile, the resistor, R5, was added in series with the coils of the same phase, namely phase C, to disconnect this phase from the circuit and force the current in this phase to zero by setting the value of this resistance to a very large number, say 100000Ohms to simulate the open phase condition.

5.3.2 Case studies and analysis

5.3.2.1 Open-loop constant (V/f) control

Case study A:

The first case study to be analyzed in this chapter is an open-loop, constant (V/f), motor-drive system. The compensation controller proposed and introduced earlier in Chapter 3 was deactivated. The motor was running at its rated speed, 124 rad/sec, while it was loaded to half of its rated load value that is a torque of 15 Nm. A short-circuit occurred at time t=0.4 sec across the coil BC9, see Fig.5.4, and the faulty phase was electrically isolated at time t=0.5 sec. It should be highlighted that the fault resistance was considered to be equal to zero in order to consider the worst case scenario. Thus, the faulty loop current was only limited by the coil resistance and leakage reactance. The simulation was run under the two-phase open-Delta mode of operation with the faulty phase disconnected in order to examine the system's performance under this faulty

condition. In this study, the monitored variables are the line currents, the circulating faulty loop current, the airgap flux density, the airgap Magnetic Vector Potential, MVP, and the motor torque.

The waveforms of the motor line currents are shown in Fig.5.5 in which the magnitudes of the line currents (IAL, IBL, and ICL) were increased upon the occurrence of the fault to almost 2.5 times their values under normal operation. Upon the isolation of the faulty phase (phase C), the magnitudes of the line currents IBL, and ICL were reduced to a value almost equal to the rated line current. Meanwhile, the magnitude of the line current IAL was equal to 2.5 times the pre-fault value of the line current. Again, it should be noticed that the unbalance in the machine resulted from two factors. The first factor is the unbalance created in the machine as a result of the two-phase open-Delta mode of operation. The second factor is the magnetic unbalance and disturbance due to the circulating faulty loop current in the faulty coil BC9. The waveform of the faulty loop current "the current in the resistor R4" is depicted in Fig.5.6. It can be observed that initial value of this current was equal to zero at normal operating condition, the magnitude of the current then increased to a very high value, 170A, "almost equal to seventeenth times the rated phase current of the machine". This current was then significantly reduced to 100A upon the isolation of this faulty phase. In spite of the fact that the faulty loop current was reduced after disconnecting the faulty phase, the magnitude of this current in both cases is very high which would have produced sever thermal stresses that would have jeopardized the whole winding had this been done in the laboratory and would have accelerated the propagation of the fault with severe consequences to the motor.

The corresponding motor output torque is depicted in Fig.5.7, in which torque ripples with a magnitude of 50% of the developed torque at this operating conditions can be observed at time, t=0.4 sec. These torque ripples are mainly produced by the pulsating field resulting from the faulty loop current in the shorted-coil as described earlier in this chapter. Upon the isolation of the faulty phase C at time, t=0.5sec, the magnitude of these torque ripples was increased to 200% of the developed torque at these operating conditions. These torque ripples are now produced by the magnetic unbalance in the machine due to the two-phase open-Delta mode of operation, and the pulsating field resulting from the faulty loop current in the faulty coil, see Fig.5.7.

The waveform of the airgap flux density at a given time instant during normal operation is given in Fig.5.8a, while the corresponding airgap flux density waveform while the coil BC9 was shorted and the faulty phase was still connected to the supply is given in Fig.5.8b. Meanwhile, the airgap flux density waveform when the coil BC9 was shorted while the faulty phase was disconnected from the supply is depicted in Fig.5.8c. In the meantime, the corresponding waveforms of the MVP conditions at the same above mentioned three operating conditions are depicted in Fig.5.9a, Fig.5.9b and Fig.5.9c, respectively. A detectable distortion in the waveforms of the airgap flux density and the MVP can be observed for the case of the existence of the short-circuit in coil BC9 when the three phases are still connected and in the case of two-phase open-Delta mode of operation while coil BC9 is still under short-circuit.

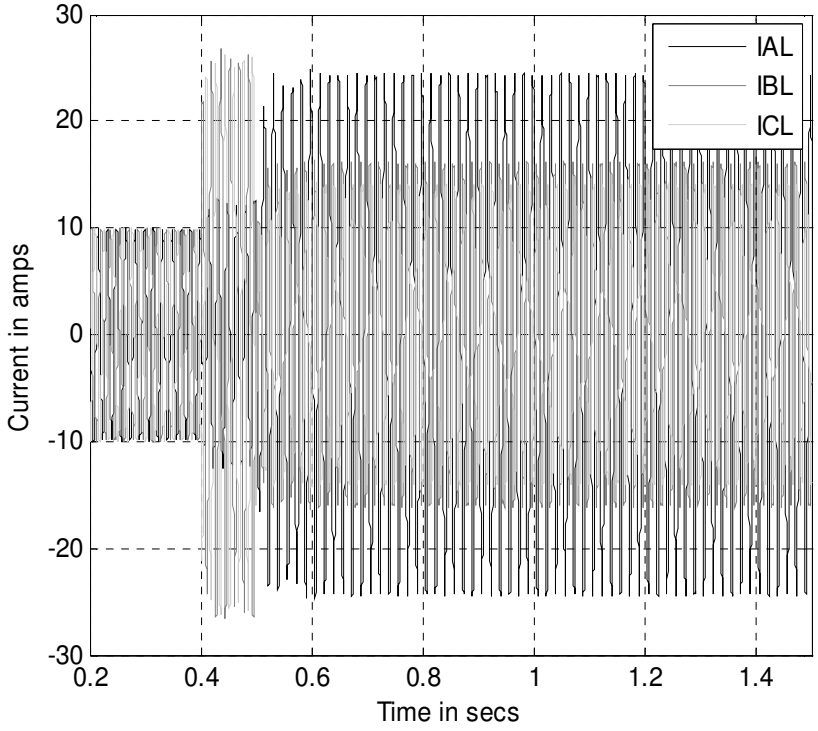

Fig.5.5 Motor line currents, case study A, open-loop mode, coil BC9 shorted at t=0.4sec, faulty phase isolated t=0.5sec

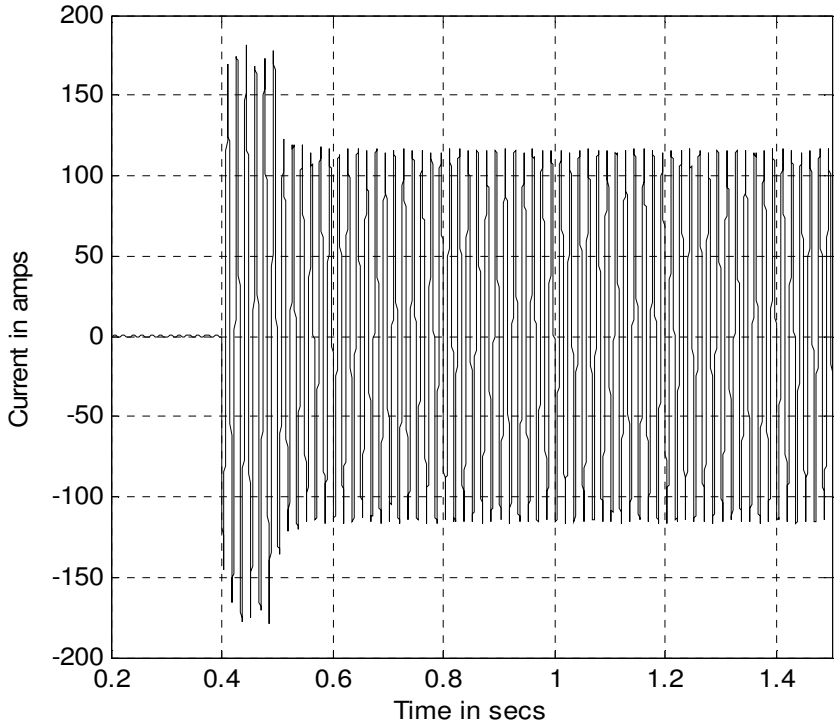

Fig.5.6 The circulating faulty loop current resulting from the faulty condition, case study A, open-loop mode.

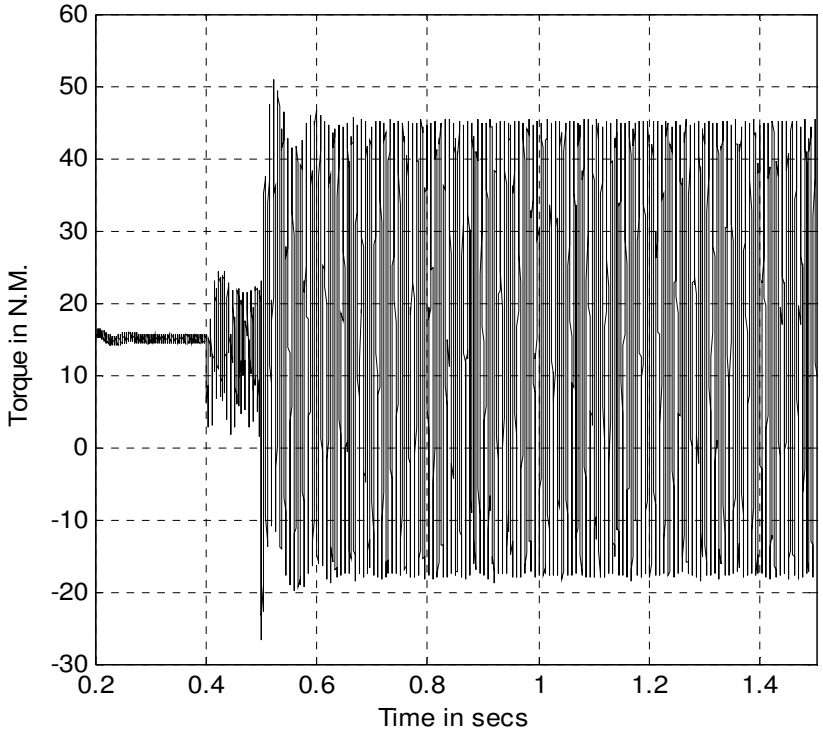

Fig.5.7 Motor's output torque, case study A, open-loop mode, coil BC9 shorted at t=0.4sec, faulty phase isolated t=0.5sec.

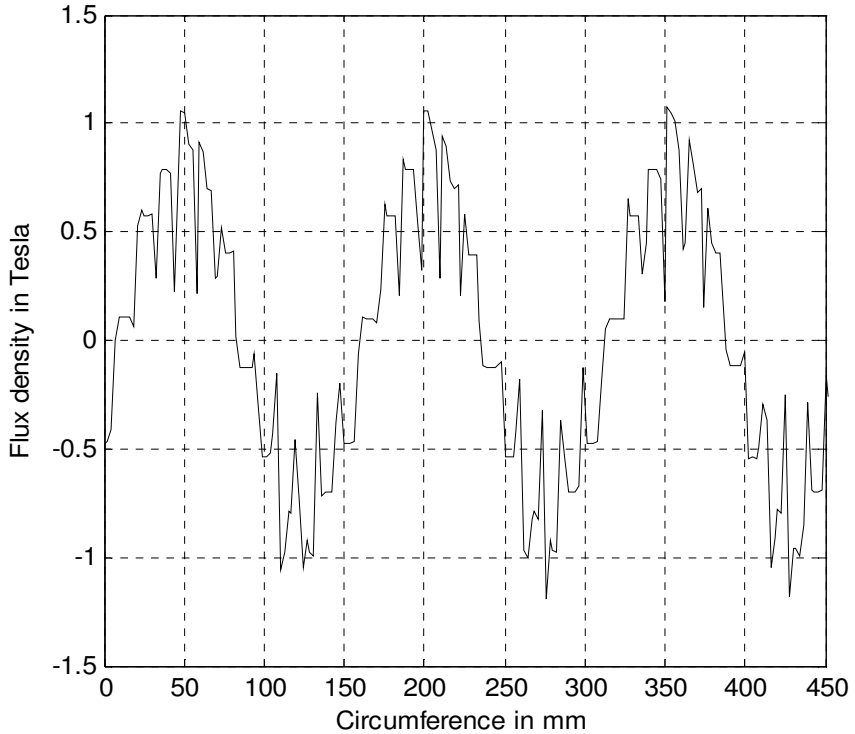

Fig.5.8a Airgap flux density, case study A, open-control mode, normal operation.

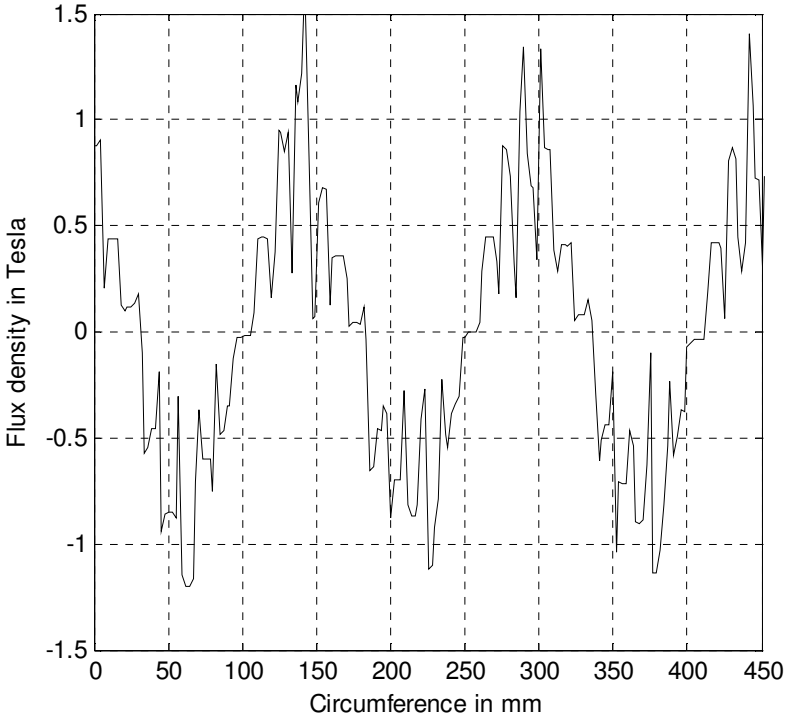

Fig.5.8b Airgap flux density, coil BC9 shorted, case study A, open-loop mode, the faulty phase is still connected to the supply.

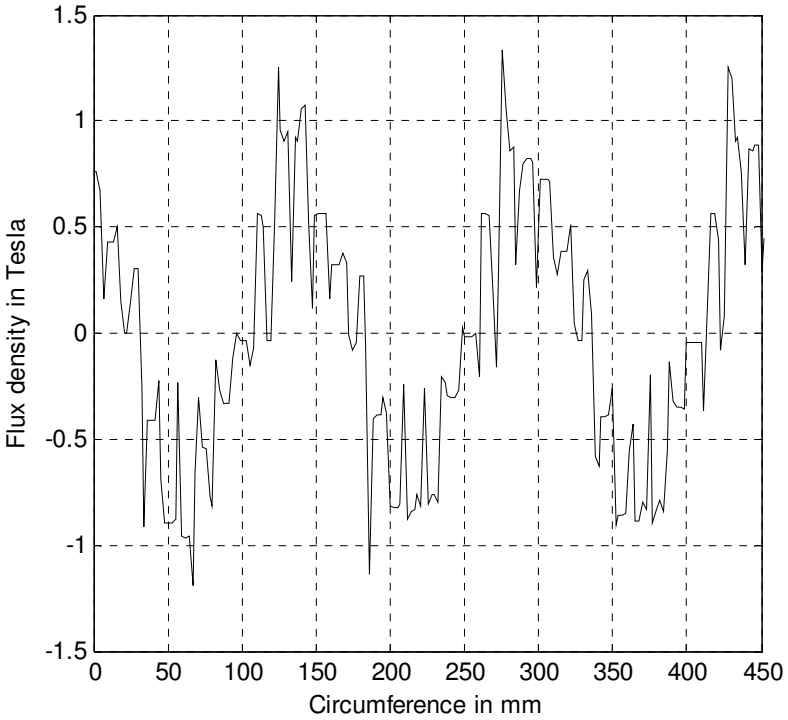

Fig.5.8c Airgap flux density, coil BC9 shorted, case study A, open-loop mode, the faulty phase is disconnected from the supply.

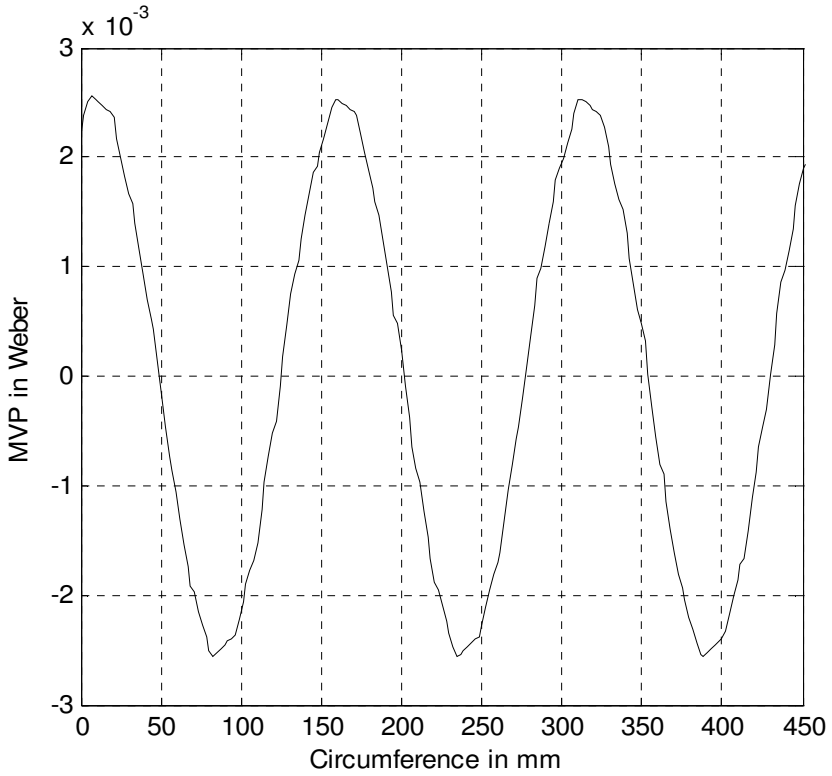

Fig.5.9a Airgap MVP, case study A, open-loop mode, normal operation

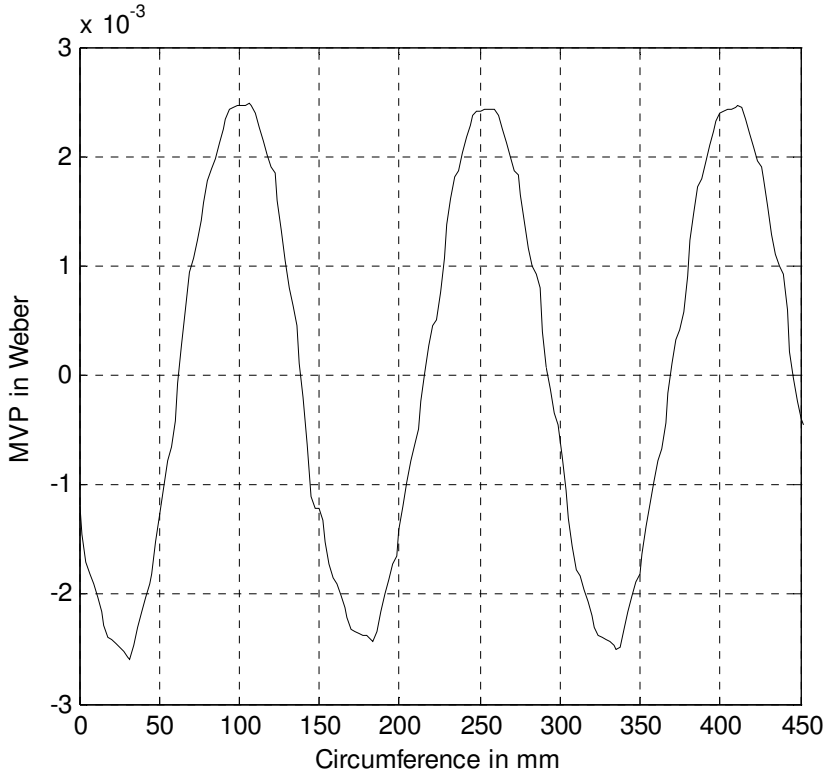

Fig.5.9b Airgap MVP, case study A, open-loop mode, coil BC9 shorted, while the faulty phase is still connected to the supply

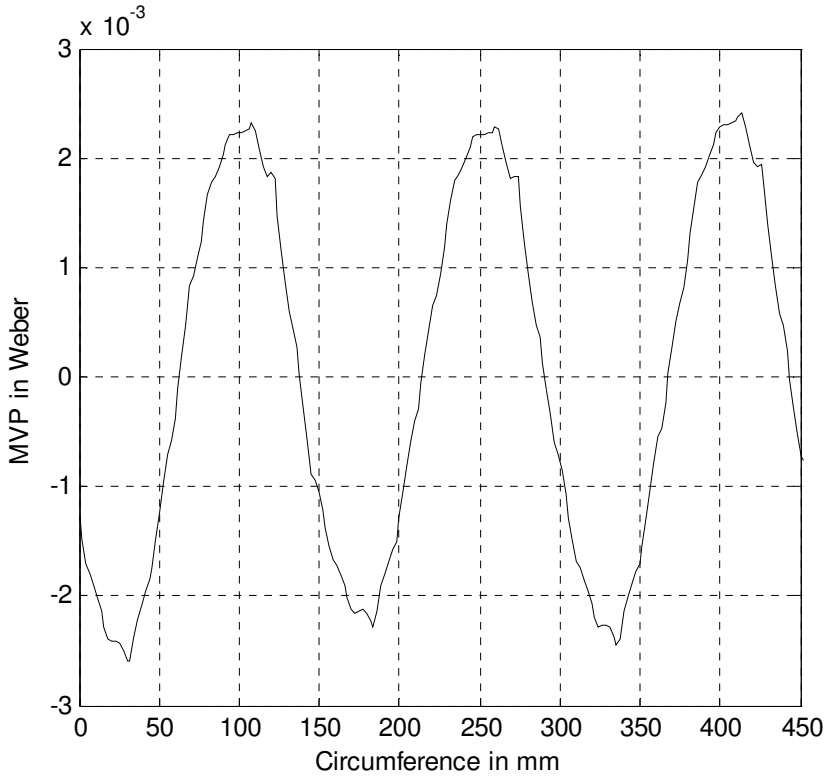

Fig.5.9c Airgap MVP, case study A, open-loop mode, coil BC9 shorted, while the faulty phase is isolated from the supply

Case study B:

The effect of the motor's operating speed on the faulty loop circulating current is studied in this case. In this case study, the motor was running at an operating speed of 30 rad/sec, the motor output torque was 50% of its rated value (15 Nm). The voltage and the frequency are controlled in such a manner so as to keep the airgap flux constant. The coil BC9 was shorted at time t=1.2sec. The compensation controller introduced in Chapter 3 was deactivated. Upon the detection of the fault, the faulty phase was disconnected at time t=1.3 sec. The motor then continued to run under two-phase open-Delta mode of operation while the coil BC9 was shorted.

The waveforms of the motor line currents are depicted in Fig.5.10. Upon the occurrence of the short-circuit fault, it can be noticed that the line currents were slightly

increased at time, t=1.2 sec. Meanwhile, a significant unbalance in the line currents can be observed after the disconnection of this faulty phase at time, t=1.3 sec. This unbalance is mainly caused by the magnetic unbalance in the machine resulting from the two-phase open-Delta mode of operation. The faulty loop current circulating in the coil BC9 is depicted in Fig.5.11. It can observed that this current was reduced to double the rated phase current of the machine under normal operation which shows a significant reduction in the magnitude of this current compared to the case study A explained earlier. At this point, it should be pointed out that reducing the faulty loop current helps to extend the operation of the faulty machine. However, the accurate estimation of the period of operation should be based on accurate thermal analysis of the machine understudy which is beyond the scope of this work.

The motor output torque is shown in Fig.5.12 in which torque ripples, with a magnitude that is equal to 66% of the developed torque, were developed upon the occurrence of the short-circuit fault at time, t=1.2 sec. These torque ripples were significantly increased upon the isolation of the faulty phase at time t=1.3 sec. This is due to the unbalance resulting from the two-phase open-Delta mode of operation.

The waveforms of the airgap flux density are depicted in Fig.5.13a for the case of normal operation, Fig.5.13b for the case of short-circuit in the coil BC9 while the three phases are remaining active, and Fig.5.13c for the case of the two-phase open-Delta mode of operation while the coil BC9 is still experiencing a short-circuit. The corresponding three waveforms of the MVP are depicted in Fig.5.14a, Fig.5.14b, and Fig.5.14c for the same cases, respectively. It can be noticed from these figures that the distortion in the airgap flux density and the MVP in the two abnormal conditions is more significant at

lower speed than their counterparts shown earlier for high speed operation in Fig.5.8b and Fig.5.8c of the case study A. This is mainly due to the increase of the voltage drop across the stator impedance at low speed operation compared to high speed operation. This stator voltage drop is not symmetrical in the two active phases as a result of the unbalance in the line currents. Consequently, this leads to a set of unbalanced voltages applied across machine's magnetizing reactance (airgap backemf).

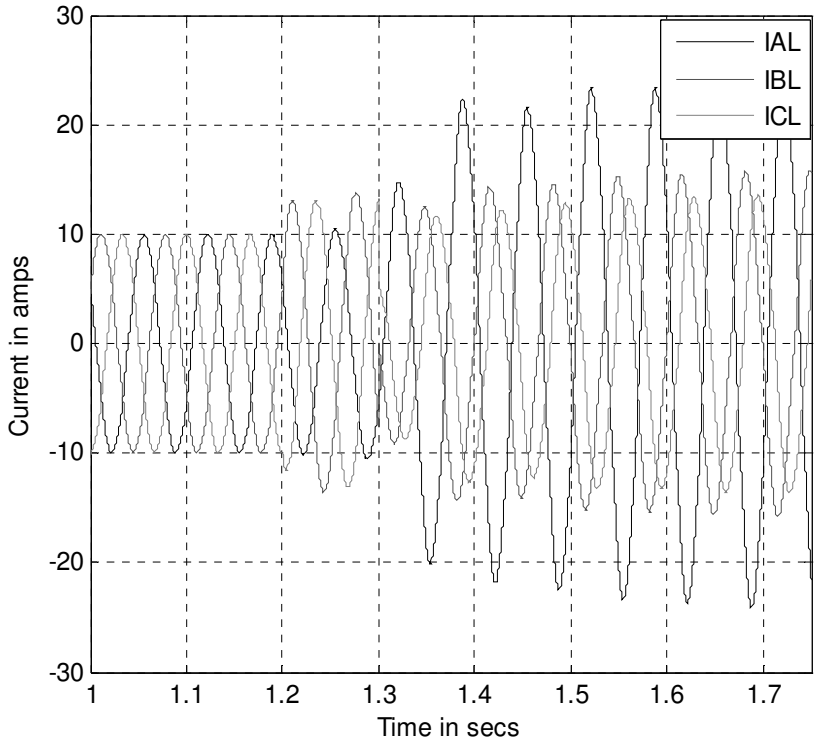

Fig.5.10 Motor line currents, case study B, open-loop mode, coil BC9 shorted at t=1.2sec, faulty phase isolated t=1.3 sec

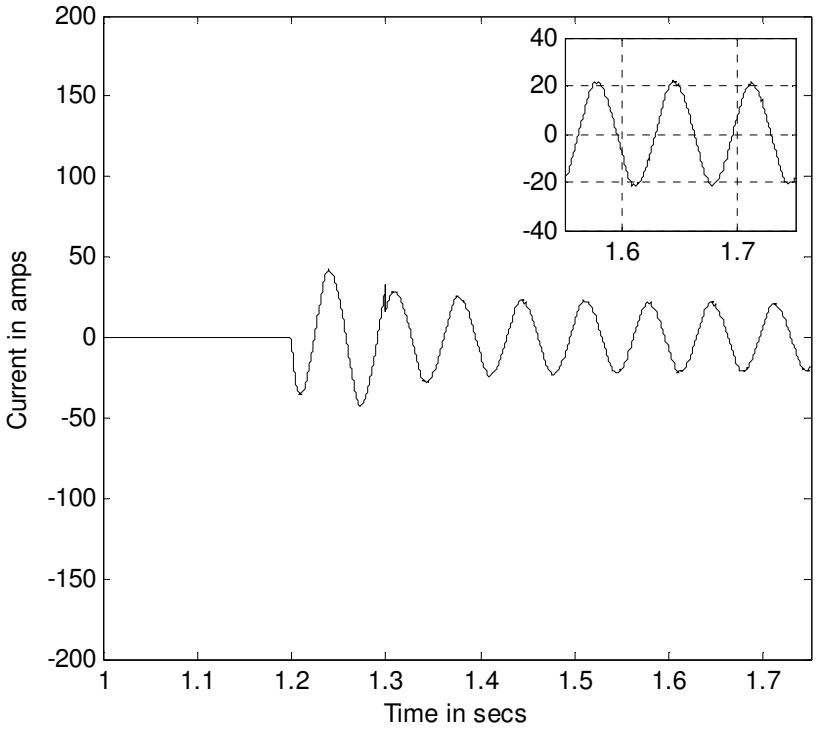

Fig.5.11 The circulating current in the shorted-coil, "coil BC9", case study B, open-loop mode.

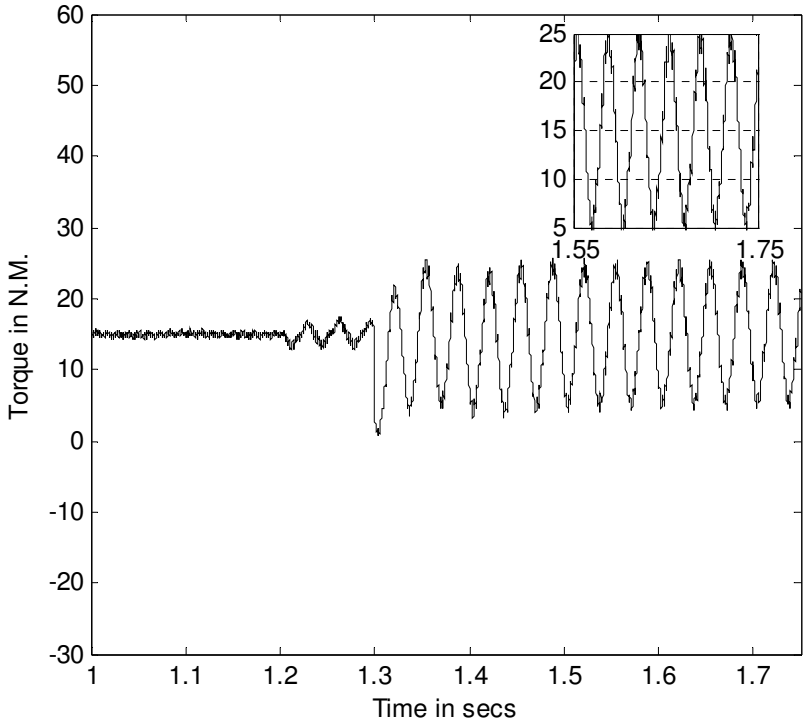

Fig.5.12 Motor's output torque, case study B, open-loop mode, coil BC9 shorted at t=1.2sec, faulty phase isolated t=1.3 sec.

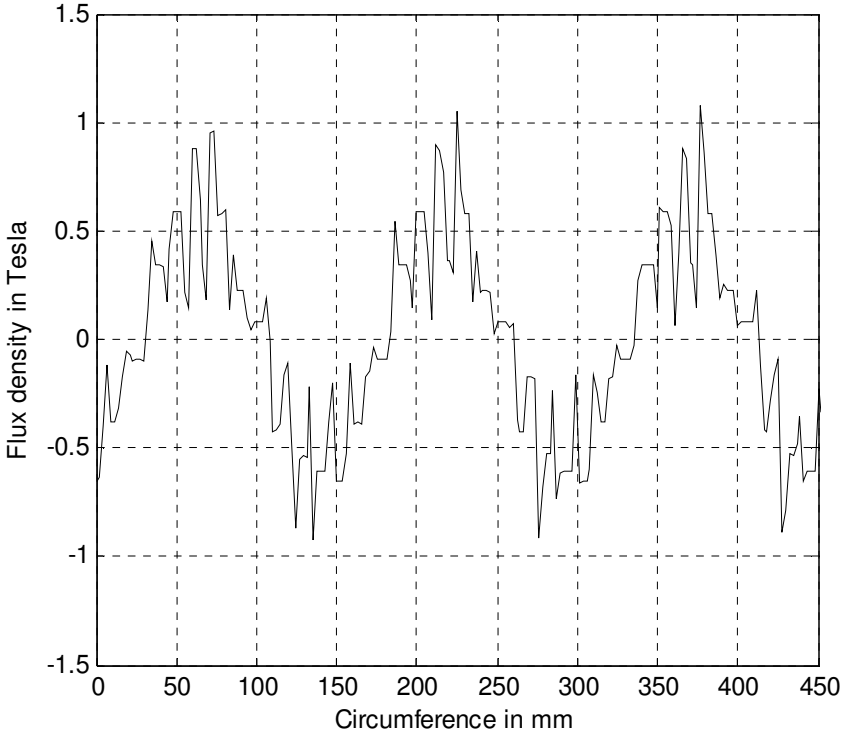

Fig.5.13a Airgap flux density, case study B, open-loop mode, during normal operation.

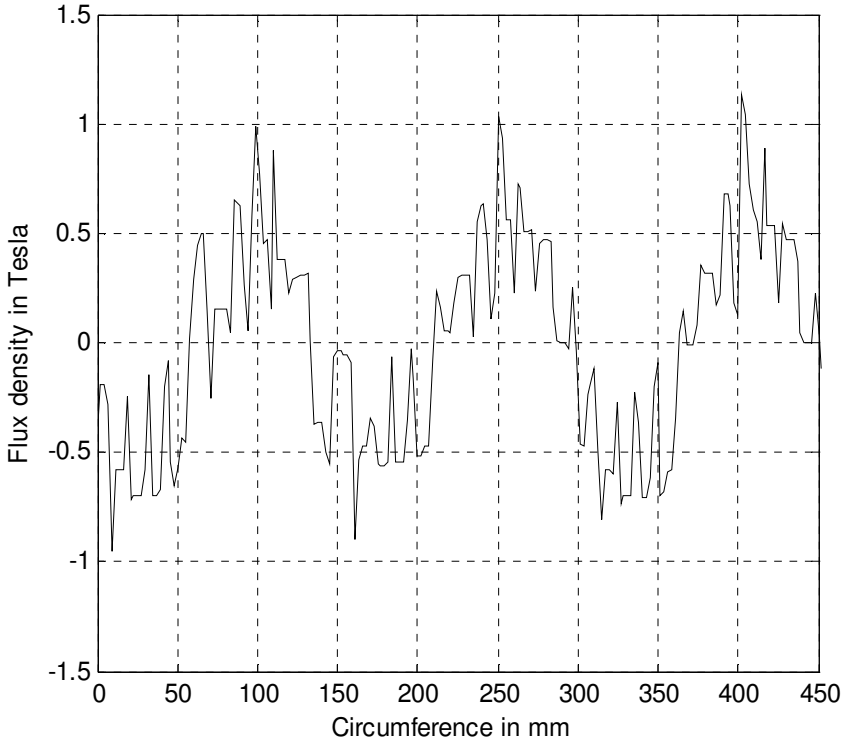

Fig.5.13b Airgap flux density, coil BC9 shorted, case study B, open-loop mode while the faulty phase is still connected to the supply.

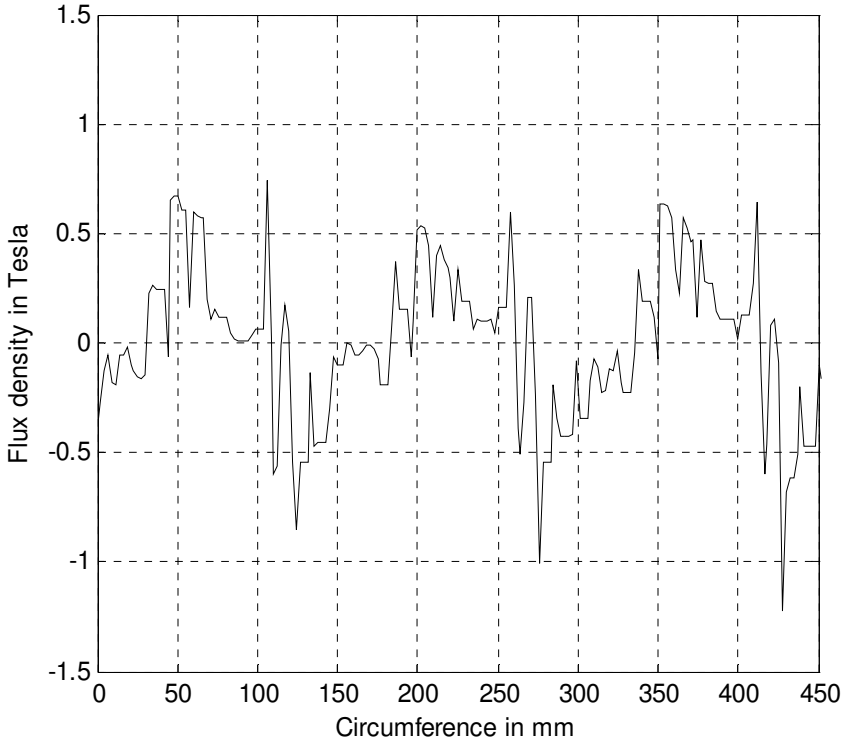

Fig.5.13c Airgap flux density, coil BC9 shorted, open-loop mode, case study B, while the faulty phase is isolated.

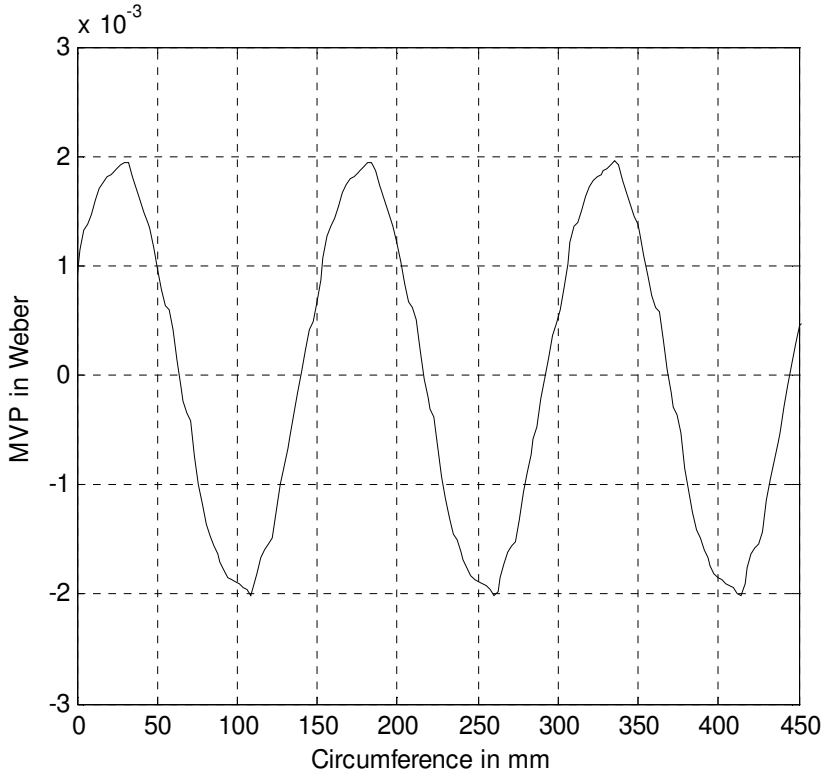

Fig.5.14a Airgap MVP, case study B, open-loop mode, during normal operation

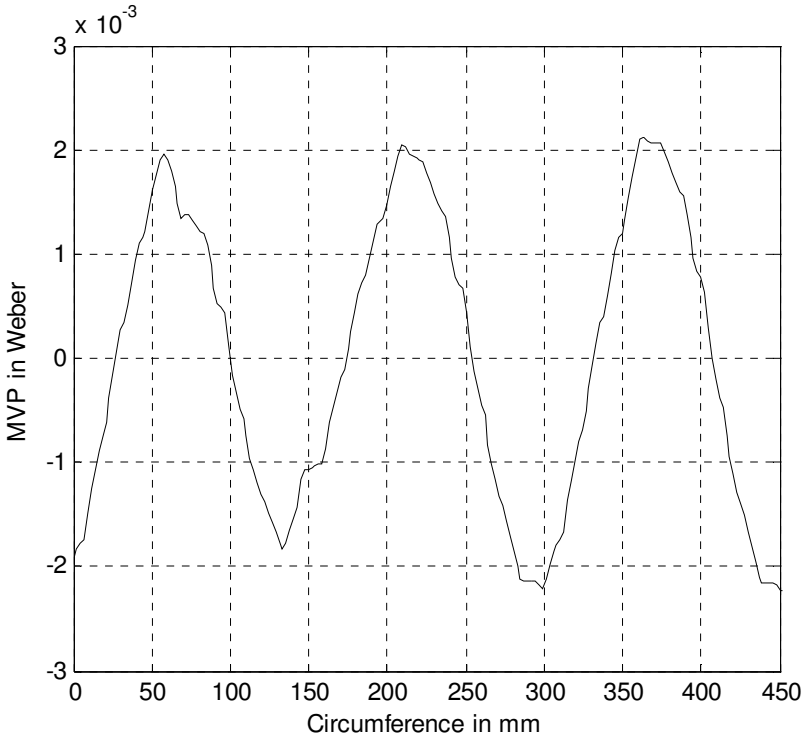

Fig.5.14b Airgap MVP, case study B, open-loop mode, coil BC9 shorted, while the faulty phase is still connected to the supply

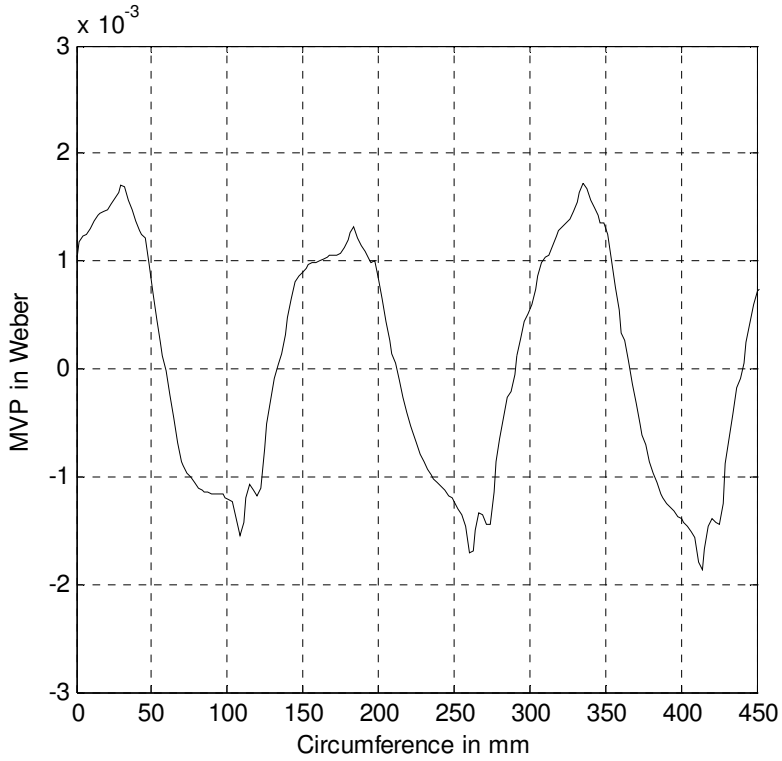

Fig.5.14c Airgap MVP, case study B, open-loop mode, coil BC9 shorted, while the faulty phase is isolated from the supply.

Case study C:

In this case study, the effects of a shorted-coil in the motor's stator phase windings are further investigated while the motor speed was reduced to 15 rad/sec (143 r /min) and the compensation algorithm was deactivated. The terminal voltage was reduced to a value such that the airgap flux density was reduced to half of its rated value. This is in order to minimize the circulating current in the faulty coil. Consequently, the load torque had to be reduced to 7.5 Nm (25% of its rated value) in order to maintain a phase rms current under the motor's rated value.

Inspection of the line current waveforms, depicted in Fig.5.15, shows a slight increase in the line currents upon the occurrence of the fault at time, t=1.25. Therefore, the fault at this operating speed can not be detected by traditional protection methods, and requires an advanced fault detection algorithm such as the techniques proposed in the literature in references [43-62]. In addition, a significant unbalance in the line currents can be noticed upon the isolation of the faulty phase. Meanwhile, it can be noticed that the faulty loop current was limited to the rated phase currents at this operating conditions as shown in Fig.5.16. The time-domain profile of the output torque is shown in Fig.5.17 in which torque ripples of 80% of the average developed output torque can be observed after the isolation of the faulty phase at time, t= 1.3sec.

The waveforms of the airgap flux density are depicted in Fig.5.18a for the case of normal operation, Fig.5.18b for the case of short-circuit in coil BC9 while the three phases are remaining active, and Fig.5.18c for the case of the two-phase open-Delta mode of operation while coil BC9 is still experiencing a short-circuit. It should be pointed out that the distortion is more observable in the two-phase open-Delta mode of operation of

Fig.5.18c.The corresponding waveforms of the MVP are depicted in Fig.5.19a, Fig.5.19b, and Fig.5.19c for the same above mentioned cases, respectively. Again, a significant distortion in the waveforms of the MVP can be noticed in the two-phase open-Delta mode of operation while coil BC9 was shorted.

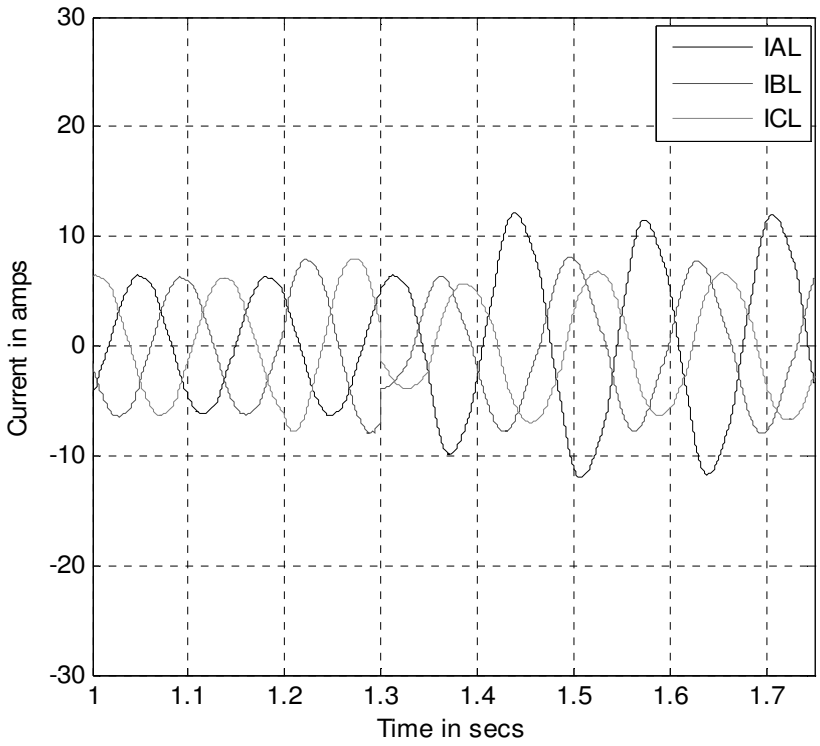

Fig.5.15 Motor line currents, case study C, open-loop mode coil BC9 shorted at t=1.2sec, faulty phase isolated t=1.3 sec

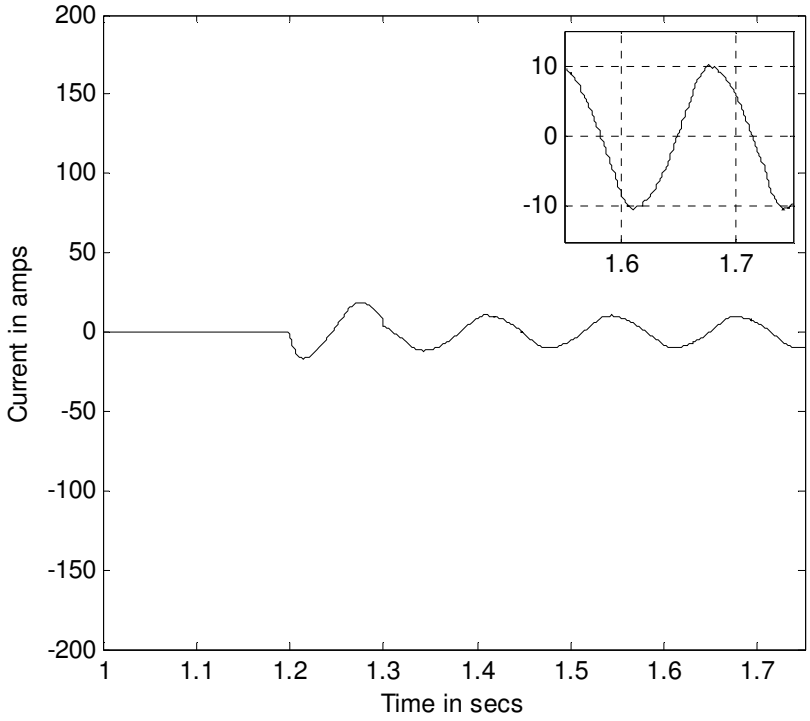

Fig.5.16 The circulation current in the shorted-coil, case study C,open-loop mode, coil BC9 shorted at t=1.2sec, faulty phase isolated t=1.3 sec

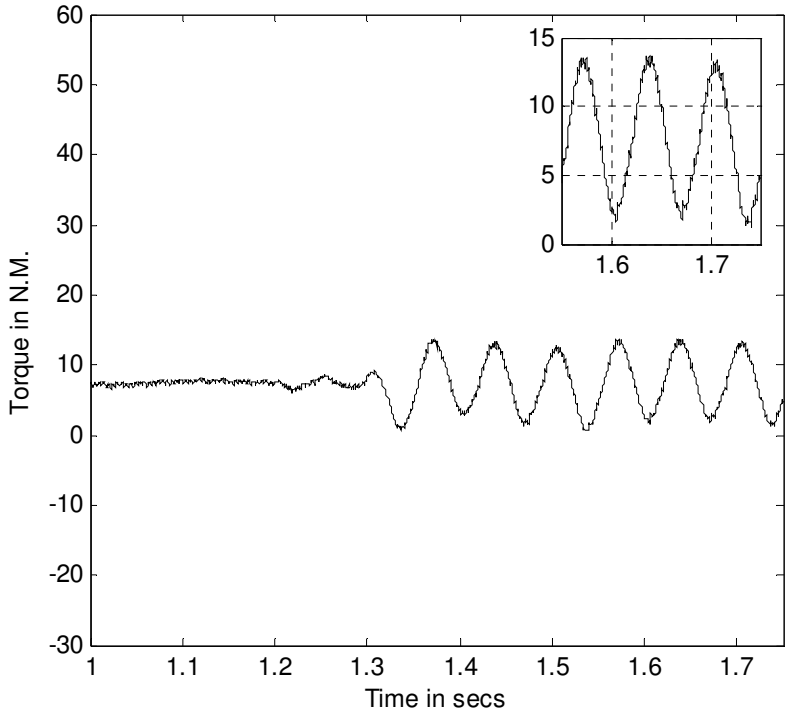

Fig.5.17 Motor's output torque, case study C, open-loop mode, coil BC9 shorted at t=1.2sec, faulty phase isolated t=1.3 sec.

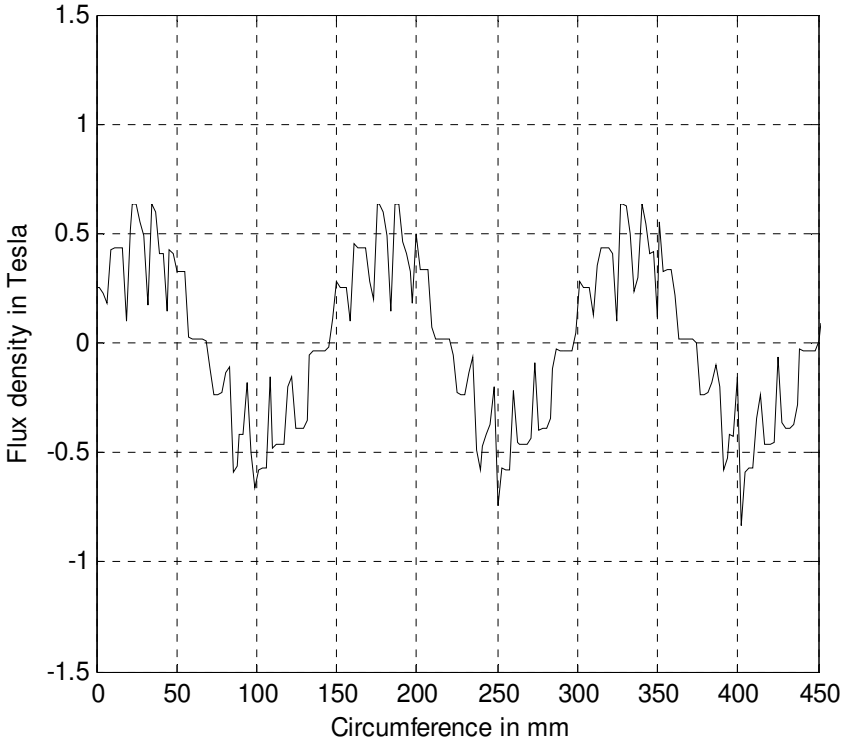

Fig.5.18a Airgap flux density, case study C, open-loop mode, during normal operation.

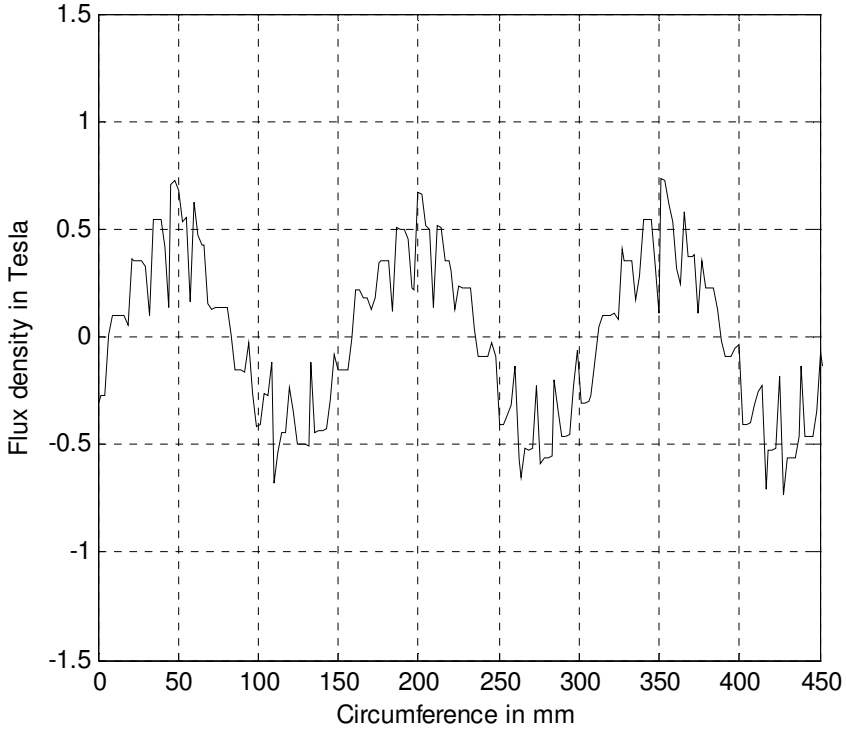

Fig.5.18b Airgap flux density, coil BC9 shorted, case study C, open-loop mode, while the faulty phase is still connected to the supply.

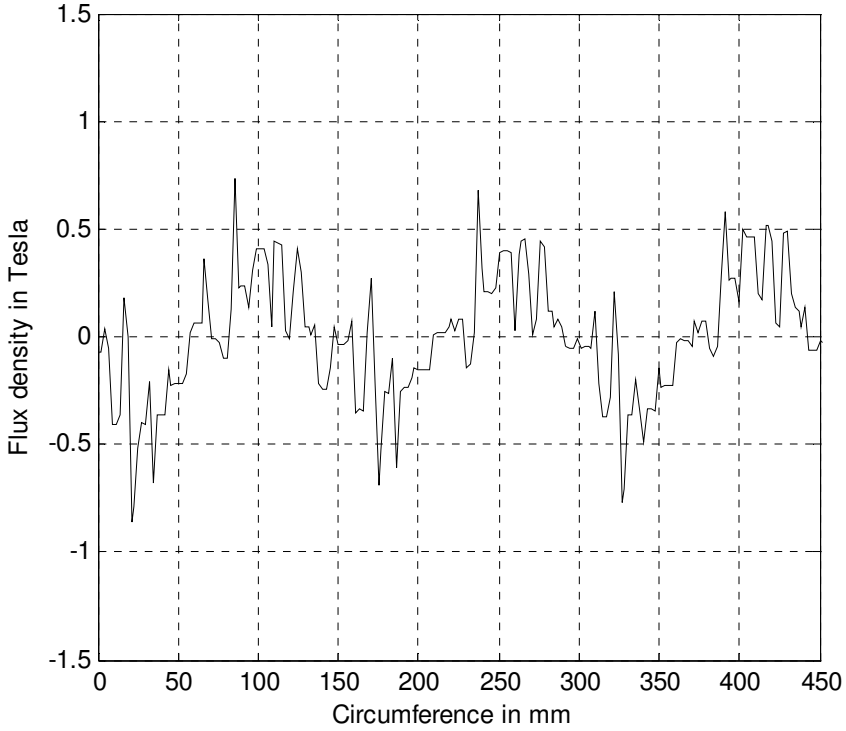

Fig.5.18c Airgap flux density, coil BC9 shorted, case study C, open-loop modewhile the faulty phase is isolated.

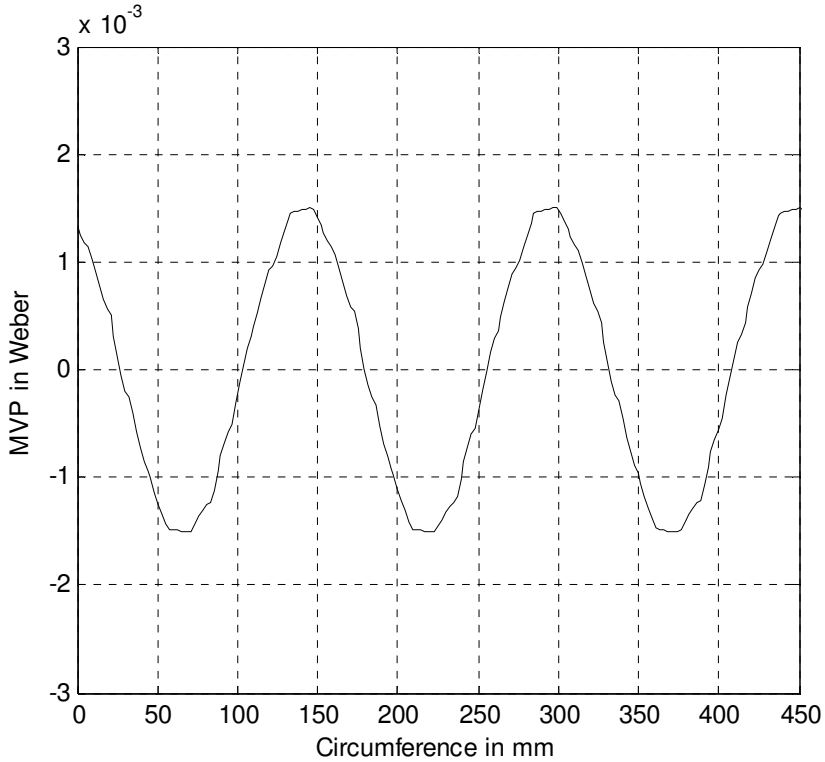

Fig.5.19a Airgap MVP, case study C, open-loop mode, during normal operation.

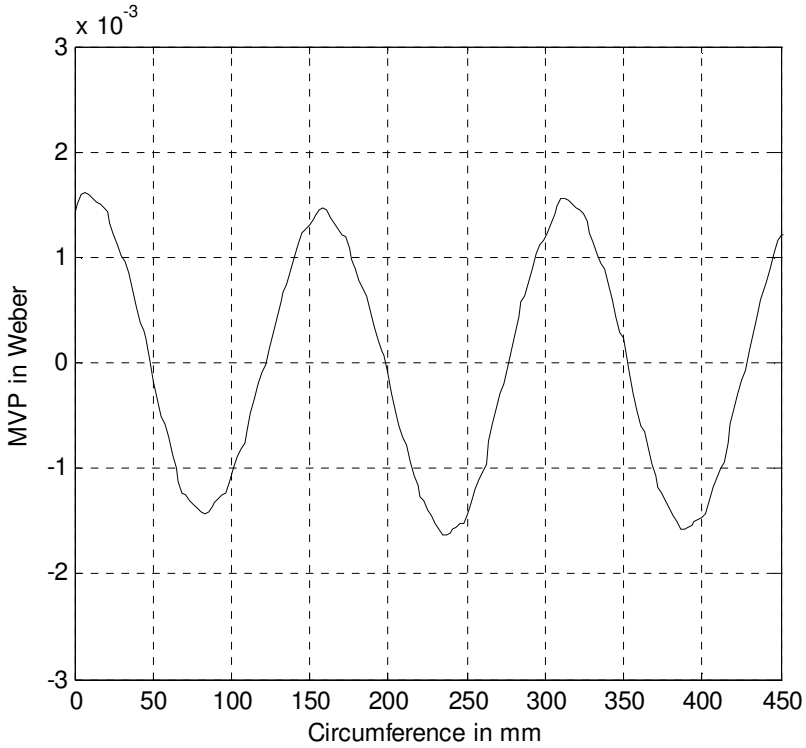

Fig.5.19b Airgap MVP, case study C, open-loop mode, coil BC9 shorted, while the faulty phase is still connected to the supply

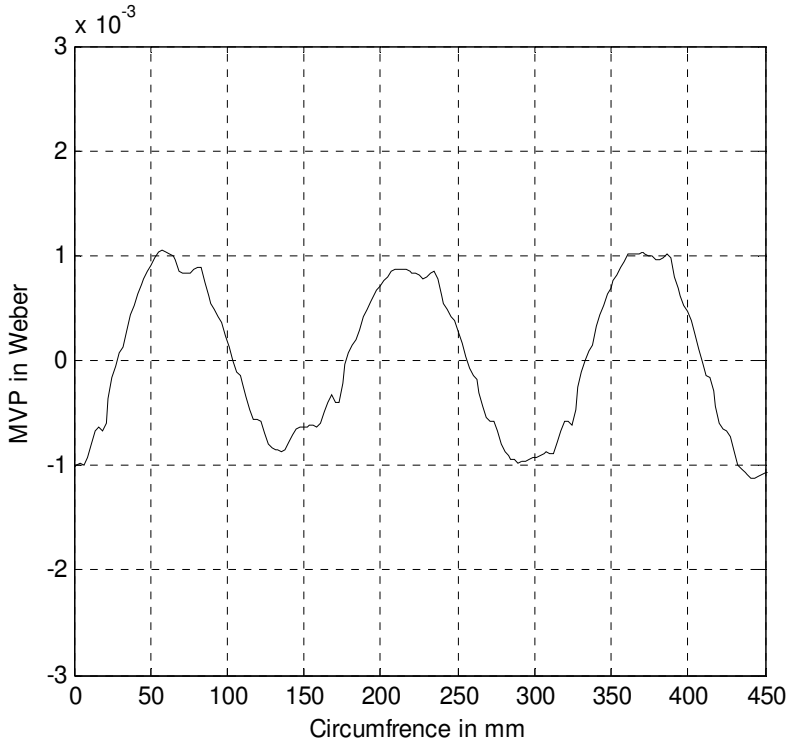

Fig.5.19c Airgap MVP, case study C, open-loop mode, coil BC9 shorted, while the faulty phase is isolated from the supply.

Case study D:

In this case study, the effect of activating the introduced compensation algorithm on the circulating faulty loop current and torque pulsations is investigated. Consequently, the operating conditions for case study C were not altered here. Again, coil BC9 was shorted at time, t=0.75 sec, while the faulty phase was isolated at time, t=0.8sec. Again, the motor line currents, the circulating faulty loop current, motor's output torque, airgap flux density, and magnetic vector potential waveforms are reported for examination of the system's performance.

The motor line currents are shown in Fig.5.20. It can be noticed that the compensation algorithm was able to significantly reduce the unbalance in the motor's line currents. Here, the currents in Fig.5.15 should be compared with those in Fig.5.20 to observe the degree of "effectiveness" of the compensation algorithm in balancing the motor line currents. This demonstrates the efficacy of the introduced compensation algorithm in mitigating the unbalance in the motor line currents for the case of a two-phase open-Delta mode of operation. The faulty loop current is shown in Fig.5.21. It can be noticed that the circulating faulty loop current has a magnitude which equals 120% of the full load rated phase current of the machine. The increase in the faulty loop current compared to its value in case study C can be attributed to the increase in the airgap densities and flux as a result of the effect of the compensation algorithm on the motor's operating flux.

The time-domain profile of the output torque is shown in Fig.5.22, in which a reduction in the magnitude of the torque ripples can be observed after the isolation of the faulty phase at time, t=0.8 sec. In this case the magnitude of these torque ripples is 44%

of the average developed torque. This is in comparison to a magnitude of 80% torque ripples in case study C, see Fig.5.17. These torque ripples are mainly originated by the torque pulsations produced by the faulty loop current in the faulted coil.

The waveforms of the airgap flux density are depicted in Fig.5.23a for the case of normal operation, in Fig.5.23b for the case of a short-circuit in coil BC9 while the three phases are remaining active, and in Fig.5.23c for the case of the two-phase open-Delta mode of operation while coil BC9 is still experiencing a short-circuit. The corresponding waveforms of the airgap MVP are depicted in Fig.5.24a, Fig.5.24b, and Fig.5.24c for the same above mentioned cases, respectively. An increase in the magnitudes of the airgap flux density waveforms and the MVP waveforms can be noticed in this case study D with an activated controller, in comparison to the corresponding airgap flux density waveforms of Fig.5.18a, Fig.5.18b and Fig.5.18c and MVP waveforms of Fig.5.19a, Fig.5.19b, and Fig.5.19c of case study C with a deactivated controller. This difference is mainly due to the compensation action of the introduced controller that resulted in rendering a set of nearly balanced line currents for the case of a two-phase open-Delta mode of operation.

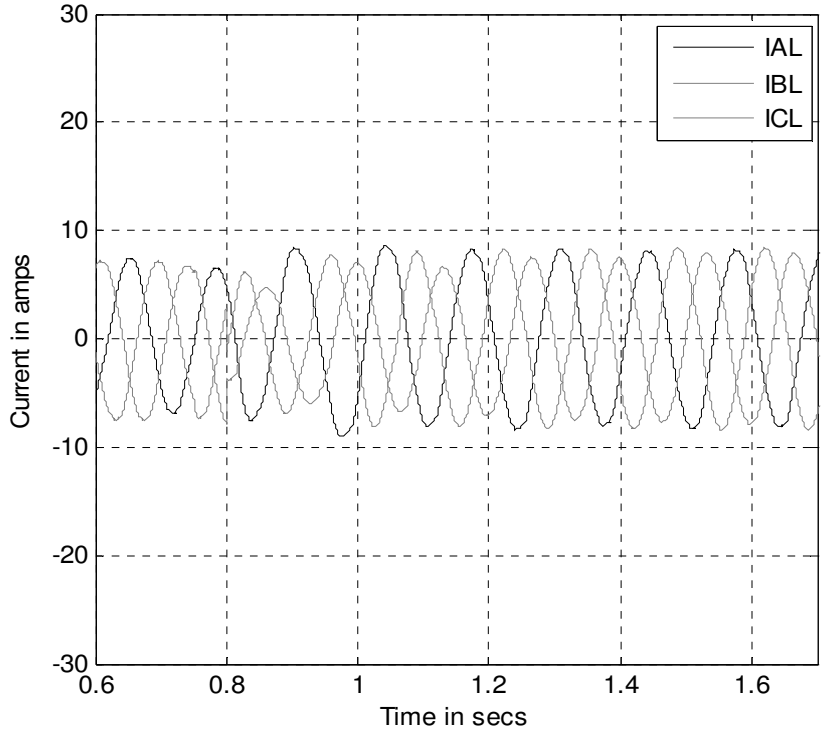

Fig.5.20 Motor line currents, case study D, open-loop mode, coil BC9 shorted at t=0.75 sec, faulty phase isolated t=0.8 sec

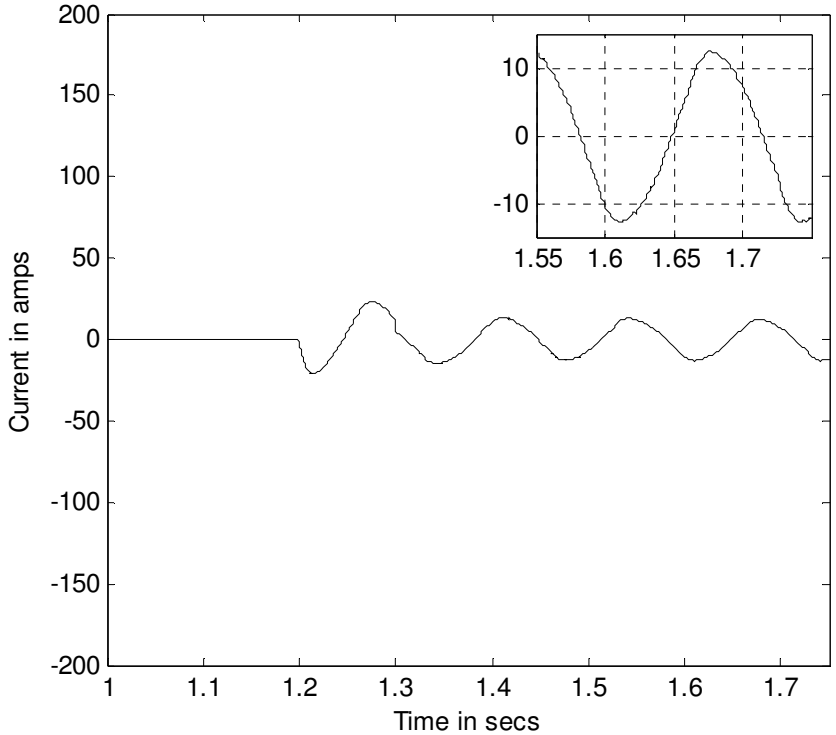

Fig.5.21 The circulating current in the shorted-coil, “coil BC9”, case study D, open-loop mode.

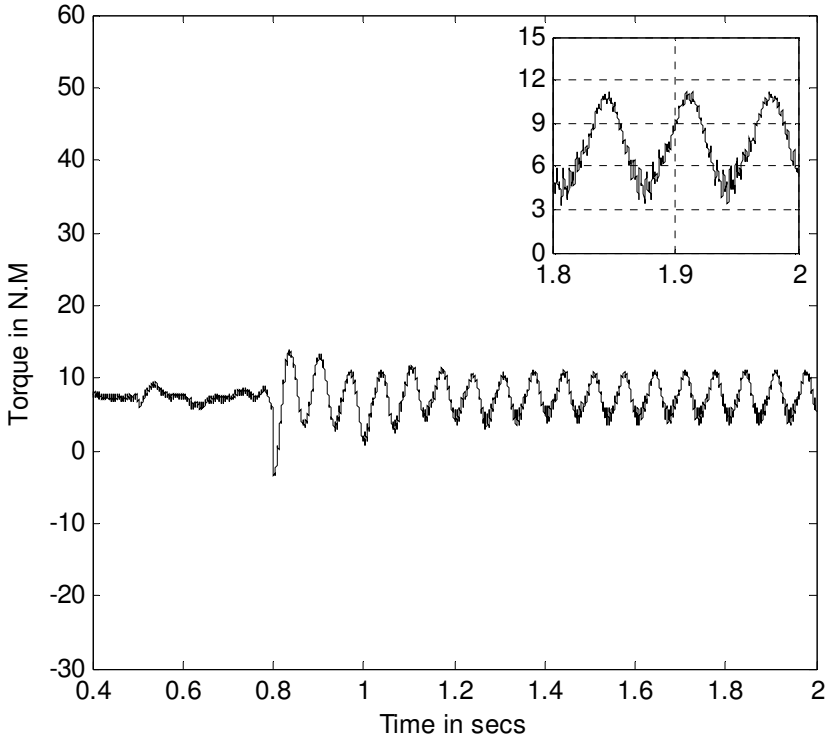

Fig.5.22 Motor's output torque, case study D, open-loop mode, coil BC9 shorted at t=0.75sec, faulty phase isolated t=0.8 sec.

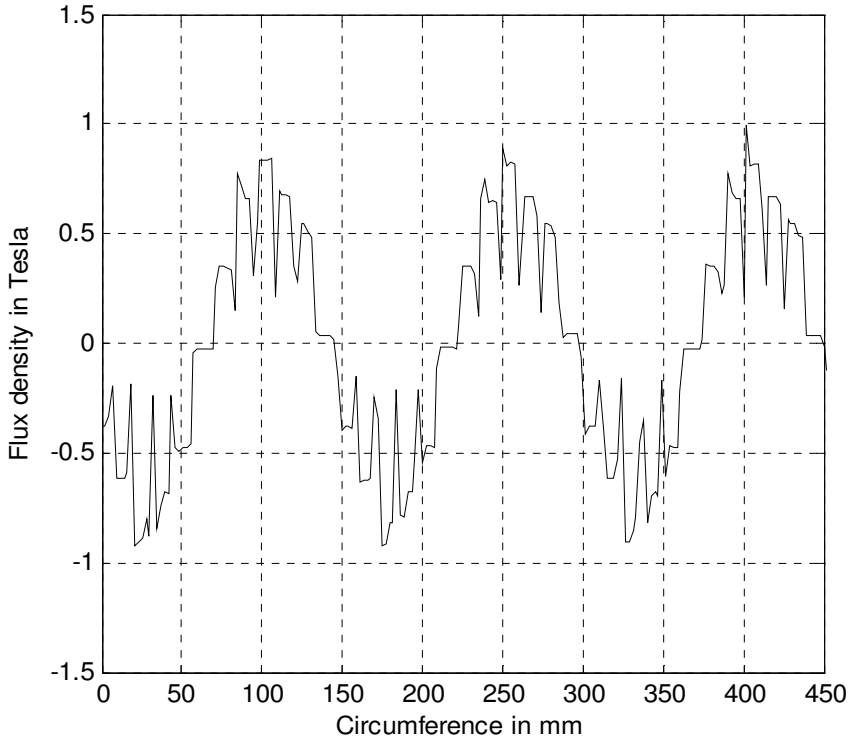

Fig.5.23a Airgap flux density, case study D, open-loop mode, during normal operation.

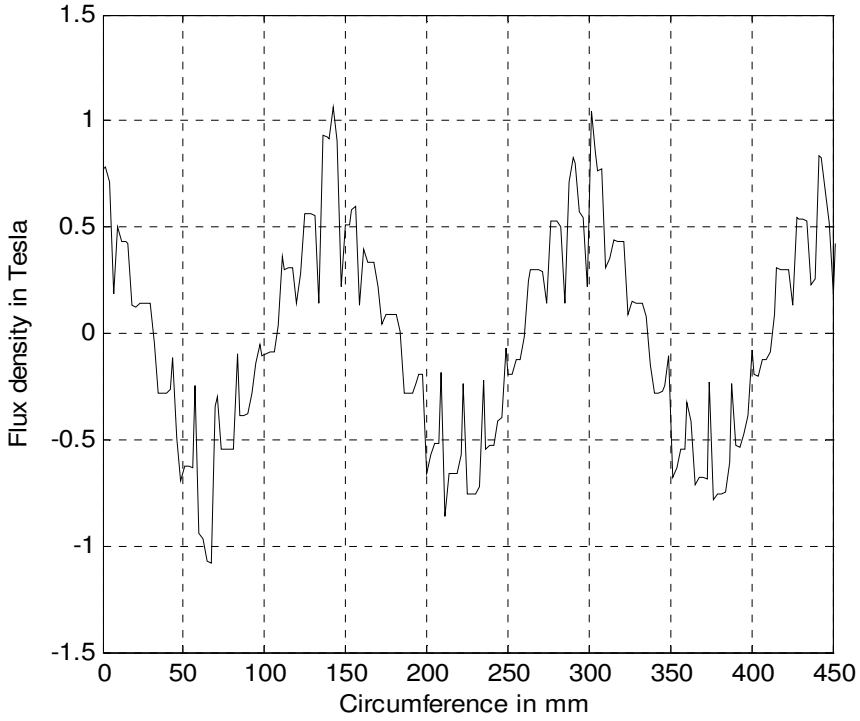

Fig.5.23b Airgap flux density, coil BC9 shorted, case study D, open-loop mode, while the faulty phase is still connected to the supply.

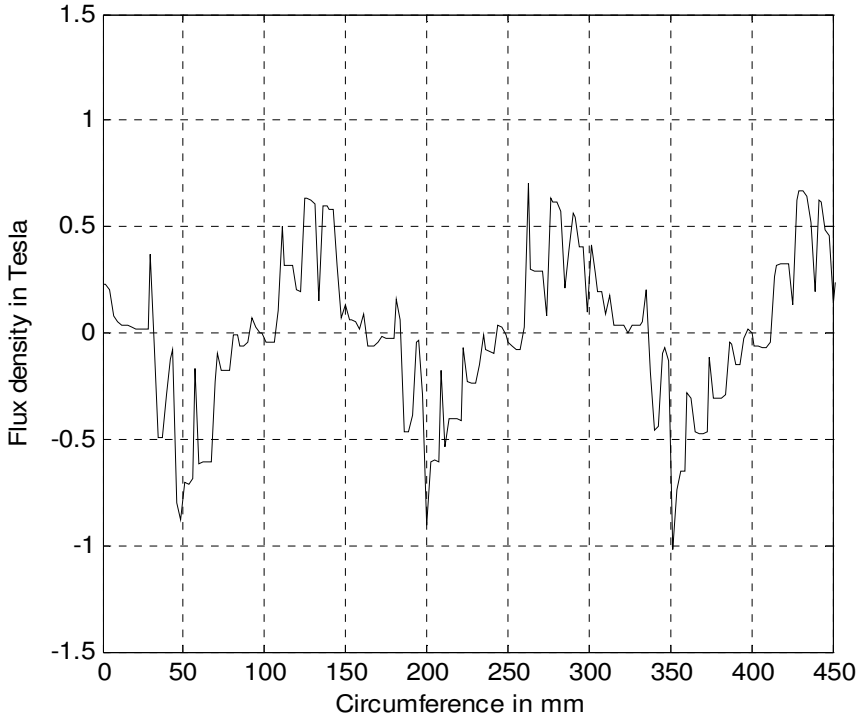

Fig.5.23c Airgap flux density, coil BC9 shorted, case study D, open-loop mode, while the faulty phase is isolated.

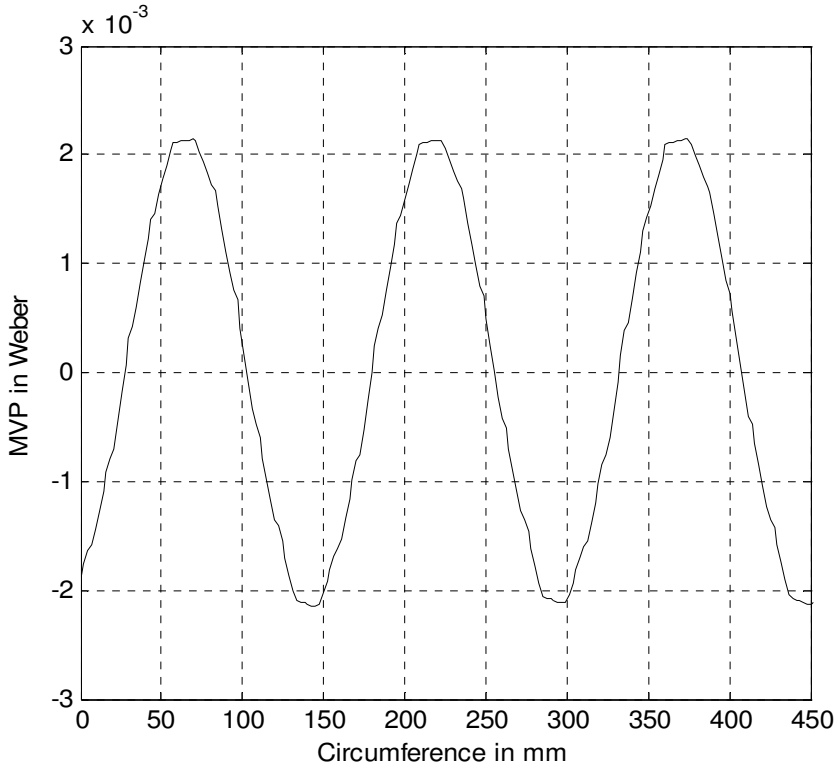

Fig.5.24a Airgap MVP, case study D, open-loop mode, during normal operation.

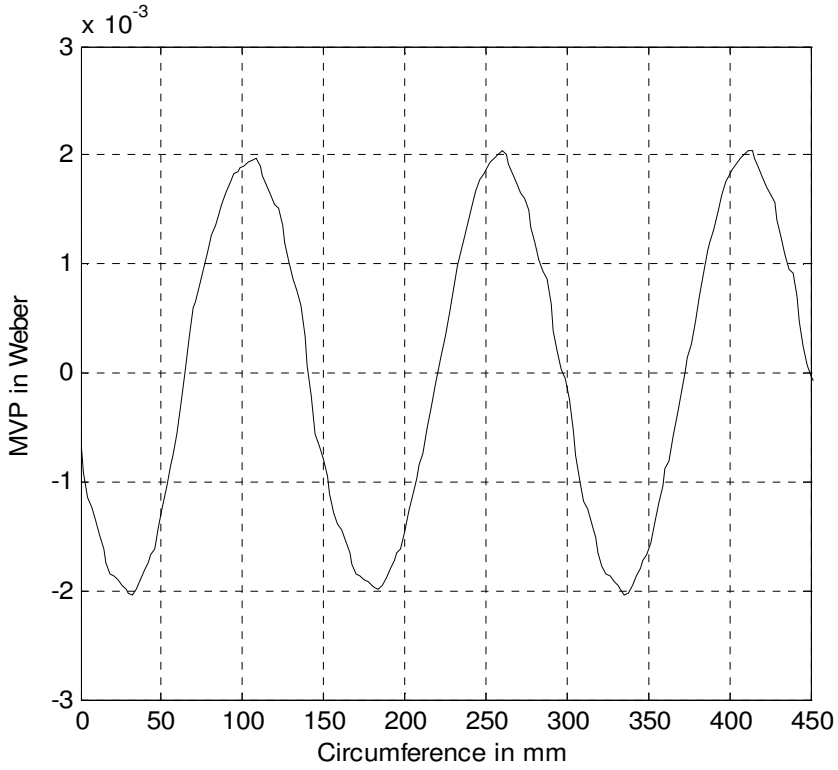

Fig.5.24b Airgap MVP, case study D, open-loop mode, coil BC9 shorted, while the faulty phase is still connected to the supply

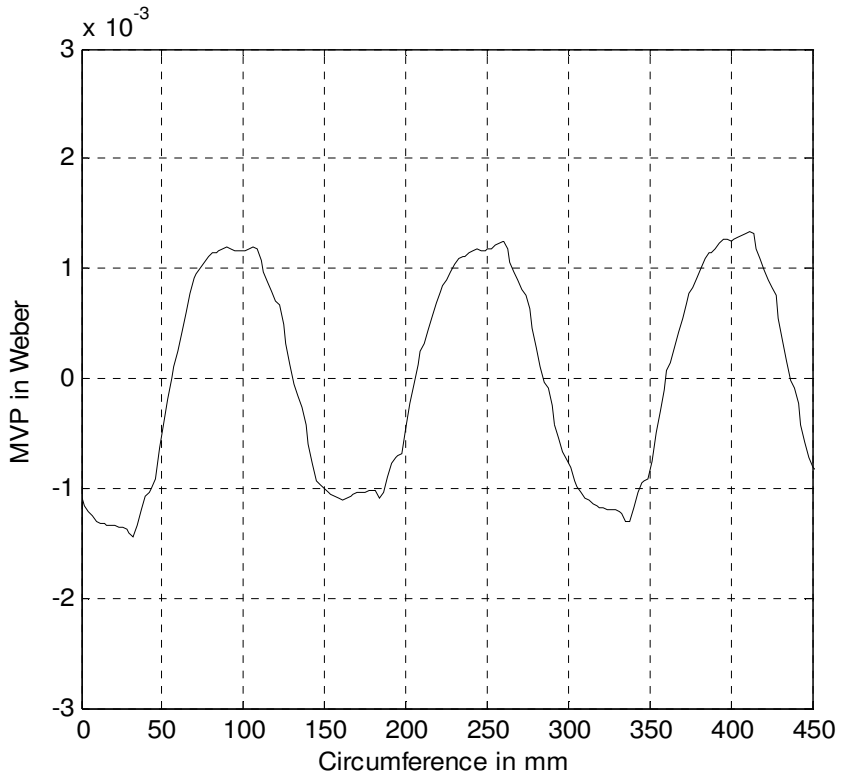

Fig.5.24c Airgap MVP, case study D, open-loop mode, coil BC9 shorted while the faulty phase is isolated from the supply.

Case study E:

In this case study, the system's transient performance was examined after detecting a solid short-circuit fault across coil BC9 when the compensation controller is activated. It should be mentioned that the inter-turn fault conditions may be detected at an earlier stage of the fault. It was claimed in reference [56] that an inter-turn shot-circuit condition may be detected when the faulty loop current, current in R4 in this FE model, exceeds the rated current of the machine. However, as mentioned earlier, the analysis performed in this chapter considers an advanced stage of the fault in which the faulty coil, BC9 in the FE model, is solidly shorted and hence the faulty loop current is only limited by the resistance and the leakage reactance of the shorted-coil.

In this case study “E”, one considers a scenario in which the motor was running at rated full load condition, rated speed and rated torque, while an inter-turn short-circuit fault occurred at a time instant ,t= 0.55 sec. Upon the detection of the fault, the motor speed was reduced to 15 rad/sec “143 r/min”, in order to limit the faulty loop current, and the load torque was reduced to 7.5 Nm Meanwhile, the faulty loop was electrically isolated at a time instant, t=0.75 sec.

The waveforms of the three phase line currents are shown in Fig.5.25. Upon the occurrence of the fault, a significant increase in the magnitude of these line currents can be observed at time, t=0.55. The magnitudes of these line currents were further increased at time instant, t=0.65 sec. The later is a temporary increase that is not related to the fault, and is mainly due to the braking action of the drive in order to reduce the motor speed and consequently limit the faulty loop current. Upon reaching steady-state, it can be observed that the line currents are nearly balanced. This is due to the compensation action of the activated controller as discussed earlier in case study D.

Meanwhile, the waveform of the faulty loop current is depicted in Fig.5.26. Upon the occurrence of the fault at time, t=0.55 sec, a significant increase in the magnitude of this current can be observed. It can be observed that the current was almost 15 times that of the rated value. This current was almost reduced to 1.3 times of its rated value as a result of the fault mitigation control action taken by the drive that included significant reduction in the motor speed and the airgap flux. In this case, the permissible duration of operation is mainly limited by the thermal capability of the motor.

The motor output torque is also depicted in Fig. 5.27. Examining this torque shows the existence of torque ripples with a magnitude that is equal to 46% of the

average developed torque. Again, the existence of these torque ripples is mainly due to the magnetic field pulsations resulting from the circulation of the faulty loop current in the shorted-coil.

The waveforms of the airgap flux density are depicted in Fig.5.28a for the case of normal operation, in Fig.5.28b for the case of short-circuit in coil BC9 while the three phases are remaining active, and in Fig.5.28c for the case of the two-phase open-Delta mode of operation while coil BC9 is still experiencing a short-circuit. The corresponding waveforms of the MVP for the above mentioned operating condition are shown in Fig.5.29a, Fig.5.29b, and Fig.5.29c, respectively. A distortion in the waveforms of the airgap flux density and MVP as a result of the magnetic disturbance produced by the circulating faulty loop current in the shorted-coil can be observed in Fig 5.28b and Fig.5.29b. Meanwhile, the distortion in the airgap flux density and the MVP waveforms resulting from the two-phase open-Delta mode of operation including the effect of circulating current in the faulty loop are depicted in Fig.5.28c, and Fig.5.29c, respectively.

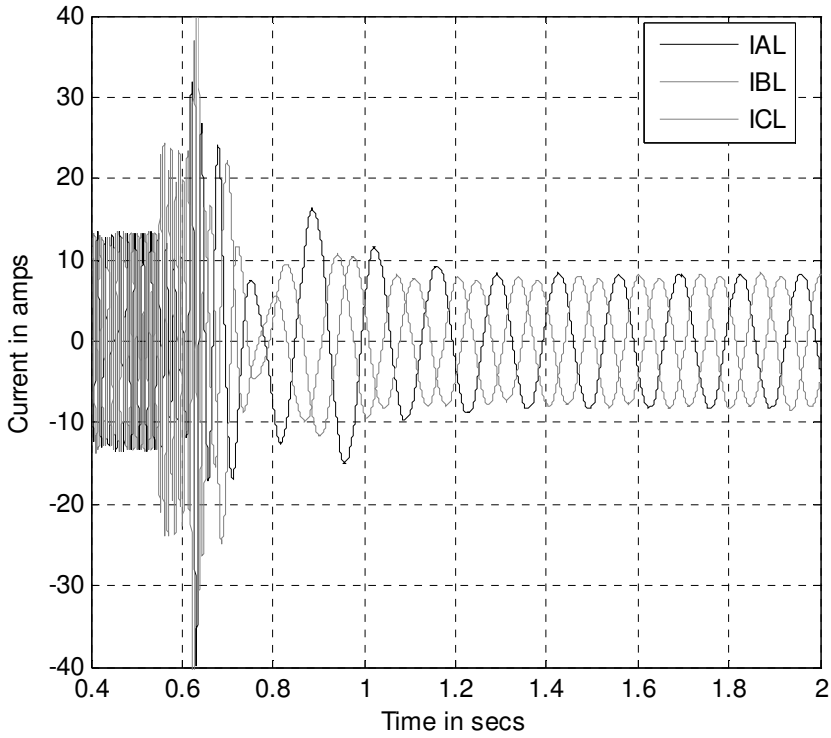

Fig.5.25 Motor line currents, case study E, open-loop mode, coil BC9 shorted at t=0.55sec, faulty phase isolated t=0.75sec.

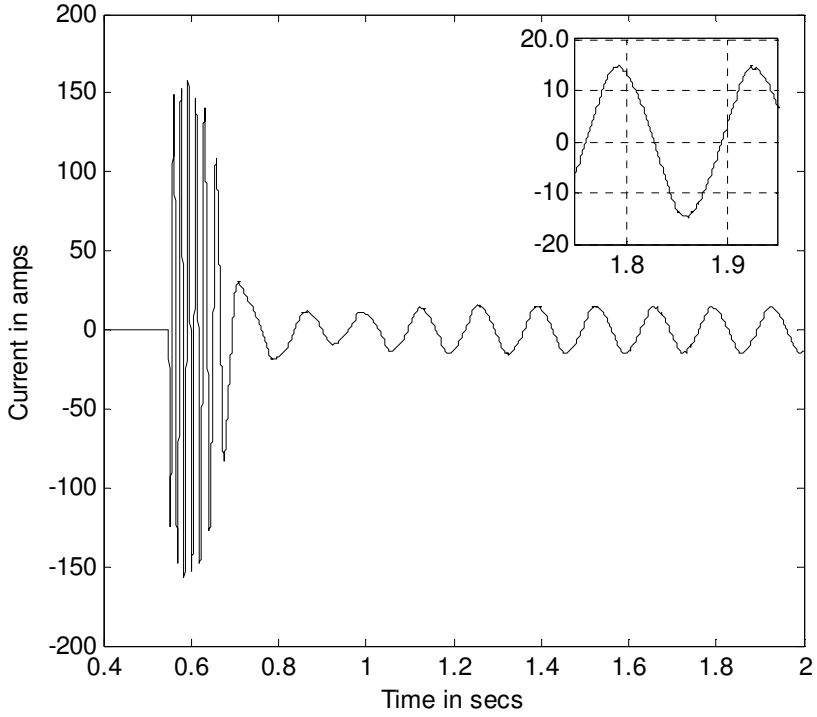

Fig.5.26 The circulating current in the shorted-coil, “coil BC9”, case study E, open-loop mode.

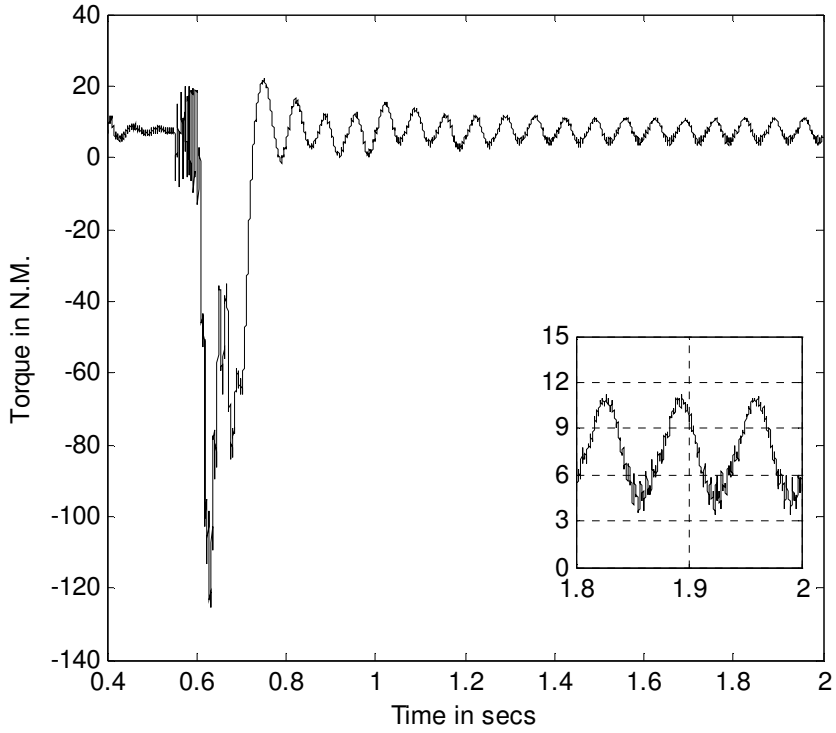

Fig.5.27 Motor's output torque, case study E, open-loop mode, coil BC9 shorted at t=0.55sec, faulty phase isolated t=0.75sec.

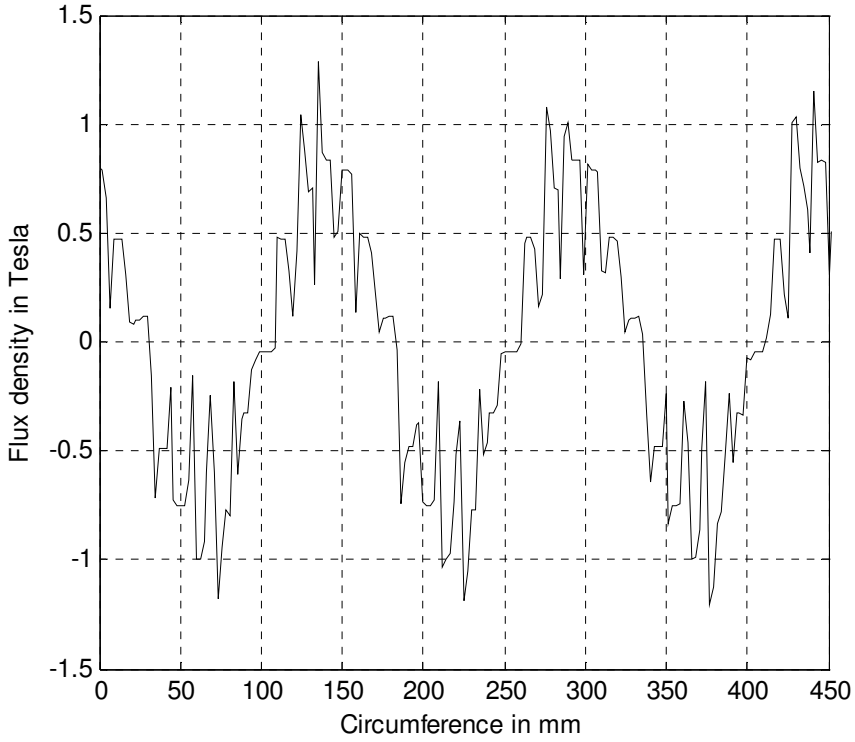

Fig.5.28a Airgap flux density, case study E, open-loop mode, during normal operation

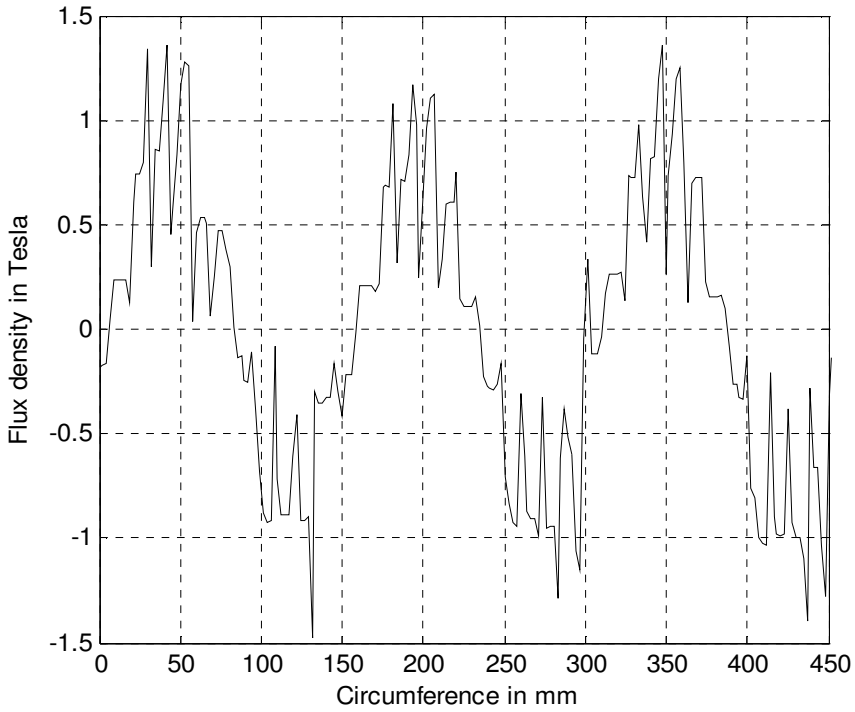

Fig.5.28b Airgap flux density, coil BC9 shorted, case study E, open-loop mode, while the faulty phase is still connected to the supply.

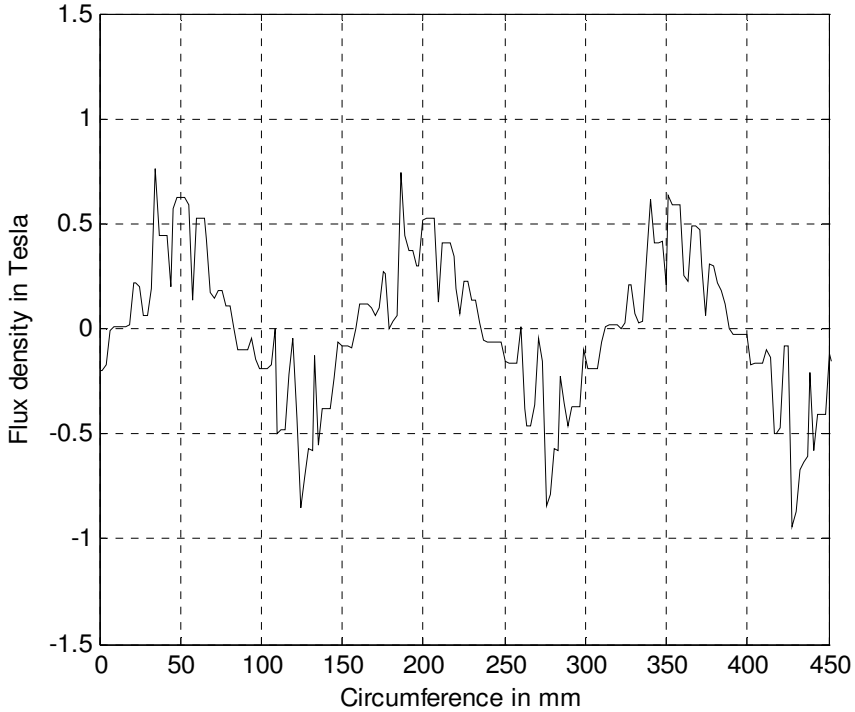

Fig.5.28c Airgap flux density, coil BC9 shorted, case study E, open-loop mode, while the faulty phase is isolated.

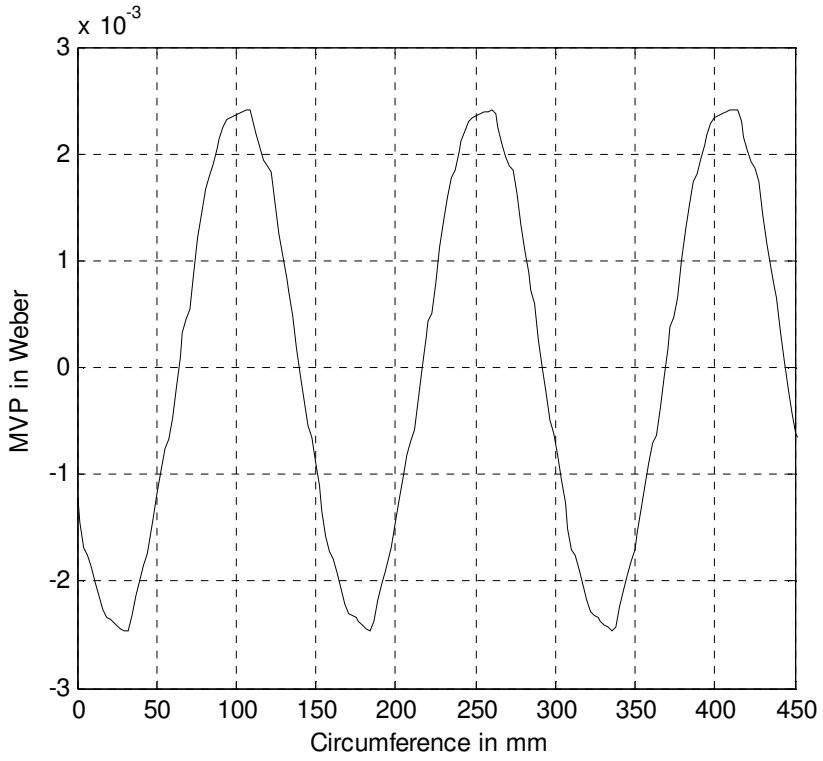

Fig.5.29a Airgap MVP, case study E, open-loop mode, during normal operation

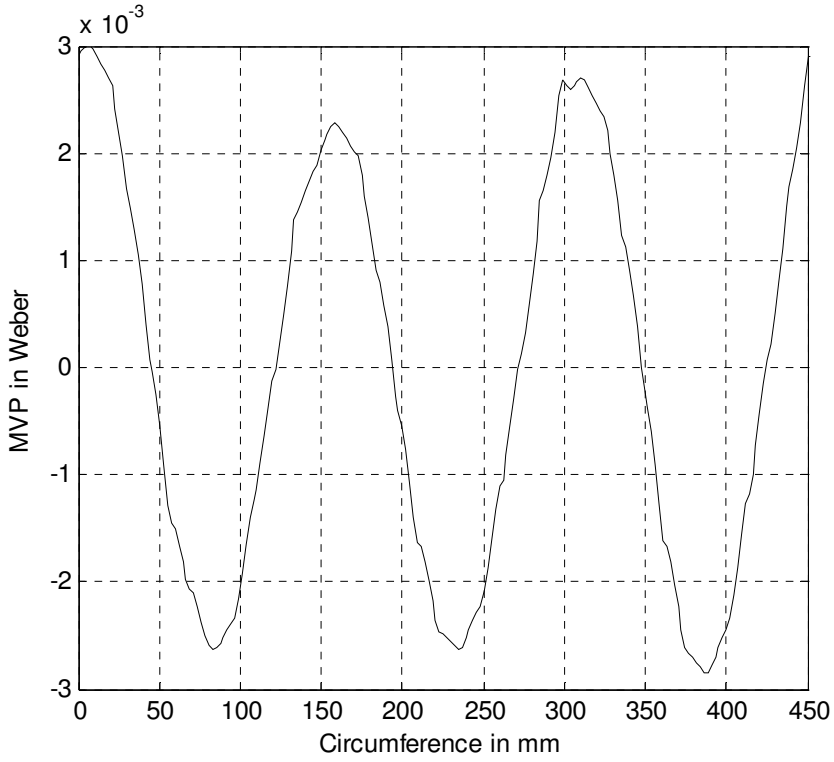

Fig.5.29b Airgap MVP, case study E, open-loop mode, coil BC9 shorted, while the faulty phase is connected to the supply

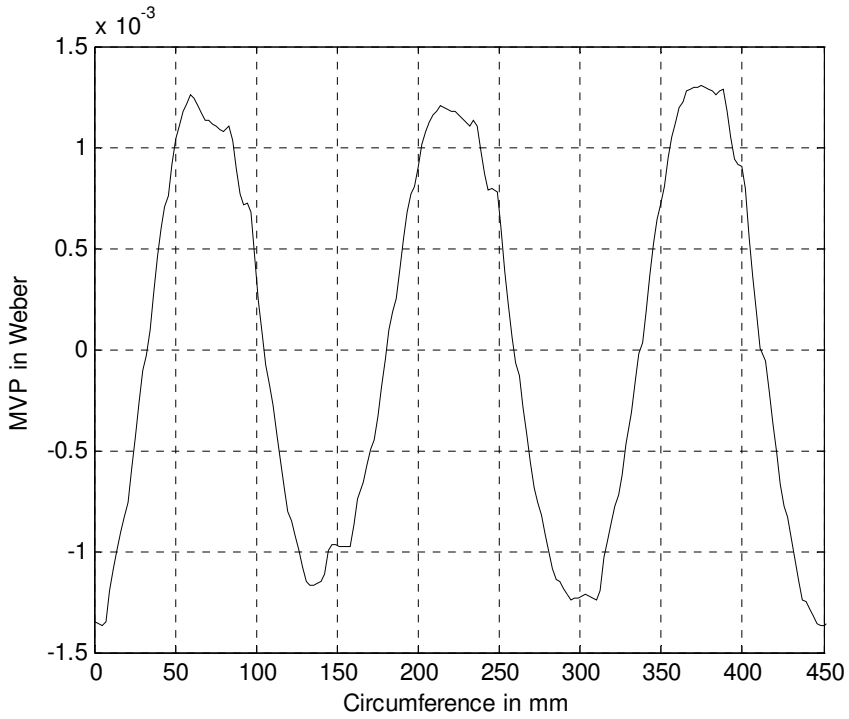

Fig.5.29c Airgap MVP, case study E, open-loop mode, coil BC9 shorted, while the faulty phase is isolated from the supply.

5.3.2.2 Vector-control motor-drive systems

Case study A:

The first case study considered in this section is a vector-controlled closed-loop motor-drive system in which the fault compensation controller introduced earlier in Chapter 4 was deactivated. It was assumed that short-circuit occurred in one of the coils, coil BC9 shown in Fig.5.4, at time, t=0.4 sec and the complete phase was isolated at time, t= 0.5 sec. The motor's flux and the motor speed were kept constant before and after the occurrence of the fault. The motor load was set to 50% of its rated value in order to avoid any damage to the machine as a result of potential overloading condition at this mode of operation.

The monitored variables are the line currents, the circulating current in the faulty coil, the airgap flux density waveforms, the airgap Magnetic Vector Potential "MVP" waveforms, and the motor's torque.

The motor line current waveforms are depicted in Fig.5.30. A sudden increase in the line currents can be observed at the instant of the occurrence of a solid short-circuit in coil BC9 at time, t=0.4sec. The faulty phase is assumed to have been isolated at time, t=0.5sec. Meanwhile, the waveform of the current in the shorted-coil is depicted in Fig.5.31. It can be noticed that the magnitude of the fault's circulating current in the faulted coil is equal to almost thirteen times the magnitude of the normal phase current at healthy conditions, in a real event of this level the phase winding will not survive. However, these simulations were carried out to demonstrate the consequences of such an event. A significant decrease in this current can be also observed as soon as the faulty phase was electrically isolated. However, even after electrically isolating the shorted-phase, the magnitude of the current in the shorted-coil is still very large "six to seven times the normal value of the phase current". Again, the thermal stresses associated with such high current values may produce potential failure in the machine.

The corresponding motor output torque is depicted in Fig.5.32, in which a sudden increase in this torque can be observed at the instant of the coil failure, at time, t=0.4 sec. This can be related to the sudden increase in the motor line currents as a result of the drive controller's transient response in an attempt to regulate the motor's torque and airgap flux. This is followed by significant torque pulsations with a magnitude of 80% of the average developed torque which can still be observed after the isolation of the faulty phase. These torque pulsations are produced due to the magnetic field unbalance resulting

from the two-phase open-Delta operation of the machine, and the consequent pulsating magnetic field produced by the circulating current in the faulty coil as explained earlier in this chapter. Comparing the output torque profile for this case with its counterpart in the open-loop control mode, see Fig.5.7, shows that the current controller in the vector-controlled mode has suppressed these torque pulsations from 400% for the case of the open-loop mode to 80% for the case of vector-controlled mode.

The waveforms of the airgap flux density are depicted in Fig.5.33a for the case of normal operation, in Fig.5.33b for the case of short-circuit in coil BC9 while the three phases are remaining active, and in Fig.5.33c for the case of the two-phase open-Delta mode of operation while coil BC9 is still experiencing a short-circuit. A significant distortion in the airgap flux density waveforms can be observed for the case of short-circuit in coil "BC9" when the faulty phase is connected to the inverter, and when the faulty phase is electrically isolated. The corresponding waveforms of the MVP for the three above operating conditions are depicted in Fig.5.34a, Fig.5.34b, and Fig.5.34c, respectively. The distortions in the airgap flux density and MVP waveforms are resulting from the drive's controller compensation action, in an attempt to suppress these torque pulsations and mitigate the unbalance in the line currents, by outputting a set of unbalanced voltages that manifest themselves as distortions in the airgap flux density waveforms.

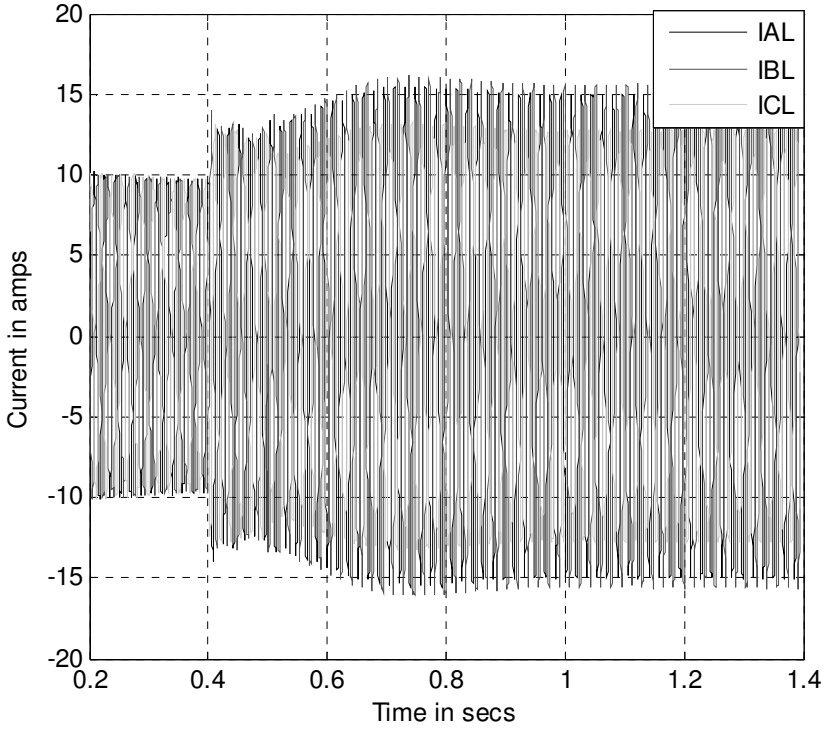

Fig.5.30 Motor line currents, case study A, vector-control mode, coil BC9 shorted at t=0.4sec, faulty phase isolated at t=0.5sec.

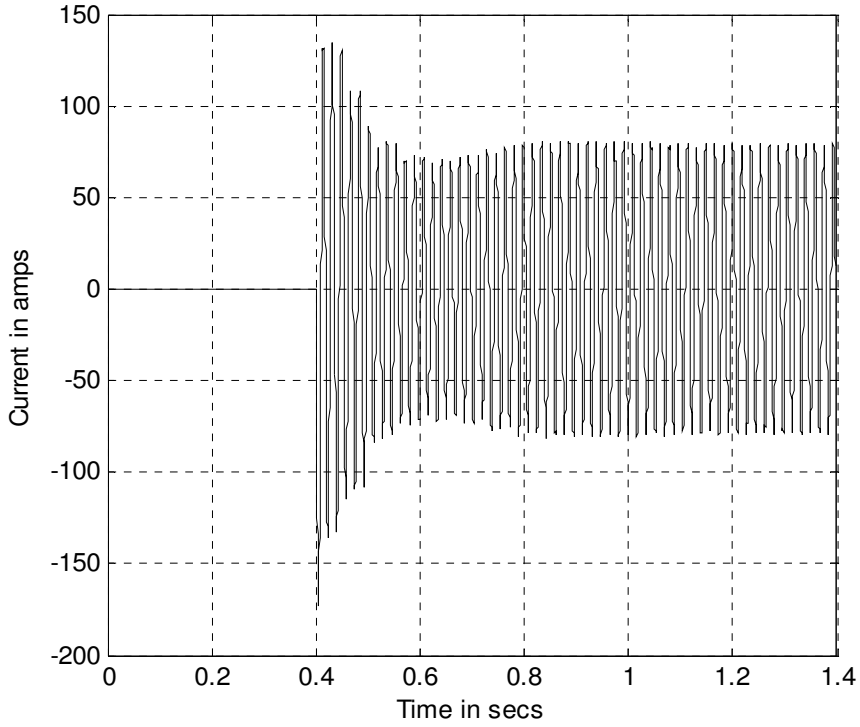

Fig.5.31 The circulating current in the shorted-coil, “coil BC9”, case study A, vector-control mode.

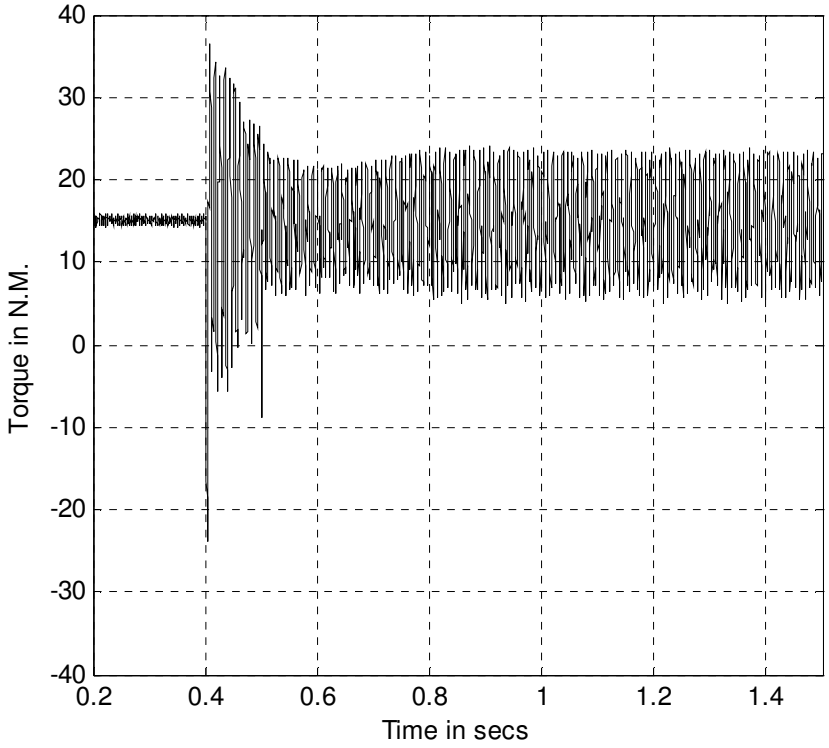

Fig.5.32 Motor's output torque, case study A, vector-control mode, coil BC9 shorted at t=0.4sec, faulty phase isolated at t=0.5sec.

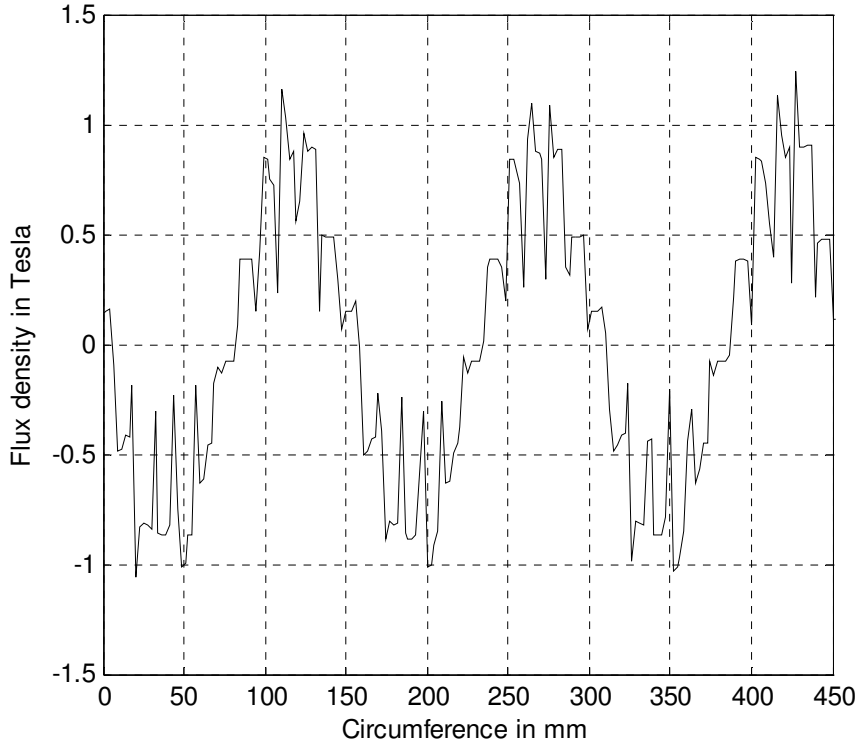

Fig.5.33a Airgap flux density, case study A, vector-control mode, during normal operation.

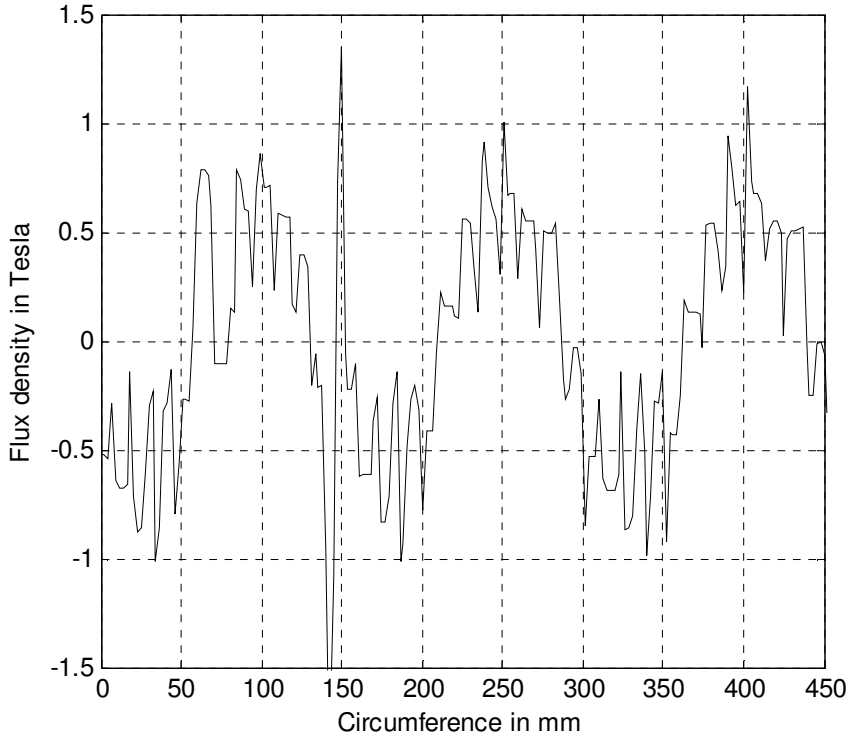

Fig.5.33b Airgap flux density, coil BC9 shorted, case study A, vector-control mode, while the faulty phase is still connected to the supply.

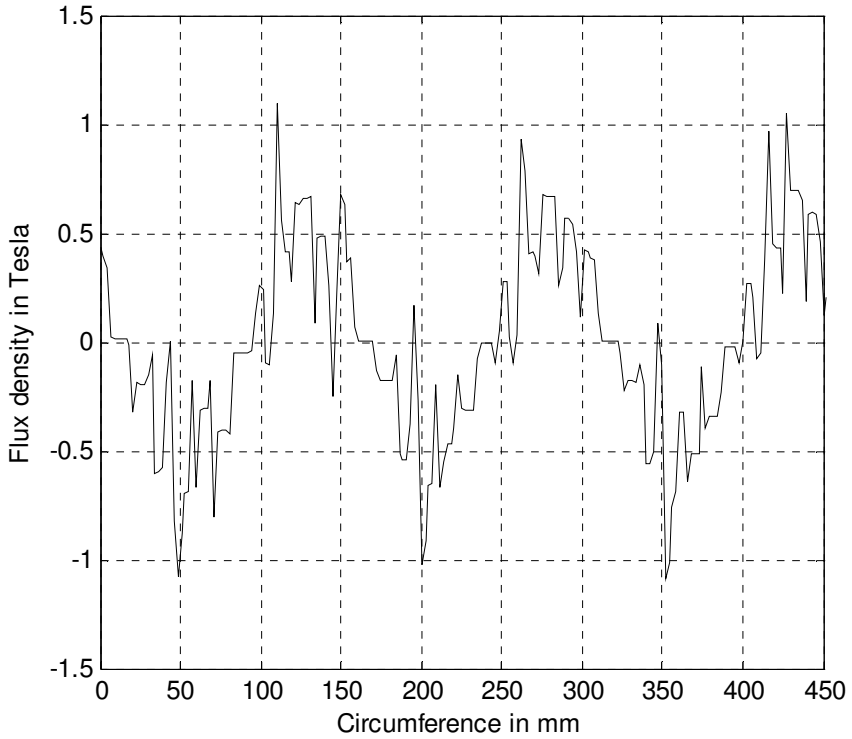

Fig.5.33c Airgap flux density, coil BC9 shorted, case study A, vector-control mode, while the faulty phase electrically is isolated from the supply.

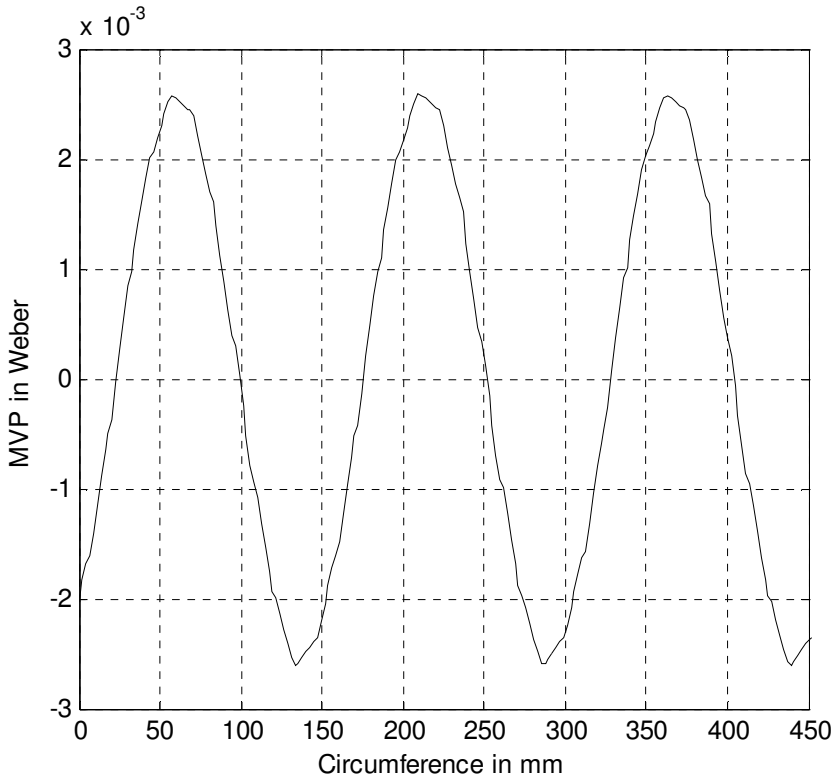

Fig.5.34a Airgap MVP, case study A, vector-control mode, during normal operation

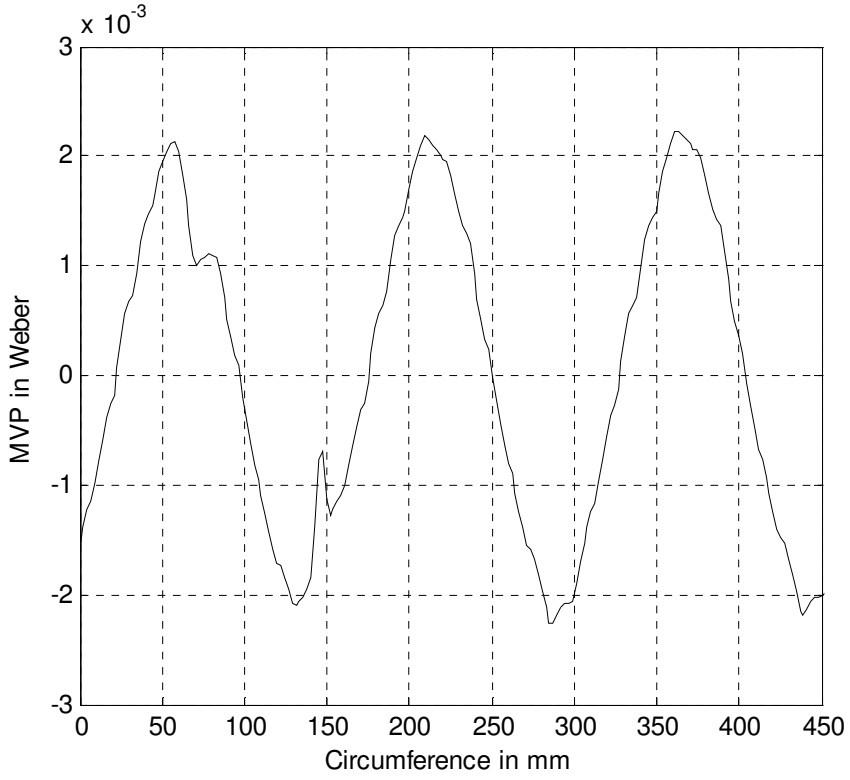

Fig.5.34b Airgap MVP, case study A, vector-control mode, coil BC9 shorted, while the faulty phase is still connected to the supply

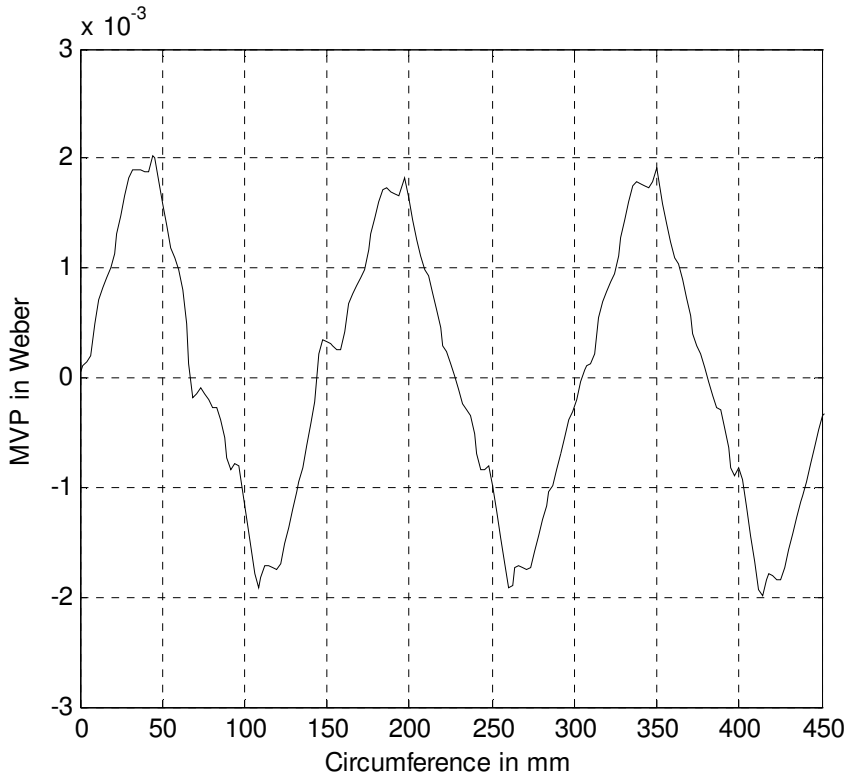

Fig.5.34c Airgap MVP, case study A, vector-control mode, coil BC9 shorted , while the faulty phase is isolated from the supply

Case study B:

The second case study in this section is similar to the same operating conditions of case A. However, the operating speed was set to 30 rad/sec (286.5 r/min) instead of 120 rad/sec (1146 r/min). Again, coil BC9 was shorted at time, t=0.4 sec, and the faulty phase was electrically isolated at time, t=0.5 sec. The motor speed and flux references are kept constant before and after the fault.

The motor line current waveforms are depicted in Fig.5.35. Again, it can be noticed that the increase in the line currents as result of this fault is insignificant at this low speed, and it can not be detected by a traditional protection device. Therefore, an advanced inter-turn short-circuit diagnostic scheme may be required to detect the fault at this operating condition. Meanwhile, the circulating current waveform in the faulty coil is

depicted in Fig.5.36. It can be noticed that the magnitude of this faulty loop current for this case at a speed of 30 rad/sec (286.5 r/min) is much less than the magnitude of the faulty loop current for case A at a speed equals 120 rad/sec (1146 r/min). However, the magnitude of the faulty loop current at this speed is equal to four times the magnitude of the normal phase current. This reduction in the magnitude of the faulty loop current was expected as expressed in (5.13) given earlier in this chapter. However, this magnitude is also very high, and may cause complete winding failure in a very short period.

The motor output torque profile at these operating conditions is depicted in Fig 5.37. The existence of torque pulsations with a frequency equal to double the line frequency can be also observed. Again, these torque pulsations are mainly caused by the interaction between the pulsating magnetic field produced by the shorted-coil and other MMFs in the machine. This is in addition to the magnetic unbalance in the machine resulting from the two-phase open-Delta mode of operation of the motor which takes place after isolating the faulty phase.

The waveforms of the airgap flux density are depicted in Fig.5.38a for the case of normal operation, in Fig.5.38b for the case of short-circuit in coil BC9 while the three phases are remaining active, and in Fig.5.38c for the case of the two-phase open-Delta mode of operation while coil BC9 is still experiencing a short-circuit. The corresponding waveforms of the MVP for the above mentioned three operating conditions are depicted in Fig.5.39a, Fig.5.39b, and Fig.5.39c, respectively. The distortion in the airgap flux density when coil BC9 was shorted in both the three-phase mode of operation and the two-phase open-Delta mode of operation can be observed through examining Fig.5.38b, and Fig.5.38c. Meanwhile, the distortion in the MVP waveform under the same cases can

be observed through examining Fig.5.39b, and Fig.5.39c. In addition, comparing the airgap flux density waveforms obtained from the simulation runs in case study A while coil BC9 was shorted and the faulty phase was connected to the supply, see Fig.5.33b, and while coil BC9 was shorted and the faulty phase was isolated, see Fig.5.33c, to the flux density waveforms under the two above operating conditions, see Fig.5.38b and Fig.5.38c , respectively, shows that the distortion in the airgap flux density waveform in this case , case B, is less than the distortion observed in case A.. The same observation can be concluded from comparing the corresponding waveforms of the MVP shown in Fig.5.39b and Fig.5.39c, respectively, to Fig.5.34b and Fig.5.34c, respectively. This is due to the fact that the magnitude of the faulty loop circulating current at this low speed is much less that its counterpart at high speed operation of case A. Consequently, the "ampere-turn" effect of the circulating faulty loop current on the resultant MMF in the airgap in case b is less than its counterpart in case A.

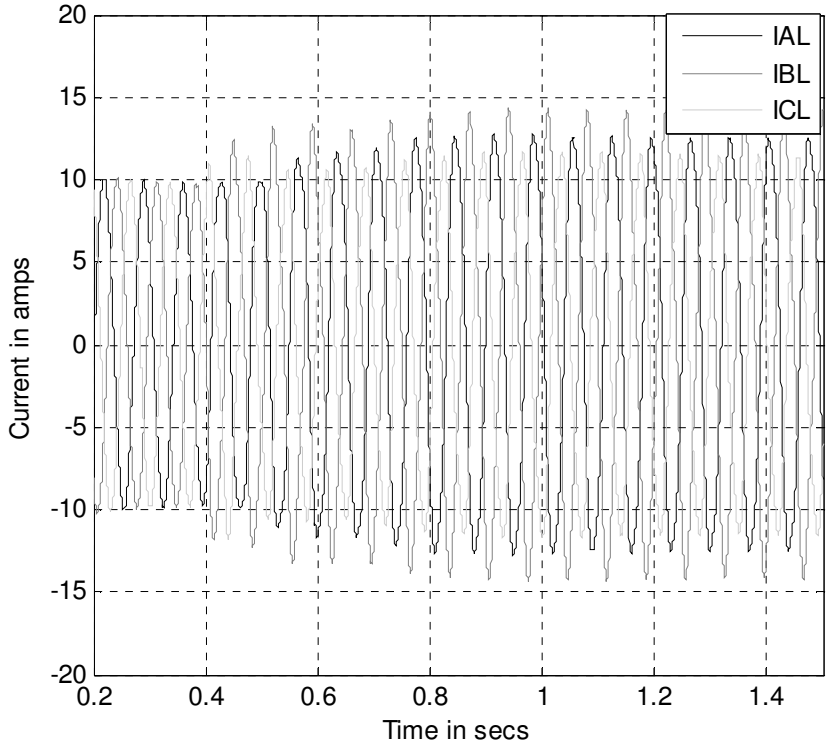

Fig.5.35 Motor line currents, case study B, vector-control mode, speed=30 rad/sec, coil BC9 shorted at t=0.4sec, faulty phase isolated at t=0.5sec.

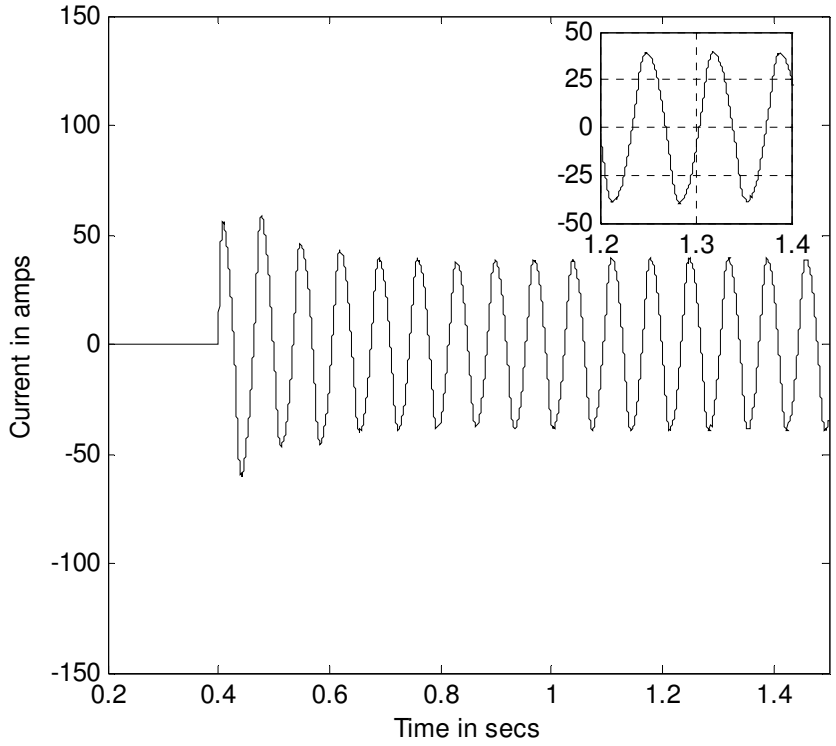

Fig.5.36 The circulating current in the shorted-coil "coil BC9", case study B, vector-control mode.

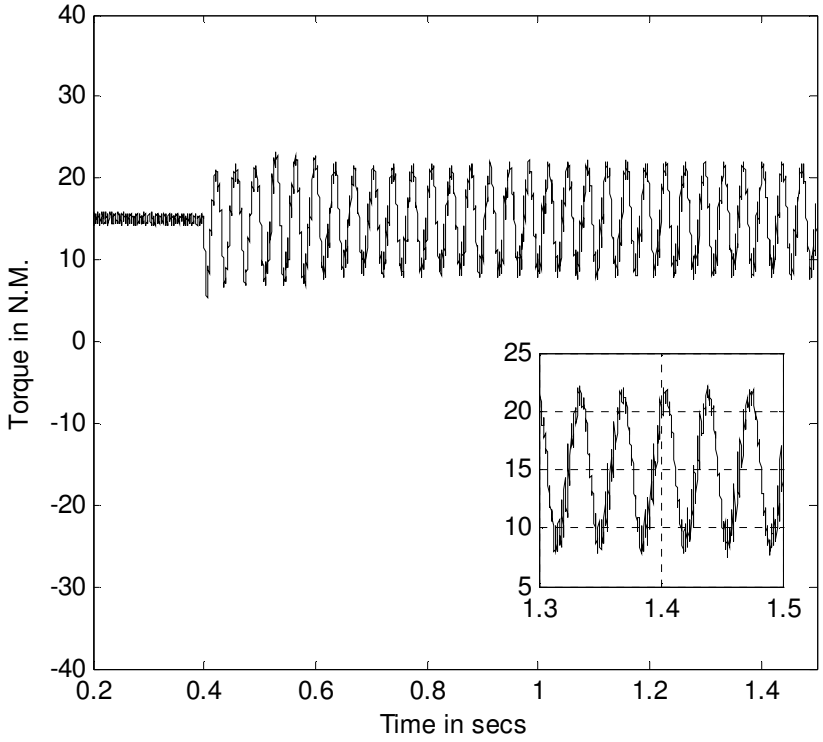

Fig.5.37 Motor's output torque during normal operation through normal operation, case study B, vector-control mode, coil BC9 shorted at t=0.4 sec, faulty phase disconnected at time t=0.5 sec.

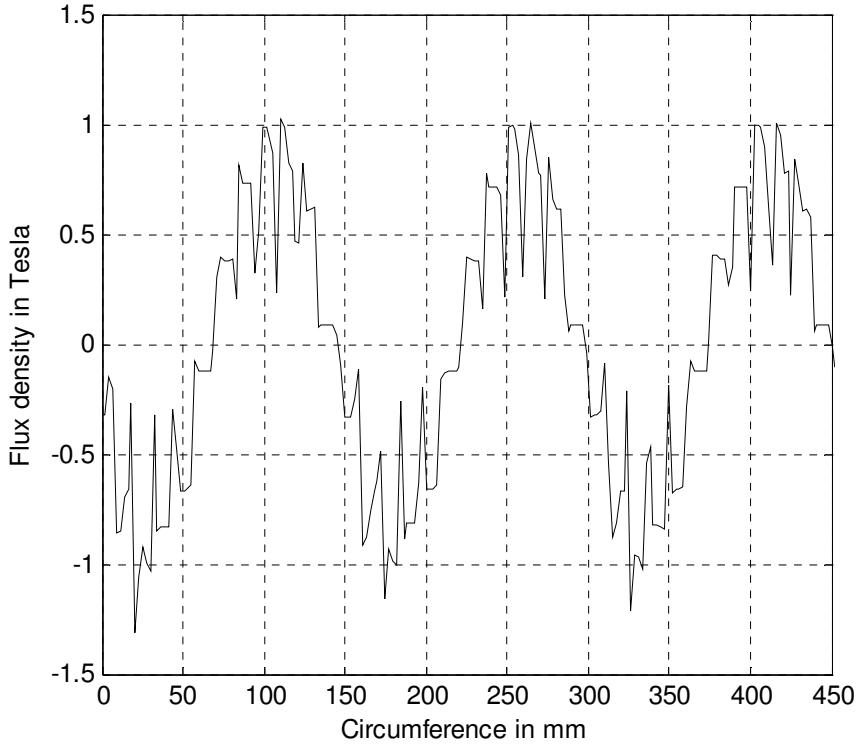

Fig.5.38a Airgap flux density, case study B, vector-control mode, during normal operation.

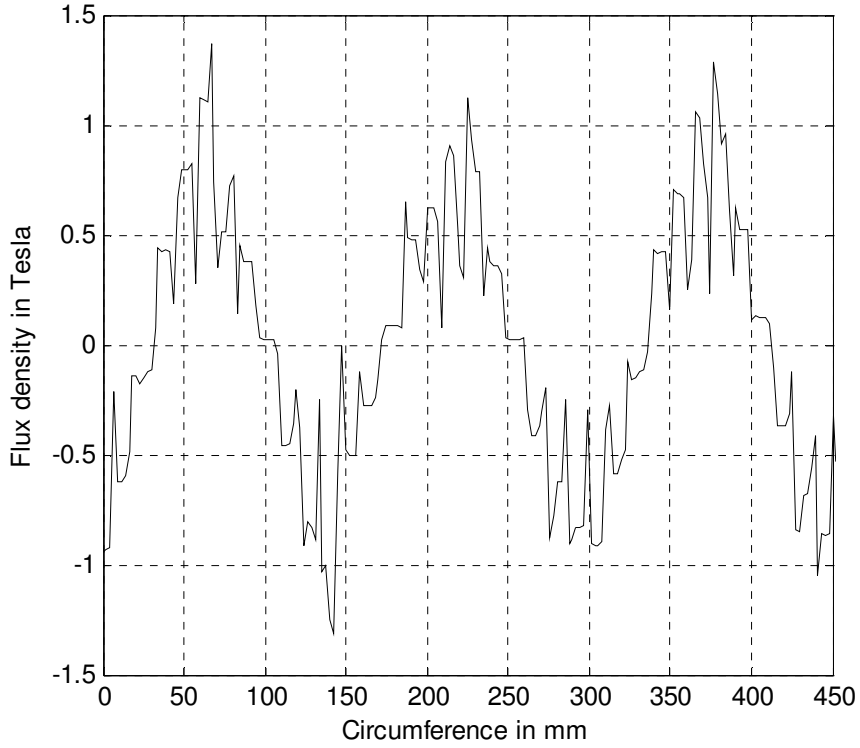

Fig.5.38b Airgap flux density, case study B, vector-control mode, coil BC9 shorted, while the faulty phase is still connected to the supply.

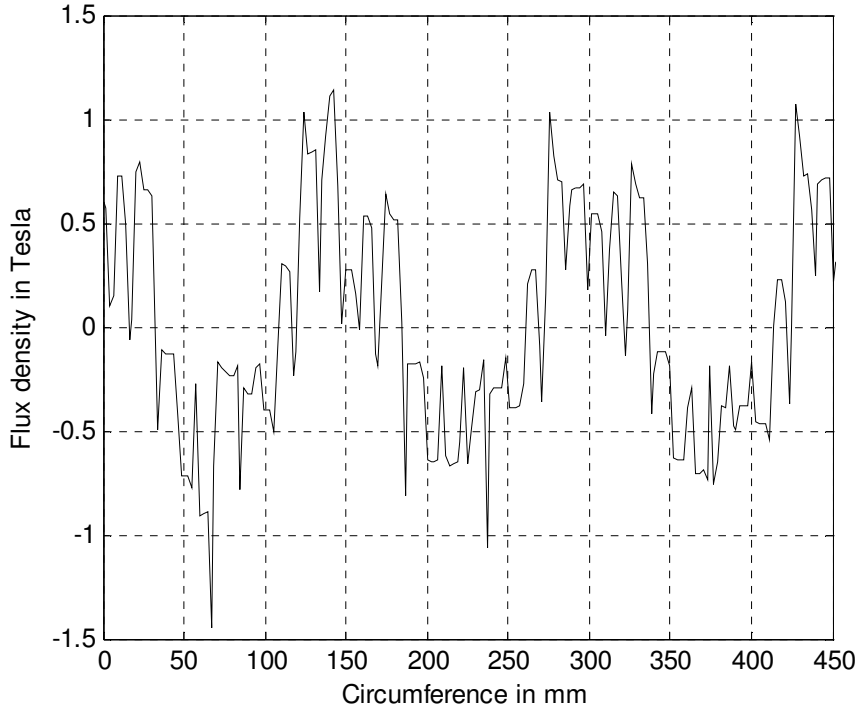

Fig.5.38c Airgap flux density, case study B, vector-control mode, coil BC9 shorted, while the faulty phase is isolated from the supply.

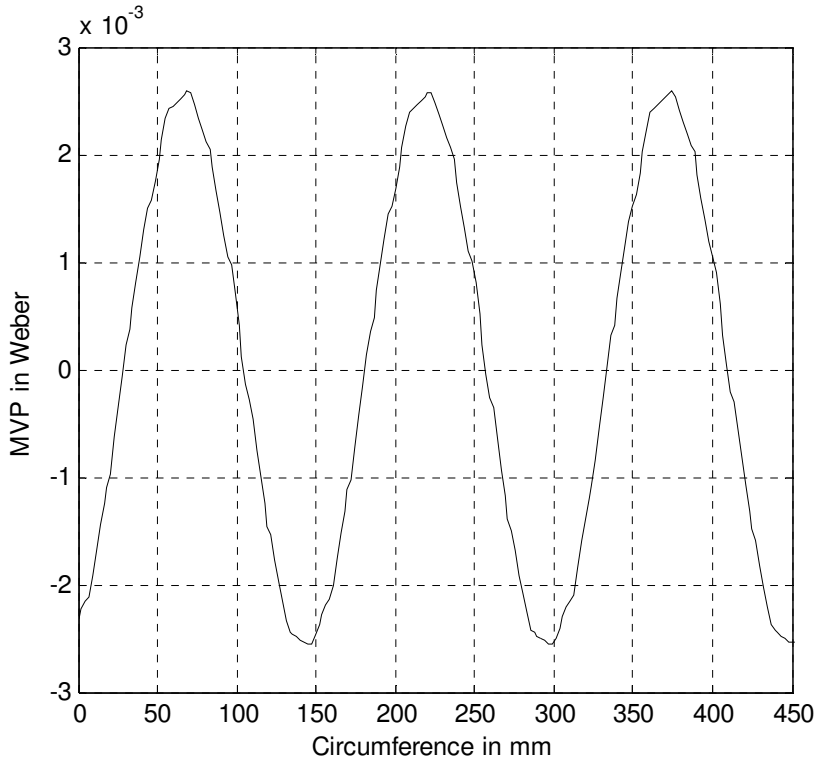

Fig.5.39a Airgap MVP, case study B, vector-control mode, during normal operation.

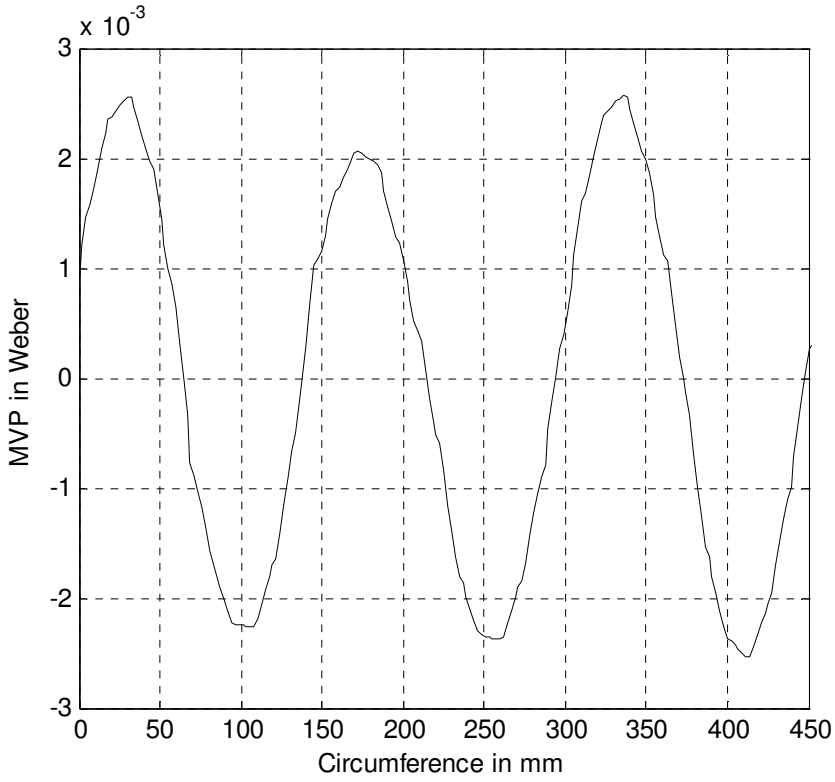

Fig.5.39b Airgap MVP, case study B, vector-control mode, coil BC9 shorted, while the faulty phase is connected to the supply.

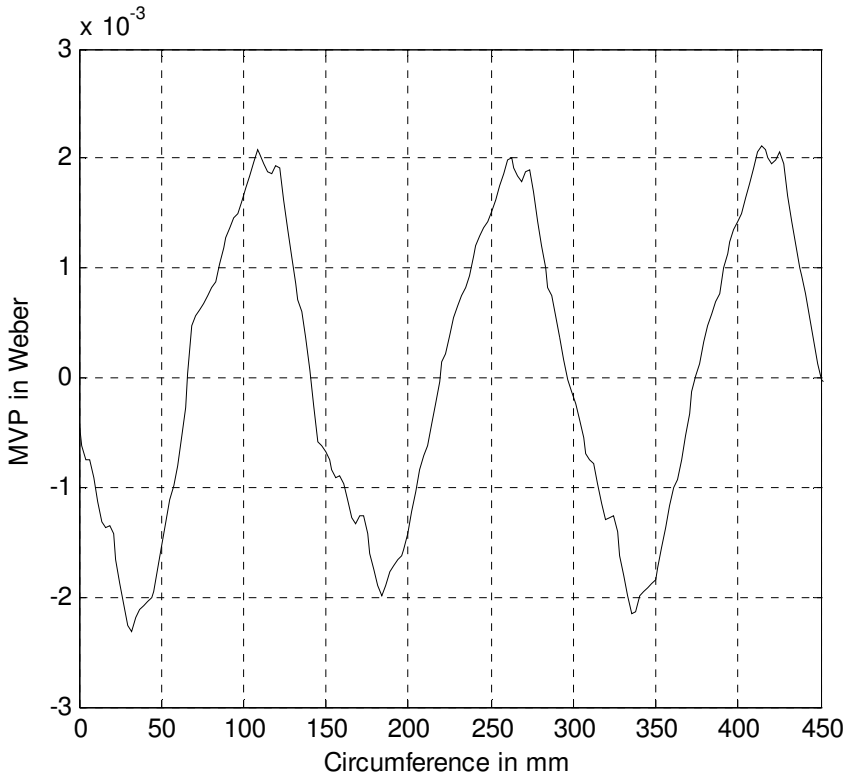

Fig.5.39c Airgap MVP, case study B, vector-control mode, coil BC9 shorted, while the faulty phase is isolated from the supply

Case study C:

The operating condition of the third case study is similar to the operating condition of case study B. However, in this case, the speed was further reduced to 15 rad/sec (143 r/min), reference flux was reduced to half of its value, and accordingly the load torque was reduced to 25% of its rated value. This is in order to reduce the induced voltage in the shorted-coil as shown earlier in section 5.2. Again, coil BC9 was shorted at time, t=0.4 sec, and the faulty phase was completely disconnected at time, t=0.5 sec. The compensation controller introduced in Chapter 4 was deactivated. The motor line currents waveforms are depicted in Fig.5.40 in which a significant current unbalance can be noticed in the line currents. Meanwhile, the faulty loop current is depicted in Fig.5.41. Inspection of Fig.5.41 shows that the magnitude of the circulating current is equal to

130% of the normal phase current of the machine at this operating condition which may enable the operation of the machine for an extended period of time after the occurrence of the fault. The operating time under this faulty condition can be calculated based on machine thermal models such as the work presented in references [124, 170], which is not addressed in this dissertation and beyond the scope of this research. The motor output torque is depicted in Fig.5.42 in which a significant torque oscillation can be observed, of magnitude of 73% of the average developed torque. The waveform of the airgap flux density under normal operation is depicted in Fig.5.43a. Meanwhile, the waveform of the airgap flux density when coil BC9 was shorted while the motor was operating at its rated speed and flux is depicted in Fig.5.43b. In addition, the waveform of the airgap flux density when the motor speed was reduced to 15 rad/sec (143 r/min), the flux was reduced to half of its rated value, and the faulty phase was disconnected is depicted in Fig.5.43c. The waveforms of the airgap MVP that correspond to the three previously mentioned operating conditions are depicted in Fig.5.44a, Fig.5.44b, and Fig.5.44c, respectively. The distortion in the airgap flux density for the case of the existence of a solid short-circuit in coil BC9 with the faulty phase connected to the supply, see Fig.5.43b, and for of the existence of a solid short-circuit in coil BC9 with the faulty phase electrically isolated, see Fig.43c, is less than their counterparts in case study A, see Fig. 5.33b and Fig.5.33c, respectively. The same observation can be concluded from examining the waveforms of the MVP under the same set of operating conditions, see Fig.5.44b and Fig.5.44c, respectively, to their counterparts in case study A, see Fig. 5.34b and Fig.34c, respectively .

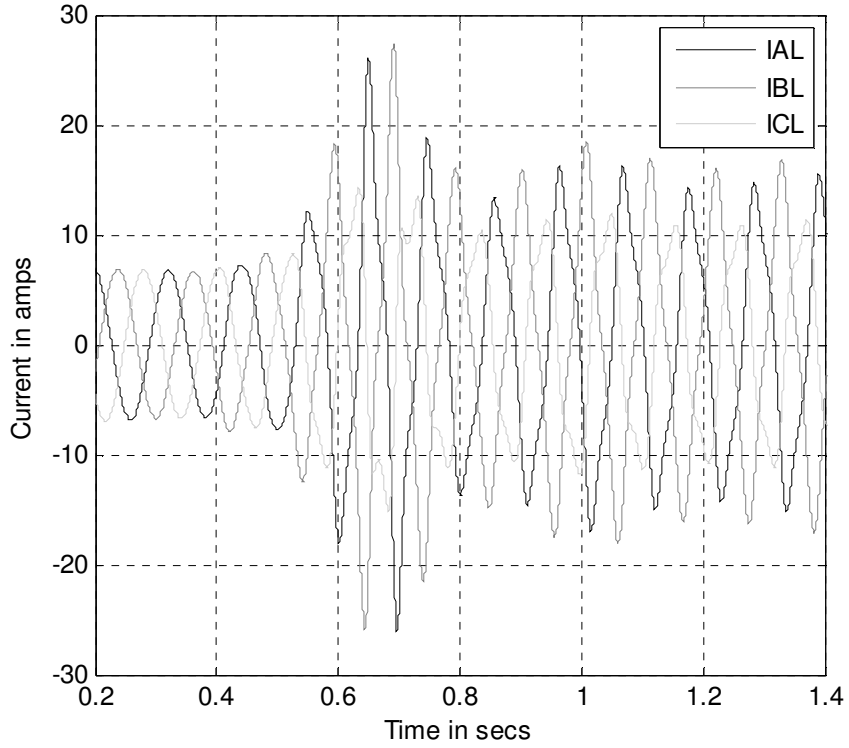

Fig.5.40 Motor line currents, case study C, vector-control, speed=15 rad/sec, coil BC9 shorted at t=0.4sec, faulty phase isolated at t=0.5sec.

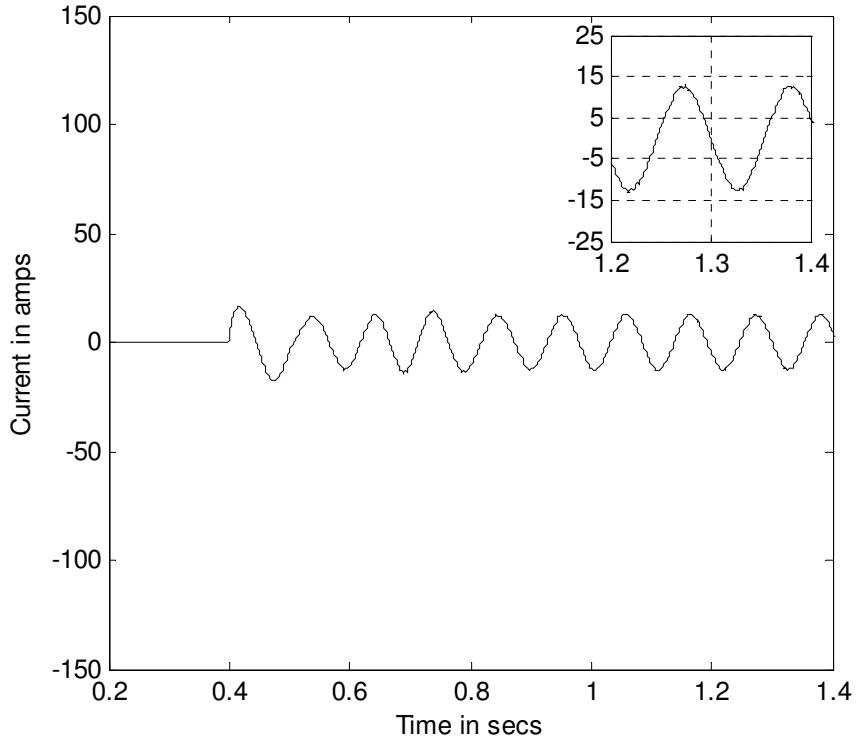

Fig.5.41The circulating current in the shorted-coil "coil BC9", case study C, vector-control mode.

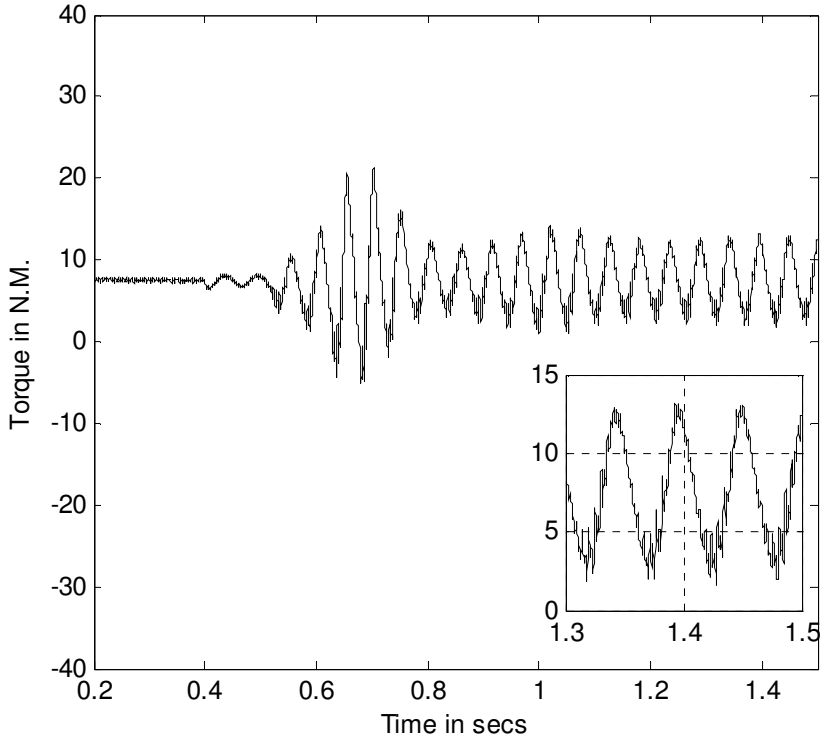

Fig.5.42 Motor's output torque, case study C, vector-control mode, coil short-circuit at t= 0.4 sec, faulty phase disconnected at t=0.5 sec.

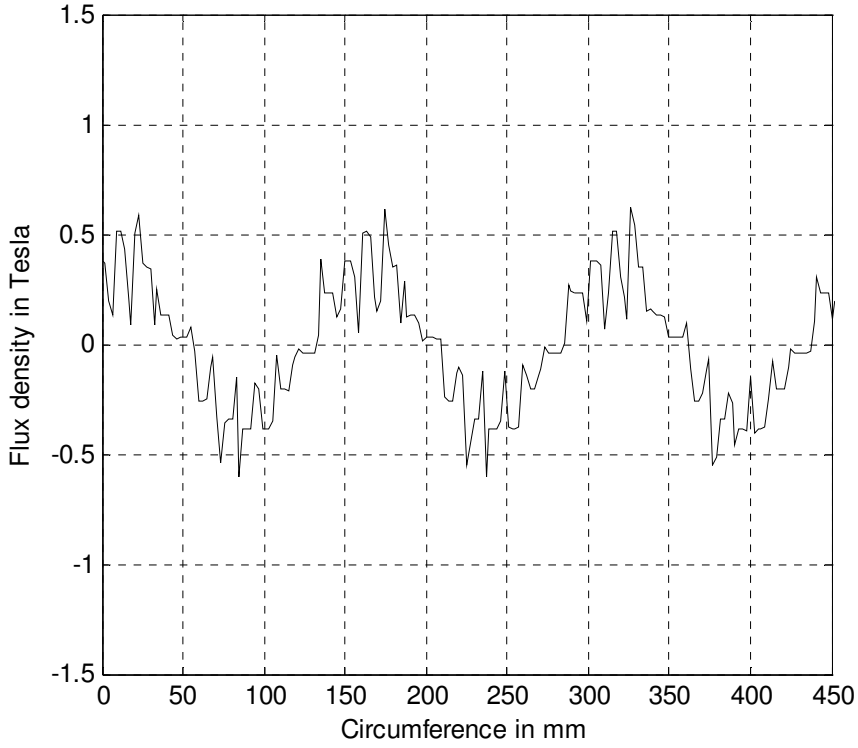

Fig.5.43a Airgap flux density, case study C, vector-control mode, during normal operation

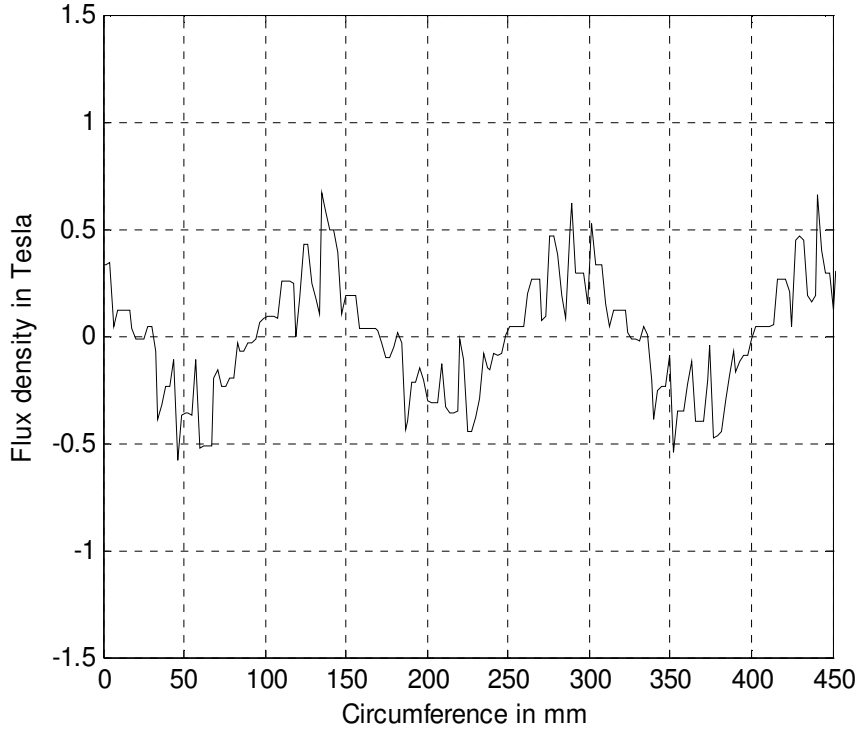

Fig.5.43b Airgap flux density, case study C, vector-control mode, during short-circuit operation while the faulty phase is connected to the supply

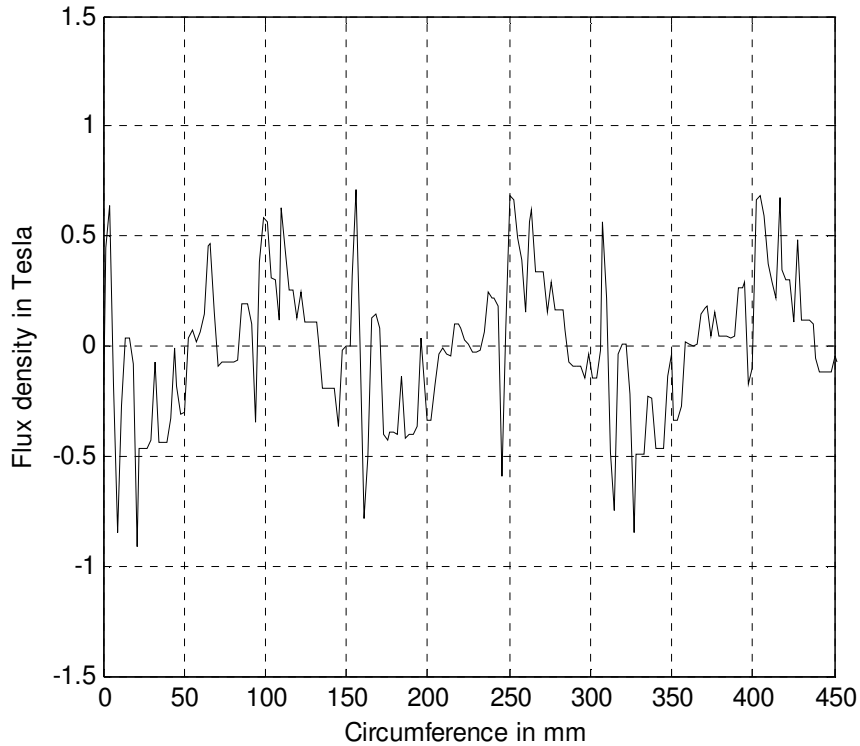

Fig.5.43c Airgap flux density, case study C, vector-control mode, coil BC9 shorted, while the faulty phase is isolated from the supply.

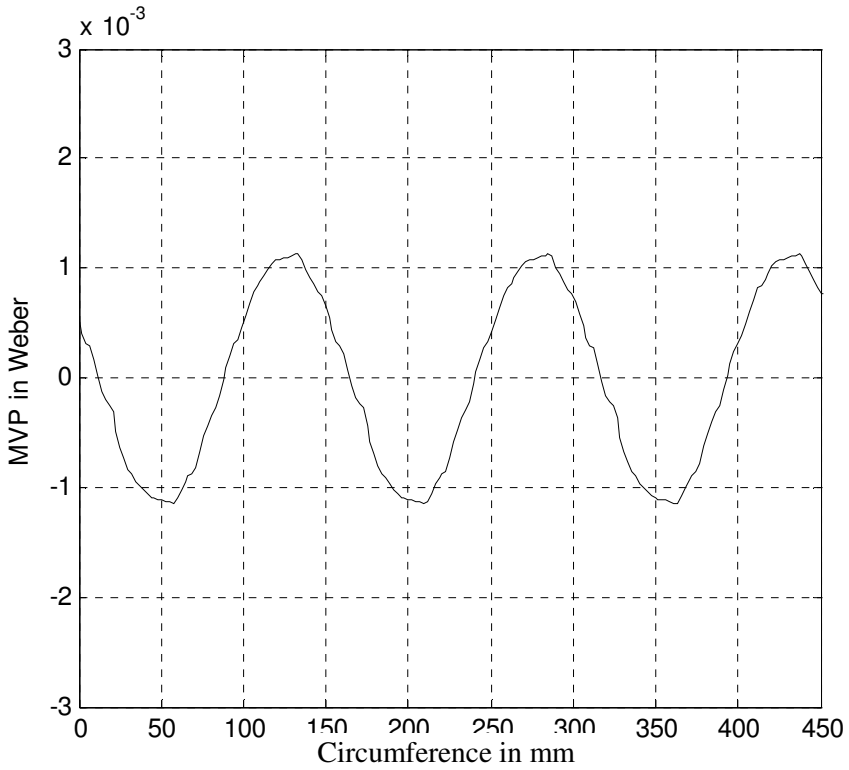

Fig.5.44a Airgap MVP, case study C, vector-control mode, during normal operation.

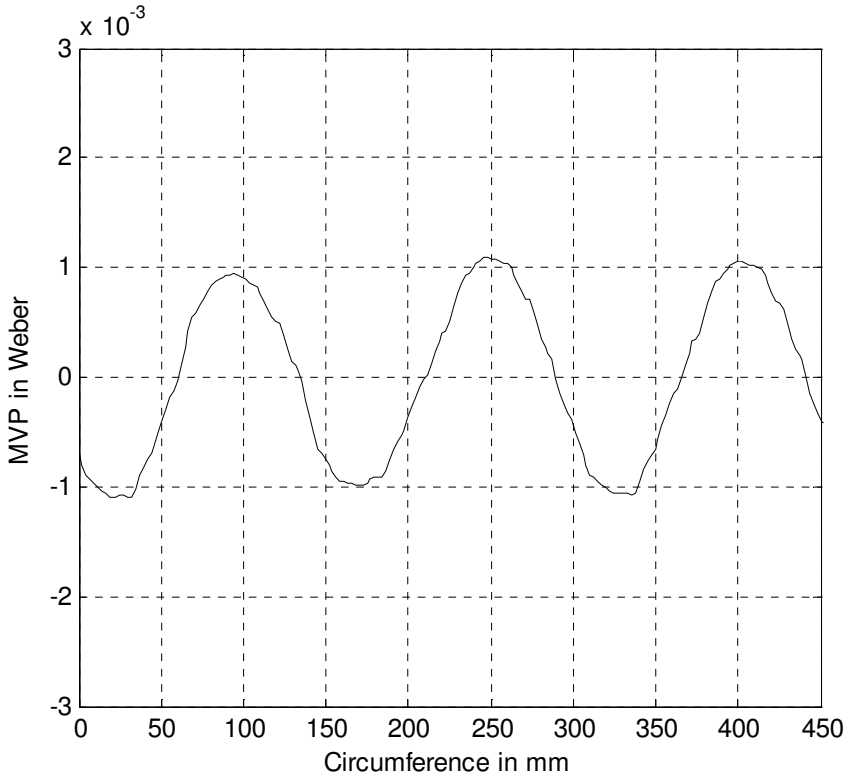

Fig.5.44b Airgap MVP, case study C, vector-control mode coil BC9 shorted, while the faulty phase is connected to the supply.

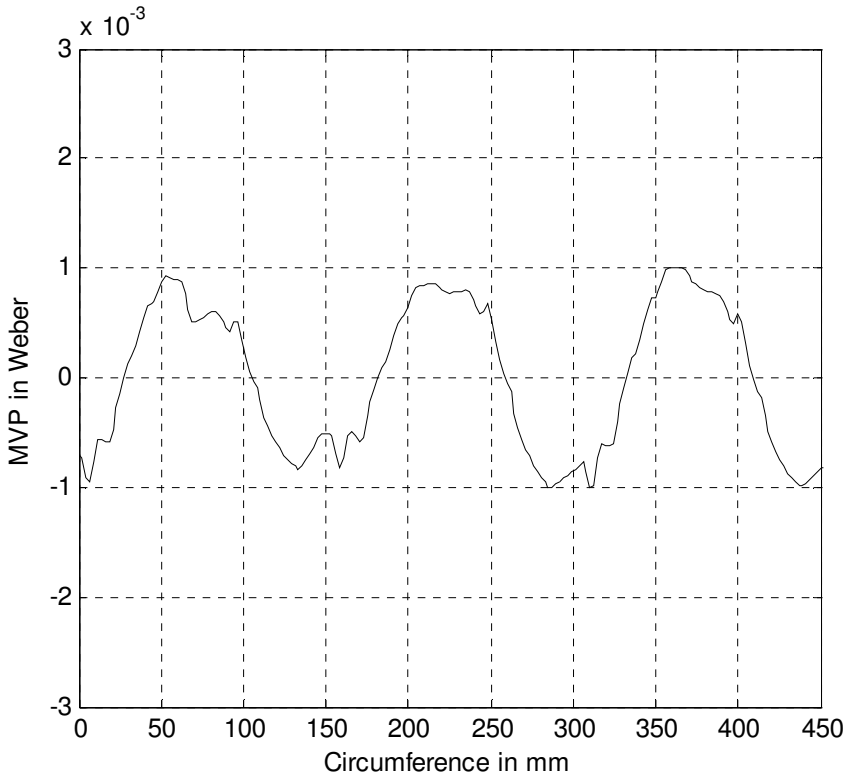

Fig.5.44c Airgap MVP, case study C, vector-control mode, coil BC9 shorted, while the faulty is phase isolated from the supply.

Case study D:

In this case, an application of a fan or a propulsion system was considered. The load torque was set to be proportional to the motor's mechanical speed. In these applications, reducing the motor's speed results in reducing the motor's load torque as well as reducing the induced voltage in the shorted-coil, thus reducing the faulty loop current. Therefore, in this case study, the motor was initially running at 120 rad/sec (1145 r/min), coil BC9 was shorted at time, t=0.48 sec. Upon detection of the fault at time, t=0.5sec, the faulty phase was electrically isolated, the speed of the motor was reduced to15 rad/sec (143 r/min), and the motor's flux was reduced to half of its normal value. This is in order to reduce the magnitude of the circulating current in the faulty coil. As described before in Chapter 4, torque ripples resulting from the unbalance in the line

current associated with the two-phase open-Delta mode of operation can be suppressed by the current controller in the synchronously rotating CCW frame of reference at low operating speed. Hence, the current controller in the synchronously rotating CW frame of reference can be deactivated at this speed without affecting the system's performance.

The waveforms of the motor line currents are depicted in Fig.5.45, in which an increase in the magnitude of the line currents can be observed due to the fault conditions at the time instant, t=0.48 sec. It can be also noticed that the magnitude of the motor line currents was further increased, at time, t=0.5 sec, to the preset current limit during braking mode initiated by the drive's controller in order to reduce the motor's speed to the commanded speed that is 15 rad/sec (143 r/min). The motor line currents were reduced at the new operating conditions that correspond to this case study. The waveform of the faulty loop current in coil BC9 is depicted in Fig.5.46. A significant reduction in the magnitude of this current to a value approximately equal to 130% of the magnitude of the motor's rated phase current can be noticed after reducing the motor speed and reference flux. This enables operating the motor for an extended period of time and hence avails a permissible time to safely shutdown the system or start up a standby unit. Meanwhile, examining the output torque depicted Fig.5.47 shows that the motor was initially producing the rated torque at normal operation, the appearance of torque pulsations can be observed at the instant of the occurrence of the short-circuit at time instant time, t =0.48 sec, followed by a braking torque to reduce the motor speed from 120 rad/sec (1146 r/min) to 15 rad/sec (143 r/min). Torque ripples with a magnitude equal to 30% of the average developed torque can be observed during the two-phase open-Delta mode of operation. These torque ripples are mainly originating due to the

pulsating field produced by the faulty current in the shorted-coil BC9 since the unbalance in the motor line currents is not significant as shown in Fig.5.45. The waveform of the airgap flux density under normal operation is depicted in Fig.5.48a. Meanwhile, a significant distortion in the waveform of the airgap flux density can be observed when coil BC9 was shorted while the motor was running at normal operating speed and normal rated flux as depicted in Fig.5.48b. It can also be noticed that this distortion was reduced when the speed was set to15 rad/sec (143 r/min) and the reference flux was reduced to half of its normal value as depicted in Fig.5.48c. The corresponding MVP waveforms for the same previously mentioned three operating conditions are depicted in Fig.5.49a, Fig.5.49b and Fig.5.49c, respectively.

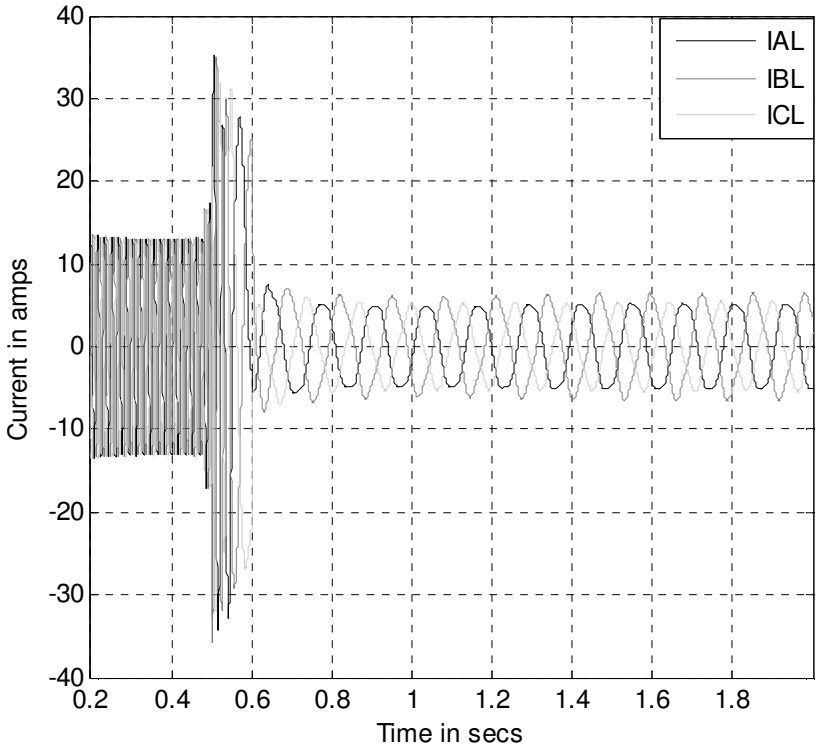

Fig.5.45 Motor line currents, case study D, vector-control mode, final speed=15 rad/sec, coil BC9 shorted at t=0.48sec, speed and flux reduced at t=0.5sec, faulty phase disconnected at t=0.5sec.

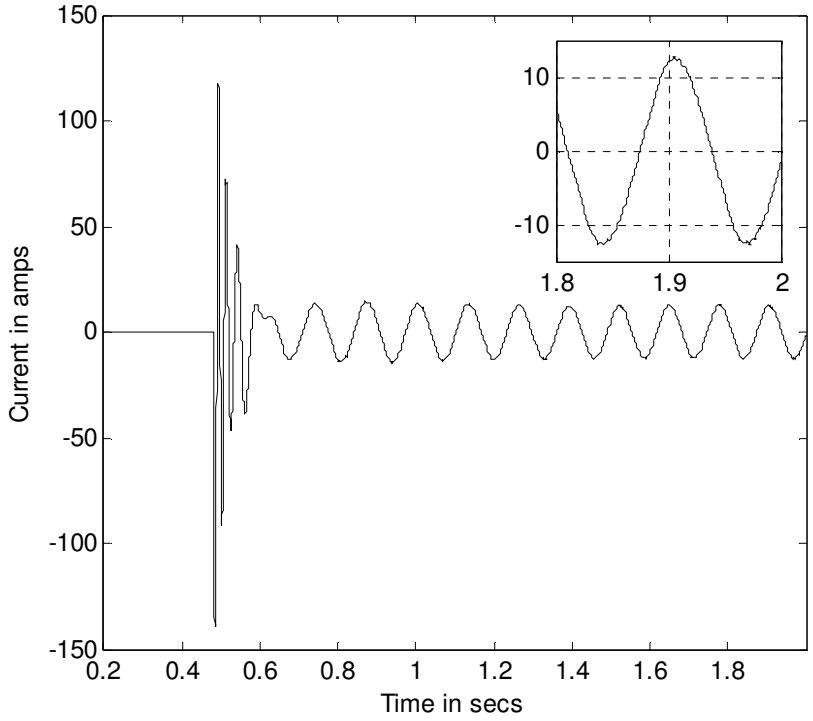

Fig.5.46 The circulating current in the shorted-coil, case study D, vector-control mode, final speed= 15rad/sec, final flux density is equal to half of the rated flux density.

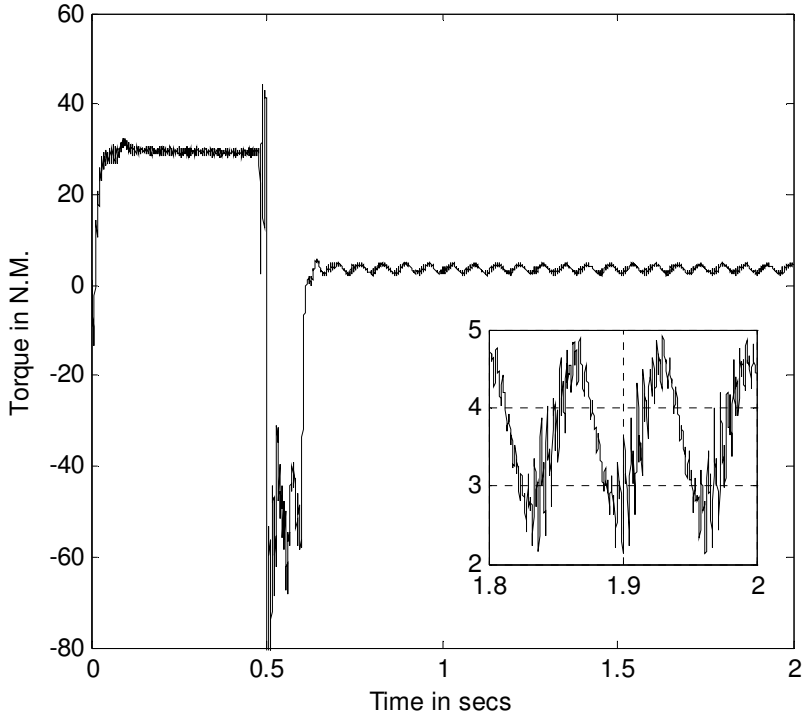

Fig.5.47 Motor's output torque during normal operation, case study D, vector-control mode, and during faulty operation, coil short-circuit at t= 0.48 sec, flux and speed reduced at t=0.5 sec, faulty phase disconnected at t=0.5 sec.

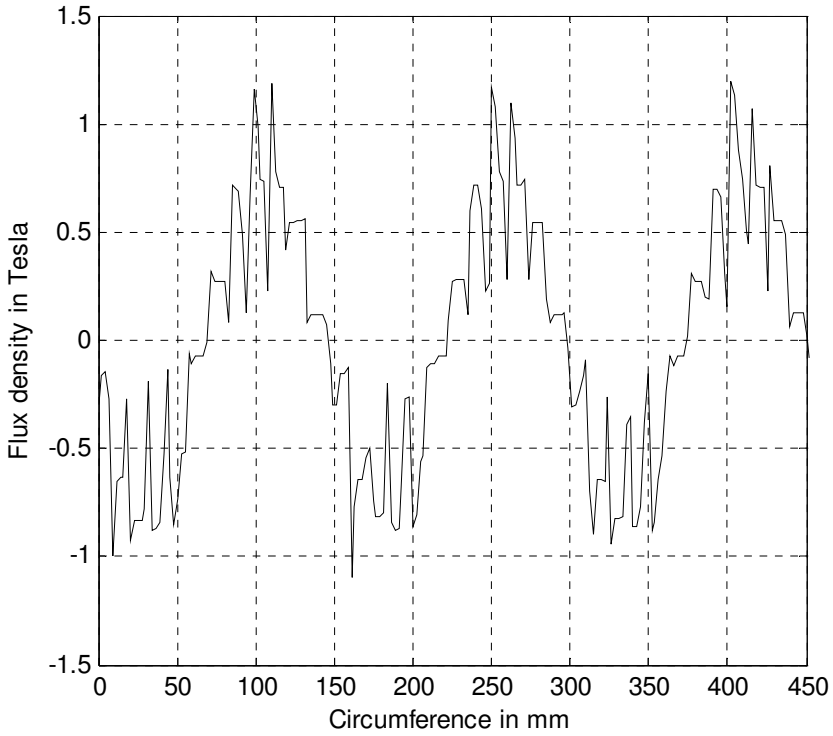

Fig.5.48a Airgap flux density, case study D, vector control mode, operating speed= 120rad/sec, rated flux density.

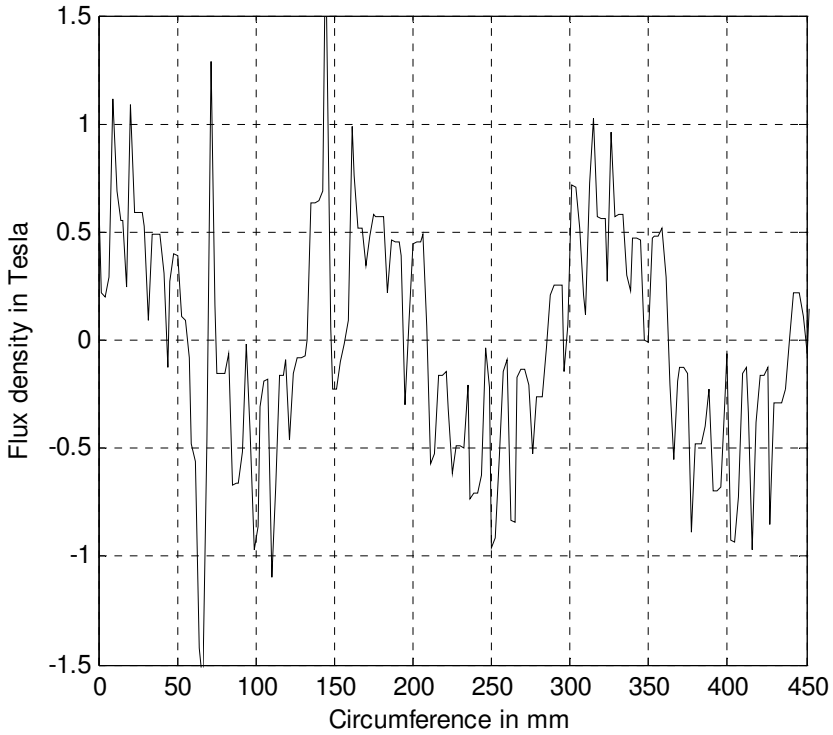

Fig.5.48b Airgap flux density, case study D, vector-control mode, during short-circuit condition while the faulty phase is connected to the supply, operating speed=120 rad/sec, rated flux density.

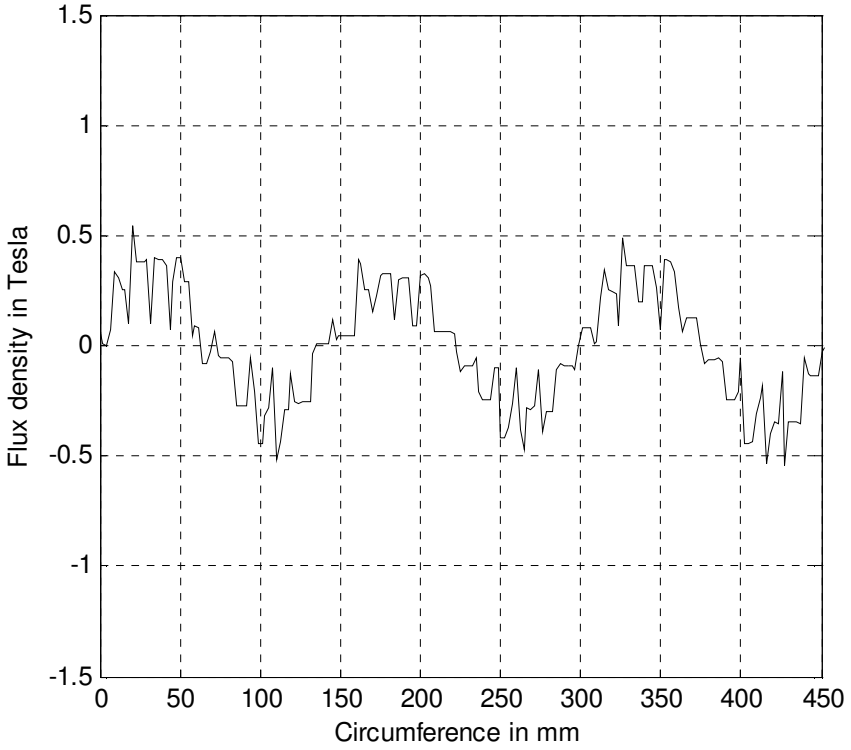

Fig.5.48c Airgap flux density, case study D, vector-control mode, coil BC9 shorted, two-phase open-Delta mode of operation, operating speed=15 rad/sec, flux density was reduced to half its rated value.

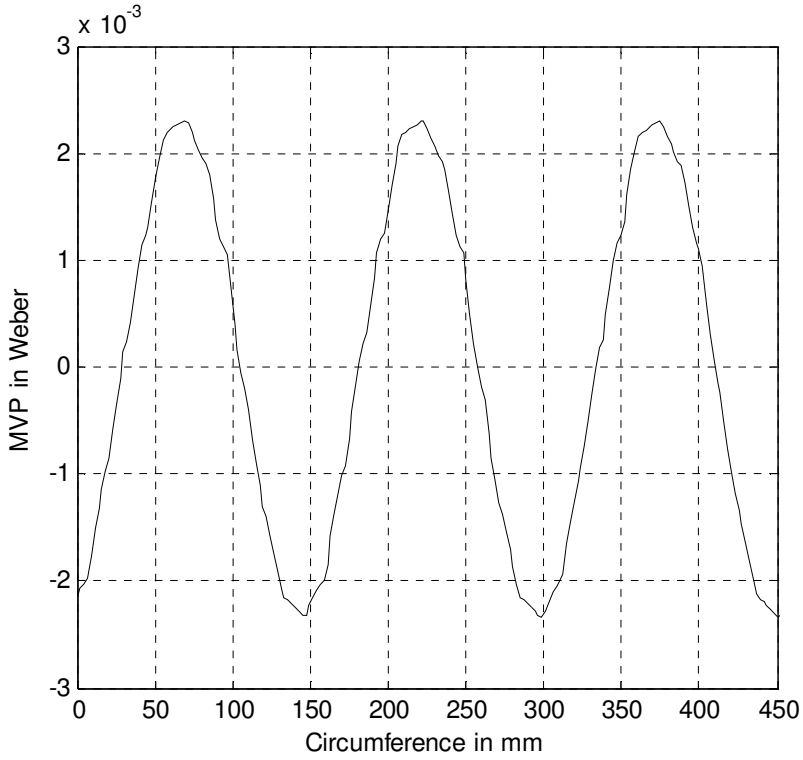

Fig.5.49a Airgap MVP, case study D, vector-control mode, during short-circuit condition, operating speed=120 rad/sec, rated flux density.

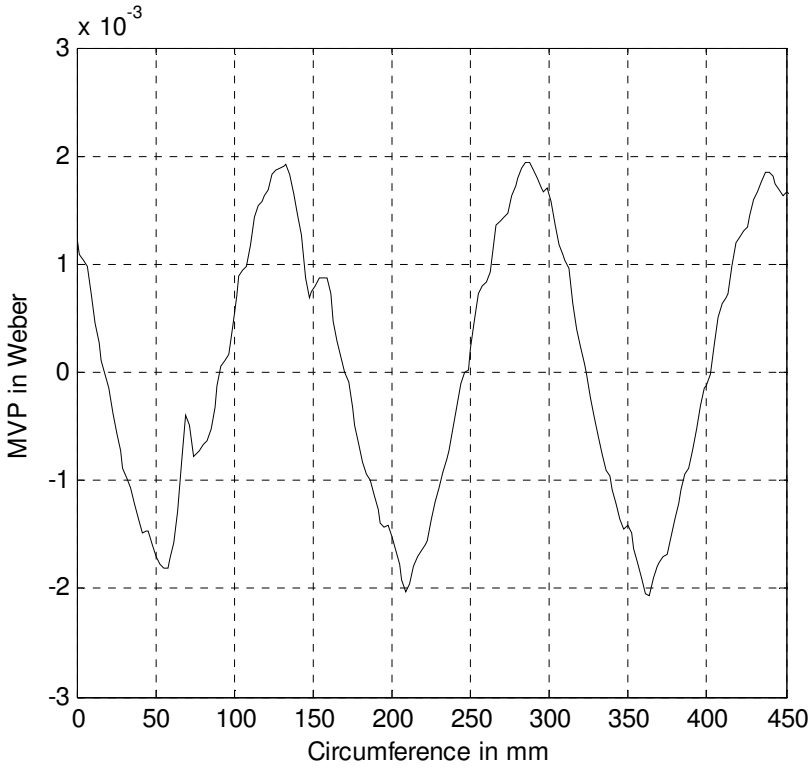

Fig.5.49b Airgap MVP, case study D, vector-control mode, during short-circuit condition while the faulty phase is connected to the supply, operating speed=120 rad/sec, rated flux density

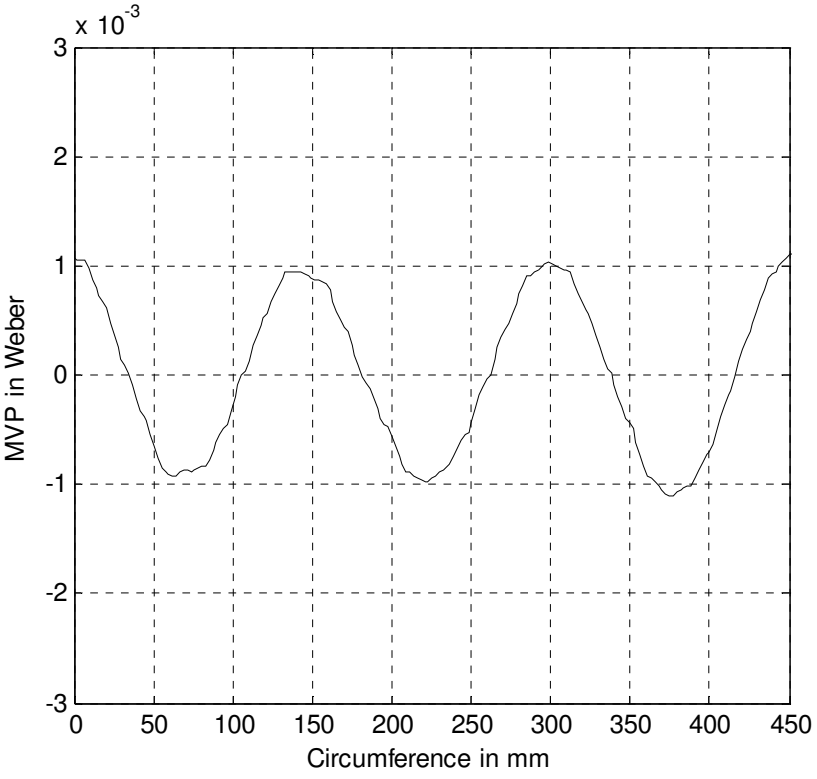

Fig.5.49c Airgap MVP, case study D, vector-control mode, coil BC9 shorted, two-phase open-Delta mode of operation, operating speed=15 rad/sec, flux density was reduced to half its rated value.

Case study E:

In this case study, unlike previous cases presented earlier in this chapter, the faulty phase was not electrically isolated. Coil BC9 was shorted at a time instant, t=0.4sec. Meanwhile, upon detection of the fault at time, t=0.5 sec, the motor reference flux was reduced to a value equal to half of its rated value, and the speed was reduced from 120 rad/sec (1145 r/min) to 15 rad/sec (143 r/min). The reduction in the motor's flux and speed resulted in a significant reduction in the circulating current in the faulty coil as will be shown later. The motor load was assumed to be a typical fan load in which the load torque is proportional to the speed, which is the same load in case study D.

The motor line current waveforms are depicted in Fig.5.50, in which the magnitudes of the line currents were increased due to the existence of the fault in coil BC9. These magnitudes were further increased to the maximum setting of the current limits in the controller as a result of the braking action associated with reducing the speed command to 15 rad/sec (143 r/min). The magnitudes of the line currents were reduced when the motor's speed reached the steady state operation at the commanded reference speed. It should be also noticed that in this case the electrical power is converted to a mechanical power through the three phases instead of two phases since the faulty phase was not isolated. Consequently, the magnitudes of the phase currents in this case are less than the magnitudes of the phase currents in the two-phase open-Delta mode of operation. However, as will be shown later, the circulating current in the faulty coil is higher than the two-phase open-Delta mode of operation since the faulty phase is connected to the supply. In spite of the fact that a significant reduction can be observed in the circulating current in the faulty coil when the motor's speed and flux were reduced, the magnitude of

this current, depicted in Fig.5.51, is higher than the magnitude of the current in the faulty coil for the case C by approximately 30%. The latter current is obtained at the same operating condition with the faulty phase electrically isolated. This increase is mainly due to the effect of electrically connecting the faulty phase to the source. Hence, a further reduction in the machine flux may be required to reduce the magnitude of this current to a value corresponds to the value obtained in the case study C. The motor's output torque is depicted in Fig.5.52 in which the machine was developing its rated torque at rated flux and at rated speed, significant torque ripples with a magnitude equal to 30% of the developed average torque can be observed upon the occurrence of the fault at time, t=0.4 sec. These torque ripples are mainly originated by the effect of the pulsating magnetic field produced by the circulating current in the faulty coil. These torque ripples were significantly reduced after the motor's speed and flux were reduced and consequently the circulating current in the faulty coil was also reduced. The waveform of the airgap flux density at normal operation is depicted in Fig.5.53a. Meanwhile, examining Fig.5.53b shows the distortion in the waveform of the airgap flux density during the existence of the short-circuit fault in coil BC9. It can be observed that the distortion corresponds to the location of the shorted-coil "BC9". The waveform of the airgap flux density, when the coil BC9 was shorted while the motor's speed and the flux were reduced, is depicted in Fig.5.53c. The waveforms of the corresponding MVP are depicted in Fig.5.54a, Fig.5.54b, and Fig.5.54c at these three time instants, respectively.

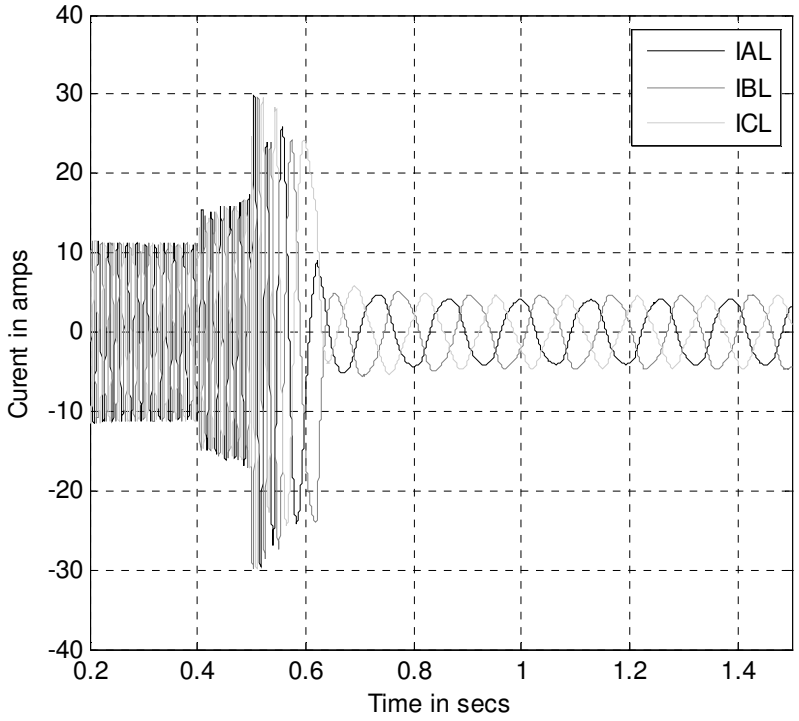

Fig.5.50 Motor line currents, case study E, vector-control, final speed=15 rad/sec, coil BC9 shorted at t=0.4sec, speed and flux reduced at t=0.5sec.

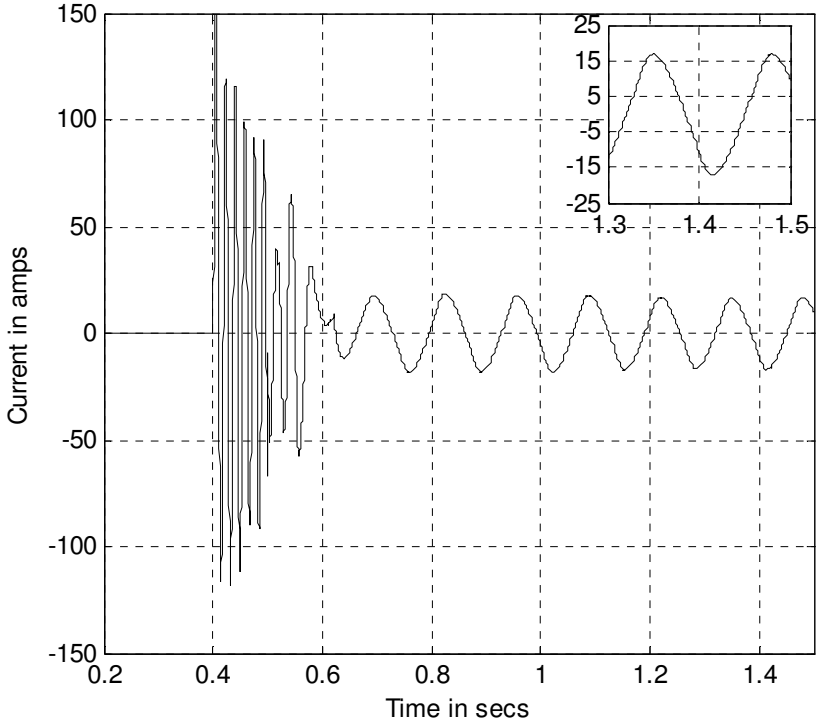

Fig.5.51 The circulating current in the shorted-coil, case study E, vector-control mode, final speed= 15rad/sec, final flux density is equal to half of the rated flux density.

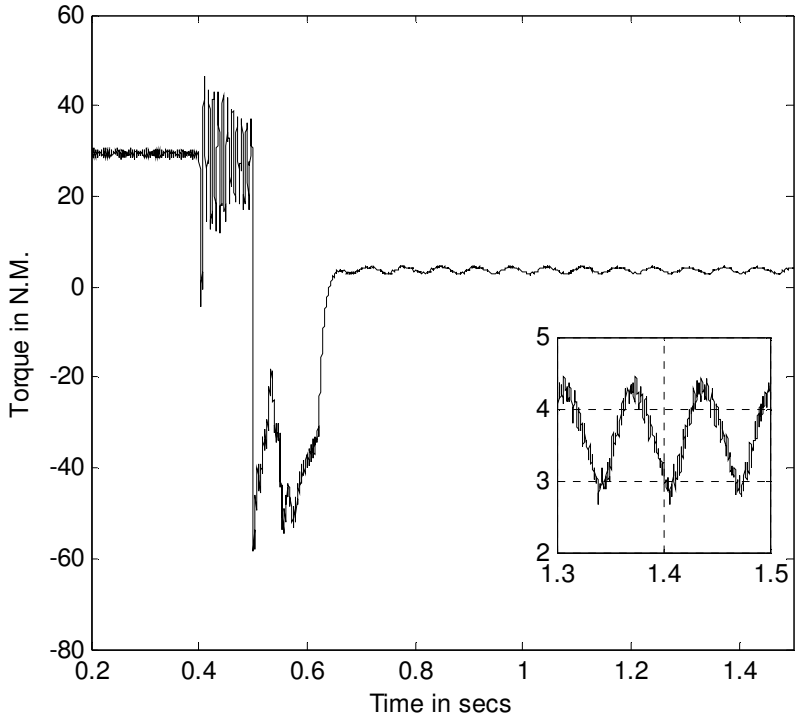

Fig.5.52 Motor's output torque during normal operation and during faulty operation, case study E, vector-control mode,coil short-circuit at t= 0.48 sec, flux and speed reduced at t=0.5 sec

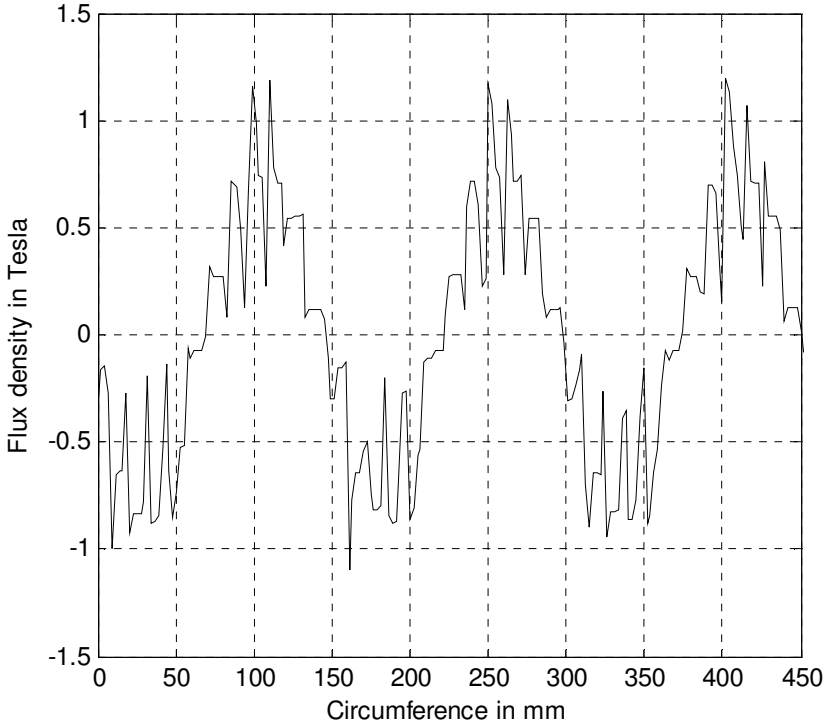

Fig.5.53a Airgap flux density, case study E, vector-control mode, operating speed= 120rad/sec, rated flux density.

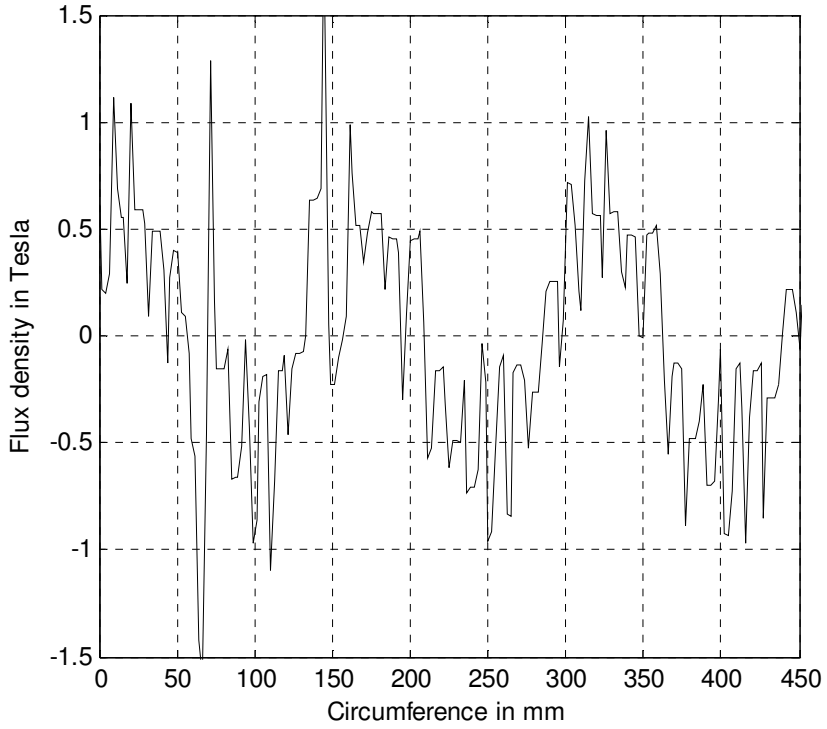

Fig.5.53b Airgap flux density, case study E, vector-control mode, during short-circuit condition, operating speed=120 rad/sec, rated flux density

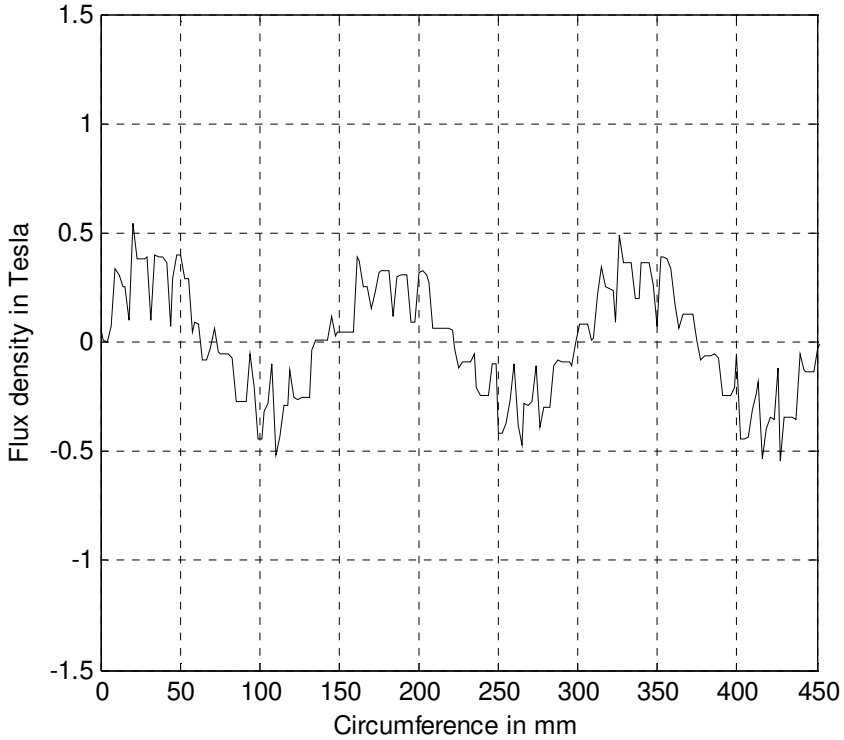

Fig.5.53c Airgap flux density, case study E, vector-control mode, coil BC9 shorted, operating speed=15 rad/sec, flux density was reduced to half its rated value.

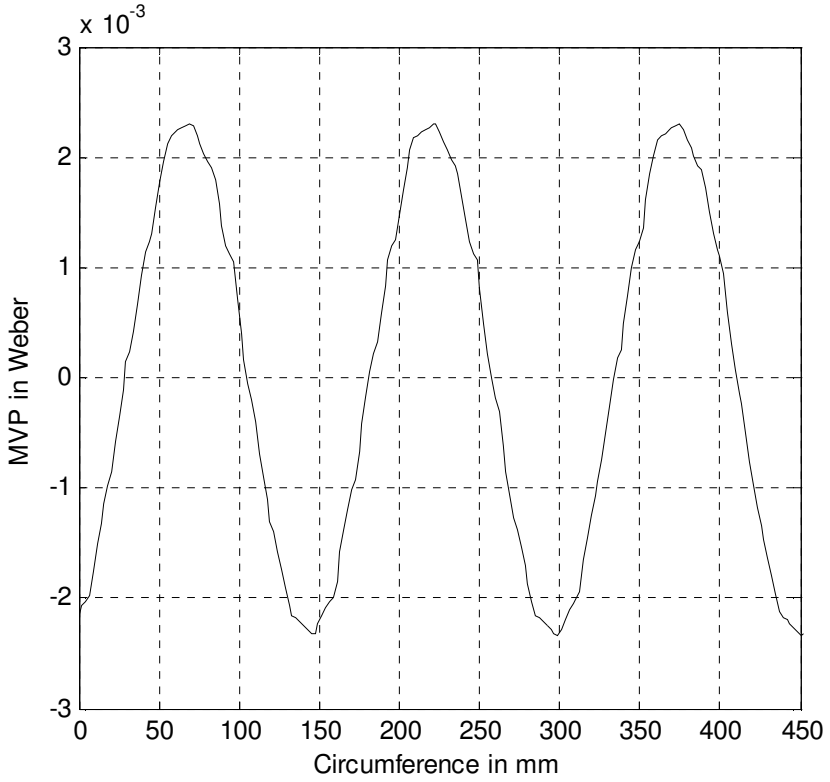

Fig.5.54a Airgap MVP, case study E, vector-control mode, during short-circuit condition, operating speed=120 rad/sec, rated flux density.

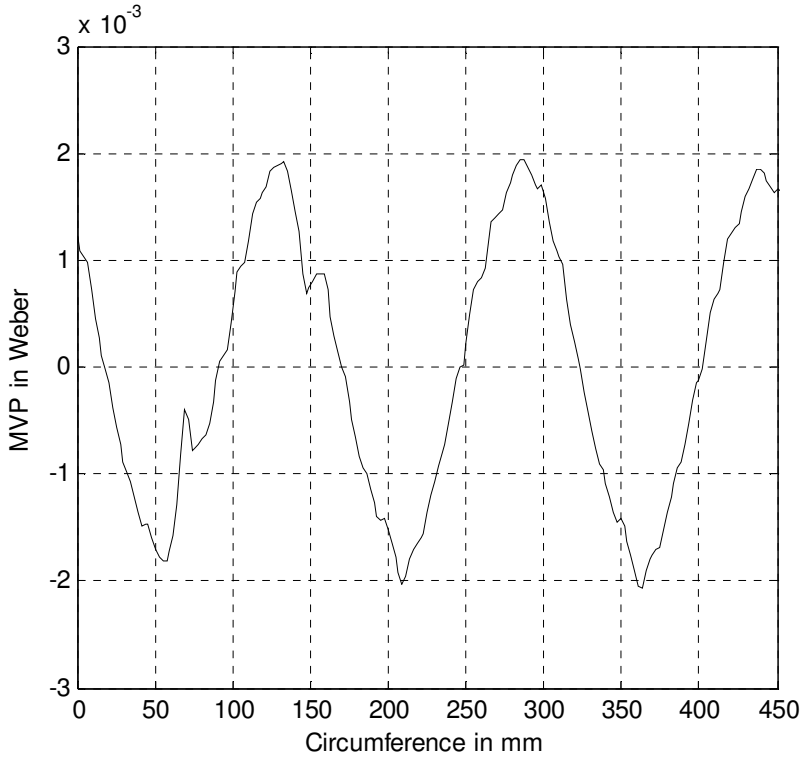

Fig.5.54b Airgap MVP, case study E, vector-control mode, during short-circuit condition, operating speed=120 rad/sec, rated flux density.

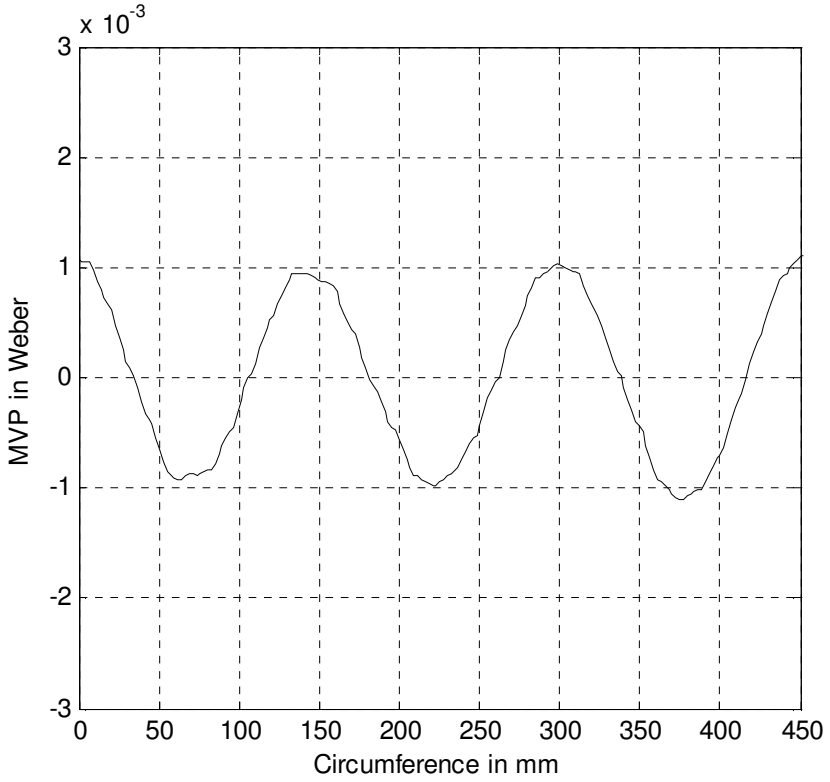

Fig.5.54c Airgap MVP, case study E, vector-control mode, during short-circuit condition, operating speed=15 rad/sec, the flux density was reduced to half of its rated value.

5.4 Summary

In this chapter, the mode of operation that involves operating a motor-drive, while one of the coils in one of the stator phase windings is shorted, was discussed and analyzed in-depth using the TSFE based Simulink/Flux2D model. This model was discussed and utilized earlier in Chapters 3 and 4 to carry out rigorous analysis of a motor-drive system considering a case in which the motor was running at "open-Delta" mode of operation, while one if its phases was disconnected from the inverter as a result of an open-coil fault, or for the case in which an inter-turn short-circuit fault was detected and isolated at an early stage, so that the "ampere-turn" effect of the circulating faulty loop is not significant and can be ignored. The efficacy of the Coupled Simulink/Flux2D

model was validated and verified in Chapters 3 and 4 through several experimental tests at various operating conditions. This model rigorously accounts for detailed winding layout, magnetic circuit saturation effects, interaction between the drive's controller and the prototype motor detailed in the TSFE model. Therefore, this model was utilized in this chapter to simulate such kind of destructive fault types that would have jeopardized the actual prototype motor utilized in this research if actually attempted in the laboratory.

The analysis included in this chapter covered two different control schemes for motor-drive systems, namely the open-loop constant (V/f) control mode, and vector-controlled closed-loop control mode. The analysis included the effects of such a fault condition on the motor line currents, motor output torque, airgap flux density, magnetic vector potential, and the faulty loop current. This faulty loop current was a key variable in determining the permissible range of operation of the faulty machine. The optimal condition is to limit the faulty loop circulating current to values close to the rated current of the machine, thus preventing localized heating of the stator windings that may cause rapid fault propagation and a complete failure of the motor.

It was also shown throughout the analysis included in this chapter for both open-loop control and vector-control closed-loop systems that reducing the faulty loop current may require significant reduction in the faulty motor's flux and operating speed.

In addition, the analysis and the discussion throughout this chapter showed that torque pulsations with a frequency equal to double the line frequency will also be originating during the mode of "open-Delta" while one of the stator's coil was shorted. These torque pulsations are resulting from two different sources. The first source is mainly resulting from the unbalance in the line current due to the disconnection or

electrical isolation of one of the motor phases. This was discussed and analyzed in Chapters 3 and 4 in which it was shown that these torque ripples can be compensated for by adding two current control loops in the CW frame of reference that is rotating with a speed equal to the synchronous speed. The second source is resulting from the "ampere-turn" effect originating by the circulating faulty loop current in the shorted-coil as discussed earlier in this chapter. These torque pulsations are not compensated for by the two current controllers added in the CW frame of reference and are very difficult to estimate. However, their effect can be minimized by reducing the magnitude of the faulty loop current in this shorted-coil.

It was also underlined that the main difference between the performance of an open-loop motor-drive system and a vector-controlled closed-loop motor-drive system is that the torque pulsations resulting from the two-phase open-Delta mode of operation can be suppressed by the conventional CCW current control loop in a vector-controlled motor-drive system at low operating speeds, provided that the bandwidth of these current control loops are much higher than the frequency of these torque oscillations. Thus, for vector-controlled motor-drive systems, the CW current control loop introduced earlier in Chapters 3 and 4 can be deactivated while the motor is running in an open-Delta mode of operation without adversely affecting the system's performance.

CHAPTER 6

6.RESEARCH SUMMARY, CONTRIBUTIONS, AND RECOMMENDATIONS FOR FUTURE WORK

6.1 Preface

The main contribution of this dissertation is to the diagnostics and fault mitigation of stator winding faults in ac motor-drive systems. Therefore, these contributions can be integrated into a drive's controller in order to render a comprehensive and reliable capability of fault diagnostic and mitigation into motor-drive systems that can be utilized in critical industrial applications.

A comprehensive survey that addresses the development of induction motor-drive systems, since the invention of the polyphase induction motor by Nichola Tesla in 1888, was conducted in Chapter 1. This survey showed that three-phase induction motors were well known for their reliable and rugged construction that significantly increased their service life and reduced maintenance cost in comparison to their dc counterparts. However, dc motors prevailed in applications that required rigorous and wide-ranging speed and torque control. That was mainly due to the superior torque-speed performance characteristics of such motors that could not be matched by existing induction motors. Intensive research efforts in the field of power electronics, digital microprocessors, and advanced machine control techniques unleashed the well known constant (V/f) control

schemes that enabled a wide range of speed control of induction motor-drive systems. This is in addition to more advanced field oriented control methods (techniques) that enabled precise speed and torque control of such induction motor-drive systems. The breakthroughs in the area of power electronics, and induction motor-drive systems enabled these motor-drive systems to substitute and replace their dc counterparts in most of current industrial applications.

It was also shown in the survey conducted in Chapter 1 that the widespread use of induction motor-drive systems in several critical applications mandated extreme levels of reliability and survivability that rendered a premature failure of such systems unacceptable. That is because of the fact that severe financial consequences or even life threatening events may occur as a result of failures in such critical applications. That was the main incentive to trigger intensive research efforts by numerous investigators in the areas of motor diagnostics and fault mitigation of such types of systems. The main target of these previous investigators was to detect a faulty condition in a premature/incipient stage and shutdown the system in order to avoid catastrophic failure of the motor or the drive. The other alternative was to isolate the fault and provide a reconfigurable arrangement that enables continued operation of such a motor-drive system with a tolerable, though partially impaired, performance. Special attention in a substantial amount of this research was centered on winding faults, either for cases of inter-turn short-circuit faults, or for cases of open-coil faults. Also, to the best of this author's knowledge, it was shown in Chapter 1 that despite the ongoing intensive research, this area is still in its immature stage with a considerable amount of gaps that need to be bridged.

The rate of propagation of a stator's winding fault is very high, allowing a very short-time between the incipient stage of such a fault and the complete failure of such windings. This hurdle rendered early diagnosis and feasible remedy of such kind of faults very difficult to achieve with a sufficient promptness/speed such that one can avoid affecting the productivity of an industrial process. A little concern was given to the problem of the identification of the faulty phase in a polyphase winding, which is considered to be vital information for a post-fault control mitigation strategy. The proposed techniques available in the literature for this purpose required the insertion of intrusive sensors or accessibility to the neutral point of such polyphase windings in order to localize and identify the faulty phase. Another technically challenging hurdle in the area of motor diagnostics is that the interaction between a drive's controller and a corresponding faulty motor fed by this drive is a very complex phenomenon that depends on the tuning of the associated controller, the programmed control mode, this in addition to possible inevitable manufacturing imperfections leading to asymmetries in the phase windings of such machines, as well as magnetic saturation that is based on such machines' loading conditions. Meanwhile, despite the intensive research efforts in the area of fault-tolerant ac motor-drive systems, research in fault-tolerant open-loop motor-drive systems are scarce to find in the literature. In addition, most of earlier research efforts were directed towards Wye-connected ac motors. Investigations centered on Delta-connected ac motor-drive systems are almost absent from the literature. Given the above mentioned technical challenges, the scope of the research which was highlighted and defined in Chapter 1, led to the present work which resulted in the contribution summarized at the end of this chapter.

6.2 Research summary

In Chapter 2, causes and mechanisms of a motor's stator winding failures were briefly described based on the research and experiments carried out by several investigators in this area. It was shown that elevated temperature rise, repetitive voltage spikes that exceed the rated voltage of the winding's insulation, and ageing, are the main factors that result in winding failures. A magnetic field based analysis of a three-phase induction motor, when one of its phases encounters an inter-turn short-circuit fault in an early stage, was studied in this chapter. Accordingly, the first main contribution in this dissertation is the conception of a new method for identifying the specific faulty phase based on this magnetic field analysis, this method can be used as a foundation for an advanced artificial intelligent algorithm to reliably identify the faulty phase in a faulty polyphase machine . This capability of identifying the faulty phase is considered to be vital information for a post-fault mitigation strategy in any motor-drive system. It was also shown that this technique does not require detailed design information regarding a stator windings' layout for the class of concentric wound machines. This is mainly due to the fact that for concentric wound armatures, the magnetic axis of any coil located in a specific phase coincides with the magnetic axis of that phase. On the other hand, for lap wound machines, the magnetic axis of a specific coil does not necessarily coincide with the magnetic axis of the phase that contains this shorted-coil. Therefore, detailed winding design information may be required for this class of armatures.

In addition, the second contribution of this dissertation is the finding of a new approach for diagnosing an inter-turn short-circuit fault in vector-controlled motor-drive systems, which was also conceived and detailed in this chapter. This new technique

unmasks the effects of controller compensation which follows the occurrence of an inter-turn short, thus it extends and supersedes the concept of the magnetic field/ MMF pendulous oscillation that was utilized earlier in the diagnosing of an inter-turn short-circuit fault in open-loop drives and line-fed induction machines, therefore, rendering this new method effective in fault diagnostics of cases which involve closed-loop vector-controlled motor-drive systems. The basic principle of this technique is to monitor the fluctuation of both the stator voltage space-vector and the stator current space-vector with respect to two reference angles that are generated by two distinct phase locked loop systems which are not affected by the faulty condition. Again, this approach can be also utilized as a foundation for an advanced artificial intelligent algorithm in order to detect such kind of faults. The details on the findings and the investigations related to these two previously mentioned contributions were summarized in Section 5 of Chapter 2.

The third contribution in this dissertation was given in Chapter 3. This contribution mainly consists of a new robust control strategy for Delta-connected induction motors in open-loop ac motor-drive systems. This robust control strategy tackles a fault that involves an open-coil in one of the stator phase windings, which can occur due to rupture in the internal wiring of a machine's stator coils due to loose connections in the internal windings, excessive vibrations that result in cracking a stator's bars in large size machines, inter-turn short-circuits resulting in excessive thermal stresses that lead to rupturing/melting of a faulted-coil. Another possible scenario for the utilization of this control technique involves cases that include inter-turn short-circuit faults in their early stages that are diagnosed and isolated, in which such resulting faulty loop currents are limited and do not present hazardous (fire) conditions.

The main aim and accomplishment of this technique was to maintain a quality of performance of a two-phase open-Delta mode of operation of a faulty motor as close as possible to the quality of performance of such a motor under normal healthy Delta-connection. That is, such a procedure would be triggered after the process of isolating the faulty phase is accomplished successfully. Accordingly, the work was directed towards the analysis of Delta-connected stator windings under a healthy three-phase mode of operation and under a two-phase open-Delta mode of operation, see Section 3 of Chapter 3. The analysis introduced in this section showed that the main advantage of a two-phase open-Delta mode of operation is the inherently provided extra degree of freedom for the currents in this type of a stator winding connection. That is, the phase currents in the two remaining active phases can be controlled independently. On the other hand, a two-phase mode of operation of Wye-connected stator windings provides only one degree of freedom. That is, the phase currents in the two remaining active phases are dependent on each other and therefore can not be controlled independently, unless the neutral point of the Wye-connection is made accessible. In addition, the analysis presented in this section, showed that a perfect Counter-ClockWise (CCW) rotating field can be theoretically obtained if the phase currents in the two remaining active phases of a two-phase open-Delta mode of operation are controlled in such a manner that they have equal magnitudes and maintained an angular phase shift of 60 degree.elect. between each other. This fact was previously mentioned by other investigators for a two-phase mode of operation of Wye-connected stator windings. However, as mentioned above, in such cases the neutral point of a motor had to be made accessible and connected to the mid-point of the dc bus to provide an additional degree of freedom that is necessary to control the remaining two

active phases independently. Moreover, a significant oversizing of such a drive and a motor is necessary to accommodate significant increases in the line currents, neutral current, as well as severe stresses on the dc bus capacitors resulting from the unbalance in these line currents.

Furthermore, the analysis in Chapter 3 revealed another interesting finding that is inherently provided by a two-phase open-Delta winding connection regarding the conditions necessary to produce a perfect CCW rotating field. This finding is that while it is mandatory to control phase currents in the remaining two active phases in such a manner that these currents should have equal magnitudes and maintain an angular phase shift of 60 degree.elect between each other, this always results in a set of balanced three-phase line currents. That is, at this operating condition, a nearly balanced load will be seen by the drive without any significant unbalance in the line currents. Therefore, the drive's power components will not be subjected to any consequent stresses resulting from phase unbalances under this mode of operation.

An additional interesting and important finding is that the control algorithm associated with the two-phase open-Delta mode of operation does not require any modification of a power structure of a drive. Thus, it only requires the addition of two current control loops in a synchronously rotating ClockWise (CW) frame of reference for mitigating an open-coil fault. The main function of these current control loops is to regulate the line currents in order to compensate for the unbalance in the machine and render a balanced set of three-phase line currents, while the phase currents in the remaining two active phases are rendered with equal magnitudes, and maintained at a 60 degree.elect angular phase shift between each other. It was also shown in this section that

this controller can be activated under a healthy three-phase mode of operation as well as under a faulty two-phase open-Delta mode of operation. Thus, another novel aspect of the introduced controller is that it enhances the "robustness" of an ac motor-drive system, and avoids inevitable system transients encountered at the instant of the transfer between two different control algorithms upon the detection of a faulty condition.

The design of these current control loops was described in detail in the sixth section of Chapter 3. First, different models for a three-phase induction machine were analyzed and investigated. These models have different orders as well as different degrees of complexity. The main incentive of this study was to utilize a simple model that can be used to design the newly introduced controller, without affecting the accuracy of the system. The study concluded that a first order model that is a function of stator and rotor resistances and leakage inductances is adequate to represent the motor transfer function for such types of applications, provided that the inverter's switching frequency is above 2 kHz. The design was mainly based on the well-known Bode-plot technique, and it was achieved using a commercial control design toolbox, namely MATLAB Control Design Toolbox. The theoretical system stability, open-loop response, as well as closed-loop response of the system were analyzed and discussed in this section.

Simulation models utilized in this work for preliminary verification of the concept and for examining the system's performance were described in Section 7 of Chapter 3. Two different simulation models were presented in this section. The first model is a time-domain simulation that includes the system's controller, a model of the drive's power circuit including the transistors' switching effects, and a lumped parameter model of the case study 5-hp motor. Meanwhile, the effects of MMF space harmonics and magnetic

circuit configuration, as well as magnetic nonlinearities due to saturation were not accounted for in that simplified model. On the other hand, the second model is a time-domain simulation that includes the system's controller implemented in MATLAB/Simulink coupled to a detailed Time Stepping Finite Element (TSFE) model that is implemented using a commercial software, namely MAGSOFT-Flux2D, in which the effects of MMF space harmonics and magnetic circuit configuration as well as magnetic nonlinearities due to saturation were rigorously accounted for. The main advantage of such a detailed model is to carryout a rigorous analysis that includes the interaction between the controller dynamics and airgap MMF space harmonics as well as nonlinear effects in the prototype machine. In addition, this model provided access to key magnetic quantities such as airgap flux density waveforms, and other magnetic field distributions throughout the magnetic circuit of the machine. The inverter's switching transients were not accounted for in this model due to limitations in the software and the excessive computational time that would be required to accommodate such switching transient events. However, the inverter was represented in this simulation as a controlled voltage source whose instantaneous time-domain output voltage was dictated by the controller-motor interaction.

The system's performance was validated using several simulation runs and experimental tests in Section 8 of this chapter. The results obtained from the simulation runs of the two previously mentioned models were compared to the results obtained from actual experimental tests of the prototype motor at a healthy three-phase mode of operation. This is to verify the validity of these simulation models and to examine the system's performance while the compensation controller was activated and the motor was

running under a healthy three-phase mode of operation. It was shown that the experimental results were in closer agreement to the results obtained from the coupled Simulink/ TSFE model. This is mainly due to the rigorous representation of the magnetic nonlinearities and effects of airgap MMF space harmonics that are higher than the fundamental component in this Simulink/TSFE model. It should be recalled that these harmonic components were not accounted for in the simpler Simulink/Simpowersystem model. It was also shown from these results that the effect of activating the compensation controller is not detectable under the healthy three-phase mode of operation which validates the analysis and results presented earlier in Chapter 3.

Another set of results was obtained when the prototype ac motor-drive system was running under two-phase open-Delta mode of operation while this newly introduced controller was activated, and when this controller was inactive. These results confirmed the validity of the present compensation strategy and demonstrated its efficacy in rendering a nearly balanced set of three-phase line currents with minimized output torque pulsations. This is in comparison to a significant unbalance that was observed in the motor line currents, with corresponding substantial pulsations in the output torque when the motor was tested under the same two-phase open-Delta mode of operation, while this controller was deactivated.

In Chapter 4, the newly introduced control strategy presented in Chapter 3 was extended for the case of vector-controlled (closed-loop) motor-drive systems. The basic principles of vector-controlled motor-drive systems were reviewed in this chapter. Also, in this chapter, several fault mitigation topologies pertaining to vector-controlled motor-drive systems were revisited and analyzed in more detail. This is in order to compare and

distinguish between the state of the art of the advances already achieved in this area, and the newly conceived control topology presented in this chapter. In this case, in addition to conventional current control loops in the CCW frame of reference that are provided to regulate a motor's torque and flux, two additional current control loops in the CW frame of reference were provided to compensate for unbalance effects resulting from the two-phase open-Delta mode of operation. Again, these two additional CW frame of reference controllers can be activated in both a healthy three-phase mode of operation and a faulty two-phase open-Delta mode of operation, without having any adverse effect on the quality of the performance of the motor-drive system operating under a healthy condition. This enhances the "robustness" of the system. This is because this approach avoids the inevitable transients that occur during the transfer between a control algorithm that is provided to control the machine under a healthy operating condition, and another control algorithm that is provided to control the machine under a faulty operating condition "fault mitigation algorithm". In the fifth section of Chapter 4, the design of the conventional current control loops in the CCW frame of reference, and the newly introduced current control loops in the CW frame of reference were discussed in detail. This design was achieved using the conventional Bode-plot technique, and a commercial control design toolbox, namely MATLAB Control Design Toolbox. The time-domain simulation models described in Chapter 3 for the case of open-loop motor-drive system control were extended to the case of the vector-controlled motor-drive system in this chapter.

The analysis presented earlier in this chapter was validated using numerous results obtained from several simulation runs as well as experimental tests. The validity of the simulation models were first examined through comparing the results obtained

from the simulation runs under a healthy three-phase mode of operation to the corresponding results obtained from the experimental tests conducted in the lab. Again, it was shown that the results obtained from the detailed TSFE model were in closer agreement with the results obtained from the experimental tests in comparison to the results obtained from the lumped parameter simplified model described earlier in Chapter 3. Then, the effect of the newly introduced controller on the system's performance was examined for a case in which the motor was running at a healthy three-phase mode of operation when this newly introduced controller was activated. It was shown that this controller does not have any detectable adverse effect on the system's performance while it is running under a healthy three-phase mode of operation. In addition, in this section, numerous results were obtained from several simulation runs as well as experimental tests under a faulty two-phase open-Delta mode of operation, when the newly introduced controller was activated, and when this controller was deactivated. These results demonstrated the effectiveness of the introduced controller in diminishing the unbalance in the motor's line currents, as well as minimizing the output torque pulsations that would have otherwise resulted from this faulty mode of operation had this controller not been activated. In addition, it was shown that conventional current control loops in the CCW frame of reference were able to suppress these output torque pulsations at low operating speeds, provided that the bandwidth of these current control loops is much higher than the frequency of these torque pulsations.

In Chapter 5, the case that involves an inter-turn short-circuit fault across one of the coils in the stator windings of the prototype machine was discussed. The analysis carried out in this chapter was supported by numerous simulation results obtained from

several simulation runs using the coupled Simulink/ TSFE model that was described earlier in Chapter 3. The model was modified to simulate a solid short-circuit fault across one of the coils in the stator windings. In this study, the monitored variables were the line currents, the circulating faulty loop current, the airgap flux density waveform, the airgap Magnetic Vector Potential (MVP) waveform and the motor torque. Also, in this chapter, a simplified theoretical analysis of a three-phase induction motor while one of the coils in the stator phase windings is shorted, was presented. This theoretical analysis showed that, in this case the faulty loop current will be only limited by the resistance and the leakage reactance of this shorted-coil. In addition, it was also shown that even if the phase which contains the shorted-coil was electrically isolated, and the motor was running under a two-phase open-Delta mode of operation, a voltage will still be induced in this shorted-coil. This is mainly due to the mutual coupling between this shorted-coil and the other energized coils in the machine. It was also shown that the faulty loop current is proportional to the magnitude of this induced voltage, which consequently depends on the motor operating conditions. This analysis also demonstrated that this induced voltage is proportional to the motor operating speed and operating flux. Moreover, in this chapter, it was shown that significant torque pulsations were produced by the pulsating field resulting from the circulation of the faulty loop current in this shorted-coil. The magnitude of these torque pulsations depends mainly on the magnitude of the faulty loop current and the number of shorted-turns.

Furthermore, the performance of an ac motor-drive system, while one of the coils in its stator phase windings is encountering a short-circuit fault, was studied and analyzed in Chapter 5 through simulations. This analysis was based on numerous results obtained

from several simulation runs at different operating conditions for the case of an open-loop control mode, and for the case of a vector-control mode. The simulation results showed that the motor operating speed and flux should be significantly reduced in order to minimize the induced voltage in the shorted-coil and consequently minimize the circulating faulty loop current. It was also shown that the newly introduced controller was able to suppress the torque pulsations resulting from the unbalance in the motor when this motor was running under a two-phase open-Delta mode of operation. However, torque pulsations resulting from the effects of the pulsating field produced by the circulation of the faulty loop current in this shorted-coil can not be suppressed by this newly introduced controller. However, the effect of the pulsating field on the torque quality can be minimized by reducing the magnitude of the faulty loop current in this shorted-coil. It was also shown in this chapter that conventional current control loops in the CCW frame of reference were able to significantly suppress the torque pulsations resulting from the unbalance in the motor, while it was running under two-phase open-Delta mode of operation. Thus, the newly introduced controller can be deactivated at low operating speeds without adversely affecting the system's performance in vector-controlled motor-drive systems.

6.3 Contributions and conclusions

The main three contributions of this work can be best summarized as follows:

- The first contribution is establishing a new theoretical foundation that can be utilized as a basis for an artificial intelligent algorithm to detect and identify the faulty phase and estimate the fault severity for inter-turn short-circuit

faults in polyphase induction motors. This technique does not require any additional hardware sensors to be installed in the machine, or knowledge of machine design details such as special wiring constrains, for the case of concentric wound machines. However, the knowledge of the winding layouts for cases of lap wound machines is necessary. The proposed technique has been verified through several simulation and experimental test results. This author believes that this technique could present a powerful tool which can be utilized in future research on prognosticating a faulty motor remaining life and providing fault mitigation strategies for this type of faults.

- The second contribution is the conception of a new theoretical foundation that can be utilized as a basis for an artificial intelligent algorithm to detect an inter-turn short-circuit fault in one phase of a stator winding of a polyphase induction motor energized from a vector-controlled drive. This technique enables one to overcome the fault masking difficulties associated with using conventional motor current signature analysis, or the concept of depending on the pendulous oscillations, which are observed between the conventional voltage and current space-vectors. This technique is based on a so-called "flux-pendulous oscillation" phenomenon being newly introduced here in this dissertation. This is in addition, and not to be confused with the magnetic field/MMF pendulous oscillation previously introduced and addressed in prior publications. The new fault detection approach was verified through experimental results which were presented here in this work.

- The third and main contribution is the conception of a new robust fault mitigation strategy that enables an inverter-fed three-phase induction motor with Delta-connected stator windings to operate under a two-phase open-Delta mode of operation, with a resulting set of nearly balanced line currents and minimized torque pulsations. This technique can be applied when one of the coils in a stator's phase windings encounters an open-coil fault due to winding rupture. Another application of this control technology is that when one of the coils in a stator's phase windings encounters an inter-turn short-circuit fault that has been diagnosed and isolated at an early stage of the fault. This is provided that the effect of this circulating current is not significant enough to represent a hazardous condition to the electrical installation. This technique was applied to a case study motor-drive system when operating in an open-loop control mode, and when operating in a vector-control mode. The efficacy of this control strategy has been verified through numerous results obtained from several simulation runs and corresponding experimental tests. The time-domain simulation model used in this work was based on utilizing a detailed coupled Simulink/ TSFE "Time Stepping Finite Element" model. The unique feature of this time-domain simulation model is that the controller dynamics and its' interaction with the motor's nonlinearities, such as airgap MMF space harmonics and saturation effects, are fully accounted for. The experimental results confirmed the results of the numerical simulations of this detailed TSFE-based model.

6.4 Recommendations for future work

As mentioned earlier in Chapter 1, diagnostics and robust control of ac motor-drive systems under faulty conditions is a rather complex and wide-ranging topic that can not be covered in one dissertation, but rather in continued research efforts. From this author's point of view, despite the above mentioned significant contributions to the areas of fault diagnostics and mitigation contained in this dissertation, there are still substantial amount of research tasks that can extend these contributions presented here further.

In this dissertation, a new technique for diagnosing inter-turn short-circuit faults in vector-controlled motor-drive systems has been presented. This technique may be further enhanced by means of monitoring the machine's developed airgap torque through use of a suitable torque observer based on using only terminal voltages and currents, while applying modern artificial intelligence techniques for decision making purposes.

Another contribution contained in this dissertation is that of a new control strategy that enables the operation of inverter-fed three-phase motors with Delta-connected stator windings in a two-phase open-Delta mode of operation, upon the failure of a coil in one of the three phases, without adverse line current unbalance and torque pulsation effects. As an extension of this work, it would be beneficial to industry to conduct and investigate the possibility of implementing a comprehensive diagnostic/fault mitigation system that integrates the benefits of this new control strategy introduced in this dissertation for tackling stator winding faults in Delta-connected motors, with the additional benefits of other research efforts that were mainly directed towards mitigating the effects of a failure

in one or more of the drive's power components, thus prolonging the operation of such faulty motor-drive systems with faults in both motor and drive.

In addition, a detailed study that is centered on the analysis of system transient performance at a faulty two-phase open-Delta mode of operation for applications that require frequent speed acceleration/deceleration and improved torque performance would be a very interesting topic for a future research in this area.

Moreover, the concepts and the methods introduced and verified in this dissertation should be extended to application to other types of ac three-phase machines such as field wound and permanent magnet synchronous ac machines and permanent magnet brushless dc machines. Therefore, one of the possible topics for future research in this area is to generally extend and experimentally verify the methods presented in this dissertation to applications that include wider classes of ac polyphase three-phase machines, including machines with inherently fault-tolerant designs, and analyze in depth extra losses that might be resulting from this mode of operation.

Appendix A

AN INSIGHT INTO THE CASE-STUDY MACHINE AND THE FINITE-ELEMENT MODELING

A.1 Introduction

The main design characteristics/particulars of the 5-hp prototype induction machine utilized in the experimental work of this dissertation are described in this appendix. This machine was specifically designed to operate from either a three-phase supply or a six-phase supply, which enhances the flexibility and reliability of the machine for this current as well as future research work. The machine can be reconfigured from six-phase operation to three-phase operation and vice-versa through changing the external connections of the windings. It should be highlighted that the machine is only briefly described here, thus interested readers should refer to reference [1] for a complete description of the machine design, modeling and analysis.

A.2 Motor design

The prototype machine was originally designed for the commercial market by Reliance-Electric as a three-phase, 6-pole induction machine. The original winding layout of this machine is shown in Table A.1. The machine has 36 stator slots, and 45 rotor bars with closed rotor slots as shown in Fig.A.1. The re-designed machine was based on the same stator core as the original design, thus the machine's mechanical dimensions, stator

and rotor slot geometries and numbers were not altered. In addition, it was also required/ stipulated that the new machine design should allow it to develop the same rated power as the original design. These design constrains implied a new six-phase stator winding layout with one slot per pole per phase (1 slot/pole/phase). The physical location of the coils of the winding in the stator slots is the same for the case of the three-phase connection-mode of operation and for the case of six-phase connection-mode of operation, except for the different phase labelings. The winding layout for the new design is shown in Table A.2 for the six-phase mode of operation and in Table A.3 for the three-phase mode of operation. In addition, the connection for the six-phase mode of operation is depicted in Fig.A.2a, see Table A.2. Meanwhile, the winding connection for the three-phase mode of operation is depicted in Fig.A.2b for a Wye-configuration and Fig.A.2c for a Delta-configuration, see Table A.3. The corresponding MMF waveforms for the winding layout of the modified three-phase mode are shown in Fig.A.3. In the design calculations, it was stipulated that the peak airgap design flux density is the same for both the three-phase and six-phase connection modes, see reference [1].

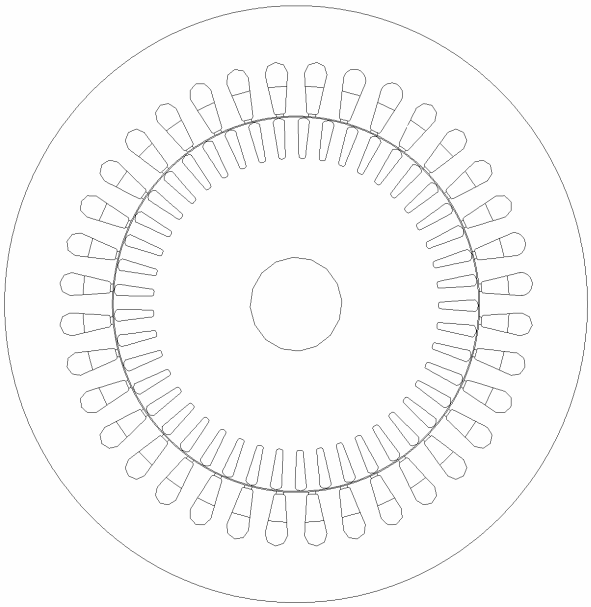

Fig.A.1 Geometry of the prototype 5-hp

	1	2	3	4	5	6	7	8	9	10	11	12	13	14	15	16	17	18
Top	A7	C5-	C6-	B8	B7	A1-	A2-	C12	C11	B1-	B2-	A12	A11	C1-	C2-	B12	B11	A3-
Bottom	A1	A2	C12-	C11-	B1	B2	A12-	A11-	C1	C2	B12-	B11-	A3	A4	C10-	C9-	B3	B4
	19	20	21	22	23	24	25	26	27	28	29	30	31	32	33	34	35	36
Top	A4-	C10	C9	B3-	B4-	A10	A9	C3-	C4-	B10	B9	A5-	A6-	C8	C7	B5-	B6-	A8
Bottom	A10-	A9-	C3	C4	B10-	B9-	A5	A6	C8-	C7-	B5	B6	A8-	A7-	C5	C6	B8-	B7-

Table A.1 Cross-Sectional view of stator slots showing the winding distributions of the three-phases for the short-pitched design (original design).

	1	2	3	4	5	6	7	8	9	10	11	12	13	14	15	16	17	18
Top	D5-	D6-	E5-	E6-	F5-	F6-	A1-	A2-	B1-	B2-	C1-	C2-	D1-	D2-	E1-	E2-	F1-	F2-
Bottom	A1	A2	B1	B2	C1	C2	D1	D2	E1	E2	F1	F2	A3	A4	B3	B4	C3	C4
	19	20	21	22	23	24	25	26	27	28	29	30	31	32	33	34	35	36
Top	A3-	A4-	B3-	B4-	C3-	C4-	D3-	D4-	E3-	E4-	F3-	F4-	A5-	A6-	B5-	B6-	C5-	C6-
Bottom	D3	D4	E3	E4	F3	F4	A5	A6	B5	B6	C5	C6	D5	D6	E5	E6	F5	F6

Table A.2 Cross-Sectional view of stator slots showing the winding distributions of the six-phase for the full-pitched design (modified winding layout).

	1	2	3	4	5	6	7	8	9	10	11	12	13	14	15	16	17	18
Top	A8	A7	C5-	C6-	B8	B7	A1-	A2-	C12	C11	B1-	B2-	A12	A11	C1-	C2-	B12	B11
Bottom	A1	A2	C12-	C11-	B1	B2	A12-	A11-	C1	C2	B12-	B11-	A3	A4	C10-	C9-	B3	B4
	19	20	21	22	23	24	25	26	27	28	29	30	31	32	33	34	35	36
Top	A3-	A4-	C10	C9	B3-	B4-	A10	A9	C3-	C4-	B10	B9	A5-	A6-	C8	C7	B5-	B6-
Bottom	A10-	A9-	C3	C4	B10-	B9-	A5	A6	C8-	C7-	B5	B6	A8-	A7-	C5	C6	B8-	B7-

Table A.3 Cross-Sectional view of stator slots showing the winding distributions of the three-phases for the full-pitched design (modified winding layout).

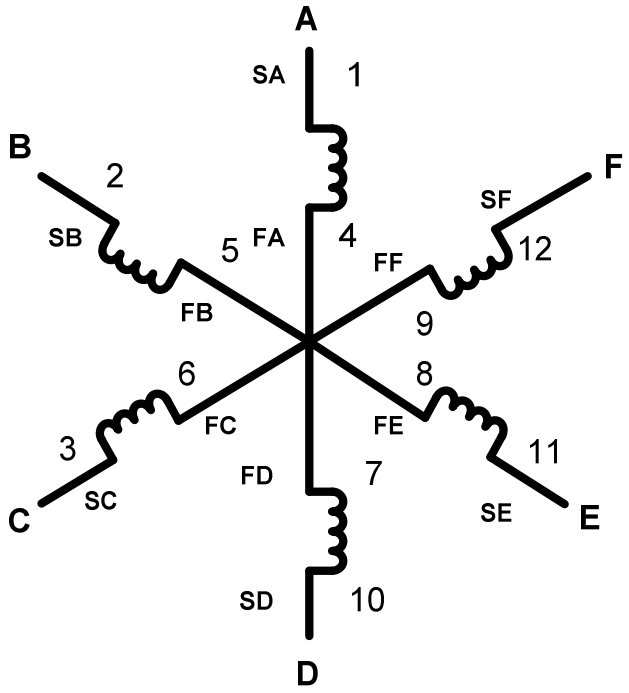

Fig.A.2a Winding connection for six-phase mode of operation.

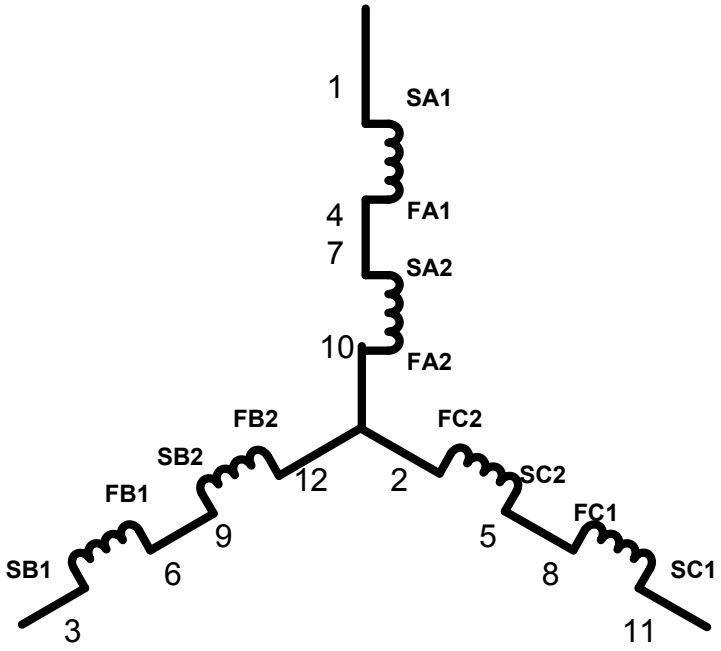

Fig.A.2b Winding connection for three-phase mode of operation (Wye-connection).

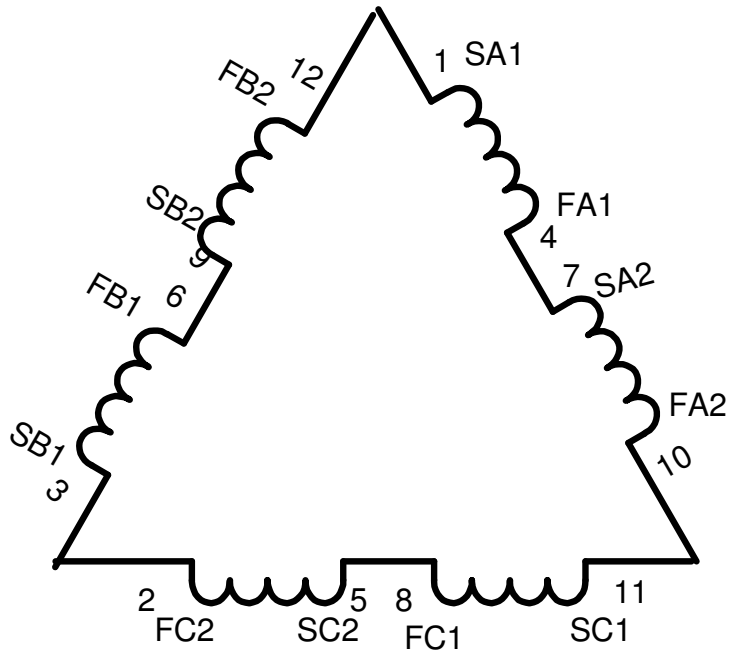

Fig.A.2c Winding connection for three-phase mode of operation (Delta-connection).

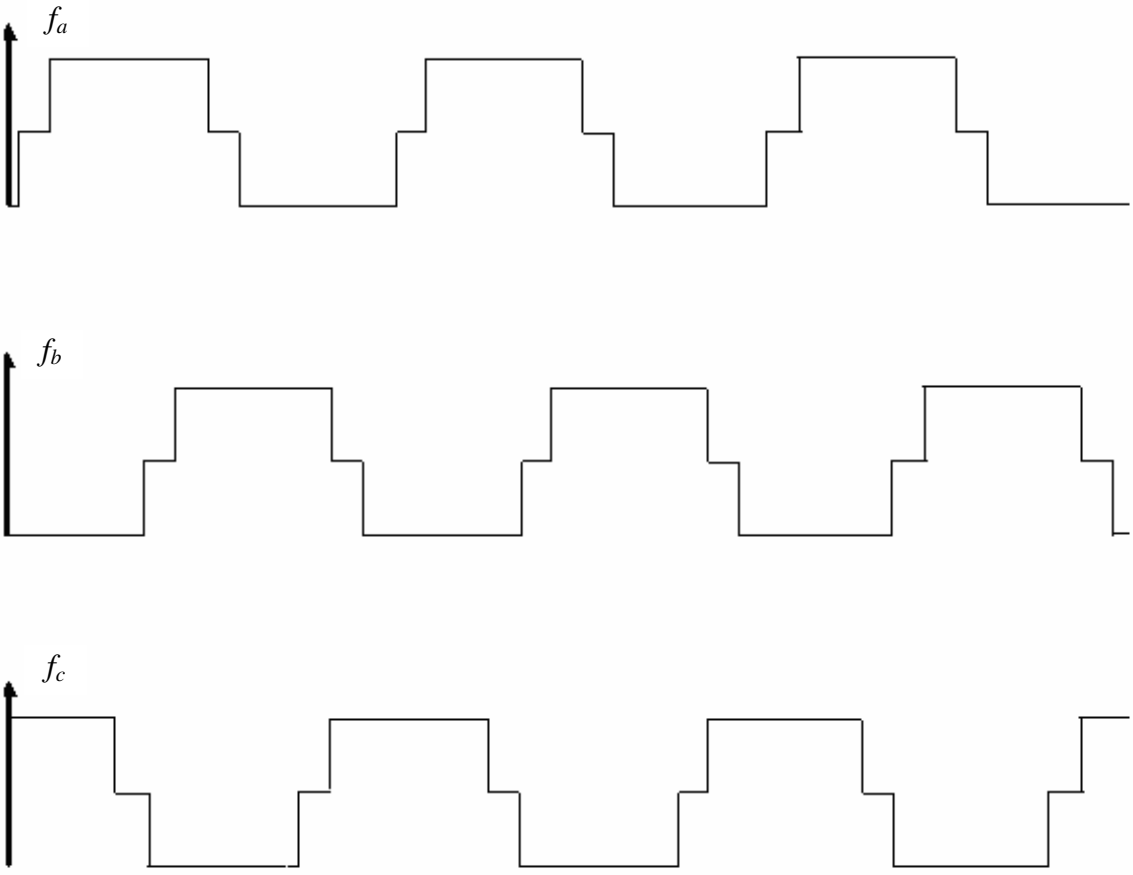

Fig.A.3 MMF distribution for the three-phase configuration (modified design).

Examining the MMF waveforms of Fig.A.3 shows that the design constrains for the new winding layout implied the existence of space harmonics with higher magnitudes in comparison to the original design because of the existence of a pitch factor in this original design. These space harmonics result in higher torque pulsations, increased time harmonics in the phase currents as well as the line currents, and increased leakage inductance, [2]. The machine design parameters are summarized in Table A.4

Rated power	5-hp
Stator Connection	Wye/Delta
Rated Voltage(line-to-line)	460/265 volt
Rated Current (line)	6.5/11.5 amps
Rated Frequency	60 Hz
Rated Speed	1185 rpm
Rated Torque	30 N.M
Phases	3/6
Number of Poles	6
Stator Resistance	1.2417
Rotor Resistance	1.0217
Stator Leakage inductance	0.00563277
Rotor Leakage inductance	0.0056
Magnetizing Inductance	0.21345

TableA.4 Design parameters of the 5-hp machine.

A.3 The Time-Stepping Finite Element (TSFE) Modeling

A.3.1 An overview

The Finite Element (FE) method is a "distributed-parameter/ fields-based" general approach that enables investigators to obtain a detailed insight into a device's performance in several engineering/science areas such as structures, fluid mechanics, thermal analysis, and electromagnetic analysis, etc. The application of the FE method in electromagnetic analysis and thermal analysis were shown over the last three to four decades to be efficient and reliable in electrical machine design and analysis work. The accuracy and the reliability of this technique enabled investigators to verify machine design/performance using in-depth simulations rather than relying on building expensive and time consuming prototypes. The main concept of this technique is to divide the physical domain of a device under study into small elements such that a numerical solution of the field variable can be found within each of these elements. The adequate number of elements depends on the complexity of the geometry and the required accuracy of the solution. It should be highlighted that the required computational power and memory utilization are proportional to the total number of elements covering the physical domain of the device being analyzed/ modeled. Generally, there are three main stages associated with any FE solution, [3]. The first stage is known as the pre-processing stage that includes inputting machine design specifications such as machine geometry including meshing the geometry or creating the finite element grid, material properties, boundary conditions, and if one is dealing with a time-stepping solution in the context of connecting an electrical machine at its terminals to external circuits, one needs to describe such external circuit configuration, etc. The second stage is the processing stage

which includes solving a set of partial differential equations that characterizes the physics of the problem in both space and time. The third stage is the post-processing stage in which final solutions can be obtained such as winding currents, flux plots, color shade plots of flux densities, etc. Nowadays, several commercial software packages [4-6] have been developed that only require the user to input the machine geometry and the details of the external circuit connection. The software is responsible for creating an adequate mesh for a given device/machine geometry, solving the system of equations and hence having the final results available for the user. These steps are all done without the need for an in-depth knowledge from the user about the details of the Time Stepping Finite Element (TSFE) technique. However, the user is required to have a full understanding of the problem under study and the main concepts of the TSFE technique. Instead of solving a problem at a certain time instant that corresponds to a specified rotor position, the TSFE solution simulates the entire system performance (machine and external circuit) at successive time instants that correspond to numerous numbers of rotor versus stator positions, which cover a sufficient period of time that reaches steady state ac cyclical variation of all the state variables, covering at least one or more ac cycles of operation. In the TSFE model, the equation of motion can be also included into the system of equations if a motor starting transient or sudden load changes are being studied. This is achieved through performing four consequent steps at each time instant. These steps can be summarized as follows, [3-6]:

- Solve Maxwells' equations and compute the electromagnetic torque acting on a machine's rotor at a given rotor position at a given time instant.

- Solve the rotational dynamic equation of motion, and compute the speed and the acceleration at the same time instant. Compute the new position of the rotor for the next time step.
- Move the rotor to the new position, and re-mesh the physical domain covering the device's cross-section at the new rotor position. Check whether steady state has been reached, if yes end.
- If no, steady state has not been reached, return to the first step and repeat.

A.3.2 Finite element formulation

A commercial software package, namely "MAGSOFT-Flux2D", was used in this dissertation to carryout the TSFE analysis of the machine under study. As elaborated in Chapters 3 and 4, the TSFE model is linked to the control algorithms implemented in MATLAB/ Simulink using Flux2D to Simulink technology, see reference [7]. The basic principles of the transient electromagnetic field solution, upon which the formulation of Flux2D is based, are briefly described in the next paragraph. Most of these principles are general electromagnetic field concepts upon which other software tools available in the market are based, [3-6].

The equations used in the Flux2D software can be divided into two sets. The first set is Maxwells' equations, and the second set is the constitutive equations that describe properties of materials. Maxwells' equations in a domain without moving bodies are as follows, [3]:

$$\nabla.\vec{D} = \rho \quad \text{(Maxwell-Gauss)} \tag{A.1}$$

$$\nabla \times \vec{E} = -\frac{\partial \vec{B}}{\partial t} \quad \text{(Maxwell Farady)} \tag{A.2}$$

$$\nabla.\vec{B} = 0 \quad \text{(Gauss law for magnetism)} \tag{A.3}$$

$$\nabla \times \vec{H} = \vec{J} + \frac{\partial \vec{D}}{\partial t} \quad \text{(Maxwell-Ampere)} \tag{A.4}$$

In the above equations, $\vec{D}$ is the electric flux density (displacement), ρ is the electric charge density, $\vec{E}$ is the electric field intensity, $\vec{B}$ is the magnetic flux density, $\vec{H}$ is the magnetic field intensity, and $\vec{J}$ is the conduction current density.

The constitutive equations that describe the characteristics of the material are as follows, [3]:

$\vec{J} = \sigma\vec{E}$, characteristic of conducting media. (A.5)

$\vec{B} = \mu\vec{H}$ or $\vec{H} = \upsilon\vec{B}$, characteristic of magnetic media. (A.6)

$\vec{D} = \varepsilon\vec{E}$, characteristic of dielectric media. (A.7)

In the previous equations, σ is the electrical conductivity of the material, μ is the magnetic permeability, υ is the magnetic reluctavity , and ε is the electrical permittivity.

There are mainly three types of applications associated with electromagnetic field problems. These are: Magnetostatic, Electromagnetic AC steady state, and Transient-Electromagnetic. The Magnetostatic problem is an application in which the magnetic field is produced by a DC current or stationary current. Practical examples of this application may be force computation in magnetic bearings and electromagnetic contactor, calculation of self inductance and mutual inductance and magneticfield solutions for a given set of excitation currents at a given instant in time in a device, etc. The second application is the AC steady state magnetic application that allows studying

devices at sinusoidal steady state operating conditions. This application takes into account the current induced in the conduction region (eddy current) skin effect. In this application, all of the computed physical quantities are sinusoidally time varying in nature and are expressed using their phasor complex numbers. Nonsinusoidal time varying physical quantities can be treated as a summation of series of sinusoidal time varying quantities with different frequencies and phase shifts. Typical simulation examples are steady state analysis, induction heating, etc. The third application is the Transient-Electromagnetic problem which is quite similar to Magnetostatic but the physical quantities are time dependent. It was found that the Transient-Electromagnetic method is the most adequate for the purposes of the work presented in this dissertation. This is due to the fact that in this approach the simulation model did include interaction between the control system implemented in MATLAB/ Simulink and the TSFE model of the electrodynamics of the electrical machine, as well as the mechanical motor-load system dynamics. In this application, the computation is concerned only with the magnetic flux density, $\vec{B}$, the magnetic field intensity, $\vec{H}$, and the electric field intensity, $\vec{E}$. On the other hand, due to the low frequencies associated with these types of problems, the displacement current density, $\frac{\partial \vec{D}}{\partial t}$, is always considered negligible. Meanwhile, the magnetic vector potential, $\vec{A}$, can be defined as follows:

$$\vec{B} = \nabla \times \vec{A} \tag{A.8}$$

From (A.8), one can write the following:

$$\vec{B} = \mu \vec{H} = \nabla \times \vec{A} \tag{A.9}$$

Hence,

$$\vec{H} = \frac{1}{\mu}(\nabla \times \vec{A}) = \upsilon(\nabla \times \vec{A}) \tag{A.10}$$

Upon substituting for $\vec{H}$ from (A.10) into (A.4) with the neglect of the $\frac{\partial \vec{D}}{\partial t}$ term gives:

$$\nabla \times \vec{H} = (\nabla \times \frac{1}{\mu}(\nabla \times \vec{A})) = (\nabla \times \upsilon(\nabla \times \vec{A})) = \vec{J} \tag{A.11}$$

Recall that:

$$\nabla \times \vec{E} = -\frac{\partial \vec{B}}{\partial t} = -\frac{\partial(\nabla \times \vec{A})}{\partial t} \tag{A.12}$$

Hence, one can express the electric field intensity, $\vec{E}$, as a the time domain derivative of the magnetic vector potential, $\vec{A}$, and the gradient of an electric scalar potential, ∇V as follows,[3]:

$$\vec{E} = (\frac{\partial \vec{A}}{\partial t} + \nabla V) \tag{A.13}$$

Upon which from (A.5), one can write :

$$\vec{J} = \sigma(\frac{\partial \vec{A}}{\partial t} + \nabla V) \tag{A.14}$$

Hence substituting (A.14) into (A.11) yields:

$$(\nabla \times \frac{1}{\mu}(\nabla \times \vec{A})) = (\nabla \times \upsilon(\nabla \times \vec{A})) = \sigma(\frac{\partial \vec{A}}{\partial t} + \nabla V) \tag{A.15}$$

The partial differential formulation of (A.15) is solved within MAGSOFT-Flux2D package to yield the magnetic vector potential, $\vec{A}$, at each node in the FE grid at all time instants (rotor positions) within the solution period of time . See references [3-9] for details.

A.3.3 The Finite Element modeling of the prototype machine

Mainly, the TSFE modeling includes three main stages; the pre-processing stage, the processing stage, and the post-processing stage. As mentioned earlier, the TSFE model includes all of the machine design details such as winding layout, machine geometry, magnetizing and saturation characteristics of the stator core and rotor core. Therefore, the model includes MMF space harmonics, saturation effects, and slot leakage inductance effects associated with the shape of the stator and rotor slots. Therefore, an accurate description of the machine geometry, magnetic materials, and winding layout are necessary to obtain the sought results. These details are entered into Flux2D through the pre-processor module "Geometry & Physics". In this module, the geometry of the problem is divided into regions and faces which are consequently divided to finite number of elements. In addition, the discretized region must be bounded in the two-dimensional x-y plan in which external boundary conditions must be specified. For example, a Dirichlet boundary condition, [3], was assigned to the outer surface of the machine as shown in the machine geometry depicted in Fig.A.4. Also, examining Fig.A.4 demonstrates the variation in the mesh density in the different region throughout the machine cross section. It can be noticed that a very fine mesh is required in the airgap region and its surrounding regions because of the high concentration of magnetic field stored energy in this region. In addition, it is highly desirable to obtain elements as close as possible to equilateral triangles to avoid numerical errors due to ill-conditioning. Meanwhile, coarse meshing can be utilized in regions towards the motor shaft and towards the outer surface of the stator core. Notice that it is not desirable to have

unnecessary fine meshing where it may not be required, because this fine meshing may increase the required processing time and memory utilization unnecessarily.

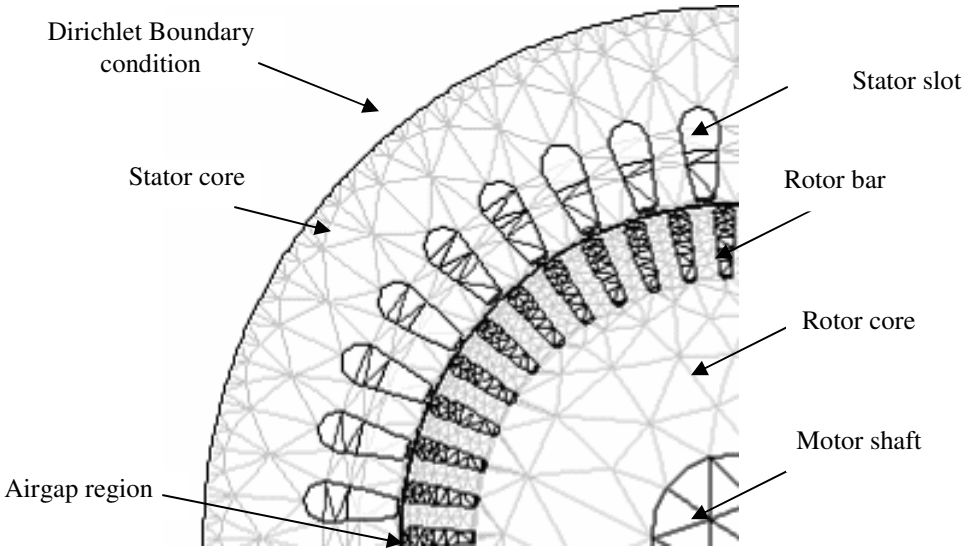

Fig.A.4 Geometry mesh for the 5-hp prototype machine.

The second step in the machine modeling is to build the circuit associated with the winding connection. The circuit diagram consists of voltage sources, the motor's stator coils and the rotor circuit as shown in Fig.A.5. It can be noticed from Fig.A.5 that the stator windings are connected in Delta. Coils BA1 through BA12 are connected in series in order to constitute phase A. Meanwhile, coils BC1 through BC12 are connected in series in order to constitute phase C, and coils BB1 through BB12 are connected in series to constitute phase B. In additional to the stator coils, two virtual resistors are added to the circuit, R4 to simulate a short-circuit fault across coil BC9, and R5 connected in series with phase C, to be used as a switch to electrically isolate phase C. The second step in the pre-processing stage is to link the coils defined in the circuit to their corresponding physical location in the geometry of the machine. This process is very similar to placing the winding coils in the stator slots in an actual manufacturing process. At this point, the

machine dimensions and winding connections are completely defined and ready for the second stage.

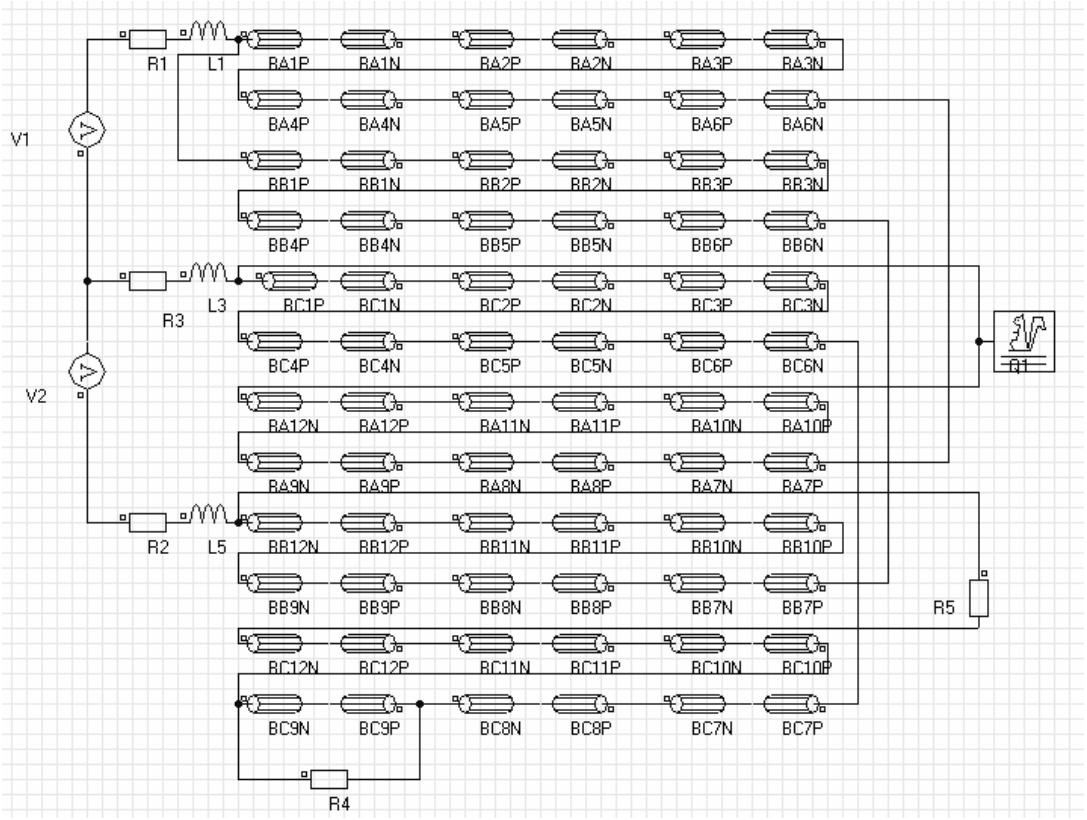

Fig.A.5 Circuit connection for the 5-hp prototype machine.

In the second stage, the defined problem is solved by a proper solver-engine in Flux-2D. The solution is carried out in sequence of time steps as described earlier in Chapter 3. The user is required to set the time duration of the simulation and the corresponding step size. Choosing an adequate time step is mainly dependent on the dynamics of the system under study. The solution process is delineated in several references such as [3, 8] for interested readers.

The third and last stage is the post-processing stage in which the results are made available for the user for analysis and inspection. As shown in Chapters 3, 4 and 5, in addition to the motor line, phase, and winding currents, The TSFE method avails to the

user other key magnetic quantities such as the nodal magnetic vector potentials, flux densities, equi-magnetic vector potential flux lines (flux plots), developed electromagnetic torque, core losses, etc. Some of these physical quantities have been utilized to gain an insight into the machine performance under various operating conditions throughout the work of this dissertation. It should be mentioned that not all of these physical quantities are calculated during the solving process. Mainly, the magnetic vector potentials are calculated from the partial differential equation of (A.15), consequently the other physical quantities can be calculated in the post-process stage based on (A.8) for flux densities, (A.10) for the field intensities, (A.14) for the current densities, [9].

Bibliography:

[1] Anushree Anantharaman Kadaba, "Design and Modeling of a Reversible 3-Phase to 6-Phase Induction Motor for Improved Survivability under Faulty Conditions" M.S., Department of Electrical and Computer Engineering, Marquette University, May 2008

[2] Ion Boldea , and Syed A. Nasar " The induction machine handbook", CRC press LLC, 2002.

[3] Chari M.V.K, and Silvester P.P. "Finite Elements in Electrical and Magnetic Field Problems " J.Wiley & Sons, New York, 1980

[4] Ansoft corporation, "MAXWELL2D brochure", www.ansoft.com

[5] Magsoft, " Flux2D brochure" , www.magsoft.com

[6] Magneforce, "MAGNEFORCE brochure", www.magneforce.com

[7] Cedrat, "Flux2D to Simulink user manual", www. cedrat.com

[8] Joao Pedro A.Bastos, Nelson Sadowski "Electromagnetic modeling by finite element methods" Marcel Dekker, 2003

[9] Cedrat, " Flux2D user manual", www.cedrat.com

Appendix B

EXPERIMENTAL PROTOTYPE AND DSP CONTROL IMPLEMENTATION

B.1 Introduction

The experimental prototype utilized to verify the theoretical and simulation results of this dissertation is described in this appendix. The hardware design details of the power converter were delineated in [1], therefore it will only be briefly described here. The main focus of this appendix is to discuss key subjects that are very important for the implementation of the control algorithms discussed in this dissertation in a fixed-point processor. This is in order to enable the replication of this work if required for further study and analysis. The control architecture described in Chapters 3 and 4 of this dissertation can be implemented in several types of modern DSP chips. However, the DSP chip TMS320F2812 was utilized here as a typical example of modern DSP chips available nowadays in the market.

B.2 Prototype architecture overview

The experimental prototype consists of the following:

- Power converter
- Pre-charge circuit.
- Gate drive circuit.
- Current transducers and associated signal conditioning circuit.

- DSP based control board
- The test motor
- A DC-dynamometer with associated torque transducer

The power converter is a 15-hp IGBT based ac drive manufactured by Cutler-Hammer which was integrated into a pre-charge circuit and a gate drive circuit to form the power structure of the drive. The pre-charge circuit utilized was a resistor connected in series with the drive to guarantee a smooth charging of the dc-link capacitor during the power-up stage. This resistor is manually bypassed by a contactor after the dc-link capacitors are charged. The gate drive circuit consists of a 3.3V to 5V level shifter and gate drive module, SKHI 61, which has an integrated instantaneous over-current protection. The three-phase line currents were measured using three current transducers model , LF-305s, in conjunction with the proper signal conditioning circuit that is connected to the DSP chip which has a built-in ADC that can support up to 16 analog inputs through a multiplexer. Again, the hardware design details are described in [1] and therefore will not be repeated here. The power converter utilized in this work is shown in Fig.B.1a while the prototype motor described earlier in Appendix A is shown in Fig.B.1b

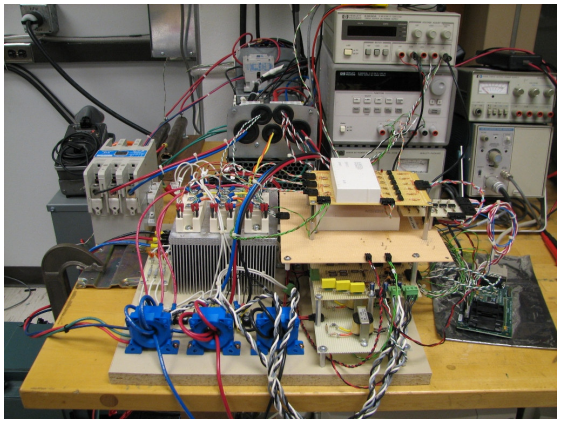

Fig.B.1a Power converter utilized in the experimental testing

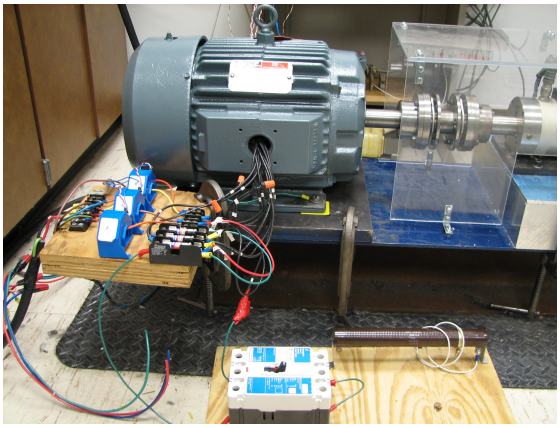

Fig.B.1b Case study motor utilized in the experimental set up

TMS320F2812 main features

The main features of this DSP can be summarized as follows, [2-8]:

1. 150MHz clock.
2. 128 K Flash memory
3. 18K Static RAM.
4. Motor control peripherals: Two event managers which can generate pulse width modulation, space vector PWM, several interrupts, etc.
5. 12 Bit ADC, 16 channels.
6. Two serial communications interface SCI, standard UART.
7. Software development tools debugging/ emulation through CCS and XDS510 emulator or any other emulator that can support the C2000 family.
8. A virtual floating point engine IQ Math Library.
9. Motor control library that includes several functions that are commonly used in motor control applications.
10. Supported by embedded Real Time Workshop / Target Support Package provided by Mathworks/Matlab that provides very simple means for DSP programming using automatic code-generation.

Torque measurement:

The torque measurement was a key element in the experimental phase of this research in order to examine system performance under a healthy three-phase mode of operation and a faulty two-phase mode of operation. This measurement was mainly achieved using a torque transducer that is mechanically coupled to the motor shaft from the Drive End (DE) side. Flexible coupling were utilized in the set-up to couple the

motor's DE to the torque transducer and the torque transducer to the DC Dyne DE. The torque transducer details are summarized in Table B.1

Torque transducer model	MCRT-2904T
Signal conditioner and amplifier	66042
Signal conditioner bandwidth	500 Hz
Torque meter installation	Foot mounted

Table B.1. Torque transducer main data

B.3 Description of the algorithm program that controls the state machine

The operation of the control system is controlled through a pre-programmed state machine. The state machine usually handles the sequence of operations of the interrupt service routines and the process of reading the analog signals. The state machine includes several stages which are mainly the initialization stage, sampling the analog signals, algorithms for execution of the control scheme, loading the corresponding PWM registers, and finally back to sampling the analog signals. Each of these states is briefly described below:

Initialization:

The initialization stage is the first executed routine as it controls the operation of the DSP along with its peripherals. The initialization code is usually included in the main program. This stage includes setting the DSP registers to determine the clock frequency,

the operation of the analog to digital converters, hardware interrupt service routines, configuring the digital outputs and digital inputs, setting the PWM channel, and inverter switching frequency. This is in addition to other peripherals such as serial communication, direct memory access, etc. The routine is usually ended by an infinite for-loop. This infinite for-loop is interrupted by an Interrupt Service Routine "ISR" which causes the program counter of the processor to jump to the address of the code that includes the main control algorithms. In this work, the ISR was set to execute the control algorithm every 100μsec for the case of open-loop control and every 200μsec for the case of vector-controlled closed-loop control. The frequency of the control algorithms depend on several factors such as the required system performance, maximum switching frequency, and code execution time.

The initialization process of the control software utilized in the experimental prototype can be summarized in the main following points:

- Initialize main clock & peripherals' clocks
  - Set the main high speed clock to 150MHz.
  - Set the low speed clock to 37.5 MHz.
  - Set the ADC clock to 25MHz.
- Initialize the PWM peripheral
  - Enable the timer associated with the PWM
  - Set the switching frequency to 5 kHz for closed-loop control system and 10 kHz for open-loop.
  - Set a dead time of 4μsec to prevent overshooting between two transistors in the same leg.

- Initialize the analog to digital module
  - Enable and power up ADC peripheral.
  - Set ADC to start conversion on the event of under flow of the PWM counter
  - Set an interrupt on the event of end of conversion. This interrupt was used to invoke the main control algorithms
- Initialize the main variables and program constants

Sampling of the analog input signals:

It was described earlier in Chapters 3 and 4 of this dissertation, that the three-phase line currents should be sampled and processed by the control algorithms. Sampling of analog signals requires special attention to guarantee proper operation of the control algorithms. The DSP chip TMS320F2812 has a built-in 16 analog input 12bit channels through two independent multiplexers. Each multiplexer is connected to a sample & hold unit which are consequently connected to one ADC converter with a conversion time of 80ns, [2]. The DSP has the capability of sampling the 16 channels either in sequential mode or simultaneous mode with the capability of sampling two channels simultaneously, [3]. The sequential mode is to sample the first channel, then sample the second channel, and so on. In simultaneous mode channel 1 and channel 9 are simultaneously sampled, and then channel 2 and channel 10 are simultaneously sampled, and so on. Generally, it is of paramount importance to sample the analog input current signals simultaneously or fast enough such that input current values processed by the control algorithm are captured approximately at the same time instant. Here, channel 1

"line current A", channel 9 "line current B", and channel 2 "line current C" were set to be sampled in cascade mode one after another, fast enough in order to avoid degradation of the control system performance. The acquisition window "the period of which the sampling circuit is connected to the measured signal" should allow enough time to allow the interface circuit to correctly capture the instantaneous value of the input signal. On the other hand, it should be also fast enough to allow fast sampling of the other analog signals. It was found that an acquisition window of 640 nsec guarantee proper and fast sampling of the current signals. Another important factor that should be considered when sampling analog signals is to maximize the signal to noise ratio especially in a noisy operating environment like a variable speed drive which includes hard switching from positive dc-bus to negative dc-bus in hundreds of nanoseconds. The switching frequency is usually in the range of 2 kHz-20 kHz depending on the application and the design of the power structure. The interruption of the current in the IGBT devices at switching instants cause ElectroMagnetic Interference noise (EMI) due to the inevitable existence of the parasitic inductances in the circuit. This noise affects and distorts the measured analog signals and may propagate to the control algorithms and affect the controller performance or it might lead to system instability. Therefore, the analog signals should be sampled at the time instants such that there are no switching events such as the time instants of the underflow or overflow of the PWM modulator as shown in Fig.B.2.

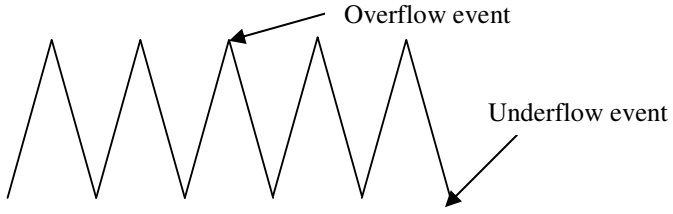

Fig.B.2 PWM counter under flow and over flow interrupt events

Main Interrupt Service Routine:

The interrupt is an event that causes the program to invoke and execute a specific algorithm. The DSP chip TMS320F2812 can handle several interrupts that can be user programmed and prioritized based on the user requirement, [6]. These interrupts can also control the DSP peripherals such as ADCs, serial communications, etc. The code which contains the main control algorithms resides in an interrupt called the main ISR. This ISR can be invoked in several scenarios as described in [6]. The description here is limited to the implementation of the control algorithms in the experimental phase of this dissertation. It was mentioned earlier that the input current signals should be sampled at the time instant of an underflow event or an overflow event of the PWM modulator's counter. Therefore, the DSP was programmed to initiate an ISR on the event of the underflow of the PWM modulator's counter. This ISR starts the operation of the ADC. Meanwhile, the ADC peripheral is programmed to invoke the main ISR, which contains the main control algorithm, upon the end of the conversion process. The DSP was programmed such that the main ISR is invoked every 200μsec for the case of vector-controlled closed-loop and every 100μsec for the case of open-loop control. It is very critical to verify that the execution time of the main ISR is less than the time between two interrupts. The state machine for the program is outlined in Fig.B.3.

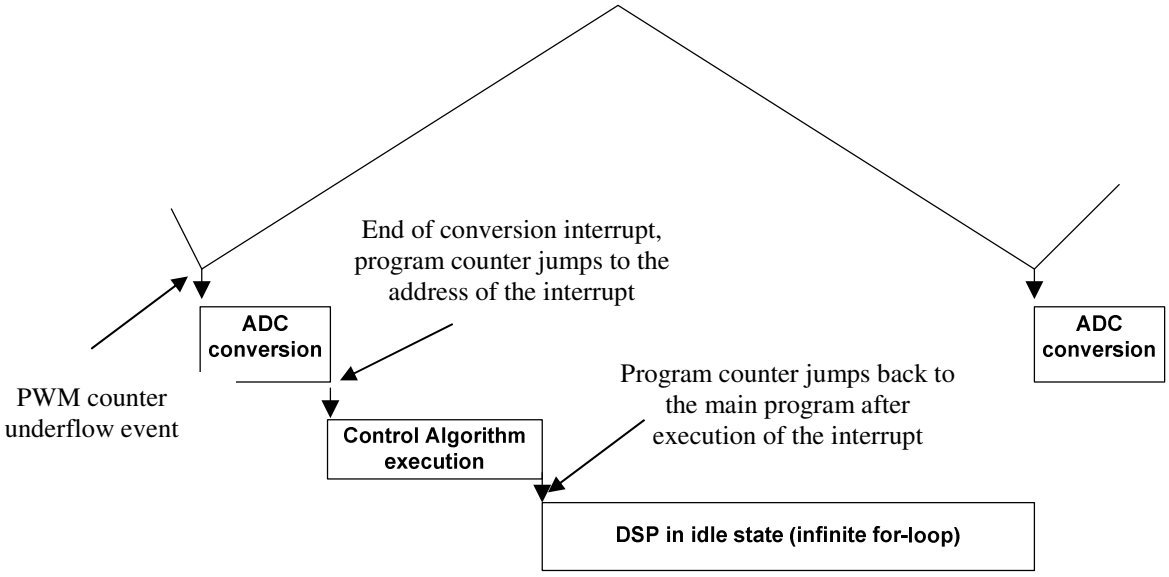

Fig.B.3 Software sequence of events (not drawn to scale)

Therefore, the sequence of the software operation is to start the ADC on an underflow event of the PWM counter, the current signals are sampled and loaded to the corresponding registers. The values in these registers are read and processed by the control algorithms in each execution cycle. The ADC initiates an interrupt at the end of each conversion event. This interrupt invokes the code implementing the main control algorithms described earlier in Chapter 3 for the case of open-loop control mode and in Chapter 4 for the case of closed-loop control mode. The values of the reference signals for the next execution cycle are then loaded to the PWM comparator shadow registers, these values are then uploaded from the comparator shadow registers to the comparator main registers to be compared with the carrier signal, [9].The execution speed and memory utilization of the software control algorithms for both cases, open-loop control and closed-loop control, are summarized in Table B.2.

Program	Execution time	Memory	Compensation Algorithm execution time	Compensation Algorithm Memory
Open loop without comp. algorithm	13.6µsec	2.950K		
Open loop with comp. algorithm	21.6µsec	3.233k		
			8µsec	0.283k
Vector control without comp. algorithm	25.6µsec	3.288k		
Vector control with comp. algorithm	34µsec	3.597k		
			8.4µsec	0.309k

Table B.2 Algorithm execution time and memory utilization.

B.4 Programming with a fixed point processor

In most applications, the main theoretical concept is verified using preliminary simulation studies that can give the investigator an initial step to verify the concept of operation. In most cases, these simulations are run on a computer program using floating point processors. Then, after verifying the concept through simulation, the next stage is to implement an experimental prototype to validate the concept of operation in the real-world. At this stage, the immigration of a control algorithm that is implemented in computer based simulation software to a fixed point DSP requires special attention taking other factors into consideration. These factors are fixed point arithmetic manipulation, numerical dynamic range, word length, quantization effects, and additional digital filters if required, [7].

Fixed point processors are designed to support operations with only integer data. These processors are usually very fast and they have the lowest price by Million Instruction Per Second (MIPS), [7]. On the other hand, these processors have a limited dynamic range. In addition, conventional ANSI C code that converts floating point numbers to fixed point code results in an extensive computation code with an increased

memory and execution time. For this reason, TI has supported these fixed point DSPs with a virtual floating point library rather than depending on the standard ANSI C floating point library. It was shown in [7] that utilization IQmath-Library is more efficient in memory and speed rather than utilizing the floating point standard ANSI C compiler. The IQ math library provides the user with several representations of the floating point number to a 32-bit fixed-point data-type. The designer has to pick the adequate formatting based on the required resolution and the required dynamic range. For instance, _IQ1 has a dynamic range from -1073741824 to 1073741823.500000000 with a resolution of 0.5, and _IQ30 has a dynamic range from -2 to 1.999999999 with a resolution of 0.000000001 , [8], the question is that which one we should choose in a motor control algorithm implemented on a fixed point processor.

It can be noticed that although _IQ1 has a very wide dynamic range, the corresponding resolution is very low. That will make the control algorithm unstable. On the other hand, _IQ30 has a very good resolution but the dynamic range is very limited which makes it very probable that the registers may overflow. In both cases, the routine might be unstable and may cause unexpected performance. Now, let us consider _IQ22, in this case the dynamic range is from -512 to 511.999999762 with a resolution of 0.000000238. This dynamic range is sufficient enough for motor control applications. At the same time, the resolution of 0.000000238 provides a sufficient accuracy for the control algorithm. Therefore, this data presentation was chosen in the implementation of the code of the control system in the experimental prototype used in the work of this dissertation. In addition to choosing the right data representation, efficient code practices to prevent overflow can be followed. For example, the designer should have an

approximate idea about the range of the numbers, and therefore limiters can be used to guarantee that the instantaneous values of the variables in this control will not exceed the range of these limiters and cause overflow. It is also very important to make sure that the results of any multiplication or division will not lead to erroneous results or overflows. It is also recommended to filter the input analog signals with first order digital low pass filters with a reasonable cut-off frequency in order to prohibit propagation of noise to the control algorithm.

Bibliography:

[1] Chia-Chou Yeh "Fault tolerant operation of induction motor-drive systems" Ph.D. dissertation, Department of Electrical and Computer Engineering, Marquette University 2008.

[2] Texas Instruments, "TMS320F2812 Data Manual", SPRS174O.

[3] Texas Instruments, "TMS320X281X Analog-to-Digital (ADC) Converter Reference Guide", SPRU060B.

[4] Texas Instruments, "Code Composer Studio Development tools V3.3", SPRU590H.

[5] Mathworks, "Target Support Package C2000, User's Guide".

[6] Texas Instruments, "TMS320x281x DSP, System Control and Interrupts, Reference Guide", SPRU078D.

[7] Texas Instruments, "Comparing fixed- and floating-point DSPs", SPRY061.

[8] Texas Instruments, "IQ Math library, Module User's Guide"

[9] Texas Instruments, " Event Manager, Module User's Guide"

BIBLIOGRAPHY

[1] Nicola Tesla, “Electric Motor”, Dec 3 1889, US Patent No.416,194.

[2] Ion Boldea , and Syed A. Nasar “ The induction machine handbook”, CRC press LLC, 2002.

[3] Russel J.Kerkman, Gary L.Skibinski, and David W.Schlegel “AC drives: year 2000 (Y2K) and beyond” Applied power electronics conference and exposition, 1999, APEC’99

[4] W.Schockley “Circuit element utilizing semiconductor material”, Sept 25 1951, US Patent No.2,569,347

[5] Michael Riordan “How Europe missed the transistor” IEEE Spectrum Vol.42, issue 11, Nov.2005, pp.52-57.

[6] Philip T.Krein “Elements of power electronics” Oxford University Press, 1998.

[7] D.Grahame Holmes, and Thomas A.Lipo “Pulse width modulation for power converters, principles and practices” IEEE series on power engineering, 2003.

[8] F. Blaschke, “A new method for the structural decoupling of A.C. induction machines,” in Conf. Rec. IFAC, Duesseldorf, Germany, Oct. 1971,pp. 1–15.

[9] K. Hasse, “Drehzahlgelverfahren fÄur schnelle umrichterantriebe mit stromrichtergespeisten asynchron – urzschlusslÄaufermotoren”, Regelungstechnik, pp. 60-66, 1972.

[10] M. Akamatsu, K.Ikeda, H.Tomei, and S.Yano “ High performance IM drive by coordinate control using a controlled current inverter” IEEE Transactions on Industry Applications, 1982, IA-18 382-392.

[11] F.Loeser and P.K.Sattler “Identification and compensation of the rotor temperature of a.c. drives by an observer” IEEE Transaction on Industry Applications, 1985, IA-21, pp.1387-1393

[12] P.P. Acarnley, and J.W. Finch“ Review of control techniques for field orientation in ac drives” 22 Universities Power Engineering conference,1987, Sunderland, paper 9.08

[13] A.Fratta, A.Vagatti, and F. Villata “Vector control of induction motors without transducers” IEEE power electronics specialists conference, 1988, Kyoto, pp. 839-846

[14] P.Vas “Vector control of ac machines” Oxford university press, 1990

[15] A.Ferrah, K.J.Bradley, and G.M Asher “Sensoreless speed detection of inverter fed induction motors using rotor slot harmonics and fast Fourier transforms” IEEE Power Electronics Specialists meeting,1992, pp.279-286

[16] P.Vas “Electrical machines and drives: a space-vector theory approach” Oxford university press,1992

[17] H.Grotstollen, and J.Wiesing “ Torque capability and control of a saturated induction motor over a wide range of flux weakening” IEEE Transaction on Industrial electronics, Vol.42,1995, pp.374-381

[18] Y.R.Kim, and S.K.Sul “ Maximum torque control of an induction machine in the field-weakening region” IEEE Transaction on Industrial Applications,Vol.31,No.3, 1995, pp.787-794

[19] H.Hofman, S.R.Sanders and C.Sullivan“ Stator-flux-based vector control of induction machines in magnetic saturation” IEEE Industrial Application Society meeting, 1995,Orlando, pp.152-158.

[20] Brian J.Seibel, Russel J.Kerkman, and Timothy M.Rowan “Transient inductance tune for motor control” US patent 5,965,995, Oct.1999

[21] Alberto Abbondanti, and Michael B.Brennen “Variable speed motor drives use electronic slip calculator based on motor voltages and currents” IEEE Transactions on Industry Applications, Vol.IA-11, No.5, Sept/Oct 1975, pp.483-488.

[22] Allen Bradley Bulletin 1336 plus slip compensation, Application note # 1336S-20, www.ab.com

[23] Torma, “Slip compensation method in a squirrel cage induction motor” ,U.S patent 5463302.

[24] Siemens, “MM410 user manual”, www.siemens.com

[25] P. Vas “Sensoreless vector and direct torque control”, Oxford science publications, 1998

[26] Bimal Bose “ Modern power electronics and AC drives” Prentice Hall PTR, 2002

[27] Russel J. Kerkman, David Leggate, and Gary L. Skibinski “Interaction of drive modulation and cable parameters on AC motor transients” IEEE Transactions on Industry Applications Vol.33, No.3 May/June 1997, pp.722-731.

[28] David Leggate, Jeff Pankau, David W. Schlegel, Russel J. Kerkman, and Gary L. Skibinski “Reflected waves and their associated current” IEEE Transactions on Industry Applications Vol.35, No.6 Nov/Dec 1999, pp.1383-1392.

[29] Gary L. Skibinski, Russel J. Kerkman, David Leggate, Jeff Pankau, and David W. Schlegel “Reflected wave modeling techniques for PWM AC motor drives” Applied Power Electronics Conference and Exposition, 1998. APEC '98. Conference Proceedings 1998., Thirteenth Annual.

[30] Doyle Busse, Jay Erdman, Russel J. Kerkman, Dave Schlegel, and Gary Skibinski “Bearing currents and their relationship to PWM drives” IEEE Transactions on Power Electronics, Vol.12, No.2, March 1997,pp.243-252.

[31] Rockwell Automation “Inverter-driven induction motors shaft and bearing current solutions” Industry white paper,www.ab.com.

[32] Shaotang Chen, and Thomas A. Lipo “Bearing currents and shaft voltages of an induction motor under hard- and soft-switching inverter excitation” IEEE Transactions on Industry Applications, Vol.34, No.5, Sep/Oct 1998,pp.1042-1048.

[33] Russel J. Kerkman, Jeff Theisen, and Kirti Shah “PWM inverters producing torsional components in ac motors” IEEE PCIC 2008, 55th

[34] Gary L. Skibinski, Russel J. Kerkman, and Dave Schlegel “EMI emissions of modern PWM AC drives” IEEE Industry Application Magazine, Vol.5, No.6, Nov/Dec 1999, pp.47-81 .

[35] Qian Liau “Modular approach for characterizing and modeling conducted EMI emissions in power converters” Ph.D dissertation, Blacksburg ,Virginia, Nov 2005.

[36] Jaroslaw Luszcz, and Krzysztof Iwan “Conducted EMI propagation in inverter-fed ac motor” Electrical power quality and utilization, Magazine, Vol.II, No.1, 2006.

[37] Bhim Singh, G.Bhuvaneswari, and vipin Garg “ Power quality improvements in vector-controlled induction motor drive employing pulse multiplication in AC-DC converters” IEEE Transaction on Power Delivery,Vol.21, No.3, July 2006, pp.1578-1586.

[38] Kurf Stockman, Frederik D’hulster , Jan Desmet, and Ronnie J.M. Belmans “ Torque behavior of A RFO induction motor drive under voltage sag conditions”,10th international conference on Harmonics and Quality of power,2002, Vol.1,pp. 359-364.

[39] C. Klumpner, and F. Blaabjerg, "Experimental evaluation of ride-through capabilities for a matrix converter under short power interruptions," IEEE Trans. on Industrial Electronics, Vol. 49, No.2, April 2002, pp. 315-324

[40] IEEE Committee Report, “Report of large motor reliability survey of industrial and commercial installation, Part I and Part II,” IEEE Transactions on Industry Applications, vol.21, July/August 1985, pp.853-872.

[41] “IEEE Guide for AC Motor Protection”, IEEE std C37.96-2000, Sponsor: Power system relaying committee of the IEEE power engineering society.

[42] Mark Fenger, Steven R.Campbell, and Jan Pedersen “Motor winding problems” IEEE Industrial Application Magazine, July/August 2003.

[43] J. Sottile and J. L. Kohler, “An on-line method to detect incipient failure of turn insulation in random-wound motors,” IEEE Transaction on Industry Applications, Vol. 28,No.4 , Jul./Aug. 1992, pp. 921–937 .

[44] J. Penman, H. G. Sedding B. A. Lloyd, and W. T. Fink “Detection and location of interturn short circuits in the stator winding of operating motors,” IEEE Transaction on Energy Conversion, Vol. 9,No.4, Dec. 1994, pp. 652-658.

[45] G. M. Joksimovic and J. Penman “The Detection of Inter-turn Short Circuits in the Stator Windings of Operating Motors,” IEEE Trans. On Industrial Electronics, Vol. 47, No.5, Oct. 2000, pp.1078-1084.

[46] S.M.A. Cruz, and A.J.M. Cardoso, "Stator winding fault diagnosis in three-phase synchronous and asynchronous motors, by the extended Park’s vector approach,"

IEEE Transactions on Industry Applications, Vol.37, No.5, September/October 2001, pp.1227-1233.

[47] Marcus Alex Cash, and Thomas G. Habetler "Insulation Failure Prediction in AC Machines Using Line–Neutral Voltages" IEEE Trans. On Industrial Applications, Vol. 34, No.6 Nov./Dec 1998, pp.1234-1239.

[48] A. Stavrou, H. G. Sedding, and J. Penman "Current Monitoring for Detecting Inter-Turn Short Circuits in Induction Motors," IEEE Transaction on Energy Conversion, Vol. 16, No.1, March 2001, pp.32-37.

[49] Sergio M.A.cruz, and A.j.Marques Cardoso "Diagnosis of stator inter-turn short circuit s in DTC induction motor drives" IEEE Transaction on Industry Applications, Vol. 40, No.5 Sept/Oct 2004,pp.1349-1360.

[50] Rangarajan M. Tallam "Current-based sensoreless detection of stator winding turn faults in induction machines" Ph.D. Dissertation, Georgia Institute of Technology 2001.

[51] Subhasis Nandi, and Hamid A. Toliyat "Novel frequency-domain-based technique to detect stator interturn faults in induction machines using stator-induced voltages after switch-off" IEEE Transaction on Industry Applications, Vol.38, No.1, Jan/February 2002, pp.101-109.

[52] Rangarajan M. Tallam, Thomas G. Habetler, and Ronald G. Harley "Stator winding turn-fault detection for closed-loop induction motor drives" IEEE Transaction on Industry Applications, Vol.39, No.3, May/Jun 2003,pp.720-724.

[53] Sang-Bin Lee, Rangarajan M. Tallam, and Thomas G. Habetler "A Robust, On-Line Turn-Fault Detection Technique for Induction Machines Based on Monitoring the Sequence Component Impedance Matrix" IEEE Transaction on Power Electronics, Vol.18, No.3, May 2003,pp. 865-872.

[54] B. Mirafzal, and N.A.O. Demerdash, "On innovative methods of induction motor inter-turn and broken-bar fault diagnostics" IEEE Transaction on Industry Applications, Vol.42, No.2, March/April 2006 ,pp.405-414

[55] S. Nandi, H. A. Toliyat, and X. Li "Condition Monitoring and Fault Diagnosis of Electrical Motors-A Review," IEEE Transaction on Energy Conversion, Vol. 20, No.4, Dec. 2005, pp.719-729.

[56] Behrooz Mirafzal "Incipient Fault Diagnosis in Squirrel-Cage induction Motor" Ph.D. Dissertation, Department of Electrical and Computer Engineering Marquette University 2005.

[57] R. Romary, R. Corton, D. Thailly and J.F. Brudny "Induction machine fault diagnosis using an external radial flux sensor" The European Physical Journal Applied Physics.Issue: 32 ,pp.125-132 (2005).

[58] Marian Dumitru Negrea "Electromagnetic flux monitoring for detecting faults in electrical machines" Ph.D. Dissertation , Helsinki University of Technology 2006.

[59] John David Heinzmann, John B.Morrell, and Jason Michael sachs "Model based fault-detection in a motor drive" US patent number 7,091,724 B2, 2006.

[60] J. Aguayo, A. Claudio, L.G. Vela, and S. Gentile "Stator winding-fault detection for the induction motor drives" Proceedings of Electronics, Robotics and Automative mechanics conference, IEEE 2006

[61] Noah Bethel, PDMA corporation " Fault zone analysis "stator"" Revolutionizing electrical reliability magazine, 2nd Quarter 2002, www.pdma.com

[62] Rangarajan M. Tallam, Sang Bin Lee,Greg C. Stone,Gerald B. Kliman, Jiyoon Yoo, Thomas G. Habetler, and Ronald G. Harley "A survey of methods for detection of stator-related faults in induction machines" IEEE Transaction on Industry Applications, Vol. 43, No.4, July/August 2007, pp.920-933.

[63] Allen Bradley, PowerFlex 700 user manual , http://www.ab.com/drives/

[64] ABB , ACS600, https://www.abb-drives.com/StdDrives

[65] M. Aníbal Valenzuela, Juan A. Tapia, and James A. Rooks "Thermal evaluation for TEFC induction motors operating on frequency-controlled variable-speed drives" IEEE Trans. Industrial Applications, Vol.40, No.2, March/April 2004,pp.692-698.

[66] S. Williamson, and A. C. Smith, "Steady state analysis of 3-phase cage motors with rotor broken bar and end ring faults," IEE Proc., Vol.129,No.3, May 1982, pp.93-100.

[67] W. Deleroi, "Squirrel cage motor with broken bar in the rotor-Physical phenomena and their experimental assessment," in Proc. of International Conference on Electrical Machines, September 1982, pp.767-700.

[68] S. Williamson, and K. Mirzoian, "Analysis of cage induction motors with stator winding faults," in Conference record of IEEE-PES, 1984.

[69] S. Williamson and K. Mirzoian, "Analysis of cage induction motors with stator winding faults," IEEE Transaction on Power Apparatus System, Vol.PAS-104,No.7, July 1985, pp.1838-1842

[70] G.B. Kliman, R.A. Koegl, J. Stein, R.D. Endicott, and M.W., "Noninvasive detection of broken rotor bars in operating induction machines," IEEE Transaction on Energy Conversion, Vol.3,No.4,December 1988, pp.873-879

[71] N.M. Elkasabgy, A.R. Eastham, and G. E. Dawson, "Detection of broken bars in the cage rotor on an induction machine," IEEE Transactions on Industry Applications, Vol.28,No.1, January/February 1992, pp.165-171.

[72] P. Vas, Parameter Estimation, Condition Monitoring and Diagnosis of Electrical Machines, Oxford University Press, 1993.

[73] A. Cardoso, S. Cruz, J.F.S. Carvalho, and E. Saraiva, "Rotor cage fault diagnosis in induction motors by Park's vector approach," in Conference record of IEEE-IAS Annual Meeting, Orlando, FL, October 1995, pp.642-646.

[74] R.R. Schoen, and T.G. Habetler, "Evaluation and implementation of a system to eliminate arbitrary load effects in current-based monitoring of induction machines," IEEE Transactions on Industry Applications, Vol.33, No.6, November/December 1997, pp.1571-1577.

[75] Caryn M. Riley, Brian K. Lin, Thomas G. Habetler, and Randy R. Schoen "A method for sensorless on-Line vibration monitoring of induction Machines" IEEE Transactions on Industry Applications, Vol.34, No.6, Nov/Dec 1998, pp.1240-1245.

[76] R. Wieser, C. Kral, F. Pirker, and M. Schagginger, "On-line rotor cage monitoring of inverter-fed induction machines by means of an improved method," IEEE Transactions on Power Electronics, Vol.14,No.5 , September 1999, pp.858-865.

[77] D. Kostic-Perovic, M. Arkan, and P. Unsworth, "Induction motor fault detection by space vector angular fluctuation," in Conference record of IEEE-IAS Annual Meeting 2000, pp.388-394.

[78] F. Filippetti, G. Franceschini, C. Tassoni, and P. Vas, "Recent developments of induction motor drives fault diagnosis using AI techniques," IEEE Transactions on Industrial Electronics, Vol.47,No.5, October 2000, pp.994-1003.

[79] A. Bellini, F. Filippetti, G. Franceschini, and C. Tassoni, "Closed-loop control impact on the diagnosis of induction motors faults" IEEE Transactions on Industry Applications, Vol.36, No.5, September/October 2000,pp.1318-1329.

[80] A. Bellini, F. Fillippetti, G. Franceschini, C. Tassoni, and G.B. Kliman, "Quantitative evaluation of induction motor broken bars by means of electrical signature analysis" IEEE Transactions on Industry Applications, Vol.37,No.5, September/October 2001, pp.1248-1255.

[81] M. Haji, and H.A. Toliyat, "Pattern Recognition-A technique for induction machines rotor broken bar detection" IEEE Transactions on Energy Conversion, Vol.16, No.4, December 2001, pp.312-317.

[82] F.C. Trutt, J. Sottile, and J.L. Kohler, "Online condition monitoring of induction motors" IEEE Transactions on Industry Applications, Vol.38, No.6, November/December 2002, pp.1627-1632.

[83] A. Bellini, F. Filippetti, G. Franceschini, C. Tassoni, R. Passaglia, M. Saottini, G. Tontini, M. Giovannini, and A. Rossi, "On-field experience with online diagnosis of large induction motors cage failures using MCSA" IEEE Transactions on Industry Applications Vol.38, No.4 July/August 2002, pp.1045-1053.

[84] R. Bartnikas, and R. Morin "Multi-Stress aging of stator bars with electrical, thermal, and mechanical stresses as simultaneous acceleration factors" Trans. On Energy Conversion, Vol.19, No.4, Dec 2004, pp.702-714.

[85] Ming Xu, and Tom Alford "Motor current analysis and its applications in induction motor fault diagnosis" Enterk IRD web site

[86] Austin H. Bonett & Timothy Albers "Motor bearing systems" IEEE Industry Application Magazine, Sept /Oct 2002, pp.58-73.

[87] R.F. Schiferl and M.J Melfi "Bearing current remediation options" IEEE Industry Application Magazine, July /August 2004, pp.40-50.

[88] G. Gentile, N. Rotondale, and M. Tursini " Investigation of inverter-fed induction motors under faulty conditions" Power Electronics Specialists conference, Vol.1, July 1992.

[89] Debaprasad Kastha, and Bimal K. Bose "Investigation of fault modes of voltage-fed inverter system for induction motor drive" IEEE Transactions on Industry Applications, Vol.30, No.4, July/August 1994, pp.1028-1038.

[90] Michael L. Gasperi "Life prediction modeling of bus capacitors in AC variable-frequency drives" IEEE Transactions on Industry Applications, Vol.41, No.6, Nov/Dec 2005, pp.1430-1435.

[91] R. S. Alwitt, and R.G. Hills "The chemistry of failure of aluminum electrolytic capacitors" IEEE Transactions on Parts, Materials and Packaging, Vol.1, No.2, Sep 1965, pp.28-34.

[92] Hao Ma, and Linguo Wang "Fault diagnosis and failure prediction of aluminum electrolytic capacitors in power electronic converters" Industrial Electronics Society, IECON 2005. 31st Annual Conference of IEEE, pp. 6-10

[93] Afroz M. Imam, "Condition monitoring of electrolytic capacitors for power electronics applications" Ph.D dissertation, Georgia Institute of Technology, May 2007

[94] CDE Cornell Builder "Application Guide, Aluminum Electrolytic Capacitors" http://www.cde.com/

[95] Sam G. Parler "Selecting and applying aluminum electrolytic capacitors for inverter applications" White paper, http://www.cde.com/

[96] Gerhard Mitic, and Guy Lefranc "Localization of electrical-insulation and partial-discharge failures of IGBT modules" IEEE Transactions on Industry Applications, Vol.38, No.6, Jan/Feb. 2005,pp.175-180.

[97] Chih-Chieh Shen, Allen R. Hefner, David W. Berning, and Joseph B. Bernstein "Failure dynamics of the IGBT during turn-off for unclamped inductive loading conditions" IEEE Transactions on Industry Applications, Vol.36, No.2, March/April 2000, pp.614-624.

[98] " Fuji IGBT Application Manual", http://www.fujisemiconductor.com

[99] R. S. Chokhawala, J. Catt, and L. Kiraly, "A discussion on IGBT short-circuit behavior and fault protection schemes" IEEE Transaction on Industry Applications, Vol. 31,No.2 , Mar./Apr. 1995, pp. 256–263.

[100] T.Jahns " Improved reliability in solid-state drives for large asynchronous ac machines by means of multiple-independent phase-drive units" Ph.D thesis, MIT , Cambridge,Apr.1978

[101] T.Jahns "Improved reliability in solid-state drives for large asynchronous ac machines by means of multiple-independent phase-drive units" IEEE Transaction on Industry Applications,Vol.1A-16, No.3, May/June 1980

[102] Lawrence W. Langley et al "Motor with redundant windings" US patent number 4,434,389.Feb 28,1984

[103] Jayant G. Vaidya "Redundant multiple channel electric motors and generators" Us patent number 4,550, 267.Oct 29, 1985

[104] Sebastiao E.M de Oliveira "Operation of three-phase induction motors connected to one phase supply" IEEE Transaction on Energy Conversion, Vol.5, No.4, Dec.1990, pp.713-718

[105] Parasad N.Enjeti, and Wajiha Shireen "A new technique to reject DC-link voltage ripple for inverters operating on programmed PWM waveforms" IEEE Transaction on power electronics, Vol.7, No.1, January 1992, pp.171-180.

[106] M.Chomat and L.Schreier "Control method for DC link voltage ripple cancellation in voltage source inverter under unbalanced three-phase voltage supply conditions" IEEE IEMDC , Vol.2, June 2003, pp.869-875.

[107] Jiri Klima, "Analytical investigation of influence of dc-link voltage ripple on PWM VSI fed induction motor drive", IEEE ICIEA 2006.

[108] Jinhwang Jung, Sunkyoung Lim, and Kwanghee Nam " A feedback linearization control scheme for a PWM converter-Inverter having a very small dc link capacitor" IEEE Transaction on Industry Application, Vol.35, No.5, Sept./Oct. 1999, pp.1124-1131

[109] Tian-Hua Liu, Jen-Ren Fu, and Thomas A.Lipo " A strategy for improving reliability of field-oriented controlled induction motor drives" IEEE Transaction on Industry Applications, Vol.29, No.5, Sept/Oct 1993, pp.910-918.

[110] T.Elch-Heb, and J.P. Hautier " Remedial strategy for inverter-induction machine system faults using two-phase operation" Power Electronics and Applications 1993,13-16 Sept 1993, pp 151-156, Vol.5

[111] M.G.Say "The performance and design of alternating current machines" Sir ISAAC Pitman & sons. LTD. 1965

[112] Jen-Ren Fu, and Thomas A. Lipo "Disturbance-free operation of a multiphase current-regulated motor drive with an opened Phase" IEEE Transactions on Industry Applications, Vol.30, No.5, Sept./Oct. 1994, pp.1267-1274.

[113] Debaprasad Kastha, and Bimal K. Bose "Fault mode single-phase operation of a variable frequency induction motor drive and improvement of pulsating torque characteristics" IEEE Transactions on Industrial Electronics, Vol.41, No.4, August 1994,pp.1151-1156.

[114] Debaprasad Kastha, and Bimal K. Bose "On-line search based pulsating torque compensation of a fault mode single-phase variable frequency induction Motor Drive" IEEE Transactions on Industry Applications, Vol.30, No.4, July/August 1995, pp.463-470.

[115] Colin Huggett, and Gabor Kalman "Fault tolerant variable speed induction motor drive" US patent number 5,568,034. Oct 22,1996.

[116] Bradley A. Targo, and Robert E. Lordo "Fault tolerant electric machine" US patent number 5,929,549.Jul.27,1999

[117] James A.Haylock, Barrie C.Mecrow, Alan G.Jack and David J.Atkinson "Operation of fault tolerant machine with winding failures" IEEE Transaction on Energy Conversion, Vol.14, No.4, Dec 1999.

[118] Raymond B.Seper Jr., and John Miller "Fault tolerant operation of induction motor drives with automatic controller reconfiguration" Electric Machine and Drives conference 2001, IEMDC 2001 ,pp.156-162

[119] R.L.A.Ribeiro, C.B.Jacobina,E.R.C da Silva, and A. M. N. Lima "A fault tolerant motor-drive system by using a compensated strategy on the PWM-VSI topology" IEEE Power Electronics Specialists Conference, 2001,pp.1191- 1196.

[120] N.Erturgi, W.soong, G.Dostal, and D.Saxon "Fault tolerant motor drive system with redundancy for critical applications" Power Electronics Specialists Conference 2002, Vol.3, pp.1457-1462.

[121] James Stanley Smith and Abdul Rehman Bilal "Synchronous machine fault tolerant arrangement" US Patent No. 6,504,281 B1.Jan.7, 2003.

[122] Brian A. Welchko, Thomas M. Jahns, and Thomas A. Lipo "Short-circuit fault mitigation methods for interior PM synchronous machine drives using six-leg inverters" The 35th Annual PESC, 2004, pp.2134-2140

[123] Brian A. Welchko, Thomas A. Lipo, Thomas M. Jahns, and Steven E. Schulz "Fault tolerant three-phase AC motor drive topologies: A comparison of features, cost, and limitations" " IEEE Transactions on Power Electronics, Vol.19, NO.4, July 2004, pp.1108-1116.

[124] C. Gerada , K. J. Bradley , M. Sumner , and P. Wheeler "Operating induction motor drives with turn to turn faults" IEEE IEMDC 2005, May 2005, pp.770-776

[125] Steven E.Schulz, Nitinkumar R.Patel,James M.Nagashima, Yu-Seok Jeong, and Seung Ki Sul "Methods and apparatus for fault-tolerant control of electric machines" US Patent No.6,989,641 B2.Jan.24, 2006

[126] Brian A.Welchko, Jackson Wai, Thomas M.Jahns, and Thomas Lipo "Magnet flux nulling control of interior PM machine drives for improved response to short-circuit faults" IEEE Transaction on Industry Applications Vol.42,No.1, Jan/Feb 2006, pp.113-120.

[127] Youngkook, and Habetler "A stator turn fault tolerance strategy for induction motor drives in safety critical applications" Power Electronics Specialists Conference, 2006, PESC'06 ,37th IEEE.

[128] J.E.Timperley " Root cause analysis of machine stator failures" Doble Engineering Strategies, www.doble.com

[129] M.Kaufhold, G.Borner, M.Eberhardt, and J.Speck "Failure mechanism of the interturn insulation of low voltage electric machines fed by pulse controlled inverters" Electrical Insulation and Dielectric Phenomena Conference 1995, pp.254-257.

[130] R.S. Miranda, H.A.Toliyat, C.B.Jacobina, and A.M.N lima "Short-circuit fault mitigation in six-phase induction machine drives" IEEE Vehicle Power and Propulsion Conference 2007, pp.370-376.

[131] Gui-Jia Su, John W.Mckeever, and Kelly S.Samons " Design of a PM brushless motor drive for hybrid electrical vehicle application" PCIM 2000, MA, October 1-5, 2000.

[132] Ayman M.ElRafie, and Manoj R.Shah "Comparison of induction machine performance with distributed and fractional-slot concentrated windings" IEEE Industry Applications Society meeting, 2008.

[133] Z.Q.Zhu, K.Utaikaifa, K.Hoang,Y.Liu, and D.Howe " Direct torque control of three-phase PM brushless AC motor with one phase open-circuit fault" Electric Machine and Drives conference 2009, IEMDC 2009 ,pp.1408-1415

[134] Ayman EL-Rafie " Fault-tolerant PM machines: A review" Electric Machine and Drives conference 2009, IEMDC 2009 ,pp.2063-2071

[135] Paul C.Krause, and James R.Hakes "Method of multiple reference frames applied to rectifier-inverter induction motor-drive system" IEEE Transaction on Power Appartus and Systems, Vol. PAS-88, No.11, November 1969.

[136] Kyung-Hwan Kim, Nam-Joo park, and Dong Seok Hyun " Advanced synchronous reference frame controller for three-phase UPS powering unbalanced and nonlinear loads" IEEE PESC 2005, pp.1699-1704

[137] IEEE Standard for Petroleum and Chemical Industry-Sever Duty Total Enclosed Fan Cooled (TEFC) Squirrel Induction Motors –up to and Including 370KW (500 hp), std-841-2001

[138] G.C. Montanari "Aging and life models for insulation systems based on PD detection" IEEE Transaction on Dielectrics and Electrical Insulation, Vol.2, No.4, August 1995, pp.667-675.

[139] P.Cygan, and J.R. Laghari "Models for insulation aging under electrical and thermal multistress" IEEE Transaction on Electrical Insulation, Vol.25. No.5,October 1990, pp.923-934

[140] G.Mazzanti, and G.C.Montanari "Electrical aging and life models: the role of space charges" IEEE Transaction on Dielectrics and Electrical Insulation, Vol.12,No.5, October 2005, pp.876-890

[141] Jean-Pierre Crine, and Laurent Lamarre "A tentative model for electrical aging of the insulation of rotating machines" IEEE Annual Report Conference on Electrical Insulation and Dielectric Phenomena,2004, pp.283-285

[142] John D.Kueck, Howard D Haynes, and Robert H. Staunton " Stator insulation degradation test uses ASD switching frequency" IEEE Power Engineering Review, January 2007

[143] Austin H.Bonnet "A comparison between insulation systems available for PWM-inverter-fed motors" IEEE Transaction on Industry applications, Vol.33, No.5, September/October 1997, pp.1331-1341

[144] Weijun Yin "Failure mechanism of winding insulations in inverter-fed motors" IEEE Electrical Insulation Magazine, Vol.13, No.6, November/December 1997, pp.18-23

[145] Mike Melfi, A. M. Jason Sung, Sidney Bell, and Gary L. Skibinski, "Effect of Surge Voltage Risetime on the Insulation of Low-Voltage Machines Fed by PWM Converters," IEEE Transaction on Industry Applications, Vol. 3, No.4, July/August, 1998, pp.766-775.

[146] Magsoft Flux2D Finite Element Software, www.magsoft-flux.com.

[147] Lícia Neto Arruda, Sidelmo Magalhães Silva, and Braz J. Cardoso Filho "PLL structures for utility connected systems" Industry Applications Conference, 2001. Thirty-Sixth IAS Annual Meeting. Conference Record of the 2001 IEEE

[148] Guan-Chyun Hsieh, and James C. Hung "Phase-locked loop techniques-a survey" IEEE Transaction on Industrial Electronics, Vol. 43, No. 6, Dec. 1996,pp.609-615.

[149] Brian A. Welchko, Thomas M. Jahns, and Thomas A. Lipo "IPM synchronous machine response to a single-phase open circuit fault" IEEE Transaction on Power Electronics Vol.17,No.5,September 2002, pp.764-770.

[150] Mathworks " Simpowersystem tool box, user manual"www.mathworks.com

[151] A.E.Fitzgerald, Charles Kingsley, Stephen D.Umans "Electric Machinery" sixth edition, MC Graw Hill, 2003.

[152] Paul C.Krause " Analysis of Electric Machinery" McGraw-Hill Book Company, 1986

[153] Nabeel Demerdash, "EECE123 class notes", Marquette University.

[154] Chen "Analog & Digital control system design", Saunders College Publishing,1993

[155] Nabeel Demerdash, "EECE 285 class notes", Marquette University

[156] Nabeel Demerdash, "EECE 281 class notes", Marquette University.

[157] J. F. Bangura, and N. A. O. Demerdash, "Comparison between characterization and diagnosis of broken bars/end-ring connectors and airgap eccentricities of

induction motors in ASD's using a coupled finite element-state space method", IEEE Transactions on Energy Conversion, Vol. 15, No.1, March 2000, pp 48-56.

[158] J. F. Bangura, and N. A. O. Demerdash, "Effects of broken bars/end-ring connectors and airgap eccentricities on ohmic and core losses of induction motors in ASDs using a coupled finite element-state space method", IEEE Transactions on Energy Conversion, Vol. 15, No.1, March 2000, pp 40-47.

[159] J. F. Bangura, "Diagnosis of Normal and Abnormal Operations of Induction Motors in ASDs by a Coupled Finite Element-Network Technique" Ph.D. dissertation, Department of Electrical and Computer Engineering, Marquette University, August 1999.

[160] Anushree Anantharaman Kadaba, "Design and Modeling of a Reversible 3-Phase to 6-Phase Induction Motor for Improved Survivability under Faulty Conditions" M.S., Department of Electrical and Computer Engineering, Marquette University, May 2008

[161] William L.Brogan "Modern Control Theory" Third Edition, Prentice-Hall Inc.1991

[162] Mathworks " Control Design tool-box, user manual" www.mathworks.com

[163] CEDRAT, Flux2D to Simulink User Manual , www. Cedrat.com

[164] Texas Instrumentations, "ezdsp F2812, Technical Reference" , www.ti.com

[165] Ahmet Hava, "Carrier Based PWM-VSI Drives in The Overmodulation Region" Ph.D dissertation, University of Wisconsin Madison, 1998

[166] Texas Instrumentation "DMC library, Technical Reference", www.ti.com.

[167] William T.Thomson, and Mark Fenger "Current signature analysis to detect induction motor faults" IEEE industry application magazine, July/August 2001, pp.26-34.

[168] William T.Thomson "On-line MCSA to diagnose shorted turns in low voltage stator windings of 3-phase induction motor prior to failure" IEEE international conference of electrical machines and drives, Boston, May 2001, pp.891-898.

[169] M.G Melero, M.F. Cabanas, C.Rojas, G.A Orcajo, J.M. Cano,and J.Solares "Study of an induction motor working under stator winding inter-turn short-circuit condition" SDEMPED 2003, Atlanta, GA, USA, August 2003.

[170] YoungKook "A stator turn fault detection method and fault-tolerant operating strategy for interior PM synchronous motor drives in safety-critical applications" Ph.D dissertation ,Georgia Institute of Technology, August 2007.

[171] Ahmed Sayed-Ahmed, Chia-Chou Yeh, Behrooz Mirafzail, and Nabeel A.O. Demerdash " Analyasis of stator winding inter-turn short-circuit faults in induction machines for the identification of the faulty phase" IAS2006, Tampa, pp.1519-1525